



TESIS DOCTORAL

Catalytic fast-pyrolysis of lignocellulosic residues for advanced biofuels production: development of multifunctional catalysts, optimisation and bench-scale demonstration

Autor:

Héctor Hernando Marcos

Directores:

Javier Feroso Domínguez

David P. Serrano Granados

**Programa de Doctorado en Tecnologías Industriales: Química, Ambiental,
Energética, Electrónica, Mecánica y de los Materiales**

Escuela Internacional de Doctorado

Madrid, 2019

D. DAVID P. SERRANO GRANADOS, Catedrático de Universidad en el área de Ingeniería Química del Departamento de Tecnología Química, Energética y Mecánica de la Universidad Rey Juan Carlos, y Director y Jefe de la Unidad de Procesos Termoquímicos del Instituto IMDEA Energía,

Y

D. JAVIER FERMOSE DOMÍNGUEZ, Investigador Titular de la Unidad de Procesos Termoquímicos del Instituto IMDEA Energía,

CERTIFICAN:

Que el presente trabajo de investigación, titulado: “*Catalytic fast-pyrolysis of lignocellulosic residues for advanced biofuel production: development of multifunctional catalysts, optimisation and bench scale demonstration*” constituye la memoria que presenta el ingeniero químico **D. Héctor Hernando Marcos** para aspirar al grado de *Doctor en Ingeniería Química* por la Universidad Rey Juan Carlos, y que ha sido realizado en los laboratorios de la Unidad de Procesos Termoquímicos del Instituto IMDEA Energía bajo nuestra dirección.

Y para que conste, firmamos el presente certificado en Móstoles, a 24 de junio de 2019.

Fdo.: D. David P. Serrano Granados

Fdo.: D. Javier Fermofo Domínguez

*“The two most important days in your life are
the day you are born and the day you find out why”*

Mark Twain

AGRADECIMIENTOS - ACKNOWLEDGMENTS

Cuando empecé mi andadura en esta Tesis Doctoral no me hacía a la idea lo difícil que se me haría llegar a este momento. La realización de esta memoria supone la culminación de muchos años de duro trabajo y esfuerzo, desde el minuto uno al último, en los que tengo y tendré que agradecer mucho a mucha gente, tanto en lo profesional como en lo personal.

En primer lugar, quería expresar mi más profunda gratitud por mis directores de Tesis, Javier Feroso y David Serrano. Sin vosotros nada de esto hubiera sido posible. Gracias por todo el tiempo, esfuerzo y paciencia que me habéis dedicado. No hubiera imaginado tener mejores ejemplos a seguir, os debo gran parte de lo que soy hoy en día como investigador, y también mucho en lo personal. Pero sobre todo, gracias por confiar en mí y haber sabido sacar lo mejor de mí mismo.

Del mismo modo quería agradecer a Patricia Pizarro, Juan Coronado e Inés Moreno, de vosotros he aprendido mucho y me habéis ayudado siempre que lo he necesitado.

A mis compañeros de unidad, tanto los que están como los que ya se fueron, Alfon, Antuán, Sergio, Laura, Cris, Prabhas, Celaya, Javi Marcos, Sankar, Santi, Sastre, Eva, Sandra, Curro, Almu, Julio, Ari... y a las chicas fotoactivadas, que para mí sois de la unidad igual, gracias Patri, Alba, Carmen, Elena... Mención aparte merecen los técnicos, Laura, ME y Fer que me han tenido que aguantar la tonelada de muestras que les he enviado durante este tiempo para que me las analizaran, gracias por todos ellos y por tantos “favorcillos” (al menos al final llegaron los bombones ☺). Y por supuesto al resto, que Dios mío, sois muchísimos y no os puedo poner a todos, ¡¡muchísimas gracias a todo IMDEA!!

Quería agradecer también a todos los estudiantes de Grado y Master que habéis estado conmigo todo este tiempo, habéis sido de gran ayuda. Don Víctor, Doña Gema, Rubén, Gabri, Dani, Celia, Paula y Edu. ¡Muchísimas gracias por vuestro trabajo chicos!

También quería dar las gracias a Gotzon por haberme dado la oportunidad de trabajar en la Universidad, y a todos los que habéis sido mis compañeros este último año, especialmente a Laura, a Gema y a mis compis de antesala.

I would also like show my gratitude to Prof. Pieter Buijninx and Prof. Bert Weckhuysen for giving me the opportunity to make my predoctoral stay in Utrecht, I have learned so much from you. Quería agradecer especialmente a Ana, no solo por ayudar a asentarme allí y por presentarme a todos, también quería darte las gracias por tu bendita paciencia conmigo y por haberme enseñado todo lo que he aprendido allí. Also I wanted to thank to Dong Long, Kang, Max, Egor, Carlos, Juan and all the rest of Utrecht University mates, you are the best!!

Quería agradecer a todos los que habéis sido importantes en lo personal para mí en estos últimos años, especialmente a mis amigos de toda la vida, Iván y Jorge.

Y por último, pero no menos importante, a mi familia, a mi hermana Paula y sobre todo a mis padres, Eugenio y María Jesús, porque a vosotros os lo debo todo. Gracias por hacer de mí la persona que soy hoy en día, no he podido tener más suerte. Ésta Tesis va dedicada a vosotros.

SCIENTIFIC PRODUCTION DURING THE DOCTORAL THESIS

SCIENTIFIC PUBLICATIONS INCLUDED IN THE DOCTORAL THESIS

- **H. Hernando**, A.M. Hernández-Giménez, S. Gutierrez-Rubio, T. Fakin, A. Horvat, P. Pizarro, J. Feroso, E. Heracleous, P.C.A. Bruijninx, A.A. Lappas, B.M. Weckhuysen, D.P. Serrano, "Scaling-Up of Bio-Oil Upgrading during Biomass Pyrolysis over ZrO₂/ZSM-5-Attapulgitite ", *ChemSusChem*, 2019, **12**, 2428-2438.
 - **H. Hernando**, C. Ochoa-Hernández, M. Shamzhy, I. Moreno J. Feroso, P. Pizarro, J.M. Coronado, J. Čejka, D.P. Serrano, "The crucial role of clay binders on the performance of ZSM-5 based materials for biomass catalytic pyrolysis", *Catalysis Science & Technology*, 2019, **9**, 789-802.
 - **H. Hernando**, A.M. Hernández-Giménez, C. Ochoa-Hernández, P.C.A. Bruijninx, K. Houben, M. Baldus, P. Pizarro, J.M. Coronado, J. Feroso, B.M. Weckhuysen, J. Čejka, D.P. Serrano, "Engineering the acidity and accessibility of the zeolite ZSM-5 for efficient bio-oil upgrading in catalytic pyrolysis of lignocellulose", *Green Chemistry*, 2018, **20**, 3499-3511.
 - **H. Hernando**, J. Feroso, C. Ochoa-Hernández, M. Opanasenko, P. Pizarro, J.M. Coronado, J. Čejka, D.P. Serrano, "Performance of MCM-22 zeolite for the catalytic fast-pyrolysis of acid-washed wheat straw", *Catalysis Today*, 2018, **304**, 30-38.
 - J. Feroso, **H. Hernando**, S. Jiménez-Sánchez, I. Moreno, P. Pizarro, J.M. Coronado, D.P. Serrano, "Bio-oil production by lignocellulose fast-pyrolysis: isolating and comparing the effects of indigenous versus external catalysts", *Fuel Processing Technology*, 2017, **161**, 1, 563-574.
 - **H. Hernando**, I. Moreno, J. Feroso, C. Ochoa-Hernández, P. Pizarro, J.M. Coronado, J. Čejka, D.P. Serrano, "Biomass catalytic fast pyrolysis over hierarchical ZSM-5 and Beta zeolites modified with Mg and Zn oxides", *Biomass Conversion and Biorefinery*, 2017, **7**, 289-304.
 - **H. Hernando**, J. Feroso, I. Moreno, P. Pizarro, J.M. Coronado, D.P. Serrano, "Thermochemical valorization of camelina straw waste via fast pyrolysis", *Biomass Conversion and Biorefinery*, 2017, **7**, 3, 277-287.
 - **H. Hernando**, S. Jiménez-Sánchez, J. Feroso, P. Pizarro, J.M. Coronado, D.P. Serrano, "Assessing biomass catalytic pyrolysis in terms of deoxygenation pathways and energy yields for the efficient production of advanced biofuels", *Catalysis Science & Technology*, 2016, **6**, 2829-2843.
 - J. Feroso, **H. Hernando**, P. Jana, I. Moreno, J. Přeč, C. Ochoa-Hernández, P. Pizarro, J.M. Coronado, J. Čejka, D.P. Serrano, "Lamellar and pillared ZSM-5 zeolites modified with MgO and ZnO for catalytic fast-pyrolysis of eucalyptus woodchips", *Catalysis Today*, 2016, **277**, 171-181.
-

OTHER SCIENTIFIC PUBLICATIONS

- L.M. López-Renau, L. García-Pina, **H. Hernando**, G. Gómez-Pozuelo, J.A. Botas, D.P. Serrano; "Enhanced bio-oil upgrading in biomass catalytic pyrolysis using KH-ZSM-5 zeolite with acid-base properties"; *Biomass Conversion and Biorefinery*, **Accepted Manuscript**.
- E.K.L. Morais, S. Jiménez-Sánchez, **H. Hernando**, P. Pizarro, A.S. Araujo, D.P. Serrano, "Catalytic co-pyrolysis of lignocellulose and polyethylene blends over HBeta zeolite", *Industrial & Engineering Chemistry Research*, 2019, **58**, 16, 6243-6254.
- E. Tomas-Pejó, J. Feroso, E. Herrador, **H. Hernando**, S. Jiménez-Sánchez, M. Ballesteros, C. González-Fernández, D.P. Serrano, "Valorization of steam-exploded wheat Straw through a biorefinery approach: bioethanol and bio-oil co-production", *Fuel*, 2016, **199**, 403-412.

CONTRIBUTION TO CONGRESSES

- **H. Hernando**, A.M. Hernández-Giménez, C. Ochoa-Hernández, P.C.A. Bruijninx, P. Pizarro, J.M. Coronado, J. Feroso, J. Čejka, B.M. Weckhuysen and D.P. Serrano, “Improving the efficiency of biomass catalytic pyrolysis by tailoring the physicochemical properties of technical ZSM-5 based catalysts”. 19th International Zeolite Conference (IZC'19), July 2019, Perth (Australia). (“Oral”)
 - **H. Hernando**, C. Ochoa-Hernández, M. Shamzhy, I. Moreno J. Feroso, P. Pizarro, J.M. Coronado, J. Čejka, D.P. Serrano, “A decisive step in biomass catalytic pyrolysis: Effect of clay binders on the performance of ZSM-5 based materials”. 4th Euro Asia Zeolite Conference, January 2019, Taormina (Italy). (“Oral”)
 - **H. Hernando**, I. Moreno, J. Feroso, C. Ochoa-Hernández, P. Pizarro, J.M. Coronado, J. Čejka, D.P. Serrano, “Pirólisis catalítica sobre zeolitas ZSM.5 y Beta jerarquizadas modificadas con óxidos de Mg y Zn”, XXVI Congresso Ibero-Americano de Catálise. September 2018, Coimbra (Portugal). (“Oral”)
 - **H. Hernando**, S. Jiménez-Sánchez, J. Feroso, P. Pizarro, J.M. Coronado, D.P. Serrano, “Assessing biomass catalytic pyrolysis for the efficient production of advanced biofuels”. III Encuentro de Jóvenes Investigadores de la SECAT, June 2018, Valencia (Spain). (“Oral”)
 - J. Feroso, **H. Hernando**, S. Jiménez-Sánchez, A.A. Lappas, E. Heracleous, P. Pizarro, J.M. Coronado, D.P. Serrano; “Effect of indigenous and external catalysts on the bio-oil production by catalytic fast-pyrolysis”. WCCE10, October 2017, Barcelona (Spain) (“Oral”)
 - **H. Hernando**, J. Feroso, S. Jiménez-Sánchez, C. Ochoa-Hernández, Á. Peral, I. Moreno, P. Pizarro, J.M. Coronado, D.P. Serrano, “Performance of hierarchical ZSM-5 in catalytic fast-pyrolysis of de-ashed wheat straw”. GEZ Summer School on Zeolites, September 2017, Móstoles (Spain). (“Oral and Poster”)
 - J. Feroso, C. Ochoa-Hernández, **H. Hernando**, S. Jiménez-Sánchez, M. Opanasenko, P. Pizarro, J.M. Coronado, D.P. Serrano, “Performance of MCM-22 zeolite for upgraded bio-oil production by lignocellulose catalytic pyrolysis”. CIS-7, June 2017, Třešť (Czech Republic). (“Oral”)
 - **H. Hernando**, C. Ochoa-Hernández, J. Přeč, J. Feroso, S. Jiménez-Sánchez, P. Pizarro, J.M. Coronado, D.P. Serrano, J. Čejka, “Catalytic fast pyrolysis of lignocellulosic biomass over 2D-ZSM-5 pillared with different metal oxides”. VI International Workshop on Layered Materials, September 2016, Kutná-Hora (Czech Republic). (“Oral”)
 - **H. Hernando**, J. Feroso, C. Ochoa-Hernández, P. Jana, I. Moreno, J.M. Coronado, D.P. Serrano, “Pirolisis rápida catalítica de astillas de eucalipto sobre catalizadores de ZnO soportado sobre ZSM-5 de porosidad jerarquizada”. II Encuentro de Jóvenes Investigadores de la SECAT, June 2016, Ciudad Real (Spain). (“Poster”)
-

- **H. Hernando**, J. Feroso, S. Jiménez-Sánchez, C. Ochoa-Hernández, Á. Peral, I. Moreno, P. Pizarro, J.M. Coronado, D.P. Serrano. “Performance of hierarchical ZSM-5 in catalytic fast-pyrolysis of de-ashed wheat straw”. CASCATBEL Workshop 2016, June 2016, Porto Carras, Thessaloniki (Greece). (“Poster”)
 - **H. Hernando**, J. Feroso, S. Jiménez-Sánchez, C. Ochoa-Hernández, Á. Peral, I. Moreno, P. Pizarro, J.M. Coronado, D.P. Serrano, “Performance of hierarchical ZSM-5 in catalytic fast-pyrolysis of de-ashed wheat straw”. Biomass Resources for Renewable Energy Production Workshop, June 2016, Móstoles (Spain). (“Oral”)
 - **H. Hernando**, J. Feroso, P. Pizarro, J.M. Coronado, D.P. Serrano, J. Přeč, “Catalytic fast pyrolysis of eucalyptus woodchips over lamellar and pillared ZSM-5”. WORKSHOP on LAYERED MATERIALS, September 2015, Třešť (Czech Republic). (“Poster”)
 - **H. Hernando**, J. Feroso, P. Jana, I. Moreno, P. Pizarro, J.M. Coronado, D.P. Serrano, J. Přeč, C. Ochoa-Hernández, J. Čejka, “Pirólisis catalítica de astillas de eucalipto sobre ZSM-5 bidimensionales dopadas con MgO y ZnO”. SECAT’15, July 2015, Barcelona (Spain). (“Oral”)
-

INDEX

SUMMARY	1
RESUMEN	7
1. INTRODUCTION.....	13
1.1. BACKGROUND: CURRENT SITUATION AND PERSPECTIVES IN THE TRANSPORTATION SECTOR.....	15
1.2. BIOMASS TO BIOFUELS	16
1.3. PYROLYSIS OF LIGNOCELLULOSIC BIOMASS	17
1.3.1. <i>Effect of the biomass source and pretreatments</i>	18
1.3.2. <i>Effect of the operation conditions</i>	19
1.3.3. <i>Type of reactors</i>	20
1.3.4. <i>Bio-oil properties</i>	21
1.4. BIO-OIL CATALYTIC UPGRADING TECHNOLOGIES	22
1.4.1. <i>Hydrodeoxygenation</i>	22
1.4.2. <i>Upgrading by condensation reactions</i>	23
1.4.3. <i>Catalytic fast-pyrolysis</i>	24
2. MOTIVATION AND OBJECTIVES.....	27
3. EXPERIMENTAL PROCEDURES.....	31
3.1. CATALYST SAMPLES	33
3.1.1. <i>MCM-22 zeolite</i>	33
3.1.2. <i>Hierarchical Beta by seed silanisation</i>	33
3.1.3. <i>Hierarchical ZSM-5 by seed silanisation</i>	33
3.1.4. <i>Two dimensional ZSM-5's</i>	33
3.1.5. <i>Hierarchical ZSM-5 by desilication</i>	34
3.1.6. <i>Nanocrystalline ZSM-5</i>	34
3.2. CATALYST CHARACTERISATION	34
3.2.1. <i>Inductively coupled plasma-optical emission spectroscopy (ICP-OES)</i>	34
3.2.2. <i>X-Ray diffraction (XRD)</i>	34
3.2.3. <i>Argon physisorption at 87 K</i>	35
3.2.4. <i>Scanning Electron Microscopy (SEM) and Transmission Electron Microscopy (TEM)</i>	35
3.2.5. <i>Ammonia/Carbon dioxide Temperature Programmed Desorption (NH₃/CO₂- TPD)</i>	35

3.2.6. Desorption of Pyridine/Carbon dioxide monitored by Fourier Transform Infrared Spectra (Pyr/CO ₂ -FTIR).....	35
3.2.7. 4-Fluorestyrene oligomerisation.....	36
3.2.8. Magic angle spinning solid state nuclear magnetic resonance (MAS ssNMR).....	36
3.3. CATALYTIC PYROLYSIS TESTS	36
3.3.1. Laboratory reaction system	36
3.3.2. Bench reaction system.....	38
4. RESULTS AND DISCUSSION	39
4.1. EFFECT OF INDIGENOUS AND EXTERNAL CATALYSTS IN THE CATALYTIC FAST-PYROLYSIS OF BIOMASS.....	41
4.2. PERFORMANCE OF DIFFERENT CATALYSTS IN THE PYROLYSIS VAPORS UPGRADING.....	46
4.3. OPTIMISATION OF THE NANOCRYSTALLINE ZSM-5 SYSTEM WITH DE-ASHED BIOMASS: EFFECTS OF THE TEMPERATURE, CATALYST TO BIOMASS RATIO AND FINE TUNING OF THE ACIDITY AND ACCESSIBILITY	53
4.4. ON THE ROAD TO INDUSTRY: STUDY OF THE EFFECT OF CLAY BINDERS TO PRODUCE TECHNICAL CATALYSTS AND SCALING-UP	60
5. CONCLUSIONS AND OUTLOOK	67
5.1. GENERAL CONCLUSIONS	69
5.2. RECOMENDATIONS FOR FUTURE WORKS.....	71
6. REFERENCES.....	73
LIST OF FIGURES.....	87
LIST OF TABLES.....	89
APPENDIX.....	91

LIST OF ABBREVIATIONS

AAEM	Alkali and Alkaline Earth Metals
ATP	Attapulgit
BAS	Brønsted Acid Sites
BBR	Bubbling-Bed Reactor
BET	Branauer, Emmett y Teller
Bio-oil*	Bio-oil in water free basis
BJH	Barret-Joyner-Halenda
BNT	Bentonite
C/B	Catalyst to Biomass ratio
CFP	Catalytic Fast-Pyrolysis
CS	Camelina Straw
D_p	Pore Diameter
ECCP	European Climate Change Programme
EU	Eucalyptus Woodchips
FCC	Fluid Catalytic Cracking
FP	Fast-Pyrolysis
FBR	Fixed-Bed Reactor
FTIR	Fourier Transformed Infrared Spectroscopy
GHG	Greenhouse gases
GC	Gas Chromatography
GC-MS	Gas Chromatography coupled to Mass Spectrometry
HDO	Hydrodeoxygenation
ICP-OES	Inductively Coupled Plasma-Optical Emission Spectroscopy
IUPAC	International Union of Pure and Applied Chemistry
KF	Karl-Fischer titration
LAS	Lewis Acid Sites
MIS	Mischanthus

LIST OF ABBREVIATIONS

MFI	Code of zeolite ZSM-5 structure
Mtoe	Millions of tons petroleum equivalent
MS	Mass Spectroscopy
NL-DFT	Non-Local Density Functional Theory
OECD	Organisation for Economic Co-operation and Development
ppmv	Parts per million in volume
S_{BET}	Total BET Surface Area
SEM	Scanning Electron Microscopy
SEM-EDX	Scanning Electron Microscopy coupled to Energy-dispersive X-ray spectroscopy
$S_{\text{MESO+EXT}}$	Mesopore + External Surface Area
S_{MICRO}	Micropore Surface Area
TCD	Thermal Conductivity Detector
TEM	Transmission Electron Microscopy
TG	Thermogravimetry
TGA	Thermogravimetric Analysis
TPD	Temperature Programmed Desorption
TPR	Temperated Programmed Reduction
VGO	Vacuum Gas-oil
$V_{\text{MESO+EXT}}$	Mesopore + External Volume
V_{MICRO}	Micropore Volume
V_{T}	Total Pore Volume
WS	Wheat Straw
XRD	X-Ray Diffraction
ZSM-5	Zeolite Socony Mobil - 5

SUMMARY

The present Doctoral Thesis has been developed in the laboratories of the Thermochemical Processes Unit of IMDEA Energy Institute, in the research line of “Sustainable fuels”, focused on the advanced biofuels production from lignocellulose through the catalytic fast pyrolysis process. Likewise, this scientific work has been carried out within the framework of CASCATBEL Project, “CAScade deoxygenation process using tailored nanoCATalysts for the production of BiofuELs from lignocellulosic biomass” (Ref. 604307), financed by the European Union Seventh Framework Programme (FP7/2007-2013).

First generation biofuels have shown important drawbacks to replace the traditional fuels and climate change mitigation, besides the biofuel versus food controversy. Lignocellulosic biomass, consisting in three main components: cellulose, hemicellulose and lignin, may hold the key for the sustainable advanced biofuels production for transportation.

Due to the high complexity of the lignocellulose, this material requires a high cost of processing. In this field, biomass fast pyrolysis is a promising technology, being able to produce a high throughput of liquid fuels. This process consists in a thermal decomposition of the lignocellulose in inert atmosphere to yield non-condensable gases, a solid residue denoted as char and a liquid called bio-oil, which can be used as fuel. The use of high heating rates, moderate temperatures (500-550 °C) and short residence times for the vapors, maximises the production of bio-oil.

The bio-oil presents a high potential as liquid fuel, being able to retain up to 70% of the chemical energy initially contained in the biomass. However, the bio-oil possesses important limitations, which hinders its direct use in transportation, especially regarding its high oxygen content, strong corrosiveness (pH = 2-4), low physicochemical stability and less than half of the high heating values of traditional fuels. Hence, pyrolytic oils require an upgrading for that purpose. Among the technologies allowing this necessary chemical transformations, catalytic pyrolysis of biomass stands out. By the incorporation of a catalyst, commonly a solid acid and more specifically a zeolite, a series of secondary reactions can be promoted, including cracking, oligomerisation, cyclisation, aromatisation and deoxygenation reactions, among others. The deoxygenation may proceed through the formation of CO (decarbonylation), CO₂ (decarboxylation) and H₂O (dehydration).

Within this context, the present work aims to study the catalytic performance of different zeolites with enhanced textural properties and therefore, lesser diffusional limitations, finely modified by the incorporation of metal oxide nanoparticles over their surface (ZnO, MgO and ZrO₂). These modifications allow the acidity and basicity of the parent zeolites to be tuned, adding new functionalities and hence, opening new interesting reaction pathways. Thus, the present work was divided in the next chapters tackling different topics concerning the ex-situ catalytic pyrolysis, aiming to a better understanding of the process mechanisms and the catalyst design, from laboratory to bench-scale.

I. Effect of indigenous and external catalysts in the catalytic fast-pyrolysis of biomass. In this chapter the different types of reactions that take place in the catalytic pyrolysis are decoupled for their analysis, including intrinsically thermal and catalytic reactions, by both indigenous (mineral matter naturally presented in the biomass) or external materials (n-ZSM-5 zeolite). The experimental results showed that the incorporation of both types of catalysts diminished the bio-oil yields. However, while n-ZSM-5 conducted an effective decrease of the

bio-oil oxygen concentration, this parameter was barely affected by the presence of minerals, since these promoted the formation of additional char and the deoxygenation was mostly produced over this solid fraction. Changes in the route of deoxygenation were also observed, being CO₂ the main pathway for mineral components, while CO was the major oxygenated molecule produced over n-ZSM-5. Regarding the chemical composition of the bio-oils, both resulted in considerable depolymerisation of lignin oligomers and high conversion of furans and anhydrosugars. n-ZSM-5 was the only of both catalysts able to convert these molecules into non-oxygenated aromatics.

II. Performance of different catalysts in the pyrolysis vapors upgrading. This chapter is devoted to the study of promising catalysts with enhanced properties (MCM-22, hierarchical Beta and ZSM-5 and 2-dimensional ZSM-5's zeolites), some of them modified by metal oxides deposition (ZnO and MgO). This chapter proves that zeolites of improved accessibility and medium acidity are suitable and promising catalysts for this process. Among the studied structures, the medium pore size of the ZSM-5 seems to produce a higher selectivity towards non-oxygenated aromatics. In addition, the modification of the type and strength of the active sites with the metal oxides, suppressing the strongest Brønsted acidity and generating additional Lewis acid/basic sites, resulted in more selective deoxygenation pathways. Thus, for hierarchical ZSM-5, the incorporation of MgO nanoparticles produced a bio-oil with around 28 wt% oxygen concentration and retaining about 45% of the chemical energy from biomass, the best result of all the studied in this chapter.

III. Optimisation of the nanocrystalline ZSM-5 system with de-ashed biomass: Effects of the temperature, catalyst to biomass ratio and fine tuning of the acidity and accessibility. In the first part of this chapter, an extensive study is deployed regarding the temperature influence in both thermal and catalyst bed zones affecting the catalytic fast pyrolysis over a MFI zeolite with improved external surface area. Aiming to scale-up the process afterwards, the catalyst selected this time was a commercial nanocrystalline ZSM-5 (n-ZSM-5). Different catalyst loadings were tested in order to obtain better information about the reaction pathways. The acidic properties of this zeolite were modified by the amphoteric properties of the ZrO₂, incorporated by wet impregnation. It was also compared with other commercial ZSM-5 with additional mesoporosity, this time by desilication (h-ZSM-5). The ZrO₂ incorporation to the n-ZSM-5 sample showed the most promising results, minimising the occurrence of overcracking and polymerisation reactions, leading to a more selective deoxygenation. Additionally, this supported active phase promoted the conversion of larger oligomers, increasing the fraction of the bio-oil detectable by the GC-MS technique.

IV. On the road to industry: Study of the effect of clay binders to produce technical catalysts and scaling-up. With the goal of producing technical catalysts from the previously studied ZrO₂/n-ZSM-5 catalyst, the influence of two clay binders: bentonite (BNT) and attapulgite (ATP) in its physicochemical properties and reaction performance is investigated. The lesser suppression of the Brønsted acidity and the emergence of new Lewis acid/basic sites in the catalyst extruded with attapulgite, caused by Zr-clay interactions, resulted in positive synergetic effects regarding the bio-oil deoxygenation selectivity and oligomer conversion. The promising results of the ZrO₂/n-ZSM-5-ATP multifunctional catalyst was deeply studied in laboratory and demonstrated at bench-scale, leading up to 60% deoxygenation degree and energy yield of

approximately 70% with respect the starting bio-oil coming from the thermal reference reaction.

RESUMEN



La presente tesis doctoral se ha desarrollado en los laboratorios de la Unidad de Procesos Termoquímicos del Instituto IMDEA Energía, en la línea de investigación de “Combustibles sostenibles”, centrada en la producción de biocombustibles avanzados a partir de la biomasa lignocelulósica mediante el proceso pirólisis rápida catalítica. Asimismo, el trabajo científico realizado ha formado parte del proyecto CASCATBEL: “Proceso de desoxigenación en CASCada utilizando nanoCATalizadores a medida para la producción de biocombustibles a partir de biomasa lignocelulósica” (Ref. 604307), el cual ha sido financiado por el Séptimo Programa Marco de la Unión Europea (FP7/2007-2013).

Los biocombustibles de primera generación han mostrado tener importantes inconvenientes tanto para reemplazar a los combustibles tradicionales como en la mitigación del cambio climático, además de la controversia generada por la competencia entre biocombustibles y alimentos. La biomasa lignocelulósica, que consta de tres componentes principales: celulosa, hemicelulosa y lignina, puede ser la clave para la producción sostenible de biocombustibles avanzados para el sector transporte.

Debido a la elevada complejidad de la lignocelulosa, este material requiere un alto coste de procesamiento. En este campo destaca la pirólisis rápida de biomasa al ser capaz de producir un alto rendimiento de combustibles líquidos. Este proceso consiste en una descomposición térmica de la lignocelulosa en una atmósfera inerte para producir gases no condensables, un residuo sólido denominado char y un líquido llamado bio-oil, que se puede usar como combustible. El uso de altas velocidades de calentamiento, temperaturas moderadas (500-550 °C) y tiempos de residencia cortos para los vapores de reacción permite maximizar la producción de bio-oil.

El bio-oil presenta un alto potencial como combustible líquido, siendo capaz de retener hasta el 70% de la energía química presente inicialmente en la biomasa. Sin embargo, el bio-oil posee importantes limitaciones que impiden su uso directo en el transporte, especialmente por su alto contenido de oxígeno, fuerte corrosividad (pH = 2-4), baja estabilidad fisicoquímica y menos de la mitad de poder calorífico que los combustibles tradicionales. Por lo tanto, los bio-oils requieren una mejora para este propósito. De entre las tecnologías que permiten esta transformación destaca la pirólisis catalítica de biomasa. Mediante la incorporación de un catalizador, comúnmente un sólido ácido y más específicamente una zeolita, se pueden promover una serie de reacciones secundarias, que incluyen reacciones de craqueo, oligomerización, ciclación, aromatización y desoxigenación, entre otras. La desoxigenación puede proceder de la formación de CO (descarbonilación), CO₂ (descarboxilación) y/o H₂O (deshidratación).

En este contexto, el presente trabajo tiene como objetivo estudiar el comportamiento catalítico de diferentes zeolitas con propiedades texturales mejoradas y, por lo tanto, menores limitaciones difusionales, modificadas con la incorporación de nanopartículas de óxidos metálicos sobre su superficie (ZnO, MgO y ZrO₂). Esta modificación permite modular la acidez y basicidad de las zeolitas de partida, añadiendo nuevas funcionalidades y, por lo tanto, abriendo nuevas rutas de reacción de interés. De este modo, el presente trabajo se ha dividido en los siguientes capítulos que abordan diferentes temas relacionados con la pirólisis catalítica ex-situ, con el objetivo de comprender mejor el mecanismo del proceso y el diseño del catalizador, desde el laboratorio hasta escala “bench”.

- I. Efecto de los catalizadores internos y externos en la pirolisis catalítica de biomasa.** En este capítulo se separan los diferentes tipos de reacciones que tienen lugar en la pirólisis catalítica, incluidas las reacciones intrínsecamente térmicas y catalíticas, tanto promovidas por las cenizas (materia mineral presente de forma natural en la biomasa) como por catalizadores externos (zeolita n-ZSM-5). Los resultados experimentales mostraron que tras la incorporación de ambos tipos de catalizadores disminuyó el rendimiento a bio-oil. Sin embargo, mientras que la n-ZSM-5 llevó a cabo una disminución de la concentración de oxígeno del bio-oil de forma efectiva, este parámetro apenas se vio afectado por la presencia de minerales, ya que promovieron la formación de char adicional, además de que la desoxigenación se produjo principalmente en esta fracción sólida. También se observaron cambios en las rutas de desoxigenación, siendo el CO₂ el principal producto para los componentes minerales, mientras que el CO fue la principal molécula oxigenada producida sobre n-ZSM-5. Con respecto a la composición química de los bio-oils, ambos dieron lugar a una considerable despolimerización de los oligómeros de lignina y una alta conversión de furanos y azúcares anhidro. La zeolita n-ZSM-5 fue el único de los dos catalizadores capaz de convertir estas moléculas en compuestos aromáticos no oxigenados.
- II. Comportamiento de diferentes catalizadores en el “upgrading” de vapores de pirolisis rápida.** Este capítulo está dedicado al estudio de zeolitas con propiedades texturales mejoradas (MCM-22, Beta y ZSM-5 jerarquizadas y ZSM-5 bidimensionales), algunas de ellas modificadas mediante impregnación de óxidos metálicos (ZnO y MgO). En este capítulo se demuestra que este tipo de zeolitas con mayor accesibilidad y acidez media son catalizadores adecuados y prometedores para este proceso. De entre todas las estructuras estudiadas, la zeolita ZSM-5 es la que tiene mayor selectividad a compuestos aromáticos no oxigenados. Además, la modificación de la naturaleza y fuerza de los centros activos tras la incorporación de óxidos metálicos, suprimiendo la acidez de Brønsted de mayor fuerza y generando nuevos centros ácidos/básicos de Lewis, dio lugar a rutas de desoxigenación más selectivas. De este modo, la incorporación de nanopartículas de MgO produjo un bio-oil con aproximadamente un 28 p/p% de concentración de oxígeno reteniendo un 45% de la energía química de la biomasa, el cual fue el mejor resultado de todos los obtenidos en este capítulo.
- III. Optimización de la zeolita ZSM-5 nanocristalina: Efecto de la temperatura, relación catalizador-biomasa y modificación de la acidez y basicidad.** En la primera parte de este capítulo se ha realizado un estudio sobre la influencia de la temperatura, en la zona térmica y en el lecho de catalizador, en la pirolisis catalítica sobre una zeolita tipo MFI con alta superficie externa. Con el objetivo de escalar el proceso posteriormente, el catalizador seleccionado esta vez fue una zeolita ZSM-5 nanocristalina comercial (n-ZSM-5). Se probaron diferentes cargas de catalizador para obtener una información más detallada sobre las rutas de reacción. A continuación, se modificaron las propiedades ácidas de esta zeolita mediante las propiedades anfóteras del ZrO₂, incorporado por impregnación húmeda, y se compararon con otra ZSM-5 con mesoporosidad adicional, obtenida por desilicación (h-ZSM-5). La incorporación de ZrO₂ a la muestra n-ZSM-5 mostró los resultados más prometedores de todos los catalizadores ensayados, minimizando las reacciones de craqueo excesivo y polimerización, llevando a una desoxigenación más selectiva. Adicionalmente, esta fase activa soportada promovió la conversión de los oligómeros de mayor tamaño, incrementando la fracción de bio-oil detectable por GC-MS.

IV. El camino a la industria: Estudio del efecto de arcillas como aglomerantes para producir catalizadores técnicos y escalado del proceso. Con el objetivo de producir catalizadores técnicos a partir del catalizador ZrO_2/n -ZSM-5 estudiado previamente en este capítulo, se analiza la influencia de dos arcillas usadas como aglomerantes: bentonita (BNT) y atapulgita (ATP) en sus propiedades fisicoquímicas y en el rendimiento de la reacción. La menor supresión de la acidez Brønsted y la generación de nuevos centros ácidos/básicos de Lewis, causadas por interacciones Zr-Mg en el catalizador extruido con atapulgita, dieron como resultado efectos sinérgicos positivos con respecto a la selectividad de desoxigenación del bio-oil y la conversión de oligómeros. Los prometedoros resultados del catalizador multifuncional ZrO_2/n -ZSM-5-ATP se estudiaron en profundidad en laboratorio y se demostraron en escala “bench”, dando lugar a grados de desoxigenación del 60% y rendimientos energéticos de aproximadamente el 70% con respecto al bio-oil de partida procedente de la reacción térmica.

1. INTRODUCTION

1.1. BACKGROUND: CURRENT SITUATION AND PERSPECTIVES IN THE TRANSPORTATION SECTOR

The evolution of the human society is inevitably associated to an increasing in population, resources consumption and energy demand. The projections predict that energy consumption will grow between 23-45% worldwide in the period 2015 to 2040, being this increase especially sharp in non-OECD countries.¹ Traditionally, fossil fuels and, in particular, petroleum has been, since the Industrial Revolution of XVIII Century, one of the main economic drivers of our era,² not only holding great part of that energy consumption, also generating other commodities (plastics, lubes, asphalts, chemicals, etc.). Nevertheless, fossil fuels are unsustainable at long term due to economic^{3,4} and environmental reasons.^{5,6}

Figure 1.1 represents the final energy production from different sources and its consumption in the main activity sectors in EU28 in 2015. The transportation sector has the second highest primary energy demand with 34% of the total,⁷ and presents the highest GHG's emissions in the EU (24% of the total in 2015).⁸ While emissions in other sectors historically have decayed over the last twenty-five years in Europe, transportation sector is still an exception, being its associated GHG's emissions 20% higher in 2012 than in 1990.⁹ The reason of this fact is also shown in Figure 1.1: more than the 94% of the energy consumption in the transportation sector comes from a petroleum source.¹⁰

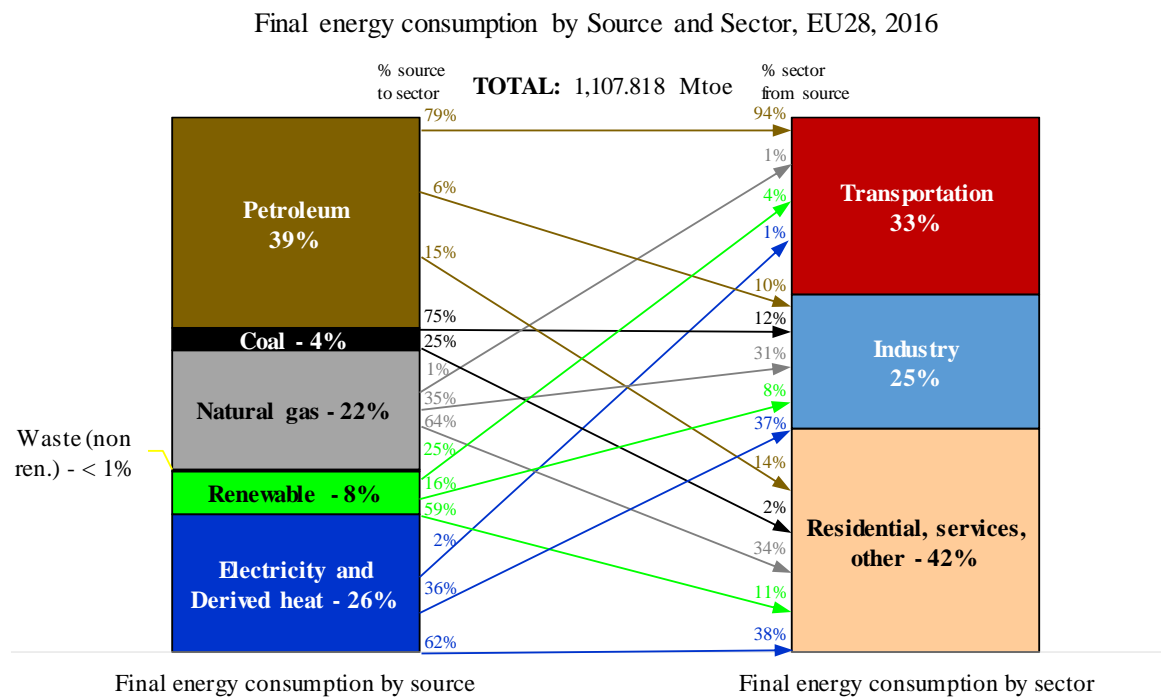


Figure 1.1. European Final Energy Consumption by Source and Sector in 2016. Data from ¹⁰.

It is in this scenario where biofuels can have a main role because they can answer all the previously commented problems. Using biomass as energy source can decrease global CO₂ and GHG's emissions, and therefore, the global warming, reducing also the oil dependence of regions like Europe. Furthermore, they act directly in the transportation sector, which historically had unfinished business regarding to oil consumption and CO₂ emissions,⁹ and can be specially effective for aviation, shipping and long distances road transport, where the electric motor cannot reach. But

in addition, a sustainable biofuel and bio-commodities production can be a critical component for a successful circular economy, proven by practical examples such as the ECO3 Business Area in Finland.¹¹

1.2. BIOMASS TO BIOFUELS

Biomass can be defined as biological material derived from living, or former living organisms, plant and animal (natural biomass) and anthropogenic sources (residual biomass or energy crops), and which has not suffered deep changes in its composition, such as mineralisation processes. Despite this is a general definition, biomass is used mainly for referring to plant based biomass.¹²

The use of biomass as a fuel is an important source of heat and electricity.⁶ Nevertheless, the use of biomass is diverse, and can also be transformed in commodities, such as food or biochemicals, or other energy products such as biofuels. Actually, the biomass is the only renewable source able to produce either solid, liquid and gaseous fuels.

Attending to their origin, the biomass, which is destined to biofuels production can be classified as follows:¹³⁻¹⁵

- Saccharides: biomass with high share of sugars (i.e. sugar cane, sugar beet, sorghum, etc.).
- Starchy: biomass with high content of starch (i.e. maize, wheat, barley, etc.).
- Oleaginous: biomass with high percentage in triglycerides, either vegetal oils (i.e. rapeseed, soybean, jatropha, palm, camelina, etc.) or animal fat.
- Aquatic: biomass that grows in aquatic media (i.e. algae, water hyacinth, etc.). They can also be grouped in either saccharides or oleaginous, depending on their composition.¹⁶⁻¹⁸
- Lignocellulosic: biomass formed by three main types of macropolymers: cellulose (30 - 50 wt%), hemi-cellulose (15 - 30 wt%) and lignin (10 - 40 wt%).¹⁹⁻²¹ It may contain also mineral compounds, whose quantity depends strongly on the biomass source, either woody (0.5 - 2 wt%) or agricultural residues (5 - 20 wt%).^{21,22} The rest is composed by organic extractives such as fat, waxes, starch, proteins, etc. (5-10 wt%).^{21,23}
- Other waste materials: organic residues from anthropogenic activities.

Lignocellulosic resources may satisfy a significant quantity of the energy consumption in the transportation sector,²⁴ being crucial to satisfy the European 7th Environment Action Programme,²⁵ Horizon 2020 Programme,²⁶ and related SET Plan.²⁷ However, the main disadvantage of using lignocellulose as raw material for biofuels production is its complexity, which requires intensive labor and a high cost of processing. For this reason, the research community is devoted to improve the feasibility of these technologies.²⁸

Figure 1.2 shows a scheme of the main routes for converting biomass into biofuels, which can be classified as follows:¹³

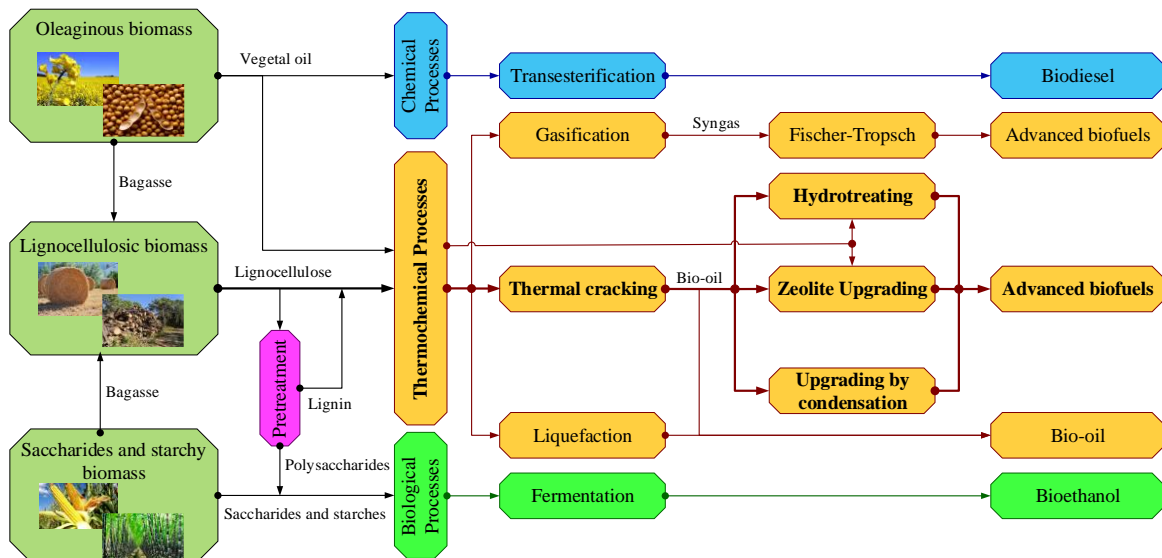


Figure 1.2. Main routes for the conversion of continental biomass into liquid biofuels.^{13,29,30}

- **Chemical processes.** It is the case of conversion of vegetable oils and animal fats into biodiesel by transesterification, normally in a stirred tank type reactor at low temperatures and using homogeneous basic or acid catalysts.
- **Thermochemical processes.** They include all the processes that transform the biomass into different biofuels at high temperatures. The most developed technologies are catalytic cracking or hydrotreatment of vegetable oils, gasification coupled to Fischer-Tropsch process, liquefaction and fast-pyrolysis.
- **Biological processes.** They involve the conversion of mono- and polysaccharides from sugar, starchy and lignocellulosic biomass into bioethanol (or other alcohols) by enzymes and other microorganisms.

Biofuels can also be classified into first and second generation, depending whether food-competing crops are harvested and used as raw material, or in the contrary, energy crops and wastes are used, respectively. Most of the efforts are now being focused on the second generation biofuels, producing biomass that is not intended for the food industry or even residues.

Fast-pyrolysis is a very versatile technology, which can transform the biomass directly into large extents of a denser liquid fuel or chemicals at the most reduced time of all technologies above mentioned. Together with its flexibility in the feedstock (lignocellulose, lignin residues, oils, plastics of other type of wastes), the added advantage that the current petroleum industry facilities can also be used to this purpose with small modifications,³¹ makes this technology very attractive, promising, and interesting to be explored.³²

1.3. PYROLYSIS OF LIGNOCELLULOSIC BIOMASS

Simply stated, pyrolysis (from the Greek: *pyro* “fire” and *lysis* “splitting”), means the irreversible thermal decomposition of an organic material in absence of oxygen. The traditional use of pyrolysis has been focused on the production of charcoal with higher heating value than biomass, using mound kilns for that purpose.³³

Today, pyrolysis is being researched to produce different types of fuels and commodities from biomass sources or other solid wastes.^{34–37} The depolymerisation reactions of lignocellulose are important in the range of 250 and 600 °C.³⁸ When the biomass is heated up, thermal cracking of the components leads to a variety of products and fractions. Some fractions can cross-link to form a carbonaceous solid product, called *char* (*charcoal* or *biochar*),^{38,39} others can depolymerise into permanent gases, most of them formed by CO and CO₂,⁴⁰ or into oligomeric oxygenated products to form a liquid product called *bio-oil* (or *pyrolytic oil*).^{41–43} Most of the pyrolytic water remains in liquid state together with the bio-oil.⁴⁴ The yields of each fraction can be controlled by the biomass nature,^{45–48} the particle size,^{49–51} the ash and alkali and alkali earth metals (AEEM) contents,^{52–54} operation conditions, such as temperature,⁵⁵ residence time of the pyrolysis vapors in the reactor,^{56–58} pressure^{59–61} and heating rate.^{38,56,57}, and the reactor design, in which the reaction is carried out.⁶²

A study of the different parameters which affect the pyrolysis reaction and their impact in the product yields will be described in the next sections.

1.3.1. *Effect of the biomass source and pretreatments*

Many works are found in bibliography studying the pyrolysis of the individual components of the lignocellulosic biomass:^{63–65} cellulose,^{52,63,66,67} hemicellulose^{63,66,67} and lignin.^{66–68} Each major component leads to unique reaction pathways, yields and products.^{64,66,69} In this line, cellulose decomposes following two pathways: one leading to the formation of small oxygenated molecules (furans, levoglucosan and other sugar derivatives, and light oxygenates), the other one leads to cellulose oligomers that can be subsequently cracked down into the previous molecules, char and permanent gases (most of them formed by CO).^{63,70} Hemicellulose is a smaller chain polymer and easier to be defragment in small molecules than cellulose (levoglucosan, furans and light oxygenates) and more gases (mostly CO₂).^{63,71} Finally, the lignin is the main responsible of the formation of oxygenated aromatics in the pyrolysis reaction. It also gives rise to larger quantities of heavier compounds and char than the rest of biopolymers.^{66,72,73} Generally, the higher the quantity of lignin the lower bio-oil is obtained, being more viscous and with lesser water content.⁶⁸ Nevertheless lignin possesses a huge potential for the production of high valuable green chemicals and fuels.⁷⁴

All biomasses contain ash-forming mineral components in the form of cations, bounded to the organic matrix of biomass at carboxylic/phenolic groups or in the form of precipitates.⁷⁵ These minerals can act as indigenous catalysts in the thermal degradation of biomass, especially alkali metals, such as potassium and sodium, and alkali earth metals in lesser extent, like calcium and magnesium.^{76–78} Thus, wood wastes, which are poorer in mineral content, generally give rise to more bio-oil and lower water and gas yields than agricultural residues.⁴⁶

An additional cause that may greatly modify the pyrolysis yields are pretreatments applied to the raw biomass. The simplest pretreatment that can be carried out is grinding to reduce the particle size. Biomass is a poor heat conductor and therefore, it may have associated a sharp temperature gradient across the particles during pyrolysis reaction. In general terms, the smaller the particle size the more limited are reactions such as secondary cracking or repolymerisation, which produce higher yields of non-liquid products (gas and char, respectively).^{20,72}

Drying is a pretreatment which is usually applied to pyrolysis since it is considered beneficial for maximising the bio-oil* (bio-oil in water free basis)⁷² and reduce operational energy and costs if done efficiently.⁷⁹ Furthermore, removing moisture can be even more convenient in Catalytic-

Fast Pyrolysis (CFP) processes, since an excess of it may induce irreversible changes in the zeolite catalysts by dealumination.⁸⁰

Other less standard pretreatments that stand out are demineralisation processes such as water leaching^{68,81–83} and acid washing (solutions of HCl, HNO₃, HF, etc.).^{81–83} These pretreatments aim to eliminate or minimise the effect of AAEM in the reaction. Pretreatment with acidic solutions is more effective than simple water washing, being the strength and concentration of the acid important parameters to take into account.⁸³

Torrefaction at atmospheric pressure and low temperatures (200-300 °C) is other pretreatment, which improves both energy density and grindability of the biomass.⁸⁴ Generally, the application of torrefaction as a pretreatment leads to an increase in char and gas yields, and despite bio-oil yield is decreased, it has lower oxygen content, less water concentration and better quality as a fuel.^{85,86}

1.3.2. Effect of the operation conditions

The operation conditions of the pyrolysis process are one of the most key parameters influencing the yields and characteristics of the final products. Generally, according to the employed temperature, heating rate and residence time of the vapors inside the reactor, the pyrolysis processes can be classified into three main categories: slow, fast and flash pyrolysis (Table 1.1).

Table 1.1. Main types of pyrolysis according to operation parameters and respective product yields^{20,29,87–90}

Operation Parameter	Slow	Fast	Flash
Heating rate (°C/s)	0.1-1	10-200	10 ³ -10 ⁴
Temperature (°C)	400-800	400-650	450-1200
Residence time (s)	450-1800	0.5-10	<0.5
Particle size (mm)	5-50	<2	<0.5
Product yield (wt%)			
Bio-oil	15-30	50-75	75-80
Char	25-40	15-20	10-15
Gas	20-50	10-30	10-15

Slow pyrolysis consists in subjecting the biomass to a moderate temperature at slow heating rate and long vapors residence time. It is the most traditional process and it is used to maximise the production of char.^{20,33,90–92} In contrast, in fast and flash pyrolysis, the feedstock is rapidly heated at >100 °C·s⁻¹ and using very short residence time (< 2 s). Both are aimed for bio-oil production and are being deeply researched and developed in the last decades.

The reaction temperature plays an important role towards yield and composition of products. In this way, bio-oil yield is maximised at moderate temperatures (450-600 °C).^{20,72} Temperatures higher than 600 °C favor secondary decomposition and cracking reactions, decreasing bio-oil and char contents.²⁰ Temperatures over 700 °C produces a bio-oil with higher carbon content and larger polyaromatics concentrations due to extensive decarboxylation and dehydration reactions.⁷² Further and more detailed information of the influence of the temperature in pyrolysis can be found in Chapter 4.3 of this memory.

Heating rate is other key parameter, which can affect the performance of the reaction in great extent.^{19–21,72} The faster heating rates, the lower mass and heat transfer limitations; conditions that favor the formation of volatiles at the same time that secondary reactions, such as overcracking or repolymerisation, are minimised.⁷²

Residence time is other important parameter to consider in pyrolysis. In order to obtain optimum yields of bio-oil, a few seconds of vapor residence times are advisable (<10 s), which minimises the extent of secondary reactions. Nevertheless, due to the heat and mass transfer difficulties that the biomass and char particles experience, longer residence times are recommended for these fractions.⁹³ Fast purging of the pyrolysis vapors is achieved by high flow rates of inert gas (N₂ or Ar) or by vacuum pyrolysis. Rapid quenching of hot vapors after reaction is also required to limit cracking reactions.^{20,72}

1.3.3. Type of reactors

The choice of the reactor is another essential parameter to keep in mind since this decision will determine the heat transfer, the residence time and also the feasibility of operating during long term reactions by continuously feeding biomass and removing products.^{32,62} There is a large number and variety of reactors that have been developed and applied in pyrolysis process;⁹⁴ among which, some of the most relevant are commented in this section.

- Fixed-Bed Reactor (FBR). The main advantage of this configuration is its simplicity. Nevertheless, this type of reactor normally does not operate in the optimum conditions required for fast-pyrolysis regarding their lower heat transfer coefficients,⁶² and therefore, its use is limited to small scales.⁹⁵ A variation from the fixed-bed can be considered the free-fall reactor, which can be modified to operate in a continuous mode,⁹⁶ but also is difficult to scale up.
- Bubbling-Bed Reactor (BBR). Bubbling-beds are a well-known technology with a relative simple construction and operation. They provide outstanding heat transfer to the biomass particles due to the high fluidised solid density in movement (normally hot sand) that favors turbulence. Fluid bed pyrolysers give rise to high liquid yields, over 65 wt% of dry biomass. Small biomass particles sizes (< 2 mm) and high nitrogen flow rates, which control vapor and char residence times, are required for this type of set up. Char yield is about 15 wt% of the total biomass fed and needs to be removed by ejection and entrainment followed by separation in cyclones and high temperature filters.⁹⁷ An additional problem found in these type of configurations is that the high flow rate of inert gases needed for their operation results in very low partial pressures for the condensable vapors, making their condensation and recovery a challenge. A combination of various types of heat exchangers, quench coolers, coalescent filters and electrostatic precipitators are often needed to fully recover the bio-oil so produced.⁶² Figure 1.3 depicts an example of a flow diagram of a pyrolysis bubbling-bed reactor set up.

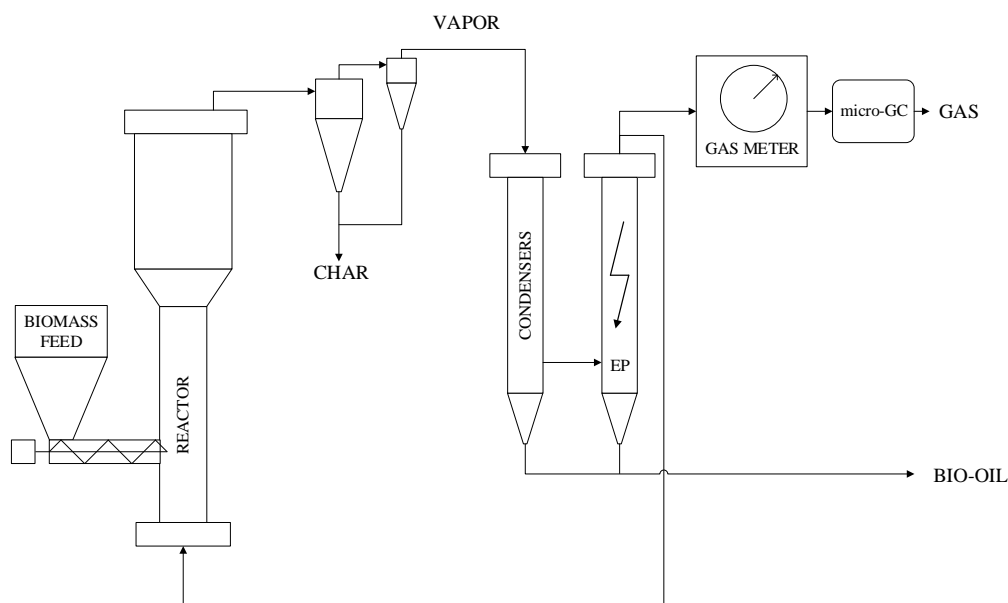


Figure 1.3. Process flow diagram of a bubbling-bed reactor for the pyrolysis of biomass.⁶²

- Other fast-pyrolysis reactors. Other important types of configurations applied to large scale set-ups or even industrial facilities are the circulating fluid-bed,⁶² rotating cone^{98,99} and the spouted-bed reactors.^{100–102} Less conventional designs that also have been applied to fast-pyrolysis are the auger,^{62,96} ablative,^{62,103–105} vacuum moving bed,¹⁰⁶ entrained flow¹⁰⁷ and microwave pyrolysis reactors.^{108,109}

1.3.4. Bio-oil properties

Pyrolysis bio-oils from lignocellulosic biomass are not standardised products, so they may exhibit a wide range of physicochemical properties, which will depend on the feedstock, the operation conditions, the reactor and the use or not of a catalyst. Table 1.2 shows the typical values of conventional and catalytic bio-oils and its comparison with commercial fossil fuels.

Conventional bio-oils generally present poor properties as fuels, limiting their use for being burned in adapted boilers for steam and electricity generation.^{32,89} Bio-oils are a complex mixture of more than 400 oxygenated compounds, which explains its high oxygen content, typically over 40 wt%. One of the direct causes of this composition is the poor heating values (15–20 MJ kg⁻¹) of thermal bio-il, less than half of commercial gasoline or diesel. Additionally, a significant part of this oxygen comes from the high content of carboxylic acids, which provides the bio-oil with an acidic pH, fact that no only provoke corrosiveness, but promotes dehydration and polycondensation reactions, which disfavor bio-oil stability along time.⁴⁴ This fact results in an increase of the viscosity of the bio-oils and water content. Fine char particles can act as catalysts of these condensation reactions if they are present in the liquid fraction.¹¹⁰

There have been many attempts to introduce conventional bio-oil in refineries by means of co-feeding with vacuum gasoil (VGO) in FCC units^{111–113} but immiscibility, thermal instability and coke formation hinder its utilisation. For this reason, it is recognised that bio-oil upgrading may be necessary prior to its feeding into refineries¹¹⁴

1. INTRODUCTION

At present, there is huge interest in the physical or chemical upgrading of bio-oils to obtain better quality fuels. Chemical transformation technologies imply deeper transformations in the bio-oil composition, involving typically the use of catalysts. The main goal of these catalytic routes aims to reduce the oxygen content of the bio-oils, increasing the miscibility with fossil fuels and producing valuable compounds. In this way, the most studied and promising catalytic technologies that allow these transformations are catalytic pyrolysis, upgrading by condensation reactions (aldol condensation, ketonisation and esterification) and hydrodeoxygenation (HDO). All of them present strengths and weaknesses and are focused on different type of target molecules, which are commented below. Because of this, a smart and viable concept of bio-oil upgrading could consist in a combination of these technologies.²⁹

Table 1.2. Typical properties of conventional and catalytic bio-oils and traditional fuels^{4,115-117}

Parameter	Conventional Bio-oil	Catalytic Bio-oil	Diesel	Gasoline
Water (wt%)	15-30	30-40	Traces	Traces
TAN (mg _{KOH} /g)	75-200	20-30	15-30	5-10
Density (g/cm ³)	1.05-1.25	0.76-1.12	0.78-0.86	0.72-0.76
Viscosity (CSt)	40-100	40-60	2-4	0.5-1
HHV (kJ/kg)	15-20	25-30	47	45.7
C (wt%)	50-65	65-75	87	85.5
H (wt%)	5-7	6-8	13	14.5
N (wt%)	<0.4	<0.4	-	-
S (wt%)	<0.05	<0.05	<0.5	<0.5
O (wt%)	30-45	15-30	<2.1	<2.1
H/C (mol/mol)	0.9-1.6	1-1.5	2	1-2
O/C (mol/mol)	0.4-0.6	0.15-0.45	0	0

1.4. BIO-OIL CATALYTIC UPGRADING TECHNOLOGIES

1.4.1. Hydrodeoxygenation

The traditional approach to deoxygenate thermal pyrolysis bio-oil is the hydrotreating, or more specifically, hydrodeoxygenation (HDO). The reaction involves the processing of the bio-oil at moderate temperatures (200-350 °C), under high pressures of hydrogen (50-150 bar) and requires the presence of a catalyst. Ideally, the products coming from HDO should have a negligible oxygen content, and they could be directly blended with conventional fuels.

The starting catalyst know-how of this reaction came from the conventional refinery reaction of hydrosulfuration (HDS), based on sulfided NiMo and CoMo supported on Al₂O₃.^{118,119} However this first generation of catalysts presented important limitations.^{62,120} New generations of catalysts based on noble metals as active phases (Ru, Pd, Pt, Rh and Re)¹²¹ was developed, but their commercial use is hindered by their high cost. For these reasons, the focus is now on the development of active phases based on low cost transition metals (Ni and Cu)¹²²⁻¹²⁵ and even more in metal phosphides (Ni, Co, Fe and Mo),¹²⁴⁻¹²⁶ achieving higher conversions of the initial ones.¹²⁷

Regarding the supports, in which these metal phases are dispersed, the best results up to date have been achieved using carbon^{127,128}, zeolitic¹²⁹ and ordered mesoporous based materials.¹²⁶

Despite all these advances, the amount of hydrogen required to remove the high oxygen content of the conventional bio-oils is an important hindrance to reach the economic feasibility. For this cause, together with the savings in fixed assets and operational costs that would supposed to handle a stabilised and less complex bio-oil before this step, calls for the implementation of one or more upgrading techniques listed in the next chapters, especially those involving transformations in vapor phase, before the bio-oil condensation.

1.4.2. Upgrading by condensation reactions

Another possibility in terms of upgrading the bio-oil consists in the promotion of different types of condensation reactions. In these processes, a highly selective oxygen removal is promoted by the formation of additional CO₂ and water. These reactions may narrow the chain length distribution of the molecules that comprise the bio-oil, promoting the formation of C-C bonds in the lower chain oxygenates, such as light acids or ketones, whereas depolymerisation of the larger biopolymer fractions also occurs.

- Esterification: The occurrence of the formation of esters may allow the concentration of carboxylic acids and oxygen content to be significantly decreased. The concentration of carboxylic acids in bio-oil ranges from 1-10 wt%, which are mostly composed by acetic acid.¹³⁰ Esterification by adding an external alcohol (usually methanol or ethanol) has been proven to decrease the acidity and viscosity, stabilising the resultant bio-oils,¹³¹ but not to produce an effective deoxygenation.¹³² Thus, an interesting approach would be promoting reactions between components already present in the bio-oil, as shown in Figure 1.4, removing oxygen via dehydration.¹³²

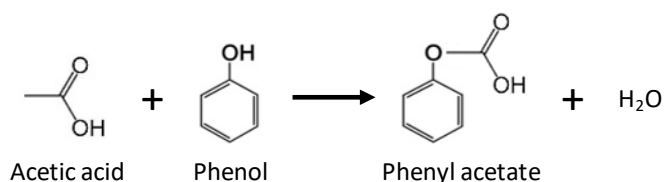


Figure 1.4. Esterification reaction between acetic acid and phenol.

- Aldol condensation: Aldol condensation involves the reaction between two molecules with carbonyl compounds. After the formation of a C-C bond that results in an aldol, these last dehydrate to form unsaturated ketones and a molecule of water.¹³³ Since bio-oils present a significant number of ketones and aldehydes in their composition, this process is seen as a possible route for their upgrading, not only due to the oxygen removed in the form of water but also because it may prevent the loss of low chain molecules that would be released as non-condensable hydrocarbons in a hypothetical consecutive HDO treatment. Additionally, the increase in the concentration of unsaturated molecules may improve the octane number of the resultant biofuel. A model aldol-condensation reaction is illustrated in Figure 1.5.

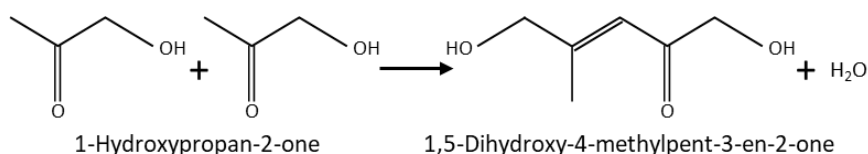


Figure 1.5. Aldol-condensation reaction of 1-hydroxypropan-2-one.

- **Ketonisation:** Ketonisation is probably the most studied process of bio-oil upgrading by condensation reactions. The reaction involves the formation of a C-C bond between two carboxylic acid molecules to yield a higher chain length ketone with $2n-1$ carbon atoms and oxygen removal through the formation of water and CO_2 , as shown in Figure 1.6. Theoretical studies based on density functional theory calculations have shown that ketonisation reaction takes place by the formation of an enolised acetate as an intermediate specie.¹³⁴ Since bio-oils contain a significant amount of small chain acids,¹³⁰ this upgrading approach becomes really convenient.

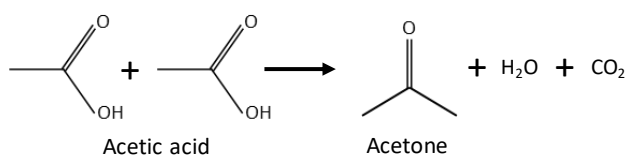


Figure 1.6. Ketonisation reaction of acetic acid.

1.4.3. Catalytic fast-pyrolysis

Catalytic fast-pyrolysis (CFP) allows the production of lower oxygenated bio-oils with higher stability and heating values. The main advantage of this technology is its simplicity, since it works at atmospheric pressure and does not require the consumption of external hydrogen. CFP can be conducted *in-situ* or in a second reactor close-coupled to the pyrolysis system (*ex-situ*),^{135–137} being the last option advisable to reduce the poisoning and deactivation of the catalyst and to operate at separate optimum conditions for the thermal and catalytic steps. In both configurations, the pyrolysis vapors in contact with the surface of the catalyst may undergo a series of complex reactions such as catalytic cracking, oligomerisation, cyclisation, aromatisation, and deoxygenation. The latter may proceed by decarbonylation (CO), decarboxylation (CO_2) or dehydration (H_2O) reactions.

The type of materials that have been used as catalysts in biomass pyrolysis is wide diverse, including amorphous silica-alumina,^{138,139} ordered mesoporous materials,^{140–142} metal oxides,^{143–147} clays,^{117,144,148} and even red mud.^{117,149,150} However, zeolites are the most studied catalysts in CFP.^{111,136,151–155} The combination of crystallinity and acidic properties of these materials provide them with high activity and chemical stability in the reaction media.¹⁵¹ Figure 1.7 shows a general scheme of the reaction routes that are promoted over acid catalysts.

Regarding the zeolite type, the two main factors that affect the distribution of pyrolysis products are the textural and acidic properties, which are largely determined by its topology. Thus, a wide number of zeolite frameworks can be found in the scientific literature tested in catalytic pyrolysis.^{111,136} Among all the structures, the ZSM-5 zeolite, with its MFI topology, stands out.^{152,156–158} Thanks to its adequate acidic properties and pore structure, the ZSM-5 possesses a high selectivity towards aromatic hydrocarbons and a relatively low coke deposition.^{159,160} These effects

have mainly been associated to its medium pore size and strong acidity.¹⁵² Jae et al.¹⁶⁰ studied the selectivity to aromatics as a function of the pore size of different zeolite topologies. Zeolites with medium pore sizes produced more aromatics with the same conditions and similar Si/Al ratios, achieving ZSM-5 the highest yield (35.5 wt%). On the other hand, larger pore zeolites (e.g. Beta, SSZ-55, and Y zeolite) produced low extent of aromatics and larger amounts of coke.¹⁶⁰

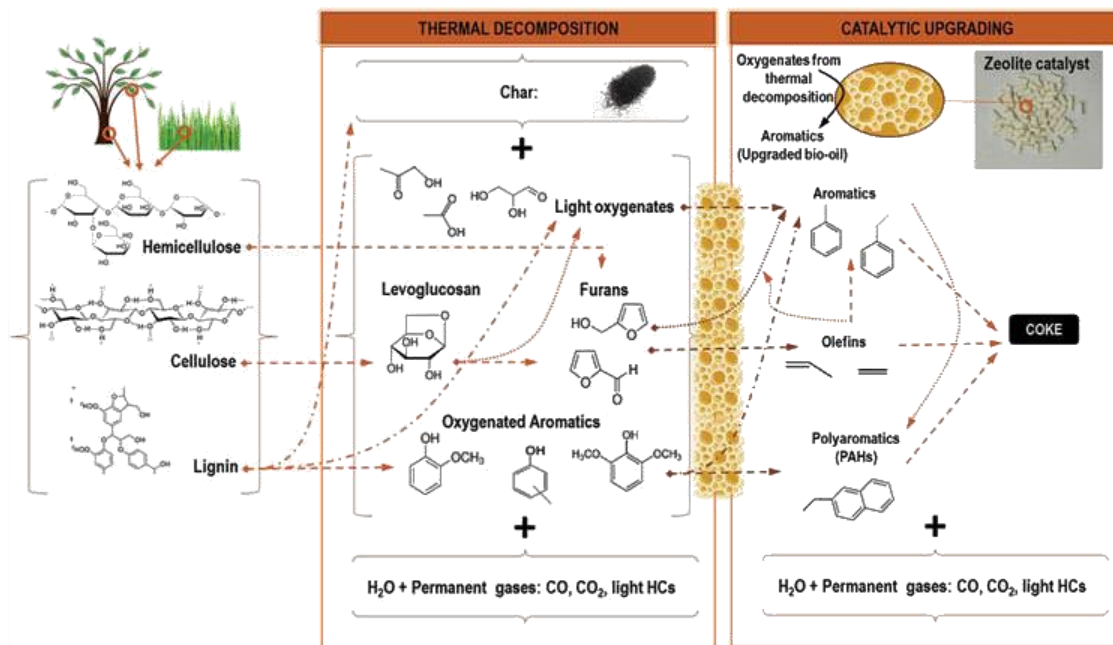


Figure 1.7. General scheme of the main CFP reaction pathways over acid catalysts.¹⁵¹

Zeolites, and in particular ZSM-5, are limited by the sole presence of microporous channels, which inevitably restrict the diffusion of bulky reactants and products into and out of the microporous networks, lowering the reaction rate or even deactivating the catalysts.¹⁶¹ To tackle this drawback, a strong research effort has been dedicated to develop zeolitic materials with enhanced accessibility and minor internal diffusional limitations. These strategies include the reduction of the crystal size of the zeolite,^{158,162} the introduction of a secondary porosity in the range of mesopores^{163,164} or the use of 2D materials.¹⁵²

Other key parameter that greatly affects the activity and product distribution is the acidity of the catalyst. A high amount of acid sites, specially Brønsted, generally leads to higher conversion and deeper bio-oil* deoxygenation.¹⁶⁵ Nevertheless, a strong acidity causes also a sharp decrease in the liquid yield, due to the occurrence of overcracking and extensive coking, resulting in a fast catalyst deactivation⁶³ and increases the amount of polyaromatic hydrocarbons in the bio-oil, which is harmful since the environmental points of view. For that reason, it is important to select an adequate acidity in order to find a good balance between activity and selectivity to bio-oil.

On the other hand, the incorporation of additional phases and functionalities in the catalyst design is an interesting strategy that is currently becoming a hot topic within the scientific community. Thus, there are numerous works in the literature, in which the zeolites are modified by deposition of metal or metal oxides over their surface, including Pt, Pd, Ni, Ga, Mg, Zn, Zr, Co and Fe.^{166–169} The incorporation of additional active phases on the zeolitic materials generally moderates

1. INTRODUCTION

the Brønsted acidity, while generates new types of Lewis acid sites, opening new interesting reaction pathways.

An additional challenge that must be taking into account to develop a process to industrial scale resides in the necessity of having the catalysts in a technical form. For that purpose, it is usually used a certain amount of a binder additive, making possible to accomplish the catalyst shaping with adequate physical properties. However, these binders are often far from inert, and may act as diluents or even inhibitors of the catalytic activity of the parent zeolites due to the occurrence of pore blockage or neutralisation of active sites.^{170,171} Clays, apart from providing physical strength, possess intrinsic catalytic properties that make them interesting binder candidates to be explored.¹¹⁷ Thus, they open the possibility of tailoring additional acid/basic features of the parent catalysts.¹¹⁷ Unfortunately, the information about binders and their influence in the catalytic properties of the pyrolysis catalysts is scarce in the literature review, and only few examples can be found applied to the pyrolysis of biomass.¹⁷²⁻¹⁷⁴ Both binders and matrix components are essential parts of technical zeolitic catalysts and, therefore, their interactions and catalytic effects are worthy of greater consideration than that has been the case to date.¹⁷⁵

The last barrier that a process developed at laboratory scale has to overcome is the scaling-up into a larger facility. Thus, fluid and solid dynamics, thermodynamics and heat transfer among others, are important parameters that must be taken into consideration when scaling a process to bench or pilot plant, which at laboratory scale can be in the background.¹⁷⁶ Additionally, in large biomass pyrolysis plants, engineers must face tricky situations, such as separation of solids at high temperature or condensation issues of bio-oil vapors inside the pipes due to the occurrence of cold spots. Besides, bio-oil recovery becomes extremely difficult due to the low vapor pressure of some of its components, especially when operating at high nitrogen flow rates.^{62,176}

2. MOTIVATION AND OBJECTIVES

As discussed in the Introduction chapter, the lignocellulosic biomass residues may become a raw material of crucial relevance to reduce the energy demand from fossil sources and to mitigate the global warming in the next decades, especially in the transportation sector. In this line, the biofuels production from fast-pyrolysis bio-oils presents a growing attraction for the industry and the scientific community, especially due to its potential high-throughput of liquid fuels, relative simplicity and adaptability to traditional refineries and engines. Nevertheless, the poor properties of the resultant fuel, as a consequence of its high oxygen concentration, poor heating values, low physicochemical stability and acidic nature; bio-oil upgrading technologies are required to produce a valuable final product. In this context, the present Doctoral Thesis is focused on the biomass catalytic fast-pyrolysis process, and more specifically, in the design and development of new multifunctional catalytic materials to increase the quality of the upgraded bio-oils and the process energy efficiency.

To accomplish the main objective, this work has been divided into different specific objectives that correspond with the chapters included next.

I. Effect of indigenous and external catalysts in the catalytic fast-pyrolysis of biomass. The general objective of this chapter is to study the influence of different materials with catalytic activity that can be found in the fast-pyrolysis process.

- Evaluation of the catalytic effect of the biomass mineral matter in the fast-pyrolysis process.
- Evaluation of the effect of the presence of a typical external catalyst (H-ZSM-5) over the fast-pyrolysis of different biomass sources.

II. Performance of different catalysts in the pyrolysis vapors upgrading. The global objective of this chapter is to study the performance of a variety of acid-based solid catalysts in order to select one system for further studies.

- Screening of different zeolite structures of enhanced accessibility (MCM-22, h-Beta, h-ZSM-5 and 2D-ZSM-5) in the catalytic fast-pyrolysis reaction.
- Study of the modification of the parent zeolites with the incorporation of additional functionalities via wet impregnation of metal oxide nanoparticles.
- Establish a correlation between the physicochemical properties of the catalysts (accessibility and acid/basic properties) and their performance in biomass fast-pyrolysis.

III. Optimisation of the nanocrystalline ZSM-5 system with de-ashed biomass: Effects of the temperature, catalyst to biomass ratio and fine tuning of the acidity and accessibility. The main goal of this chapter is to find an optimised catalytic material in powder form.

- Study of the influence of the temperature and catalyst to biomass ratio in the ex-situ catalytic fast-pyrolysis of the nanocrystalline ZSM-5 zeolite.
- Effect of the acidity and type of mesoporosity of two ZSM-5 zeolites with enhanced textural properties in the catalytic fast-pyrolysis.
- Fine tuning of the acidic properties of the ZSM-5 parent zeolite by wet impregnation of ZrO₂ nanoparticles and its effects in the reaction products yields.

IV. On the road to industry: Study of the effect of clay binders to produce technical catalysts and scaling-up. Starting from the $\text{ZrO}_2/\text{n-ZSM-5}$ in powder form selected as optimum catalyst, the objective of this last chapter is to compare different technical catalysts and their scaling-up testing from laboratory to bench-scale.

- Study of the effect of two natural clays, bentonite and attapulgite, used as binders to produce agglomerated shaped catalysts on the physicochemical properties and their impact on the activity and selectivity.
- Study the catalytic performance of the selected $\text{ZrO}_2/\text{n-ZSM-5-ATP}$ at lab-scale
- Scaling-up to a bench set up and comparison with the laboratory results, allowing implementation into larger scales.

3. EXPERIMENTAL PROCEDURES

3.1. CATALYST SAMPLES

During the present work, the synthesis of different zeolitic materials were carried out in order to be tested in the catalytic fast pyrolysis reaction.

3.1.1. MCM-22 zeolite

Two MCM-22 with Si/Al ratios of 20 and 40 were prepared following the procedure proposed by Corma et al.^{177,178} A detailed description of the synthesis procedure can be found in Article 3 included in this work.

The catalysts were synthesised by the group of Prof. J. Čejka in the J. Heyrovský Institute of Physical Chemistry of Prague.

3.1.2. Hierarchical Beta by seed silanisation

Hierarchical Beta zeolite (h-Beta) was synthesised by silanisation of zeolitic units as described by Aguado et al.¹⁷⁹ In this case, the synthesis gel was prepared with the following molar composition: 1 Al₂O₃: 60 SiO₂: 15.5 TEAOH: 1000 H₂O. 8% of PHAPTMS in molar basis respecting the silica content of the gel was added as silanising agent.

The acidity of h-Beta was tuned by MgO and ZnO deposition wet impregnation with ethanol as solvent, using Mg(NO₃)₂.6H₂O and Zn(NO₃)₂.6H₂O as salt precursors.

These catalysts were synthesised in IMDEA Energy.

3.1.3. Hierarchical ZSM-5 by seed silanisation

The hierarchical ZSM-5 (h-ZSM-5) was synthesised following the procedure proposed by Serrano et al.,¹⁸⁰ based on the silanisation of protozeolitic units. The synthesis gel of the zeolite was prepared with the next molar composition: 1 Al₂O₃: 80 SiO₂: 14.4 TPAOH: 2015 H₂O. 8% of (phenylaminopropyltrimethoxysilane, PHAPTMS) in molar basis with respect to the silica content of the initial gel was added as silanising agent.

The h-ZSM-5 material was also modified by MgO and ZnO deposition by ethylic wet impregnation, using Mg(NO₃)₂.6H₂O and Zn(NO₃)₂.6H₂O as salt precursors.

These catalysts were entirely synthesised in IMDEA Energy.

3.1.4. Two dimensional ZSM-5's

The synthesis of the lamellar ZSM-5's (L-ZSM-5) with Si/Al = 22 was prepared following the recipe of Choi, et al.¹⁸¹, and its structure directing agent was prepared as proposed by Na et al.¹⁸².

The pillared ZSM-5's (Pi-ZSM-5) was synthesised from the lamellar zeolites using TEOS as pillaring agent, following the procedure of He, et al.¹⁸³

Both materials, L-ZSM-5 and Pi-ZSM-5, were modified by MgO and ZnO deposition afterwards, following the same precursors and impregnation method as the previous zeolites.

These supports were both synthesised by the group of Prof. J. Čejka in the J. Heyrovský Institute of Physical Chemistry of Prague. and impregnated in IMDEA Energy Institute.

3. EXPERIMENTAL PROCEDURES

3.1.5. Hierarchical ZSM-5 by desilication

Desilicated ZSM-5 support was prepared by SILKEM, d.o.o. (ref: MFI-12-DS). It was subjected to desilication by treatment with a 1.4 M NaOH solution at 65 °C for 30 min (solution/zeolite mass ratio = 5) to generate mesopores, then ion-exchanged and calcined at 550 °C to obtain the zeolite in protonated form.

This sample was modified afterwards by ZrO₂ nanoparticles deposition in IMDEA Energy, which was carried out by wet impregnation with Zr(C₅H₇O₂)₄ in ethanol.

3.1.6. Nanocrystalline ZSM-5

Nanocrystalline ZSM-5 zeolite is a commercial catalyst from CLARIANT (ref: HCZP-90). It was calcined at 550 °C prior the catalytic tests like the rest of previous materials.

The properties of this catalyst were also tuned by ZrO₂ impregnation, similarly to the desilicated ZSM-5 sample.

Additionally, the ZrO₂/n-ZSM-5 was also extruded with two clay binders (bentonite and attapulgite) with a ratio catalyst:binder of 70:30, to produce technical catalysts with cylindrical shape of 1 mm diameter and 3 mm length.

These catalysts were entirely synthesised in IMDEA Energy.

3.2. CATALYST CHARACTERISATION

Each catalytic system evaluated in the present work, was characterised by different analytic techniques with the goal of evaluating their physicochemical properties and relating them with the experimental catalytic results.

3.2.1. Inductively coupled plasma-optical emission spectroscopy (ICP-OES)

The optical or atomic emission spectroscopy has been used for the quantification of most of the existing elements, even when their concentration is in the range of traces. In the present work this technique has been used in order to measure the aluminum content of the aluminosilicates, and their associated Si/Al molar ratio. In the case of bifunctional and technical catalysts, the amount of active phases (Zn, Mg, Zr) and/or other metals, such as those present in the clay binders, have been also determined.

In order to prepare the liquid samples, an acid digestion of the solid samples is carried out with a mixture of nitric and hydrofluoric acid 2:1 in volume, in an Anton Paar Multi-wave 3000 microwave. The ICP-OES set-up used was a Perkin Elmer Optima 7300AD instrument with an argon flow of 15 l min⁻¹ and 1.5 ml min⁻¹ of sample.

3.2.2. X-Ray diffraction (XRD)

X-ray diffraction technique was used to determine the crystallography of the assayed catalytic materials. Additionally, the mesoscopic order of some of the assayed materials was determined by low angle X-ray diffractograms. The analyses were carried out employing a Philips PW 3040/00 X'Pert MPD/MRD diffractometer using Cu K α radiation ($\lambda = 1.54178 \text{ \AA}$), with 40 mA intensity and 45 kV potential. The crystal phases were identified using the X'Pert HighScore Plus software and the ICSD and Crystallography Open Database (COD) of 2012.

3.2.3. Argon physisorption at 87 K

The adsorption-desorption of argon (87 K) has been used for studying the textural properties of the synthesised catalysts, in a AUTOSORB iQ equipment from Quantachrome Instruments. A small amount of sample (≈ 0.1 g) was firstly degassed at 300 °C during 3 h at high vacuum.

The specific surface area was determined by applying the Brunauer-Emmet-Teller (BET) equation in the range of $P/P_0 = 0.05-0.2$. An estimation of the contributions of microporous and mesoporous + external surface areas in the case of MCM-22 and clay binders were done with the t-plot method, applied in the range of $0.3 < P/P_0 < 0.6$, which corresponds to 4.5-7.5 Å.^{184,185} On the other hand, the pore size distribution was determined applying the Non Local Density Functional Theory (NL-DFT) method,¹⁸⁶ by means of the “NL-DFT-Ar zeolite/silica adsorption branch at 87 K” model, valid for cylindrical pores with diameters in the range of 3.5-1000 Å. A more accurate determination of the micro and mesopore surface areas was carried out by means of the NL-DFT method, for ZSM-5 and Beta based materials. High crystalline zeolites are used to determine the relation coefficient α , which is enounced as the relation between microporous surface and volume. In the present work, α values of 1681 and 1654 m² cm⁻³ were calculated from reference zeolites for the MFI and BEA structures, respectively.

3.2.4. Scanning Electron Microscopy (SEM) and Transmission Electron Microscopy (TEM)

Scanning electron microscopy (SEM) was used to study the morphology of the samples. SEM micrographs were taken with a Hitachi TM-100 microscope without any pretreatment of the sample.

Likewise, transmission electron microscopy (TEM) was utilised to measure the different zeolite crystal sizes and morphologies at high resolution. In the case of bifunctional catalysts, this microscopy technique has been employed for measuring the size and dispersion of the active phases over the supports. TEM images were obtained using a Philips Tecnai 20T microscope. Samples were previously dispersed in acetone and sonicated for 5 min.

3.2.5. Ammonia/Carbon dioxide Temperature Programmed Desorption (NH₃/CO₂-TPD)

Temperature programmed desorption has been used for measuring the quantity and strength of the acid and basic sites of the catalysts, using ammonia and carbon dioxide as adsorbates, respectively. These analyses have been carried out in a Micromeritics AUTOCHEM 2910, with a thermal conductivity detector (TCD).

3.2.6. Desorption of Pyridine/Carbon dioxide monitored by Fourier Transform Infrared Spectra (Pyr/CO₂-FTIR)

The Brønsted and Lewis acid sites (BAS and LAS, respectively) were quantified by pyridine desorption, followed by FTIR spectroscopy. Both types of acid centers were quantified considering the bands assigned to ν_{19b} vibration mode of pyridine and their corresponding integrated molar extinction coefficients.¹⁸⁷ To measure the strength of both BAS and LAS, the type and amount of adsorbed pyridine over the catalyst was determined at increasing temperatures (150, 250, 350 and 450 °C).

Likewise, adsorption of CO₂ monitored by FTIR was used to qualitative identify the amount and nature of the basic sites. FTIR spectra show CO₂ adsorbed on extraframework cations ($\Delta\nu_3$ shift

3. EXPERIMENTAL PROCEDURES

at 2400-2200 cm^{-1}) and chemisorbed CO_2 in the form of different type of carbonates (C-O stretching at 1400-1700 cm^{-1}).

These analyses were entirely carried out by the group of Prof. J. Čejka in the J. Heyrovský Institute of Physical Chemistry of Prague.

3.2.7. 4-Fluorestyrene oligomerisation

In order to assess the strength of the Brønsted acid sites and their accessibility, the 4-fluorestyrene reaction at 100 °C was carried out. This technique consists in the identification of the type of oligomers formed and the time of reaction, followed by UV-Vis and/or Confocal Fluorescence Microscopy. Ex-situ examination of the sample allows a determination of the accessibility of the technical catalysts, by comparison between the surface and the cross section of the pellet, as shown in Article 9.

These analyses were performed by the group of Prof. B.M. Weckhuysen in Utrecht University.

3.2.8. Magic angle spinning solid state nuclear magnetic resonance (MAS ssNMR)

^{27}Al MAS ssNMR technique was employed in the study of the local environment of the aluminium in the zeolite. Additionally, a zero-quantum (ZQ) filtered multiple-quantum magic angle spinning (MQ-MAS) pulse-sequence was used to correlate the ^{27}Al isotropic chemical shift (F1) with the quadrupolar line-shape (F2). These analyses allow the quantification of tetrahedrally coordinated Al species (Al^{IV}) or extraframework aluminium (Al^{V} or Al^{VI}).

The NMR analyses included in this work were performed by the group of Prof. B.M. Weckhuysen in Utrecht University.

3.3. CATALYTIC PYROLYSIS TESTS

3.3.1. Laboratory reaction system

Figure 3.1 shows a schematic diagram of the experimental lab-scale set-up and their parts, where the thermal and ex-situ catalytic pyrolysis tests were carried out.

The reaction system was formed by a downdraft fixed-bed stainless steel reactor (16 mm i.d. and 400 mm length) divided in two zones physically separated by internal tubes, metallic perforated plates and quartz wool. Both zones were heated by separate electrical furnaces, being the temperature controlled externally. The reaction temperature is measured by two internal type K thermocouples, one placed in the char bed (primary thermal pyrolysis), and the other on the catalyst bed (catalytic zone). The reaction operates in discontinuous mode and the operation conditions were 100 ml min^{-1} flow rate of nitrogen (inerting agent and carrier gas) and atmospheric pressure. Char and coke, which is deposited over the catalyst particles, remain inside the reactor and are recovered separately after the reaction. The bio-oil is collected in a series of four 125 ml condensers afterwards, submerged in an ice-water bath (0-4 °C), while the gaseous fraction is collected after these in a sampling bag. All the catalysts in powder form were previously pelletised with a size of 180-240 μm , in order to avoid excessive pressure drop during the reaction.

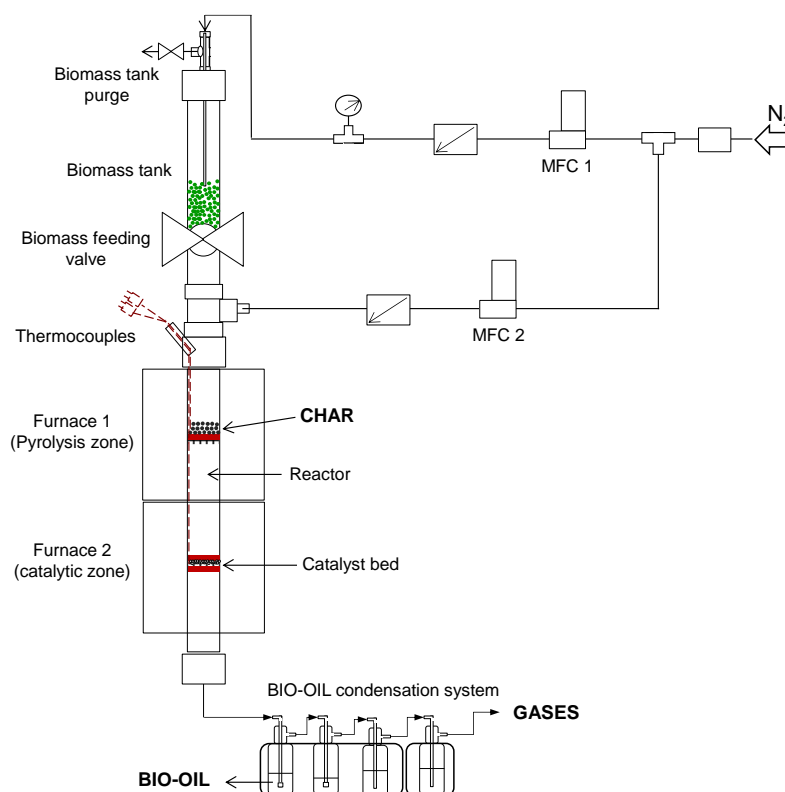


Figure 3.1. Laboratory experimental set-up catalytic fast-pyrolysis set up.

The most relevant analytic techniques used in the present work employed in the characterisation of the biomass pyrolysis products are enounced and briefly described as follows:

- Inductively coupled plasma-optical emission spectroscopy (ICP-OES). This technique was applied in the analysis of the feedstock to determine the elemental composition of the ash.
- Thermogravimetric analysis (TGA). TGA was applied to quantify the weight loss with a determined temperature program and atmosphere conditions. Thus, volatile matter in the initial biomass and char samples were determined by weight difference of a previously dried sample at 900 °C during 10 min in an inert atmosphere granted by 80 cm³ min⁻¹ Ar flow. On the other hand, the amount of coke deposited over the post-reaction catalysts was calculated by measuring the weight loss occurred during combustion under 80 cm³ min⁻¹ air flow, using a heating rate of 20 °C min⁻¹ up to 550 °C for 3 h. The TGA model was a NETZSCH STA 449.
- Organic elemental analysis (CHNS-O). The C, H, N and S (O by difference) elemental composition of the biomass, char, coke and bio-oil fractions were determined by an Organic Elemental Analyser Thermo Scientific FLASH 2000 CHNS/O).
- Karl-Fischer titration. The water content of bio-oil was determined using Karl-Fischer volumetric titrations in a Mettler-Toledo V20S compact volumetric KF titrator.
- Gas chromatography (GC). Permanent gases and light hydrocarbons (C₁-C₄) collected in a sampling bag during the pyrolysis tests were analysed in a dual channel Agilent® CP-4900 Micro Gas Chromatograph (Micro-GC), which is equipped with molecular sieve (Molsieve 5 Å) and HayeSep A columns and a thermal conductivity detector (TCD). Helium was used as carrier gas. The TCD is periodically calibrated with standard gas mixtures containing different concentrations of N₂ (internal standard), O₂, H₂, CO, CO₂, CH₄, C₂H₄, C₂H₆, C₃H₆, C₃H₈, C₄H₈

3. EXPERIMENTAL PROCEDURES

and C_4H_{10} . The gas mass yield, elemental composition (C, H and O) and chemical energy were calculated from the individual values of their compounds.

- Gas chromatography coupled to mass spectroscopy (GC-MS). The individual components of the bio-oil* fraction were analysed by a gas chromatograph coupled to a triple quadrupole mass spectrometer (GC-MS), Bruker® SCION 436-GC. The gas chromatograph column is a WCOT fused silica with a non-polar stationary phase (95% Dymethyl–5% diphenylpolisiloxane) with the next specifications: Maximum working temperature: 350 °C; Dimensions: Length: 30 m x Diameter: 0.25 mm ID x Stationary phase thin: 0.25 μ m. Bio-oil samples were diluted 1:25 in ethanol prior to their injection. In order to identify the components, NIST EI-MS spectral library (v2.0) was used.

3.3.2. Bench reaction system

The bench scale set up consist in two coupled reactors, which are a fluidised and a fixed bed configuration for the thermal and catalytic pyrolysis, respectively. A screw feeder for the biomass allows this reaction system to operate in continuous mode. 5 l min^{-1} of N_2 are introduced at the bottom to grant inert atmosphere and fluidisation. The pyrolysis vapors generated at 550 °C in the first stage are passed through the second reactor containing the catalyst at 450 °C. Bio-oil is recovered in two separate vessels, which are mixed in one single sample for its analysis. On the other hand, char and coke were measured together during the regeneration stage, introducing air to the reaction system and increasing the bed temperature of both reactors to 650 °C.

The bench-scale reactions included in this work were performed by the group of Prof. A.A. Lappas in the CERTH/CPERI of Thessaloniki.

4. RESULTS AND DISCUSSION

4.1. EFFECT OF INDIGENOUS AND EXTERNAL CATALYSTS IN THE CATALYTIC FAST-PYROLYSIS OF BIOMASS

The results obtained in this chapter are reported in Articles 1 and 2. Both manuscripts analyse the catalytic effects of the different materials that can be found in the pyrolysis reaction: the mineral matter contained in the biomass (indigenous catalysts) and the presence or not of an external catalyst (H-ZSM-5 in this case). The most important conclusion from both manuscripts is that the mineral content of the biomass plays a major role in the pyrolysis reaction that cannot be overlooked. The highlights of each manuscript are described next.

Article 1 investigates four biomasses of different sources: two herbaceous/agricultural residues (wheat straw and miscanthus) and two woody/forestry biomasses (eucalyptus and oak), in both raw and de-ashed forms. De-ashed biomass samples were obtained removing the mineral components by an acid washing treatment, which especially affected the alkali and alkaline earth metals (AAEM) that are known for possessing a high catalytic activity,¹⁸⁸ as shown in Table 4.1.

The results obtained show that both, indigenous and external, catalysts reduce the bio-oil* yield, regardless their origin. However, the catalytic effect of mineral matter in most of the cases was not really effective for bio-oil deoxygenation, since it promotes an excessive amount of char formation, retaining in some cases more than 40% of the energy coming from the initial biomass. In counterpart, the presence of the external nanocrystalline n-ZSM-5 (named as HZSM-5 in Articles 1 and 2) catalyst, promotes a higher extent of deoxygenation reactions, as seen in Figure 4.1.

Table 4.1. Proximate and elemental analyses of the raw (dry) and acid-washed biomass samples

	EU	EU-ac	OAK	OAK-ac	MIS	MIS-ac	WS	WS-ac
Proximate Analysis (wt%)^a								
Ash	1.9	0.3	0.5	0.2	2.5	1.6	4.7	3.5
Volatile Matter	74.7	80.4	80.0	81.4	77.4	85.3	75.3	83.1
Fixed Carbon	23.4	19.3	19.5	18.4	20.1	13.1	20.0	13.4
Ash removal (%)	-	84.2	-	60.0	-	36.0	-	25.5
Elemental Analysis (wt%)^b								
C	51.3	50.9	49.5	49.2	48.8	48.8	47.8	49.1
H	5.9	6.0	5.9	6.0	5.9	5.9	5.9	6.0
N	0.1	0.1	0.0	0.0	0.2	0.2	0.5	0.5
S	-	-	-	-	-	-	-	-
O	42.7	43.0	44.6	44.8	45.1	45.1	45.8	44.4
HHV (MJ/kg_{ab})	20.0	20.3	19.5	19.5	18.8	19.0	17.9	18.9

^a In a dry basis (db)

^b In a dry and ash-free basis (daf)

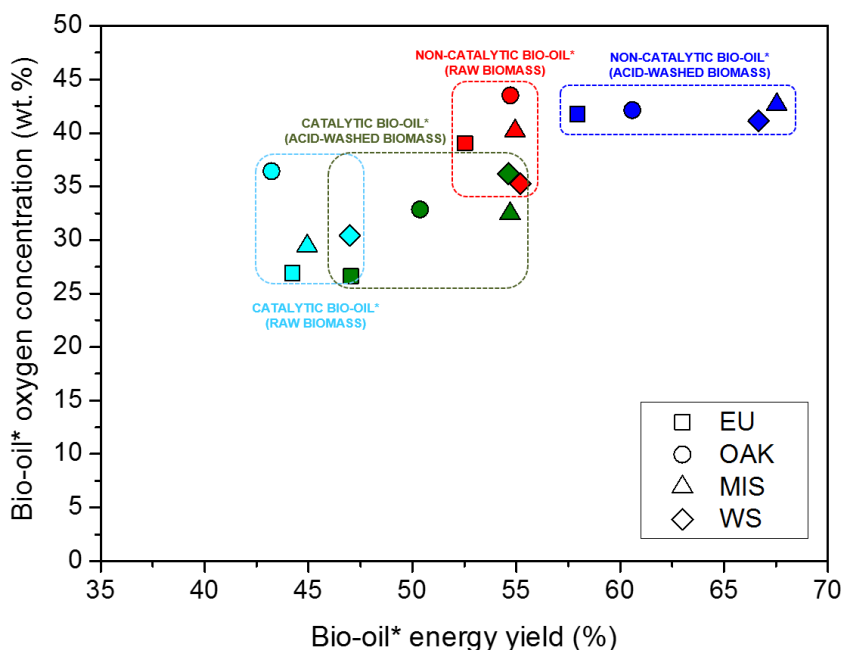


Figure 4.1. Oxygen concentration versus energy yield of the bio-oil* fraction obtained in the fast-pyrolysis tests (catalytic and non-catalytic) of de-ashed and raw biomass samples.

Likewise, the routes in which oxygen is removed are different in each case: dehydration is the major route when no catalyst is present, mineral matter promotes the formation of CO_2 ; while n-ZSM-5 zeolite favors decarbonylation reactions (CO). It is important to note that the deoxygenation in the case of the indigenous catalysts is produced in the char fraction, which is not effective to reduce the oxygen content in the bio-oil. Finally, the molecular composition of the produced bio-oils obtained by GC-MS (Figure 4.2) reveals that these catalysts present common features: both depolymerise in a considerable extent the lignin oligomers, as shown by the increase of detectable oxygenated aromatics, and also they efficiently converting furan compounds and sugar derivatives presented in the pyrolysis vapors. The main difference between both catalysts is that while mineral matter decomposed these molecules into light oxygenates (especially acids) the external n-ZSM-5 catalyst is the only able to form non-oxygenated aromatics.

Based on the results collected in this manuscript, a simplified reaction scheme is proposed, as shown in Figure 4.3, illustrating the influence of both indigenous and external catalysts on the deoxygenation pathways.

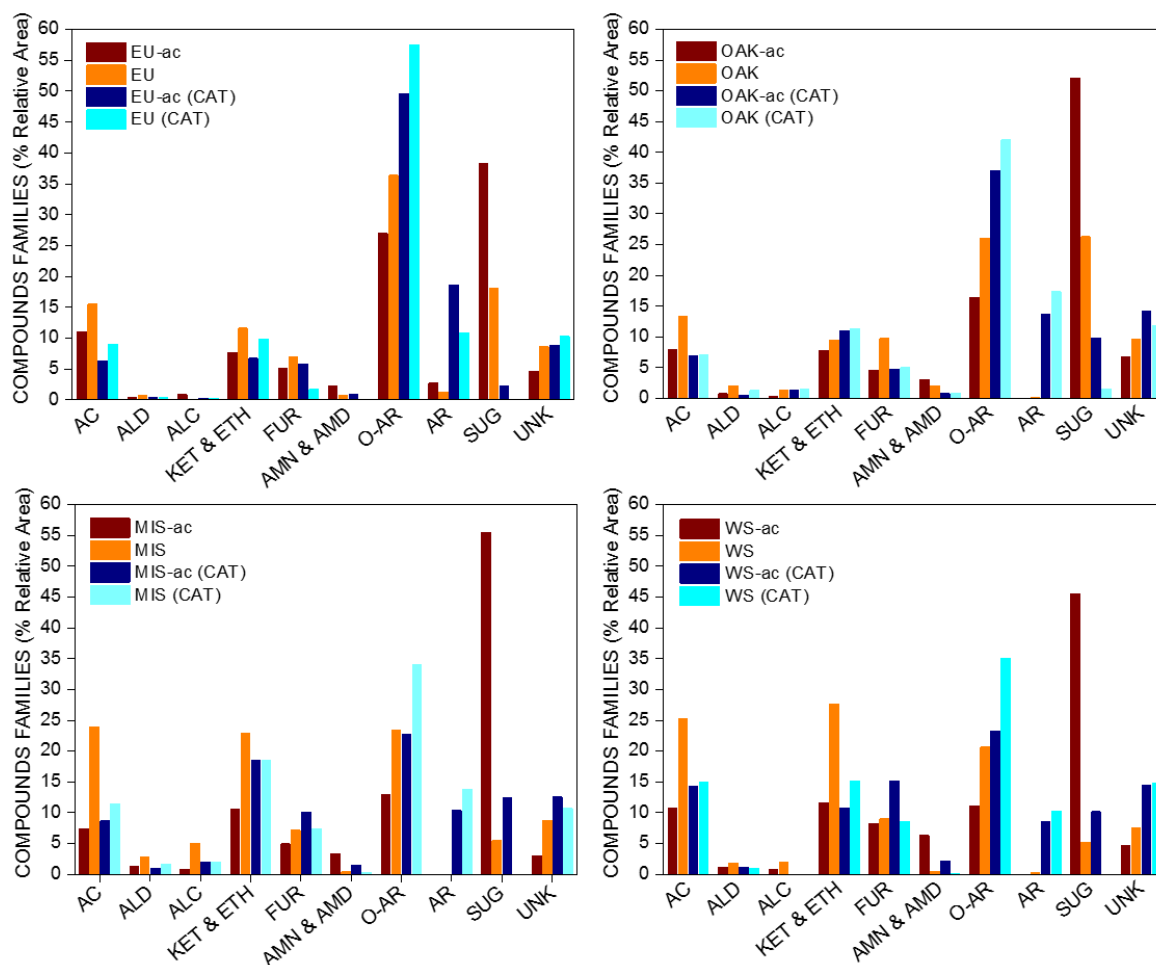


Figure 4.2. Main compound families in the bio-oil obtained by fast-pyrolysis of raw and de-ashed biomass samples.

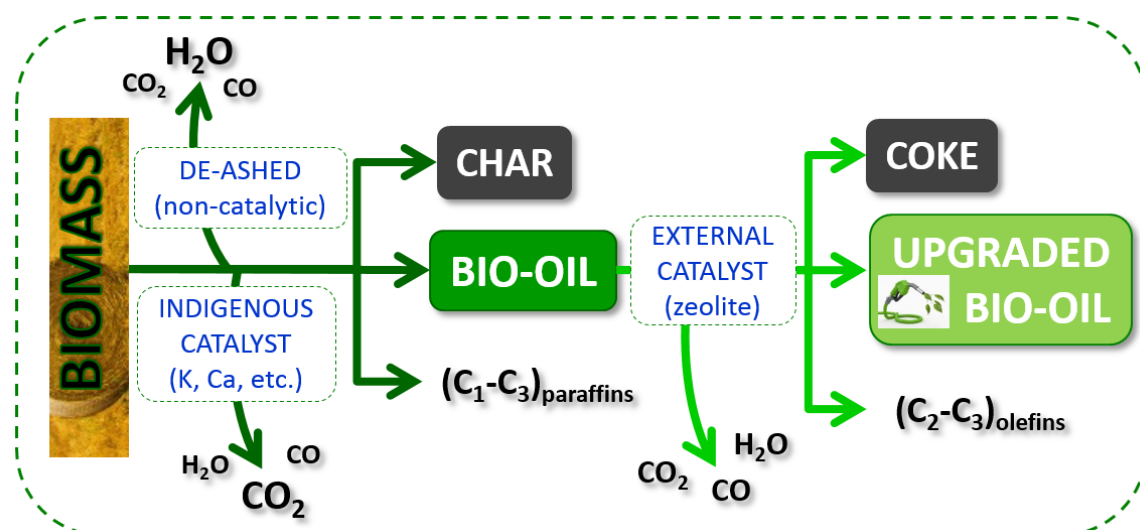


Figure 4.3. Simplified scheme of the main pathways in the non-catalytic (de-ashed) and catalytic (indigenous and/or external catalyst) lignocellulose fast-pyrolysis.

Article 2, that shares the same topic, is focused on a special feedstock: the camelina straw. Camelina Sativa is seen as an interesting crop for the production of biodiesel or green diesel, being a renewable source that presents high resistance to weather conditions and low water and

4. RESULTS AND DISCUSSION

maintenance requirements. Thereby, the waste straw from this plant can be also valorised producing fuels via fast-pyrolysis. The effect of the high content of mineral matter of this herbaceous plant was investigated as in the previous paper by acid-washing treatment. As expected, the removal of these inorganics increases the bio-oil* mass and energy yields, but in this case at the expense of a notable higher oxygen content. This trend was already observed in the herbaceous biomasses in Article 1 (see Figure 4.1), but in the case of camelina straw is more noticeable because it possesses the highest amount of mineral matter of all the feedstocks included in this Thesis. Actually, the occurrence of a synergetic effect when combining the catalytic effect of both indigenous and external H-ZSM-5 catalysts is observed in this case, yielding lower amounts of bio-oil but highly deoxygenated, as summarised in Table 4.2.

Regarding the rest of reaction parameters, for both internal and external catalysts, including the product distribution, they are not different from those included in Article 1 and briefly discussed above.

Table 4.2. Parameters of the bio-oil* obtained in the catalytic pyrolysis tests of camelina sativa over the n-ZSM-5 zeolite

Sample	%H ₂ O	Elemental analysis, db (wt.%)				H/C	HHV (MJ/kg _{db})	Mass yield (wt%)	Energy yield (%)
		C	H	N	O				
CS-ac	21.2	52.3	6.4	0.1	41.1	0.12	21.6	55.0	65.8
CS	31.3	56.9	8.2	0.2	34.8	0.14	25.9	35.8	54.5
CS-ac (CAT)	31.4	57.4	7.5	0.2	34.9	0.13	25.2	38.9	54.2
CS (CAT)	45.3	69.1	12.8	0.2	18.0	0.19	37.3	20.1	44.4

An additional key point, which is incorporated in Article 2 is the regeneration of the n-ZSM-5 external catalyst. For this purpose, this material was regenerated in a furnace at 550 °C. Results show that the regenerated catalyst maintained the activity in comparison with the fresh sample, as shown in Figure 4.4. This suggests that n-ZSM-5 not only performs adequately in the catalytic pyrolysis reaction, but it is also resistant to the harsh conditions and the high amounts of coke deposited over its surface. This fact is crucial, since the implementation of this process at industrial scale requires the continuous regeneration of the catalyst.

To sum up, regardless of their origin, common trends in different biomasses pyrolysis are obtained. This fact is of high importance since industrial pyrolysis facilities may rely of a wide variety of biomass sources.^{22,29} On the other hand, demineralisation process by acid-washing treatment has been proved to increment the bio-oil yield. This result, which also diminishes the variations and interferences of the indigenous catalysts (AAEM), makes this process desirable, especially when agricultural residues are used.

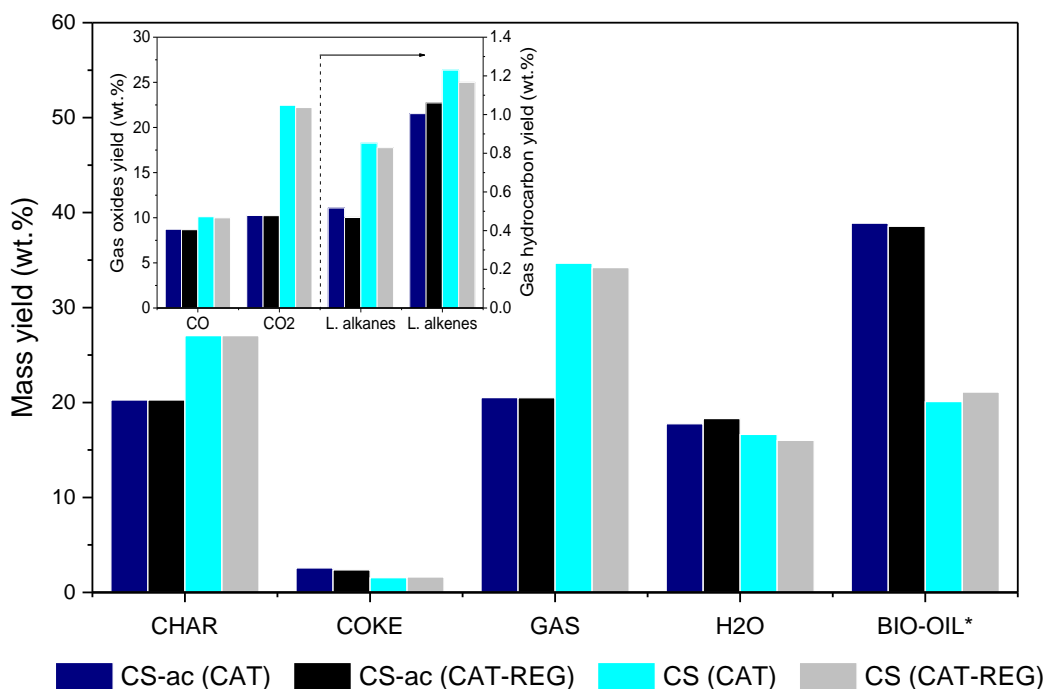


Figure 4.4. Product yield distribution in the catalytic fast-pyrolysis tests of the raw and de-ashed camelina straw with fresh and regenerated catalyst.

Article 1

“Bio-oil production by lignocellulose fast-pyrolysis: Isolating and comparing the effects of indigenous versus external catalyst”

J. Feroso, H. Hernando, S. Jiménez-Sánchez, A. A. Lappas, E. Heracleous, P. Pizarro, J.M. Coronado, D.P. Serrano

Fuel Processing Technology, 2017, 161, 1, 563-574

Article 2

“Thermochemical valorization of camelina straw waste via fast pyrolysis”

H. Hernando, J. Feroso, I. Moreno, P. Pizarro, J.M. Coronado, D.P. Serrano

Biomass Conversion and Biorefinery, 2017, 7(3), 277–287

4.2. PERFORMANCE OF DIFFERENT CATALYSTS IN THE PYROLYSIS VAPORS UPGRADING

The results obtained in this chapter are discussed in detail in Articles 3, 4 and 5. A brief summary of the major results of those works is disclosed in this section.

The catalytic pyrolysis process evolves molecules of large dimensions, such as cellulose and/or lignin derived oligomers. This fact, together with the fast reaction rates, causes that the limiting stage is the internal diffusion of such molecules. For this reason, a key parameter in the design of a pyrolysis catalyst is the surface area and accessibility to the active sites. The combination of the shape selectivity of the zeolite micropores with a secondary porosity (in the range of mesopores) and/or high share of external surface area, that allows a better diffusion, makes nanosized,¹⁸⁹ hierarchical¹⁹⁰ or 2D¹⁵² zeolites and mesostructured materials^{140,141} strong candidates in this process. Acidic catalysts, and specially zeolites, are well known to promote cracking reactions,^{136,191} but there are also other examples used in catalytic pyrolysis, including ordered mesoporous materials,^{140,141} amorphous silica-alumina,^{138,139} molten salts,^{52,192–195} metal oxides^{144,145,196,197} and bifunctional catalysts.^{159,169,198}

In general terms, the higher and stronger the acidity of the catalyst, the more accentuated the activity and the higher the aromatics production.¹⁶⁵ Nevertheless, an excessive acidity leads to unnecessary gas and coke formation, diminishing the selectivity to bio-oil and provoking a faster catalyst deactivation due to solids deposition that hinders the accessibility to the active sites. Additionally, it provokes an increase of the polyaromatic hydrocarbons in the final fuel composition, which is undesirable according to environmental and health points of view.¹⁹⁹ Thus, a mild acidity normally meets the optimum equilibrium between activity and selectivity. Finally, it is important to take into account that not only the amount and the strength, but also the nature of the acidity matters. In this line, Brønsted acid sites are more effective for promoting aromatics and light olefins production.¹⁵¹

Thereby, Article 3 discusses the performance of two MCM-22 zeolites with different Si/Al ratios, 20 and 40 respectively. XRD patterns show that both samples are highly crystalline and present the three distinctive reflections at 7, 24.9 and 25.9°, matching with the intralayer reflections (1 0 0), (2 2 0) and (3 1 0) of the MWW topology, respectively. The characterisation of the textural properties show that both materials are provided with high BET areas, with a high contribution of the external surface. The synthesised sample with higher Al amount possesses lower particle size and therefore enhanced textural properties, which is in agreement with previous reported results.²⁰⁰ Regarding the acidic properties assessed by pyridine TPD, these MCM-22 zeolites followed the expected trend: the sample with more aluminum content showed higher concentration of acid sites, with more Brønsted than Lewis sites in both samples. The results obtained after the integration of the FTIR bands at 1545 cm⁻¹ (PyH⁺ band) and 1461 + 1454 cm⁻¹ (PyL band) are depicted in Figure 4.5.

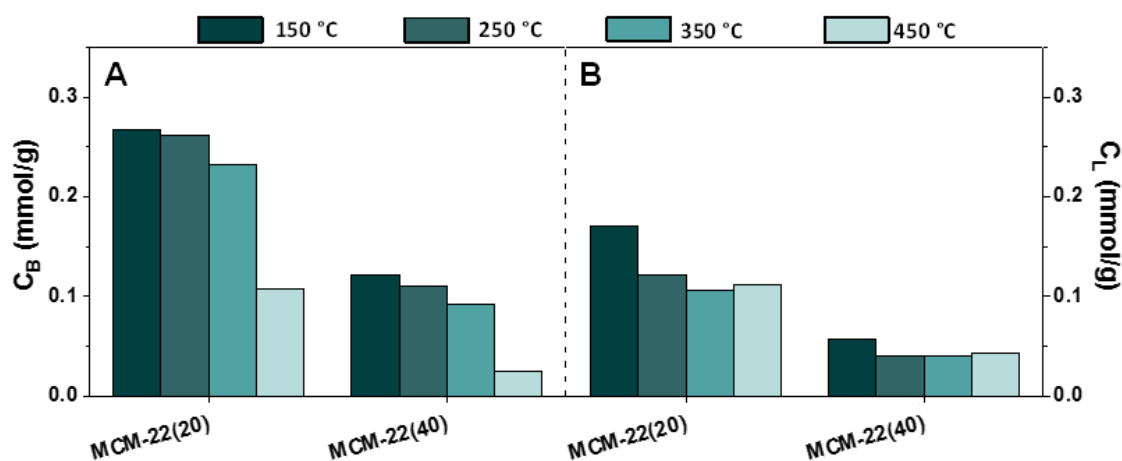


Figure 4.5. Concentration of Brønsted, C_B (A) and Lewis, C_L (B) acid sites measured for the MCM-22 samples after desorption of pyridine at different temperatures, monitored by FTIR.

Despite suitable and selective bio-oil deoxygenation was achieved, the weaker acidity of these zeolites resulted in a lower formation of non-oxygenated aromatics than other zeolite structures, such as the ZSM-5. Other important aspect is that the bigger pore sizes of the cavities of MCM-22 zeolite, caused larger amounts of coke deposition than the mentioned ZSM-5. This coke contains relevant amounts of oxygen, suggesting that its formation is in a significant part mediated by oxygenated compounds. Despite decreasing the Si/Al of the MCM-22 zeolite resulted in higher conversions, the best results in terms of deoxygenation/bio-oil selectivity were achieved with the MCM-22 (40) zeolite at 450 °C.

The next step in the catalysts design consists in the incorporation of additional functionalities by adding metallic or metal oxide nanoparticles over the zeolite. Taking into account what was mentioned in Section 1.4.2, metal oxides showing acid, basic or redox properties promote condensation reactions, which selectively remove oxygen in the bio-oil*. At the same time, they increase the chain length of the lower molecular weight oxygenates and moderate the acidity of the catalyst. In addition, they are a good combination with the stronger acid sites, shape selectivity and accessibility that offer the modified zeolites as supports.

Article 4 is focused on the performance of two hierarchical zeolites synthesised by the seed silanisation method,¹⁸⁰ Beta and ZSM-5, modified by deposition of MgO and ZnO nanoparticles. The presence of a secondary mesoporosity and/or a high share of external surface area provide hierarchical zeolites with a high accessibility for processing sterically demanding compounds and for supporting active phases as co-catalysts. Mg and Zn oxides, for their side, have been reported to be effective catalysts in the pyrolysis of biomass with promising results.^{143,144,201,202}

Regarding the characterisation of the catalysts, the materials before and after impregnation show high crystallinity, with the characteristic peaks of the MFI and BEA topologies for the h-ZSM-5 and h-Beta based catalysts, respectively. No diffraction peaks of any phase of the metal oxides were found in the diffractograms despite the relative high loading added, indicating a good dispersion of the active phases. This fact is reinforced with the TEM images, where no regions of different electronic density, which would be associated with the presence of particles of the oxides, are appreciable. In these images it can be observed the characteristic morphology of globular agglomerates of very small zeolite entities, own to these hierarchical zeolites.

4. RESULTS AND DISCUSSION

The Ar physisorption at 87 K of the hierarchical materials shows hybrid isotherms between types I and IV, according to the IUPAC classification. Thus, a significant adsorption is observed at low relative pressures ($P/P_0 < 0.1$), associated with the micropores of the zeolites, and also at intermediate relative pressures ($0.1 < P/P_0 < 0.9$) due to the mesopore+external surface area of this type of hierarchical molecular sieves. Nevertheless, as shown in Table 4.3, there is an important difference between the two supports when incorporating the active phase. In the case of h-Beta, there is a 20-30% reduction in the micropore surface area, while in h-ZSM-5 this reduction is just 7-12%, which matches with the quantities of metal loading. Despite in both hierarchical zeolites the deposition of the active phase is preferential over the external surface, a partial pore blockage occurs in the case of h-Beta, probably because its larger pore size allows this undesired phenomena, while in case of the h-ZSM-5 that effect is non-existent.

Table 4.3. Chemical and textural properties of the hierarchical catalysts

Catalysts	(Si/Al) _{MOL} ^a	Metal oxide ^a (wt%) ^a	S _{BET} ^b (m ² /g)	V _{MZ} ^c (cm ³ /g)	V _{MS} ^c (cm ³ /g)	S _{MZ} ^c (m ² /g)	S _{MS} ^c (m ² /g)
h-ZSM-5	58	--	562	0.149	0.425	243	319
MgO/h-ZSM-5	58	8.4	398	0.132	0.374	215	183
ZnO/h-ZSM-5	58	9.7	434	0.138	0.370	225	209
h-Beta	24	--	779	0.256	0.251	434	345
MgO/h-Beta	24	8.7	400	0.174	0.136	295	105
ZnO/h-Beta	24	10.0	524	0.203	0.170	343	181

The quantity, nature and strength of the acid sites of the materials have been measured by NH₃-TPD and pyridine desorption monitored by FTIR. After incorporating the metallic component, there is a dramatic decrease in the Brønsted acidity, that reached more than 70% reduction at 150 °C in all cases. Since this reduction is more pronounced than that of the textural properties, this suggests that the BAS are preferential anchoring points of the oxides. On counterpart, the impregnated samples, and especially the samples with Zn, present an enhanced population of Lewis sites. Finally, temperature programmed desorption of carbon dioxide analyses are shown in Figure 4.6, which reveals an increased basicity in the impregnated samples, reaching the highest values with the samples with MgO.

All the samples were tested in the catalytic pyrolysis of dried eucalyptus woodchips at the same conditions of catalyst to biomass ratio (C/B) of 0.2 and 500 °C for the thermal and catalytic zones. Zeolites with bigger pore sizes, like h-Beta, tend to yield larger coke deposits. However, in this case, their values are quite close for both zeolites, probably because of the larger contribution of the external surface area of the h-ZSM-5 zeolites. The deposition of the metal oxides originates a reduction of 20-35% in the yield of coke due to the partial suppression of Brønsted acidity. There is a logical drop in the bio-oil* yield in all catalytic experiments, but the difference between both supports is clear: h-ZSM-5 largely promotes deoxygenation reactions, decreasing the bio-oil* oxygen concentration in 18-25%, whilst h-Beta is inefficient in this term, only reducing 0-5%. The better performance of the h-ZSM-5 is also reflected in the chemical composition of bio-oils*, analysed by GC-MS (Figure 4.7). Those analyses show that h-ZSM-5 presents higher conversion of anhydrosugars and higher aromatics content.

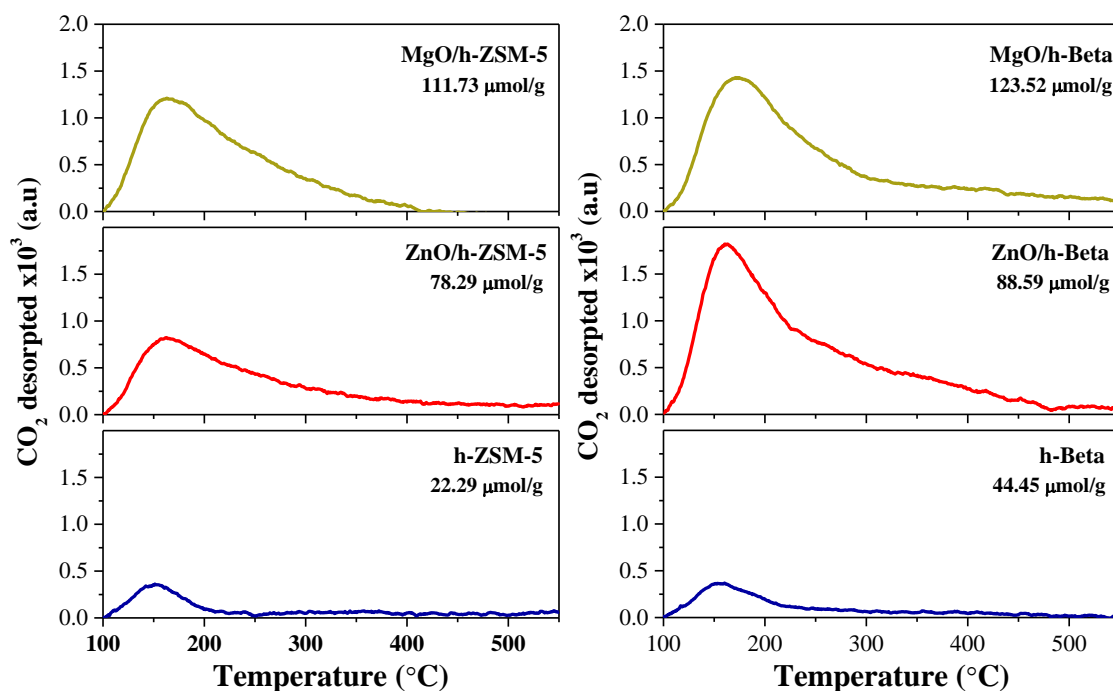


Figure 4.6. CO₂-TPD curves and overall basicity values of the hierarchical catalysts.

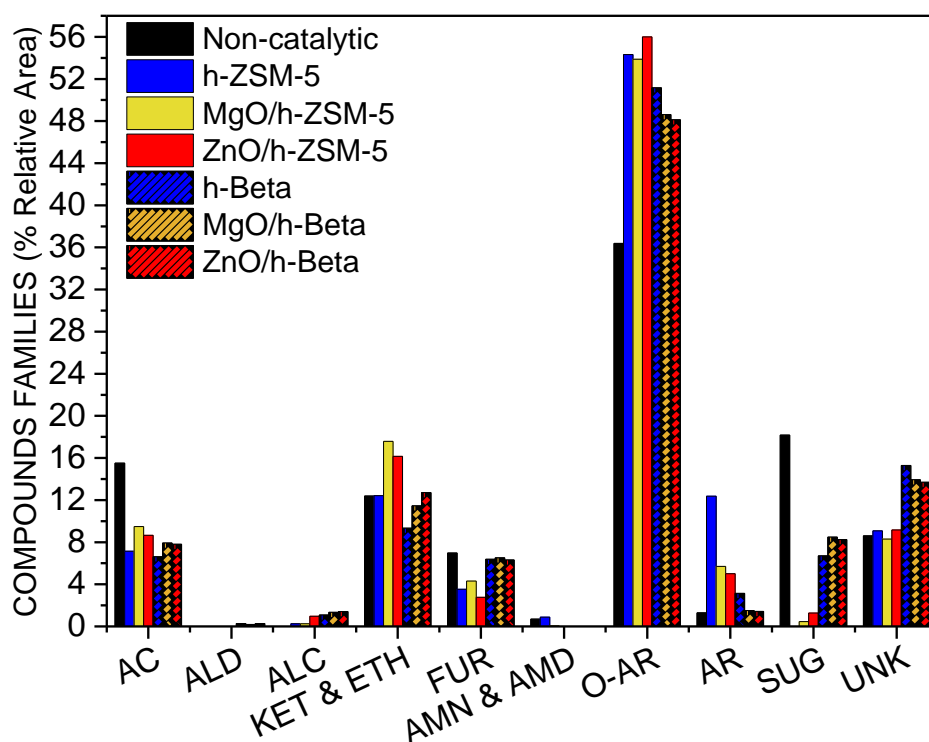


Figure 4.7. Bio-oil* composition in terms of organic compounds families (% of relative area from GC-MS analyses), obtained in the thermal and catalytic fast pyrolysis of eucalyptus woodchips over the hierarchical zeolites. (AC: acids; ALD: aldehydes; ALC: alcohols; KETÐ: ketones and ethers; FUR: furans; AMN&AMD: amines and amides; O-AR: oxygenated aromatics; AR: aromatics; SUG: anhydro sugars; UNK: unidentified chemicals).

4. RESULTS AND DISCUSSION

The moderation of the Brønsted and the generation of additional Lewis acid/basic sites in the bifunctional catalysts provoke an increase in the bio-oil* yield respecting the parent zeolites, and lower the gases formation. An interesting feature is observed in the case of ZnO loaded samples that consists in the formation of additional CO₂ and H₂, probably caused by the promotion of the water-gas shift reaction, which has been previously reported over this oxide.^{201,202} The best results, in terms of deoxygenation selectivity, are obtained with the MgO/h-ZSM-5 due to a balanced concentration of acid/basic sites.

A zeolite is considered 2D when one dimension of its crystals is formed by a maximum of one or two unit cells. In this case the accessible external surface area is greatly enhanced in comparison with 3D zeolites.¹⁵² In Article 5, the performance on biomass pyrolysis of 2D lamellar and pillared ZSM-5 zeolites and their modification by depositing MgO and ZnO nanoparticles over their surface was investigated. XRD reveals the characteristic peaks of a crystalline MFI structure, and at low angle they show a reflection at 1.34-1.39°, assigned to the formation of ZSM-5 lamellas.²⁰³ This morphology is clearly appreciated in TEM images (Figure 4.8). Both materials present high total BET areas and an outstanding contribution of the external surface, and therefore they improve the dispersion of the active phases and the internal diffusion of the reaction molecules. The introduction of silica pillars in the 2D zeolites, led to an additional 20% increase in the BET area. After the incorporation of the metal oxides, textural properties sharply decrease in the whole range of porosity, suggesting the existence of micropore blocking.

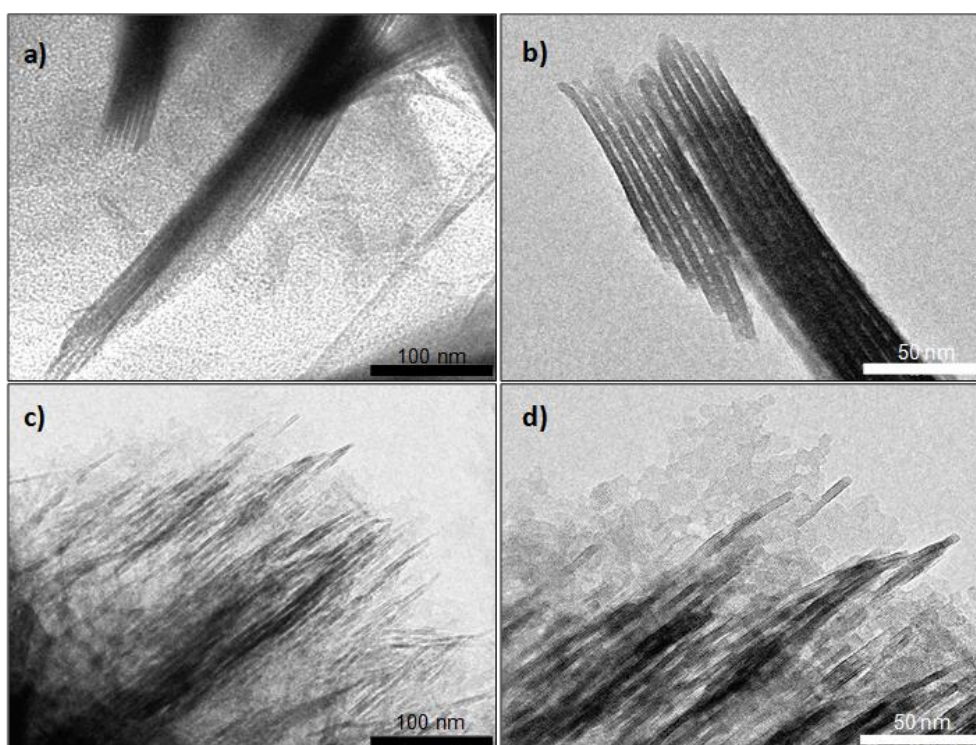


Figure 4.8. TEM images of the parent materials after calcination: (a, b) PI-ZSM-5 and (c, d) L-ZSM-5.

Regarding the acidity characterisation of the materials, pyridine desorption analyses reveal that the incorporation of the active phases induces severe changes in the concentration, strength and nature of the active sites. Thus, as it occurred in Article 4 with hierarchical zeolites, after the zeolite impregnation there is a drop in the Brønsted sites concentration. On the other hand, a new type of

Lewis sites is generated in the region of 1615-1623 cm^{-1} of the FTIR spectra. These changes are expected to play a major role in the pyrolysis reaction.

The activity tests were carried out at 500 °C for thermal and catalytic zones with a catalyst to biomass ratio of 0.2 for all the experiments. In addition to char, coke yields are about 3 wt% in the parent zeolites, decreasing 3–23% when incorporating the active phases. Gas phase yield largely increases from 12 wt% (thermal test) to values of 20-24 wt%, where CO and CO₂ are the major compounds. An important increase in the gaseous olefins is also noticeable, without a clear trend between all the evaluated materials. The bio-oil, initially in form of one single phase (thermal pyrolysis), is separated in two (aqueous and organic) phases, mostly due to the changes in polarity generated by bio-oils dehydration reactions promoted over these catalysts. The increase in the yield of gas phase compounds and water formation originate a significant descent in the bio-oil* yield, from 42 wt% to 24-30 wt% in the catalytic experiments. However, this decrease is accompanied by an improvement in the oxygen concentration, which moves from 39 wt% down to 27-34 wt%.

As shown in the GC-MS analyses (Figure 4.9), the products distribution of bio-oils* is also improved, in which sugar derivatives are practically transformed into light oxygenates and furans by dehydration. On the other hand, furans tend to form aromatics through successive dehydration and Diels-Alder condensation with olefins.

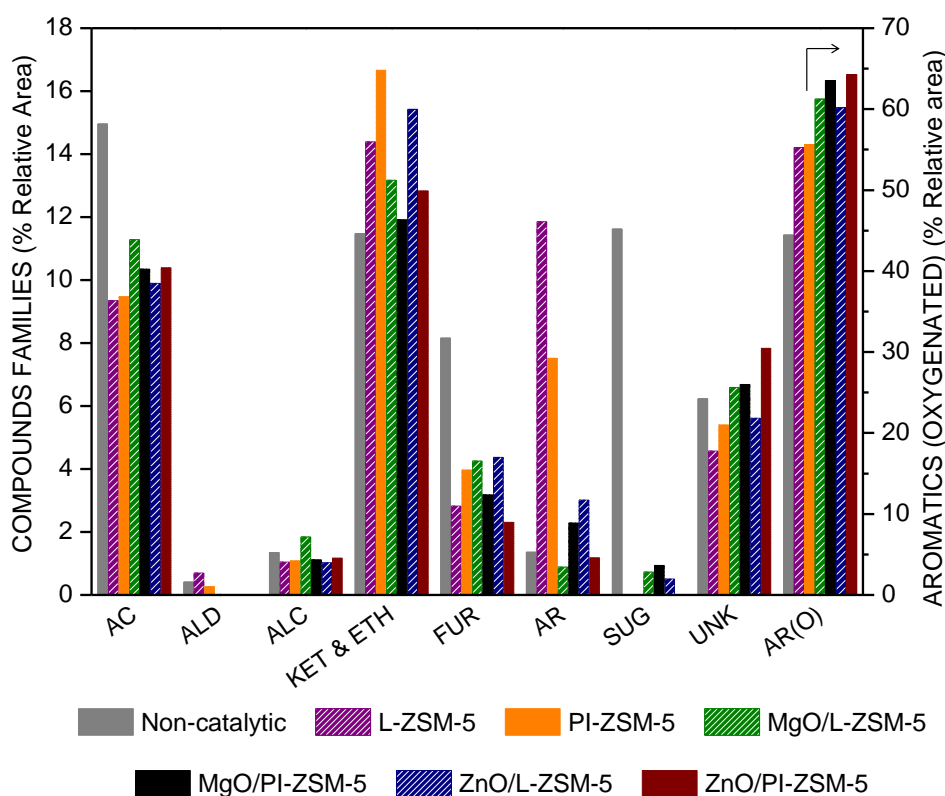


Figure 4.9. Composition of the bio-oil* in term of organic compounds families (% of relative area from GC-MS analyses) obtained in the different fast-pyrolysis tests (catalytic and non-catalytic) of eucalyptus woodchips.

The yield of aromatic hydrocarbons decreases in favor of oxygenated aromatics after the metal oxide deposition due to the lowering of the Brønsted sites concentration in these materials. The carboxylic acids concentration also decreases, being converted in gaseous molecules, specially olefins and CO, or ethers/ketones formed by condensation reactions.

4. RESULTS AND DISCUSSION

In conclusion, both lamellar and pillared 2D-ZSM-5 zeolites appear to be promising supports for well dispersed active phases and as catalysts in biomass pyrolysis vapor upgrading, although they would present important limitations in the scaling-up of the process due to their high synthesis cost.

Taking into account the results and discussion of this section, it seems logical to select a catalyst based on ZSM-5 of medium acidity and enhanced textural properties as a support, since it has been proven to be more active and selective in terms of deoxygenation and aromatics production than other zeolite structures. Fine tuning by means of oxides with acid/basic or redox properties has been also shown as a useful tool to promote condensation reactions and to moderate the Brønsted acidity, reducing the overcracking and coke formation, and resulting in more selective deoxygenation pathways.

Article 3

“Performance of MCM-22 zeolite for the catalytic fast-pyrolysis of acid- washed wheat straw”

H. Hernando, J. Feroso, C. Ochoa-Hernández, M. Opanasenko, P. Pizarro, J.M. Coronado, J. Čejka, D.P. Serrano

Catalysis Today, 2018, 304, 1, 30-38

Article 4

“Biomass catalytic fast pyrolysis over hierarchical ZSM-5 and Beta zeolites modified with Mg and Zn oxides”

H. Hernando, I. Moreno, J. Feroso, C. Ochoa-Hernández, P. Pizarro, J.M. Coronado, J. Čejka, D.P. Serrano

Biomass Conversion and Biorefinery, 2017, 7(3), 289–304

Article 5

“Lamellar and pillared ZSM-5 zeolites modified with MgO and ZnO for catalytic fast-pyrolysis of eucalyptus woodchips”

J. Feroso, H. Hernando, P. Jana, I. Moreno, J. Přech, C. Ochoa-Hernández, P. Pizarro, J.M. Coronado, J. Čejka, D.P. Serrano

Catalysis Today, 2016, 277, 171-181

4.3. OPTIMISATION OF THE NANOCRYSTALLINE ZSM-5 SYSTEM WITH DE-ASHED BIOMASS: EFFECTS OF THE TEMPERATURE, CATALYST TO BIOMASS RATIO AND FINE TUNING OF THE ACIDITY AND ACCESSIBILITY

Among all the materials tested in catalytic pyrolysis, the ZSM-5 zeolite is the most studied in literature due its outstanding selectivity to produce aromatic hydrocarbons,^{159,162,204,205} which has been also demonstrated in the previous articles of this Thesis. This effect has been related to the medium pore size and strong acidity of ZSM-5, which confers this material a high selectivity to aromatics.²⁰⁶

Following this statement, Article 6 is based on the optimisation of the pyrolysis conditions, decoupling the thermal and catalytic steps and using a nanocrystalline ZSM-5 (n-ZSM-5) of intermediate Si/Al = 40. For that purpose, de-ashed wheat straw (WS-ac) was selected as biomass feedstock, to avoid the catalytic interferences caused by AAEM present in the mineral matter, as it was previously demonstrated in Section 4.1 of this Thesis (Articles 1 and 2).

The temperature in the thermal pyrolysis zone was varied from 475 to 600 °C in order to establish an optimum value for the first stage. The increase in the temperature reduces the char yield due to a larger devolatilisation and favored steam gasification. Dehydration is the main deoxygenation pathway under thermal conditions, followed by decarboxylation and decarbonylation. It is important to notice that the origin of most of the oxygen so removed proceed from the char fraction, being poorly effective in lowering the bio-oil* oxygen content. The maximum bio-oil* yield is reached at 550 °C, which is fixed as optimum for this biomass and experimental set-up.

The next step consists in the optimisation of the catalytic zone temperature, where the n-ZSM-5 zeolite is added. Considering a catalyst to biomass ratio (C/B) of 0.2, the temperature of the catalytic furnace was varied in the range of 400-500 °C, increasing the gas formation at the expense of the bio-oil* yield. Decarbonylation is predominant from 450 °C and above, whereas dehydration reactions seem to be unaffected by increasing temperature. The most selective deoxygenation pathway over this material was achieved at 400 °C.

In order to have a better understanding of the pyrolysis reaction pathways, the catalyst (n-ZSM-5) to biomass ratio is another important parameter to be studied. Therefore, adjusting thermal and catalytic temperatures to 550 and 400 °C, respectively; C/B ratio was varied in the range of 0.1-0.7. The increase of the catalyst weight results in a linear decrease in the bio-oil* yield (Figure 4.10A), while in parallel increases the gas formation, specially CO, CO₂ and gaseous olefins (Figure 4.10B). The larger surface available when increasing the C/B allows greater quantities of coke to be produced. At the highest C/B ratio tested, the n-ZSM-5 was able to reduce the bio-oil* oxygen concentration to 10 wt%, but at the expense of losing notable amounts of mass and energy yields.

In order to study semiquantitatively the compounds present in the bio-oil*, GC-MS analyses of this fraction were carried out. As expected, the increase in the C/B ratio sharply changes the chemical composition of the bio-oil*, enhancing the aromatic production whereas sugars, furans and light oxygenates are almost completely converted. Based on the results of the mass balances and chemical composition of the bio-oil*, a scheme of the possible reaction pathways is proposed in Figure 4.11.

4. RESULTS AND DISCUSSION

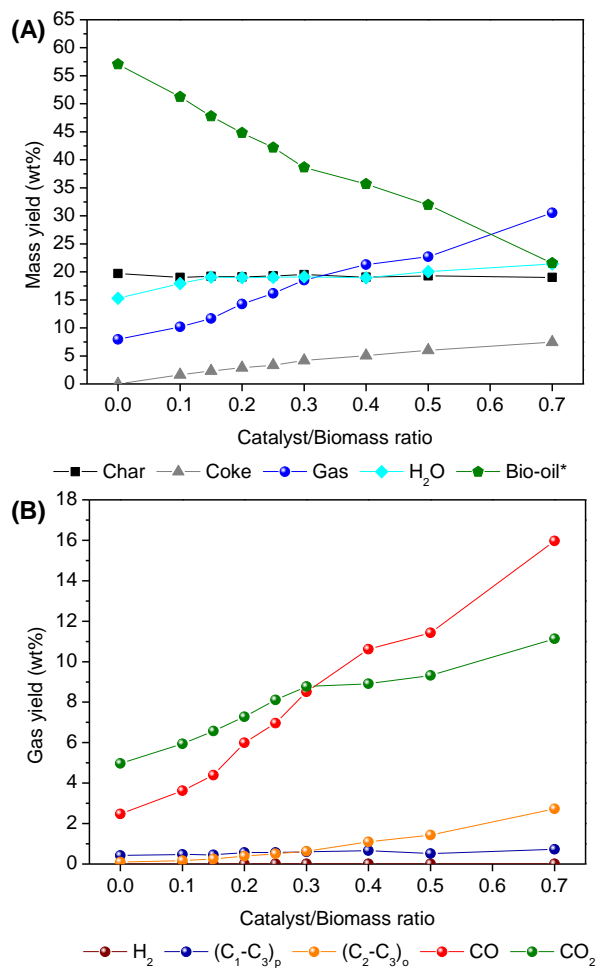


Figure 4.10. Products yield (A), and gas composition (B) in the catalytic fast-pyrolysis of WS-ac as function of the catalyst to biomass ratio (0.0-0.7). Pyrolysis/Catalyst temperature zones: 550°C/400°C. (C₁-C₃)_p: paraffins; (C₂-C₃)_o: olefins.

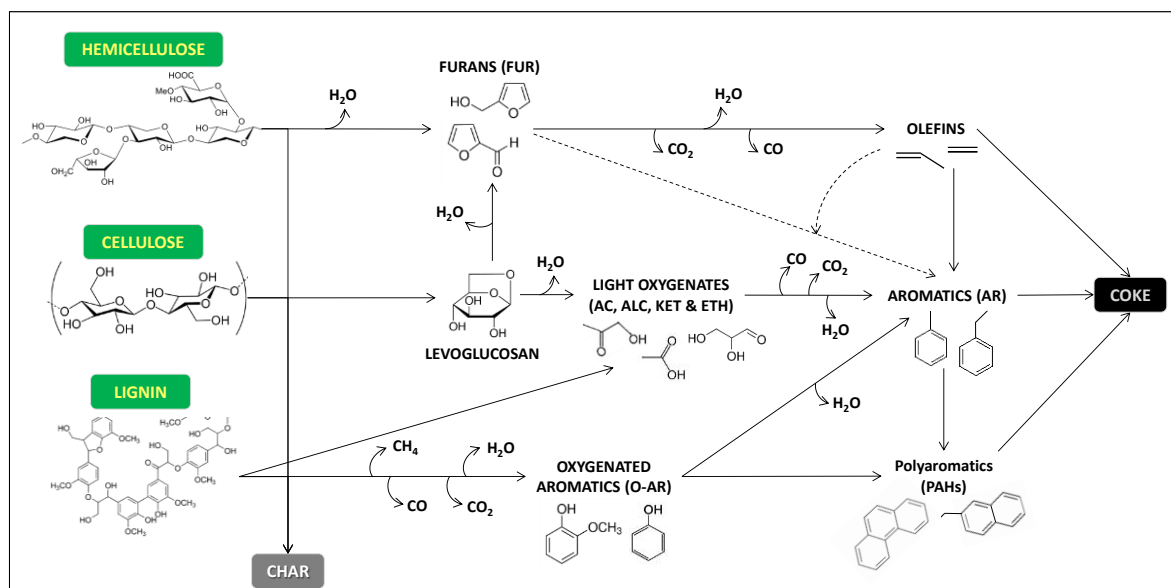


Figure 4.11. Scheme proposed showing the main pathways for the catalytic fast-pyrolysis of lignocellulose over the n-ZSM-5.

The modification with additional functionalities, by means of supported metal/metal oxides phases, can improve the bio-oil deoxygenation selectivity of the zeolitic materials, as discussed in Section 4.2. In spite of the good performance of the ZSM-5 zeolite, especially with enhanced textural properties, it still suffers from important limitations due to an excessive cracking and coke formation, which drastically decrease the selectivity to bio-oil*. Article 7 is focused on the fine tuning of the acidity and accessibility of two ZSM-5 zeolites with high mesopore/surface areas. Thus, a nanocrystalline ZSM-5 (denoted as n-ZSM-5, used in previous studies), and a hierarchical ZSM-5 prepared by desilication (h-ZSM-5) were modified by wet impregnation of ZrO_2 nanoparticles. ZrO_2 catalysts have been reported to be useful not only in catalytic pyrolysis,²⁰⁷ but also in condensation reactions such as ketonisation,¹³⁴ aldol condensation^{208–210} and esterification.^{210,211}

The physicochemical characterisation of these materials reveals that both zeolites present high shares of mesopore/external surface area, especially in the case of the desilicated h-ZSM-5. However, there is a notorious reduction in their textural properties once the ZrO_2 nanoparticles are deposited over their surface. This effect is more accentuated in the surface area included in the micropores range for the h-ZSM-5, suggesting that ZrO_2 preferred location is within the zeolite channels, preventing the entrance of argon into these. On the other hand, the reduction of the mesopore/external surface area in the case of the n-ZSM-5 indicated that the nanoparticles cover the outer part of the zeolite crystals in this case. This supposition is confirmed by TEM images, where a fine coating of different electronic density can be appreciated over the crystals of 25–50 nm of the n-ZSM-5, as shown in Figure 4.12.

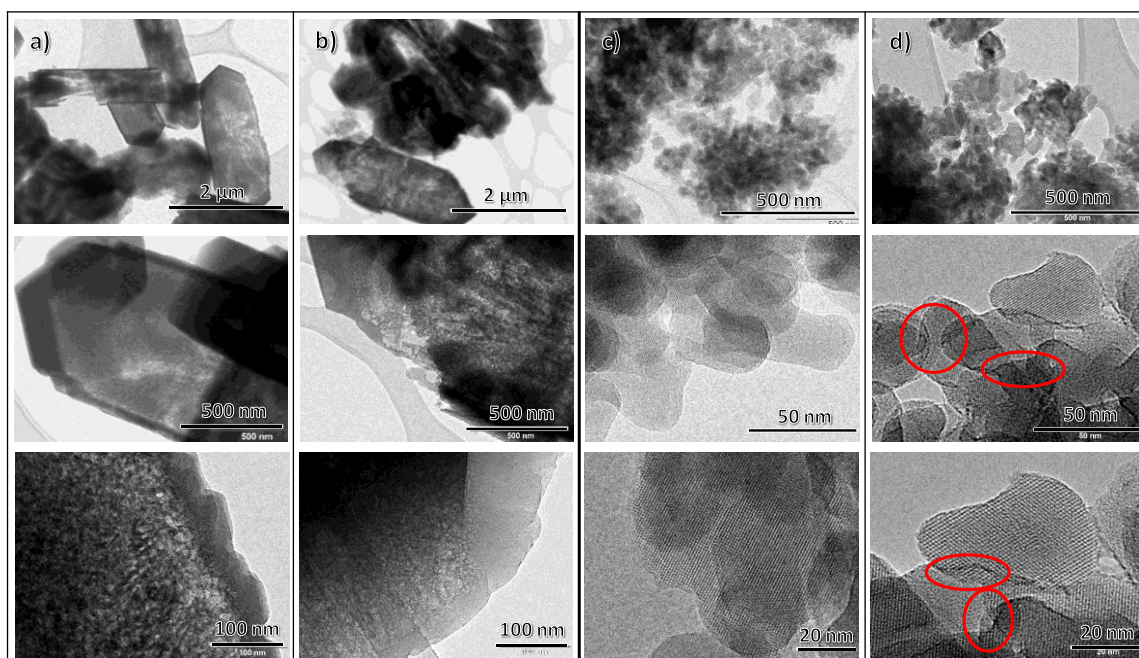


Figure 4.12. TEM images of h-ZSM-5 (a), ZrO₂/h-ZSM-5 (b), n-ZSM-5 (c) and ZrO₂/n-ZSM-5 (d). The marked areas in d correspond to regions rich in ZrO₂ nanoparticles.

The acidity and accessibility to the active sites of the catalysts was assessed by a combination of analytic techniques, including ²⁷Al MAS ssNMR, temperature programmed desorption of pyridine and 4-fluorestyrene oligomerisation. With respect to the Al coordination of the samples, most of it is in the zeolite framework in the case of the n-ZSM-5 and just a negligible peak of octahedrally coordinated is seen. When analysing data from h-ZSM-5, significant amounts of different extraframework aluminum species are detected, which is a direct consequence of the desilication treatment with which this sample was treated for generating the mesoporosity. Barely changes after ZrO₂ deposition are observed regarding the coordination state of aluminum in the samples, just small peaks in the extraframework Al of the h-ZSM-5 due to the occurrence of Al-Zr interactions. Regarding the acidity, the addition of ZrO₂ provoke a notorious decrease in both Brønsted and Lewis sites concentration, due to the interaction of the Zr with the former active sites or due to the above mentioned pore obstruction. The effects are different in case of n-ZSM-5 zeolite, where the concentration of Brønsted sites is loosely shielded and new types of Lewis sites are generated. The oligomerisation of 4-fluorestyrene followed by Confocal Fluorescence Spectroscopy (CFM) and UV-Vis confirmed the reduction of the accessible BAS of the ZrO₂/h-ZSM-5 sample, whereas the acidity moderation in the case of the ZrO₂/n-ZSM-5 is softer.

The catalytic activity tests have been performed in a laboratory ex-situ catalytic pyrolysis set-up, using de-ashed wheat straw as feedstock and operating at 550 and 400 °C, for thermal and catalytic zones, respectively, same conditions that those optimised in Article 6. Figure 4.13a) depicts the mass yield distribution of the different products, whereas Figure 4.13b) shows the bio-oil* oxygen concentration. The tuning of the acidity after Zr modification leads to larger bio-oil* yields combined with higher deoxygenation degrees. As demonstrated by Figure 4.13c), this is a result of the reduction of the overcracking and polymerisation reactions, and also of the lower selectivity towards deoxygenation through decarbonylation, extensively promoted by the now suppressed strongest Brønsted sites.

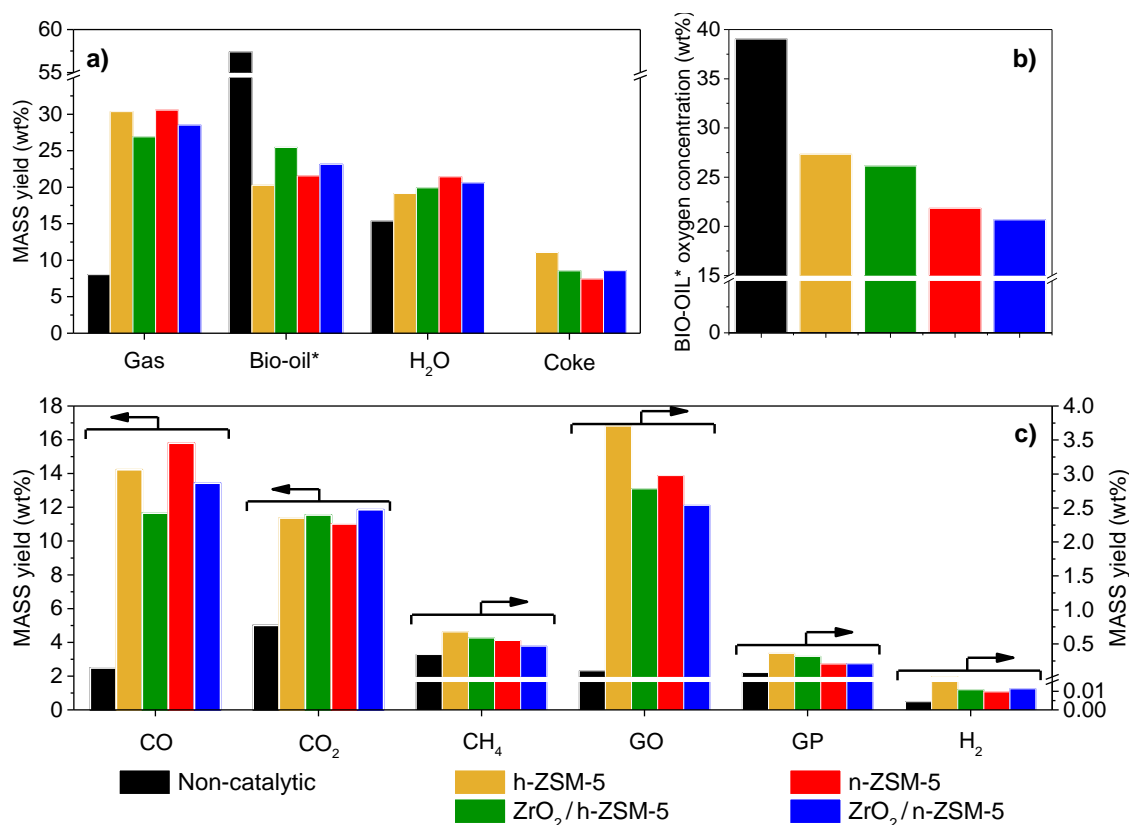


Figure 4.13. Products yield distribution (wt%) (a), Bio-oil* oxygen concentration (wt%, dry basis) (b) and gaseous components yield (wt%) (c), in the fast-pyrolysis of WS-ac over ZrO₂ modified ZSM-5's (Catalyst/Biomass = 0.7 g/g, T = 550/400 °C). GO: gaseous olefins (C₂–C₄); GP: gaseous paraffins (C₂–C₄).

Attending to the GC-MS analyses, in which an external calibration of major compounds was carried out (Figure 4.14), ZrO₂-modified samples show considerably enhanced conversion of the larger, undetected oligomers in the GC-MS, suggesting that the new generated Lewis sites participate in these reactions. The ZrO₂/n-ZSM-5, which is the most promising catalyst, looking at their textural and acidic properties as discussed above, shows the most selective deoxygenation pathway, in terms of both bio-oil* mass and energy yields, and also lower contents of oligomeric species.

In summary, in this Chapter can be concluded that the ZrO₂ deposition over the nano-sized ZSM-5 of intermediate Si/Al ratio produces the best results of all the studied catalysts, due to an enhanced bio-oil* deoxygenation and lower promotion of undesired reactions, such as excessive cracking and coke formation. But also, it promotes that oligomers are more easily converted than over the parent material. Therefore, this material appears as a promising candidate to be scaled-up and investigated in technical form.

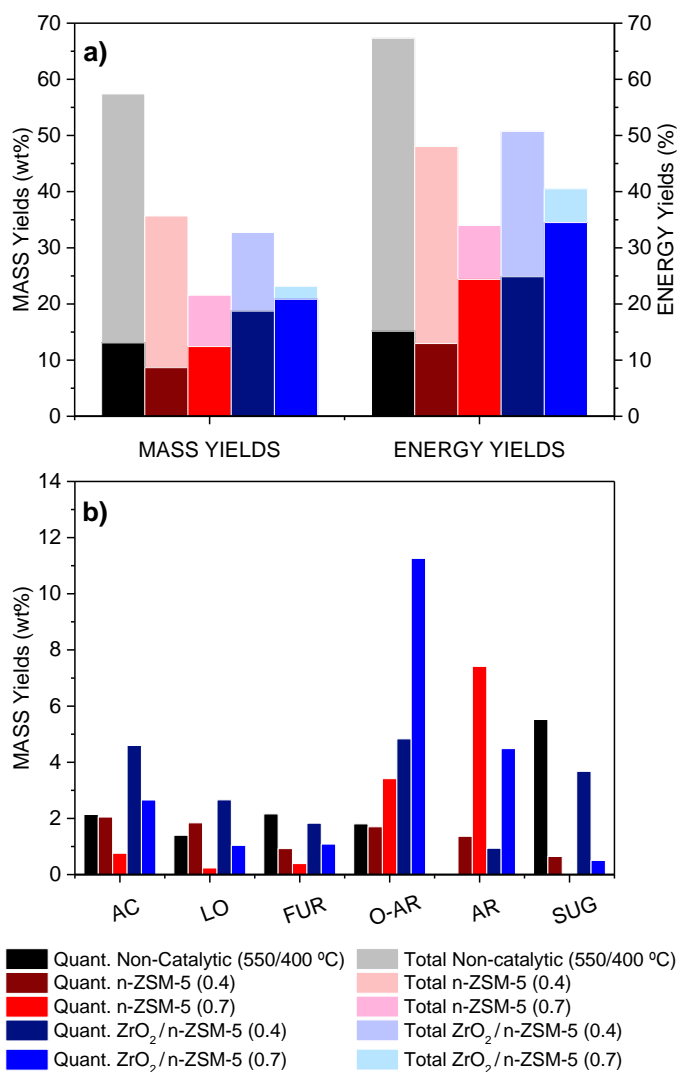


Figure 4.14. Total/quantified bio-oil* components (a), and bio-oil* components mass yields in terms of main organic compounds families (b) obtained in the fast-pyrolysis of WS-ac over the ZrO₂ modified nanocrystalline ZSM-5 and parent zeolite (Catalyst to biomass weight ratio indicated in brackets, T = 550/400 °C).

Article 6

“Assessing biomass catalytic pyrolysis in terms of deoxygenation pathways and energy yields for the efficient production of advanced biofuels”

H. Hernando, S. Jiménez-Sánchez, J. Feroso, P. Pizarro, J.M. Coronado, D.P. Serrano

Catalysis Science and Technology, 2016, 6(8), 2829-2843

Article 7

“Engineering the acidity and accessibility of the zeolite ZSM-5 for efficient bio-oil upgrading in catalytic pyrolysis of lignocellulose”

H. Hernando, A.M. Hernández-Giménez, C. Ochoa-Hernández, P.C.A. Bruijninx, K. Houben, M. Baldus, P. Pizarro, J.M. Coronado, J. Feroso, B.M. Weckhuysen, J. Čejka, D.P. Serrano

Green Chemistry, 2018, 20(15), 3499-3511

4.4. ON THE ROAD TO INDUSTRY: STUDY OF THE EFFECT OF CLAY BINDERS TO PRODUCE TECHNICAL CATALYSTS AND SCALING-UP

As shown in the previous Chapter of this Thesis, ZrO₂/n-ZSM-5 has proven to be an effective catalyst in terms of both deoxygenation selectivity and depolymerisation of larger oligomers. Once the catalytic components of the technical catalyst have been selected, next step consists on the search of an appropriate binder in order to produce such catalysts suitable for their utilisation at industrial scale. Nevertheless, as reflected in the introduction, binders and matrix components tend to dilute or even inhibit the catalytic activity of the parent materials, neutralising the active sites by ionic-exchange or obstructing the access to their pores.^{170,171}

In this line, Article 8 addresses the use of two clay binders, namely bentonite (BNT) and attapulgite (ATP), for the ZrO₂/n-ZSM-5 and their effect on the resultant catalyst in technical form. These catalysts have been evaluated at lab-scale using de-ashed wheat straw at 550 °C and 400 °C for the thermal and catalytic zones temperatures, respectively. The results of the reactions have been correlated with the textural and acidic/basic properties, monitoring the desorption of probe molecules (pyridine and carbon dioxide) with FTIR.

The characterisation of the textural properties is included in Table 4.4. Binder materials possess significant BET area, but a completely absence of microporosity. The agglomerated catalysts reveal a reduction of the resultant BET surface area respecting the starting ZrO₂/n-ZSM-5 material. Nevertheless, this reduction fitted well with the expected dilution effect of the materials with 30 wt% of each clay, considering both catalyst and binder independently. This confirms the almost complete absence of pore blockage, maintaining the enhanced accessibility of the nanocrystalline zeolite.

Concerning the catalytic experiments, agglomeration caused opposite effects depending on the clay. The use of BNT as binder is detrimental to the deoxygenation ability of ZrO₂/n-ZSM-5, which is attributed to an almost complete loss of the Brønsted acidity due to ionic exchange with the Na⁺ cations of this clay. On the contrary, the catalyst agglomerated with ATP exhibited a boosted activity, leading to a change in the deoxygenation pathways, with major contributions of decarbonylation and especially decarboxylation. This results in a bio-oil* with significantly lower oxygen content than that produced over the initial ZrO₂/n-ZSM-5 (13.5% less oxygen concentration, in relative terms), as shown in Figure 4.15.

Table 4.4. Physicochemical properties of both pure clays and ZSM-5 based catalysts

Catalyst	ZrO ₂ ^a (wt%)	Rupture test (N)	S _{BET} ^b (m ² /g)	S _{MES+EXT} ^c (m ² /g)	S _{MIC} ^d (m ² /g)	V _T ^e (cm ³ /g)	V _{MIC} ^f (cm ³ /g)	Acidity ^g (mmol/g)	
								C _B	C _L
BNT	-	20 ± 1	57	57	-	0.099	-	-	0.008
ATP	-	24 ± 3	107	107	-	0.455	-	0.004	0.039
ZrO ₂ /n-ZSM-5	9.2	-	375	91	284 ^d	0.378	0.169	0.116	0.091
ZrO ₂ /n-ZSM-5-BNT	9.8	16 ± 1	269	77	192 ^d	0.326	0.114	0.018	0.121
ZrO ₂ /n-ZSM-5-ATP	10.5	12 ± 1	296	65	231 ^d	0.382	0.138	0.059	0.088

^a Measured by ICP-OES. ^b BET surface area. ^c Mesopore + external surface area. ^d Micropore surface area. ^e Total pore volume at P/P₀ ≈ 0.98. ^f Micropore volume. ^g From FTIR/pyridine, values calculated from desorption at 150 °C

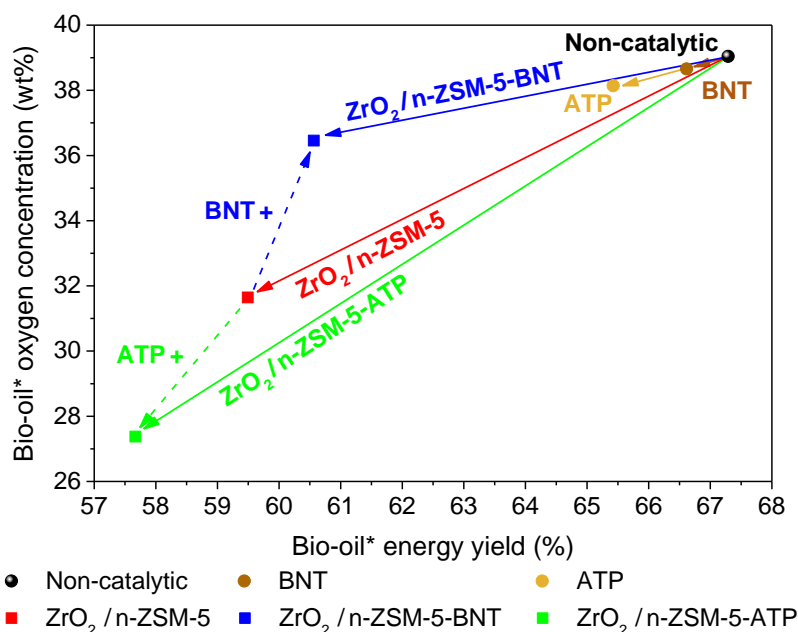


Figure 4.15. Bio-oil* oxygen concentration versus bio-oil* energy yield obtained in the WS-ac pyrolysis over both pure clays and ZSM-5 based catalysts.

Advanced and detailed characterisation of the acidity and basicity by FTIR of the materials explain the improved activity of the ZrO₂/n-ZSM-5-ATP technical catalyst. There is a migration of Mg²⁺ cations from the attapulgite towards the zeolitic component and the ZrO₂ nanoparticles, but it results in lesser decrease of Brønsted acidity. Actually, the migrated Mg²⁺ species interact with the ZrO₂ phase, deposited over the outer part of the nanocrystals, creating new types of Lewis acidity and more interestingly, a wide variety of basic sites, as seen in the FTIR spectra after CO₂ adsorption of Figure 4.16.

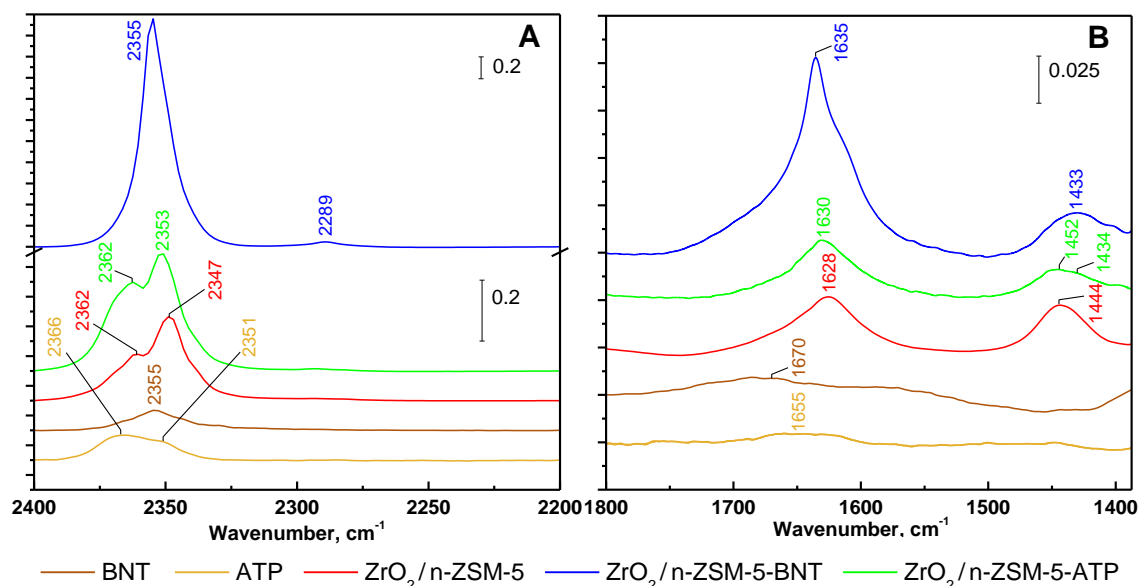


Figure 4.16. FTIR spectra of adsorbed CO₂ (~30 μmol g⁻¹ catalyst) over both pure clays and ZSM-5 based materials in the ranges of 2200-2400 cm⁻¹ (A) and 1300-1800 cm⁻¹ (B).

4. RESULTS AND DISCUSSION

Thus, the lower exchange capability of Mg^{2+} respecting Na^+ of the BNT caused a minor reduction in the Brønsted acidity, while a variety of new types of acid/basic Lewis acid sites were generated by the interaction of the Mg and Zr species. The equilibrated acid/basic properties of the ZrO_2/n -ZSM-5-ATP demonstrated by FTIR analyses explain the better performance in the biomass catalytic pyrolysis of this technical catalysts in comparison with the starting materials.

The last manuscript included in this Thesis, named as Article 9, is aimed to explore more in detail the performance of the ZrO_2/n -ZSM-5-ATP technical catalyst at lab-scale for the advanced biofuels production, varying the catalyst to biomass ratio and providing information about the reaction pathways. Finally, experimental results operating at bench scale in continuous mode and at different operation conditions are also shown in this manuscript. Some similarities and common trends between both different scale installations are reported, which confirms the excellent performance of the designed ZrO_2/n -ZSM-5-ATP technical catalyst.

The characterisation comprised in this article includes acidity/basicity by NH_3/CO_2 TPDs, Al environment by ^{27}Al NMR and morphology by SEM, TEM and SEM-EDX.

The overall acidity and basicity is increased after the impregnation of the powder sample, thanks to the amphoteric properties of the ZrO_2 . The agglomeration with attapulgite does not alter the total acidity of the material, but creates new basic sites thanks to the migration of the Mg^{2+} cations and their interactions with the zeolite and Zr species, as previously reported. Thus, the final ZrO_2/n -ZSM-5-ATP technical catalyst presents a combination of multiple Brønsted and Lewis acidic sites and also multiple basic sites of different nature, thus confirming the remarks performed by the FTIR analyses of the Article 8.

4-fluorestyrene oligomerisation reaction was performed over the technical catalysts and their parent materials in powder form to analyse the Brønsted acidity and accessibility of those active sites. When agglomerating with attapulgite, a partial loss of the Brønsted acidity is observed, mainly caused by the dilution effect in the mix with the clay, which is compensated by an increment in the Lewis acid sites, as mentioned before. The diffusion of the styrene oligomers produced in the reaction is really high, as seen in the cross-section of the catalyst after the reaction, showing higher intensity bands in the core region than in the surface of the catalyst cylinders. Regarding the morphology and dispersion of the different components, microscopy images and specially SEM-EDX show that Zr and Mg are evenly distributed along the catalyst surfaces, with ratios of Si/Zr \sim 43 and Si/Mg \sim 21, respectively. Regarding the Al environment, the addition of attapulgite to the ternary ZrO_2/n -ZSM-5-ATP sample lead to a distortion in the coordination of aluminum, broadening the band of Al^{IV} and increasing the anisotropy, as shown in the 2D-NMR. Additionally, extraframework Al^V and Al^{VI} , which also appeared in the pure attapulgite, are also present in the extruded sample.

Regarding the catalytic tests at lab-scale, a wide range of C/B ratios of ZrO_2/n -ZSM-5-ATP was investigated, varying between 0.1 and 0.7 wt, using de-ashed wheat straw as feedstock at temperatures of 550 and 400 °C for the thermal and catalytic zones, respectively. Bio-oil* oxygen concentration is reduced in 56.5% (in relative terms) in the case of the catalyst ratio 0.7 respecting the initial thermal bio-oil*, which confirms the extraordinary deoxygenation ability of this multifunctional catalyst. The analysis of the mass yields and deoxygenation selectivity towards H_2O , CO and CO_2 show interesting results, depicted in Figure 4.17: dehydration and CO_2 formation increase with the lowest C/B ratios and then stabilises; while CO, light olefins and coke increase linearly in the whole range of catalyst to biomass ratios assayed. Thus, catalytic deoxygenation

selectivity through decarbonylation, which is secondary at lower amounts of catalyst, linearly increases until been the predominant deoxygenation pathway at 0.7 g g^{-1} .

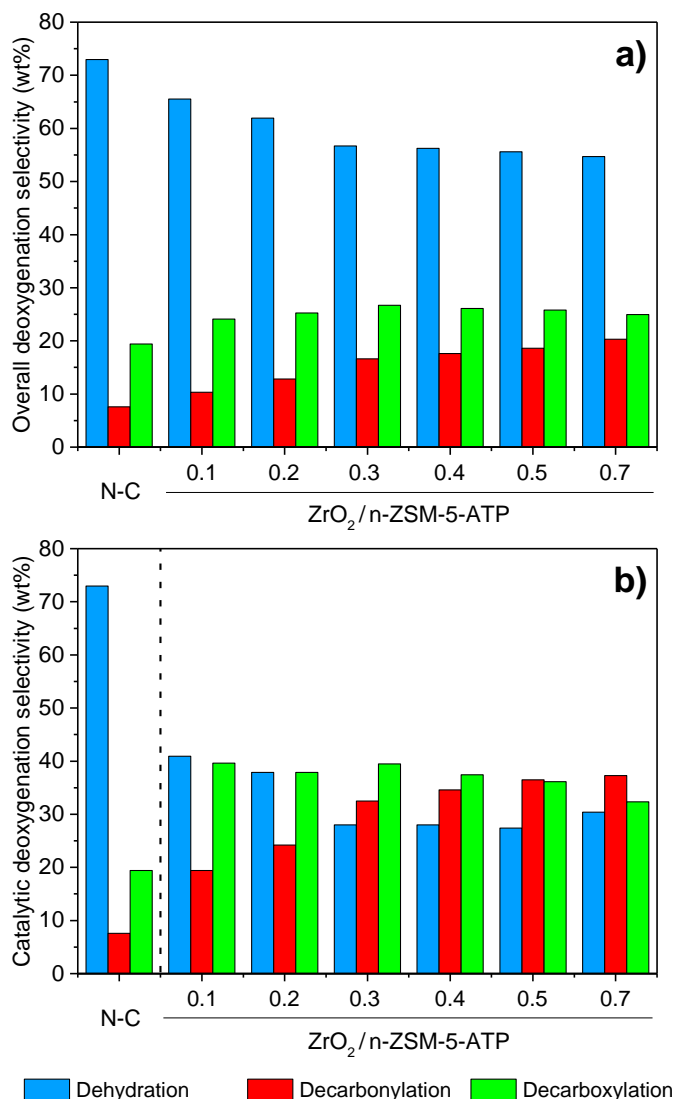


Figure 4.17. Overall deoxygenation selectivity (a) and catalytic deoxygenation (b), obtained in the WS-ac pyrolysis over the $\text{ZrO}_2/\text{n-ZSM-5-ATP}$ catalyst using different C/B ratios. N-C: non-catalytic.

The bio-oil* deoxygenation selectivity of the multifunctional technical catalyst is much higher than the parent nanocrystalline ZSM-5, which would be considered as the state-of-the-art catalyst in all the range of C/B ratios. Thus, for a bio-oil* oxygen concentration of 22 wt%, $\text{ZrO}_2/\text{n-ZSM-5-ATP}$ is able to retain more than 53% chemical energy than the starting zeolite, in relative terms.

The last barrier that tackles Article 9 is the scaling-up of the catalyst into an ex-situ bench-scale facility. It is composed by a bubbling bed reactor, with silica sand as bed material; and a fixed-bed, in which the $\text{ZrO}_2/\text{n-ZSM-5-ATP}$ is loaded. A total of 100 g of oak woodchips as raw biomass was fed with a rate of 5 g min^{-1} , and the temperature of the thermal and catalytic zones were established at 550 and 450 °C, respectively, for all the experiments. Concerning the catalyst to biomass ratio, it was varied between 0.2-0.5 g g^{-1} .

4. RESULTS AND DISCUSSION

The results obtained at bench scale present slight different features in comparison with those obtained at lab-scale. However, in order to make a proper comparison of the reactions at both scales, results must be normalised taking into account the important differences produced in the thermal step, where a different biomass feedstock, vapor residence time and reactor configuration profoundly affect the vapors inlet composition to the catalytic step. As illustrated in Figure 4.18, by subtracting the thermal contribution, thus considering only the bio-oil* oxygen concentration and energy yield in the catalytic step, results of both scales match quite well, indicating that whatever the scale and operation conditions, $ZrO_2/n-ZSM-5-ATP$ catalyst provides deoxygenation degrees of up to 60% with energy yields of approximately 70% with respect to those of the thermal bio-oils.

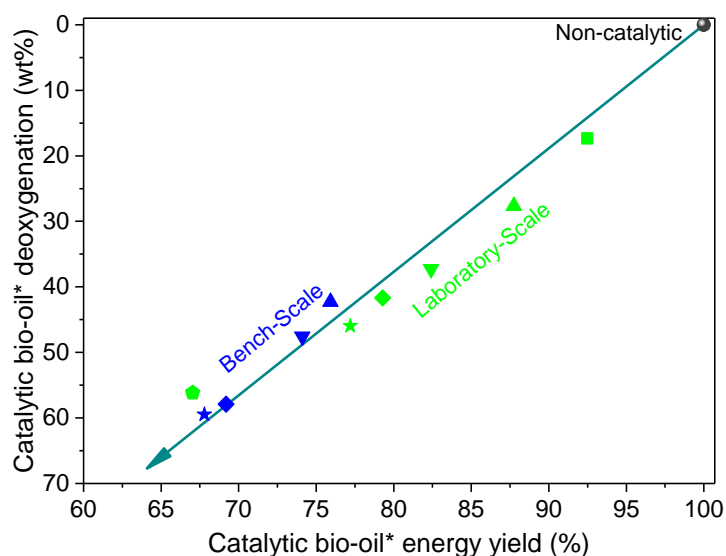


Figure 4.18. Bio-oil* deoxygenation degree versus bio-oil energy yield of the catalytic step (referred to those of the thermal bio-oil), obtained in the biomass pyrolysis at laboratory and bench scales over the $ZrO_2/n-ZSM-5-ATP$ catalyst using different C/B ratios.

The organic part was isolated and analysed separately. The GC-MS of this fraction reveals that it mainly consists in monoaromatics (35%), phenolics (20%), polyaromatic hydrocarbons (14%) and aliphatic compounds (7%), with very low content of light oxygenates, including carboxylic acids; which is consistent with the high deoxygenation activity promoted over the $ZrO_2/n-ZSM-5-ATP$.

In summary, the experimental results included in Articles 8 and 9 demonstrate the superior activity of the catalyst $ZrO_2/n-ZSM-5-ATP$, which is based on two pillars: 1) enhanced textural properties and accessibility, and 2) the existence of diverse active sites, including both Brønsted and Lewis acid sites, as well as multiple basic centers, thanks to the synergetic effects of its different components, as shown by a variety of advanced analytic techniques. These results have been successfully validated at laboratory and bench scales, making that $ZrO_2/n-ZSM-5-ATP$ presents a promising prospect for the lignocellulose catalytic pyrolysis at large scale.

Article 8

“The crucial role of clay binders on the performance of ZSM-5 based materials for biomass catalytic pyrolysis”

H. Hernando, C. Ochoa-Hernández, M. Shamzhy, I. Moreno J. Feroso, P. Pizarro, J.M. Coronado, J. Čejka, D.P. Serrano

Catalysis Science and Technology, 2019, 9, 789-802

Article 9

“Scaling-up of Bio-oil Upgrading during Biomass Pyrolysis over ZrO₂/ZSM-5-Attapulgite”

H. Hernando, A.M. Hernández-Giménez, S. Gutierrez-Rubio, T. Fakin, A. Horvat, R.M. Danisi, P. Pizarro, J. Feroso, E. Heracleous, P.C.A. Bruijnincx, A.A. Lappas, B.M. Weckhuysen, D.P. Serrano

ChemSusChem, 2019, 12, 2428-2438

5. CONCLUSIONS AND OUTLOOK

5.1. GENERAL CONCLUSIONS

The main conclusions derived from the Results and Discussion Chapter have already been presented in each section. Therefore, this chapter only contains the most relevant corollaries obtained throughout this Doctoral Thesis, which are summarised as follows:

- The biomass type and its origin can strongly vary the pyrolysis results, which however present common trends. In general, the mineral matter intrinsically presented in the biomass promotes polymerisation and secondary cracking reactions, diminishing the bio-oil production with poor deoxygenation. Biomass acid-washing has been proved to increment the bio-oil yield. This fact, which also diminishes the variations and interferences of indigenous catalysts, makes this process desirable, especially when agricultural residues, with higher mineral content, are used.
- Char fraction is a solid residue formed during the primary decomposition of the biomass, so its yield and composition only depends on the biomass source and the conditions of the thermal step. Therefore, it is not affected by the presence or not of a catalyst. This carbonaceous solid possesses lower oxygen concentration than the initial biomass (in the range 9 to 17 wt% in the experiments compiled in this work) and high energy yields (29-44%). For this reason, the energetic exploitation of the char is a key factor in the process efficiency.
- The ex-situ configuration seems to be more adequate in catalytic fast pyrolysis, in order to operate at the optimum conditions for each thermal and catalytic steps. In this way, working with poor mineral or de-ashed biomass samples, the optimum pyrolysis thermal temperature is around 550 °C, while for the catalytic pyrolysis step, the optimum stays at lower temperatures, in the range of 400-450 °C, despite they also depend on the catalyst and reactor configuration. Furthermore, the ex-situ configuration is also advisable to reduce catalyst deactivation and poisoning due to direct contact with the metals present in the biomass.
- Among the wide variety of catalysts that have been studied in bibliography, medium pore size zeolites, and specially ZSM-5, is one of the most adequate for the process, thanks to its strong acidity and high selectivity to aromatics. The incorporation of additional mesoporosity/external surface area to overcome the diffusional limitations of bulky molecules and to supply a good dispersion of active phases is a good synthesis approach. Among all the strategies used for this purpose, reducing the crystal size through nano- or seed silanised zeolites have shown the best results in the present work.
- The higher and stronger the catalyst acidity the larger the activity; but at the expense of promoting an excessive cracking and coke deposition. Accordingly, the best results are reached at intermediate aluminum contents ($\text{Si/Al} = 20\text{-}60$), which meet the equilibrium between activity and selectivity.
- Despite the high activity of zeolite ZSM-5, incorporating additional functionalities like impregnation with other actives phases, especially metal oxides can improve the performance of the parent zeolites. Thus, ZnO, MgO and especially ZrO₂, through softening the strong Brønsted acid sites and creating new Lewis and even basic sites, have proven to enhance the catalytic activity and deoxygenation selectivity.
- Binders and matrix components are essential not only in the formulation of technical catalysts, but they can also drastically change their catalytic performance. Taking into account that Lewis acid/basic sites promote efficient deoxygenation through condensation reactions, clays are

5. CONCLUSIONS AND OUTLOOK

attractive binders for the process. More specifically, the use of attapulgite was highly adequate to increase the activity and selectivity of the initial catalyst, thanks to a lower ionic exchange with the zeolite and the generation of new Lewis acid/basic sites created when the migrated Mg^{2+} interacted with the catalyst.

- The good performance of the ZrO_2/n -ZSM-5-ATP catalyst, selected in this Thesis as the best material, have been validated in two pyrolysis set-ups at different scale, laboratory and bench. Besides the different biomass sample, conditions and operation mode, comparable results were found in both reactions systems when results are referenced to the thermal bio-oil. Thus, ZrO_2/n -ZSM-5-ATP provides deoxygenation degrees of up to 60% with energy yields around 70% with respect to those of the non-catalytic reaction, demonstrating the good deoxygenation efficiency of this catalyst.

5.2. RECOMENDATIONS FOR FUTURE WORKS

Taking into account the results and conclusions included in the present Thesis, regarding the design of catalysts and catalytic pyrolysis as a process to obtain advanced biofuels, the next recommendations are enounced for future works:

- To study the effect of different loadings of ZrO₂ active phase, and also different amounts of ATP binder in the technical catalyst in order to find an optimum for the process.
- To analyse the coke nature, the deactivation of the catalysts and their regenerability. Although it has not been included in this Thesis, there are some works in preparation related to this topic, which will be published shortly.
- To perform an economic assessment of the process taking into account the data included in this Thesis and a Life Cycle Analysis (LCA) to calculate the environmental impact of the process and the savings that would result in CO₂ emissions.
- To consider the valorisation of the other byproducts of the pyrolysis, with their different destinations, apart from the energetic one. Thus, the char can be used as soil amendment, raw material for electrodes in electrochemistry, or activated to produce pollutants adsorbents or support for catalysts. On the other hand, olefins included in the gas phase can be destined for petrochemistry, including the production of bioplastics. Finally, the extraction of some high valuable molecules included in the bio-oil can be destined to petrochemistry. These considerations can make the biomass catalytic pyrolysis more economically feasible.
- To co-feed of biomass with hydrogen rich materials, such as plastics, vacuum gas oil or vegetable oils to search synergetic effects, lowering the char formation and favoring the biomass deoxygenation. Besides, these raw materials can also enrich the chemical composition of the resultant oils in aliphatics and aromatics, formed through H-transfer and Diels-Alder condensation reactions.

6. REFERENCES

- 1 US Energy Information Administration (EIA), *International Energy Outlook 2017 Overview*, 2017.
- 2 Y. Sun and J. Cheng, *Bioresour. Technol.*, 2002, **83**, 1–11.
- 3 S. Mayer, *J. Int. Relations Dev.*, 2008, **11**, 251–278.
- 4 A. K. Agarwal, *Prog. Energy Combust. Sci.*, 2007, **33**, 233–271.
- 5 European Commission, Climate action. Causes of climate change, https://ec.europa.eu/clima/change/causes_en, (accessed 29 December 2017).
- 6 G. Myhre et al, *Anthropogenic and Natural Radiative Forcing in Climate Change 2013: The Physical Science Basis. Contribution of Working Group I to the Fifth Assessment Report of the Intergovernmental Panel on Climate Change*, Cambridge University Press, 2013.
- 7 European Commission, *Estatistical Pocketbook 2017. EU transport in figures*, Luxembourg: Publications Office of the European Union, 2017.
- 8 European Commission, Eurostat. Greenhouse Gas Emission Statistics, http://ec.europa.eu/eurostat/statistics-explained/index.php/Greenhouse_gas_emission_statistics#Further_Eurostat_information, (accessed 29 December 2017).
- 9 Commission Staff Working Document, *A European Strategy for Low-Emission Mobility*, 2016.
- 10 Eurostat, Eurostat - Energy balances (June 2017 edition), <http://ec.europa.eu/eurostat/web/energy/data/energy-balances>, (accessed 28 December 2017).
- 11 ECO3, ECO3, <http://www.eco3.fi/en/>, (accessed 3 March 2018).
- 12 M. Cabrera, A. Vera, J. Cornejo, I. Ordás, E. Tolosana, Y. Ambrosio, I. Martínez, S. Vignote, N. Hotait, A. Lafarga and J. Garraza, *Evaluación del potencial de energía de la biomasa. Estudio técnico per 2011-2020*, IDAE (Instituto para la Diversificación y Ahorro de la Energía), 2011.
- 13 J. C. Serrano-Ruiz and J. A. Dumesic, *Energy Environ. Sci.*, 2011, **4**, 83–99.
- 14 G. W. Huber and A. Corma, *Angew. Chemie*, 2007, **46**, 7184–7201.
- 15 S. Vaz Jr, *Biomass and Green Chemistry: Building a Renewable Pathway*, Springer International Publishing, 1st edn., 2018.
- 16 R. P. John, G. S. Anisha, K. M. Nampoothiri and A. Pandey, *Bioresour. Technol.*, 2011, **102**, 186–193.
- 17 P. M. Schenk and S. R. Thomas-hall, *Bioenergy Res.*, 2008, **1**, 20–43.

6. REFERENCES

- 18 J. Singh and S. Gu, *Renew. Sustain. Energy Rev.*, 2010, **14**, 2596–2610.
- 19 S. Yaman, *Energy Convers. Manag.*, 2004, **45**, 651–671.
- 20 T. Kan, V. Strezov and T. J. Evans, *Renew. Sustain. Energy Rev.*, 2016, **57**, 1126–1140.
- 21 D. Mohan, C. U. Pittman and P. H. Steele, *Energy & Fuels*, 2006, **20**, 848–889.
- 22 D. Carpenter and T. Westover, *Green Chem.*, 2014, **16**, 384–406.
- 23 C. Roy, H. Pakdel and D. Brouillard, *J. Appl. Polym. Sci.*, 1990, **41**, 337–348.
- 24 C. Panoutsou, J. Eleftheriadis and A. Nikolaou, *Energy Policy*, 2010, **37**, 5675–5686.
- 25 European Commission, Environment Action Programme to 2020, <http://ec.europa.eu/environment/action-programme/index.htm>, (accessed 28 December 2017).
- 26 European Commission, HORIZON 2020 - The EU Framework Programme for Research and Innovation, <https://ec.europa.eu/programmes/horizon2020/>, (accessed 28 December 2017).
- 27 European Commission, *Strategic Energy Technology (SET) Plan*, Publications Office of the European Union, 2017.
- 28 A. Limayem and S. C. Ricke, *Prog. Energy Combust. Sci.*, 2012, **38**, 449–467.
- 29 J. Feroso, P. Pizarro, J. M. Coronado and D. P. Serrano, *Adv. Rev.*, 2017, **6**, 1–18.
- 30 E. Tomás-Pejó, J. Feroso, E. Herrador, H. Hernando, S. Jiménez-Sánchez and M. Ballesteros, *Fuel*, 2017, **199**, 403–412.
- 31 Y. Makar and E. T. Ganda, *Renew. Sustain. Energy Rev.*, 2018, **81**, 69–75.
- 32 D. Meier, B. van de Beld, A. V Bridgwater, D. C. Elliott, A. Oasmaa and F. Preto, *Renew. Sustain. Energy Rev.*, 2013, **20**, 619–641.
- 33 F. Ronsse, in *Biochar: A Regional Supply Chain Approach in View of Climate Change Mitigation*, Cambridge University Press, 2016, pp. 199–226.
- 34 S. M. Al-Salem, P. Lettieri and J. Baeyens, *Waste Manag.*, 2009, **29**, 2625–2643.
- 35 S. L. Wong, N. Ngadi, T. A. T. Abdullah and I. M. Inuwa, *Renew. Sustain. Energy Rev.*, 2015, **50**, 1167–1180.
- 36 R. Miandad, M. A. Barakat, A. S. Aburiazaiza, M. Rehan and A. S. Nizami, *Process Saf. Environ. Prot.*, 2016, **102**, 822–838.
- 37 S. Dayana, A. Sharuddin, F. Abnisa, W. Mohd and A. Wan, *Energy Convers. Manag.*, 2016, **115**, 308–326.
- 38 J. Montoya, B. Pecha, D. Roman, F. Chejne and M. Garcia-perez, *J. Anal. Appl.*

- Pyrolysis*, 2017, **123**, 347–363.
- 39 J. B. Wooten, J. I. Seeman and M. R. Hajaligol, *Energy & Fuels*, 2004, **18**, 1799–1807.
- 40 R. J. M. Westerhof, S. R. G. Oudenhoven, P. S. Marathe, M. Engelen, M. Garcia-Perez, Z. Wang and S. R. A. Kersten, *React. Chem. Eng.*, 2016, **1**, 555–566.
- 41 P. J. Dauenhauer, J. L. Colby, C. M. Balonek, J. Suszynski and L. D. Schmidt, *Green Chem.*, 2009, **11**, 1555–1561.
- 42 J. Montoya, B. Pecha, F. C. Janna and M. Garcia-Perez, *J. Anal. Appl. Pyrolysis*, 2016, **122**, 106–121.
- 43 M. R. Pelaez-Samaniego, V. Yadama, M. Garcia-Perez, E. Lowell and A. G. McDonald, *J. Anal. Appl. Pyrolysis*, 2014, **109**, 222–233.
- 44 V. Mamleev, S. Bourbigot, M. Le Bras and J. Yvon, *J. Anal. Appl. Pyrolysis*, 2009, **84**, 1–17.
- 45 D. Carpenter, T. L. Westover, S. Czernik and W. Jablonski, *Green Chem.*, 2014, **16**, 384–406.
- 46 A. Oasmaa, Y. Solantausta, V. Arpiainen, E. Kuoppala and K. Sipil, *Energy & Fuels*, 2010, **24**, 1380–1388.
- 47 C. Di Blasi, G. Signorelli, C. Di Russo and G. Rea, *Ind. Eng. Chem. Res.*, 1999, **38**, 2216–2224.
- 48 I. D. V. Torri, V. Paasikallio, C. Schmitt Faccini, R. Huff, E. Bastos Caramão, V. Sacon, A. Oasmaa and C. Alcaraz Zini, *Bioresour. Technol.*, 2016, **200**, 680–690.
- 49 J. Shen, X. Wang, M. Garcia-perez, D. Mourant, M. J. Rhodes and C. Li, *Fuel*, 2009, **88**, 1810–1817.
- 50 R. J. M. Westerhof, H. S. Nygard, W. P. M. van Swaaij, S. R. A. Kersten and D. W. F. Brilman, *Energy & Fuels*, 2012, **26**, 2274–2280.
- 51 S. Zhou, M. Garcia-perez, B. Pecha, A. G. Mcdonald and R. J. M. Westerhof, *Fuel*, 2014, **125**, 15–19.
- 52 P. R. Patwardhan, J. A. Satrio, R. C. Brown and B. H. Shanks, *Bioresour. Technol.*, 2010, **101**, 4646–4655.
- 53 D. Mourant, Z. Wang, M. He, X. S. Wang, M. Garcia-Perez, K. Ling and C.-Z. Li, *Fuel*, 2011, **90**, 2915–2922.
- 54 A. Oasmaa, I. Fonts, M. R. Pelaez-samaniego, M. E. Garcia-perez and M. Garcia-perez, , DOI:10.1021/acs.energyfuels.6b01287.
- 55 X. Wang, S. R. A. Kersten, W. Prins and W. P. M. Van Swaaij, *Ind. Eng. Chem.*

6. REFERENCES

- Res.*, 2005, **44**, 8786–8795.
- 56 E. Hoekstra, R. J. M. Westerhof, W. Brilman, W. P. M. Van Swaaij, S. R. A. Kersten, K. J. A. Hogendoorn and M. Windt, *AIChE J.*, 2012, **58**, 2830–2842.
- 57 E. Hoekstra, W. P. M. Van Swaaij, S. R. A. Kersten and K. J. A. Hogendoorn, *Chem. Eng. J.*, 2012, **187**, 172–184.
- 58 S. Zhou, M. Garcia-perez, B. Pecha, A. G. McDonald, S. R. A. Kersten and R. J. M. Westerhof, *Energy & Fuels*, 2013, **27**, 1428–1438.
- 59 W. Shu-lai, *Ind. Eng. Chem. Res.*, 1992, **31**, 1162–1166.
- 60 A. Chaala, H. Pakdel, D. Kretschmer and C. Roy, *J. Anal. Appl. Pyrolysis*, 2007, **78**, 104–116.
- 61 W. A. De Jongh, M. Carrier and J. H. H. Knoetze, *J. Anal. Appl. Pyrolysis*, 2011, **92**, 184–193.
- 62 A. V Bridgwater, *Biomass and Bioenergy*, 2012, **38**, 68–94.
- 63 C. Liu, H. Wang, A. M. Karim, J. Sun and Y. Wang, *Chem. Soc. Rev.*, 2014, **43**, 7594–7623.
- 64 K. Raveendran, A. Ganesh and K. C. Khilar, *Fuel*, 1996, **75**, 987–998.
- 65 M. S. Talmadge, R. M. Baldwin, M. J. Bidy, R. L. McCormick, G. T. Beckham, G. A. Ferguson, S. Czernik, K. A. Magrini-bair, T. D. Foust, P. D. Metelski and M. R. Nimlos, *Green Chem.*, 2014, **16**, 407–453.
- 66 S. D. Stefanidis, K. G. Kalogiannis, E. F. Iliopoulou, C. M. Michailof, P. A. Pilavachi and A. A. Lappas, *J. Anal. Appl. Pyrolysis*, 2014, **105**, 143–150.
- 67 P. Giudicianni, G. Cardone and R. Ragucci, *J. Anal. Appl. Pyrolysis*, 2013, **100**, 213–222.
- 68 R. Fahmi, A. V Bridgwater, I. Donnison, N. Yates and J. M. Jones, *Fuel*, 2008, **87**, 1230–1240.
- 69 H. Yang, R. Yan, H. Chen, D. H. Lee and C. Zheng, *Fuel*, 2007, **86**, 1781–1788.
- 70 M. S. Mettler, S. H. Mushrif, A. D. Paulsen, A. D. Javadekar, D. G. Vlachos and P. J. Dauenhauer, *Energy Environ. Sci.*, 2012, **5**, 5414–5424.
- 71 K. Wu, M. Yang, W. Pu, Y. Wu, Y. Shi and H. sheng Hu, *ACS Sustain. Chem. Eng.*, 2017, **5**, 3509–3516.
- 72 J. Akhtar, N. Saidina and P. Wood, *Renew. Sustain. Energy Rev.*, 2012, **16**, 5101–5109.
- 73 K. G. Kalogiannis, S. Stefanidis, A. Marianou, C. Michailof, A. Kalogianni and A. Lappas, *Waste and Biomass Valorization*, 2015, **6**, 781–790.

- 74 R. E. Key and J. J. Bozell, *ACS Sustain. Chem. Eng.*, 2016, **4**, 5123–5135.
- 75 M. Nik-Azar, M. R. Hajaligol, M. Sohrabi and B. Dabir, *Fuel Process. Technol.*, 1996, **51**, 7–17.
- 76 R. J. Evans and T. A. Milne, *Energy & Fuels*, 1987, **1**, 123–137.
- 77 D. Nowakowski, J. Jones, R. Brydson and a Ross, *Fuel*, 2007, **86**, 2389–2402.
- 78 Q. Hao, B. Li, L. Liu, Z. Zhang, B. Dou and C. Wang, *J. Fuel Chem. Technol.*, 2015, **43**, 34–41.
- 79 J. F. Peters, F. Petrakopoulou and J. Dufour, *Fuel Process. Technol.*, 2014, **119**, 245–255.
- 80 H. Yang, R. J. Coolman, P. Karanjkar, H. Wang, Z. Xu and H. Chen, *Green Chem.*, 2015, **17**, 2912–2923.
- 81 P. Das, A. Ganesh and P. Wangikar, *Biomass and Bioenergy*, 2004, **27**, 445–457.
- 82 T. Wigley, A. C. K. Yip and S. Pang, *Energy*, 2016, **109**, 481–494.
- 83 S. D. Stefanidis, E. Heracleous, D. Th, K. G. Kalogiannis, C. M. Michailof and A. A. Lappas, *Biomass and Bioenergy*, 2015, **83**, 105–115.
- 84 A. Ohliger, M. Förster and R. Kneer, *Fuel*, 2013, **104**, 607–613.
- 85 D. Chen, Y. Li, M. Deng, J. Wang, M. Chen, B. Yan and Q. Yuan, *Bioresour. Technol.*, 2016, **214**, 615–622.
- 86 A. Zheng, Z. Zhao, S. Chang, Z. Huang, F. He and H. Li, *Energy & Fuels*, 2012, **26**, 2968–2974.
- 87 M. I. Jahirul, M. G. Rasul, A. A. Chowdhury and N. Ashwath, *Energies*, 2012, **5**, 4952–5001.
- 88 M. Tripathi, J. N. Sahu and P. Ganesan, *Renew. Sustain. Energy Rev.*, 2016, **55**, 467–481.
- 89 D. Vamvuka, *Int. J. Energy Res.*, 2011, **35**, 835–862.
- 90 P. Roy and G. Dias, *Renew. Sustain. Energy Rev.*, 2017, **77**, 59–69.
- 91 K. Słopiecka, P. Bartocci and F. Fantozzi, *Appl. Energy*, 2012, **97**, 491–497.
- 92 F.-X. Collard and J. Blin, *Renew. Sustain. Energy Rev.*, 2014, **38**, 594–608.
- 93 D. S. Scott, P. Majerski, J. Piskorz and D. Radlein, *J. Anal. Appl. Pyrolysis*, 1999, **51**, 23–37.
- 94 J. A. García-Nunez, M. R. Pelaez-Samaniego, M. E. García-Pérez, I. Fonts, J. Abrego, R. J. M. Westerhof and M. García-Pérez, *Energy & Fuels*, 2017, **31**, 5751–5775.
- 95 M. Grønli, M. J. Antal and G. Várhegyi, *Ind. Eng. Chem. Res.*, 1999, **38**, 2238–2244.

6. REFERENCES

- 96 S. Papari and K. Hawboldt, *Renew. Sustain. Energy Rev.*, 2015, **52**, 1580–1595.
- 97 Y. Mei and R. Liu, *Fuel Process. Technol.*, 2017, **161**, 204–219.
- 98 B. M. Wagenaar, J. A. M. Kuipers, W. Prins and W. P. M. van Swaaij, in *Advances in Thermochemical Biomass Conversion*, 1993, pp. 1122–1133.
- 99 B. M. Wagenaar, R. H. Venderbosch, J. Carrasco, R. Strenziok and B. J. Aa, van der, in *Progress in thermochemical biomass conversion*, 2008, pp. 1268–1280.
- 100 M. Amutio, G. Lopez, M. Artetxe, G. Elordi, M. Olazar and J. Bilbao, *Resour. Conserv. Recycl.*, 2012, **59**, 23–31.
- 101 J. Makibar, A. R. Fernandez-Akarregi, I. Alava, F. Cueva, G. Lopez and M. Olazar, *Chem. Eng. Process. Process Intensif.*, 2011, **50**, 790–798.
- 102 A. R. Fernandez-Akarregi, J. Makibar, G. Lopez, M. Amutio and M. Olazar, *Fuel Process. Technol.*, 2013, **112**, 48–56.
- 103 D. A. Johnson, D. Maclean, J. F. Eller, J. Diebold and H. L. Chumt, *Biomass and Bioenergy*, 1994, **7**, 259–266.
- 104 G. Peacocke and A. Bridgwater, *Biomass and Bioenergy*, 1995, **7**, 147–154.
- 105 A. V. Bridgwater, D. Meier and D. Radlein, *Org. Geochem.*, 1999, **30**, 1479–1493.
- 106 C. Roy, I. Pyrolysis and P. Development, in *Biomass Gasification and Pyrolysis: State of the Art and Future Prospects*, eds. M. Kaltschmitt and A. V. Bridgwater, CPL Scientific Ltd., Newbury, Berkshire UK, 1997.
- 107 J. A. Knight, C. W. Gorton and R. J. Kovac, *Biomass*, 1984, **6**, 69–76.
- 108 B. Zhang, Z. Zhong, P. Chen and R. Ruan, *Bioresour. Technol.*, 2015, **197**, 79–84.
- 109 M. Bartoli, L. Rosi, A. Giovannelli, P. Frediani and M. Frediani, *J. Anal. Appl. Pyrolysis*, 2016, **119**, 224–232.
- 110 R. M. Baldwin and C. J. Feik, *Energy & Fuels*, 2013, **27**, 3224–3238.
- 111 P. S. Rezaei, H. Shafaghat and W. M. A. W. Daud, *Appl. Catal. A Gen.*, 2014, **469**, 490–511.
- 112 A. de R. Pinho, M. B. B. de Almeida, F. L. Mendes, L. C. Casavechia, M. S. Talmadge, C. M. Kinchin and H. L. Chum, *Fuel*, 2017, **188**, 462–473.
- 113 Á. Ibarra, E. Rodríguez, U. Sedran, J. M. Arandes and J. Bilbao, *Ind. Eng. Chem. Res.*, 2016, **55**, 1872–1880.
- 114 C. Freeman, S. Jones and A. Padmaperuma, *Initial assessment of US refineries for purposes of potential bio-based oil insertions*, 2013.
- 115 V. Paasikallio, K. Kalogiannis, A. Lappas, J. Lehto and J. Lehtonen, *Energy Technol.*, 2017, **5**, 94–103.

-
- 116 K. E. Pankin, Y. V. Ivanova, R. I. Kuz'Mina and S. N. Shtykov, *Chem. Technol. Fuels Oils*, 2011, **47**, 8–10.
- 117 A. Veses, M. Aznar, J. M. López, M. S. Callén, R. Murillo and T. García, *Fuel*, 2015, **141**, 17–22.
- 118 A. H. Zacher, M. V. Olarte, D. M. Santosa, D. C. Elliott and S. B. Jones, *Green Chem.*, 2014, **16**, 491–515.
- 119 N. Tran, Y. Uemura, S. Chowdhury and A. Ramli, in *Applied Mechanics and Materials*, 2014, pp. 255–258.
- 120 A. Popov, E. Kondratieva, J. M. Goupil, L. Mariey, P. Bazin, J. P. Gilson, A. Travert and F. Maugé, *J. Phys. Chem. C*, 2010, **114**, 15661–15670.
- 121 H. Wang, J. Male and Y. Wang, *ACS Catal.*, 2013, **3**, 1047–1070.
- 122 T. M. Sankaranarayanan, A. Berenguer, C. Ochoa-Hernández, I. Moreno, P. Jana, J. M. Coronado, D. P. Serrano and P. Pizarro, *Catal. Today*, 2015, **243**, 163–172.
- 123 T. M. Sankaranarayanan, M. Kreider, A. Berenguer, S. Gutiérrez-Rubio, I. Moreno, P. Pizarro, J. M. Coronado and D. P. Serrano, *Fuel*, 2018, **214**, 187–195.
- 124 D. A. Ruddy, J. A. Schaidle, J. R. Ferrell III, J. Wang, L. Moens and J. E. Hensley, *Green Chem.*, 2014, **16**, 454–490.
- 125 M. Saidi, F. Samimi, D. Karimipourfard, T. Nimmanwudipong, B. C. Gates and M. R. Rahimpour, *Energy Environ. Sci.*, 2014, **7**, 103–129.
- 126 A. Berenguer, T. M. Sankaranarayanan, G. Gómez, I. Moreno, J. M. Coronado, P. Pizarro and D. P. Serrano, *Green Chem.*, 2016, **18**, 1938–1951.
- 127 J. Wildschut, F. H. Mahfud, R. H. Venderbosch and H. J. Heeres, *Ind. Eng. Chem. Res.*, 2009, **48**, 10324–10334.
- 128 P. M. Mortensen, J. D. Grunwaldt, P. A. Jensen, K. G. Knudsen and A. D. Jensen, *Appl. Catal. A Gen.*, 2011, **407**, 1–19.
- 129 A. M. Robinson, J. E. Hensley and J. Will Medlin, *ACS Catal.*, 2016, **6**, 5026–5043.
- 130 C. A. Mullen, A. A. Boateng, N. M. Goldberg, I. M. Lima, D. A. Laird and K. B. Hicks, *Biomass and Bioenergy*, 2010, **34**, 67–74.
- 131 A. R. K. Gollakota, M. Reddy, M. D. Subramanyam and N. Kishore, *Renew. Sustain. Energy Rev.*, 2016, **58**, 1543–1568.
- 132 J. . Diebold and S. Czernik, *Energy & Fuels*, 1997, **11**, 1081–1091.
- 133 W. Shen, G. A. Tompsett, R. Xing, W. C. Conner and G. W. Huber, *J. Catal.*, 2012, **286**, 248–259.
- 134 G. Pacchioni, *ACS Catal.*, 2014, **4**, 2874.
-

6. REFERENCES

- 135 R. French and S. Czernik, *Fuel Process. Technol.*, 2010, **91**, 25–32.
- 136 A. Galadima and O. Muraza, *Energy Convers. Manag.*, 2015, **105**, 338–354.
- 137 G. Yildiz, F. Ronsse, R. van Duren and W. Prins, *Renew. Sustain. Energy Rev.*, 2016, **57**, 1596–1610.
- 138 M. Zabeti, T. S. Nguyen, L. Lefferts, H. J. Heeres and K. Seshan, *Bioresour. Technol.*, 2012, **118**, 374–381.
- 139 M. Zabeti, J. Baltrusaitis and K. Seshan, *Catal. Today*, 2016, **269**, 156–165.
- 140 Q. Lu, Z. Tang, Y. Zhang and X. Zhu, *Ind. Eng. Chem. Res.*, 2010, **49**, 2573–2580.
- 141 E. H. Lee, M. J. Jeon, J. K. Jeon, D. J. Suh, S. H. Park, B. Seo, S. H. Joo and Y. K. Park, *J. Nanosci. Nanotechnol.*, 2014, **14**, 2343–2351.
- 142 F. Yu, L. Gao, W. Wang, G. Zhang and J. Ji, *J. Anal. Appl. Pyrolysis*, 2013, **104**, 325–329.
- 143 E. Pütün, *Energy*, 2010, **35**, 2761–2766.
- 144 S. D. Stefanidis, S. A. Karakoulia, K. G. Kalogiannis, E. F. Iliopoulou, A. Delimitis, H. Yiannoulakis, T. Zampetakis, A. A. Lappas and K. S. Triantafyllidis, *Appl. Catal. B Environ.*, 2016, **196**, 155–173.
- 145 X. Zhang, L. Sun, L. Chen, X. Xie, B. Zhao, H. Si and G. Meng, *J. Anal. Appl. Pyrolysis*, 2014, **108**, 35–40.
- 146 T. S. Nguyen, M. Zabeti, L. Lefferts, G. Brem and K. Seshan, *Bioresour. Technol.*, 2013, **142**, 353–360.
- 147 M. Auta, L. M. Ern and B. H. Hameed, *J. Anal. Appl. Pyrolysis*, 2014, **107**, 67–72.
- 148 A. M. Elfadly, I. F. Zeid, F. Z. Yehia, M. M. Abouelela and A. M. Rabie, *Fuel Process. Technol.*, 2017, **163**, 1–7.
- 149 S. Wang, Z. Li, X. Bai, W. Yi and P. Fu, *Bioresour. Technol.*, 2019, **278**, 66–72.
- 150 S. Wang, Z. Li, X. Bai, W. Yi and P. Fu, *J. Anal. Appl. Pyrolysis*, 2018, **136**, 8–17.
- 151 D. P. Serrano, J. A. Melero, G. Morales and J. Iglesias, *Catal. Rev.*, 2018, **60**, 1–70.
- 152 J. Přeč, P. Pizarro, D. P. Serrano and J. Čejka, *Chem. Soc. Rev.*, 2018, **47**, 8263–8306.
- 153 T. S. Nguyen, M. Zabeti, L. Lefferts, G. Brem and K. Seshan, *Biomass and Bioenergy*, 2013, **48**, 100–110.
- 154 D. P. Gamliel, H. J. Cho, W. Fan and J. A. Valla, *Appl. Catal. A Gen.*, 2016, **522**, 109–119.
- 155 D. M. Alonso, J. Q. Bond and J. A. Dumesic, *Green Chem.*, 2010, **12**, 1493–1513.
- 156 T. C. Hoff, D. W. Gardner, R. Thilakarathne, J. Proano-Aviles, R. C. Brown and J. P.

- Tessonnier, *Appl. Catal. A Gen.*, 2017, **529**, 68–78.
- 157 T. C. Hoff, D. W. Gardner, R. Thilakaratne, K. Wang, T. W. Hansen, R. C. Brown and J. P. Tessonnier, *ChemSusChem*, 2016, **9**, 1473–1482.
- 158 A. Zheng, Z. Zhao, S. Chang, Z. Huang, H. Wu, X. Wang, F. He and H. Li, *J. Mol. Catal. A Chem.*, 2014, **383–384**, 23–30.
- 159 Y. T. Cheng, J. Jae, J. Shi, W. Fan and G. W. Huber, *Angew. Chem. Int. Ed.*, 2012, **51**, 1387–1390.
- 160 J. Jae, G. A. Tompsett, A. J. Foster, K. D. Hammond, S. M. Auerbach, R. F. Lobo and G. W. Huber, *J. Catal.*, 2011, **279**, 257–268.
- 161 W. Khan, X. Jia, Z. Wu, J. Choi and A. Yip, *Catalysts*, 2019, **9**, 127.
- 162 T. C. Hoff, M. J. Holmes, J. Proano-Aviles, L. Emdadi, D. Liu, R. C. Brown and J. P. Tessonnier, *ACS Sustain. Chem. Eng.*, 2017, **5**, 8766–8776.
- 163 L. Y. Jia, M. Raad, S. Hamieh, J. Toufaily, T. Hamieh, M. Bettahar, G. Mauviel, M. Tarrighi, L. Pinard and A. Dufour, *Green Chem.*, 2017, **19**, 5442–5459.
- 164 K. Ding, Z. Zhong, J. Wang, B. Zhang, M. Addy and R. Ruan, *J. Anal. Appl. Pyrolysis*, 2017, **125**, 153–161.
- 165 K. S. Triantafyllidis, E. F. Iliopoulou, E. V. Antonakou, A. A. Lappas, H. Wang and T. J. Pinnavaia, *Microporous Mesoporous Mater.*, 2007, **99**, 132–139.
- 166 H. Zhang, J. Zheng and R. Xiao, *BioResources*, 2013, **8**, 5612–5621.
- 167 S. Kelkar, C. M. Saffron, Z. Li, S.-S. Kim, T. J. Pinnavaia, D. J. Miller and R. Kriegel, *Green Chem.*, 2014, **16**, 803–812.
- 168 Y. Zheng, F. Wang, X. Yang, Y. Huang, C. Liu, Z. Zheng and J. Gu, *J. Anal. Appl. Pyrolysis*, 2017, **126**, 169–179.
- 169 D. P. Gamliel, G. M. Bollas and J. A. Valla, *Energy Technol.*, 2017, **5**, 172–182.
- 170 M. A. Uguina, J. L. Sotelo and D. P. Serrano, *Appl. Catal.*, 1991, **76**, 183–198.
- 171 A. de Lucas, J. L. Valverde, P. Sánchez, F. Dorado and M. J. Ramos, *Ind. Eng. Chem. Res.*, 2004, **43**, 8217–8225.
- 172 K. Iisa, R. J. French, K. A. Orton, S. Budhi, C. Mukarakate, A. R. Stanton, M. M. Yung and M. R. Nimlos, *Top. Catal.*, 2016, **59**, 94–108.
- 173 E. Kantarelis, W. Yang and W. Blasiak, *Fuel*, 2014, **122**, 119–125.
- 174 A. Aho, N. Kumar, K. Eränen, M. Hupa, T. Salmi and D. Y. Murzin, *Stud. Surf. Sci. Catal.*, 2008, **174**, 1069–1074.
- 175 J. S. J. Hargreaves and A. L. Munnoch, *Catal. Sci. Technol.*, 2013, **3**, 1165–1171.
- 176 D. Gertenbach and B. L. Cooper, *Pap. 509f, Present. AIChE Natl. Meet.*

6. REFERENCES

- 177 A. Corma, C. Corell and J. Pérez-Pariente, *Zeolites*, 1995, **15**, 2–8.
- 178 J. Pavlatová, P. Chlubná, W. J. Roth and M. Kub, 2012, **179**, 35–42.
- 179 J. Aguado, D. P. Serrano and J. M. Rodríguez, *Microporous Mesoporous Mater.*, 2008, **115**, 504–513.
- 180 D. P. Serrano, J. Aguado, J. M. Escola, J. M. Rodríguez and A. Peral, *Chem. Mater.*, 2006, **18**, 2462–2464.
- 181 M. Choi, K. Na, J. Kim, Y. Sakamoto, O. Terasaki and R. Ryoo, *Nature*, 2009, **461**, 246–250.
- 182 K. Na, C. Jo, J. Kim, W.-S. Ahn and R. Ryoo, *ACS Catal.*, 2011, **1**, 901–907.
- 183 Y. . He, G. . Nivarthi, F. Eder, K. Seshan and J. . Lercher, *Microporous Mesoporous Mater.*, 1998, **25**, 207–224.
- 184 B. Lippens and J. H. de Boer, *J. Catal.*, 1965, **4**, 319–323.
- 185 J. H. de Boer, B. G. Linsen and T. J. Osinga, *J. Catal.*, 1965, **4**, 643–648.
- 186 J. Jagiello and M. Thommes, *Carbon N. Y.*, 2004, **42**, 1227–1232.
- 187 C. A. Emeis, *J. Catal.*, 1993, **141**, 347–354.
- 188 N. Wang, D. Chen, U. Arena and P. He, *Appl. Energy*, 2017, **191**, 111–124.
- 189 D. P. Serrano, J. Aguado, J. M. Rodríguez and A. Peral, *J. Anal. Appl. Pyrolysis*, 2007, **79**, 456–464.
- 190 K. Qiao, X. Shi, F. Zhou, H. Chen, J. Fu, H. Ma and H. Huang, *Appl. Catal. A Gen.*, 2017, **547**, 274–282.
- 191 T. Carlson, J. Jae, Y. Lin, G. Tompsett and G. Huber, *J. Catal.*, 2010, **270**, 110–124.
- 192 K. Wang, J. Zhang, B. H. Shanks and R. C. Brown, *Appl. Energy*, 2015, **148**, 115–120.
- 193 D. J. Nowakowski and J. M. Jones, *J. Anal. Appl. Pyrolysis*, 2008, **83**, 12–25.
- 194 E. Jakab, E. Mészáros and J. Borsa, *J. Anal. Appl. Pyrolysis*, 2010, **87**, 117–123.
- 195 S. Soares, G. Camino and S. Levchik, *Polym. Degrad. Stab.*, 1998, **62**, 25–31.
- 196 D. Fabbri, C. Torri and V. Baravelli, *J. Anal. Appl. Pyrolysis*, 2007, **80**, 24–29.
- 197 M. I. Nokkosmäki, E. T. Kuoppala, E. A. Leppämäki and A. O. I. Krause, *J. Anal. Appl. Pyrolysis*, 2000, **55**, 119–131.
- 198 E. F. Iliopoulou, S. Stefanidis, K. Kalogiannis, A. C. Psarras, A. Delimitis, K. S. Triantafyllidis and A. A. Lappas, *Green Chem.*, 2014, **16**, 662–674.
- 199 C. Liu, H. Wang, A. M. Karim, J. Sun and Y. Wang, *Chem. Soc. Rev.*, 2014, **43**, 7594–7623.
- 200 C. Delitala, M. D. Alba, A. I. Becerro, D. Delpiano, D. Meloni, E. Musu and I.

- Ferino, *Microporous Mesoporous Mater.*, 2009, **118**, 1–10.
- 201 L. Zhou, H. Yang, H. Wu, M. Wang and D. Cheng, *Fuel Process. Technol.*, 2013, **106**, 385–391.
- 202 W. L. Fanchiang and Y. C. Lin, *Appl. Catal. A Gen.*, 2012, **419–420**, 102–110.
- 203 K. Na, M. Choi, W. Park, Y. Sakamoto, O. Terasaki and R. Ryoo, *J. Am. Chem. Soc.*, 2010, **132**, 4169–4177.
- 204 C. Hu, R. Xiao and H. Zhang, *Bioresour. Technol.*, 2017, **243**, 1133–1140.
- 205 A. A. Lappas, K. G. Kalogiannis, E. F. Iliopoulou, K. S. Triantafyllidis and S. D. Stefanidis, *Wiley Interdiscip. Rev. Energy Environ.*, 2012, **1**, 285–297.
- 206 D. Kubička, I. Kubičková and J. Čejka, *Catal. Rev. Sci. Eng.*, 2013, **55**, 1–78.
- 207 X. Chen, Y. Chen, H. Yang, X. Wang, Q. Che, W. Chen and H. Chen, *Bioresour. Technol.*, 2019, **273**, 153–158.
- 208 W. Shen, G. A. Tompsett, K. D. Hammond, R. Xing, F. Dogan, C. P. Grey, W. C. Conner, S. M. Auerbach and G. W. Huber, *Appl. Catal. A Gen.*, 2011, **392**, 57–68.
- 209 D. Liang, G. Li, Y. Liu, J. Wu and X. Zhang, *Catal. Commun.*, 2016, **81**, 33–36.
- 210 S. Wang and E. Iglesia, *J. Phys. Chem. C*, 2016, **120**, 21589–21616.
- 211 M. Signoretto, F. Menegazzo, L. Contessotto, F. Pinna, M. Manzoli and F. Boccuzzi, *Appl. Catal. B Environ.*, 2013, **129**, 287–293.

LIST OF FIGURES

Figure 1.1. European Final Energy Consumption by Source and Sector in 2016. Data from ¹⁰ .15	15
Figure 1.2. Main routes for the conversion of continental biomass into liquid biofuels. ^{13,31,32} ..17	17
Figure 1.3. Process flow diagram of a bubbling-bed reactor for the pyrolysis of biomass. ⁶³21	21
Figure 1.4. Esterification reaction.23	23
Figure 1.5. Aldol-condensation reaction.24	24
Figure 1.6. Ketonisation reaction.24	24
Figure 1.7. General scheme of the main CFP reaction pathways over acid catalysts. ¹⁵³25	25
Figure 3.1. Laboratory experimental set-up catalytic fast-pyrolysis set up.....37	37
Figure 4.1. Oxygen concentration versus energy yield of the bio-oil* fraction obtained in the fast-pyrolysis tests (catalytic and non-catalytic) of de-ashed and raw biomass samples.42	42
Figure 4.2. Main compound families in the bio-oil obtained by fast-pyrolysis of raw and de-ashed biomass samples.43	43
Figure 4.3. Product yield distribution in the catalytic fast-pyrolysis tests of the raw and de-ashed camelina straw with fresh and regenerated catalyst.45	45
Figure 4.4. Concentration of Brønsted, C_B (A) and Lewis, C_L (B) acid sites measured for the MCM-22 samples after desorption of pyridine at different temperatures, monitored by FTIR.47	47
Figure 4.5. CO ₂ -TPD curves and overall basicity values of the hierarchical catalysts.....49	49
Figure 4.6. Bio-oil* composition in terms of organic compounds families (% of relative area from GC-MS analyses), obtained in the thermal and catalytic fast pyrolysis of eucalyptus woodchips over the hierarchical zeolites. (AC: acids; ALD: aldehydes; ALC: alcohols; KETÐ: ketones and ethers; FUR: furans; AMN&AMD: amines and amides; O-AR: oxygenated aromatics; AR: aromatics; SUG: anhydro sugars; UNK: unidentified chemicals).....49	49
Figure 4.7. TEM images of the parent materials after calcination: (a, b) PI-ZSM-5 and (c, d) L-ZSM-5.50	50
Figure 4.8. Composition of the bio-oil in term of organic compounds families (% of relative area from GC-MS analyses) obtained in the different fast-pyrolysis tests (catalytic and non-catalytic) of eucalyptus woodchips.....51	51

LIST OF TABLES

- Figure 4.9.** Products yield (A), and gas composition (B) in the catalytic fast-pyrolysis of WS-ac as function of the catalyst to biomass ratio (0.0-0.7). Pyrolysis/Catalyst temperature zones: 550°C/400°C. (C₁-C₃)_p: paraffins; (C₂-C₃)_o: olefins.....54
- Figure 4.10.** Scheme proposed showing the main pathways for the catalytic fast-pyrolysis of lignocellulose over the n-ZSM-5.....55
- Figure 4.11.** TEM images of h-ZSM-5 (a), ZrO₂/h-ZSM-5 (b), n-ZSM-5 (c) and ZrO₂/n-ZSM-5 (d). The marked areas in d correspond to regions rich in ZrO₂ nanoparticles.....56
- Figure 4.12.** Products yield distribution (wt%) (a), Bio-oil oxygen concentration (wt%, dry basis) (b) and gaseous components yield (wt%) (c), in the fast-pyrolysis of WS-ac over ZrO₂ modified ZSM-5's (Catalyst/Biomass = 0.7 g/g, T = 550/400 °C). GO: gaseous olefins (C₂-C₄); GP: gaseous paraffins (C₂-C₄).57
- Figure 4.13.** Total/Quantified bio-oil* components (a), and bio-oil* components mass yields in terms of main organic compounds families (b) obtained in the fast-pyrolysis of WS-ac over the ZrO₂ modified nanocrystalline ZSM-5 and parent zeolite (Catalyst to biomass weight ratio indicated in brackets, T = 550/400 °C).....58
- Figure 4.14.** Bio-oil* oxygen concentration versus bio-oil* energy yield obtained in the WS-ac pyrolysis over both pure clays and ZSM-5 based catalysts.....61
- Figure 4.15.** FTIR spectra of adsorbed CO₂ (~30 μmol g⁻¹ catalyst) over both pure clays and ZSM-5 based materials in the ranges of 2200-2400 cm⁻¹ (A) and 1300-1800 cm⁻¹ (B).....61
- Figure 4.16.** Overall deoxygenation selectivity (a) and catalytic deoxygenation (b), obtained in the WS-ac pyrolysis over the ZrO₂/n-ZSM-5-ATP catalyst using different C/B ratios. N-C: non-catalytic.63
- Figure 4.17.** Bio-oil* deoxygenation degree versus bio-oil energy yield of the catalytic step (referred to those of the thermal bio-oil), obtained in the biomass pyrolysis at laboratory and bench scales over the ZrO₂/n-ZSM-5-ATP catalyst using different C/B ratios.64

LIST OF TABLES

Table 1.1. Main types of pyrolysis according to operation parameters and respective product yields. ^{20,31,89-92}	19
Table 1.2. Typical properties of conventional and catalytic bio-oils and traditional fuels. ^{4,113-115}	22
Table 4.1. Proximate and elemental analyses of the raw (dry) and acid-washed biomass samples	41
Table 4.2. Parameters of the bio-oil* obtained in the catalytic pyrolysis tests of camelina sativa over the n-ZSM-5 zeolite.....	44
Table 4.3. Chemical and textural properties of the hierarchical catalysts.	48
Table 4.4. Physicochemical properties of both pure clays and ZSM-5 based catalysts.....	60

APPENDIX

Article 1

Bio-oil production by lignocellulose fast-pyrolysis: Isolating and comparing the effects of indigenous versus external catalysts

Fuel Processing Technology, 2017, 161, 1, 563-574

Fuel Processing Technology 167 (2017) 563–574

Contents lists available at [ScienceDirect](#)



Fuel Processing Technology

journal homepage: www.elsevier.com/locate/fuproc



Bio-oil production by lignocellulose fast-pyrolysis: Isolating and comparing the effects of indigenous versus external catalysts



Javier Feroso^a, Héctor Hernando^a, Sergio Jiménez-Sánchez^a, Angelos A. Lappas^b, Eleni Heracleous^{b,c}, Patricia Pizarro^{a,d}, Juan M. Coronado^a, David P. Serrano^{a,d,*}

^a Thermochemical Processes Unit, IMDEA Energy Institute, 28935 Móstoles, Madrid, Spain
^b Chemical Process and Energy Resources Institute (CPERI), Centre for Research and Technology Hellas (CERTH), Thessaloniki, Greece
^c School of Science & Technology, International Hellenic University, 57001 Thessaloniki, Greece
^d Chemical and Environmental Engineering Group, ESCET, Rey Juan Carlos University, 28933 Móstoles, Madrid, Spain

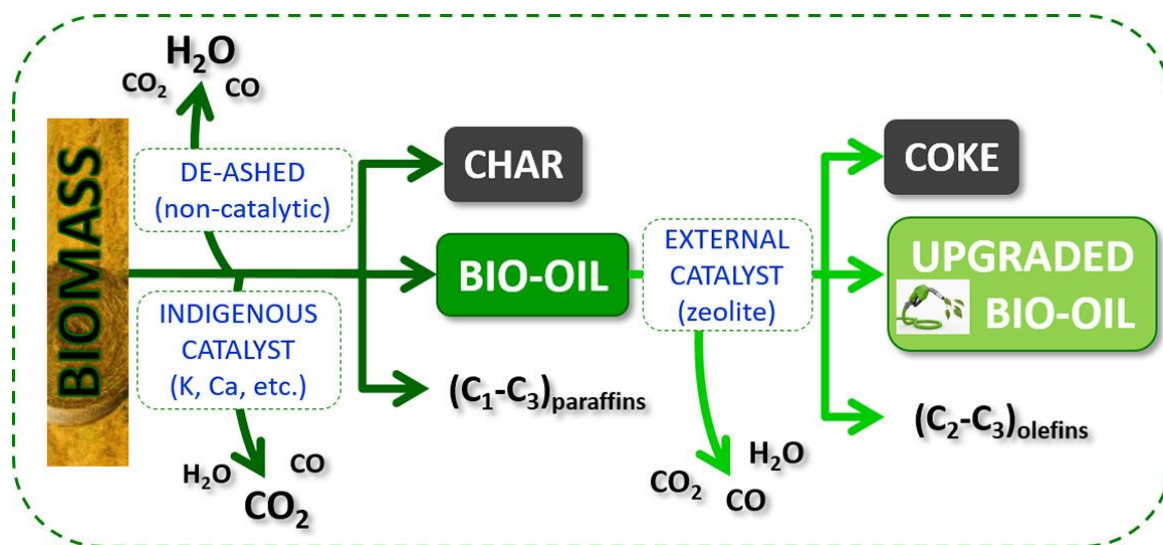
Impact JCR factor, (JCR 2017): 3.956
Category: Applied Chemistry. 8 of 72 (Q1)

ABSTRACT

The effect of both indigenous (mineral components) and external (HZSM-5 zeolite) catalysts on bio-oil production by biomass fast-pyrolysis has been isolated and compared for two herbaceous and two woody biomass samples. Thereby, a variety of lignocellulosic biomasses (in both raw and de-ashed forms) have been subjected to fast pyrolysis tests. Mineral components present in the raw biomasses were removed by an acid-washing treatment. The results obtained showed that both types of catalysts decreased the bio-oil* yield (water-free basis). However, whereas the indigenous catalysts almost did not affect the bio-oil* oxygen content, this parameter was significantly reduced when using the HZSM-5 zeolite. This finding denotes that mineral components are not really effective for bio-oil deoxygenation since they mainly promote the formation of additional char, which retains about 40 % of the chemical energy contained in the raw biomass. In contrast, the external catalyst does favour oxygen removal from the bio-oil. Likewise, the deoxygenation route was strongly dependent on the type of catalyst. In the non-catalytic process dehydration was predominant, the indigenous catalysts favoured decarboxylation, whereas for the external HZSM-5 catalyst decarbonylation became the major deoxygenation pathway. Regarding the bio-oil* composition, both indigenous and external catalysts promoted the conversion of sugars and the formation of carboxylic acids, aldehydes and oxygenated aromatics. However, aromatic hydrocarbons were only produced over the external HZSM-5 catalyst, with a high proportion of alkyl-substituted benzenes and naphthalenes.

Keywords: lignocellulosic biomass, fast-pyrolysis, indigenous catalyst, de-ashing, bio-oil, HZSM-5

GRAPHICAL ABSTRACT



1. Introduction

Lignocellulosic biomass is a widely available and renewable resource with high potential for the production of liquid, solid and gaseous fuels.^{1,2} Fast-pyrolysis, in which biomass is rapidly heated to moderate temperatures (450-550 °C), followed by a fast quenching of vapours and aerosols (< 2 s of residence time) gives rise to three main product categories: solid char, non-condensable gases (H₂, CO, CO₂ and light hydrocarbons), and a dark brown liquid phase including water, with a distinct smoky odour, which is known as bio-oil. This last product may represent up to 70 wt% of the raw biomass, which renders the process highly efficient.³ The bio-oil obtained from non-catalytic fast-pyrolysis (NCFP) consists of a complex mixture of hundreds of oxygenated species derived from the fragmentation of the three main biomass constituents. Contrary to fossil fuels, bio-oils are highly polar, dense and viscous liquids, containing typically a significant amount of water (15-30 wt%) and having acidic nature (pH of 2-3).⁴ Moreover, bio-oils are usually not miscible with hydrocarbons, which limits their direct use as fuels, which is a consequence of their chemical composition and, in particular, of its really high oxygen content (about 40 wt%), as bio-oils consist of a great variety of oxygenated functionalities, including acids, aldehydes, esters, alcohols, ethers, ketones, phenols, sugars and furans.^{4,5}

The quality of bio-oils can be improved by reducing the oxygen content while products are still in the vapour phase (prior to condensation), either by external (*ex situ*) or internal (*in situ*) catalytic fast-pyrolysis (CFP), depending on the placement of the catalyst bed with respect to the pyrolysis reactor.⁵ Catalytic fast-pyrolysis is considered a first bio-oil upgrading step to convert this liquid product into a conventional transport fuel, something that requires almost full deoxygenation.⁶⁻⁹ When pyrolysis vapours enter the pores of the catalyst they undergo a complex series of reactions, including among others cracking, aromatization, ketonization, aldol condensation, isomerization, oligomerization and dehydrogenation. Ideally, deoxygenation should occur mainly through decarboxylation and dehydration. In this fashion, most of the biomass chemical energy is retained in the so produced catalytic bio-oil. However, deoxygenation also takes place by decarbonylation, releasing CO, whereas additional losses of carbon and hydrogen occur due to coke formation and gaseous hydrocarbons production as a consequence of the vapours cracking.^{6,8,10-12}

The final composition of catalytic bio-oils is influenced by several factors, such as the catalyst type and properties, operating conditions and type of biomass. The latter has a strong influence on the quality of the obtained bio-oil, which is an aspect of high relevance considering that commercial catalytic fast-pyrolysis facilities would eventually rely on diverse feedstocks.^{4,13} The determination of the char, gas, and liquid yield of different feedstocks is a very important factor for assessing the viability of biomass fast-pyrolysis. Some authors have reported in the literature that the yield of the main pyrolysis products could be predicted reasonably well from the biopolymers content of the raw biomass, according to the additivity law.¹⁴⁻¹⁶ Nevertheless, according to other studies, it is not that simple as an additive law concerning the biopolymers since the interaction between the released vapours and other factors, such as ash composition,¹⁷⁻²² or catalyst presence^{6,8,10-12,23} may also have significant effects on the final product distribution.

All biomasses contain ash-forming mineral components in the form of cations, which are bound to the organic matrix of biomass at carboxylic and/or phenolic groups, or in the form of precipitates, such as salts.²⁴ These indigenous minerals included in the biomass structure, such as the alkali metals potassium and sodium, and to a lesser extent the alkaline earth metals, calcium and magnesium, are known to catalyse the thermal degradation of biomass.^{25,26} Alkali and alkaline earth

metals (AAEM) are also known to promote secondary cracking and several thermolysis reactions that modify the pyrolysis product distribution by increasing yields of char, water, and gases^{17-19,22,27} resulting in lower yield and quality of liquid organic compounds. These inorganics can be removed from biomass via various demineralization treatments.^{20,28,29} Ash-removal was reported to have a major impact on the non-catalytic biomass fast-pyrolysis products, with demineralized biomasses producing more organic liquid fraction and lower char and gas products, especially CO₂. The composition of the liquid product was also significantly affected as well, with overall higher oxygen content for bio-oil produced from de-ashed feedstocks.

While a number of works in the literature has been focused on the effects derived from the removal of the mineral components for lignocellulose fast pyrolysis, little attention has been paid in the comparison of the catalytic properties of these indigenous catalysts with those of external ones, such as zeolites. Assessing the differences and similarities between these two types of catalysis is relevant to gain further insight into the factors affecting the yield and the quality of pyrolysis bio-oils, and it can help to exploit possible synergies for the upgrading of this liquid fraction. In this context, the present work reports the results of a systematic study aimed at better understanding the effects of both indigenous (mineral components) and external (HZSM-5 zeolite) catalysts in lignocellulose fast-pyrolysis. The results obtained have been interpreted in terms of mass yield, elemental and chemical composition of the produced bio-oil, as well as taking into account the overall energy yield of this fraction with regard to the raw biomass. Remarkable differences have been found between the catalytic effects induced by these two types of catalysts on both the predominant deoxygenation pathway and their effectiveness for bio-oil upgrading. In this way, a simplified pyrolysis scheme has been proposed, illustrating the effect of both indigenous and external catalysts on the bio-oil production by lignocellulose fast pyrolysis.

2. Experimental section

2.1. Materials

The biomass samples selected to carry out this study included forestry residues: woodchips from eucalyptus (EU) and oak (OAK); energy crops: miscanthus (MIS); and agricultural residues: straw from wheat (WS). The biomass samples were ground with a cutter mill and sieved to the desired particle size (0.5-1 mm).

To study the role of minerals on the pyrolysis performance, the biomass samples were partially de-ashed by means of a mild acid-washing pretreatment. The procedure used was as follows:²⁹ 50 g of the biomass were added to 1000 ml of 1 wt% HNO₃ aqueous solution and were subjected to continuous stirring at 50 °C for 2 h. After this pretreatment, the solution was vacuum filtered and the remaining biomass was washed with mili-Q water until reaching pH=6-7. Then, the sample was dried at 105 °C for 2 days. The acid-washed samples are denoted as X-ac (X: EU, OAK, MIS and WS).

For catalytic fast-pyrolysis tests with external catalyst, HZSM-5 zeolite (Si/Al = 42) supplied by CLARIANT was employed. Prior to the pyrolysis tests, the zeolite sample was pelletized, crushed and sieved to the desired particle size of 180-250 µm.

2.2. Thermogravimetric analysis

A TGA analyser (NETZSCH STA 449) was employed to study the effect of the ash on the devolatilisation profile of the raw and acid-washed biomass samples. For that purpose, 10 mg of the sample mass were heated at $10\text{ }^{\circ}\text{C min}^{-1}$ up to $900\text{ }^{\circ}\text{C}$ in an Ar flow of 100 ml min^{-1} .

2.3. Pyrolysis tests

The schematic diagram of the lab-scale experimental setup used for the fast-pyrolysis experiments of raw and acid-washed biomass samples is shown in Fig. 1. It consists of a downdraft fixed-bed stainless steel reactor (16 mm i.d. and 400 mm length) heated by two electrical furnaces. The reaction temperature is measured by two type K thermocouples, placed in the pyrolysis zone and inserted into the catalyst bed, respectively. For the catalytic experiments, the reactor was loaded with 1 g of zeolite

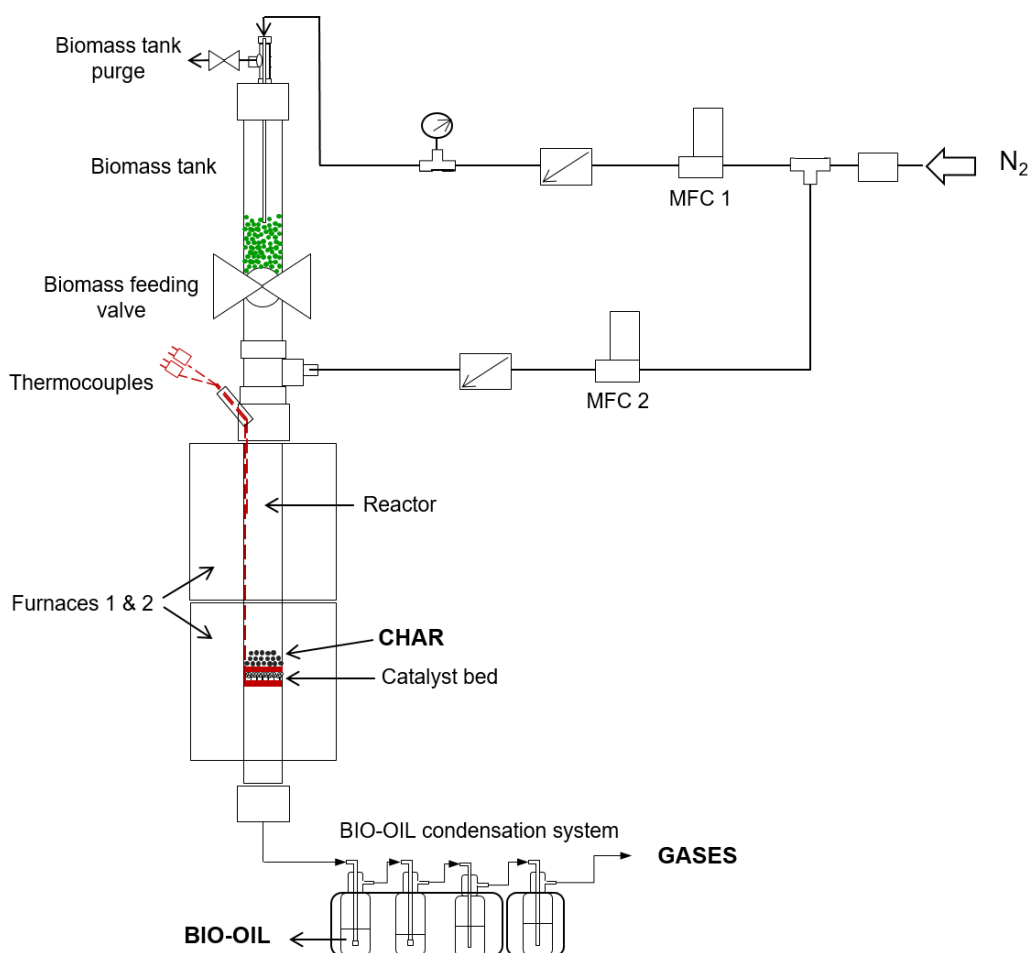


Fig. 1. Schematic diagram of the experimental setup used for the biomass fast pyrolysis experiments.

to attain a biomass/catalyst mass ratio of 5. The biomass sample (5 g) was placed in the biomass tank and kept at room temperature. A quartz wool sheet and a metallic plate were placed over the catalyst particles to avoid physical contact and possible mixing between the char particles and the catalyst bed. The pyrolysis tests were carried out at $500\text{ }^{\circ}\text{C}$ and atmospheric pressure.

Prior to each pyrolysis experiment and during the heating of the reactor, the biomass tank and all the reaction system was purged with N₂ delivered by mass flow controllers to obtain O₂

concentration levels lower than < 0.1 vol%, ensuring that pyrolysis occurs in inert atmosphere. Once the reactor temperature reached the desired set point, the biomass was inserted in the reactor via a feeding valve and was pyrolyzed to form a solid carbonaceous residue (char) and vapours. The volatiles generated in the pyrolysis zone were swept by a N_2 flow of 100 ml min^{-1} and passed through the catalyst bed to leave rapidly the reaction zones, passing through a condensation system composed by four flasks (125 ml each) connected in series and refrigerated by an ice-water bath where the bio-oil components were condensed. Permanent gases and light hydrocarbons (C_1 - C_4) were finally collected in a sampling bag.

2.4. Analytical techniques

European standards were considered for performing the proximate analysis of the biomass samples: moisture content (UNE-EN 14774-1:2010), ash content (UNE-EN 14775:2010), volatile matter (UNE-EN 15148:2010) and fixed carbon (determined by difference). In addition, the elemental analyses were carried out in a micro-elemental analyser (Thermo Scientific) to determine the content of C, H, N, S and O (by difference).

The ash content of the different biomasses was determined by controlled burning of 20 g of each sample, both raw and acid-washed, in a muffle furnace at $815 \text{ }^\circ\text{C}$ in air flow for 2 h and measuring the weight of the remaining solid. The chemical composition of the ash (considering 25 elements in total) was measured by inductively coupled plasma-optical emission spectroscopy (ICP-OES) analyses in a Perkin Elmer Optima 3300 DV instrument. Previously, a representative amount of the ash was digested in a mixture of HF and HNO_3 in an Anton Paar microwave oven (MW3000).

The composition of the gas component was determined in a dual channel Agilent® CP-4900 Micro Gas Chromatograph (Micro-GC), equipped with molecular sieve (Molsieve 5 Å) and HayeSep A columns and a thermal conductivity detector (TCD), using Helium as carrier gas. The Micro-GC was periodically calibrated with a standard gas mixture containing N_2 (internal standard), O_2 , H_2 , CO , CO_2 , CH_4 , C_2H_4 , C_2H_6 , C_3H_6 and C_3H_8 .

The bio-oil was analysed by several techniques. For the catalytic fast-pyrolysis tests, bio-oil was separated into two phases by centrifugation. The water content of bio-oil was determined using a Karl-Fischer titration instrument (ASTM E203-08), whilst its elemental composition of C, H, N, S and O (the latter by difference) was obtained with a Thermo-Scientific micro analyser. The bio-oil fraction was considered in a water-free basis, denoted as bio-oil*. The components present in bio-oil were analysed by a Gas Chromatograph Mass Spectrometer, GC-MS, Bruker® SCION 436-GC, (Electron Energy 70eV, Emission 300V; He flow rate: 1 ml min^{-1} ; Column WCOT fused silica $30 \text{ m} \times 0.25 \text{ mm ID} \times 0.25 \text{ } \mu\text{m}$). NIST EI-MS spectral library (v2.0) was used for the compounds identification (with a minimum match score of 700). Bio-oil compounds were further grouped in families according to their main functional groups.

The chemical composition of the zeolite was determined by ICP-OES. Argon physisorption isotherms at $-186 \text{ }^\circ\text{C}$ were measured on an AUTOSORB iQ system (Quantachrome). The surface area was determined using the Brunauer–Emmet–Teller (BET) equation and the micropore volume was obtained by application of the t-plot method. The acidity of the zeolite was measured by temperature programmed desorption (TPD) of NH_3 using an AUTOCHEM 2910 system (Micromeritics). The procedure applied for the TPD measurements has been earlier described.³⁰

2.5. Experimental methods and data evaluation

After each pyrolysis experiment, the char and the used catalyst were collected for further investigation. Char was characterized in the same way as the biomass, proximate and elemental analyses being performed. In the case of the coke fraction, its amount was determined as the weight loss experienced by the used catalyst in a TGA test with a heating program of 20 °C min⁻¹ up to 550 °C in air atmosphere. Moreover, elemental analysis of coke was carried out in the same way as that of biomass and char samples.

Finally, from the weight of the bio-oil and char fractions and those calculated for coke and gas fractions, the total mass balance was closed to the amount of biomass fed with an experimental error lower than 5 wt% in all tests.

Then, the mass yield of any product fraction was calculated according to Eq. (1):

$$\text{Mass yield } i \text{ (wt\%)} = 100 \cdot [\text{mass } i \text{ (g)} / \text{biomass (g)}] \quad (1)$$

where i = gas, char, bio-oil* (bio-oil in water-free basis), water and coke. In addition, Eq. (2) was used to estimate the mass yield of the different components of the gas fraction:

$$\text{Mass yield } j \text{ (wt\%)} = 100 \cdot [\text{mass } j \text{ (g)} / \text{biomass (g)}] \quad (2)$$

where j = H₂, (C₁-C₃)_{paraffins}, (C₂-C₃)_{olefins}, CO and CO₂.

In addition, the high heating value (HHV) of the biomass and of the different fractions was calculated according to Eq. (3), which is a correlation reported to be valid for solid, liquid and gaseous fuels:³¹

$$\text{HHV}_i \text{ (MJ/kg}^{-1}\text{)} = 0.3491 \cdot C + 1.1783 \cdot H + 0.1005 \cdot S - 0.1034 \cdot O - 0.0151 \cdot N - 0.0211 \cdot A \quad (3)$$

where C, H, O, N, S and A represents carbon, hydrogen, oxygen, nitrogen, sulfur and ash contents of i , expressed in wt% on dry basis. Then, the energy yield of any i fraction was calculated according to Eq. (4):

$$\text{Energy yield } i \text{ (\%)} = 100 \cdot [\text{HHV}_i \cdot \text{mass yield } i / \text{HHV}_{\text{biomass}}] \quad (4)$$

The deoxygenation selectivity to k , being k : H₂O (dehydration), CO (decarbonylation) or CO₂ (decarboxylation), was estimated according to Eq. (5):

$$\text{Deoxygenation } k \text{ (wt\%)} = 100 \cdot [[\text{O}_{k \text{ (cat)}} \text{ (g)} - \text{O}_{k \text{ (de-ashed sample)}} \text{ (g)}] / \text{O}_{\text{biomass}} \text{ (g)}] \quad (5)$$

where $\text{O}_{k \text{ (cat)}}$ is the oxygen content in k obtained in the cat experiments (with raw samples and de-ashed samples with HZSM-5 catalyst); $\text{O}_{k \text{ (de-ashed sample)}}$ is the oxygen content in k obtained with de-ashed samples; and $\text{O}_{\text{biomass}}$ is the oxygen content in the biomass feed. The incremental selectivity corresponding to the two types of catalysts (indigenous and external) was determined by subtracting the CO, CO₂ and H₂O yields obtained in the non-catalytic pyrolysis tests (with de-ashed biomass) from the overall yields of these compounds in the catalytic pyrolysis experiments.

3. Results and discussion

3.1. Catalyst characterization

A commercial HZSM-5 catalyst was used in the present study. The analysis of chemical composition of the zeolite was performed by ICP-OES giving a Si/Al molar ratio of 42. The zeolite surface area was determined using the Brunauer–Emmet–Teller (BET) method and the micropore

volume was obtained by application of the t-plot method. The specific surface area and micropore volume showed values of $445 \text{ m}^2 \text{ g}^{-1}$ and $0.512 \text{ cm}^3 \text{ g}^{-1}$, respectively. The NH_3 TPD curve of the HZMS-5 zeolite exhibited a desorption peak centred at about $396 \text{ }^\circ\text{C}$, with a total amount of adsorbed ammonia of $0.223 \text{ mmol NH}_3 \text{ g}^{-1}$, which is consistent with its Al content.

3.2. Biomass composition and properties

Table 1 presents the chemical composition according to proximate and elemental analyses, as well as the heating value of the four raw biomass samples employed in the present work. The feedstocks were selected as to include both woody and herbaceous biomasses, being representative of largely available feedstock in the form of forestry and agriculture residues, as well as energy crops. The as-received samples (in dry basis) contain between 75-80 wt% of volatile matter, typical of this type of sources. The ash content varies from very low values, as in the case of forestry residues (0.5 wt% in OAK), up to relatively high amounts in the case of MIS (2.5 wt%) and WS (4.7 wt%).

Table 1. Proximate and elemental analyses of the raw (dry) and acid-washed biomass samples

	EU	EU-ac	OAK	OAK-ac	MIS	MIS-ac	WS	WS-ac
Proximate Analysis (wt%)^a								
Ash	1.9	0.3	0.5	0.2	2.5	1.6	4.7	3.5
Volatile Matter	74.7	80.4	80.0	81.4	77.4	85.3	75.3	83.1
Fixed Carbon	23.4	19.3	19.5	18.4	20.1	13.1	20.0	13.4
Ash removal (%)	-	84.2	-	60.0	-	36.0	-	25.5
Elemental Analysis (wt%)^b								
C	51.3	50.9	49.5	49.2	48.8	48.8	47.8	49.1
H	5.9	6.0	5.9	6.0	5.9	5.9	5.9	6.0
N	0.1	0.1	0.0	0.0	0.2	0.2	0.5	0.5
S	-	-	-	-	-	-	-	-
O	42.7	43.0	44.6	44.8	45.1	45.1	45.8	44.4
HHV (MJ/kg_{ab})	20.0	20.3	19.5	19.5	18.8	19.0	17.9	18.9

^a In a dry basis (db)

^b In a dry and ash-free basis (daf)

All materials present elemental compositions typical of lignocellulose with C and O in the range of 47.8-51.3 and 42.7-45.8 wt%, respectively, whereas the H content is about 6 wt% for all the samples. Accordingly, the heating value (HHV) varies in a short range from 17.9 for WS up to 20 MJ kg^{-1} for EU.

Table 2 shows the ash composition expressed as wt% of dry raw samples. It should be noted that only the elements with a content superior to 0.1 wt% are included in this table. It can be observed that Ca and K are the main ash constituents in forestry residues: 0.0263 and 0.0075 wt% respectively for EU, and 0.0081 and 0.007 wt% respectively for OAK. EU also contains significant amounts of P (0.006 wt%) and Mg (0.0037 wt%). In the case of herbaceous samples, MIS and WS, the highest content by far corresponds to Si with values of 0.891 wt%, followed by K (0.251 wt% and 0.28 wt%, respectively) and Ca (0.229 and 0.173 wt%, respectively). Comparison of the

composition of the raw and de-ashed biomass samples denotes that the treatment with dilute aq. nitric acid results in the removal of a great part of the inorganic components, in agreement with previous findings.²⁹ The overall de-ashing effectiveness of the acid-washing procedure significantly varied from 26% for WS to more than 84% for EU, owing to both the easiness of removal for each element and the biomass type. Thus, as shown in Table 2, K and Mg were very effectively removed (91-98%) from all the samples, regardless of the biomass source. On the contrary, Ca was almost entirely eliminated (98-99%) from herbaceous biomasses (MIS and WS), but was partly removed in the case of eucalyptus (79%) and hardly removed from oak (7%). Silicon, present in large amounts in herbaceous biomasses, was barely removed with ratios of 45 and 2% for MIS and WS samples, respectively.

Table 2. ICP analysis of the raw (dry) and acid-washed biomass samples

Element	Element (wt% · 10 ⁻²)							
	EU	EU-ac	OAK	OAK-ac	MIS	MIS-ac	WS	WS-ac
Al	0.2	0.1	---	---	0.9	0.6	1.0	0.6
Ba	---	---	---	---	0.1	---	0.3	---
Ca	26.3	5.6	8.1	7.5	22.9	0.6	17.3	0.2
Fe	1.9	0.1	---	---	0.8	0.4	0.6	0.3
K	7.5	0.2	7.0	0.5	25.1	1.9	28.0	0.6
Mg	3.7	0.3	0.1	---	3.0	0.2	5.0	0.1
Mn	2.5	0.2	0.1	---	0.4	0.1	0.3	---
Na	2.1	---	---	---	1.5	0.5	4.4	0.1
P	6.0	1.3	0.1	---	1.8	0.2	4.7	0.6
Si	1.0	0.8	0.3	0.7	88.1	48.3	89.1	87.2
Sn	2.3	0.1	---	---	0.9	0.4	0.6	0.3
Sr	0.1	---	---	---	0.1	---	0.3	---
Ti	0.1	0.1	---	---	0.1	0.1	0.1	0.1
Zn	0.1	---	---	---	0.1	---	0.1	---

Interestingly, the acid-washing pretreatment had an effect not only on the ash and on minerals content, but it also modified other parameters related with the composition of biomass. The data in Table 1 clearly show that the volatile matter of the acid-washed samples was 8-10% higher than for the raw materials, thereby depleting the biomasses in fixed carbon.³² The only exception was OAK, where very similar proximate analyses were obtained before and after the acid-washing treatment. This can be attributed to the originally very low ash content of this biomass.

Catalytically active elements, such as K and divalent elements like Ca and Mg, have been found to act as cross-links to stabilize the 3-D structure of lignin or between lignin and cellulose/hemicellulose, causing further breakdown of weak bonds to produce lighter components in bio-oil.³³ This finding agrees well with the above-commented increase in the proportion of volatile matter at the expense of fixed carbon in the de-ashed biomasses. On the other hand, the elemental analyses (in dry, ash-free basis) of both raw and acid-washed samples are fairly similar for all the biomass samples, with just relatively small variations observed in the C, H, N and O content. Consequently, the acid-washing treatment has little effect on the HHV of the biomass

feedstocks, with the exception of WS where a significant enhancement of the HHV is detected after the acid-washing treatment.

The thermal decomposition of both raw and de-ashed samples in inert atmosphere was investigated with TG analyses. Fig. 2 plots TGA results showing that lignocellulose conversion occurs through a series of transformations in a broad temperature range.^{34,35} The first peak observed in the differential weight loss curves, with maximum between 270-300 °C, is attributed to the decomposition of hemicellulose, which presents the least stable structure (200-300 °C). The second peak corresponds to cellulose, which is the component in biomass showing the highest decomposition rate, its maximum being located between 330 and 355 °C. Finally, lignin degradation occurs in a very wide temperature range (200-500 °C), leading to broadening of the DTG curve.^{32,36}

Removal of minerals increases the overall TG weight loss, which agrees well with the higher volatile matter content of the de-ashed biomass samples. Moreover, for the latter, a shift towards higher temperatures is observed in the position of the peak maxima for both cellulose and hemicellulose. This suggests that the activation energy for the pyrolysis of the holocellulose components increases after the removal of the inorganic species, which is in agreement with the previously reported catalytic role of minerals in biomass pyrolysis.^{26,32,37} Oak constitutes an exception, due to its extremely low ash content, with the TGA curves being very similar before and after acid treatment, as also occurred in the case of the proximate analysis results.

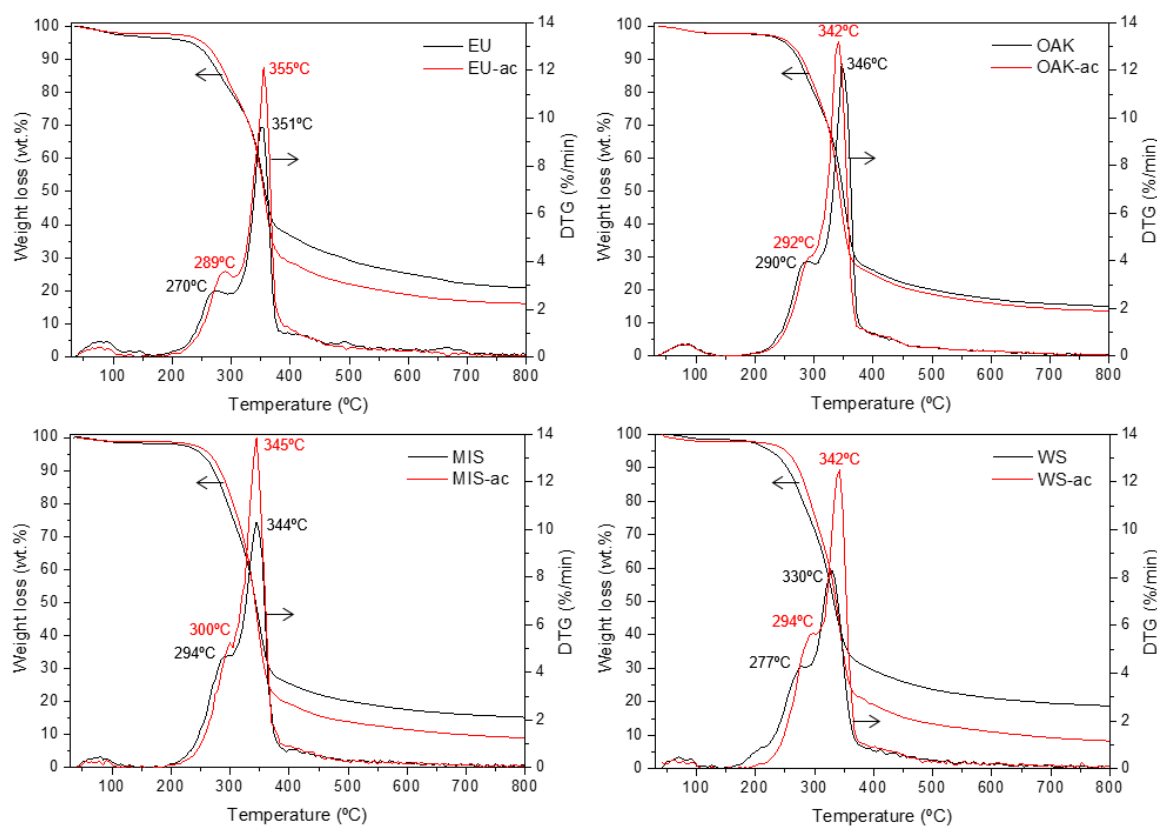


Fig. 2. Thermogravimetric analysis, TG and DTG curves, of raw and de-ashed biomass samples. (Reaction conditions: 100 ml min⁻¹ Ar; heating rate, 10 °C min⁻¹, from room temperature to 800 °C).

3.3. Biomass fast-pyrolysis in absence of external catalyst

Before considering catalytic fast-pyrolysis by coupling the thermal treatment with a zeolite HZSM-5 bed, it is important to keep in mind that biomass contains within its structure a variety of elements that can act as catalysts susceptible to participate in the pyrolysis process. These indigenous catalysts are mostly alkali and alkaline earth metals (AAEM) that form part of the ash, their content varying depending on the biomass feedstock as discussed above. In addition, it is important to keep in mind that the char produced in the pyrolysis process can also play a role in promoting secondary reactions of the vapours, such as dehydration and tar cracking, at the relatively high temperature of operation used in this study.³⁸ Accordingly, even in absence of the zeolite catalyst, not purely primary reactions of thermal cracking are observed in these tests.

The four different biomass samples were first subjected to thermal fast-pyrolysis, before and after the acid-washing pretreatment. The mass yields obtained for the different fractions are shown in Fig. 3. It can be observed that ash removal leads to an improvement in the bio-oil* production at the expense of gas, water and char fractions, in accordance with other literature studies.^{22,39} These changes are more pronounced for herbaceous biomasses (WS and MIS), which demonstrate a noteworthy improvement in the bio-oil* yield upon removal of the mineral components (principally K), mainly at the expense of gases. These results confirm that mineral components in ash (particularly potassium), which are most likely dispersed in the char fraction and accordingly in contact with the liberated vapours, catalyse decarbonylation and decarboxylation reactions,¹⁰ giving rise to enhanced production of gases compared to de-ashed biomass. This effect is illustrated in Fig. 4, showing a linear relationship between the production of CO and CO₂ and the K content in biomass, regardless of the biomass type. This dependence is more remarkable in the case of CO₂ formation, suggesting that potassium preferentially promotes decarboxylation as deoxygenation route. Moreover, the production of light hydrocarbons, mostly CH₄, seems to increase also with the K content in biomass. CH₄ formation is mainly attributed to the fragmentation of the methoxyl O-CH₃ groups present in lignin constituents.^{34,35}

Water is another key product of biomass pyrolysis. It is produced from various dehydration reactions of the original biomass biopolymers and/or dehydration of the primary and secondary pyrolysis products. Water is recovered as a component of the bio-oil fraction, its concentration being determined by Karl-Fisher titration. The elimination of the inorganic material from the biomass samples also affects the water content of the obtained bio-oils, decreasing from 24-31 wt% for the raw materials to 18-24 wt% for the de-ashed samples (Fig. 3). However, no clear trend can be observed, as water yield decreases slightly for EU and WS, but does not change in the case of OAK and MIS after the acid-washing treatment.

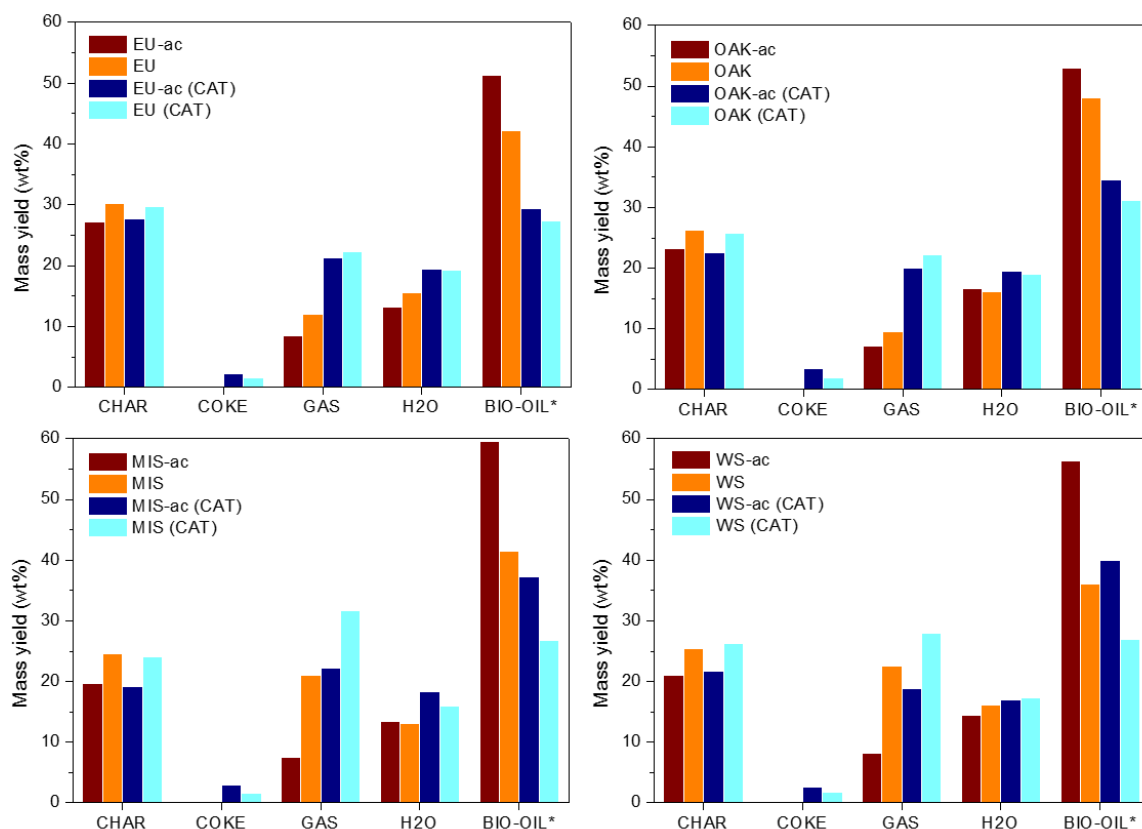


Fig. 3. Products yield in the fast-pyrolysis tests, non-catalytic and catalytic, of de-ashed and raw biomass samples.

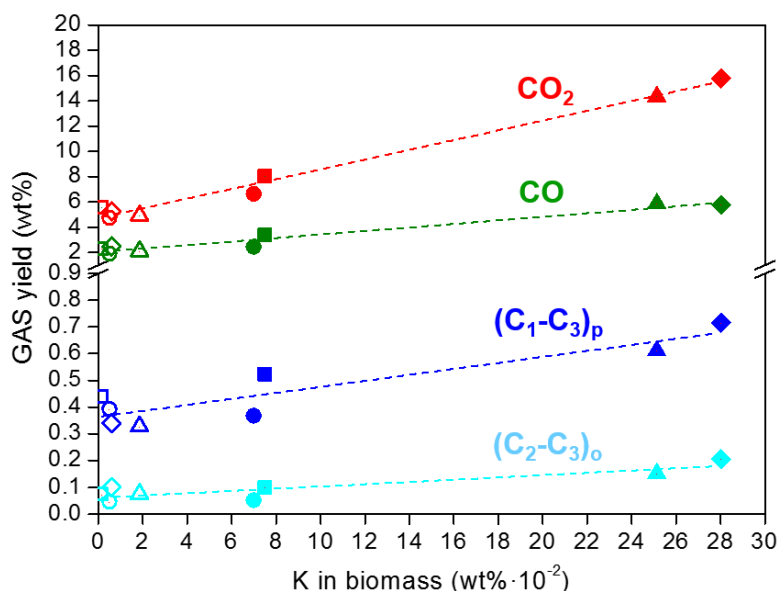


Fig. 4. Production of different gas components in the non-catalytic (open symbols) and internal catalytic (filled symbols) fast pyrolysis of biomass samples as a function of the potassium (K) content in biomass. (C₁-C₃)_p: paraffins; (C₂-C₃)_o: olefins.

In order to get further insights about the different deoxygenation pathways, the selectivity towards dehydration, decarbonylation and decarboxylation is plotted in Fig. 5. In the absence of any catalytically-active component, i.e. when employing de-ashed biomasses (Fig. 5(A)),

dehydration is clearly the predominant pathway (68-77%), followed by decarboxylation and finally decarbonylation. In the case of the non-treated raw biomasses (Fig. 5(B)), the incremental deoxygenation selectivity induced by the indigenous catalysts was calculated by subtracting the production of CO, CO₂ and H₂O corresponding to the de-ashed biomasses. These data reveal that decarboxylation becomes the main deoxygenation route over indigenous catalysts with some contribution of decarbonylation, whilst dehydration route is hardly promoted with regard to the level observed for de-ashed biomass samples. Only in the case of EU, dehydration remains the most significant route over indigenous catalysts, followed by decarboxylation.

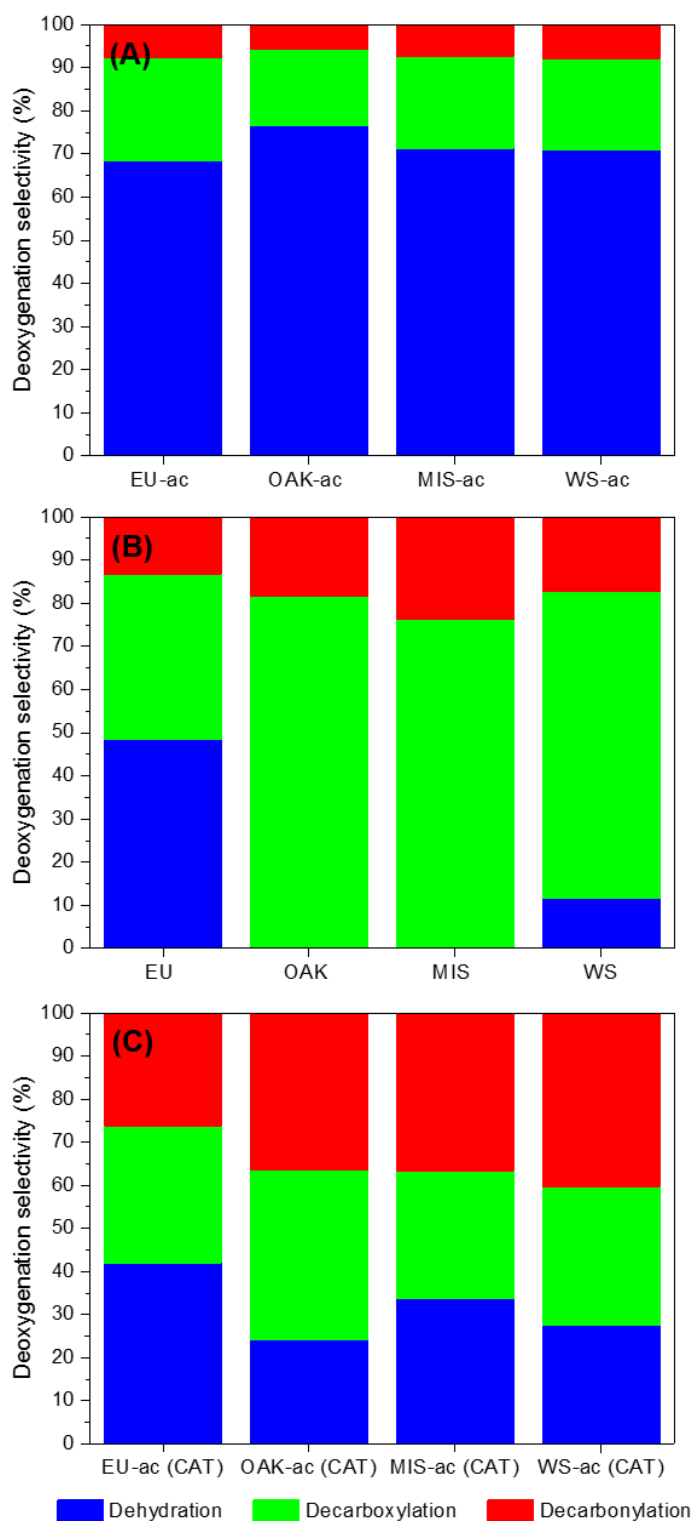


Fig. 5. Deoxygenation selectivity obtained in the non-catalytic fast-pyrolysis tests of de-ashed biomass samples (A), and incremental selectivity of those catalytically obtained by the internal (B) and external (C) catalysts.

The production of char, which is an important by-product of the pyrolysis process, is linked to the biomass ash content since some of its inorganics components may also catalyse carbonization reactions.⁴⁰⁻⁴² Indeed, char production decreased in all samples after de-ashing biomass (Fig. 3), in accordance with the TGA results discussed earlier (Fig. 2). The solid char from biomass pyrolysis

possesses high carbon content, as it retains between 40–47 wt% of the carbon contained in the initial raw biomass. The oxygen content of the char fraction is significant, and it shows appreciable differences between types of biomass, as shown in Table 3. Thus the amount of oxygen in the char obtained from EU is in the range 13–16 wt%, whereas for WS is about 9 wt%. In average, the following order of oxygen content in the char is denoted: EU > OAK > MIS > WS. Moreover, for most biomasses the char oxygen content is lower for the raw samples compared to the acid-washed ones. In contrast, the hydrogen proportion of the char is in all cases relatively similar ranging from 2.9–3.8 wt%, whereas the nitrogen content is in all cases lower than 1 wt%. Consequently, due to the reduced oxygen proportion in the char, a great part of the chemical energy of the raw biomass is retained in the char as summarizes Table 3, with values in the range 38–44% in the case of the raw biomass samples, being lost in terms of energy available in the liquid bio-oil* product. Interestingly, this value is significantly reduced for the de-ashed biomasses; although even in the best cases (WS-ac and MIS-ac), it represents at least $\approx 30\%$ of the biomass chemical energy yield due to the high carbon proportion (> 80 wt%) of this solid product. This is also reflected in the high heating values of the obtained char, which vary from 27 to almost 32 kJ kg⁻¹. This result highlights the relevance of decreasing the formation of char or, alternatively, of using this char in the co-production of energy for the overall pyrolysis process to be truly efficient.^{43,44}

Table 3. Elemental analysis, heating values, and energy yields of the char obtained in the fast-pyrolysis of different raw and de-ashed biomass samples with and without external HZSM-5 catalyst

	Char elemental analysis (wt%) ^a					Char HHV (kJ/kg _{Char}) ^b	Energy Yield (%)
	C	H	N	S	O		
EU-ac	80.1	3.0	0.3	-	16.6	29.4	39.3
EU	83.4	2.9	0.2	-	13.5	29.0	43.8
EU-ac (Cat)	80.0	3.0	0.3	-	16.6	29.4	40.1
EU (Cat)	83.5	2.9	0.2	-	13.4	29.0	43.0
OAK-ac	83.1	3.2	0.5	-	13.2	31.1	37.0
OAK	85.7	3.1	0.1	-	11.1	31.8	42.6
OAK-ac (Cat)	83.2	3.2	0.5	-	13.2	31.1	35.9
OAK (Cat)	85.7	3.1	0.1	-	11.1	31.8	41.8
MIS-ac	83.3	3.4	0.3	-	12.9	29.0	30.0
MIS	87.3	3.5	0.3	-	8.9	30.1	39.3
MIS-ac (Cat)	83.5	3.4	0.3	-	12.8	29.0	29.3
MIS (Cat)	87.1	3.8	0.3	-	8.8	30.2	38.6
WS-ac	86.6	3.6	0.8	-	9.0	27.6	30.6
WS	86.7	3.4	0.7	-	9.2	27.0	38.3
WS-ac (Cat)	86.1	3.6	0.8	-	9.6	27.5	31.5
WS (Cat)	86.9	3.4	0.7	-	9.0	27.0	39.6

^a In a dry and ash-free basis

^b In a dry basis

3.4. Biomass fast-pyrolysis in presence of external catalyst

This section describes the results obtained when the biomass pyrolysis vapours were upgraded by passing them over a catalyst bed of HZSM-5 zeolite. This material has been extensively employed in literature⁴⁵⁻⁵⁰ for biomass catalytic pyrolysis due to its high activity in the production of aromatic hydrocarbons. Therefore, HZSM-5 zeolite was used in this work as a common “external” pyrolysis catalyst to check and compare the catalytic pyrolysis of both raw and de-ashed biomass samples. Operation conditions such as temperature and catalyst to biomass ratio were selected according to a previous study carried out to achieve an optimal balance between energy yield and oxygen content of the bio-oil.⁴⁵

As shown in Fig. 3, the use of an external catalyst drastically reduced the bio-oil* yield over all biomasses. This result was accompanied by an enhanced production of gases and, to less extent, of water. The char yield was hardly affected by the presence of HZSM-5, a rather expected result considering that char is mainly formed before the pyrolysis vapours come into contact with the zeolite bed. Nevertheless, during catalytic reactions, a part of the primary organic vapours may undergo polymerization reactions to form coke deposited over the catalyst.⁴⁴ Accordingly, coke has been considered as a new fraction, being included in the product distribution shown in Fig. 3. It can be observed that for all the biomass types investigated in this work, coke formation is higher for the de-ashed samples compared to the raw biomasses. Interestingly, if the yield of char and coke are considered collectively, the results are very similar for the pyrolysis of biomass before and after acid treatment. This suggests that, at least in terms of solid residues formation, the mineral components of biomass and the external catalyst contribute in a similar way.

Regarding the gas fraction, Fig. 6 compares the yield into the different products obtained in the experiments carried out with and without the external catalyst. The zeolite catalyst clearly enhances the formation of gaseous hydrocarbons, mainly olefins, as it promotes cracking reactions. Among these olefins, propylene is the major product (0.5-0.6 wt%), whereas methane remains the main alkane component (0.4-0.5 wt%). Moreover, the HZSM-5 catalyst favors deoxygenation through both decarbonylation and decarboxylation routes, as denoted by the increased CO and CO₂ production. The enhancement in CO production is particularly impressive, showing yields 3.4-4.9 times higher in the catalytic tests, whilst CO₂ production is enhanced by only 1.7-2.2 times.

In the case of external catalysis over HZMS-5, catalytic bio-oils separate into two distinct phases: an aqueous and an oily, organic-rich phase. This is a result of the overall higher water production and/or the presence of less polar compounds compared to those obtained in the tests without external catalyst. The presence of water was detected in both liquid phases, indicative of the establishment of liquid-liquid equilibrium. The water content of the so-called “aqueous” bio-oil phase obtained from the de-ashed feedstocks showed values of 68 wt% (EU-ac), 62 wt% (OAK-ac), 47 wt% (MIS-ac) and 41 wt% (WS-ac). In the case of the liquid product derived from the raw biomasses, the values were larger with 76 wt% (EU), 64 wt% (OAK), 68 wt% (MIS) and 66 wt% (WS). In contrast, the “organic” phase of those bio-oils possessed quite lower water content with values ranging between 11 wt% and 16 wt% for all biomass samples, irrespective of acid pre-treatment. This should be carefully considered when comparing and discussing bio-oil yield, since the presence of water in different proportions could lead to inconsistent observations. For this reason, in the present work water and bio-oil* yields are given independently, considering only the organic components when expressing bio-oil* yield data.

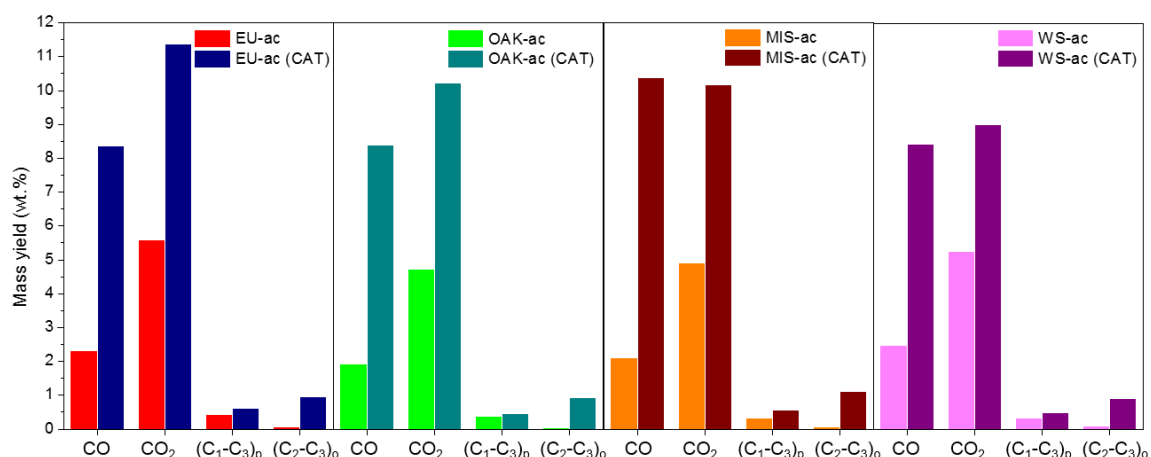


Fig. 6. Effect of the external catalyst (zeolite HZSM-5) on the production of different gas components in the fast-pyrolysis of de-ashed biomass samples. (C₁-C₃)_p: paraffins; (C₂-C₃)_o: olefins.

In relation to the deoxygenation routes, Fig. 5(C) displays the contribution of the external catalyst (zeolite HZSM-5) in terms of incremental selectivity, calculated by subtracting the CO, CO₂ and H₂O productions corresponding to the de-ashed biomasses. It can be observed that the zeolite catalyst induces higher diversity to the deoxygenation pathways in comparison with indigenous catalytic components. In general terms, the HZSM-5 zeolite promotes decarbonylation (36-40%) and decarboxylation (30-39%), in contrast with the non-catalytic pyrolysis in which dehydration was by far the most important deoxygenation route.

The increase in the decarbonylation selectivity when the pyrolysis vapours are passed through the zeolite catalyst is particularly remarkable, which is in agreement with the above commented enhancement in CO production. This HZSM-5-induced effect is not entirely positive since, although it contributes to bio-oil* deoxygenation, it also causes a loss of both mass and energy yield associated to the CO contained in the gaseous stream.

3.5. Bio-oil deoxygenation efficiency and energy yield

The bio-oil* energy yield was calculated as the proportion of the chemical energy contained in the initial biomass that remains in the liquid fraction. The energy yield is negatively affected by a number of factors, such as the formation of char, coke, gaseous hydrocarbons and CO.

Another important parameter, that largely determines the properties of bio-oil, is its oxygen content. In fact, catalytic pyrolysis aims to decreasing the oxygen content at values well below those typically found in pyrolytic bio-oils (about 40 wt%). Moreover, these two parameters are often closely related, since the reduction of the bio-oil oxygen content is usually accompanied by a decrease of its mass and energy yield. Accordingly, Fig. 7 displays all the results obtained in the present work in the form of oxygen concentration of the bio-oil* produced from catalytic and non-catalytic fast-pyrolysis of both raw and de-ashed biomass samples versus the energy yield of these bio-oils*. It can be observed that the bio-oils* derived from the non-treated biomasses, without external catalyst, possess oxygen contents very similar to those of the raw lignocellulosic materials (just in the case of WS a significant reduction of the oxygen content is observed, which is probably due to its higher content of mineral matter with a more diverse composition), while the energy yield is in the range 50-55%. This result means that in conventional thermal fast-pyrolysis, biomass is

converted into a liquid bio-oil showing no significant deoxygenation, with about half of the biomass chemical energy lost in the form of char and gases. Moreover, any deoxygenation that takes place is really associated to char formation, since the elemental composition analyses indicate that the latter is depleted in oxygen compared to the raw biomass.

The removal of mineral components from the biomass during the acid-washing treatment results in significant increase of the bio-oil* energy yield. This effect is more noteworthy in the case of the herbaceous samples, whose bio-oil* energy yield reached 67-68%.

Interestingly, the oxygen content of the bio-oils* from de-ashed biomasses presents in all cases very similar values (about 42 wt%), which are also close to those of the raw biomasses, confirming that in pure thermal pyrolysis little bio-oil deoxygenation occurs.

On the other hand, the data in Fig. 7 show that the indigenous catalysts have in most cases a negative effect as they cause a further reduction in the bio-oil* energy yield with little additional deoxygenation. Only in the case of WS, the ash mineral components seem to promote a significant bio-oil* deoxygenation, although with a strong penalty in terms of energy yield. This finding could be assigned to the high ash content of WS, as well as to the presence of relatively large proportions of some inorganic elements (in addition to K), such as Ca, Mg, Na, P and Si, which may exhibit catalytic activity for bio-oil* deoxygenation.

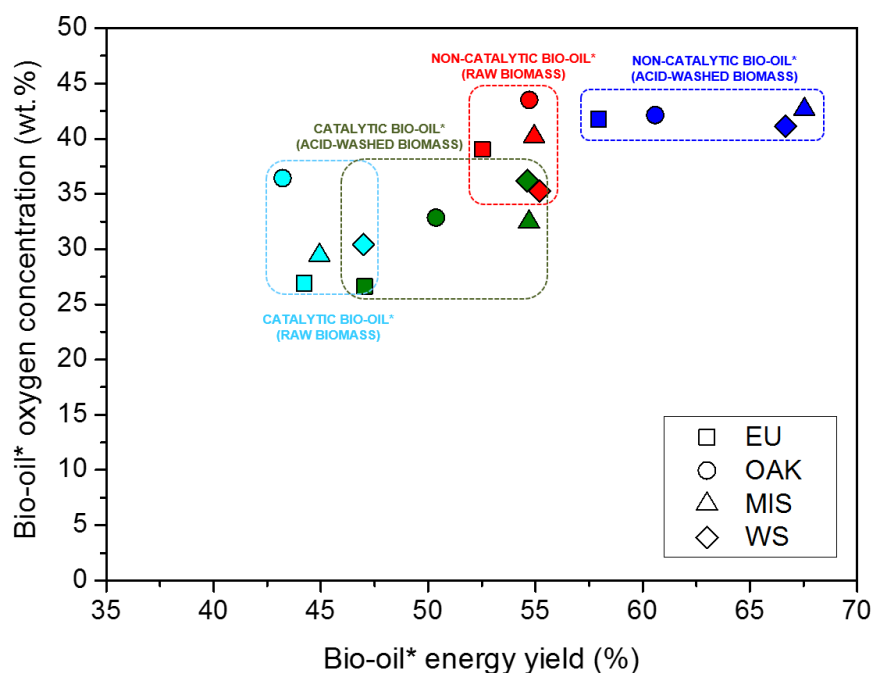


Fig. 7. Oxygen concentration versus energy yield of the bio-oil* fraction obtained in the fast-pyrolysis tests (catalytic and non-catalytic) of de-ashed and raw biomass samples.

For both raw and de-ashed biomass, the use of an external HZSM-5 catalyst causes a further decrease of the bio-oil* energy yield due to the enhanced production of CO and gaseous hydrocarbons, as well as to coke formation. Coke hardly accounts for 0.5-2 wt% of the biomass oxygen, whereas in terms of energy it represents for de-ashed and raw biomasses about 2-3 and 4-5% of the chemical energy, respectively. However, in contrast with the indigenous catalysts, the HZSM-5 zeolite also induces in most cases a reduction in the oxygen content of bio-oil*. Thus, for the non-treated raw biomasses the bio-oil* oxygen content is around 26-36wt%, i.e. clearly below

that of the raw biomasses, whereas the corresponding energy yields range between 42% and 47%. The positive effect of the de-ashing treatment is also denoted when using the zeolite catalyst, since in general terms it leads to a significant enhancement of the bio-oil* energy yield without much increase of the oxygen content. Accordingly, the combination of acid-washing for the removal of the mineral components with the use of the external HZSM-5 catalyst appears to be a convenient option for achieving partially deoxygenated bio-oils*, while maintaining the energy yield at about 50%.

3.6. Bio-oil composition

GC-MS was employed to get insight on the complex chemical composition of the obtained bio-oils. Fig. 8 provides semi-quantitative information about the composition of the thermal and catalytic fast-pyrolysis bio-oils generated from both raw and de-ashed biomasses. Catalytic tests produced, as it was previously mentioned, two-phase bio-oils that were separately analysed to determine the distribution of the different compound families in both phases. The bio-oils components are classified to nine groups of compounds: carboxylic acids (AC), aldehydes (ALD), alcohols (ALC), ketones and ethers (KET & ETH), furans (FUR), amines and amides (AMN & AMD), oxygenated aromatics (O-AR), aromatic hydrocarbons (AR), sugars (SUG) and also a group representing unidentified compounds (UNK). However, it must be taken into account that high molecular weight oligomers (molecular weight > 220 g mol⁻¹) produced by partial depolymerisation of the biomass cannot be detected by this technique. As can be seen in Fig. 8, SUG (primarily levoglucosan) represent the most abundant family in thermal bio-oils* produced from biomass samples without any type of catalyst (indigenous or external), i.e. from de-ashed samples. Levoglucosan is formed by the dehydration of glucose units, which are derived from cellulose according to a mechanism involving condensation and sequential depolymerization of the glycosidic units.^{20,25,51} These results also confirm that levoglucosan is quite stable under the pyrolysis conditions,¹⁰ remaining largely unaltered if there is no catalyst in the reaction media. In the case of bio-oils* obtained from de-ashed woody biomasses, O-AR are also detected in relatively high concentrations. Oxygenated aromatics (O-AR) are formed by lignin-derived compounds (guaiacol, syringol, 1,2,4-trimethoxybenzene and methoxyeugenol among others).

The direct use of the raw biomasses, containing indigenous catalysts, in the pyrolysis process not only influences the amount of bio-oil* produced, but also drastically alters the composition as show in Fig. 8. This change is more pronounced for herbaceous biomasses, which contain higher amounts of indigenous catalysts (AAEM elements). In the case of woody biomasses, O-AR and SUG are the main families contained in bio-oils* with minor proportions of AC, KET & ETH and FUR. In contrast, bio-oils* derived from herbaceous samples present very low content of SUG, consisting mainly by organics in the O-AR, AC and KET & ETH families. These results indicate that the mineral components present in the raw biomasses promote extensively the conversion of sugars. Likewise, O-AR were obtained in high amounts from the raw biomasses, this effect being more pronounced for herbaceous samples, suggesting that the indigenous catalysts also promote the decomposition of lignin fragments into lower molecular weight oxygenated aromatics that are detectable by GC-MS.

The use of an external catalyst (HZSM-5) in the biomass pyrolysis system significantly modifies the chemical composition of bio-oils*, which become depleted in SUG and enriched in O-AR and AR compounds (Fig. 8). Among aromatic hydrocarbons, the most abundant compounds detected in bio-oils* obtained over the HZSM-5 zeolite were alkyl benzenes (toluene, ethylbenzene, styrene,

trimethyl-benzene and especially xylene) and some polyaromatics hydrocarbons (PAHs), mostly alkyl naphthalenes (mainly methyl-naphthalene and dimethyl-naphthalene), as summarized in Table 4. In general terms, the concentrations of these main aromatic chemicals tend to increase for all types of biomass after the acid washing pre-treatment. This is the case of the xylene produced by pyrolysis of miscanthus, which shows an almost two-fold increment after de-ashing. However, for other alkyl derivatives variations the concentration changes after de-ashing are less marked and do not follow a clear trend.

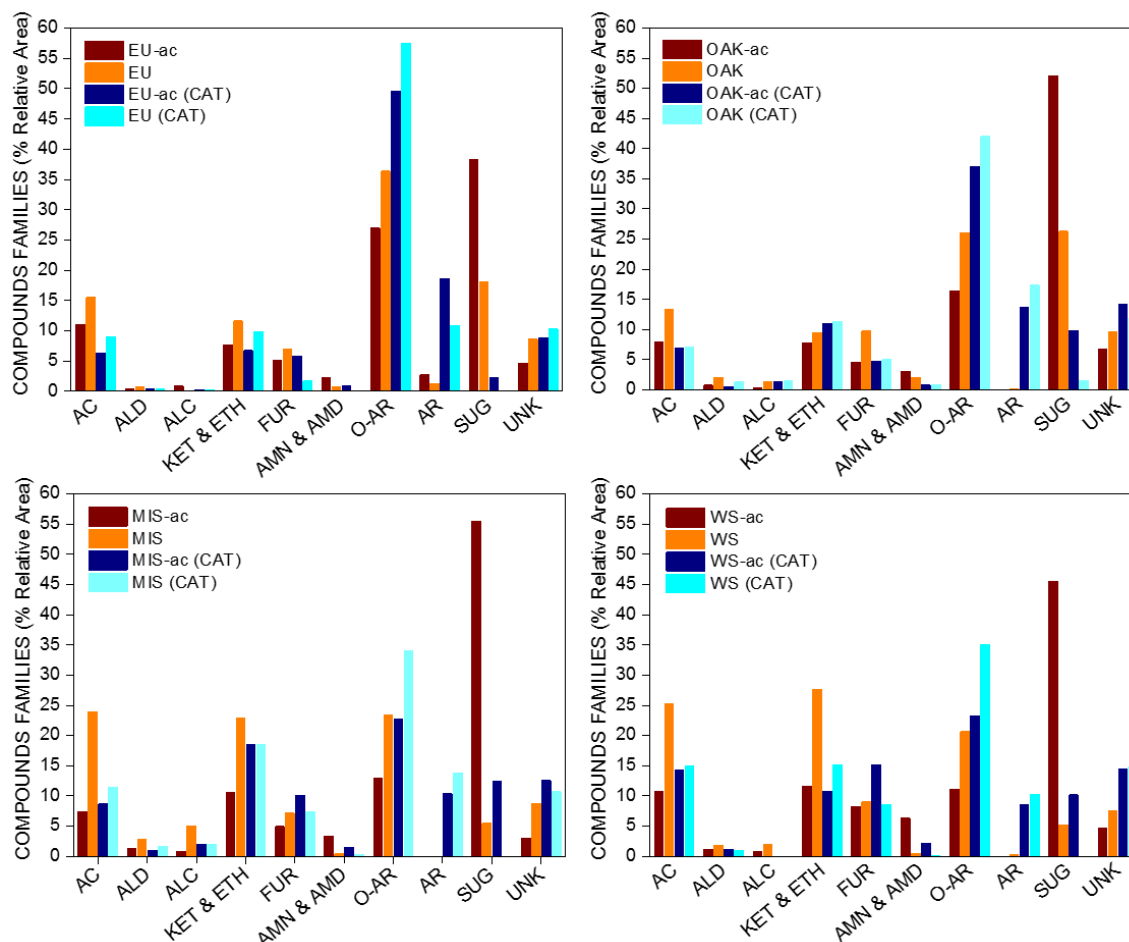


Fig. 8. Main compound families in the bio-oil obtained by fast-pyrolysis of raw and de-ashed biomass samples.

These results denote that indigenous and external catalysts exhibit some common features, such as the enhanced production of oxygenated aromatics and their ability to transform anhydrosugars. However, significant differences are observed between the two types of catalysts regarding other compound families. Thus, the bio-oils* obtained using the zeolite catalyst present a high content of aromatic hydrocarbons, which are almost completely absent in the bio-oils* produced in the presence of indigenous catalysts, confirming the higher effectiveness of the external catalyst for bio-oil* upgrading.

3.7. Deoxygenation pathways

Based on the previous results, a simplified reaction scheme (Fig. 9) is proposed, illustrating the influence of both indigenous and external catalysts on the deoxygenation pathways. Pyrolysis of

de-ashed biomass, i.e. in the absence of any catalytic effect other than that of the simultaneously formed char, proceeds mainly by dehydration with lower contribution of decarboxylation and little decarbonylation, leading to the formation of gases, char and bio-oil. In contrast, the presence of indigenous catalysts, which is constituted by the AAEM mainly accumulated in the char, promotes selectively decarboxylation reactions for most biomasses, favouring to a lower extension the decarbonylation processes. The use of an external catalyst based on HZSM-5 zeolite renders decarbonylation the predominant deoxygenation route, although accompanied by significant decarboxylation and dehydration.

In addition to the deoxygenation routes, it is equally important to consider if the deoxygenation reactions essentially affect the bio-oil* oxygen content. In the pyrolysis of both raw and de-ashed biomasses, the oxygen present in the produced bio-oil* is very similar to that of the starting biomass, since in this case deoxygenation mainly occurs in the char fraction rather than in bio-oil*. In fact, the indigenous catalysts provoke an enhancement of the char formation which is probably linked to the conversion of the anhydrous sugars promoted by the mineral matter components.

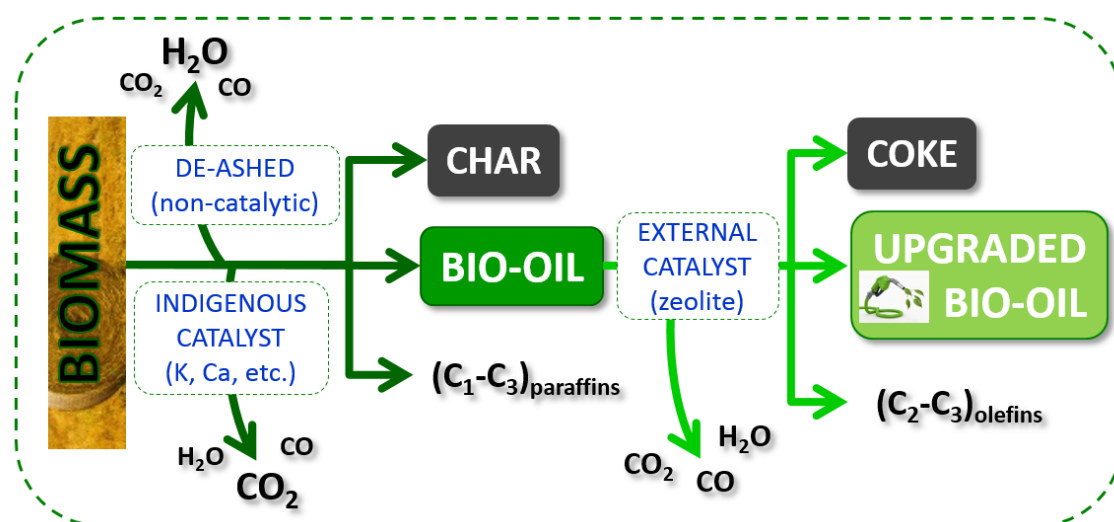


Fig. 9. Simplified scheme of the main pathways in the non-catalytic (de-ashed) and catalytic (indigenous and/or external catalyst) lignocellulose fast-pyrolysis.

These findings mean that both thermal and mineral matter-promoted deoxygenations are not equally efficient in terms of bio-oil* upgrading. In contrast, the organic liquid produced over the zeolite catalyst contains significantly lower amounts of oxygen, which denotes that in this case deoxygenation reactions do really occur in the bio-oil* fraction. Nevertheless, it must be taken into account that, when using the external catalyst, a part of the oxygen removed in the form of H₂O, CO₂ and CO is associated to the formation of other compounds and fractions different from bio-oil*, such as gaseous hydrocarbons and coke deposited over the catalyst itself, being also not productive for bio-oil* upgrading. Therefore, it can be concluded the relevance of modifying and fine-tuning the properties of the external catalyst in order to minimize the extension of non-productive transformations that do not contribute to bio-oil* deoxygenation and cause a loss of energy yield.

4. Conclusions

Four types of lignocellulosic biomass, including woody and herbaceous species, were tested for bio-oil production by fast-pyrolysis. To highlight the role of the mineral matter components on the pyrolysis performance, both raw and de-ashed biomass samples were employed. Moreover, catalytic fast-pyrolysis tests of these samples were carried out over HZSM-5 zeolite to compare the effect of indigenous (mineral components) and external catalysts.

De-ashing biomass significantly varies the distribution and composition of the products obtained from fast-pyrolysis. The bio-oil* (bio-oil in water free basis) production increases at the expense of char, water and gas fractions, this effect being more pronounced in the biomasses containing larger ash amounts (herbaceous samples). These results show that the mineral components present in the raw biomasses catalyse char formation reactions rather than transformations for bio-oil upgrading. Char contains up to 87.3 wt% of carbon and accordingly it may retain more than 40% of the initial energy content of the biomass.

The use of an external catalyst (HZSM-5) leads also to a drastic decrease in bio-oil* production for all the biomasses with enhanced formation of gases and water, in addition to the coke deposited over the zeolite catalyst. However, in contrast with the indigenous catalysts, the HZSM-5 zeolite also induces a reduction in the oxygen content of bio-oils* compared to those obtained in absence of any catalytic effect. The positive effect of the de-ashing treatment is also denoted when using the external zeolite catalyst, since in general terms it leads to a significant enhancement of the bio-oil* energy yield.

Concerning the bio-oil composition, both indigenous and external catalysts exhibit some common features, such as the increase in the production of oxygenated aromatics and the ability to transform anhydrosugars. However, significant differences are observed between both types of catalysts regarding other compounds families. Thus, the bio-oils* obtained using the zeolite catalyst present a high content of aromatic hydrocarbons, with a high proportion of alkyl substituted benzenes and naphthalenes, which are absent in the bio-oils* produced in the presence of indigenous catalysts, confirming the higher effectiveness of the external catalyst for bio-oil* upgrading.

Relevant variations in the deoxygenation routes occur depending on the type of catalyst. Dehydration was the main deoxygenation pathway for de-ashed biomasses, i.e. in the absence of any catalyst. In contrast, the presence of indigenous catalysts promotes decarboxylation as the predominant deoxygenation pathway. Finally, in the case of the external HZSM-5 catalyst, decarbonylation is the main route for oxygen removal. Another important finding is that, for both raw and de-ashed biomasses, deoxygenation is just taking place on the char fraction, but it is not productive for reducing the bio-oil* oxygen content. In contrast, the zeolite catalyst does induce deoxygenation of the bio-oil* fraction.

Acknowledgements

Authors gratefully acknowledge the financial support from the European Union Seventh Framework Programme (FP7/2007-2013) under grant agreement n°604307 (CASCATBEL project); and RESTOENE2 project. CLARIANT is highly acknowledged for supplying the HZSM-5 zeolite sample.

References

- 1 D. Kubička, I. Kubičková and J. Čejka, *Catal. Rev. Sci. Eng.*, 2013, **55**, 1–78.
- 2 A. V. Bridgwater and G. V. C. Peacocke, *Renew. Sustain. energy Rev.*, 2000, **4**, 1–73.
- 3 M. S. Talmadge, R. M. Baldwin, M. J. Bidy, R. L. McCormick, G. T. Beckham, G. A. Ferguson, S. Czernik, K. A. Magrini-bair, T. D. Foust, P. D. Metelski and M. R. Nimlos, *Green Chem.*, 2014, **16**, 407–453.
- 4 J. Feroso, P. Pizarro, J. M. Coronado and D. P. Serrano, *Adv. Rev.*, 2017, **6**, 1–18.
- 5 D. A. Ruddy, J. A. Schaidle, J. R. Ferrell III, J. Wang, L. Moens and J. E. Hensley, *Green Chem.*, 2014, **16**, 454–490.
- 6 R. H. Venderbosch, *ChemSusChem*, 2015, **8**, 1306–1316.
- 7 P. A. H. Paul T. Williams, *Biomass and Bioenergy*, 1994, **7**, 223–236.
- 8 T. R. Carlson, G. A. Tompsett, W. C. Conner and G. W. Huber, *Top. Catal.*, 2009, **52**, 241–252.
- 9 P. T. Williams and N. Nugranad, *Energy*, 2000, **25**, 493–513.
- 10 C. Liu, H. Wang, A. M. Karim, J. Sun and Y. Wang, *Chem. Soc. Rev.*, 2014, **43**, 7594–7623.
- 11 J. Adam, E. Antonakou, A. Lappas, M. Stöcker, M. H. Nilsen, A. Bouzga, J. E. Hustad and G. Øye, *Microporous Mesoporous Mater.*, 2006, **96**, 93–101.
- 12 T. R. Carlson, T. P. Vispute and G. W. Huber, *ChemSusChem*, 2008, **1**, 397–400.
- 13 D. Carpenter, T. L. Westover, S. Czernik and W. Jablonski, *Green Chem.*, 2014, **16**, 384–406.
- 14 T. Qu, W. Guo, L. Shen, J. Xiao and K. Zhao, *Ind. {&} Eng. Chem. Res.*, 2011, **50**, 10424–10433.
- 15 M. I. Hajaligol, J. B. Howard, J. P. Longwell and W. A. Peters, *Ind. Eng. Chem. Process Des. Dev.*, 1982, **21**, 457–465.
- 16 D. J. Nowakowski, A. V Bridgwater, D. C. Elliott, D. Meier and P. De Wild, *J. Anal. Appl. Pyrolysis*, 2010, **88**, 53–72.
- 17 D. J. Hayes and A. Fisheries, Biofuels, *Bioprod. Biorefining*, 2009, **3**, 500–520.
- 18 P. R. Patwardhan, J. A. Satrio, R. C. Brown and B. H. Shanks, *Bioresour. Technol.*, 2010, **101**, 4646–4655.
- 19 G. Yildiz, F. Ronsse, R. Venderbosch, R. Van Duren, S. R. A. Kersten and W. Prins, *Appl. Catal. B Environ.*, 2015, **168**, 203–211.
- 20 R. Fahmi, A. V. Bridgewater, L. I. Darvell, J. M. Jones, N. Yates, S. Thain and I. S. Donnison, *Fuel*, 2007, **86**, 1560–1569.
- 21 A. Oasmaa, Y. Solantausta, V. Arpiainen, E. Kuoppala and K. Sipil, *Energy & Fuels*, 2010, **24**, 1380–1388.

- 22 R. Fahmi, A. V Bridgwater, I. Donnison, N. Yates and J. M. Jones, *Fuel*, 2008, **87**, 1230–1240.
- 23 J. Feroso, H. Hernando, P. Jana, I. Moreno, J. Přeč, C. Ochoa-Hernández, P. Pizarro, J. M. Coronado, J. Čejka and D. P. Serrano, *Catal. Today*, 2016, **277**, 171–181.
- 24 M. Nik-Azar, M. R. Hajaligol, M. Sohrabi and B. Dabir, *Fuel Process. Technol.*, 1996, **51**, 7–17.
- 25 T. A. M. Robert J. Evans, *Energy & Fuels*, 1987, **1**, 123–137.
- 26 D. Nowakowski, J. Jones, R. Brydson and a Ross, *Fuel*, 2007, **86**, 2389–2402.
- 27 T. Wigley, A. C. K. Yip and S. Pang, *J. Anal. Appl. Pyrolysis*, 2015, **113**, 296–306.
- 28 L. Jiang, S. Hu, L. shi Sun, S. Su, K. Xu, L. mo He and J. Xiang, *Bioresour. Technol.*, 2013, **146**, 254–260.
- 29 S. D. Stefanidis, E. Heracleous, D. Th, K. G. Kalogiannis, C. M. Michailof and A. A. Lappas, *Biomass and Bioenergy*, 2015, **83**, 105–115.
- 30 T. M. Sankaranarayanan, A. Berenguer, C. Ochoa-Hernández, I. Moreno, P. Jana, J. M. Coronado, D. P. Serrano and P. Pizarro, *Catal. Today*, 2015, **243**, 163–172.
- 31 S. A. Channiwala and P. P. Parikh, *Fuel*, 2002, **81**, 1051–1063.
- 32 K. Raveendran, A. Ganesh and K. Khilar, *Fuel*, 1995, **74**, 1812–1822.
- 33 D. Mourant, Z. Wang, M. He, X. S. Wang, M. Garcia-Perez, K. Ling and C.-Z. Li, *Fuel*, 2011, **90**, 2915–2922.
- 34 H. Yang, R. Yan, H. Chen, D. H. Lee and C. Zheng, *Fuel*, 2007, **86**, 1781–1788.
- 35 E. Biagini, F. Barontini and L. Tognotti, *Ind. Eng. Chem. Res.*, 2006, **45**, 4486–4493.
- 36 K. Raveendran, A. Ganesh and K. C. Khilar, *Fuel*, 1996, **75**, 987–998.
- 37 M. R. Nimlos, S. J. Blanksby, G. B. Ellison and R. J. Evans, *J. Anal. Appl. Pyrolysis*, 2003, **66**, 3–27.
- 38 N. Wang, D. Chen, U. Arena and P. He, *Appl. Energy*, 2017, **191**, 111–124.
- 39 P. Das, A. Ganesh and P. Wangikar, *Biomass and Bioenergy*, 2004, **27**, 445–457.
- 40 I.-Y. Eom, J.-Y. Kim, S.-M. Lee, T.-S. Cho, H. Yeo and J.-W. Choi, *Bioresour. Technol.*, 2013, **128**, 664–672.
- 41 A. Trubetskaya, P. A. Jensen, A. D. Jensen, M. Steibel, H. Spliethoff and P. Glarborg, *Fuel Process. Technol.*, 2015, **140**, 205–214.
- 42 A. Saddawi, J. M. Jones and A. Williams, *Fuel Process. Technol.*, 2012, 104, 189–197.
- 43 A. V Bridgwater, *Biomass and Bioenergy*, 2012, **38**, 68–94.
- 44 H. Zhang, R. Xiao, H. Huang and G. Xiao, *Bioresour. Technol.*, 2009, 100, 1428–1434.
- 45 H. Hernando, S. Jiménez-Sánchez, J. Feroso, P. Pizarro, J. M. Coronado and D. P. Serrano, *Catal. Sci. Technol.*, 2016, **6**, 2829–2843.
- 46 O. D. Mante and F. A. Agblevor, *Green Chem.*, 2014, **16**, 3364–3377.

- 47 P. T. Williams and P. A. Horne, *Fuel*, 1995, **74**, 1839–1851.
- 48 O. D. Mante and F. A. Agblevor, *Biomass Convers. Biorefinery*, 2011, **1**, 203–215.
- 49 K. Uemura, S. Appari, S. Kudo, J. I. Hayashi, H. Einaga and K. Norinaga, *Fuel Process. Technol.*, 2015, **136**, 73–78.
- 50 R. French and S. Czernik, *Fuel Process. Technol.*, 2010, **91**, 25–32.
- 51 G. W. Huber, S. Iborra and A. Corma, *Chem. Rev.*, 2006, **106**, 4044–4098.

Article 2

Thermochemical valorization of camelina straw waste via fast pyrolysis

Biomass Conversion and Biorefinery, 2017, 7(3), 277–287

Biomass Conv. Bioref.
DOI 10.1007/s13399-017-0262-x



ORIGINAL ARTICLE

Thermochemical valorization of camelina straw waste via fast pyrolysis

H. Hernando¹ · J. Feroso¹ · I. Moreno^{1,2} · J. M. Coronado¹ · D. P. Serrano^{1,2} · P. Pizarro^{1,2}

Received: 15 January 2017 / Revised: 10 April 2017 / Accepted: 19 April 2017
© Springer-Verlag Berlin Heidelberg 2017

Impact JCR factor, (JCR 2017): 1.310
Category: Energy & Fuels. 71 of 97 (Q3)

ABSTRACT

The present work investigates the thermochemical valorization of camelina straw, which is a waste generated during the harvesting of *Camelina sativa*, an oilseed crop for the production of biodiesel or hydrotreated vegetable oil (HVO). In particular, it is focused on obtaining bio-oil via thermal or catalytic fast pyrolysis, which would be the first stage on a sequence of chemical processes for biofuel production. The catalytic interference of the inorganic matter present in the biomass was studied by preparing a batch of de-ashed camelina straw by washing with diluted nitric acid. Chemical analysis revealed this treatment effectively removed alkaline (K and Na) and alkaline earth (Ca and Mg) metals. Pyrolysis of de-ashed camelina straw led to higher mass and energy yields of bio-oil in water-free basis (bio-oil*), but with higher oxygen concentration. Catalytic pyrolysis over HZSM-5 was also studied in both raw and de-ashed feedstocks. This catalyst promoted mainly decarbonylation and decarboxylation reactions of the pyrolysis vapors, leading to much higher gas yields and lower of bio-oil*, but with better quality. Catalytic pyrolysis of untreated camelina straw exhibited a synergetic effect between both the inorganic matter and the external HZSM-5 catalyst, so that bio-oil* yield was the lowest (20 wt%) due to an extensive deoxygenation (18 wt% oxygen content), which resulted in the highest HHV obtained (37.3 MJ/kg_{db}). Significant differences were also found on the molecular composition of the bio-oils* with larger proportion of anhydro sugars when the biomass was de-ashed, while HZSM-5 strongly promoted the formation of oxygenated aromatics and aromatic hydrocarbons.

Keywords: *Camelina sativa*. HZSM-5 nanozeolite. Pyrolysis. De-ashed.

1. Introduction

Biofuels can play a crucial role reducing the dependence of petroleum and their associated GHGs emissions,^{1,4} especially in the transportation, a sector with a high fossil fuel demand.⁵ Lignocellulosic biomass, which is a mixture of three main macromolecules (cellulose, hemicellulose, and lignin), a certain quantity of mineral matter and organic extractives, is an attractive source of renewable energy because of its high availability.^{6,7} Among the thermochemical routes which allow the transformation of this resource into biofuels, fast pyrolysis is considered of high prominence.^{8,9} In this process, lignocellulose is rapidly heated up to moderate temperatures (450–550 °C), at low residence times (< 2 s) and fast cooling, to produce an enhanced yield of liquid fraction (bio-oil), along with a solid residue (char) and non-condensable gases (H₂, CO, CO₂, and light hydrocarbons) as by-products.^{10,11}

The bio-oil obtained from conventional thermal (non-catalytic) pyrolysis consists of a complex mixture of hundreds of oxygenated organic compounds, such as acids, aldehydes, ketones, alcohols, ethers, esters, phenols, furans, and sugars, formed by thermal decomposition of the macromolecules of lignocellulose into lighter molecules.

The reaction mechanisms and pathways of non-catalytic fast pyrolysis (NCFP) have been widely studied in literature for each individual macromolecule forming the lignocellulosic biomass. Cellulose is the main responsible in the formation of light oxygenates (especially acetic acid), sugar derivatives (most of them levoglucosan), and it has a moderate contribution to the generation of furans.¹² Hemicellulose leads to the formation of furans, with a minor contribution of light oxygenates, pyrans and additional sugars.¹³ Lignin breakdown produces most of the oxygenated aromatics compounds observed in bio-oil and a minor formation of light oxygenates.¹⁴ Regarding the mass yield of each product of the NCFP, it has been reported that both cellulose and hemicellulose produce more bio-oil (around 60–70 wt%) than lignin (~20–30 wt%), being the concentration of this last component the main factor in the formation of char. Although yields can be roughly predicted using an additive law of the three main macromolecules in lignocellulose,¹⁵ mineral matter present in the biomass can play an important role in the pyrolysis reaction and final product composition, acting as an indigenous catalyst.¹⁶⁻²⁰ All natural biomass contains a certain amount of inorganic components, which usually represents between 1 and 10 wt%, in the form of cations bounded to the organic molecules of the lignocellulose or as precipitated salts.^{7,20} Among the metals present in the biomass, the most abundant are Na, K, Ca, Si, and Mg.²¹

NCFP has proven to be an effective way of obtaining a large yield of liquid fuel from lignocellulose with higher energy density (20–25 MJ/kg). In fact, the NCFP process is already implemented at an industrial scale to produce heat or to supply electricity to the grid.²² However, bio-oil properties are far away to those of conventional fuels. The main adverse properties are as follows: large amount of oxygen (35–40 wt%), acid nature (pH of 2–4), significant amounts of water (10–30 wt%), low physicochemical stability, high viscosity, and high density.²³ Therefore, they require an upgrading treatment in order to be used in conventional transportation engines. The most effective routes for upgrading bio-oils are based on the use of heterogeneous catalysts.^{7,10,23} One alternative is to conduct the pyrolysis process in the presence of a catalyst, catalytic fast pyrolysis (CFP), which can be performed in situ or ex situ, depending on the placement of the catalyst bed in the reaction.²³ Ex situ CFP allows improving and optimizing the control of the reaction temperature and avoids unnecessary fouling of the catalyst by char particles, since the pyrolysis vapors are the only phase in contact with the catalytic bed. A wide variety of

heterogeneous catalysts have been studied in literature, but acidic zeolite catalysts, and in particular HZSM-5, are the most employed in this process due to their high activity.²⁴⁻³¹ Acidic zeolites promote a series of reactions, such as secondary cracking, oligomerization, cyclization, aromatization, and/or polymerization reactions, among others, leading to a partial deoxygenation of the vapors through the formation of CO, CO₂, and H₂O (decarbonylation, decarboxylation, and dehydration, respectively). According to the oxygen extraction occurred, the bio-oil yield decreases but its quality is significantly increased as it is enriched in aromatics in detriment of oxygenated compounds, leading to enhanced properties closer to those required in conventional liquid fuels. Nevertheless, it is important to control such acid properties, since highly acidic zeolites promote polymerization reactions, yielding higher amounts of coke and polyaromatic hydrocarbons (PAHs), which decrease dramatically the bio-oil yield and it is environmentally undesirable.³²

Second-generation lignocellulosic biofuels rely on the utilization of non-edible forestry and agriculture residues. Of particular interest for maximizing the yield is the possible exploitation of the whole plant in the case of dedicated plantations. In this respect, *Camelina sativa*, which is an herbaceous plant, has been proposed as a flexible and tough energy crop because it presents fast annual growth with a moderate to low demand of nutrients making it highly resistant to drought.

Furthermore, their seeds contain high amounts of oil (about 30–43 wt%), especially unsaturated fatty acids (90% of total oil). Most of them are linolenic, linoleic, oleic, and eicosenoic acids,^{33,34} which find application in either the food industry or the production of biofuels through thermochemical processes, such as transesterification, thermal or catalytic pyrolysis, or hydrodeoxygenation.³⁵⁻³⁷ In addition, harvesting this crop generates between 1800 to 5000 kg Ha⁻¹ of straw per year³⁸ as lignocellulosic waste. One way to valorize this lignocellulosic straw could be its conversion into second-generation biofuels through catalytic fast pyrolysis. Therefore, *C. sativa* is a very promising energy crop, since it allows an integral use for the production of advanced biofuels.

In this context, the present work approaches the energetic valorization of residual camelina straw into biofuels via thermochemical pathways. In particular, it is focused on obtaining bio-oil via fast pyrolysis, which would be the first stage on a sequence of chemical processes for the production of biofuels. Despite studies regarding the pyrolysis of this type of feedstock are very scarce, it has been already pointed out to present interesting properties due to its low N content and char yields lower than other biomasses.³⁹ In this work, we go further and study the influence of both indigenous (mineral matter present in the raw biomass) and external catalysts in the yield and the quality of the bio-oil has been investigated. The external catalyst selected was a commercial HZSM-5 nanozeolite having a mild acidity.

2. Experimental

2.1. Catalyst and biomass samples

A commercial HZSM-5 nanozeolite supplied by CLARIANT (HZCP90) was selected to be used in the catalytic activity tests. Prior the catalytic activity test, the HZSM-5 zeolite was pelletized, crushed and sieved into a particle size of 180-250 μm.

Camelina Straw (CS) was kindly supplied by Camelina Company S.L. Prior to its utilization in the pyrolysis reactor, it was ground in a cutter mill, sieved to a desire particle size between 0.5-1 mm and dried at 105 °C for 2 days. Additionally, a second batch was prepared by previously

deashing the original CS through a mild acid-washing pretreatment, which was described in literature before [40]. Through this treatment, a representative amount of biomass sample of 50 g was dispersed into 1000 ml of 1 wt% HNO₃ aqueous solution and subjected to continuous stirring at 50 °C for 2 h. The partially de-ashed camelina straw sample, denoted as CSac, was recovered by filtration, washed with mili-Q water until reaching pH = 6–7, and finally dried at 105 °C for 2 days.

2.2. Catalyst and biomass characterization

Biomass moisture was determined by drying in an oven at 105 °C for 2 days and measuring the weight loss. The ash content was estimated by burning 20 g of each biomass sample, CS and CS-ac, in a muffle at 815 °C in air flow of 100 cm³ min⁻¹ for 2 h and, then, weighing the residual solids. The elemental composition of the ash attained by calcinations was analyzed by inductively coupled plasma-optical emission spectroscopy (ICP-OES) with a Perkin Elmer Optima 3300 DV instrument. For this purpose, a representative amount of each ash sample was digested in a solution of HF and HNO₃ in an Anton Paar (MW3000) microwave oven. Biomass moisture was determined by drying in an oven at 105 °C for 2 days and measuring the weight loss. The ash content was estimated by burning 20 g of each biomass sample, CS and CS-ac, in a muffle at 815 °C in air flow of 100 cm³ min⁻¹ for 2 h and, then, weighing the residual solids. The elemental composition of the ash attained by calcinations was analyzed by inductively coupled plasma-optical emission spectroscopy (ICP-OES) with a Perkin Elmer Optima 3300 DV instrument. For this purpose, a representative amount of each ash sample was digested in a solution of HF and HNO₃ in an Anton Paar (MW3000) microwave oven.

Both the volatile matter of each biomass sample and the coke deposited on the catalysts after reaction were measured by TGA analyses in a NETZSCH STA 449 apparatus, 10 °C min⁻¹ till 800 °C, using 100 cm³ min⁻¹ of argon and air, respectively, as carrier gas.

Ultimate analyses were carried out in a micro-elemental analyzer (Thermo Scientific FLASH 2000 CHNS/O), provided with a column for the C, H, N, and S determination whereas O was attained by difference. The results were normalized in both water-free and ash-free bases. The composition of the raw and de-ashed camelina straw samples in biopolymers (cellulose, hemicellulose, and lignin) was determined by the method described elsewhere.⁴¹

The Al content of the catalyst was determined by ICP-OES, using the equipment aforementioned. Textural properties were determined by Ar isotherms at 87 K on an AUTOSORB IQ SYSTEM (Quantachrome). The surface area was determined using the Brunauer-Emmet-Teller (BET) equation. Pore size distributions and mesoporosity contribution to the surface area were calculated by applying the NL-DFT model to the adsorption branch. The total pore volume was calculated at $P/P_0 \approx 0.98$. The acidity of the zeolite was measured by temperature-programmed desorption (TPD) of NH₃ using an AUTOCHEM 2910 system (Micromeritics). The standard procedure for the TPD measurements involved the inertization of the sample by flowing He at 600 °C (1 h), cooling to 100 °C, adsorbing NH₃ from a 15% NH₃-He mixture, removing first the weakly physisorbed NH₃ by flowing He at 180 °C for 30 min, and finally carrying out the TPD experiment by raising the temperature of the catalyst sample with a ramp of 10 °C min⁻¹ till 600 °C to determine the chemisorbed NH₃.

2.3. Catalytic activity tests

All the fast pyrolysis experiments were carried out in a lab-scale fixed bed, drop-tube reactor made of stainless steel. The reaction temperature was measured by two internal type K thermocouples, placed on the pyrolysis and catalytic bed zones, respectively. The selected catalyst loading was 1 g, so the biomass to catalyst ratio was established as 5 wt%. The reactions were run at 500 °C and atmospheric pressure, using 100 ml min⁻¹ of N₂ flow as carrier gas to provide an inert atmosphere. The formed solid carbonaceous residue (char) was retained in the reactor, while the vapor fraction was swept by the N₂ carrier gas flow, passed through the HZSM-5 bed in the catalytic experiments, and then they were condensed in a series of four vessels containing an ice-water mixture (0–4 °C). The residence time of vapors, calculated taking into account the distance between the point in which char is accumulated and the exit of the reactor, was 1.97 s. Regarding the biomass heating rate, it was around 860 °C min⁻¹. Under these conditions, the requisites to be considered as fast pyrolysis were met.⁴²

The gases produced in the reaction (H₂, N₂, CO, CO₂, CH₄, C₂H₄, C₂H₆, C₃H₆, C₃H₈, and C₄H₈) were finally collected in a sampling bag for their further analysis in a dual channel Agilent® CP-4000 micro gas chromatograph (Micro-GC). More detailed explanations about the experimental set up can be found in previous works.^{40,43}

Once the experiments were finished, the char and catalyst were recovered separately from inside the reactor for further characterization. Proximate and ultimate analyses were performed to the char fraction. The total amount of coke (solid deposited over the catalyst) was determined by weight loss in the thermobalance using a heating rate of 20 °C min⁻¹ up to 815 °C in air atmosphere.

Bio-oil characterization included the following properties and techniques: (a) water determination by Karl-Fischer titrations in a Mettler-Toledo V20S compact volumetric KF titrator; (b) C, H, N, S, O elemental composition was calculated by difference applying the total mass and atomic balances to the reaction. The reliability of such calculations was verified by CHNS/O analysis in Thermo Fisher Scientific FLASH-2000 micro-elemental analyzer of some selected bio-oils; (c) molecular composition using a gas chromatograph coupled to a mass spectrometer (GC-MS) Bruker® SCION 436-GC (electron energy 70 eV, emission 300 V; He flow rate 1 cm³ min⁻¹; column WCOT-fused silica 30 m × 0.25 mm ID × 0.25 μm). Identification of the compounds separated by GC-MS was performed by means of the NIST EI-MS spectral library (v2.0). Bio-oil compounds were further grouped into families according to their main functional groups for its semiquantitative analysis. The bio-oil fraction was considered in a water-free basis, being named as bio-oil*.

Finally, from the weight of each pyrolysis fraction, the total mass balance was closed with an experimental error < 5 wt% for all the cases. Then, the mass yield of any product fraction, and so the oxygen yields, high heating values (HHV), and energy yields of each fraction were calculated according to equations described elsewhere.³⁷

All reactions were repeated, data were statistically treated, and confidence intervals were calculated in order to verify the reproducibility and reliability of the results attained.

3. Results and discussion

3.1. *Camelina straw characterization*

As stated in the introduction section, the main objective of this work was to explore the potential valorization of camelina straw, which is a residue during the harvest time of camelina crops, via pyrolysis as the first stage for biofuel production. The thermochemical behavior of any lignocellulosic biomass is strongly dependent of both its macromolecular composition and mineral content. Despite mineral or ash content in minor proportions, its composition may affect strongly the biomass feedstock behavior under the pyrolysis conditions.^{26,40} Accordingly, the experimental study here presented was applied to the raw camelina straw and to a second batch of de-ashed biomass, obtained by acid washing following the procedure described in the experimental section.

Table 1 summarizes the main characteristics of camelina straw, before and after the acid treatment, including the proximate and ultimate analysis as well as the molecular composition (cellulose, hemicellulose, and lignin content) and the high heating value (HHV). The properties and chemical composition of as-received camelina straw are consistent with the expected values for this type of feedstock:⁴⁴ typically, the volatile matter of an herbaceous biomass is higher than 75 wt%, while the fixed carbon and ashes content is lower than 20 and 4 wt%, respectively. The chemical analyses by ICP-OES technique reveal that the most abundant inorganic elements in camelina straw are K and Ca, which represent 48.8 and 35.9 wt% of the ash composition, respectively. In lower proportion, there is also Si (11.80%), Mg (4.5 wt%), P (4.21%), and Na (3 wt%).

The high efficiency of the acid washing was evidenced by the reduction of the ash content in camelina straw from 3.2 to 0.3 wt%. This reduction was especially significant for the alkali (K and Na) and alkali earth metals (Mg and Ca), exhibiting removal percentages higher than 95%. It must be remarked that these elements have been associated as responsible of catalytic reactions, such as carbonization, decarboxylation, and decarbonylation that interfere on the pyrolysis product yields.⁴⁰ The elimination of P was also important (ca. 85%) but Si represented only about 17%, which was predictable considering the limited solubility of SiO₂ in acidic conditions. Nevertheless, the expected catalytic activity of silica is rather reduced or even ineffective.

Accordingly, the acidic pretreatment induced an increase of the volatile matter content from 77.0 up to 87.7 wt%, while that of fixed carbon decreased. This effect was attributed to the elimination of inorganic material (K, Na, Mg, and Ca) able to catalyze carbonization reactions when they are present in the biomass feedstock.⁴⁰ In contrast, the elemental composition in terms of C, H, N, and O remains basically constant following this pretreatment.

Regarding the compositional analysis of camelina straw, as expected, hollocellulose (cellulose and hemicellulose) is the major fraction, accounting for about 59 wt% of the total composition (Table 1). The phenolic polymer, lignin, represents 25 wt% of the biomass. A last group of components identified as “Others” comprises organic extractives, ashes, and unidentified compounds in a percentage of 15.5 wt%. It can be clearly seen that de-ashing produces a major effect on this last group due to the extraction of mineral matter. The carbohydrate and phenolic polymers remained almost unaffected.

The thermal behavior of both raw and de-ashed camelina straw in inert atmosphere was determined by thermogravimetric tests, and the results are displayed in Fig. 1. In the case of raw biomass (CS), the derivative curve of the mass loss shows a low temperature peak at 280 °C that,

according to the literature,⁷ can be assigned to the decomposition of hemicellulose. In addition, the sharper peak at 330 °C is attributed to the pyrolysis of cellulose. The fact that this feature is more intense for the CS-ac is consistent with the observed variation in the biopolymer distribution, as summarized in Table 1. On the other hand, lignin is expected to decompose in a wide range of temperatures so it can be only appreciated as the high tailing of the derivative curve. A slight shift to higher temperatures for the decomposition of CS-ac appears, which is consistent with previous observations¹⁶⁻²⁰ and, again, it is an expected result as most of the inorganic components able to catalyze carbonization reactions have been removed.

Table 1. Proximate, ultimate, biopolymers analyses and ashes composition of the raw (CS) and acid-washed (CS-ac) camelina straw biomass.

Sample	Moisture (wt.%)	Proximate analysis, db (wt.%)			Ultimate analysis, db (wt.%)				HHV ^a (MJ/kg _{db})
		Ash	Volatile Matter	Fixed Carbon	C	H	N	O	
CS	9.0	3.2	77.0	19.8	48.4	5.9	0.3	45.4	18.5
CS-ac	-	0.3	87.7	12.0	48.6	6.0	0.3	45.2	19.3

Sample	Molecular composition, db (wt.%)				
	Cellulose	Hemicellulose	Lignin	Others ^b	Lignin/Hollocellulose ^c
CS	36.3	23.2	25.0	15.5	0.42
CS-ac	41.6	24.9	26.3	7.2	0.40

Sample	Ash element (wt.% · 10 ⁻²)													
	Al	Ba	Ca	Fe	K	Mg	Mn	Na	P	Si	Sn	Sr	Ti	Zn
CS	0.45	0.21	35.9	0.21	48.8	4.53	0.11	3.00	4.21	11.80	0.25	0.13	0.05	0.05
CS-ac	0.14	0.01	1.63	0.14	0.24	0.11	0.01	0.03	0.61	9.76	0.15	0.01	0.02	0.01

db: dry basis

a Calculated from the CHNS/O analysis using the equation reported in reference 37

b Organic extractives, ashes and unidentified compounds determined by difference

c Holocellulose: Cellulose + Hemicellulose

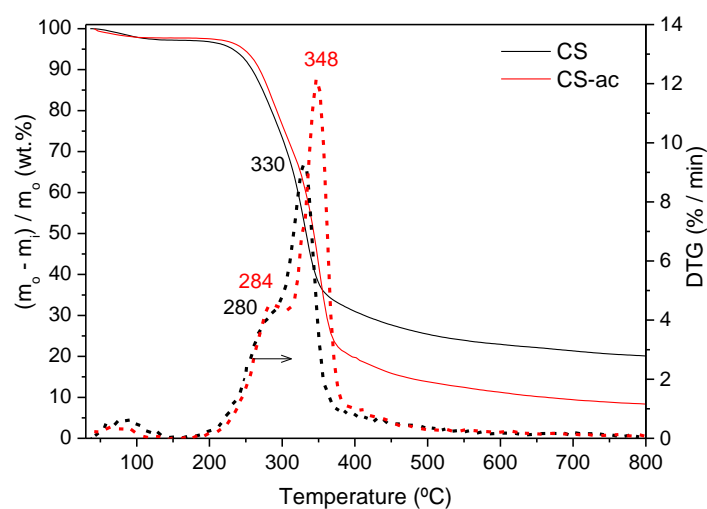


Fig. 1. Thermogravimetric analysis, TG and DTG curves, of raw and de-ashed camelina straw. (Analysis conditions: 100 ml min⁻¹ Ar; heating rate, 10 °C min⁻¹, from room temperature to 800 °C).

3.2. Pyrolysis tests

Pyrolysis reactions were performed in lab-scale fixed bed reactor at 500 °C, with and without the presence of a catalyst bed which was in contact only with the pyrolysis vapors. The catalyst selected was a commercial HZSM-5, an aluminosilicate zeolite with MFI structure, having mild

acidity in order to avoid excessive coke formation, which would penalize the mass energy yield of bio-oil. A summarize of the physicochemical properties of the catalyst is presented in Table 2. The aluminum content, measured as Si to Al ratio by ICP-OES, was 42. Regarding its textural properties, it is a zeolite with a BET surface area of $445 \text{ m}^2 \text{ g}^{-1}$, having a relatively high contribution of mesoporosity and/or external surface ($133 \text{ m}^2 \text{ g}^{-1}$). Total acidity, determined by TPD- NH_3 measurements, was 0.223 mol g^{-1} .

Although the most relevant product of fast pyrolysis is the bio-oil, because this liquid fraction can be upgraded to be used as biofuel, gases and solid char are simultaneously generated. In addition, when a catalyst is present, an additional fraction of coke deposited on this solid can be differentiated. The distribution of these fractions experimentally obtained by the thermal (non-catalytic) and catalytic pyrolysis of CS and CS-ac samples are shown in Fig. 2. Confidence intervals are also represented with sticks, revealing high reproducibility as the variation of mass yields was always below 4 points in the nominal values. In this graph, water and bio-oil in dry basis (bio-oil*) are represented separately for the sake of clarity in the discussion. It must be mentioned that non-catalytic pyrolysis produced a stable emulsion of the organic and aqueous phases, whereas they were collected as separated fractions when ZSM-5 was placed in the reactor. From Fig. 2, it is evidenced the de-ashing treatment had a profound effect in the distribution of pyrolysis products. Thus, in both catalytic and non-catalytic reactions, the CS-ac feedstock produced considerably more bio-oil* and less char and gases than untreated CS. It is evidenced, therefore, the catalytic interference of some ash constituents aforementioned. In line with this, Liu et al.²⁶ reported that mineral matter, and especially K, may catalyze decarbonylation and decarboxylation reactions of the pyrolysis vapors. Accordingly, the removal of the inorganic components by the acidic treatment reduces the contribution of these gasification reactions. As it will be discussed below, this is also consistent with the variation in the gas composition.

As expected, the use of HZSM-5 catalysts had an important influence on the product distribution obtained by pyrolysis of both CS and CS-ac biomass samples. As a general trend, an increment of the gas products and a reduction of the bio-oil* yield were observed when using the zeolite. Moreover, the non-catalytic pyrolysis produced one-phase bio-oil, while the catalytic reactions led to a two-phase bio-oil (aqueous and organic), which could be physically separated for their respective analyses. These results are consistent with the fact that HZSM-5 promoted different gasification reactions, such as decarbonylation or decarboxylation, as well as a slight increment of water generation, particularly in the case of CS-ac.

Table 2. Physicochemical properties of the catalyst

Sample	Si/Al	S_{BET} ($\text{m}^2 \text{ g}^{-1}$)	$S_{\text{MESO+EXT}}$ ($\text{m}^2 \text{ g}^{-1}$)	S_{MICRO} ($\text{m}^2 \text{ g}^{-1}$)	V_{TOTAL} ($\text{cm}^3 \text{ g}^{-1}$)	V_{MICRO} ($\text{cm}^3 \text{ g}^{-1}$)	Acidity ($\text{NH}_3 \text{ mmol g}^{-1}$)
HZSM-5	42	445	133	312	0.512	0.186	0.223

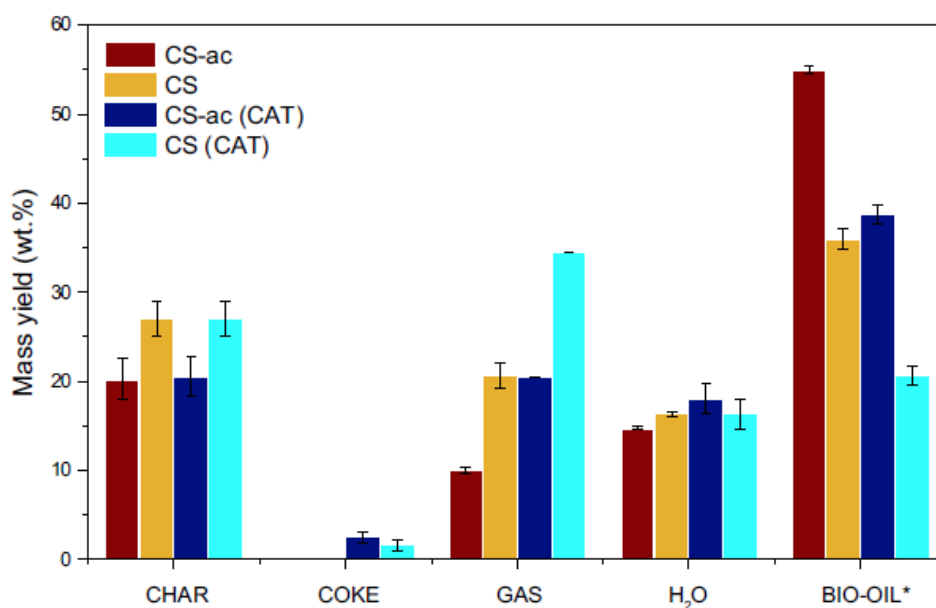


Fig. 2. Product yield distribution in the fast-pyrolysis tests, non-catalytic and catalytic, of the raw and de-ashed camelina straw.

Coke appeared as a new product in the catalytic pyrolysis experiments. As it was mentioned previously, coke represents the carbonaceous compounds deposited over the catalyst. Due to its low oxygen content, and therefore high heating value, it is desirable to minimize its production in order to not penalize the bio-oil energy yield. In this study, untreated biomass sample (CS) led to significantly lower coke amounts, which was attributed again to the catalytic effect of mineral matter, which strongly increased the gas yield. The mechanisms explaining coke formation over ZSM-5 have been already described, phenols and aldehydes in the primary pyrolysis vapors being identified as most involved components.^{45,46} Regarding the type of coke formed, the H/C ratio, determined by elemental analyses, was 0.76 and 1.04 for de-ashed and raw camelina straw, respectively. These are typical values of coke composed mainly by polyaromatics. In addition, burning the used catalyst in a thermobalance (not reported here) gives a unique peak with a maximum at 490–500 °C, which is associated to CO₂ release from coke. This means that coke deposited on the catalyst is highly reactive and, therefore, easy to remove by combustion.

Formation of char does not depend on the catalyst because it is mainly generated before the pyrolysis vapors reach the catalyst bed. It can be appreciated that its yield is significantly reduced by the pretreatment of the biomass, from ca. 27 wt% for CS to 20 wt% for CS-ac. This result fits well with the TG analysis for fixed carbon determination (Table 1) and, again, it is related with the catalytic activity of some inorganic species present in the biomass, particularly the alkali metals.⁴⁷

Regarding the gas fraction, Fig. 3 details its composition in the form of mass yields, together with their confidence intervals, of CO, CO₂, H₂, (C₁–C₃)_p: paraffins, and (C₂–C₃)_o: olefins. In all cases, CO and CO₂ were the major compounds, representing more than 90% of the total gas weight. Light paraffins and olefins were also detected but as minor constituents. The reproducibility of the reactions was again confirmed as the larger deviations were attained with the gases in minor concentrations, which is associated to analytical reasons. The gas analyses indicate that acidic washing of biomass induced a reduction in CO₂ formation and CO. The opposite effect was achieved with the incorporation of HZSM-5, which exhibited a significant rise of CO, CO₂, and light hydrocarbons, in particular methane, ethane, and propane, for both CS and CS-ac biomass

samples. According to these results, in the case of CS, the use HZSM-5 mainly promotes decarboxylation and in a lesser extent, decarbonylation. In contrast, the catalyst has a more balanced effect for the acid-washed biomass.

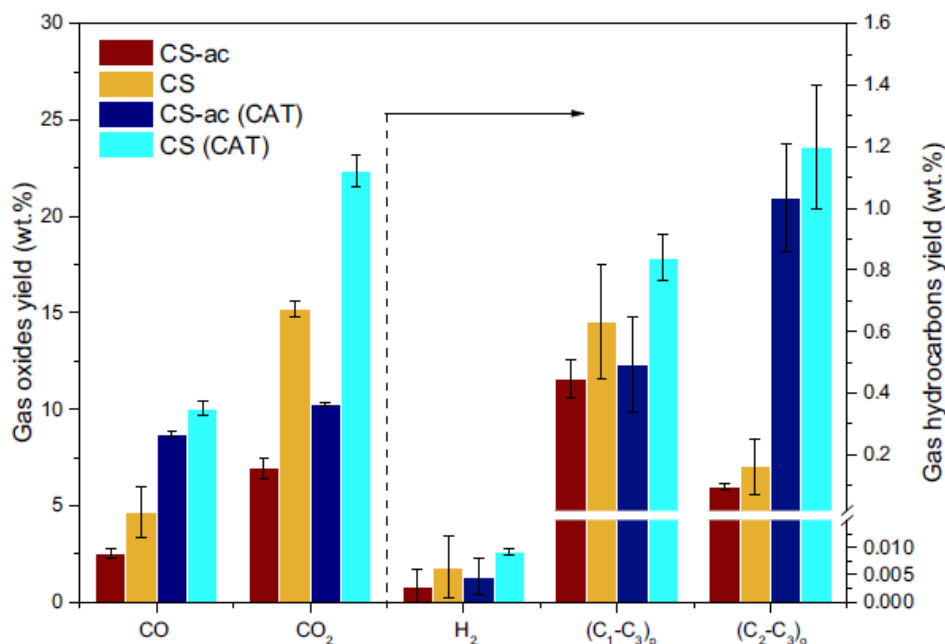


Fig. 3. Gas yield distribution in the fast-pyrolysis tests, grouped in CO, CO₂, H₂, (C₁-C₃)_p: paraffins, and (C₂-C₃)_o: olefins.

Property and product distribution in the bio-oils revealed remarkable differences depending on the presence of both the indigenous and/or external catalyst. As it can be observed in Table 3, the acidic treatment caused an increment of the mass yield, from 35.8 to 55 wt%, at expenses of increasing the oxygen content, which was larger than 40 wt% for CS-ac-derived bio-oil. The use of HZSM-5 for the pyrolysis of CS-ac partially reversed the effect of the acidic wash, so that the bio-oil* presented almost the same elemental composition, in particular the oxygen content, as well as the energy yield than that produced by thermal pyrolysis of CS. Especially remarkable are the differences attained for the catalytic pyrolysis over HZSM-5 of CS biomass, which led to a bio-oil* with a much lower oxygen content (ca. 18 wt%) and significantly higher H/C ratio. Accordingly, its HHV was the highest obtained (37.3 MJ kg_{db}⁻¹), which is significantly higher than the HHV of the raw biomass (18.5 MJ kg_{db}⁻¹). Despite the mass yield of this bio-oil* was really small, it retained 44.4% of the initial energy of the biomass. These results confirm the good deoxygenation capacity of HZSM-5, as it has been previously reported,⁴⁰ and that a synergetic effect with the mineral matter of the raw biomass seems to occur.

In order to have a more realistic output about the efficiency of the process in converting camelina straw wastes into bio-oils, the products obtained were compared in terms of energy yield. This energy yield relates the proportion of the chemical energy in the raw biomass that it is retained in each product. The comparison is presented in Fig. 4, in which the confidence intervals demonstrate the high reliability of the results. It can be clearly seen that coke, and more dramatically char, play important roles as energy drains due to its chemical composition, which are essentially based on carbon and hydrogen resulting in very high HHV. On the other hand, despite the gas yields were comparable to those of char in each experiment (Fig. 2), their contribution as chemical energy

carriers is noticeably smaller, as CO and specially H₂ and light HCs were present in minor concentrations.

Table 3. Parameters of the bio-oil* obtained in the pyrolysis tests.

Sample	%H ₂ O	Ultimate analysis, db (wt.%)				H/C	HHV (MJ/kg _{db})	Mass yield (wt%)	Energy yield (%)
		C	H	N	O				
CS-ac	21.2	52.3	6.4	0.1	41.1	0.12	21.6	55.0	65.8
CS	31.3	56.9	8.2	0.2	34.8	0.14	25.9	35.8	54.5
CS-ac (CAT)	31.4	57.4	7.5	0.2	34.9	0.13	25.2	38.9	54.2
CS (CAT)	45.3	69.1	12.8	0.2	18.0	0.19	37.3	20.1	44.4

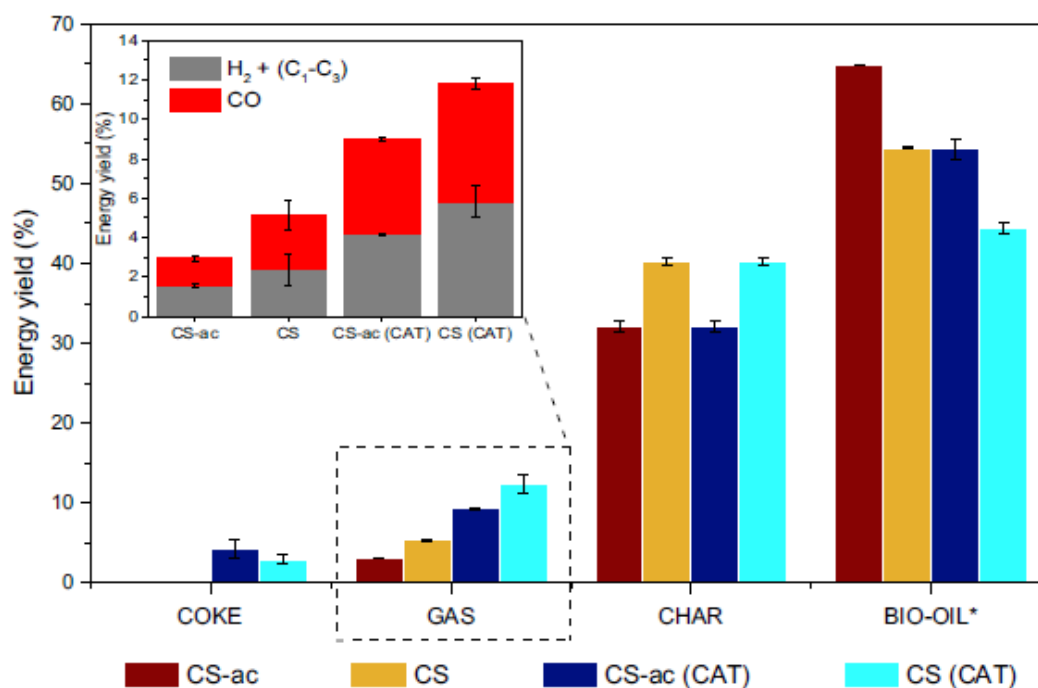


Fig. 4. Energy yield distribution among the different products corresponding to the thermal and catalytic fast-pyrolysis of the raw and de-ashed camelina straw

The pretreatment of biomass had an important effect on the composition at a molecular scale of the resulting bio-oils. Fig. 5 represents the results from GC-MS analysis of the bio-oils* in the form of compound families. The most abundant molecule detected in each family has been also drawn. It can be appreciated that the acid-washed camelina straw produced significantly less carboxylic acids, ketones, ethers, and oxygenated aromatics. In contrast, CS-ac generated a much larger proportion of furans and anhydro sugars, mainly levoglucosan. That trend is basically consistent with previous results obtained with different biomass types submitted to de-ashing treatments. These results suggest that inorganic matter, and particularly K, may play a role on promoting the transformation of sugar into smaller molecules such acids and ketones. On the other hand, the use of HZSM-5 induces the formation of a higher proportion of oxygenated aromatics and, remarkably, aromatic hydrocarbons for both CS and CS-ac, which are basically absent in thermal bio-oil*, as it can be observed in Fig. 5. In particular, arenes are more abundant in the liquid fraction obtained from the pyrolysis of CS-ac biomass over HZSM-5, while the proportion of oxygenated aromatics is higher for the pyrolysis bio-oil obtained from the CS sample. The formation of aromatics over HZSM-5 catalysts has been previously reported and, most likely, takes place through Diels-Alders condensation of light olefins which are intermediates produced by

cracking and dehydration on these solid acids.⁴⁸ This process is relevant to enhance the properties of the bio-oil as fuel.

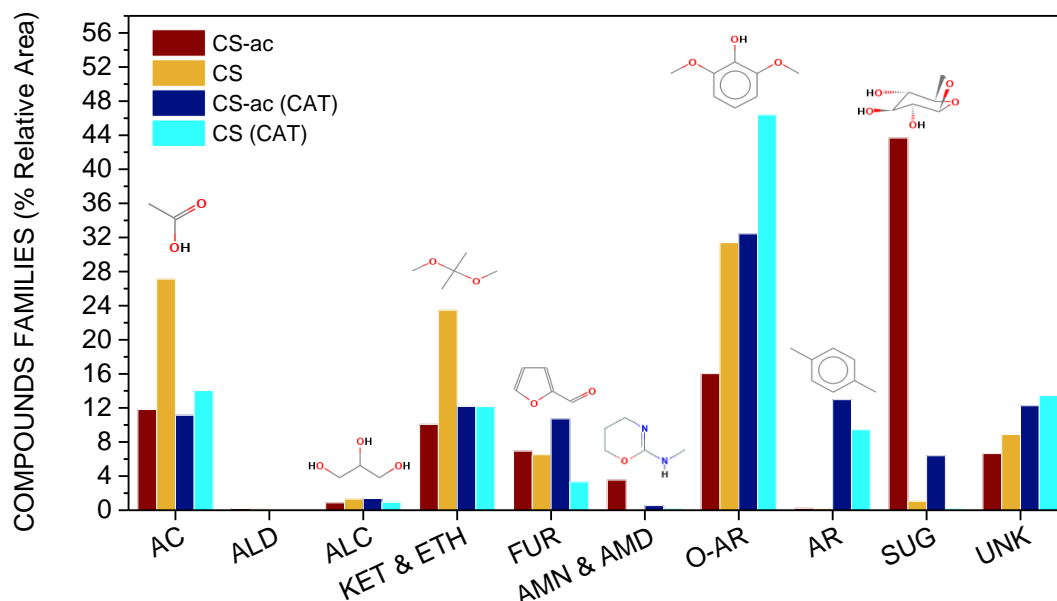


Fig. 5. Bio-oil* composition in terms of organic compounds families (% of relative area from GC–MS analyses) obtained in the different fast-pyrolysis tests. The most abundant compound detected has been drawn for each family.

Finally, regeneration of used ZSM-5 was carried out in order to evaluate the catalyst stability as it may affect the process viability. Such regeneration treatment consisted in a calcination at 550 °C, under air flow, during 4 h using a heating rate of 1.8 °C min⁻¹. Fig. 6 compares the mass yields of each pyrolysis fraction obtained, together with the gases composition, of both fresh and regenerated ZSM-5 catalyst. Negligible differences can be detected, which denotes a high stability of the catalyst during the pyrolysis reaction and also during regeneration. Despite a higher number of reaction regeneration cycles and also longer pyrolysis reactions (in larger scale and continuous operation mode) should be done, the interest in progressing the research about valorization of camelina straw by catalytic pyrolysis has been demonstrated.

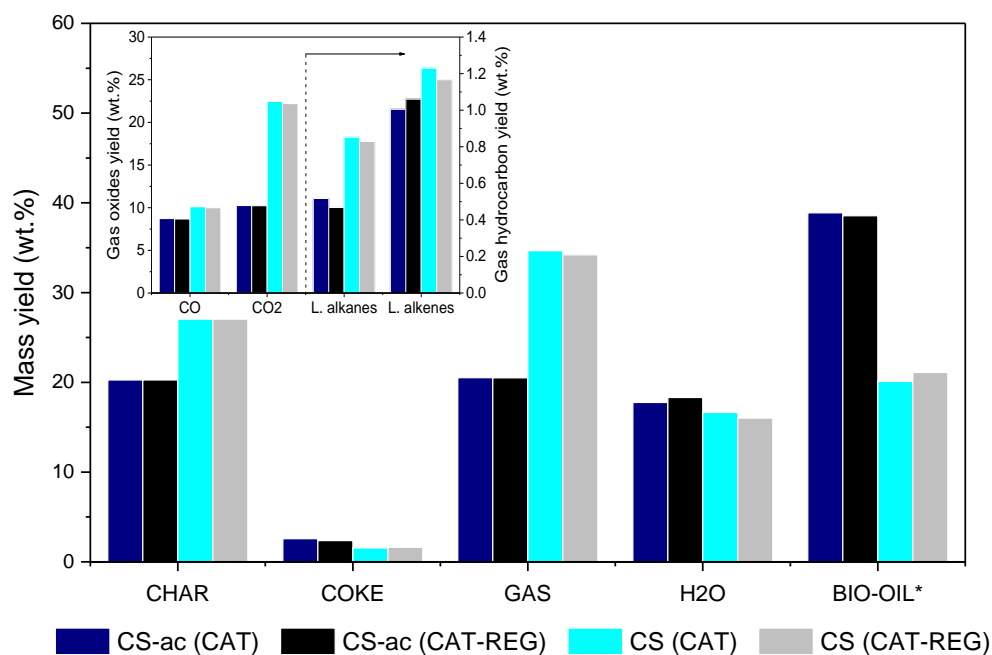


Fig. 6. Product yield distribution in the catalytic fast-pyrolysis tests of the raw and de-ashed camelina straw with fresh and regenerated catalyst.

4. Conclusions

The present work demonstrates the potential energetic valorization of camelina straw, which is a waste generated during the harvesting of *C. sativa*, an oilseed crop for the production of biodiesel or hydrotreated vegetable oil (HVO). The valorization has been attempted via both thermal and catalytic pyrolysis at 500 °C for the production of bio-oil, typically the first stage in liquid biofuel production via thermochemical pathways. The results obtained reveal that the existence of inorganic matter in the raw biomass plays an important role on the product distribution as they catalyze reactions of decarbonylation, decarboxylation, and carbonization of the pyrolysis vapors. Thus, the partial removal of such inorganics by an acid washing treatment (de-ashing) of the raw straw increases the proportion of bio-oil* (water-free basis) and the energy retained in this liquid fraction, but at expense of having a higher oxygen concentration.

Using HZSM-5 as catalyst for the pyrolysis assays promoted decarbonylation, decarboxylation, and in lower extent, dehydration reactions, resulting in a considerable increase of the gas yield. This affected to the bio-oil yield, which decreased but presented a better quality due to its lower oxygen concentration. A synergetic behavior seemed to exist when combining the catalytic effect of the inorganic matter in CS and HZSM-5. Thus, pyrolysis of the unwashed camelina straw in the presence of HZSM-5 yielded a bio-oil with rather low oxygen content (ca. 18 wt%), and the highest HHV among the bio-oils* obtained (37.3 MJ kg_{db}⁻¹). Despite the mass yield of this bio-oil* was really small (20 wt%), it retained 44.4% of the initial energy of biomass.

Analyses of molecular distribution in the bio-oil* reveal that de-ashing the feedstock led to bio-oils* with significantly less carboxylic acids, ketones, ethers, and oxygenated aromatics, but with larger proportion of anhydro sugars. On the other hand, the use of HZSM-5 promoted the formation of oxygenated aromatics and, interestingly, aromatic hydrocarbons for both types of biomass. The presence of these aromatic compounds is of interest for enhancing the properties of catalytic bio-oil from camelina straw as biofuel.

Finally, used ZSM-5 was regenerated by calcination and subsequently reused in the reaction, evidencing a high stability as negligible differences with the fresh catalyst were attained.

Acknowledgements

The authors gratefully acknowledge the financial support from the European Union Seventh Framework Programme (FP7/2007-2013) under grant agreement no. 604307 (CASCATBEL project) and the Spanish Ministry of Economy and Competitiveness Subprogram INNPACTO 2012 (IPT-2012-0219-120000).

CLARIANT is highly acknowledged for supplying HZSM-5 zeolite. Camelina Company España S.L. is acknowledged for supplying the camelina straw. CIEMAT (Spain), and in particular Dr. Ignacio Ballesteros, is acknowledged for assessing the biopolymers composition of the biomass.

References

1. M. Röder, C. Whittaker, P. Thornley, *Biomass Bioenergy*, 2014, **79**, 50–63.
2. G.W. Huber, S. Iborra, A. Corma, *Chem Rev*, 2006, **106** (9), 4044–4098.
3. D. Kubička, I. Kubičková, J. Čejka, *Catal Rev*, 2013, **55** (1), 1–78.
4. D. Meier, B. van de Beld, A.V. Bridgwater, D.C. Elliott, A. Oasmaa, F. Preto, *Renew Sust Energ Rev*, 2013, **20**, 619–641.
5. C. Azar, K. Lindgren, B.A. Andersson, *Energy Policy*, 2003, **31** (10), 961–976.
6. AEBIOM (1997) Annual Report 2015. **15**, 1–184.
7. D. Mohan, C.U. Pittman, P.H. Steele, *Energy Fuel*, 2006, **20** (3), 848–889.
8. S. Czernik, A.V. Bridgwater, *Energy Fuel*, 2004, **18** (2), 590–598.
9. J.F. Peters, D. Iribarren, J. Dufour, *Biomass Convers Biorefinery*, 2015, **5** (1).
10. D. Meier, O. Faix, *Bioresour Technol*, 1999, **68** (1), 71–77.
11. M.S. Talmadge, R.M. Baldwin, M.J. Bidy, et al, *Green Chem*, 2014, **16** (2), 407–453.
12. D.K. Shen, S. Gu, *Bioresour Technol*, 2009, **100** (24), 6496–6504.
13. P.R. Patwardhan, R.C. Brown, B.H. Shanks, *ChemSusChem*, 2011, **4** (5), 636–643.
14. W. Mu, H. Ben, A. Ragauskas, Y. Deng, *BioEnergy Res*, 2013, **6** (4), 1183–1204.
15. T. Qu, W. Guo, L. Shen, J. Xiao, K. Zhao, *Ind Eng Chem Res*, 2011, **50** (18), 10424–10433.
16. K. Raveendran, A. Ganesh, K.C. Khilar, *Fuel*, 1995, **74** (12), 1812–1822.
17. J. Robert, T.A.M. Evans, *Energy Fuel*, 1987, **1** (2), 123–137.
18. R. Fahmi, A.V. Bridgwater, L.I. Darvell, J.M. Jones, N. Yates, S. Thaind, I.S. Donnison, *Fuel*, 2007, **86** (10–11), 1560–1569.
19. R. Fahmi, A.V. Bridgwater, I. Donnison, N. Yates, J.M. Jones, *Fuel*, 2008, **87** (7), 1230–1240.
20. M. Nik-Azar, M. Hajaligol, M. Sohrabi, B. Dabir, *Fuel Process Technol*, 1997, **3820** (96).

21. J. Capablo, P.A. Jensen, K.H. Pedersen, K. Hjuler, L. Nikolaisen, R. Backman, F. Frandsen, *Energy Fuels*, 2009, **23** (4), 1965–1976.
22. Y. Solantausta, A. Oasmaa, K. Sipilä, C. Lindfors, J. Lehto, J. Autio, P. Jokela, J. Alin, J. Heiskanen, *Energy Fuels*, 2012, **26** (1), 233–240.
23. D.A. Ruddy, J.A. Schaidle, J.R. Ferrell, J. Wang, L. Moens, J.E. Hensley, *Green Chem*, 2014, **16** (2), 454–490.
24. A. Galadima, O. Muraza, *Energy Convers Manag*, 2015, **105**, 338–354.
25. P.S. Rezaei, H. Shafaghat, W.M.A. Wan Daud, *Appl Catal Gen*, 2014, **469**, 490–511.
26. C. Liu, H. Wang, A.M. Karim, J. Sun, Y. Wang, *Chem Soc Rev*, 2014, **43** (22), 7594–7623.
27. H. Zhang, R. Xiao, H. Huang, G. Xiao, *Bioresour Technol*, 2009, **100** (3), 1428–1434.
28. Y. Fan, Y. Cai, X. Li, N. Yu, H. Yin, *J Anal Appl Pyrolysis*, 2014, **108**, 185–195.
29. O.D. Mante, J. Rodriguez, S.D. Senanayake, S.P. Babu, *Green Chem*, 2015, **17** (4), 2362–2368.
30. P.T. Williams, P.A. Horne, *Fuel*, 1995, **74** (12), 1839–1851.
31. J. Jae, R. Coolman, T.J. Mountziaris, G.W. Huber, *Chem Eng Sci*, 2014, **108**, 33–46.
32. K.S. Triantafyllidis, E.F. Iliopoulou, E.V. Antonakou, A.A. Lappas, H. Wang, T.J. Pinnavaia, *Microporous Mesoporous Mater*, 2007, **99** (1–2), 132–139.
33. J. Zubr, *Ind Crop Prod*, 1997, **6** (2), 113–119.
34. J.T. Budin, W.M. Breene, D.H. Putnam, *J Am Oil Chem Soc*, 1995, **72** (3), 309–315.
35. J. Xu, J. Jiang, J. Zhao, *Renew Sust Energ Rev*, 2016, **58**, 331–340.
36. I. Kubicková, D. Kubicka, *Waste Biomass Valoriz*, 2010, **1** (3), 293–308.
37. G. Knothe, *Prog Energy Combust Sci*, 2010, **36** (3), 364–373.
38. S.S. Malhi, E.N. Johnson, L.M. Hall, W.E. May, S. Phelps, B. Nybo, *Can J Soil Sci*, 2014, **94** (1), 35–47.
39. B. Gómez-Monedero, F. Bimbela, J. Arauzo, J. Faria, M.P. Ruiz, *Energy Fuel*, 2015, **29** (3), 1766–1775.
40. H. Hernando, S. Jiménez-Sánchez, J. Feroso, P. Pizarro, J.M. Coronado, D.P. Serrano, *Catal Sci Technol*, 2016, **6**, 2829–2843.
41. J.B. Sluiter, R.O. Ruiz, C.J. Scarlata, A.D. Sluiter, D.W. Templeton, *J Agric Food Chem*, 2010, **58** (16), 9043–9053.
42. S.W. Banks, A.V. Bridgwater, *Catalytic fast pyrolysis for improved liquid quality. Handbook of biofuels production: processes and technologies*. Woodhead Publishing, 2nd ed. Elsevier, 2016, 391–429.
43. J. Feroso, H. Hernando, P. Jana, I. Moreno, J. Přech, C. Ochoa-Hernández, P. Pizarro, J.M. Coronado, J. Čejka, D.P. Serrano, *Catal Today*, 2016, **277**, 171–181.
44. Phyllis2 database for biomass and waste; ECN. No Title. 2012. <https://www.ecn.nl/phyllis2>

45. A.G. Gayubo, A.T. Aguayo, A. Atutxa, R. Aguado, J. Bilbao, *Ind. Eng. Chem Res*, 2004, **43**, 2610–2618.
46. A.G. Gayubo, A.T. Aguayo, A. Atutxa, R. Aguado, M. Olazar, J. Bilbao, *Ind Eng Chem Res*, 2004, **43**, 2619–2626.
47. M. Antal, M. Grønli, *Ind Eng Chem Res*, 2003, **42** (8), 1619–1640.
48. Y.T. Cheng, G.W. Huber, *Green Chem*, 2012, **14** (11), 3114–3125.

Article 3

Performance of MCM-22 zeolite for the catalytic fast-pyrolysis of acid-washed wheat straw

Catalysis Today, 2018, 304, 1, 30-38

Catalysis Today 304 (2018) 30–38

Contents lists available at ScienceDirect

 **Catalysis Today** 

journal homepage: www.elsevier.com/locate/cattod

Performance of MCM-22 zeolite for the catalytic fast-pyrolysis of acid-washed wheat straw 

Héctor Hernando^a, Javier Feroso^a, Cristina Ochoa-Hernández^b, Maksym Opanasenko^b, Patricia Pizarro^{a,c}, Juan M. Coronado^a, Jiří Čejka^b, David P. Serrano^{a,c,*}

^a Thermochemical Processes Unit, IMDEA Energy Institute, 28935, Móstoles, Madrid, Spain
^b J. Heyrovský Institute of Physical Chemistry, Academy of Sciences of the Czech Republic, v.v.i., 182 23, Prague 8, Czech Republic
^c Chemical and Environmental Engineering Group, ESCET, Rey Juan Carlos University, 28933, Móstoles, Madrid, Spain

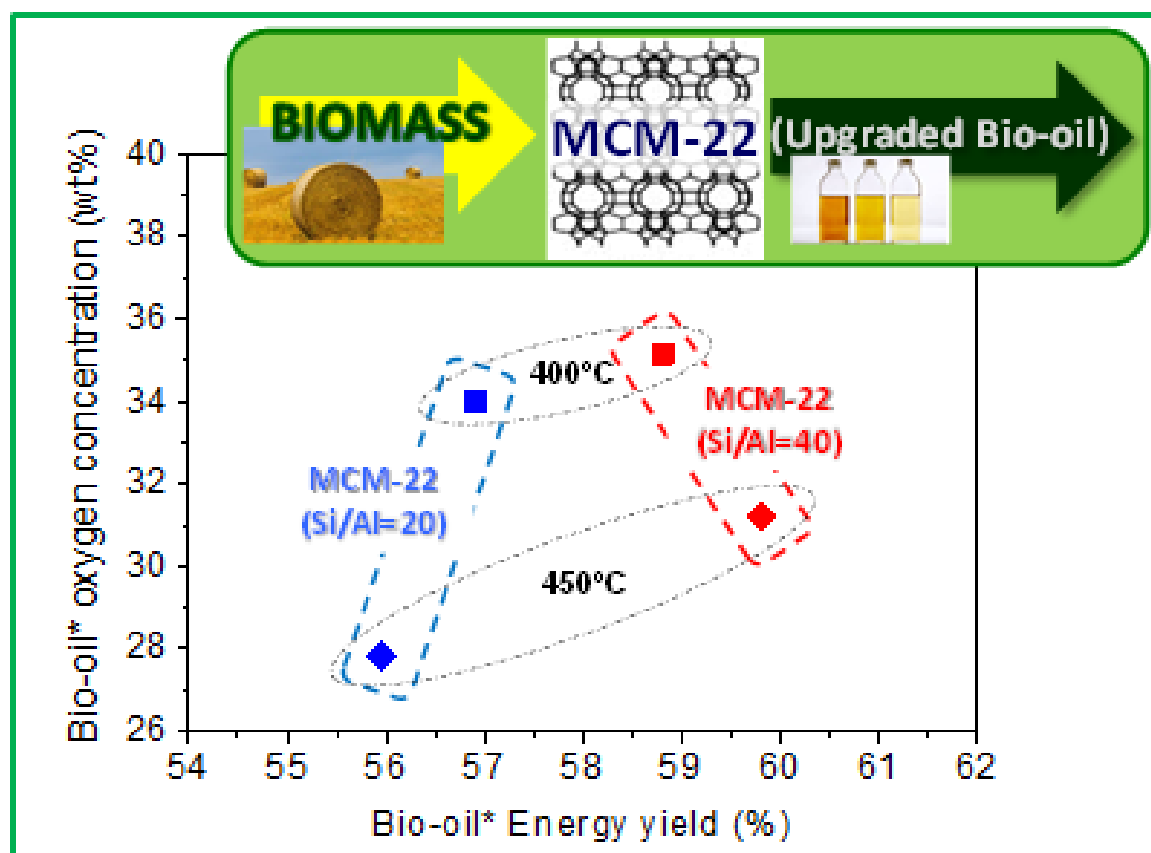
Impact JCR factor, (JCR 2017): 4.667
Category: Applied Chemistry. 6 of 72 (Q1)

ABSTRACT

MCM-22 zeolite samples, having different Si/Al ratios, have been studied for the fast-pyrolysis of acid-washed wheat straw at two catalytic pyrolysis temperatures aimed to the production of partially upgraded bio-oil. The best combination of bio-oil deoxygenation activity and energy yield is obtained when the catalytic bed was operated at 450 °C using the MCM-22 sample with the lowest Al content (Si/Al=40). Interestingly, the increase in the reaction temperature results in a lower amount of coke deposited over the zeolite. On the other hand, reducing the zeolite Si/Al ratio had a negative effect as a higher concentration of acid sites promotes non-desired reactions: severe cracking of the bio-oil vapours, leading to the enhanced production of gaseous hydrocarbons, and coke formation. Coke produced over MCM-22 zeolite exhibits high oxygen content, whereas the bio-oil fraction presents a high concentration of oxygenated aromatics. These results denote the limited aromatization activity of MCM-22 zeolite for producing aromatic hydrocarbons, in particular when compared with ZSM-5, being of interest for the selective production of phenolic compounds by biomass catalytic pyrolysis.

Keywords: lignocellulosic biomass, catalytic fast-pyrolysis, bio-oil deoxygenation, MCM-22 zeolite

GRAPHICAL ABSTRACT



1. Introduction

Lignocellulosic biomass is the most abundant and low-cost raw material for the production of biofuels with reduced environmental impact.¹ In recent years, this resource has attracted a great interest for developing new advanced biofuels from sources that do not compete with the food industry, such as energy crops and forestry and agricultural residues.^{2,3}

Fast-pyrolysis has become one of the most promising thermochemical routes investigated for the transformation of biomass into liquid fuels. In this process, biomass is quickly decomposed through rapid heating ($> 1000\text{ }^{\circ}\text{C s}^{-1}$) to moderate temperatures ($400\text{--}600\text{ }^{\circ}\text{C}$) at a short vapours residence times ($< 2\text{ s}$) under inert atmosphere to yield a solid residue (char), non-condensable gases, and a liquid (bio-oil) as main products.^{4,6} The last fraction can be used directly as fuel in thermal power stations, even when it presents poorer quality than petroleum-derived fuels. Likewise, pyrolysis bio-oil is attracting high interest to be employed for the production of advanced liquid biofuels and/or value added chemicals.^{4,7} Nevertheless, bio-oil presents numerous unfavourable properties, such as large oxygen content ($35\text{--}40\text{ wt}\%$), acid nature (pH of $2\text{--}4$), significant amounts of water ($15\text{--}30\text{ wt}\%$), low physicochemical stability, high viscosity, and high density.^{4,5,8} Chemically, this liquid consists of a very complex mixture of oxygenated species including carboxylic acids, ketones, aldehydes, furans, phenolics, etc., derived from the fragmentation of the biopolymers composing biomass.⁹

Significant improvements in the properties of the bio-oil can be achieved using a catalyst bed, either in the pyrolysis reactor (in situ catalytic pyrolysis) or in a downstream catalytic reactor (ex situ catalytic pyrolysis) due to the partial oxygen removal of the pyrolysis vapours. This route has recently arisen as one of the most efficient options for bio-oil upgrading into biofuels/biochemicals, with several technologies based on the pyrolysis process near to their commercialization.¹⁰ Accordingly, a large number of research works have been published and recently dealing with the development of catalysts and the influence of diverse operation conditions on biomass catalytic pyrolysis.^{5,11-15} The catalyst promotes a number of reactions: cracking, oligomerization, cyclization, aromatization and deoxygenation, which are coupled with those already occurring just by thermochemical degradation of the different biomass components. In particular, deoxygenation may proceed by three main pathways: decarboxylation, decarbonylation and dehydration, leading to the formation of CO_2 , CO and H_2O , respectively.

Numerous catalysts have been reported for biomass catalytic fast-pyrolysis, including zeolites¹⁶⁻¹⁹ and metal oxides^{18,20,21}. A high degree of deoxygenation has been achieved using strong acidic zeolitic catalysts, which produce large concentrations of aromatic hydrocarbons. However, high density of acidic sites of the catalyst provokes a sharp decrease in the bio-oil yield, because of excessive cracking. At the same time, the catalyst suffers from extensive coking, which results in its fast deactivation.²²⁻²⁷ Moreover, zeolites are limited by the size of their micropores hindering the accessibility to the active sites and impeding the diffusion of large molecules. To tackle this problem, recent advances have been achieved with the development of novel two-dimensional (2D) zeolites²⁸⁻³⁰ providing a high share of non-sterically limited external surface area and a combination of micro- and mesopores. Thus, Lee et al.³¹ have studied the catalytic pyrolysis of biomass constituents (cellulose, hemicelluloses and lignin) using unilamellar mesoporous ZSM-5 nanosheets (UMNs) and Al-SBA-15 catalysts. UMN showed a better performance in terms of bio-oil properties, such as lower oxygen content and higher quality, due to the higher acidity of the catalyst.

MCM-22 zeolite presents interesting properties that can be exploited for the catalytic fast pyrolysis of biomass. This material has a framework topology that consists of two independent 10-ring pore systems, one formed by two-dimensional sinusoidal channels, and the other by large cages having an inner diameter and a height of approximately 7.1 and 18.2 Å accessible via 10-ring channels, respectively.³² Only a few studies can be found in the literature employing MCM-22 zeolite for the catalytic upgrading of vapours produced by pyrolysis of biomass derived compounds, such as glucose³³ or levoglucosan^{34,35}. Likewise, lignocellulosic biomass (paddy husk) has been directly pyrolyzed over this type of zeolite.³⁶

The main goal of the present work is to investigate the performance of MCM-22 zeolite for the catalytic fast-pyrolysis of lignocellulosic biomass. Thus, the effect of both the zeolite acidity and the catalytic pyrolysis temperature during the pyrolysis tests on the bio-oil mass and energy yields, as well as on its composition, is here discussed.

2. Experimental

2.1. Biomass sample

In this work, the lignocellulosic biomass employed was wheat straw (WS). It was crushed and sieved to get a particle size of 0.5-1 mm. WS was partially demineralized by means of a mild acid-washing pre-treatment, intended to avoid the catalytic interference of the mineral matter components on the catalytic activity of the MCM-22 zeolites employed in the reaction tests.

2.1.1. Biomass acid-washing pre-treatment and characterization

50 g of wheat straw were dispersed in 1000 cm³ of an aqueous HNO₃ solution (1 wt%) and subjected to a continuous magnetic stirring at a constant temperature of 50 °C for 2 h. After this pre-treatment, the biomass suspension was vacuum filtered and washed with milli-Q water until reaching neutral pH. Then, the biomass sample was dried at 105 °C for 2 days. This acid-washed sample was denoted as WS-ac.

The composition of raw and acid-washed biomass samples in biopolymers (cellulose, hemicellulose and lignin) was determined by methods described elsewhere.³⁷

2.2. Synthesis of catalysts (MCM-22 zeolites)

MCM-22 lamellar precursors (MCM-22P) with Si/Al ratios of 20 and 40 were synthesized following the procedure reported elsewhere.^{38,39} In a general synthesis, 2.4 cm³ of NaOH (50% in H₂O, Aldrich) and the proper amount of NaAlO₂ (Riedel-de-Haën) were dissolved in 200 g of H₂O. Subsequently, 116.2 g of LUDOX AS-30 (Aldrich) and 22 cm³ of hexamethyleneimine (HMI) were added and vigorously stirred for 30 min. The final gel was loaded into a stainless-steel Parr reactor and the hydrothermal synthesis was carried out at 150 °C for 96 h under mechanical stirring (350 rpm). After cooling down the reactor, the product was recovered by filtration, washed out with water and dried at 110 °C. The sample was finally calcined using a ramp of 1 °C min⁻¹ up to 482 °C and kept for 3 h under nitrogen. Then, the temperature was increased up to 540 °C with a ramp of 1 °C min⁻¹ and kept for 8 h under a flow of air. The calcined MCM-22 material was converted into NH₄⁺ form by four cycles of ion-exchange with 1.0 M NH₄NO₃ solution at room temperature for 3.5 h. Subsequently, the sample was calcined at 480 °C for 6 h using a ramp of 2 °C min⁻¹ in order to obtain the final zeolite in H⁺ form.

2.3. Biomass pyrolysis tests

The schematic diagram of the lab-scale experimental setup used for the fast-pyrolysis experiments of WS-ac sample can be found in previous publications.²⁶ This reaction system consists of a downdraft fixed-bed stainless steel reactor (16 mm i.d. and 400 mm length) with two separated zones, pyrolytic and catalytic, heated by two independent electrical furnaces. The non-catalytic and catalytic pyrolysis temperatures are measured by two type K thermocouples, placed on the char bed and on the catalyst bed, respectively. For the catalytic experiments, the reactor was loaded with 0.8 g of catalyst, to operate with a catalyst to biomass ratio of 0.2. The WS-ac sample (4 g) was placed in the biomass tank and kept at room temperature. Two internal stainless-steel tubes were placed inside the reactor to separate the catalytic bed from the pyrolytic zone. A quartz wool plug and a metallic grid were placed over each tube and over the catalyst particles to avoid possible mixing between the char particles and the catalyst bed. The pyrolysis tests were carried out at atmospheric pressure and temperatures of 550 °C and 400-450 °C for the pyrolysis and catalytic zones, respectively.

Prior to each pyrolysis experiment and during the heating up of the reactor, the biomass tank and all the reaction system were purged with a N₂ flow supplied by mass flow controllers, until the O₂ concentration levels of the exiting gas dropped to < 0.1 vol%. Once the reactor temperature reached the desired set point, the feeding valve was open and the biomass fell into the reactor. Consequently, pyrolysis reactions occurred leading to the formation of a solid carbonaceous residue (char) and vapours. The char fraction was accumulated in the pyrolytic zone, whereas vapours were swept by a N₂ flow of 100 cm³ min⁻¹ and passed through the catalyst bed. Upgraded vapours left rapidly the reaction zones and were condensed by means of a condensation system comprising four 125 cm³ flasks connected in series and refrigerated by an ice-water bath (0-4 °C).

After the experiments, the bio-oil, char and the used catalyst were collected for their further characterization by the analytical techniques described next. The bio-oil fraction measured in water-free basis has been named as bio-oil* along the manuscript.

2.4. Analytical techniques

2.4.1. Proximate and ultimate analysis

The proximate analyses, according to European standards, included the determination of moisture (UNE-EN 14774-1:2010), ash (UNE-EN 14775:2010), volatile matter (UNE-EN 15148:2010) and fixed carbon (determined by difference) contents.

Moisture content in lignocellulosic biomass was determined by the oven drying method, calculating the weight lost undergone by a certain amount of sample after being dried in an oven at 105 °C for 3 h.

Ash content in solid samples determined by the muffle oven calcination method, calculating the weight loss achieved in a certain amount of sample (previously dried) after being calcined at 550 °C for 3 h.

Volatile matter in lignocellulosic samples was determined by thermogravimetric analysis (TGA) using a NETZSCH STA 449 apparatus, calculating the weight difference attained when a certain amount of sample (previously dried) was heated up to 900 °C for 7 min under an inert flow of N₂.

Finally, Fixed Carbon (dry basis) was determined by difference according to the following expression:

$$\text{Fixed Carbon} = 100 - \text{Volatile Matter} - \text{Ash} \quad (1)$$

where, Volatile Matter and Ash content are expressed in dry basis.

The ultimate analysis of biomass samples and pyrolysis products (bio-oil, char and coke) was carried out in a micro-elemental analyser (Thermo Scientific FLASH 2000 CHNS/O). C, H, N, S elements were directly measured whereas O was determined by difference.

The high heating value (HHV) of any sample i , including both biomass feedstocks and any product fraction, was calculated from the ultimate analysis according to the correlation reported by Channiwala and Parikh:⁴⁰

$$\text{HHV}_i (\text{MJ/kg}_i) = 0.3491 \cdot C + 1.1783 \cdot H + 0.1005 \cdot S - 0.1034 \cdot O - 0.0151 \cdot N - 0.0211 \cdot A \quad (2)$$

where C , H , O , N , S and A represent carbon, hydrogen, oxygen, nitrogen, sulfur and ash contents of sample i , expressed in wt% on dry basis. This equation is valid for solid, liquid and gaseous fuels.

2.4.2. Chemical composition

The chemical composition of both the biomass ash (mineral matter) and zeolite catalysts was measured by inductively coupled plasma-optical emission spectroscopy (ICP-OES) analyses with a Perkin Elmer Optima 3300 DV instrument. A representative amount of each ash sample was digested in a mixture of HF and HNO₃ in an Anton Paar (MW3000) microwave oven. Previous to the digestion, ash from the lignocellulosic biomass was collected by burning 20 g of wheat straw, both raw and acid-washed, in a muffle oven at 815 °C in air flow for 2 h.

2.4.3. X-ray diffraction (XRD)

Powder X-ray diffraction (XRD) analyses of the zeolites were performed on a Philips X'Pert PRO diffractometer operated at 45 kV and 40 mA with Cu K α radiation ($\lambda=1.542\text{\AA}$).

2.4.4. Ar adsorption-desorption isotherms

The textural properties of the MCM-22 zeolites were determined by argon physisorption isotherms at -186 °C on a Quantachrome AUTOSORB iQ system. The BET area was calculated applying the Brunauer-Emmet-Teller (BET) equation. Microporous surface areas and micropore volumes were determined by applying t-plot method whilst mesopore surface areas were estimated by difference between total and micropore surface areas.

2.4.5. Fourier Transform Infrared Spectroscopy (FTIR)

The acidic properties of zeolites were measured by pyridine adsorption followed by FTIR spectroscopy. Self-supporting wafers (ca. 8-12 mg cm⁻²) were prepared and activated at 450 °C for 4 h under vacuum. Subsequently, 3 torr of pyridine vapours (probe molecule) were introduced into the IR cell at 150 °C and kept inside for 20 min in order to be adsorbed over the acidic groups. Subsequently, the strength of the acid sites was studied subjecting the sample at different desorption temperatures (150, 250, 350 and 450 °C) for 20 min. All spectra were recorded with a resolution of 4 cm⁻¹ in the 4000-400 cm⁻¹ range using a Nicolet spectrometer equipped with a MCT/B detector cooled with liquid nitrogen and normalized to a 10 mg/cm² wafer. The amount of the acid sites was calculated using the following bands

(ν_{19b} vibration mode of pyridine) and integrated molar extinction coefficients: pyridine PyH^+ band at 1545 cm^{-1} ($\epsilon=1.67 \text{ cm} \mu\text{mol}^{-1}$) and pyridine PyL bands at $1461+1454 \text{ cm}^{-1}$ ($\epsilon=2.2 \text{ cm} \mu\text{mol}^{-1}$).^{41,42}

2.4.6. Karl-Fischer titration

The water content of bio-oil was determined using Karl-Fischer titrations in a Mettler-Toledo V20S compact volumetric KF titrator (ASTM E203-08).

2.4.7. Determination of coke over used catalysts

TGA was applied to quantify the amount of coke deposited on the used catalysts, by measuring the weight loss occurred during combustion under air flow, using a heating rate of $20 \text{ }^\circ\text{C min}^{-1}$ up to $550 \text{ }^\circ\text{C}$.

2.4.8. Gas chromatography (GC)

Permanent gases and light hydrocarbons ($\text{C}_1\text{-C}_4$) collected in a sampling bag during the pyrolysis tests were analysed in a dual channel Agilent[®] CP-4900 Micro Gas Chromatograph (Micro-GC), which is equipped with molecular sieve (Molsieve 5 \AA) and HayeSep A columns and a thermal conductivity detector (TCD). Helium was used as carrier gas. The TCD is periodically calibrated with a standard gas mixture containing N_2 (internal standard), O_2 , H_2 , CO , CO_2 , CH_4 , C_2H_4 , C_2H_6 , C_3H_6 and C_3H_8 . Thus, the gas mass yield and its elemental composition (C, H and O) can be calculated.

2.4.9. Gas chromatography coupled with mass spectrometry (GC-MS)

The components present in bio-oil were analysed by a Gas Chromatograph Mass Spectrometer, GC-MS, Bruker[®] SCION 436-GC, (Electron Energy 70eV , Emission 300V ; He flow rate: $1 \text{ cm}^3 \text{ min}^{-1}$; Column WCOT fused silica $30 \text{ m} \times 0.25 \text{ mm ID} \times 0.25 \mu\text{m}$). NIST EI-MS spectral library (v2.0) was used for the compounds identification (with a minimum match score of 700). Bio-oil components were further grouped in families according to their main functional groups.

2.5. Catalytic pyrolysis data evaluation

By adding the measured weights of bio-oil, char, coke and gas fractions, the total mass balance was closed to the amount of biomass fed with an experimental error lower than 5 wt% in all tests. Details on the mass balances applied to the catalytic and non-catalytic biomass pyrolysis tests can be found in a recent work.²⁶

Energy yield of any i pyrolysis product is defined as the proportion of the chemical energy (heating value) contained in the initial biomass that remains in this product. Accordingly, it is calculated by the following equation:

$$\text{Energy yield of } i \text{ (\%)} = 100 \cdot \frac{\text{HHV}_i \cdot \text{Product } i \text{ yield}}{\text{HHV}_{\text{Biomass}}} \quad (3)$$

The overall and catalytic deoxygenation selectivity to product k (being k : H_2O for dehydration; CO for decarbonylation; or CO_2 for decarboxylation), were estimated according to the following equations:

$$\text{Overall deoxygenation to } k \text{ (wt\%)} = 100 \cdot \frac{O_k(g)}{O_{\text{Biomass}}(g)} \quad (4)$$

$$\text{Catalytic deoxygenation to } k \text{ (wt\%)} = 100 \cdot \left[\frac{O_{k(\text{cat})}(\text{g}) - O_{k(\text{non-catalytic})}(\text{g})}{O_{\text{Biomass}}(\text{g})} \right] \quad (5)$$

where for the overall deoxygenation, O_k is the oxygen content in the form of k (H_2O , CO or CO_2) obtained in the any experiment (catalytic or non-catalytic), and O_{biomass} is the oxygen content in the biomass feed. The catalytic deoxygenation selectivity to either H_2O , CO or CO_2 was determined by subtracting the oxygen contained in such molecules obtained in the non-catalytic pyrolysis tests from the oxygen present in those compounds produced in the catalytic pyrolysis experiments.

3. Results and discussion

3.1. Biomass composition and properties (WS-ac)

The complete chemical characterization of the biomass sample used in the present work (WS-ac), together with that of the raw sample (WS), were analysed and described in a previous work.²⁶ In that work is shown that raw wheat straw possesses a composition consistent with that expected for this type of herbaceous feedstocks,⁴³ with a volatile matter content of 75 wt%, while the fixed carbon and ashes contents are 20 and 4.7 wt%, respectively. Interestingly, it was observed that the acid-washing pre-treatment had an effect not only on the ash content, which was reduced in more than 25%, but it also modified other parameters related to the proximate analysis. Thus, volatile matter of WS-ac was 10% higher than for the raw material, while fixed carbon was diminished in more than 33%, while some changes were also observed in the biopolymers composition.

As the main goal of the current work was to study the performance of MCM-22 zeolites on the catalytic fast-pyrolysis of biomass, only the WS-ac sample was employed as feedstock to minimize any possible interference associated to the indigenous catalysts naturally present in raw biomass (WS), such as alkali and alkali earth metals (AAEM); which has been investigated in a recent work.⁹

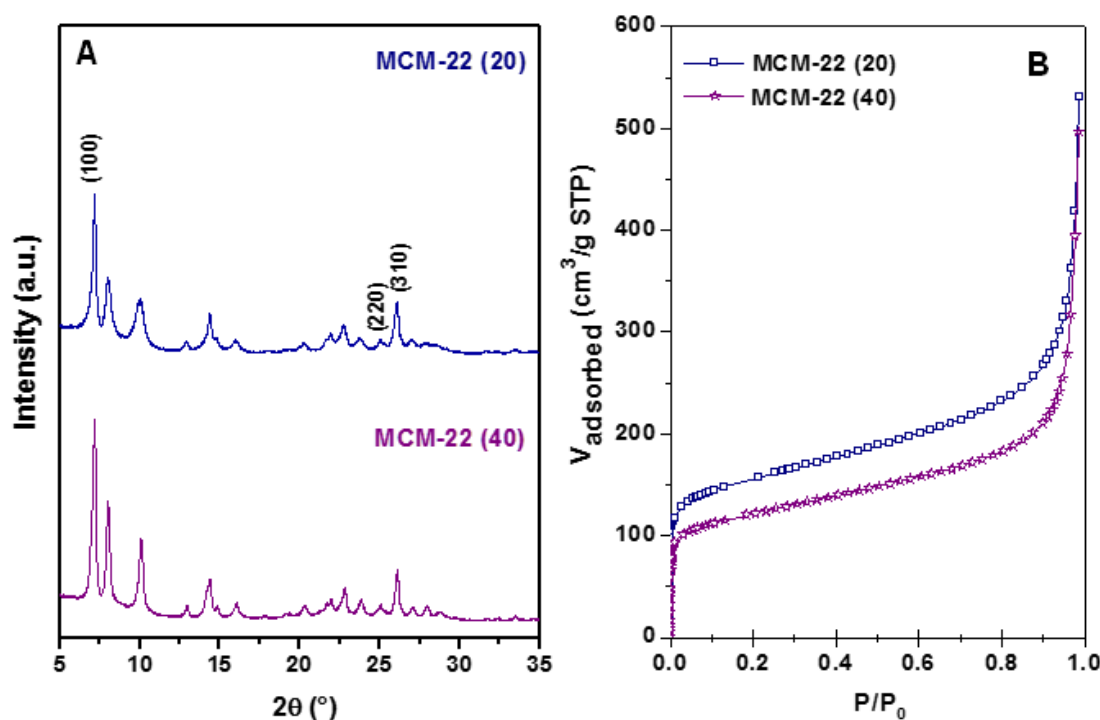
3.2. Catalysts properties

Two MCM-22 zeolite samples, having different Si/Al ratio, have been synthesized to investigate their performance in the catalytic fast-pyrolysis of acid-washed wheat straw. These samples have been characterized by different techniques to determine their physicochemical features. Aluminum content has been measured by ICP-OES (Table 1). The concentrations are quite close to the amounts added to the synthesis mixtures indicating that aluminum present in the synthesis gel has been successfully incorporated into the zeolite framework. The structure and crystallinity of the samples were assessed by X-ray powder diffraction, and the corresponding XRD patterns of the calcined samples are shown in Fig. 1. The two samples present the three distinctive reflections characteristic for materials with MWW topology. These intra-layer reflections are (1 0 0), (2 2 0) and (3 1 0) at 12.46, 3.56 and 3.43 Å d-spacing, respectively. Besides, the absence of the inter-layer diffraction line at $\sim 6.5^\circ$ (2 0 0) indicates the condensation of the layers upon calcination, yielding ordered 3-D MCM-22.^{44,45} The sharper peaks of the sample with higher Si/Al ratio indicates that the increase in the aluminum concentration results in the decrease of crystallite size of MCM-22 that is in agreement with the results reported previously.⁴⁴

Table 1. Physicochemical properties of the MCM-22 zeolite samples.

Catalysts	Si/Al ^a	S _{BET} ^b (m ² /g)	S _{EXT} ^c (m ² /g)	S _{MIC} ^d (m ² /g)	V _{MIC} ^e (cm ³ /g)	V _{Total} ^f (cm ³ /g)
MCM-22 (20)	19.4	502	196	306	0.114	0.534
MCM-22 (40)	40.0	389	160	229	0.086	0.502

^aICP-OES measurements; ^bBET surface area; ^cExternal surface area; ^dMicropore surface area; ^eMicropore volume; ^fTotal pore volume at P/P₀ ≈ 0.98.

**Fig. 1.** XRD patterns (A) and Ar physisorption isotherms (B) of MCM-22 zeolites.

Textural properties of the MCM-22 materials were determined by Ar physisorption (Fig. 1B), being summarized in Table 1. The zeolite isotherms show a high adsorption at low relative pressures, which is typical of microporous solids. However, significant adsorption takes place also at intermediate and high relative pressures, which indicates the existence of interparticle porosity, as confirmed by the values of the textural properties included in Table 1. The increase in the Si/Al molar ratio leads to both lower surface areas and total pore volume, going from 502 m²/g and 0.534 cm³/g for the MCM-22 (20) to 389 m²/g and 0.502 cm³/g for the MCM-22 (40). Likewise, a reduction is also observed in the value of the external surface area when reducing the Al content. Nevertheless, both MCM-22 samples exhibit high values of the external surface area, which can be considered a relevant and convenient feature for the conversion of bulky compounds. The values of the textural properties of the two MCM-22 samples are in agreement with those observed previously for this type of zeolite.⁴⁴

Differences in the acidic properties (type, concentration and strength of the acid sites) with the variation of Si/Al molar ratios have been analysed by adsorption of pyridine followed by FTIR. As shown in Fig. 2, it is possible to distinguish the bands ascribed to pyridine interacting with Brønsted acid sites (BAS, 1635 and 1545 cm⁻¹) and Lewis acid sites coming from the presence of coordinatively unsaturated Al³⁺ (LAS, 1622, 1610, 1464 and 1455 cm⁻¹). Acidity quantification was

performed considering the bands assigned to ν_{19b} vibration mode of pyridine and their corresponding integrated molar extinction coefficients.⁴¹ Therefore, BAS were calculated using the band at 1545 cm^{-1} and LAS, associated to the presence of partially coordinated aluminum atoms and extra-framework Al species, were determined through the bands at 1464 and 1455 cm^{-1} .

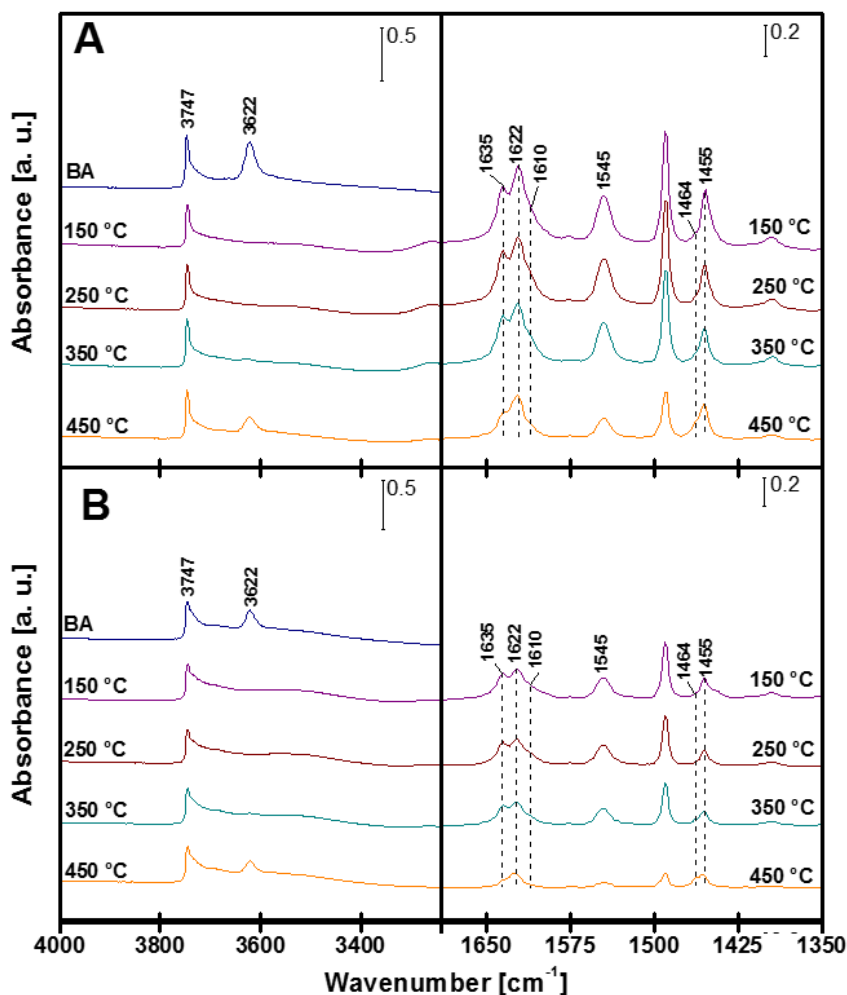


Fig. 2. FTIR spectra of MCM-22 (20) (A) and MCM-22 (40) (B) in the hydroxyl (left) and pyridine (right) vibration regions.

Fig. 3 illustrates the evolution of the concentration of Brønsted and Lewis acids sites with the pyridine desorption temperatures. As expected, comparing both Si/Al ratios (20 and 40), the higher the silica content the lower the concentration of Brønsted and Lewis acid sites. Both samples behave in a similar way regarding the evolution of the adsorbed pyridine with temperature, in the range of the desorption temperatures going from 150 to 350 °C , presenting larger amounts of BAS than LAS. In particular, the BAS/LAS ratios at 150 °C show values of 1.56 and 2.11 for MCM-22 (20) and MCM-22 (40), respectively. However, at the highest desorption temperature the decrease in the BAS and LAS concentration is more pronounced for the MCM-22 (20) sample, which evidences a slightly weaker nature of the acid sites in this material compared to MCM-22 (40).

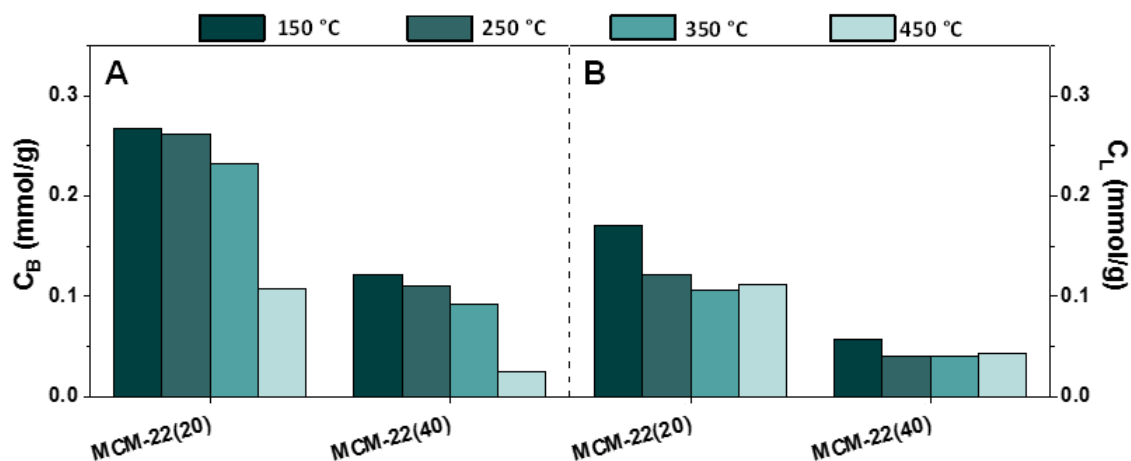


Fig. 3. Concentration of Brønsted, C_B (A) and Lewis, C_L (B) acid sites measured for the MCM-22 samples after desorption of pyridine at different temperatures, monitored by FT-IR.

3.3. Catalytic pyrolysis assays

3.3.1. Products yield and gas composition

The pyrolysis of biomass is strongly influenced by temperature, in terms of both bio-oil yield and products distribution.²⁶ Accordingly, in the current study the most favourable temperature for the pyrolytic zone (550 °C) has been selected to maximize the bio-oil* production in the lab-scale experimental setup used herein. Then, the performance of the MCM-22 samples has been tested at two different temperatures, 400 and 450 °C, for the catalytic bed zone controlled independently from the non-catalytic zone.

Fig. 4 represents the results obtained in terms of products mass yield for the non-catalytic and catalytic pyrolysis experiments, whereas Fig. 5 displays the yield of the components in the produced gases. The char fraction is not displayed since it was entirely produced through pyrolysis and retained in the first reactor zone; then, its yield was practically identical in all cases, ≈ 19 wt%, whatever the catalyst and the catalytic zone temperature employed during the pyrolysis tests. Likewise, when the temperature of the second zone of the reactor was varied from 400 to 450 °C in the experiments without catalyst, only slight variations in the products distribution and gas components yield were observed. The yield of the gas fraction generated by non-catalytic pyrolysis of WS-ac is about 8.0-8.7 wt%, being mainly composed by CO_2 and CO, as well as by minor amounts of light hydrocarbons (mostly CH_4).

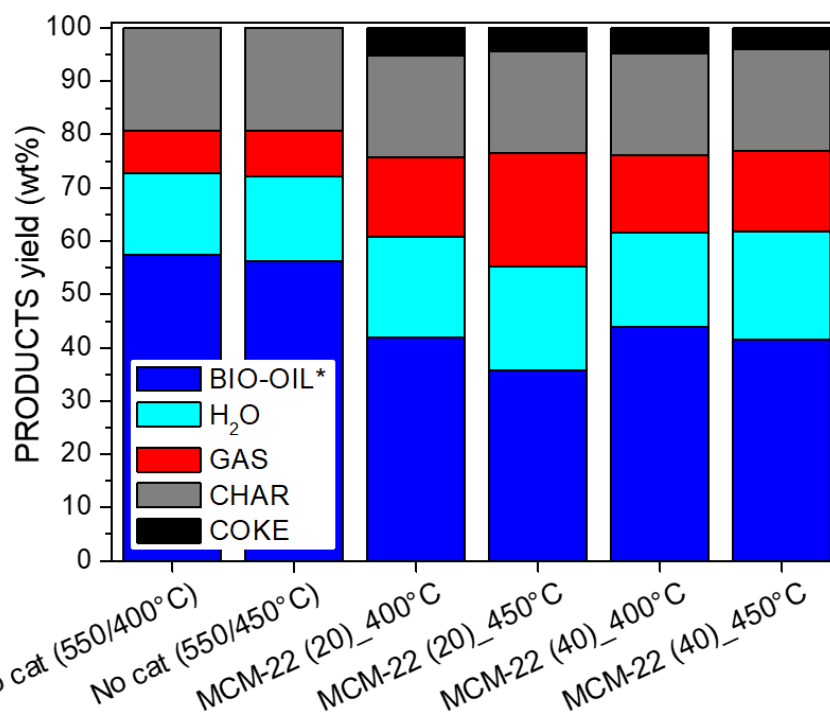


Fig. 4. Products yield distribution (wt%, dry basis) in the catalytic and non-catalytic fast-pyrolysis of WS-ac over the MCM-22 samples, as a function of the catalytic bed temperature (non-catalytic pyrolysis zone temperature: 550 °C).

The incorporation of the MCM-22 zeolites to the reaction system caused a reduction in the quantity, but also an improvement in the quality of the bio-oil* collected at both temperatures, at expense of the formation of more H₂O and gases (CO, CO₂ and light hydrocarbons). At the lower catalytic pyrolysis temperature (400 °C) the utilization of MCM-22 zeolites with Si/Al ratios of 20 and 40 caused similar reductions (13-15%) in the production of bio-oil* with respect to that obtained during the non-catalytic pyrolysis. The gas distribution was similar for both zeolite samples (Fig. 5). Nevertheless, at higher temperature (450 °C) the differences between both zeolites were more noticeable, producing more gases, especially CO₂ and CO, but also light hydrocarbons. Thus, the bio-oil* yield decreased in 37 and 26 %, with respect to the one obtained via non-catalytic pyrolysis, for the MCM-22 (20) and MCM-22 (40) catalysts, respectively (Fig. 4). Therefore, the higher the zeolite acidity the lower amount of bio-oil* collected. This effect is more significant at higher temperature.

Water is other major product of biomass pyrolysis that comes from a variety of dehydration reactions, either undergone initially by the degradation of biopolymers or subsequently by transformations of the pyrolysis vapours. Water is recovered as a part of the liquid fraction mixed with the bio-oil* fraction. The water yield in the non-catalytic pyrolysis represents 15.4 and 15.8 wt%, for temperatures of 400 and 450 °C, respectively. An increasing water formation with the temperature was also observed for the catalytic tests (see Fig. 4). The increment in the amount of water, generated when MCM-22 (20) zeolite was used increased up to 18.9 and 19.5 wt% for catalytic pyrolysis temperatures of 400 and 450 °C, respectively. While in case of MCM-22 (40) those values reached 17.8 and 20.3 wt% for the same temperatures. This result shows that the MCM-22 samples promotes the extension of dehydration reactions.

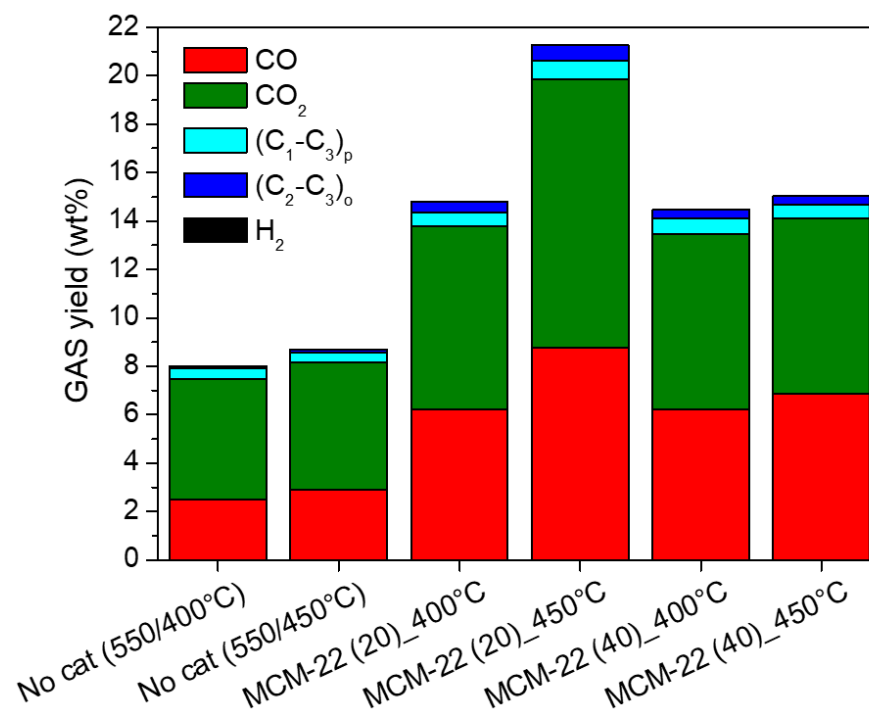


Fig. 5. Gaseous components yield in the catalytic and non-catalytic fast-pyrolysis of WS-ac over the MCM-22 samples, as a function of the catalytic bed temperature (non-catalytic pyrolysis zone temperature: 550 °C). (C₁-C₃)_p: paraffins; (C₂-C₃)_o: olefins.

On the other hand, significant amounts of coke are deposited over the MCM-22 zeolite samples during the catalytic pyrolysis tests (Fig. 4). Table 2 shows that coke deposits represent between 19.4 and 24.2 wt% of the spent catalyst weight, which account for about 3.9-5.2 wt% with respect to the biomass feed. In particular, coke formation is favored at low catalytic bed temperatures and promoted by the increase in the strength of zeolite acid sites. Thus, coke yields obtained herein are significantly higher than those obtained in a recent work (2.9-3.2 wt%), in which H-ZSM-5 (Si/Al=42) was tested under the same experimental reaction conditions and using the same biomass feedstock.²⁶ Similar behavior was observed by Jae et al.,³³ who identified a higher degree of coke formation over MCM-22 than over H-ZSM-5 zeolite during the glucose catalytic fast-pyrolysis, being associated to the presence of relatively large cages inside the MCM-22 porous structure that provide space for coke accumulation.

Table 2. Parameters of coke and light hydrocarbons in gas product obtained in the catalytic fast-pyrolysis of WS-ac as function of the Si/Al ratio of the MCM-22, and the catalytic bed temperature.

Catalyst-Temperature	COKE							Hydrocarbons [†] in GAS	
	Coke in catalyst (wt%)	Mass yield (wt%)	Elemental analysis (db, wt%)				Energy yield (%)	Mass yield (wt%)	Energy yield (%)
			C	H	N	O			
No cat 550/400°C	-	-	-	-	-	-	-	0.5	1.5
No cat 550/450°C	-	-	-	-	-	-	-	0.6	1.6
MCM-22(20)_400°C	24.2	5.2	72.8	6.6	0.7	19.9	8.9	1.0	2.8
MCM-22(20)_450°C	21.8	4.3	76.6	4.7	0.6	18.1	7.3	1.4	3.9
MCM-22(40)_400°C	22.1	4.7	72.2	4.2	0.1	23.5	7.1	1.0	2.8
MCM-22(40)_450°C	19.4	3.9	71.0	4.3	0.3	24.4	5.9	0.9	2.6

[†]: Paraffins (C₁-C₃) and olefins (C₂-C₃).

3.3.2. Deoxygenation selectivity of MCM-22

In order to get further insight about the pathways for bio-oil* deoxygenation favored by the MCM-22 zeolites, Fig. 6A displays the overall selectivity towards dehydration, decarbonylation and decarboxylation, in comparison with that obtained in non-catalytic experiments. Fig. 6B shows the deoxygenation selectivity corresponding to the catalytic step. These results reveal how the variation in the zeolite acidity and the temperature in the catalytic bed affected the deoxygenation pathways. During the non-catalytic biomass fast-pyrolysis, cellulose and hemicellulose are thermochemically decomposed via primary pyrolysis to organic volatile compounds, such as furans and light oxygenates (alcohols, acids, ketones and ethers), which involves dehydration reactions;^{4,26} but also decarbonylation and decarboxylation (from the cracking of carbonyl (C-O-C), carboxyl (C=O) and (COOH)).⁴⁶ On the contrary, lignin primary pyrolysis products are mostly monomeric oxygenated aromatics, derived from the fragmentation of lignin monolignols, and also light oxygenates (like carboxylic acids). Therefore, the importance of the different routes can be ranked according to the following trend: dehydration >> decarboxylation > decarbonylation, with selectivity towards the products formed via mentioned pathways of around 72, 20, and 8%, respectively.

The incorporation of the MCM-22 zeolites causes some changes in the relative significance of the deoxygenation routes (Fig. 6B). It is well known that acidic zeolites promote a series of reactions, such as secondary cracking, oligomerization, cyclization, aromatization, and/or polymerization reactions, among others, leading to partial deoxygenation of the primary vapours through the formation of CO, CO₂, and H₂O (decarbonylation, decarboxylation, and dehydration, respectively).^{4,26} MCM-22 (40), with low concentration of acid sites, favours the dehydration ≥ decarbonylation > decarboxylation, in such a way that the increment in dehydration occurs at higher temperature at expenses of other routes (mainly decarboxylation). In contrast, MCM-22 (20) behaves differently depending on the temperature, most likely due to higher concentration of acid sites. Thus, at low temperature dehydration is the principal deoxygenation route, whilst at higher temperature decarboxylation becomes predominant.

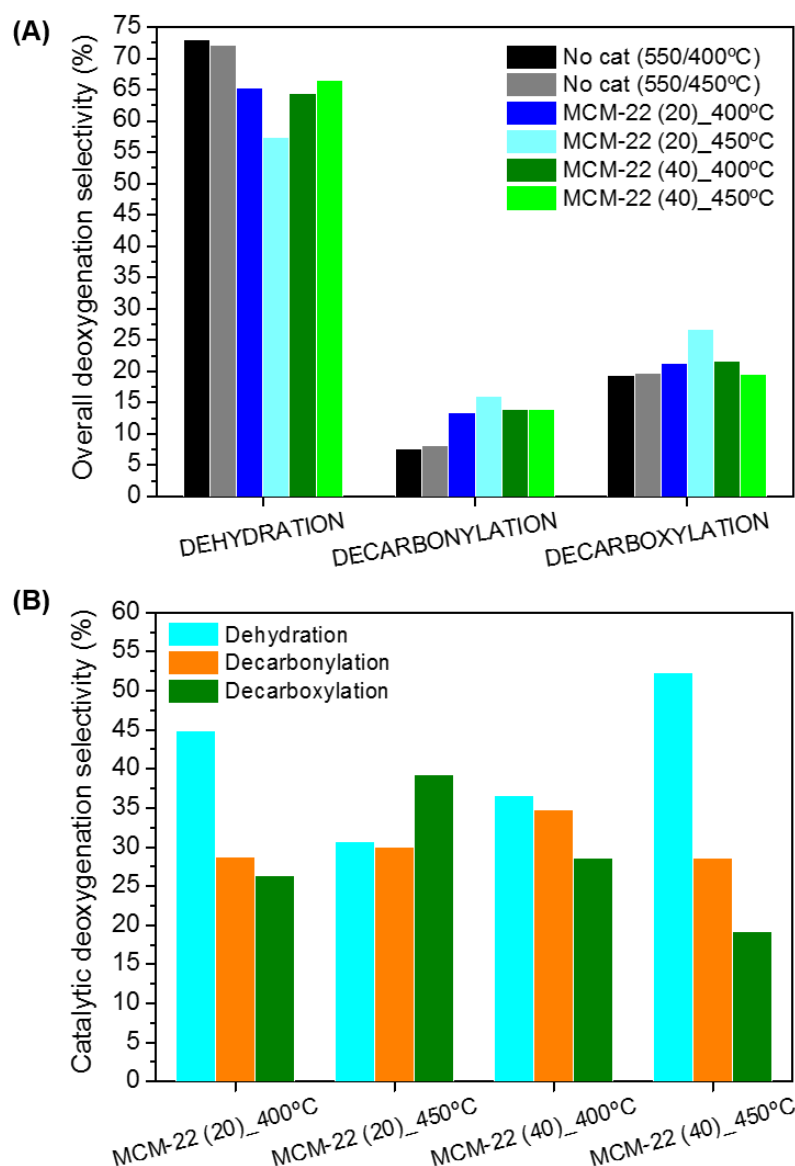


Fig. 6. Overall (A) and catalytic (B) deoxygenation selectivity over the MCM-22 samples, as a function of the catalytic bed temperature during the fast-pyrolysis of WS-ac (non-catalytic pyrolysis zone temperature: 550 °C)

3.3.3. Bio-oil properties

Reduction of the oxygen content in the liquid fraction unavoidably results in lower yields of bio-oil* (Fig. 7A). In this graph, the curves corresponding to three theoretical deoxygenation pathways (dehydration, decarboxylation and decarbonylation) have been represented starting from the point corresponding to the non-catalytic bio-oil* obtained at 550/400 °C. It must be kept in mind that, when using a catalyst, part of the oxygen removed as H₂O, CO₂ and CO is related to the formation of other compounds and fractions different from bio-oil*, such as light gaseous hydrocarbons and coke deposited over the catalyst surface, which are not productive for bio-oil* upgrading.

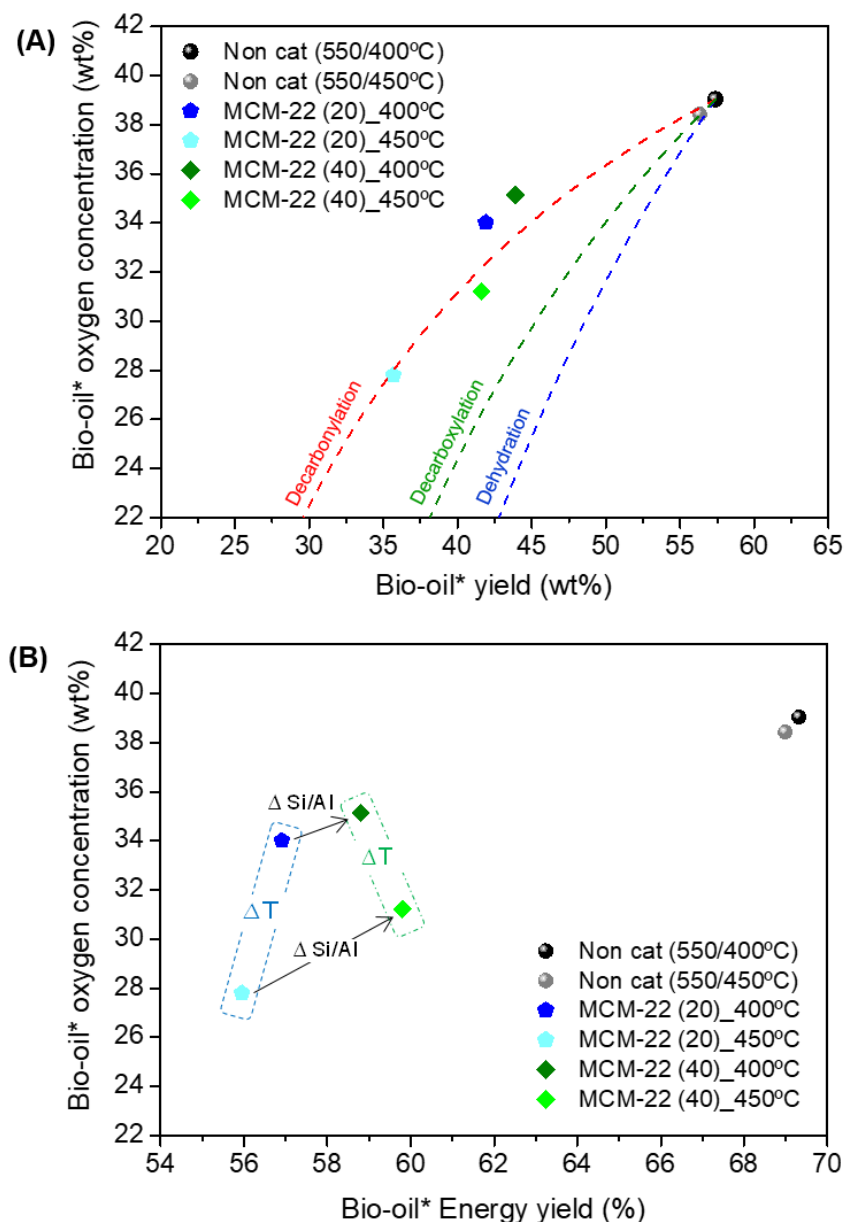


Fig. 7. Oxygen concentration versus bio-oil* mass (A) and energy (B) yields obtained over the MCM-22 samples, as a function of the catalytic bed temperature during the fast-pyrolysis of WS-ac (non-catalytic pyrolysis zone temperature: 550 °C).

Acid sites concentration of the MCM-22 zeolite affects differently the bio-oil* oxygen concentration and yield depending on the temperature. At 400 °C both MCM-22 zeolites show similar bio-oil* yield and oxygen concentration, with values around 42-44 and 34-35 wt%, respectively. The fact that the experimental points obtained with the catalytic bed at 400 °C are located at lower mass yields than the theoretical curves indicates that other processes such as the formation of coke and light hydrocarbons are also relevant. In contrast, at higher catalytic pyrolysis temperature both zeolites showed an enhanced bio-oil* deoxygenation. Moreover, at this temperature the higher the concentration of zeolite acid sites the deeper the bio-oil* deoxygenation.

Fig. 7B represents/shows the bio-oil* oxygen concentration as a function of the bio-oil* energy yield, to assess the process efficiency also in terms of chemical energy remaining in the bio-oil*

fraction regarding to that initially contained in the raw biomass. The higher is the amount of acid sites in MCM-22 the lower the energy recovered in the bio-oil*.

This effect was partially caused by the loss of chemical energy in form of coke, which was more noticeable for the more acidic zeolite. Thus, MCM-22 (20) accumulated 8.9 and 7.3% of the biomass energy as coke at 400 and 450 °C, respectively; while coke produced over MCM-22 (40) caused an energy loss of 7.1 and 5.9% at the same temperatures, as it can be observed in Table 2.

The difference in the bio-oil* energy loss between both catalysts was enlarged at the highest catalytic pyrolysis temperature (450 °C), mainly due to the larger production of light hydrocarbons, whose energy yields account for 3.9 and 2.6% in the case of MCM-22 (20) and MCM-22 (40), respectively; whilst at lower temperature these values were very similar (about 2.8%), as summarized in Table 2.

Likewise, an increase in the catalytic pyrolysis temperature hardly altered 1% of the bio-oil* energy yield, while its oxygen concentration decreased in 4 and 6 wt% for MCM-22 (40) and MCM-22 (20) samples, respectively. Hence, zeolite MCM-22 (20) provided a bio-oil* with an oxygen concentration about 28 wt% at 450 °C with still 56 % of bio-oil* energy yield.

3.3.4. Bio-oil GC-MS composition

GC-MS analytical technique was used to assess the complex chemical composition of bio-oils*, in order to provide valuable insights into the effect of the operation variables on the mechanism of catalytic pyrolysis. The identified compounds have been classified in the following groups: carboxylic acids (AC), aldehydes (ALD), alcohols (ALC), ketones and ethers (KET & ETH), furans (FUR), amines and amides (AMN & AMD), oxygenated aromatics (O-AR), aromatic hydrocarbons (AR), anhydro sugars (SUG) and a last group representing non-identified compounds (UNK). In addition, high molecular weight oligomers produced by partial depolymerisation of the biomass cannot be detected by this technique.

Fig. 8 shows the semi-quantitative results (expressed as area %) of the bio-oils* composition obtained by fast-pyrolysis of WS-ac. In a previous work, a simplified scheme has been proposed to account for the main transformation routes occurring during the biomass fast-pyrolysis.²⁶ Comparing non-catalytic with catalytic pyrolysis at 400 °C (Fig. 8A), the most noticeable differences are the increase in the content of carboxylic acids (mainly acetic acid), oxygenated aromatics and nitrogenated molecules; while the concentration of anhydro sugars, ketones and ethers decrease when the bio-oil* vapours are contacted with the MCM-22 catalysts. Just minor concentrations of aromatic hydrocarbons are observed under these conditions. These variations in the composition can be attributed to the promotion of decarboxylation and cracking reactions by the zeolite catalysts. At low operation temperature (400 °C), differences in the MCM-22 acidity does not have a significant effect and both catalysts generate bio-oils* with similar composition, although with a slightly higher proportion of furans produced over MCM-22 (40). Rising the catalytic pyrolysis temperature up to 450 °C (Fig. 8B) causes further reduction of the concentration of anhydro sugars and a slight increment in the proportion of oxygenated aromatics. Likewise, at higher temperature the concentration of ethers and ketones grow, while the amount of carboxylic acids remains similar to that obtained at 400 °C.

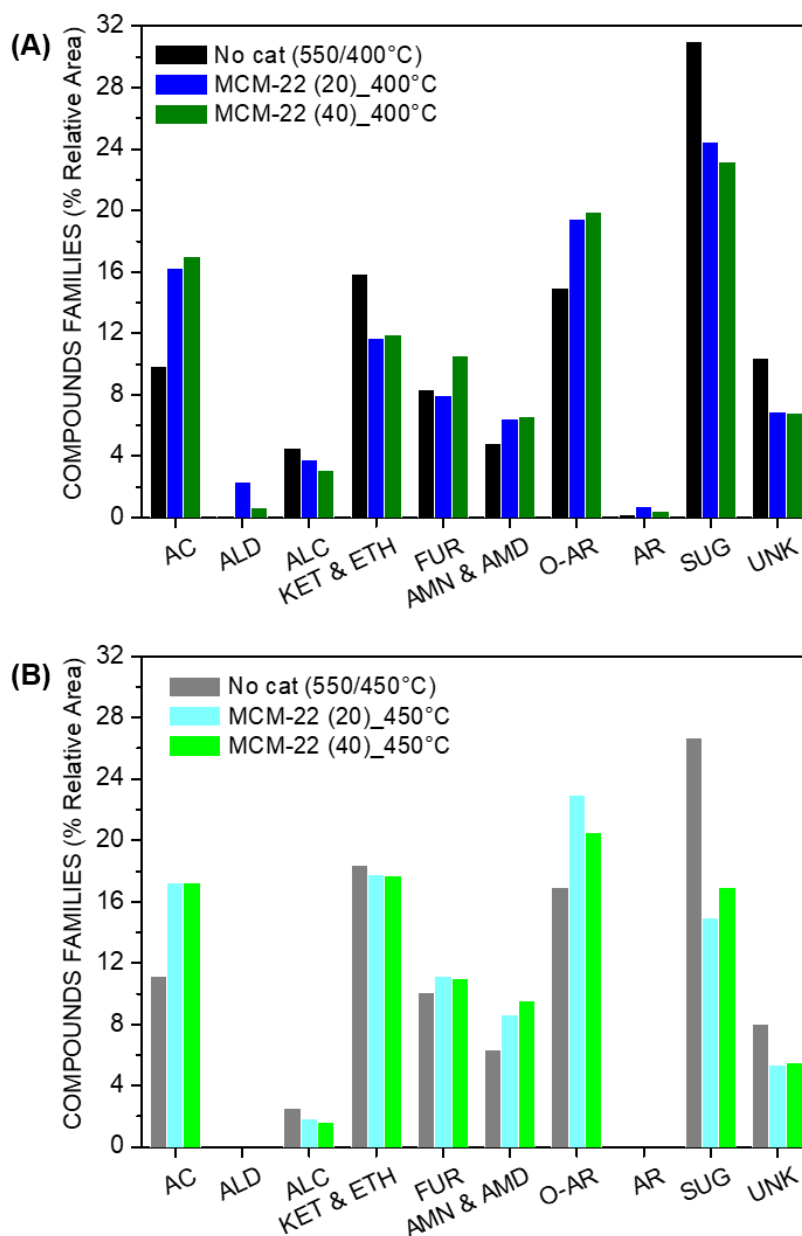


Fig. 8. Composition of the bio-oil* in terms of main organic compounds families (% of relative area from GC-MS analyses) obtained over the MCM-22 samples, as a function of the catalytic bed temperature during the fast-pyrolysis of WS-ac (non-catalytic pyrolysis zone temperature: 550 °C).

3.3.5. Comparison of MCM-22 and ZSM-5 zeolites

As above indicated ZSM-5 zeolite is the catalyst that has been more widely investigated in the literature for biomass fast catalytic pyrolysis, hence the results here obtained over MCM-22 zeolites are compared with the performance of that material reported in a recent work,²⁶ using also acid-washed wheat straw as feedstock.

In terms of overall deoxygenation degree and energy yield both zeolites exhibit a quite similar behavior. This finding is observed in spite of the formation of more coke over MCM-22 than in the case of ZSM-5, which is a consequence of the presence of larger cavities in the former material. However, MCM-22 produces lower gaseous hydrocarbons, which can be associated to the lower extension of severe cracking reactions due to the weaker acidity of this zeolite compared with ZSM-5.

Regarding the bio-oil* fraction composition, a number of differences can be appreciated with respect to the results obtained over ZSM-5. In particular, a lower proportion of aromatic hydrocarbons and a higher concentration of oxygenated aromatics are found when using MCM-22 as catalyst. These results denote the lower aromatization activity (low yields of aromatic hydrocarbons) of MCM-22 zeolite compared to ZSM-5. Moreover, the high concentration of oxygenated aromatics presented in the bio-oil produced over MCM-22 zeolite can be of interest for the selective production of phenolic compounds with commercial applications.

Likewise, the coke formed over MCM-22 presents a higher oxygen content (see Table 2) than that deposited over ZSM-5, with values of 18-24 and 9 wt%, respectively. Coke is typically generated over zeolites by a complex combination of reactions, such as olefin oligomerization and aromatics polycondensation.^{16,24,47} On the other hand, in biomass catalytic pyrolysis, the formation of carbonaceous residues may follow also a pathway mediated by oxygenated species leading to a lighter fraction of coke containing significant amount of oxygen.⁴⁸ This route for coke formation seems to be favoured in the case of the MCM-22 zeolite compared to ZSM-5.

4. Conclusions

Catalytic fast-pyrolysis of acid-washed wheat straw has been studied in a fixed-bed reactor using MCM-22 zeolites with Si/Al ratios of 20 and 40, respectively, as catalysts. Both samples present a significant amount of external surface area, which is advantageous for the conversion of bulky molecules released during the biomass thermochemical decomposition. Likewise, both MCM-22 materials exhibit a higher concentration of Brønsted acid sites than of Lewis ones.

Catalytic biomass pyrolysis performed with the MCM-22 samples led to a significant bio-oil* deoxygenation activity with moderate loss of the bio-oil* energy yield, although significant amounts of coke are deposited over the zeolite samples. The best results are obtained over the MCM-22 (40) at 450 °C. These conditions limit the formation of coke and the production of gaseous hydrocarbons. In particular, decreasing the Si/Al ratio of the zeolite has a positive effect to achieve a good balance between the deoxygenation degree of the bio-oil* and its energy yield.

Coke deposited over the MCM-22 zeolite presents significant oxygen content, denoting that over this zeolite the formation of carbonaceous residues is in great part mediated by oxygenated compounds. This finding is in agreement with the composition of the bio-oils produced over MCM-22, which present higher concentration of oxygenated aromatics and lower aromatic hydrocarbons content than those typically obtained using ZSM-5 catalysts. These differences are most likely due to the weaker acid strength of MCM-22 compared to ZSM-5, as well as to the presence of large cavities within its structure, and can be of interest for the selective production of phenolic compounds.

Acknowledgements

The authors gratefully acknowledge the financial support from the European Union Seventh Framework Programme (FP7/2007–2013) under grant agreement n° 604307 (CASCATBEL project). J. Čejka thanks the Czech Science Foundation for the financial support (P106/12/G015).

References

- 1 C. Liu, H. Wang, A. M. Karim, J. Sun and Y. Wang, *Chem. Soc. Rev.*, 2014, **43**, 7594–7623.
- 2 S. N. Naik, V. V. Goud, P. K. Rout and A. K. Dalai, *Renew. Sustain. Energy Rev.*, 2010, **14**, 578–597.
- 3 S. K. Karmee, *Renew. Sustain. Energy Rev.*, 2016, **53**, 945–953.
- 4 J. Feroso, P. Pizarro, J. M. Coronado and D. P. Serrano, in *Encyclopedia of Sustainability Science and Technology*, ed. R. A. Meyers, Springer, New York, 2017, pp. 1–33.
- 5 J. Feroso, P. Pizarro, J. M. Coronado and D. P. Serrano, *Adv. Rev.*, 2017, **6**, 1–18.
- 6 A. V Bridgwater, *Biomass and Bioenergy*, 2012, **38**, 68–94.
- 7 E. Tomás-Pejó, J. Feroso, E. Herrador, H. Hernando, S. Jiménez-Sánchez and M. Ballesteros, *Fuel*, 2017, **199**, 403–412.
- 8 R. M. Baldwin and C. J. Feik, *Energy & Fuels*, 2013, **27**, 3224–3238.
- 9 J. Feroso, H. Hernando, S. Jiménez-sánchez, A. A. Lappas, E. Heracleous, P. Pizarro, J. M. Coronado and D. P. Serrano, *Fuel Process. Technol.*, 2017, **167**, 563–574.
- 10 D. Meier, B. van de Beld, A. V Bridgwater, D. C. Elliott, A. Oasmaa and F. Preto, *Renew. Sustain. Energy Rev.*, 2013, **20**, 619–641.
- 11 A. Sharma, V. Pareek and D. Zhang, *Renew. Sustain. Energy Rev.*, 2015, **50**, 1081–1096.
- 12 M. Asadieraghi and W. M. A. Wan Daud, *Energy Convers. Manag.*, 2015, **101**, 151–163.
- 13 K. Wang, J. Zhang, B. H. Shanks and R. C. Brown, *Appl. Energy*, 2015, **148**, 115–120.
- 14 R. H. Venderbosch, *ChemSusChem*, 2015, **8**, 1306–1316.
- 15 G. Yildiz, F. Ronsse, R. van Duren and W. Prins, *Renew. Sustain. Energy Rev.*, 2016, **57**, 1596–1610.
- 16 T. Carlson, J. Jae, Y. Lin, G. Tompsett and G. Huber, *J. Catal.*, 2010, **270**, 110–124.
- 17 E. Taarning, C. M. Osmundsen, X. Yang, B. Voss, S. I. Andersen and C. H. Christensen, *Energy Environ. Sci.*, 2011, **4**, 793–804.
- 18 D. Fabbri, C. Torri and V. Baravelli, *J. Anal. Appl. Pyrolysis*, 2007, **80**, 24–29.
- 19 B. Zhang, Z. Zhong, P. Chen and R. Ruan, *Bioresour. Technol.*, 2015, **197**, 79–84.
- 20 X. Zhang, L. Sun, L. Chen, X. Xie, B. Zhao, H. Si and G. Meng, *J. Anal. Appl. Pyrolysis*, 2014, **108**, 35–40.
- 21 H. Hernando, I. Moreno, J. Feroso, C. Ochoa-Hernández, P. Pizarro, J. M. Coronado and D. P. Serrano, *Bioresour. Technol.*, 2017, **7**, 289–304.
- 22 C. Mukarakate, M. J. Watson, J. Ten Dam, X. Baucherel, S. Budhi, M. M. Yung, H. Ben, K. Iisa, R. M. Baldwin and M. R. Nimlos, *Green Chem.*, 2014, **16**, 4891–4905.
- 23 H. S. Cerqueira, P. Ayrault, J. Datka and M. Guisnet, *Microporous Mesoporous Mater.*, 2000, **38**, 197–205.

- 24 A. Aho, N. Kumar, K. Eränen, T. Salmi, M. Hupa and D. Y. Murzin, *Fuel*, 2008, **87**, 2493–2501.
- 25 D. J. Mihalcik, C. A. Mullen and A. A. Boateng, *J. Anal. Appl. Pyrolysis*, 2011, **92**, 224–232.
- 26 H. Hernando, S. Jiménez-Sánchez, J. Feroso, P. Pizarro, J. M. Coronado and D. P. Serrano, *Catal. Sci. Technol.*, 2016, **6**, 2829–2843.
- 27 J. Feroso, H. Hernando, P. Jana, I. Moreno, J. Přech, C. Ochoa-Hernández, P. Pizarro, J. M. Coronado, J. Čejka and D. P. Serrano, *Catal. Today*, 2016, **277**, 171–181.
- 28 W. Roth, P. Nachtigall, R. Morris and J. Čejka, *Chem. Rev.*, 2014, **114**, 4807–4837.
- 29 W. J. Roth, B. Gil and B. Marszalek, *Catal. Today*, 2014, **227**, 9–14.
- 30 M. V Opanasenko, W. J. Roth and J. Čejka, *Catal. Sci. Technol.*, 2016, **6**, 2467–2484.
- 31 H. W. Lee, S. H. Park, J.-K. Jeon, R. Ryoo, W. Kim, D. J. Suh and Y.-K. Park, *Catal. Today*, 2014, **232**, 119–126.
- 32 A. Corma, *J. Catal.*, 2000, **191**, 218–224.
- 33 J. Jae, G. A. Tompsett, A. J. Foster, K. D. Hammond, S. M. Auerbach, R. F. Lobo and G. W. Huber, *J. Catal.*, 2011, **279**, 257–268.
- 34 M. Källdström, N. Kumar, T. Heikkilä, M. Tiitta, T. Salmi and D. Y. Murzin, *Biomass and Bioenergy*, 2011, **35**, 1967–1976.
- 35 M. Källdström, N. Kumar, T. Heikkilä and D. Y. Murzin, *Appl. Catal. A Gen.*, 2011, **397**, 13–21.
- 36 S. R. Naqvi, Y. Uemura, S. Yusup, Y. Sugiura and N. Nishiyama, *J. Anal. Appl. Pyrolysis*, 2015, **114**, 32–39.
- 37 J. B. Sluiter, R. O. Ruiz, C. J. Scarlata, A. D. Sluiter and D. W. Templeton, *J. Agric. Food Chem.*, 2010, **58**, 9043–9053.
- 38 A. Corma, C. Corell and J. Pérez-Pariente, *Zeolites*, 1995, **15**, 2–8.
- 39 P. Chlubná, W. J. Roth, A. Zukal, M. Kubů, and J. Pavlatová, *Catal. Today*, 2012, **179**, 35–42.
- 40 S. A. Channiwala and P. P. Parikh, *Fuel*, 2002, **81**, 1051–1063.
- 41 C. A. Emeis, *J. Catal.*, 1993, **141**, 347–354.
- 42 R. A. García-Muñoz, D. P. Serrano, G. Vicente, M. Linares, D. Vitvarova and J. Čejka, *Catal. Today*, 2015, **243**, 141–152.
- 43 ECN, Phyllis2 database for biomass and waste.
- 44 C. Delitala, M. D. Alba, A. I. Becerro, D. Delpiano, D. Meloni, E. Musu and I. Ferino, *Microporous Mesoporous Mater.*, 2009, **118**, 1–10.
- 45 I. Güray, J. Warzywoda, N. Baç and A. Sacco, *Microporous Mesoporous Mater.*, 1999, **31**, 241–251.
- 46 H. Yang, R. Yan, H. Chen, D. H. Lee and C. Zheng, *Fuel*, 2007, **86**, 1781–1788.

- 47 J. M. Escola, J. Aguado, D. P. Serrano, L. Briones, J. L. Díaz de Tuesta, R. Calvo and E. Fernandez, *Energy & Fuels*, 2012, **26**, 3187–3195.
- 48 Á. Ibarra, A. Veloso, J. Bilbao, J. M. Arandes and P. Castaño, *Appl. Catal. B Environ.*, 2016, **182**, 336–346.

Article 4

Biomass catalytic fast pyrolysis over hierarchical ZSM-5 and Beta zeolites modified with Mg and Zn oxides

Biomass Conversion and Biorefinery, 2017, 7(3), 289–304

Biomass Conv. Bioref.
DOI 10.1007/s13399-017-0266-6



ORIGINAL ARTICLE

Biomass catalytic fast pyrolysis over hierarchical ZSM-5 and Beta zeolites modified with Mg and Zn oxides

Héctor Hernando¹ · Inés Moreno^{1,2} · Javier Feroso¹ · Cristina Ochoa-Hernández³ · Patricia Pizarro^{1,2} · Juan M. Coronado¹ · Jiří Čejka³ · David P. Serrano^{1,2}

Received: 15 January 2017 / Revised: 28 April 2017 / Accepted: 3 May 2017
© Springer-Verlag Berlin Heidelberg 2017

Impact JCR factor, (JCR 2017): 1.310
Category: Energy & Fuels. 71 of 97 (Q3)

ABSTRACT

Hierarchical ZSM-5 and Beta zeolites, loaded with MgO and ZnO, have been explored for the catalytic fastpyrolysis of eucalyptus woodchips. These materials exhibit a high dispersion of the MgO or ZnO phases, which is probably due to the presence of a hierarchical porosity with both micro and mesopores in the zeolitic supports. The incorporation of these metal oxides led to a significant reduction in the textural properties and to changes in the acidic properties of the parent zeolites. Thus, a decrease in the concentration of Brønsted acid sites was observed, which was accompanied by the generation of additional Lewis acid sites with medium strength. In addition, the incorporation of metal oxide promotes the formation of significant amount of basic sites, especially for the samples loaded with MgO. Catalytic fast pyrolysis experiments of eucalyptus woodchips were performed in a fixed bed reactor at 500 °C and atmospheric pressure under a nitrogen flow. In comparison with non-catalytic fast pyrolysis, the use of zeolitic catalysts caused a decrease in the bio-oil* (water free basis bio-oil) production due to enhanced formation of gases, as well as coke deposition on the catalyst. However, the quality of the bio-oil* was enhanced since the catalysts were able to decrease its oxygen content. In this way, h-ZSM-5-based catalysts showed a clearly deeper deoxygenation degree compared to those having h-Beta as support, with very low content of anhydro sugars and the formation of a significant amount of aromatics. Regarding the effect of the metal oxide phase, MgO-loaded samples provided bio-oil* with enhanced energy yields and lower oxygen content, probably due to the adequate balance of Lewis acid and basic sites. Likewise, significant differences were observed among the catalysts regarding the deoxygenation pathways and the compounds families present in the bio-oil*.

Keywords: Catalytic fast pyrolysis. Hierarchical zeolite. Bio-oil upgrading.

1. Introduction

The increasing energy demand and the rising of the CO₂ emissions are currently major driving forces fostering the exploitation of renewable sources of energy. In this way, lignocellulosic biomass is an abundant, renewable, non-edible and geographically diverse natural resource, which is considered an attractive feedstock for producing liquid biofuels.^{1,2} Lignocellulose conversion into biofuels can be conducted via two generic routes: thermochemical transformations (gasification, liquefaction and pyrolysis) and biological processes (such as enzymatic hydrolysis and fermentation into bioethanol).³ Among the thermochemical conversion processes, biomass fast pyrolysis is viewed as a promising method to produce liquid fuels directly from biomass. Through this process, biomass is decomposed into a liquid (bio-oil), a solid (biochar) and non-condensable gases, under oxygen-free conditions, atmospheric pressure and moderate temperatures (450–600 °C).⁴ The resulting pyrolysis bio-oil is considered to be a convenient energy carrier, as it can be easily transported, burned directly in thermal power stations or coprocessed in petroleum refineries for the production of higher quality hydrocarbon fuels.² However, the bio-oil contains a large variety of oxygenated compounds, which deteriorates its properties, such as the presence of a significant water concentration, high viscosity, acidic pH, low thermal and chemical stability, reduced heat value and immiscibility with fossil fuels, limiting its integration into existing petroleum-based infrastructures.^{5,6}

The bio-oil properties can be upgraded by means of oxygen removal using heterogeneous catalysts integrated into the fast pyrolysis system, commonly known as catalytic fast pyrolysis (CFP).⁷ Depending on the method employed for coupling the thermal and catalytic biomass steps, catalytic fast pyrolysis can be categorized into two different approaches: *in situ* and *ex situ*. In the first one, the biomass is contacted directly with the catalyst as the same reactor is employed for conducting the thermal and catalytic transformations, whereas in the *ex-situ* method, the vapors formed in the biomass pyrolysis are subsequently passed through the catalyst bed.^{8–10} This later approach has several advantages allowing the thermal and catalytic steps to be performed at different reaction temperatures, having a better control of the bio-oil yield and composition, and the catalyst is not mixed with the char formed in the pyrolysis zone, which makes easier its recovery and reuse.¹⁰

One of the main objectives in biomass catalytic pyrolysis is to decrease the oxygen content of the bio-oil* (typically in the range 40–45 wt%) through the occurrence of a number of deoxygenation reactions. This can be accomplished by the formation and release of CO, CO₂ and H₂O via decarbonylation, decarboxylation, and dehydration reactions, respectively.¹¹ Among them, decarbonylation is the least preferred route for deoxygenation since it implies a loss of both mass and chemical energy of the bio-oil* fraction.⁶ Accordingly, one of the main challenges in biomass catalytic pyrolysis is the development of catalytic systems that selectively reduces the oxygen content from bio-oil through a combination of decarboxylation/dehydration pathways with little contribution of decarbonylation.

During the last two decades, a large variety of catalysts has been tested in catalytic biomass pyrolysis. In particular, zeolites have led to interesting results due to a combination of well-defined acid sites and their shape selectivity arising from the uniform size of the zeolite micropores.¹² Thus, zeolites such as H-ZSM-5, H-Beta, HY, mordenite and MCM-22 have been investigated using a wide range of biomass feedstock.^{5,9,10,13} Nevertheless, low bio-oil yields and catalyst deactivation by coke deposition have been identified as major limitations for the use of zeolites in biomass

catalytic pyrolysis. Thus, the strong diffusional limitations existing within the zeolite micropores hinder the conversion of bulky oxygenates present in the bio-oil*, whereas the presence of strong acid sites promotes polymerization and coke-forming reactions.^{12,14} The use of large pore zeolites, such as H-Beta and HY, may improve internal mass transfer phenomena, enhancing the conversion of bulky oxygenates. However, these zeolites typically lead to a lower formation of aromatic hydrocarbons and higher coke generation compared to H-ZSM-5.^{15,16}

In this context, hierarchical zeolites can be considered as promising catalysts for bio-oil upgrading, since they combine, in a sole material, the improved mass transfer characteristic of mesoporous materials with the acidity and high intrinsic activity of zeolites. Consequently, several works have been published recently reporting biomass catalytic pyrolysis over hierarchical zeolites, prepared using different synthesis approaches such as the utilization of amphiphilic organosilanes or desilication treatments.^{12,15,16} In general terms, the presence of mesopores resulted in higher mono-aromatic hydrocarbons yields, decreasing the formation of polyaromatic hydrocarbons (PAHs).

On the other hand, bio-oil* upgrading has been also investigated using catalysts based on different metal oxides showing acid-basic or redox properties, which could potentially contribute to the deoxygenation of pyrolysis vapors. Thus, Lin et al. used CaO as catalyst for the pyrolysis of white pine biomass, showing that the bio-oil oxygen content and the amounts of formic and acetic acids were lower than in the bio-oil obtained by thermal pyrolysis of the same biomass.¹⁷ Likewise, MgO has been employed as catalyst for cotton seeds' fast pyrolysis, leading to an upgraded bio-oil* with higher heat values and lower oxygen content than the bio-oil obtained without catalyst.¹⁸ Among transition metal oxides, promising results have been also reported using ZnO as catalyst. In particular, catalytic fast pyrolysis of rice husk over ZnO decreased the bio-oil production, while this enhanced the yields to small molecular compounds and reduced the amount of oxygenated species present in the bio-oil.^{19,20}

Based on the previous background, the present work has been aimed to investigate the lignocellulose (eucalyptus woodchips) fast pyrolysis over catalysts based on hierarchical ZSM-5 and Beta zeolites, modified by incorporation of MgO and ZnO phases. The latter are intended to adjust and complement the acid-basic properties of the zeolites in order to optimize their catalytic performance in terms of deoxygenation pathways, bio-oil* upgrading routes, and coke formation. Moreover, the presence of a hierarchical porosity in the zeolitic supports, making available a large share of mesopore/external surface area, is expected to have at least two positive effects on the conversion of biomass. The first one is related to the decrease in steric and diffusional limitations for the conversion of bulky oxygenated compounds, whereas the second one should arise from a better dispersion of the metal oxide over the overall zeolite surface. The results have been evaluated from the point of view of both the quality and quantity of bio-oil* produced, using the oxygen concentration, the bio-oil* mass, and energy yield, as well as its composition, as main assessment parameters. Moreover, the effect of the metal oxide incorporation on the different deoxygenation pathways is also studied.

2. Experimental section

2.1. Materials

Eucalyptus woodchips were used as raw biomass for the catalytic fast pyrolysis experiments. Table 1 shows the proximate and ultimate analysis of this feedstock. The proximate analysis was carried out according to European standards in order to determine the moisture (UNE-EN 14774-1:2010), ash (UNE-EN 14775:2010) and volatile matter content (UNE-EN 15148:2010). The elemental composition of the biomass sample (ultimate analysis) was measured using a microelemental analyser from Thermo Fisher Scientific in order to calculate the content of C, H, N, S, and O. The high heating value (HHV) of the dried eucalyptus feedstock was estimated according to the literature.²¹ Previously to the catalytic tests, the eucalyptus woodchips were dried overnight at 110 °C and, subsequently, grounded in a cutter mill. Then, the obtained sawdust was sieved to get the desired particle size (0.5–1 mm).

2.2. Catalysts preparation

2.2.1. Synthesis of hierarchical ZSM-5 and Beta zeolites

h-ZSM-5 and h-Beta zeolites were prepared following a procedure based on the crystallization of silanized protozeolitic units published elsewhere.^{22,23}

For the h-ZSM-5 synthesis, a clear solution containing tetraethoxysilane (TEOS, 98 wt%, Aldrich), tetrapropylammonium hydroxide (TPAOH, 40 wt%, Alfa), aluminum isopropoxide (AIP, 98%, Aldrich) and distilled water was prepared with the following molar composition: $1\text{Al}_2\text{O}_3:80\text{SiO}_2:14.4\text{TPAOH}:2015\text{H}_2\text{O}$. The mixture was precrystallized under reflux and stirring at 90 °C for 20 h. Then, the protozeolitic nanounits so formed were functionalized by reaction with a silanization agent, phenylaminopropyltrimethoxysilane (PHAPTMS; 95 wt%, Fluka), at 90 °C for 6 h. The organosilane was added in a proportion of 8 mol% to the initial silica content in the gel. Finally, the resulting solution was crystallized in a Teflonlined stainless steel autoclave at 170 °C for 7 days. The solid products so obtained were recovered by centrifugation, washed several times with distilled water, dried overnight at 110 °C and calcined in air at 550 °C for 5 h under static air conditions.

h-Beta was prepared from a solution with the following molar composition: $1\text{Al}_2\text{O}_3:60\text{SiO}_2:15.5\text{TEAOH}:1000\text{H}_2\text{O}$, in which fumed silica (Fluka), tetraethylammonium hydroxide (TEAOH, 35 wt%; Alfa), aluminum flakes (Aldrich), and distilled water were used as reagents. The precursor solution was precrystallized in a Teflon-lined stainless steel autoclave under autogenous pressure at 135 °C during 3 days to promote the formation of protozeolitic nanounits. The gel so obtained was mixed with an aqueous solution of TEAOH (13 wt%), containing the silanization agent (PHAPTMS) with an 8 mol% proportion regarding to the silica content of the initial gel. The resulting mixture was kept under reflux at 90 °C for 6 h. Thereafter, the crystallization of the functionalized protozeolitic nanounit solution was carried out in a Teflon-lined stainless steel autoclave at 135 °C for 7 days. The solid products obtained were recovered by centrifugation, washed several times with distilled water, dried overnight at 110 °C and, finally, calcined in air at 550 °C for 5 h.

2.2.2. MgO and ZnO incorporation

MgO and ZnO were deposited over the hierarchical zeolites via wet impregnation method using ethanol as solvent and a nominal load of 10 wt%. Firstly, 50 wt% of the overall metal precursor load, $\text{Mg}(\text{NO}_3)_2 \cdot 6\text{H}_2\text{O}$ or $\text{Zn}(\text{NO}_3)_2 \cdot 6\text{H}_2\text{O}$ (Aldrich), was dissolved in 20 ml of ethanol (Sharlab). Then, 2 g of the zeolitic support was added over the previous solution, the mixture being kept under stirring for 6 h at 40 °C and, afterwards, the solvent was removed using a rota-evaporator. The recovered solid was dried overnight at 100 °C and activated at 200 °C for 10 h in a conventional oven. Then, the impregnation process was repeated using the second half of the metal precursor. Finally, the resulting solid was calcined at 500 °C for 6 h.

2.3. Catalyst characterization

X-ray diffraction (XRD) patterns of the parent and supported catalysts were recorded with a Philips PW 3040/00 X'Pert MPD/MRD diffractometer using Cu K α radiation operated at 45 kV and 40 mA. Argon adsorption–desorption isotherms at –186 °C of the catalysts were obtained using an Autosorb iQ Analyzer System from Quantachrome Instruments. The samples were previously outgassed at 300 °C under vacuum. The surface area was determined applying the Brunauer–Emmett–Teller (BET) equation. The pore size distributions, as well as surface and volume corresponding to micro- and mesopores, were calculated using the adsorption branch of the Argon isotherms by applying the NL-DFT (Non Local Density Functional Theory) model assuming cylindrical pore geometry. The Si/Al molar ratio and metal oxide contents of the catalysts were measured by ICP-OES using a Perkin Elmer Optima 7300AD instrument.

The catalyst acidity was probed by means of temperature programmed desorption of ammonia (NH_3 -TPD) using an AUTOCHEM 2910 instrument (Micromeritics) equipped with a TCD. The catalyst sample (0.1 g) was degassed under He flow at 600 °C for 6 h followed by saturation at 100 °C using a He– NH_3 mixture. After that, the sample was purged for 30 min under He flow in order to remove the weakly physisorbed ammonia. NH_3 -TPD profiles were subsequently recorded increasing the temperature from 100 to 600 °C using a ramp rate of 10 °C/min. CO_2 -TPD were performed in the same instrument. The catalysts sample (0.1 mg) was preconditioned by heating up to 600 °C during 6 h by flowing 100 ml min^{-1} of He. After cooling to 100 °C, the sample was exposed to 50 ml/min of 5% CO_2 /He gas for 30 min and then the system was then purged in flowing He for 1 h to remove physisorbed CO_2 . Finally, the catalysts were heated from 100 to 600 °C in He flow.

On the other hand, the nature, amount, and strength of acidic sites of the catalysts were evaluated by pyridine adsorption monitored by FTIR spectroscopy. Previously to the adsorption of the probe molecule (pyridine), the samples were pressed into self-supporting wafers (ca. 8–12 mg cm^{-2}), sealed in a quartz cell and activated overnight at 450 °C under vacuum. After recording the background spectra of the sample, pyridine adsorption (3 Torr) was carried out at 150 °C for 20 min. The strength of the acid sites was probed subjecting the samples at different desorption temperatures (150, 250, 350 and 450 °C) for 20 min under vacuum. A Nicolet spectrometer, equipped with a MCT/B detector cooled with liquid nitrogen, was used to record the spectra (normalized to 10 mg cm^{-2} wafer) with a resolution of 4 cm^{-1} in the 4000–400 cm^{-1} range. The following bands and integrated molar extinction coefficients were used for a quantitative characterization of acid sites: pyridinium band (PyH $^+$) at 1545 cm^{-1} ($\epsilon = 1.67 \text{ cm} \mu\text{mol}^{-1}$) and pyridine PyL bands at 1461 + 1454 cm^{-1} ($\epsilon = 2.2 \text{ cm} \mu\text{mol}^{-1}$).^{24,25}

2.4. Catalytic fast pyrolysis experiments

The biomass catalytic tests were performed under nitrogen atmosphere using a pyrolysis–catalytic fixed bed stainless steel reactor. Details of the experimental setup were given elsewhere.²⁶

The reactor consisted in two zones: the pyrolysis zone, where the purely thermal pyrolysis occurred, and the catalytic section, where the pyrolysis vapors were put in contact with the catalyst bed, being independently heated at 500 °C using two electrical furnaces. The reactor was loaded with 1 g of catalyst, operating with a biomass/catalyst mass ratio of 5. Prior to the catalytic pyrolysis experiments, the zeolite samples were pelletized, crushed and sieved to a particle size in the 180–250 µm range. Likewise, the biomass sample was placed in the biomass tank and kept at room temperature.

Once the reactor temperature reached 500 °C, the biomass was introduced into the reactor via opening the feeding valve and was rapidly decomposed into a carbonaceous solid (biochar), bio-oil vapors and non-condensable gases. In order to avoid the mixing between the char particles and the catalyst bed, a quartz wool sheet and a metallic net were placed over the catalyst particles. The vapors and gases generated in the pyrolysis section were conducted through the catalyst bed by a N₂ flow of 100 Nml min⁻¹, being rapidly passed through a condensation train composed by four 125 cm³ flasks connected in series and refrigerated by an ice-water bath (0–4 °C). In the catalytic experiments, the condensed bio-oils consisted of two phases, which were separated by centrifugation for further analysis. The water content of each bio-oil fraction was determined using a Karl Fischer titration instrument (ASTM E203-08), while its elemental composition (C, H, N, and O) was calculated with a Thermo Scientific microanalyser. In addition, bio-oil composition was analysed by a Gas Chromatograph Mass Spectrometer GC-MS, Bruker® SCION 436-GC (electron energy, 70 eV, emission, 300 V; He flow rate, 1 ml/min; column, WCOT fused silica 30 m × 0.25 mm ID × 0.25 µm). For tentative identification of pyrolysis products, all mass spectra were compared to the NIST mass spectrum library (with a minimum match score of 700). Bio-oil compounds were further grouped into different families according to their main functional groups.

Uncondensed gases (CH₄, C₂H₄, C₂H₆, C₃H₆, and C₃H₈) were collected in a sampling bag for their further analysis in a dual channel Agilent® CP-4900 Micro Gas Chromatograph (Micro-GC) equipped with a thermal conductivity detector (TCD), using helium as carrier gas. The TCD was periodically calibrated with a standard gas mixture containing N₂ (internal standard), O₂, H₂, CO, CO₂, CH₄, C₂H₄, C₂H₆, C₃H₆, and C₃H₈. After the catalytic tests, the char and the spent catalyst were recovered for their characterization. Char was subjected to both proximate and ultimate analyses in the same way as the raw biomass. Coke amount was determined by thermogravimetric analysis with a heating program of 10 °C/min up to 550 °C under air atmosphere using TGA analyser NETZSCH STA 449.

Finally, from the weight of the bio-oil and char fractions and those calculated for coke and gas fractions, the total mass balance can be closed to the amount of biomass fed. The elemental (C, H, N, and O) mass balances were also assessed from the yield of the different products and their ultimate analyses. The reproducibility of the analyses of all the products is rather good, and the standard deviation is in all cases below 5%. The bio-oil high heating value (HHV) was calculated according to the correlation reported elsewhere.²¹

3. Results and discussion

3.1. Catalyst properties

A total of six zeolite-based catalysts have been prepared and applied in this work for biomass catalytic pyrolysis. They consist of two hierarchical zeolite samples with MFI and BEA topologies (h-ZSM-5 and h-Beta, respectively), and the corresponding materials were obtained after MgO and ZnO incorporation. This section discusses the main characterization data of the catalyst samples.

Chemical composition of the catalysts is displayed in Table 2. The Al content of the h-Beta support is higher than that of h-ZSM-5. Concerning the supported materials, the values measured for the metal oxide content are close to the nominal content added during the synthesis (10 wt%). Thus, MgO-containing materials exhibit metal oxides loadings in the range 8.4–8.7 wt%, whereas for ZnO-supported samples, higher contents are observed with values between 9.7 and 10 wt%.

Table 1. Proximate and ultimate analyses of eucalyptus woodchips

Proximate analysis	wt%	Proximate analysis	wt%
Moisture	9.7	Carbon ^c	51.23
Volatiles ^a	74.7	Hydrogen ^c	5.93
Ash ^a	1.83	Nitrogen ^c	0.13
Fixed Carbon ^{a,b}	23.5	Oxygen ^{b, c}	42.71
HHV (MJ/kg)	20.04	Sulphur ^c	0.00

^a Weight percentage on dry basis

^b Determined by difference

^c Determined on dry and ash free basis

High angle XRD patterns of the catalyst samples are depicted in Fig. 1. The zeolitic supports exhibit the XRD peaks typical of MFI and BEA structures, with no amorphous background being observed, which is indicative of the high crystallinity of the samples, as it was confirmed by adsorption data. The XRD patterns of the metal oxide loaded materials display quite similar diffraction signals to those corresponding to the parent zeolites, indicating that the crystalline structure is retained after the incorporation of both metal oxides. Thus, sharp XRD peaks can be observed for the h-ZSM-5 materials in the 2θ ranges 7° – 9° and 23° – 25° , corresponding to the main diffraction signals of the MFI structure.²⁷ Similarly, XRD patterns of the h-Beta based materials present the characteristic peaks of the BEA topology located at 2θ of 7.6° , 14.6° , and 22.4° .²⁸ A slight reduction in the intensity of the XRD diffraction lines is observed after the metal oxides incorporation, which is a consequence of their addition with relatively high loadings. However, no diffraction peaks have been detected corresponding to the metal oxides. Likewise, no metal oxide particles could be clearly detected in the TEM images taken of the loaded samples, neither for Beta nor for ZSM-5 based catalysts (see Fig. 2). These results indicate that MgO and ZnO phases are present with a very high dispersion over the surface of the zeolitic supports. This effect is probably favored by the presence of mesopores in the hierarchical zeolites, which provide additional surface area for the incorporation and dispersion of the metal oxide phases. On the other hand, it cannot be discarded that at least a part of the metallic species could be introduced by ion exchange of Zn^{2+} and Mg^{2+} cations with protons of the zeolitic supports.²⁶ Nevertheless, taking into account the high

metal loading and the limited ion exchange availability of the zeolites, most of the Mg and Zn species are expected to be present in the form of metal oxide phases.

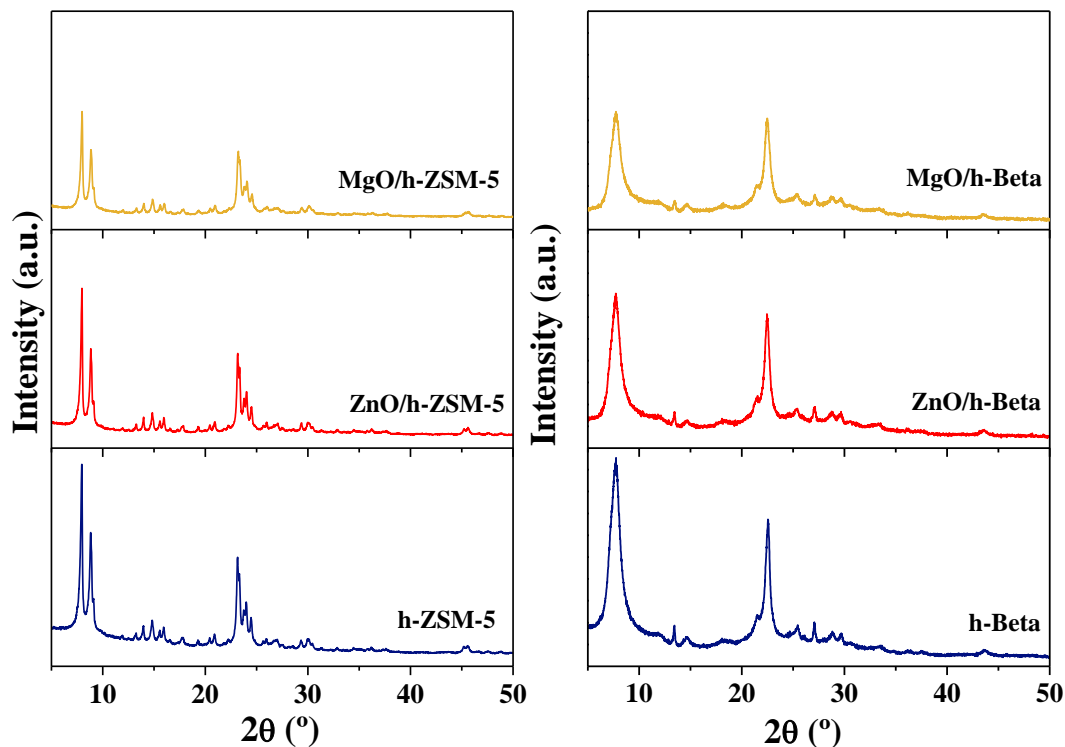


Fig. 1. XRD patterns of the catalysts.

Textural properties of the catalysts have been assessed by means of Ar adsorption–desorption isotherms at 87 K, being depicted in Fig. 3a, b. Parent zeolites, h-ZSM-5 and h-Beta exhibit an intermediate shape between type I and IV isotherms, according to the IUPAC classification. Thus, a significant adsorption is observed at low relative pressures ($P/P_0 < 0.1$) associated to the zeolitic micropores, followed by a large increase in the adsorption at intermediate relative pressures, which is ascribed to the presence of mesopores. The existence of a bimodal pore structure, which is a typical feature of hierarchical zeolites, is confirmed by the results derived from the application of the NL-DFT model, as illustrated in Fig. 3c, d in the form of pore size distribution (PSD) and cumulative pore volume curves. Thus, for both zeolitic supports, two main peaks can be observed in the respective PSD. The first one is a quite narrow peak located at about 5.5 and 6.5 Å for the h-ZSM-5 and h-Beta samples, respectively. These values agree well with the size of the micropores in the MFI and BEA structures. The second peak in the PSD is broader compared to the previous one, being centered at pore sizes in the ranges 20–45 Å and 30–60 Å for the h-Beta and h-ZSM-5 materials, respectively, denoting the presence of an important mesoporosity in both parent zeolite samples.

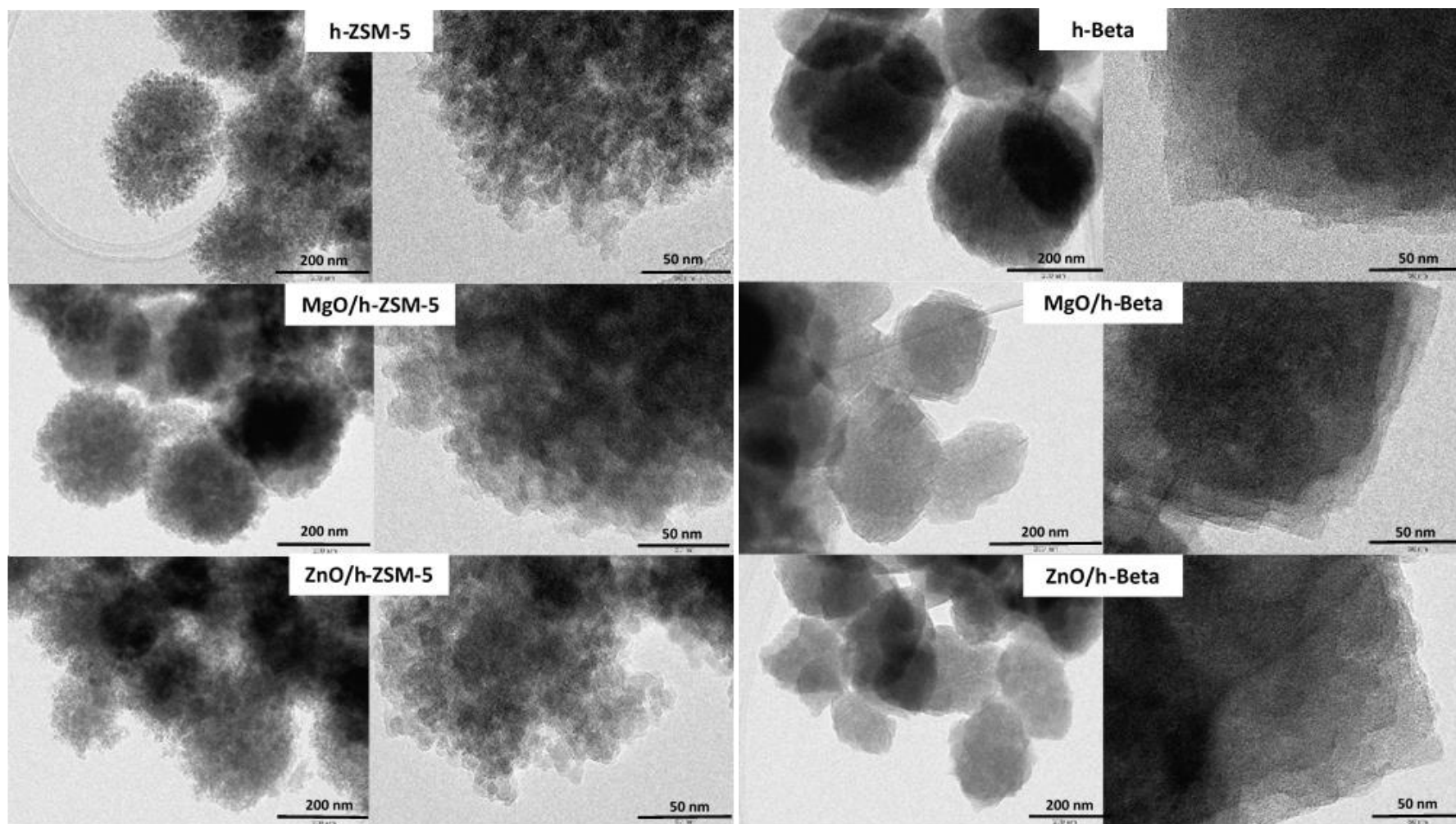


Fig. 2. TEM images at two magnifications of the different catalysts based on A) ZSM-5 zeolites and B) BETA.

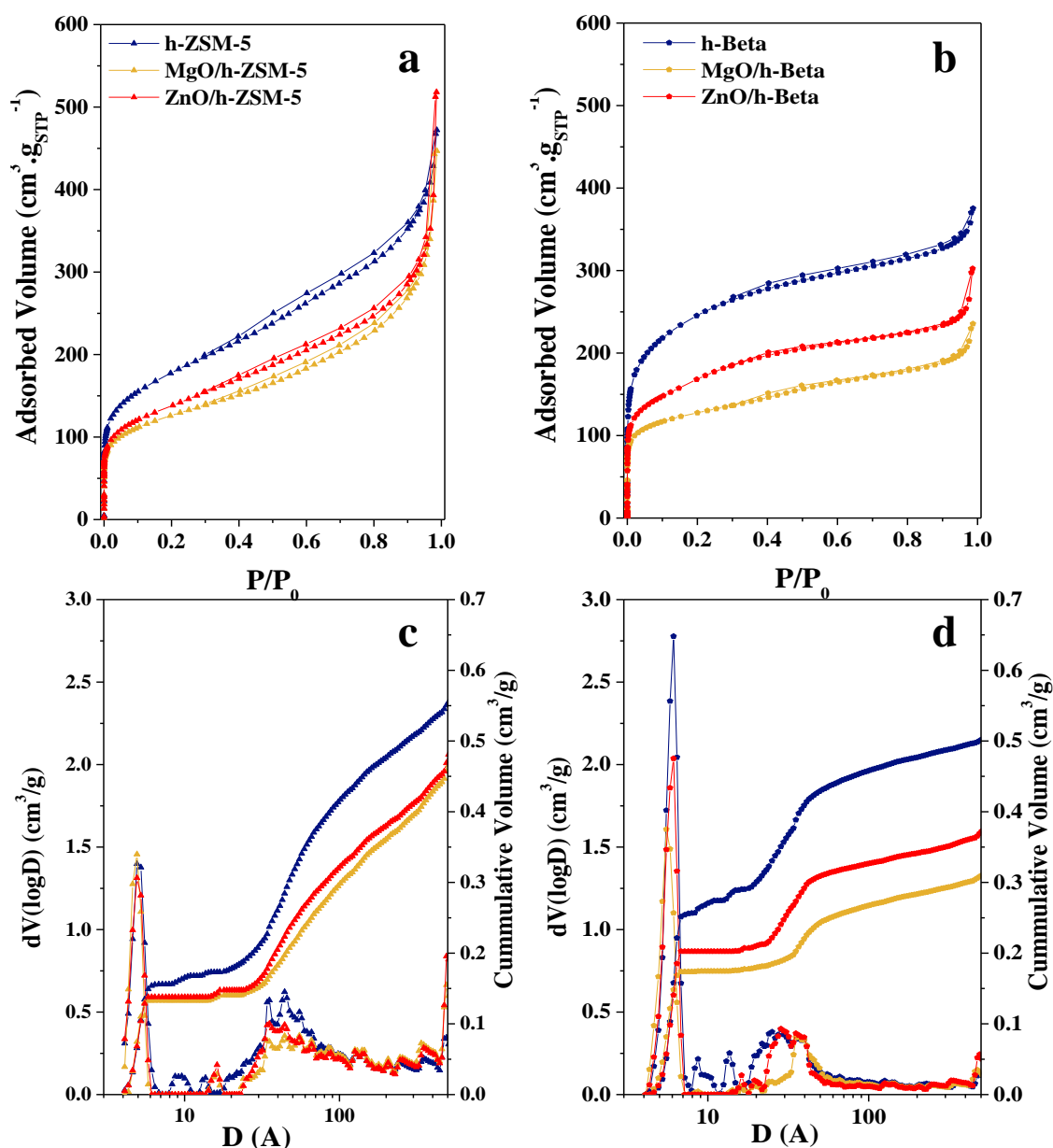


Fig. 3. Ar adsorption-desorption isotherms measured at 87 K (A, B) and NL-DFT cumulative pore volume curves and pore size distributions (C, D) of the catalysts.

After the loading of both Zn and Mg species, an important reduction of the Ar adsorption capacity occurs due to the partial zeolite surface coverage and pore blockage caused by the generated metal oxide particles. While for the h-ZSM-5 samples, both metal oxides cause similar reductions in the overall adsorption capacity, and for the h-Beta ones, this effect is quite more pronounced in the case of the MgO containing material. Table 2 provides detailed information on how the incorporation of these metal oxides affects to the textural properties of the supports. Thus, the BET area is decreased in all cases, showing reductions between 22.8% (ZnO/h-ZSM-5) and 48.6% (MgO/h-Beta). Interestingly, in all samples, this effect is more pronounced on the surface area corresponding to mesopores compared to micropores, indicating that the metal oxides are preferentially located on the mesopores of the hierarchical zeolitic supports. Thus, for h-ZSM-5-based samples the micropore surface areas are 7.4 and 11.5% lower when incorporating ZnO and MgO, respectively. Therefore, it can be concluded that for h-ZSM-5, just

a small proportion of the metal oxides are located within the micropores. In contrast, the mesopore surface area is decreased by 34 and 42% after the addition of Zn and Mg oxides, corroborating that these metal oxide phases are preferentially located on the h-ZSM-5 mesoporosity. However, the picture is somewhat different for the h-Beta samples since in this case, both micropore and mesopore surface areas are decreased after the metal oxide incorporations, denoting that in this case, the latter are distributed within both micro- and mesopores, which can be assigned to the larger micropore size of the BEA structure compared to the MFI one. Nevertheless, also for h-Beta materials, the highest decrease of the surface area is observed in the mesopore range with reductions of 47 and 70% for the ZnO/h-Beta and MgO/h-Beta samples, respectively. Other important difference between both series of catalysts is the fact that in all cases, the available mesopore volume is quite larger for the h-ZSM-5 materials compared to the h-Beta ones, which is expected to have a significant effect on the internal diffusion rate and the catalytic properties of these samples. Concerning to the metal oxide effect, it can be observed that the deposition of MgO leads to a higher reduction in the Ar adsorption capacity than ZnO, resulting in lower textural properties values for both micro- and mesopore ranges.

Table 2. Chemical and textural properties of the catalysts.

Catalysts	(Si/Al) _{MOL} ^a	Metal oxide ^a (wt%) ^a	S _{BET} ^b (m ² /g)	V _{MZ} ^c (cm ³ /g)	V _{MS} ^c (cm ³ /g)	S _{MZ} ^c (m ² /g)	S _{MS} ^c (m ² /g)
h-ZSM-5	58	--	562	0.149	0.425	243	319
MgO/h-ZSM-5	58	8.4	398	0.132	0.374	215	183
ZnO/h-ZSM-5	58	9.7	434	0.138	0.370	225	209
h-Beta	24	--	779	0.256	0.251	434	345
MgO/h-Beta	24	8.7	400	0.174	0.136	295	105
ZnO/h-Beta	24	10.0	524	0.203	0.170	343	181

^aICP-OES measurements

^bBET surface area

^cEstimated by applying the NL-DFT model assuming cylindrical pore geometry

MZ: Zeolitic micropores; MS: Mesopores

The acidic properties of the zeolite catalysts have been investigated first by ammonia TPD, as displayed in Fig. 4. In the TPD profiles corresponding to both parent zeolites, two different desorption peaks, centered at about 150 °C and 300–325 °C, can be easily distinguished. The first one is traditionally attributed to NH₃ molecules adsorbed onto weak acid sites, such as silanol groups, while the second one is related to NH₃ molecules interacting with framework Al species.^{25,29} The concentration of both strong and weak acids sites is higher for the h-Beta sample regarding the h-ZSM-5 one, which can be ascribed to the higher content of aluminum, as well as of defective silanols groups, in the former. Thus, the overall concentration of acid sites is higher for the h-Beta sample compared to the h-ZSM-5 zeolite, showing values of 0.578 and 0.36 NH₃ mmol g⁻¹, respectively. After the metal oxide deposition, the ammonia TPD profiles and acidity values are significantly modified, indicating a substantial change of the acidic properties. Thus, the overall acidity is increased after the Mg and Zn addition, showing that new acid sites associated to these metal oxides area are created, this effect being somewhat more pronounced for the Zn containing materials. This fact is clearly evidenced in the ammonia TPD

curves by the appearance of a new broad signal that extends in the temperature range between 200 and 300 °C, overlapping and masking the peaks already observed in the parent zeolites. The presence of this signal denotes the generation of new acid sites, exhibiting a medium strength, as a consequence of the metal oxide deposition.

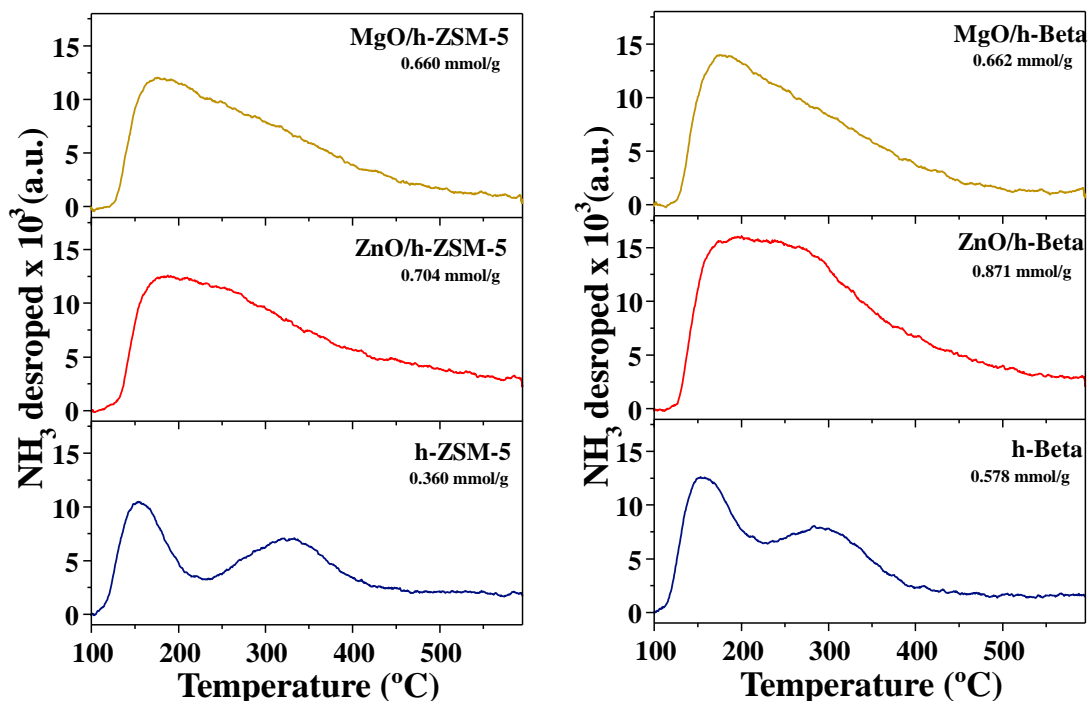


Fig. 4. NH_3 TPD curves and overall acidity values of the catalysts.

Further insights into the nature and strength of the acid sites present in the catalyst samples have been obtained by adsorption–desorption of pyridine monitored by FTIR spectroscopy. Fig. 5 depicts the pyridine vibration region of the spectra obtained after adsorption/desorption at 150 °C. For both types of zeolites (h-ZSM-5 and h-Beta), characteristic bands of Brønsted acid sites (BAS) are clearly appreciated in the parent samples at 1637 and 1547 cm^{-1} , which strongly decrease in intensity after the incorporation of the Mg and Zn species. On the other hand, important changes are also observed for the metal oxide containing samples in the bands ascribed to Lewis acid sites (LAS; 1600–1628 cm^{-1} and 1464–1445 cm^{-1}). Lewis acid sites in zeolites can be ascribed to extraframework Al species (EFAL), as well as to partially coordinated Al atoms (structure defects). The parent zeolites exhibit a steep band at 1623 cm^{-1} corresponding to pyridine strongly adsorbed on coordinatively unsaturated Al^{3+} ions (PyL, pyridine interacting with Lewis acid sites),^{29,30} which is almost suppressed in the zeolites after the metal oxide incorporation, whereas a new and intense signal appears in this region at 1613 and 1610 cm^{-1} for the Mg and Zn containing samples, respectively. Likewise, a strong increase in the intensity of the band at $\sim 1456 \text{ cm}^{-1}$ is observed after the addition of the metal oxides, which is accompanied by a bathochromic shift due to the different polarizing power of the cations ($\text{Mg}^{2+} < \text{Zn}^{2+} < \text{Al}^{3+}$), the higher wave numbers corresponding with stronger LAS.³¹ Therefore, the evaluation of the spectra indicates that the incorporation of Mg and Zn species affects not only the zeolite Brønsted acid sites but also the coordinatively unsaturated Al^{3+} ions. Moreover, new Lewis acid sites have appeared coming from the presence of the metal species.

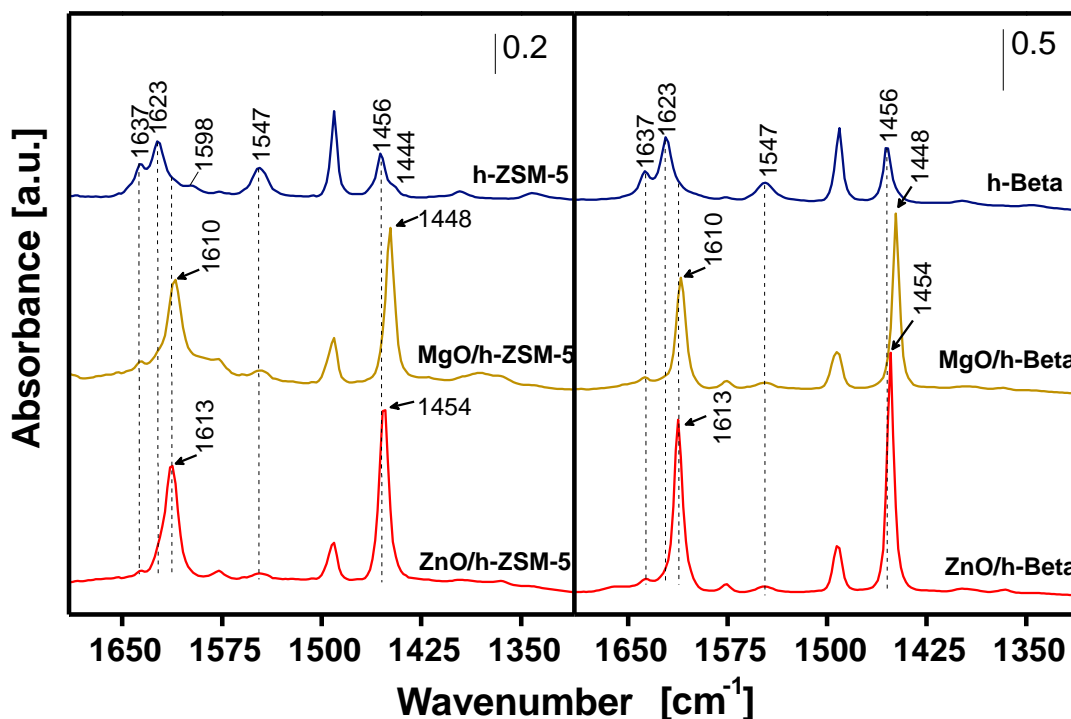


Fig. 5. FTIR spectra of the catalysts after pyridine adsorption.

Acid site concentration values, referred to the weight of the zeolitic support, were evaluated at different temperatures (150, 250, 350, and 450 °C) using the pyridine/FTIR data (Fig. 6). As expected, for the parent zeolites, the concentration of both types of acid sites is higher in h-Beta compared to h-ZSM-5, which agrees well with its superior aluminum content. On the other hand, a large difference between the Lewis acid sites concentration in both parent samples is observed, showing that the higher aluminum content exhibited by h-Beta zeolite results in a larger amount of coordinatively unsaturated Al^{3+} ions.

After metal oxide loading, the Brønsted acid sites concentration is significantly decreased for both zeolites (Fig. 6a, c). Thus, attending to the BAS concentration data determined by pyridine desorption at 150 °C, the reduction accounts for more than 70% of the BAS initially present in both parent zeolites. This result can be partially ascribed to surface coverage and pore blockage effects caused by the deposition of metal oxide species. However, if compared with reduction of the textural properties, the decrease in the BAS concentration is more pronounced, suggesting also the existence of ion exchange phenomena between the metallic species and the acidic bridging hydroxyl groups (Si-OH-Al), which is in agreement with previous literature results.³²

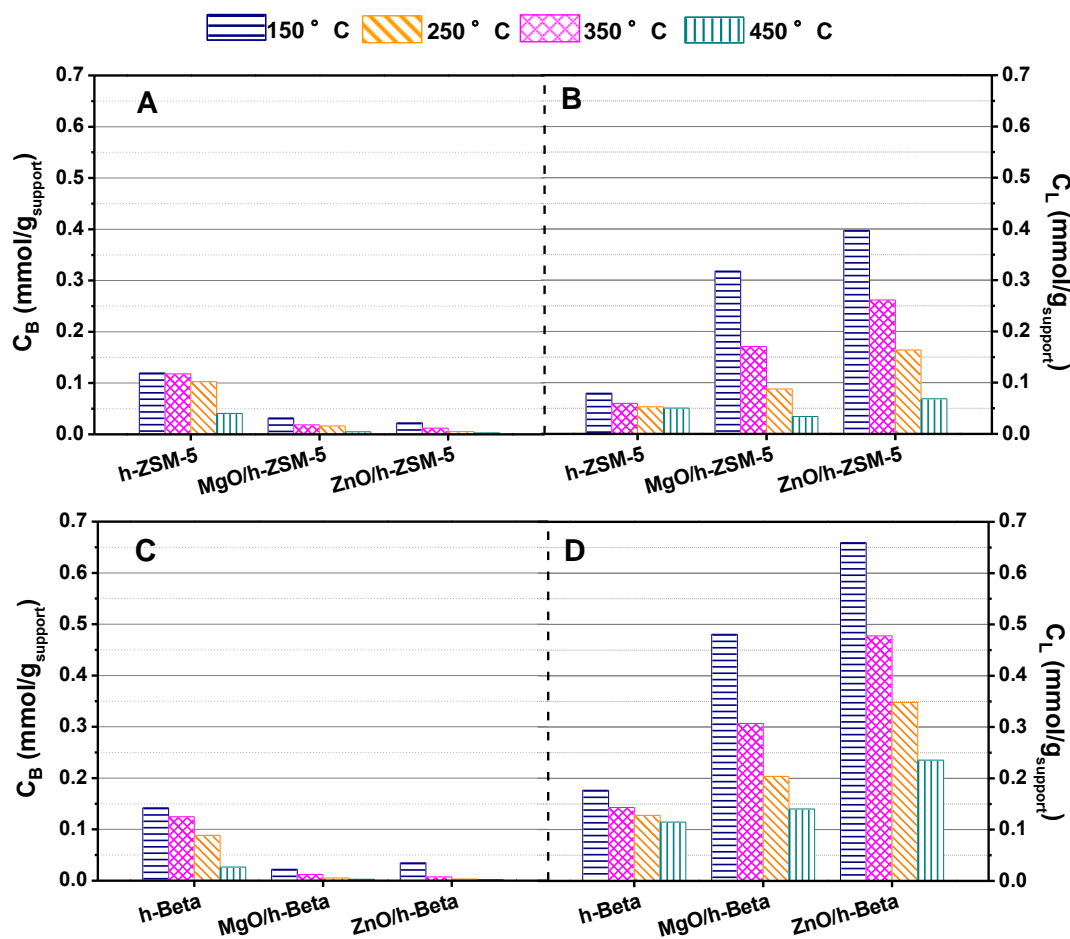


Fig. 6. Concentration of Brønsted, C_B (A, C) and Lewis, C_L (B, D) acid sites of the catalysts, probed by FT-IR/pyridine adsorption, as a function of the outgassing temperature.

Typically, the Lewis acid sites in protonic zeolites can be ascribed to extraframework Al species (EFAL) and partially coordinated Al atoms (structure defects). In addition, as it is mentioned above, the incorporation of Zn and Mg species causes the generation of new Lewis acid sites. Therefore, the total concentration of LAS present in the metal oxide containing samples will depend on the content of coordinatively unsaturated Al^{3+} ions coming from the zeolitic support, as well as on the Zn and Mg loadings. In this way, as shown in Fig. 6b, d, the presence of these metallic species leads to a considerable increase of the overall LAS Lewis concentration regarding the parent zeolites. This effect is more pronounced for the Zn-containing materials, which agrees well with the more enhanced acidity observed in the ammonia TPD tests for the latter.

Finally, CO_2 -TPDs were used to determine the basicity of the different samples, and the results are displayed in Fig. 7. In all cases, the profile of the TPD is similar with a peak at about 160 °C, which for the oxide loaded zeolites is appreciably more intense which can be attributed respectively to adsorbed CO_2 on hydroxyl groups and other centers of weak or medium strength. The TPD curves of both parent zeolites are rather similar and they show low intensity contributions of weak centers. Incorporation of the oxides results in a sharp increment of the contribution of the weak sites, which is significantly larger for the catalyst based on h-Beta zeolites, which most likely reflects a better dispersion of the oxides on this support. Differences in CO_2 adsorption between catalysts loaded with ZnO and MgO are more moderate but

significant. For the both types of zeolites, the concentration of basic sites is larger for the samples loaded with MgO, being the difference more marked in the case of the ZSM-5 catalyst.

Accordingly, these catalysts, particularly those loaded with metal oxides, present simultaneously basic and acid sites which contribute to the activity of these catalysts for the upgrading of pyrolysis vapors.

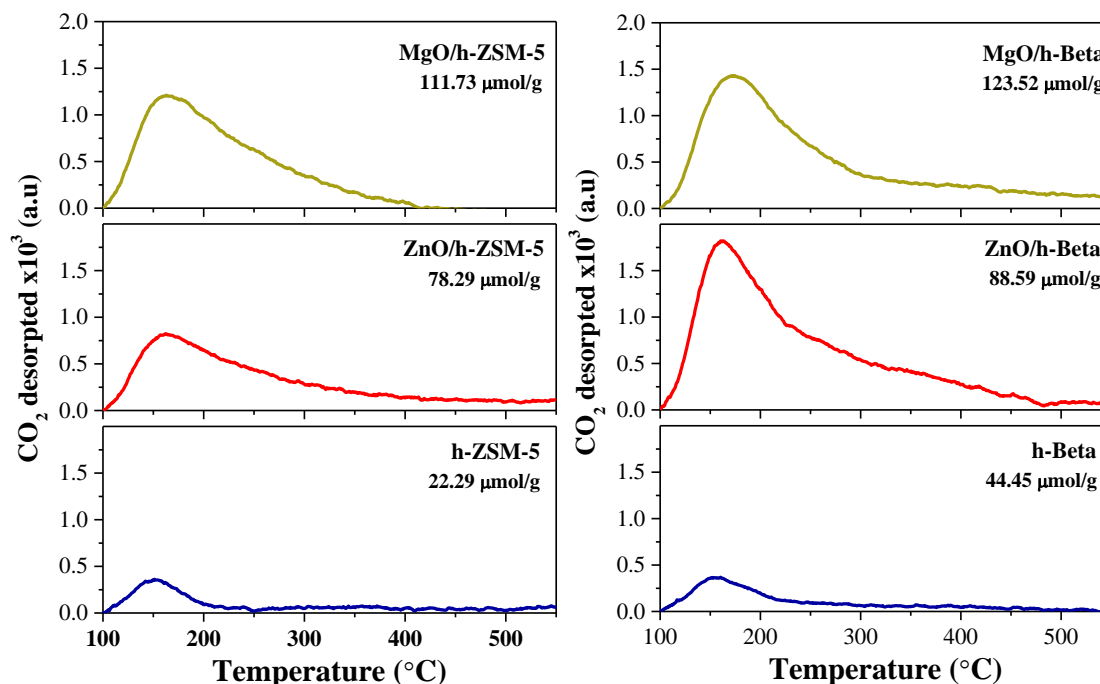


Fig. 7. CO₂-TPD curves and overall basicity values of the catalysts.

3.2. Catalytic fast pyrolysis of eucalyptus woodchips

In this section, the effect of the incorporation of ZnO and MgO on two hierarchical zeolites, h-ZSM-5 and h-Beta, has been investigated in the catalytic fast pyrolysis of eucalyptus woodchips. The same reaction temperature (500 °C) was maintained in the thermal and catalytic zones, whereas a biomass/catalysts ratio of 5 w/w was employed. Moreover, the results obtained in a non-catalytic test performed under the same experimental conditions have been also included in the study for comparison purposes.

The yields obtained in the eucalyptus pyrolysis tests corresponding to the main fractions, and expressed on basis of dry initial weight of biomass, are presented in Table 3.

Firstly, it should be noticed that char yields obtained in the catalytic and non-catalytic experiments are quite similar, showing values around 30 wt%. This fact confirms that the catalyst incorporation does not have any influence on the char yields, which is an expected result since both thermal and catalyst reaction zones are clearly separated and, therefore, the char fraction is formed in the thermal section, just before reaching the catalyst bed.

Table 3. Product distribution per fractions obtained in the fast pyrolysis of eucalyptus woodchips.

Catalysts	Product yield ^c (wt%)					Bio-oil*	HHV
	Gas	Char	Coke	Bio-oil*	Water	O conc. (wt%)	(MJ/kg bio-oil*)
Non-catalytic	12.1	30.3	0.0	42.2	15.5	39.0	23.37
h-ZSM-5	20.5	30.5	3.1	26.5	19.4	31.8	27.80
MgO/h-ZSM-5	18.7	30.8	2.5	28.4	19.7	28.4	28.84
ZnO/h-ZSM-5	23.3	30.5	2.4	25.4	18.4	29.1	29.45
h-Beta	20.0	29.9	3.5	31.8	14.8	39.1	24.82
MgO/h-Beta	16.5	30.7	2.3	34.6	15.9	37.0	24.69
ZnO/h-Beta	19.2	30.7	2.7	32.0	15.5	37.0	25.15

Bio-oil*: Free water basis

In the catalytic experiments, an additional solid carbonaceous phase, coke, is formed on the zeolite surface. Coke is generated by a complex combination of reactions, such as olefin oligomerization and aromatics polycondensation, which are mainly catalyzed by Brønsted acid sites.³³ According to the literature, large pore zeolites, such as Beta materials, typically produce higher coke yields.³⁴ However, coke amount generated over both hierarchical parent zeolites here studied is quite close (3.1–3.5 wt%, for h-ZSM-5 and h-Beta samples, respectively). In this way, it must be taken into account that the contribution of the mesopores is higher in the case of the h-ZSM-5 sample than for Beta catalysts, which may compensate its lower micropore size and volume, resulting in similar values of the overall coke formation for both materials. After the metal oxide incorporation, coke yields are decreased, being in the range 2.3–2.7 wt%. This is a positive result, as it should reduce the catalyst deactivation. Lower coke formation after the metal oxide incorporation can be related to the above commented reduction in the concentration of Brønsted acid sites and the parallel increment of basic sites. This effect takes place in spite of the observed overall enhancement of the catalyst acidity by generation of new LAS, associated to the Mg and Zn species, showing that the latter contributes little to the formation of coke deposits. Accumulation of coke can cause catalysts deactivation for successive assays. However, calcination in carefully controlled conditions to avoid the formation of hot spots, which may damage the catalyst, has been found to be a very effective procedure for recovery the activity of zeolite-based catalysts for pyrolysis.³⁵

The amount of bio-oil* produced in the catalytic tests is significantly reduced compared to the thermal process, due to the catalytic cracking of the pyrolytic vapors over the zeolite acid sites, which results in an important increase in the gas yields. Figure 8a displays the composition of the gas fraction, expressed as yield of the different components referred to the raw biomass. The gas share, in the thermal pyrolysis experiment, is 12.1 wt%, which is increased up to 20–20.5 wt% over the parent h-ZSM-5 and h-Beta zeolites. Thus, for parent zeolites, the proportion of CO₂ and CO is enhanced due to the occurrence of deoxygenation reactions by means of decarboxylation and decarbonylation pathways. However, zeolites behave differently in terms of water production. In this way, the water yield is enhanced over the h-ZSM-5 sample, as compared to the thermal test, but it remains almost constant over the h-Beta zeolite, showing a different contribution of deoxygenation through dehydration reactions depending on the zeolitic

structure. Likewise, the amount of non-condensable light hydrocarbons (such as methane, ethane, ethylene, propane, and propene) increases in the catalytic experiments due to a higher rate of deep cracking reactions. Hydrogen is also detected in the gas stream but in quite small proportions.

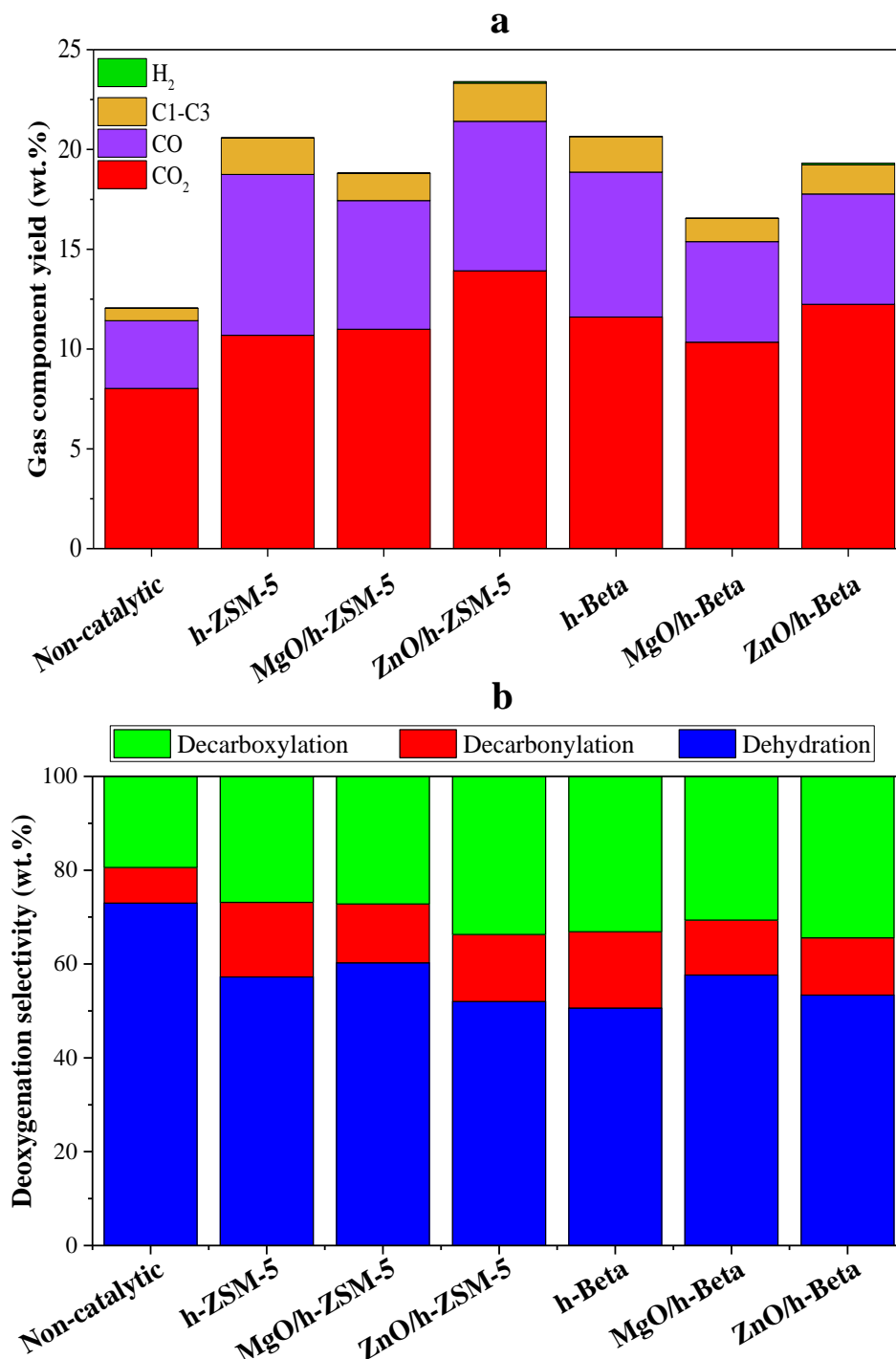


Fig. 8. a) Composition of the gaseous fraction composition obtained in the thermal and catalytic fast pyrolysis of eucalyptus woodchips. b) Deoxygenation selectivity corresponding to the thermal and catalytic fast pyrolysis of eucalyptus woodchips.

After the loading of Mg and Zn species, significant changes are produced on the product distribution by fractions (Table 3). The incorporation of the metal oxides over the zeolitic support

provokes an enhancement in the bio-oil yield and a lower gas production, with the exception of the ZnO/h-ZSM-5 sample. These results indicate that the metal-modified zeolites exhibit somewhat lower activity in the overall conversion of the pyrolytic vapors, probably due to the reduction in the BAS concentration and the generation of basic centers caused by the addition of Mg and Zn species. The presence of these two types of centers in a single material has been recently reported for Mg-loaded BEA zeolites, and they can enhance the performance of these catalysts.³⁶ However, little variation is observed in those samples regarding the water yield, evidencing that dehydration reactions are not significantly altered by the metal oxides addition to the zeolitic supports. On the other hand, it should be noted that ZnO loading enhanced somewhat the carbon dioxide and hydrogen yields, probably due to the occurrence of the water gas shift reaction between CO and H₂O, which is known to be catalysed by Zn species.^{19,20}

Comparing both series of zeolitic catalysts, the highest differences in regard to the thermal test have been obtained over h-ZSM-5-based materials. In this case, the bio-oil* yield decreased from 42.2 wt% to 25.4 and 28.5 wt%. Likewise, the water production increased from 15.5 wt% up to 18.4–19.7 wt%. This result, together with a higher CO and CO₂ production, denotes that, although h-ZSM-5 materials provide lower bio-oil* yields, they contribute significantly to promote deoxygenation reactions. This fact is corroborated by the data reported in Table 3, displaying an important reduction in the bio-oil* oxygen content. In this way, the oxygen percentage decreases from 39.0 wt%, in the thermal bio-oil*, to 31.8 wt% over the parent h-ZSM-5 zeolite. Interestingly, Mg and Zn incorporation into the h-ZSM-5 sample leads to an enhanced deoxygenation with oxygen concentrations in bio-oil* of 28.4 and 29.1 wt%, respectively. In contrast, for the h-Beta, the decrease in the bio-oil* oxygen content is much less pronounced, showing values quite close to that obtained in the non-catalytic test (in the range 37–39 wt%).

In order to compare the deoxygenation pathways favoured over each catalytic system, the deoxygenation selectivity has been estimated from the oxygen amount removed in the form of CO, CO₂, and H₂O (Fig. 8b). In the non-catalytic test, the main deoxygenation route is dehydration, with a selectivity value close to 73%, whereas the contributions of decarboxylation and decarbonylation are less significant, around 19 and 7.5%, respectively. In contrast, in the catalytic reactions, the relevance of decarboxylation reactions for deoxygenation pathway is enhanced, while decarbonylation route is also promoted but in lower degree. In fact, dehydration contribution is slightly lower for the parent h-Beta sample. Metal oxide loading induces some modification in the contribution of the different deoxygenation mechanisms. Thus, compared to the parent zeolites, MgO loading decreases oxygen removal through decarbonylation, favoring somewhat the dehydration route. In contrast, ZnO deposition increases the contribution of decarboxylation mechanism, particularly for the ZnO/ZSM-5 catalysts. As it has been earlier mentioned, this fact could be related to the occurrence of the water gas shift reaction, promoted by the Zn species, and lead to the formation of CO₂ and H₂. In terms of mass and energy efficiency, the oxygen removal through decarbonylation is the least desirable route, since only one oxygen atom is eliminated for each carbon atom, affecting negatively to the bio-oil* mass and energy yields.

Accordingly, a compromise between dehydration and decarboxylation routes is desired. In this way, the modification of the parent zeolites by the incorporation of Mg metal oxides has a positive effect on the deoxygenation pathways as the contribution of decarbonylation is reduced to some extent.

The results above commented show how the catalyst promotes bio-oil* deoxygenation, which implies a loss of bio-oil yield in terms of both mass and energy (referred to the initial biomass). In this sense, it must be taken into account that the energy yield depends on both the mass yield and the bio-oil* composition. In particular, lowering the oxygen content of the bio-oil* increases its heat value, which affects positively the bio-oil* energy yield. Accordingly, the major objective of the catalytic treatment would be to enhance the rate of the bio-oil* deoxygenation but without losing too much energy yield. In this way, Fig. 9 represents the relationship between these two parameters, i.e., bio-oil* oxygen content versus bio-oil* energy yield, for the different experiments performed in this work. Thereby, the bio-oil* energy yield has been calculated as the chemical energy contained in the bio-oil* referred to that initially present in the raw biomass.

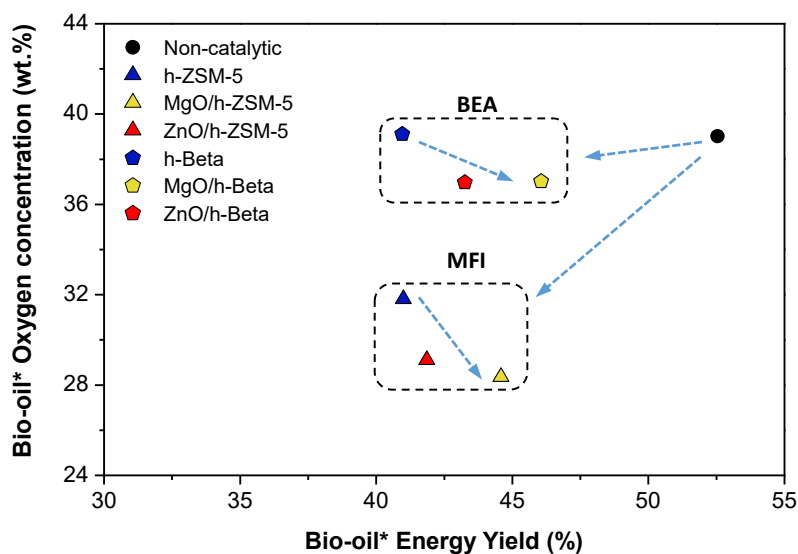


Fig. 9. Relationship between the bio-oil* oxygen content and the bio-oil* energy yield obtained in the thermal and catalytic fast pyrolysis of eucalyptus woodchips.

The data in Fig. 9 corresponding to the non-catalytic experiments show that the thermal bio-oil* has an oxygen content of 39 wt% (very close to that of the raw biomass: 42.7 wt%) and an energy yield about 55%. The rest of the chemical energy contained in the raw biomass is distributed among the char and the gaseous fractions. Compared to the thermal experiment, the catalyst incorporation causes a further reduction in the bio-oil* energy yield due to the production of more gases, as well as to the coke deposited over the catalyst. However, both types of zeolite catalysts behave quite different. Thus, those based on zeolite Beta are not really very efficient for bio-oil* upgrading since they induce little deoxygenation, due to the lower relative contribution of dehydration processes, while they cause a significant loss of energy yield. In contrast, h-ZSM-5 catalysts show clearly a better performance, leading to a deeper deoxygenation degree than h-Beta-based samples and keeping similar energy yield values. However, taking into account the higher Al content of the Beta samples, and therefore its larger acidity, a superior conversion and upgrading of the bio-oil vapors should be expected compared to h-ZSM-5. These results suggest that the acid sites in the MFI structure possess an intrinsic higher activity for bio-oil cracking and deoxygenation reactions than those of the BEA topology.

On the other hand, in all cases, the loading of Mg and Zn species over the zeolitic supports is clearly beneficial since it produces a further bio-oil* deoxygenation increasing the bio-oil*

energy content. The improved bio-oil* deoxygenation can be related with the changes provoked by the metal oxides in the acid-basic properties of the parent zeolites, decreasing the BAS concentration and generating LAS sites and new basic centers, which may promote additional deoxygenation reactions such as ketonization and aldol condensation that involve C–C bonds formation, consistently with the chemical compositions of bio-oils discussed below.³⁷ Likewise, the improved energy yield obtained over the Mg- and Zn- modified catalysts is a direct consequence of the lower production of coke and gaseous hydrocarbons, as well as to the decrease in the extension of decarbonylation reactions, as above commented. Interestingly, these positive effects derived from the incorporation of the metal oxides are more remarkable in the case of the h-ZSM-5 zeolite compared with h-Beta, despite the slightly larger concentration of basic and acidic sites on the catalyst based on this material. In particular, the MgO/h-ZSM-5 catalyst exhibits a good performance as it leads to a bio-oil* having an oxygen content of 28.4 wt% with an energy yield about 44.5%. Lower formation of light hydrocarbons, probably related to the lower Brønsted acidity with respect to the parent zeolite and the formation of specific Lewis sites, contribute to improve the energy yield obtained with these catalysts.

Finally, bio-oils* originated from thermal and catalytic tests were analysed by GC/MS in order to get insight about their chemical composition. Bio-oil is a very complex mixture of highly oxygenated compounds and its analysis by GC/MS must be interpreted with caution as it provides semi-quantitative information. Identification of these compounds has been performed comparing the mass spectra with the NIST database. The bio-oil* products have been classified, according to the main chemical functionality, into several groups: acids, aldehydes, alcohols, ketones and ethers, furans, oxygenated aromatics, sugars, and aromatic hydrocarbons. Non-identified compounds or products exhibiting a correlation match lower than 700 have been grouped as unknowns. Semiquantitative bio-oil* composition have been determined according to the relative area percentages of the compounds classified according to those groups, the results so obtained being represented in Fig. 10.

For the thermal bio-oil*, the main components detected correspond with oxygenated aromatics, ketones and ethers, sugars and carboxylic acids, followed by minor contributions of the rest of the families. In the case of the catalytic bio-oils*, the largest variations in product distribution, compared to the thermal product, are observed when using the h-ZSM-5-based samples, whereas smaller changes take place for the h-Beta catalysts. This finding agrees well with the observed variation in the bio-oil* oxygen content induced over these two types of catalysts.

Sugars are originated from holocellulose (cellulose and hemicellulose) depolymerization and their presence decreases the bio-oil* quality due to aging reactions. Bio-oils* obtained in the thermal test, as well as over h-Beta-based materials, exhibit a significant proportion of sugars, 1,6-anhydro- β -D-glucose being the main component. In contrast, sugars are almost fully converted over the h-ZSM-5-based samples, which is consistent with the superior activity observed over these materials.

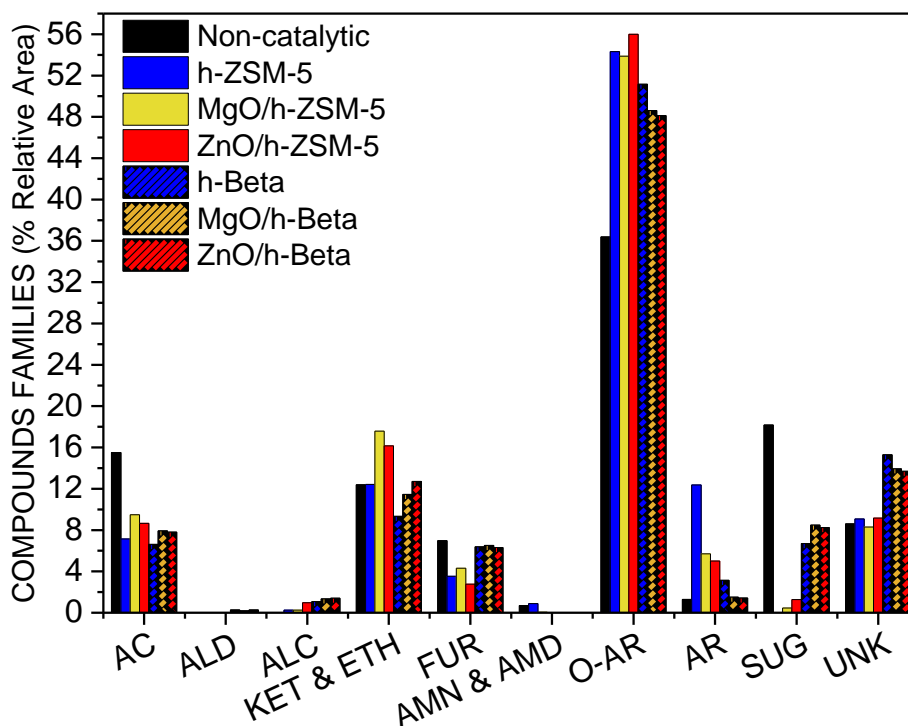


Fig. 10. Bio-oil* composition in terms of organic compounds families (% of relative area from GC-MS analyses), obtained in the thermal and catalytic fast pyrolysis of eucalyptus woodchips. (AC: acids; ALD: aldehydes; ALC: alcohols; KETÐ: ketones and ethers; FUR: furans; AMN&AMD: amines and amides; O-AR: oxygenated aromatics; AR: aromatics; SUG: anhydro sugars; UNK: unidentified chemicals)

Oxygenated aromatic compounds, which arise from the depolymerization of the lignin fraction of the biomass, represent an important share in the obtained bio-oils*. The main components detected in this group are 2-methoxyphenol, catechol and 1,2,3-trimethoxy-5-methylbenzene. For all the catalysts, the proportion of oxygenated aromatics is quite high and clearly larger than that obtained in the thermal test. This finding shows that the zeolite catalysts promote the conversion of lignin oligomers into oxygenated aromatics, being this effect more pronounced over the h-ZSM-5-based catalysts, in particular for the catalyst loaded with ZnO.

Sugar ring scission leads to light products, such as aliphatic acids, ethers, aldehydes, and ketones.³⁸ Compared to the non-catalytic test, the amounts of carboxylic acids decrease over the different catalysts, whereas no general trend is observed for other families, such as ketones, ethers, and furans. Interestingly, the concentration of ketones and ethers increased in the bio-oils* obtained over the Mg and Zn oxides containing catalysts, showing that the incorporation of metal oxides into the zeolitic supports favours the occurrence of ketonization and etherification reactions.

In the case of aromatic hydrocarbons, their concentration is almost negligible for the bio-oil* obtained in the thermal test. In the same way, h-Beta-based catalysts almost do not produce aromatic hydrocarbons. In contrast, bio-oils* from h-ZSM-5 catalysts, and especially that obtained over the parent zeolite, exhibit a larger proportion of aromatic hydrocarbons. This fact, along with the lower concentration of furans and sugars for the h-ZSM-5-based catalysts, denotes that aromatic hydrocarbon formation by Diels–Alder condensation is favoured over this type of zeolite, while the incorporation of metal oxides is not positive for this route.³⁹ In this way, the

clearly superior aromatization activity of h-ZSM-5 compared to h-Beta is in good agreement with the larger deoxygenation degree observed on the former.

4. Conclusions

Catalytic fast pyrolysis of eucalyptus woodchips has been performed in a fixed bed reactor using hierarchical zeolites (h-ZSM-5 and h-Beta), modified with MgO and ZnO, as catalysts. The physicochemical characterization of the catalysts indicates that the metal oxides are highly dispersed on the zeolitic supports, which strongly modifies both their textural and acid properties. Thus, textural parameters, such as BET surface area and total pore volume, suffered a severe reduction, which can be assigned to different phenomena such as surface coverage and partial pore blockage caused by the well dispersed metal oxide phases. This excellent dispersion is favoured by the presence of the additional mesopore system in the hierarchical zeolites used as supports. Likewise, metal oxide deposition led to an important reduction of the Brønsted acid sites concentration, showing that cation exchange between Mg and Zn species and the zeolite protons is also occurring. In addition, acidity measurements revealed that a new Lewis acidity is generated by the incorporation of the metal oxides, exhibiting medium strength. On the other hand, CO₂-TPD reveals that incorporation of metal oxides generates new weak basic centers. As a consequence, the Mg- and Zn- containing catalysts present simultaneously both acidic and basic sites, providing a very interesting reactivity.

Fast pyrolysis of eucalyptus woodchips leads to the formation of a number of fractions: char, gases, water, and bio-oil*. Compared to the non-catalytic experiment, bio-oil* yield was considerably lower when contacting the pyrolysis vapors with the zeolite catalysts, leading to an increase in the gas generation. Likewise, an additional solid phase, coke, was formed over the catalyst surface.

The incorporation of Mg and Zn species into the parent zeolites leads to positive effects in their catalytic performance, since it increases the bio-oil yield at the same time that a larger deoxygenation is achieved. Thus, the metal-modified catalysts produced lower amounts of coke and gaseous hydrocarbons, which can be attributed to a decrease in the Brønsted acid sites caused by the metal oxide deposition. In addition, the modification of the parent zeolites by the incorporation of Mg and Zn metal oxides has a positive effect on the deoxygenation pathways as the contribution of decarbonylation is reduced to some extent. As a consequence, loading of Zn and particularly Mg species on the zeolitic supports resulted in an improvement of the bio-oil* quality due to its lower oxygen concentration. This effect was more noticeable for the h-ZSM-5-based materials, since they provided a deeper deoxygenation degree, with lower anhydro sugar content, as well as a higher extension of aromatization reactions, for similar energy yields. Thus, among the catalyst tested, the best performance was obtained over the MgO/h-ZSM-5 sample, since it provides bio-oil* with the lowest oxygen concentration and the highest energy yield. The balance of Lewis acid sites with basic centers in this catalyst may explain the enhanced performance of this catalyst.

Acknowledgements

The authors gratefully acknowledge the financial support from the European Union Seventh Framework Programme (FP7/2007-2013), under grant agreement no. 604307, and from the Spanish Ministry of Economy and Competitiveness (CATPLASBIO project, Ref: CTQ2014-602209-R). JC acknowledges the Czech Science Foundation for the support of the project P106/12/G015.

References

1. D. Carpenter, T. L. Westover, S. Czernik and W. Jablonski, *Green Chem.*, 2014, **16**, 384–406.
2. D. M. Alonso, J. Q. Bond and J. A. Dumesic, *Green Chem.*, 2010, **12**, 1493–1513.
3. E. F. Iliopoulou, S. D. Stefanidis, K. G. Kalogiannis, A. Delimitis, A. A. Lappas and K. S. Triantafyllidis, *Appl. Catal. B Environ.*, 2012, **127**, 281–290.
4. T. Dickerson and J. Soria, *Energies*, 2013, **6**, 514–538.
5. D. J. Mihalcik, C. A. Mullen and A. A. Boateng, *J. Anal. Appl. Pyrolysis*, 2011, **92**, 224–232.
6. A. Imran, E. a. Bramer, K. Seshan and G. Brem, *Fuel Process. Technol.*, 2014, **127**, 72–79.
7. H. Zhang, R. Xiao, B. Jin, G. Xiao and R. Chen, *Bioresour. Technol.*, 2013, **140**, 256–262.
8. M. Asadieraghi and W. M. A. Wan Daud, *Energy Convers. Manag.*, 2015, **101**, 151–163.
9. A. Aho, N. Kumar, K. Eränen, T. Salmi, M. Hupa and D. Y. Murzin, *Fuel*, 2008, **87**, 2493–2501.
10. S. Tan, Z. Zhang, J. Sun and Q. Wang, *Chinese J. Catal.*, 2013, **34**, 641–650.
11. C. Liu, H. Wang, A. M. Karim, J. Sun and Y. Wang, *Chem. Soc. Rev.*, 2014, **43**, 7594–7623.
12. J. Li, X. Li, G. Zhou, W. Wang, C. Wang, S. Komarneni and Y. Wang, *Appl. Catal. A Gen.*, 2014, **470**, 115–122.
13. S. R. Naqvi, Y. Uemura, S. Yusup, Y. Sugiura and N. Nishiyama, *J. Anal. Appl. Pyrolysis*, 2015, **114**, 32–39.
14. A. J. Foster, J. Jae, Y. T. Cheng, G. W. Huber and R. F. Lobo, *Appl. Catal. A Gen.*, 2012, **423–424**, 154–161.
15. H. J. Park, H. S. Heo, J. K. Jeon, J. Kim, R. Ryoo, K. E. Jeong and Y. K. Park, *Appl. Catal. B Environ.*, 2010, **95**, 365–373.
16. H. J. Park, K. H. Park, J. K. Jeon, J. Kim, R. Ryoo, K. E. Jeong, S. H. Park and Y. K. Park, *Fuel*, 2012, **97**, 379–384.
17. Y. Lin, C. Zhang, M. Zhang and J. Zhang, *Energy and Fuels*, 2010, **24**, 5686–5695.

18. E. Pütün, *Energy*, 2010, **35**, 2761–2766.
19. L. Zhou, H. Yang, H. Wu, M. Wang and D. Cheng, *Fuel Process. Technol.*, 2013, **106**, 385–391.
20. W. L. Fanchiang and Y. C. Lin, *Appl. Catal. A Gen.*, 2012, **419–420**, 102–110.
21. S. A. Channiwala and P. P. Parikh, *Fuel*, 2002, **81**, 1051–1063.
22. D.P. Serrano, J. Aguado, J.M. Escola, J.M. Rodríguez, Á. Peral, *Chem. Mater.*, 2006, **18**, 2462–2464.
23. J. Aguado, D. P. Serrano and J. M. Rodríguez, *Microporous Mesoporous Mater.*, 2008, **115**, 504–513.
24. C. A. Emeis, *J. Catal.*, 1993, **141**, 347–354.
25. D. P. Serrano, R. A. García, G. Vicente, M. Linares, D. Procházková and J. Čejka, *J. Catal.*, 2011, **279**, 366–380.
26. J. Feroso, H. Hernando, P. Jana, I. Moreno, J. Přech, C. Ochoa-Hernández, P. Pizarro, J. M. Coronado, J. Čejka and D. P. Serrano, *Catal. Today*, 2016, **277**, 171–181.
27. H. Lermer, M. Draeger, J. Steffen and K. K. Unger, *Zeolites*, 1985, **5**, 131–134.
28. A. Omegna, M. Vasic, J. A. Van Bokhoven, G. Pirngruber and R. Prins, *Phys Chem Chem Phys*, 2004, **6**, 447–452.
29. R. A. García-Muñoz, D. P. Serrano, G. Vicente, M. Linares, D. Vitvarova and J. Čejka, *Catal. Today*, 2015, **243**, 141–152.
30. C. Poupin, R. Maache, L. Pirault-Roy, R. Brahmi and C. T. Williams, *Appl. Catal. A Gen.*, 2014, **475**, 363–370.
31. A. Travert, A. Vimont, A. Sahibed-Dine, M. Daturi and J. C. Lavalley, *Appl. Catal. A Gen.*, 2006, **307**, 98–107.
32. L. A. M. M. Barbosa and R. A. Van Santen, *Catal. Letters*, 1999, **63**, 97–106.
33. J. M. Escola, J. Aguado, D. P. Serrano, L. Briones, J. L. Díaz de Tuesta, R. Calvo and E. Fernandez, *Energy & Fuels*, 2012, **26**, 3187–3195.
34. J. Jae, G.A. Tompsett, A.J. Foster, K.D. Hammond, S.M. Auerbach, R.F. Lobo, G.W. Huber, *J. Catal.*, 2011, **279**, 257–268.
35. S. Cheng, L. Wei, X. Zhao, J. Julson, *Catalysts*, 2016, **195**, 6–24.
36. J. Xie, W. Zhuang, W. Zhang, N. Yan, Y. Zhou, J. Wang, *Chem Cat Chem*, 2017, **9**(6), 1076–1083.
37. S. D. Stefanidis, K. G. Kalogiannis, E. F. Iliopoulou, A. A. Lappas and P. A. Pilavachi, *Bioresour. Technol.*, 2011, **102**, 8261–8267.
38. T. S. Nguyen, M. Zabeti, L. Lefferts, G. Brem and K. Seshan, *Biomass and Bioenergy*, 2013, **48**, 100–110.
39. H. Hernando, S. Jiménez-Sánchez, J. Feroso, P. Pizarro, J. M. Coronado and D. P. Serrano, *Catal. Sci. Technol.*, 2016, **6**, 2829–2843.

Article 5

Lamellar and pillared ZSM-5 zeolites modified with MgO and ZnO for catalytic fast-pyrolysis of eucalyptus woodchips

Catalysis Today, 2016, 277, 171-181

Catalysis Today 277 (2016) 171–181



Contents lists available at [ScienceDirect](#)

Catalysis Today

journal homepage: www.elsevier.com/locate/cattod



Lamellar and pillared ZSM-5 zeolites modified with MgO and ZnO for catalytic fast-pyrolysis of eucalyptus woodchips



Javier Feroso^a, Héctor Hernando^a, Prabhas Jana^a, Inés Moreno^{a,b}, Jan Přeč^c,
Cristina Ochoa-Hernández^c, Patricia Pizarro^{a,b}, Juan M. Coronado^a, Jiří Čejka^{c,**},
David P. Serrano^{a,b,*}

^a Thermochemical Processes Unit, IMDEA Energy Institute, Móstoles, Madrid 28935, Spain

^b Chemical and Environmental Engineering Group, ESCET, Rey Juan Carlos University, Móstoles, Madrid 28933, Spain

^c J. Heyrovský Institute of Physical Chemistry, Academy of Sciences of the Czech Republic, v.v.i., 182 23, Prague 8, Czech Republic

Impact JCR factor, (JCR 2017): 4.667

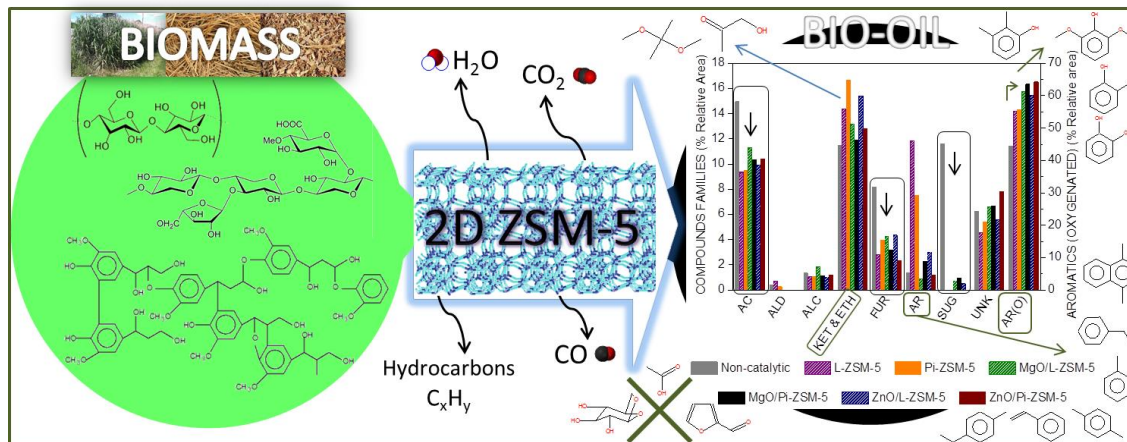
Category: Applied Chemistry. 6 of 72 (Q1)

ABSTRACT

Lamellar and pillared ZSM-5 materials modified with Mg and Zn oxides were synthesized and tested for in-situ catalytic upgrading of eucalyptus woodchips fast-pyrolysis vapors. The introduction of silica pillars into the lamellar ZSM-5 support led to a higher BET area, but also reduced the overall catalyst acidity. The incorporation of MgO and ZnO occurred with a high dispersion over the zeolitic supports, causing also a significant reduction in the value of their textural properties due to a partial blockage of the zeolite pores. Likewise, the acid features of the zeolitic supports underwent sharp changes by the addition of both MgO and ZnO with a strong decrease in the concentration of the Brønsted and Lewis acid sites present in the parent zeolite, as detected by pyridine adsorption followed FTIR spectroscopy. However, additional Lewis acid sites were created associated to the metal oxides deposited onto the zeolitic supports. Pyrolysis tests were accomplished using a lab-scale downdraft fixed-bed reactor working at atmospheric pressure and a temperature of 500 °C. The use of zeolitic catalysts increased the gas yield, mostly due to the formation of CO and CO₂, to the detriment of bio-oil production. However, the so obtained bio-oils presented higher quality in terms of H/C and O/C ratios, and larger heating values. The incorporation of MgO and ZnO allowed tailoring the zeolite activity to avoid an excessive cracking of the bio-oil, which in turn resulted in a higher yield of the organic compounds present in the bio-oil, and decreasing the formation of undesired polyaromatic hydrocarbons and coke.

Keywords: Lignocellulosic biomass. Catalytic fast-pyrolysis. Bio-oil. Two dimensional zeolite. ZSM-5.

GRAPHICAL ABSTRACT



1. Introduction

The viability, sustainability, and overall commercial readiness of biofuels are still a matter of profound debate. While the potential benefits of replacing fossil fuels by liquids from renewable sources are obvious, substantial barriers for their implementation need still to be overcome.¹ In contrast to other renewable energies (e.g., wind, solar), supplying heat and power, biomass represents the only renewable resource of liquid, solid and gaseous fuels.^{2,3}

Lignocellulosic biomass is a mixture of cellulose, hemicellulose, lignin and minor amounts of other organic and inorganic species. Lignocellulose can be decomposed by means of pyrolysis working at different heating rates and temperatures, and following a variety of pathways.⁴ Fast-pyrolysis, in which biomass is rapidly heated to relatively moderate temperatures (450–550 °C), followed by a fast quenching of vapors and aerosols (<2 s of residence time), gives rise to three main product categories: solid char, non-condensable gases (H₂, CO, CO₂ and light hydrocarbons), and a dark brown liquid phase (bio-oil). Non-catalytic fast-pyrolysis leads to a bio-oil consisting of a very complex mixture of oxygenated species derived from the fragmentation of the main components of the biomass. Unfortunately, high oxygen content (35–40 wt%) in biomass pyrolysis oil causes many undesirable properties regarding its potential application as fuel. Bio-oil contains between 15 and 30 wt% of water, it possesses a reduced calorific value and a high viscosity, is immiscible with gasoline and has acid pH (2–3).^{5,6}

Catalytic upgrading of bio-oil is an interesting route for converting it into advanced biofuels, having properties very similar to conventional transportation fuels, although it requires an almost total deoxygenation of the bio-oil. This can be accomplished either by decoupling pyrolysis and bio-oil deoxygenation steps, or by integrated catalytic pyrolysis.⁷⁻¹⁰ When pyrolysis vapors enter the pores of the catalyst they may undergo a complex series of reactions such as cracking, aromatisation, ketonisation, aldol condensation, isomerisation, oligomerisation and dehydrogenation, among others. Deoxygenation may occur removing water (dehydration), CO (decarbonylation) and CO₂ (decarboxylation). In addition, some carbon and hydrogen are lost by coke formation over the catalyst and the production of gaseous hydrocarbons as a consequence of cracking of the bio-oil vapors.^{5,7,9,11,12}

A variety of heterogeneous catalysts has been studied in the literature for their application in lignocellulosic biomass catalytic fast-pyrolysis or bio-oil upgrading.^{5,13-15} In this respect, acidic zeolite catalysts, and in particular ZSM-5, have been commonly used for catalytic pyrolysis of biomass due to its high activity, as it has been recently reviewed by Liu et al.⁵ However, these materials are limited by the size of their micropores that can hinder the accessibility to the active sites and impede the diffusion of large molecules into the pore system. To tackle this problem, recent advances have been achieved with the development of novel materials such as two-dimensional (2D) layered zeolites,^{16,17} which contain a high share of non-steric limited external surface area and a combination of micro- and mesopores. Recent achievements have shown that 2D zeolites can be synthesized not only via traditional bottom-up approach,¹⁸ but also via top-down treatment of appropriate germanosilicates.¹⁹⁻²⁰ Lee et al.²¹ have studied the catalytic pyrolysis of biomass model constituents (cellulose, hemicelluloses and lignin) using unilamellar mesoporous ZSM-5, nanosheets (UMNs) and Al-SBA-15 catalysts. The results obtained denote the improvement of the bio-oil properties, which show lower oxygen content when UMN was used as catalyst due to its superior acid properties. Nevertheless, zeolites

suffer of extensive coking and deactivation when used in lignocellulosic biomass catalytic pyrolysis because of its high acid strength.

On the other hand, base oxides have been employed as catalysts for ketonisation and aldol condensation of carboxylic acids and other compounds possessing carbonyl groups,⁵ which could be applied in the deoxygenation of bio-oil by releasing CO₂ and the formation of C-C bonds. In this way, alkaline earth metal oxides such as MgO and CaO, where the oxide ions behave as bases and their metal cations could function as Lewis acids,²² have been recently used as biomass pyrolysis catalysts.²³ Likewise, transition metal oxides, such as ZnO, ZrO₂ and TiO₂, have been also investigated for the lignocellulose catalytic fast-pyrolysis in order to promote ketonisation and aldol condensation reactions as a method for bio-oil upgrading.^{5,24,25}

The main goal of the present work is to establish the performance of novel catalysts for lignocellulose catalytic pyrolysis based on lamellar and pillared ZSM-5 (2D) zeolites, featured by having a high accessibility due to the presence of a large share of external and mesopore surface area. Moreover, these zeolites have been here used as supports for the incorporation of MgO and ZnO in order to modify and tune their acidic properties and improve their catalytic behavior in bio-oil upgrading processes.

2. Experimental

2.1. Raw biomass

Eucalyptus woodchips were selected as lignocellulosic biomass to carry out the catalytic fast-pyrolysis experiments. This biomass belongs to the hardwoods type and contains 35.5, 12.5 and 39.2 wt% of cellulose, hemicellulose and lignin, respectively. The sample was ground with a cutter mill and sieved to the desired particle size (0.5–1 mm). The proximate analysis of the sample was performed according to European standards. It included 9.7 wt% of moisture (UNE-EN 14774-1:2010), whereas the ash (UNE-EN 14775:2010), volatile matter (UNE-EN 15148:2010) and fixed carbon (determined by difference) contents, in dry basis, were 1.83, 74.70 and 23.47 wt%, respectively. In addition, the ultimate analysis of the eucalyptus sample was carried out in a micro-elemental analyser (Thermo Scientific) in order to determine the content of C, H, N, S and O (the latter by difference); which, in dry and ash free basis, were 51.23, 5.93, 0.13, 0.00 and 42.71 wt%, respectively. A literature correlation²⁶ was employed to calculate the high heating value (HHV) of the dried eucalyptus sample, resulting a value of 20.04 MJ kg⁻¹.

2.2. Catalysts preparation

2.2.1. Synthesis of lamellar ZSM-5 (L-ZSM-5)

The synthesis of lamellar ZSM-5 is based on the procedure described by Choi et al.²⁷ The structure directing agent (SDA) was prepared following the protocol detailed by Na et al.²⁸, but replacing 1-bromooctadecane by 1-bromodocosane (98%, TCI). The preparation of the gel, as well as the zeolite synthesis, were carried out in a 1000 ml stainless steel Parr 4848 autoclave with mechanical stirring. Thereby, 9.88 g of NaOH (99.5%, Penta, Czech Republic) were dissolved in 223 g of distilled water, followed by the addition of 5.91 g of Al₂(SO₄)₃·16 H₂O (95%, Fluka). After dissolution, 6.47 g of sulphuric acid (96%, Penta, Czech Republic) and 86 g of tetraethyl orthosilicate (TEOS, 98%, Aldrich) were introduced into the mixture, being then

stirred for 70 min. Thereafter, 30 g of the structure directing agent (SDA), a quarternary ammonium-type surfactant ($C_{22}H_{45}-N^+(CH_3)_2-C_6H_{12}-N^+(CH_3)_2-C_6H_{13}$) in bromide form ($C_{22-6}Br_2$) were added and the mixture so obtained was homogenized for another 30 min. Then, 35 g of water were added before closing the autoclave to compensate the ethanol evaporation, that is formed from TEOS hydrolysis. The final molar composition of the gel was $60 NaOH \cdot 2.27 Al_2(SO_4)_3 \cdot 16 H_2SO_4 \cdot 100 SiO_2 \cdot 10 SDA \cdot 3000 H_2O$.

The zeolite crystallization proceeded under hydrothermal conditions at 155 °C, stirring (350 rpm) and autogeneous pressure for 144 h. The solid product was collected by filtration, washed out with distilled water and dried at 65 °C overnight. Then, it was calcined in air at 540 °C for 8 h. The calcined sample was ion-exchanged into the NH_4^+ form by treating four-times with 1.0 M NH_4NO_3 solution for 4 h at room temperature (100 ml of solution/1 g of zeolite) and calcined at 450 °C for 90 min to convert it into the protonic form. The final product was denoted as L-ZSM-5.

2.2.2. *Synthesis of pillared ZSM-5 (PI-ZSM-5)*

The as-synthesized dry lamellar ZSM-5, obtained according to the procedure described in the earlier section, was pillared using TEOS as pillaring agent.²⁹ For that purpose, 190 ml of TEOS were mixed with 18.8 g of L-ZSM-5 and stirred in a 250 ml flask at 85 °C for 20 h. The solid material was then separated by centrifugation and dried at ambient temperature for 36 h. The as-synthesized pillared material (31.8 g) was hydrolysed in 2000 ml of water with the addition of 50 ml of ethanol at ambient temperature for 24 h. Finally, the material was filtered, dried at 65 °C overnight and calcined in air at 540 °C for 6 h with a heating ramp of 2 °C min^{-1} . The calcined pillared ZSM-5 was ion-exchanged into NH_4^+ form by treating 4-times with 1.0 M NH_4NO_3 solution for 4 h at room temperature (100 ml of solution/1 g of zeolite) and calcined again at 450 °C for 90 min using a ramp of 2 °C min^{-1} to obtain the zeolite in H^+ form. The final product was denoted as PI-ZSM-5.

2.2.3. *Mg and Zn incorporation*

Ten weight percent of MgO (or ZnO) were incorporated over the layered and pillared zeolites by wet impregnation method using ethanol as solvent. Initially, 50% of the total required metal pre-cursor $Mg(NO_3)_2 \cdot 6H_2O$ or $Zn(NO_3)_2 \cdot 6H_2O$, both from Aldrich, was dissolved in 20 ml of ethanol and then, 2 g of support were added to this solution. The mixture was then left under stirring for 6 h at 40 °C. Subsequently, the solvent was removed in a rotary evaporator and the solid was dried overnight at 100 °C in an oven, being finally oven treated at 200 °C for 10 h. In a similar way, the second half of the metal precursor was incorporated to the material obtained and the resulting solid was finally calcined at 450 °C for 6 h.

2.3. *Catalysts characterization*

Metal contents of the samples were determined by ICP-OES on a Perkin Elmer Optima 7300 DV instrument. X-ray diffraction (XRD) analyses were collected on a Philips X'Pert PRO diffractometer operated at 45 kV and 40 mA with Cu-K α radiation ($\lambda = 1.542 \text{ \AA}$). Argon physisorption isotherms at $-186^\circ C$ were measured on a Quantachrome AUTOSORB iQ system. The surface area was determined using the Brunauer–Emmet–Teller (BET) equation and the pore size distributions were calculated by applying the NLDFT model to the adsorption branch

of the isotherms. TEM images of the catalysts were obtained with a Philips TECNAI 20 instrument operating at 200 kV.

The acidic properties were determined by pyridine adsorption followed by FTIR spectroscopy. The samples were prepared as self-supporting wafers (ca. 8–12 mg/cm²) and activated overnight at 450 °C under vacuum prior to the adsorption of the probe molecule (pyridine) at 150 °C and a pressure of 3 Torr. All spectra were recorded with a resolution of 4 cm⁻¹ in the 4000–400 cm⁻¹ range using a Nicolet spectrometer equipped with a MCT/B detector cooled with liquid nitrogen and normalized to a 10 mg/cm² wafer. The strength of the acid sites was studied by recording the FTIR spectra after treating the sample at different desorption temperatures (150, 250, 350 and 450 °C) for 20 min. The quantification of the acid sites was performed using the following bands (ν_{19b} vibration mode of pyridine) and absorption coefficients: pyridine PyH⁺ band at 1545 cm⁻¹ ($\epsilon = 1.67$ cm/ μ mol) and pyridine PyL bands at 1461 + 1454 cm⁻¹ ($\epsilon = 2.2$ cm/ μ mol).^{30,31}

2.4. Biomass fast-pyrolysis tests

The schematic diagram of the lab-scale experimental setup used for the eucalyptus woodchips fast-pyrolysis tests is shown in Fig. 1. It consists of a downdraft fixed-bed stainless steel reactor (16 mm i.d. and 400 mm length) heated by two electrical furnaces. The reaction temperature is measured by two type K thermocouples, placed on the pyrolysis zone and inserted into the catalyst bed, respectively. The reactor is loaded with 1 g of catalyst, to operate with a biomass-to-catalyst ratio of 5 g g⁻¹. Previously to the pyrolysis tests, all the catalyst samples are pelletized, crushed and sieved to a particle size in the 180–250 μ m range. The biomass sample is placed in the biomass tank and kept at room temperature. A quartz wool sheet and a metallic plate are placed over the catalyst particles to avoid the physical contact and possible mixing between the char particles and the catalyst bed. The pyrolysis tests have been carried out at atmospheric pressure and 500 °C. Prior to each pyrolysis experiment and during the heating up of the reactor, the biomass tank and the reaction system are purged with a N₂ flow delivered by mass flow controllers, until the O₂ concentration levels of the exiting gas drop to <0.1 vol.%, ensuring that pyrolysis takes place in an inert atmosphere. Once the reactor temperature reaches the desired set point, the feeding valve is open and the biomass falls into the reactor, being subjected to pyrolysis to form a solid carbonaceous residue (char) and vapors. The volatiles so generated are swept by a N₂ flow of 100 Nml min⁻¹ and passed through the catalyst bed to leave rapidly the reaction zone, being condensed by means of an ice-water trap (0–4 °C). Permanent gases and light hydrocarbons (CH₄, C₂H₄, C₂H₆, C₃H₆ and C₃H₈) are finally collected in a sampling bag for their further analysis in a dual channel Agilent® CP-4900 Micro Gas Chromatograph (Micro-GC), which is equipped with molecular sieve (Molsieve 5 Å) and HayeSep A columns and a thermal conductivity detector (TCD), using Helium as carrier gas. The TCD is periodically calibrated with a standard gas mixture containing N₂ (internal standard), O₂, H₂, CO, CO₂, CH₄, C₂H₄, C₂H₆, C₃H₆ and C₃H₈. Thus, the gas mass yield and its elemental composition (C, H and O) can be calculated.

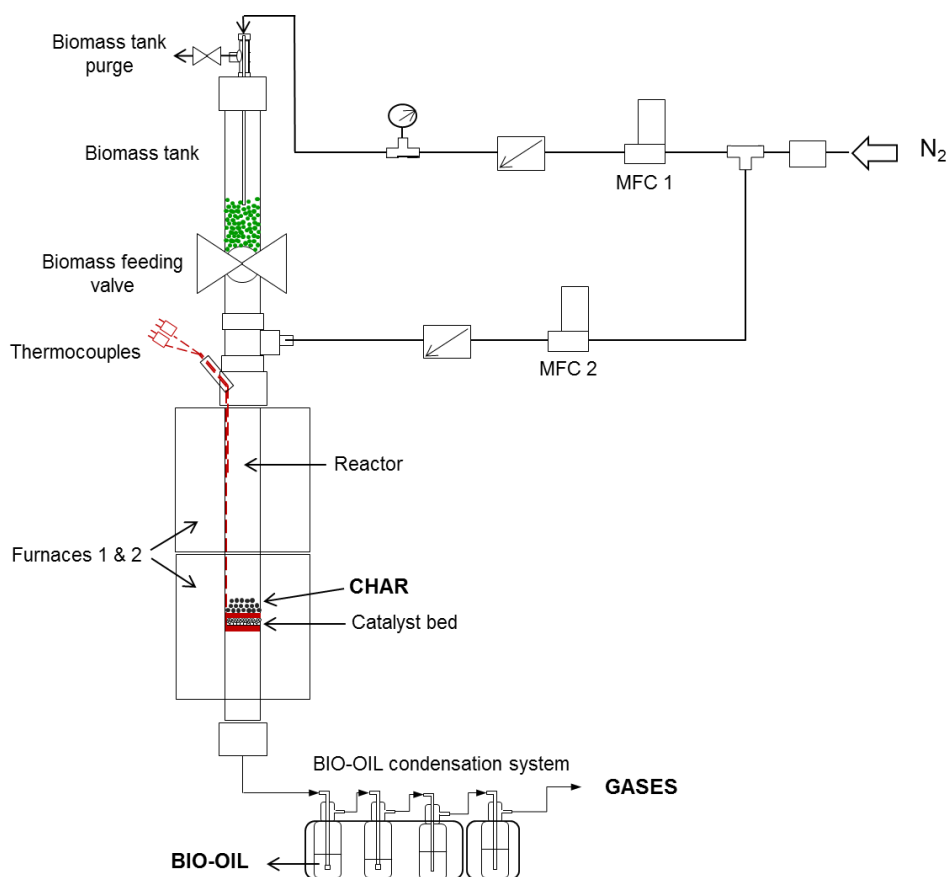


Fig. 1. Schematic flow diagram of the experimental setup used for the eucalyptus woodchips fast-pyrolysis experiments.

After the experiments, the char and the used catalyst are collected for their further characterization. Char is characterized in the same way as the raw biomass, proximate and ultimate analyses being performed. In the case of the coke fraction, its amount is determined as the weight loss experienced by the used catalyst exposed in a TGA to a heating program of $10\text{ }^{\circ}\text{C min}^{-1}$ up to $550\text{ }^{\circ}\text{C}$ in air atmosphere.

The bio-oil is characterized by several techniques. For the catalytic fast pyrolysis tests, bio-oils are formed by two phases, being separated by centrifugation for further analysis. The water content of bio-oil is determined using a Karl-Fischer titration instrument (ASTM E203-08), whilst its elemental composition of C, H, N, S and O (by difference) is calculated with a Thermo-Scientific micro analyser. Thus, the bio-oil fraction is considered in a water free basis. Bio-oils were analysed by a Gas Chromatograph–Mass Spectrometer, GC–MS, Bruker® SCION 436-GC, (Electron Energy 70 eV, Emission 300 V; He flow rate: 1 ml min^{-1} ; Column WCOT fused silica $30\text{ m} \times 0.25\text{ mm ID} \times 0.25\text{ }\mu\text{m}$). NIST EI-MS spectral library (v2.0) has been used for the compounds identification (with a minimum match score of 700). Bio-oil compounds are further grouped in families according to their main functional groups.

Finally, from the weight of the bio-oil and char fractions, and those calculated for coke and gas fractions, the total mass balance can be closed to the amount of biomass fed. The elemental (C, H and O) mass balances were also assessed from the yield of the different products and their ultimate analyses.

3. Results and discussion

3.1. Catalysts properties

Six different catalysts have been prepared and investigated in the present work for catalytic pyrolysis of eucalyptus woodchips. They consist of two zeolitic supports (layered and pillared ZSM-5) and the corresponding samples after addition of 10 wt% of MgO and ZnO. These samples have been characterized by different techniques in order to determine the effect of the metal oxides incorporation on their physicochemical properties. The amounts of aluminum, as well as the final metal oxide loadings, were determined by ICP-OES (Table 1). PI-ZSM-5 presents a higher Si/Al ratio than L-ZSM-5 due to the introduction of silica pillars. The measured metal oxide loadings are quite close to the theoretical one added onto the zeolitic supports. In the case of the two samples containing Zn, the measured amount of the metal, expressed in the form of metal oxides, is somewhat higher (around 11 wt%) than the theoretical value. This result suggests that not all the Zn species are present solely as ZnO in the final catalysts.

Low-angle X-ray diffraction pattern (Fig. S1) of calcined L-ZSM-5 exhibits a reflection at $2\theta \approx 1.34^\circ$ ($d = 6.6$ nm) ascribed to the inter-lamellar structural correlation in the multilamellar ZSM-5 material.³² After pillaring with TEOS the as-synthesized L-ZSM-5, it is appreciated a similar reflection at $2\theta \approx 1.39^\circ$ ($d = 6.4$ nm) for the calcined PI-ZSM-5, suggesting that the structural order of the lamellas have been retained by the introduction of silica pillars. These facts were corroborated by TEM analysis (Fig. S2), observing clear differences between both parent materials due to the presence of lamellas and pillars, respectively. High-angle XRD patterns are shown in Fig. 2. PI-ZSM-5 and L-ZSM-5 present diffraction lines typical of crystalline zeolites with MFI topology. It is also evident that after the incorporation of MgO and ZnO to the supports, the catalysts still exhibit a very high crystallinity. It is important to highlight that no diffractions peaks corresponding to the pure metal oxides have been detected. This fact may be assigned to different factors: existence of MgO and ZnO particles with very small size, homogeneous dispersion of the metal oxides over the zeolitic support surface, or even, the partial ion exchange of protons of the support by Mg^{2+} and Zn^{2+} cations.

Table 1. Physicochemical properties of the catalysts.

Catalysts	Si/Al ^a	Metal oxide loading (wt%) ^a	S _{BET} ^b (m ² /g)	S _{MESO+EXT} ^c (m ² /g)	S _{MICRO} ^d (m ² /g)	V _{MICRO} ^e (cm ³ /g)	V _{TOTAL} ^f (cm ³ /g)
PI-ZSM-5	64	-	623	439	184	0.110	0.640
MgO/PI-ZSM-5	64	9.25	328	228	100	0.060	0.428
ZnO/PI-ZSM-5	64	11.1	300	247	53	0.031	0.345
L-ZSM-5	22	-	493	316	177	0.110	0.750
MgO/L-ZSM-5	22	9.78	255	147	108	0.064	0.462
ZnO/L-ZSM-5	22	11.2	282	162	119	0.071	0.501

^aICP-OES measurements; ^bBET surface area; ^cMesopore + external surface area; ^dMicropore surface area; ^eMicropore volume; ^fTotal pore volume at $P/P_0 \approx 0.98$. All textural properties are expressed per gram of zeolitic support in the sample.

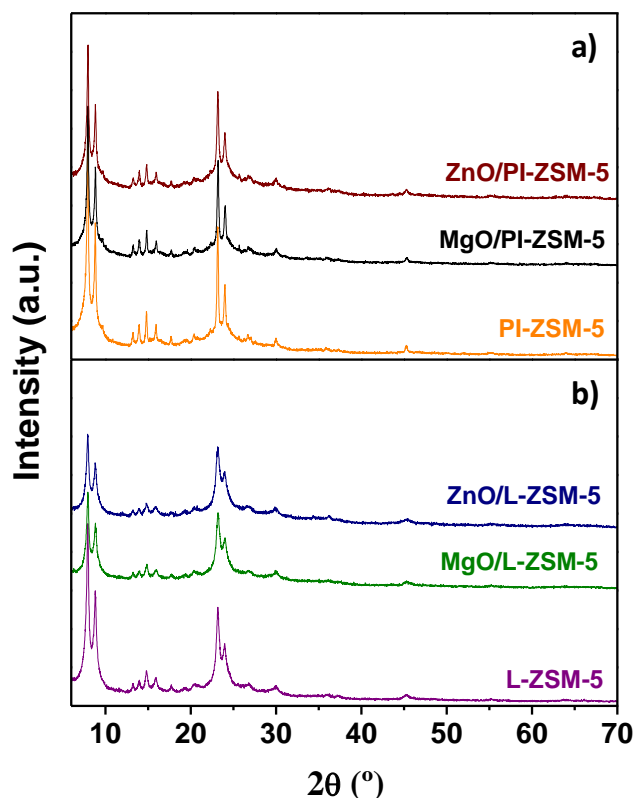


Fig. 2. XRD patterns of calcined (a) pillared and (b) lamellar ZSM-5 based materials.

TEM measurements were also performed in order to get more information about the distribution of the metal oxides particles (Fig. S3). No particles or spots are observed in the micrographs that could correspond with MgO and ZnO phases. These results reinforce the idea of the metal oxides being present in the form of very-small entities with a high dispersion over the supports.

The textural properties of the catalysts were determined from argon physisorption isotherms at $-186\text{ }^{\circ}\text{C}$ (Fig. 3a and c). The pore size distributions were calculated in the whole range of micro- and mesopores by applying the NLDFT model (Fig. 3b and d). It is well known that conventional ZSM-5 zeolite presents a type I isotherm according to the IUPAC classification. However, the presence of multilamellar structures (in L-ZSM-5) and pillars (in PI-ZSM-5) strongly modifies the typical zeolitic profile. The isotherms of the different catalysts show three main regions of adsorption (Fig. 3): (i) low pressures adsorption ($P/P_0 < 0.1$), which corresponds to the presence of micropores, (ii) intermediate relative pressure adsorption, associated with adsorption on the external surface and the filling of mesopores and (iii) adsorption at high pressures ($P/P_0 > 0.9$), which evidences the existence of interparticle voids.

Interestingly, the contribution of the mesopore + external surface area reaches very high values, 439 and 316 m^2/g , for PI-ZSM-5 and L-ZSM-5 samples, respectively (Table 1), denoting the relevance of the non-microporous textural properties in these materials. The profiles and values here obtained for the zeolitic supports are in agreement with those earlier reported for 2D ZSM-5 zeolites.³² The high availability of mesopore + external surface areas in both L-ZSM-5 and PI-ZSM-5 is an important factor as it could enable good dispersions of the metallic oxide phases. Regarding the pore size distribution, both zeolitic supports exhibit a sharp peak centered at 5.5 Å characteristic of the ZSM-5 zeolite micro-pores. On the other hand, pillared ZSM-5

possesses a quite well defined adsorption jump at a relative pressure of 0.4–0.5, denoting the presence of a mesoporosity with a narrow pore size distribution centered at 40 Å (Fig. 3b). In contrast, the increase in the Ar adsorption at intermediate relative pressures is less pronounced for L-ZSM-5, evidencing the presence of an irregular array of the zeolite layers with a significant contribution of interlamellar voids (Fig. 3d).²⁷

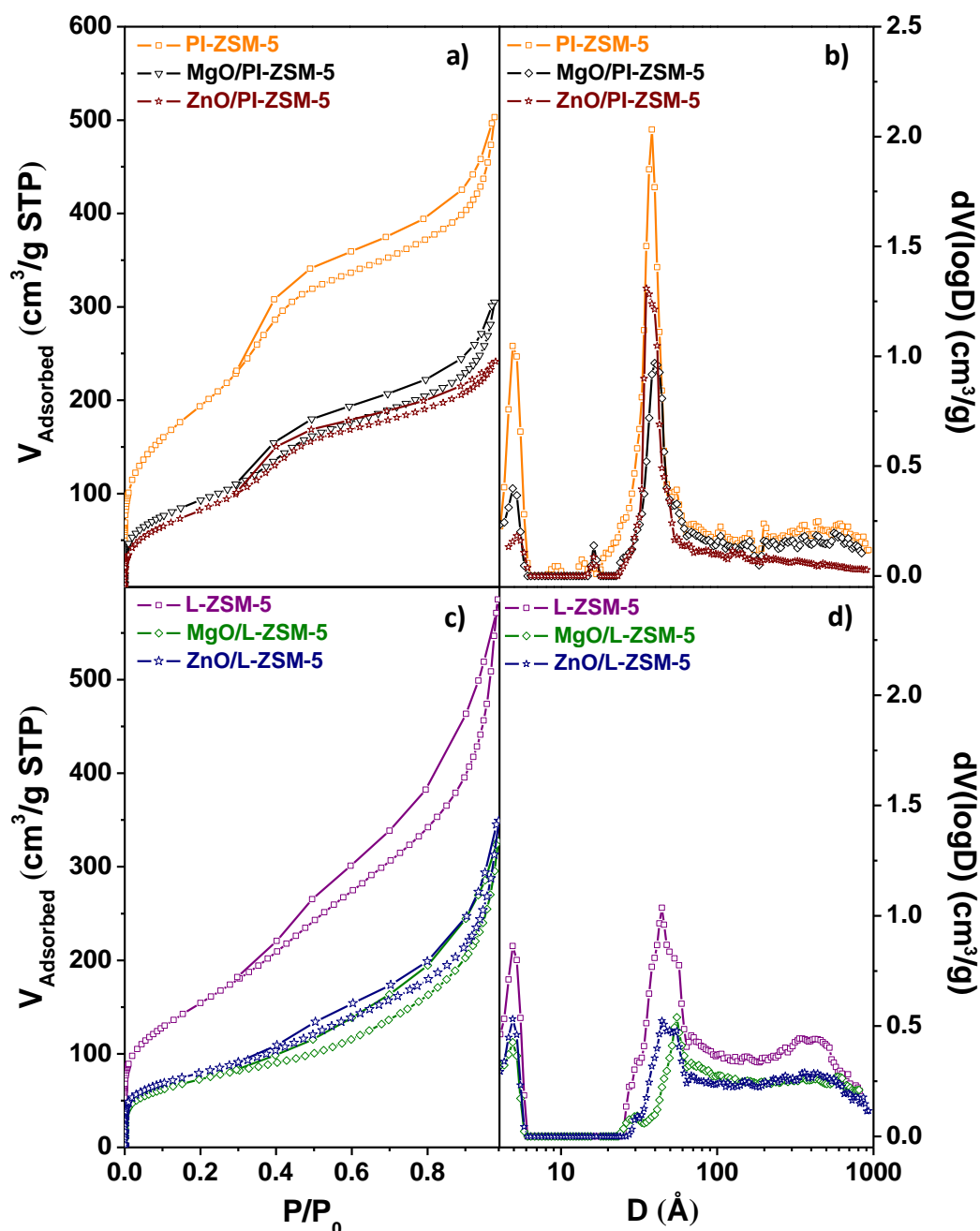


Fig. 3. Ar adsorption-desorption isotherms at -186 °C (a, c) and pore size distribution (b, d) of the catalysts determined applying the NLDFT model.

The incorporation of MgO and ZnO causes in all cases a strong decrease in the Ar adsorption in the whole range of relative pressures, suggesting that it affects strongly the support porosity. It is noticeable that the changes induced in the Ar isotherms by the metal addition are very close for both Mg and Zn, suggesting that they present quite similar dispersion and location over the

zeolitic supports. The contribution of both micro- and mesopore peaks in the pore size distribution curves undergo a significant decrease (Fig. 3b and d). This result confirms that the deposition/incorporation of the metal species occurs and affects practically to all the support surface areas (micropore, mesopore and external surface areas), which can be also considered as another indication of their high dispersion onto the zeolitic support.

The values of the BET, mesopore + external and micropore surface areas, after the Mg and Zn addition, have been expressed in relation to those corresponding to the zeolitic supports to gain further insights about the location of the metal oxides. In general, the textural properties (surface area and pore values) are clearly lower for the samples incorporating the metal oxides compared to the parent supports (Table 1). Thus, the PI-ZSM-5 sample has a BET surface area of 623 m²/g that decreases to values of 328 and 300 m²/g (referred to the weight of zeolitic support present in the catalyst) after the addition of MgO and ZnO, respectively. These figures correspond with about 50% of those determined in the parent supports. A strong reduction is also observed in this parameter for the lamellar based catalyst. The same occurs when analysing the decrease observed in the mesopore + external surface area, showing values that represents about 50% of those determined for the parent L-ZSM-5 and PI-ZSM-5 samples. Likewise, the micropore surface area shows values of 177 and 184 m²/g for the parent zeolites (L-ZSM-5 and PI-ZSM-5, respectively), which decreases to reach the range 53–119 m²/g for the metal oxide-containing materials. The latter represents about 55–66% of the micropore surface area in the raw supports, although a higher micropore surface area reduction is observed for the ZnO/PI-ZSM-5, which could be related to an enhanced accessibility of the Zn species into micropores of the pillared zeolitic support.

The strong variations observed in the Ar isotherms, and in the corresponding textural properties, may be assigned to a combination of different phenomena: location of metal oxide species within the zeolite micropores, deposition of metal oxides particles on the mesopores blocking the entrance to the zeolite micropores and ion exchange of the protons in Si-OH-Al species by Mg²⁺ and Zn²⁺. Probably all of them take place simultaneously for the systems here studied.

The incorporation of metal oxides induces also substantial changes in the acidic properties of the parent zeolites. In order to evaluate the type, concentration and strength of the acid sites, pyridine adsorption followed by FTIR was performed. As an alternative probe molecule, CO can be also employed. However, it has been reported that for layered MCM-22 and MCM-56 zeolites, the O-H frequency shift probed by an adsorbed weak base like CO is not a general indicator for ranking zeolite Brønsted acidity.^{33,34}

In the region corresponding to the stretching vibrations of hydroxyl groups (Fig. S4), the band located at 3745 cm⁻¹ is assigned to terminal silanols (Si-OH), whereas the band at 3613 cm⁻¹ is ascribed to acidic bridging hydroxyls groups (Si-OH-Al).³¹ These bands are clearly visible in the parent ZSM-5 zeolite samples (L-ZSM-5 and PI-ZSM-5). The vibrational band observed at 3613 cm⁻¹ is more marked in the case of L-ZSM-5 due to its higher content of aluminum. This absorption band disappears in all cases with the incorporation of Mg and Zn evidencing the replacement/interaction between the zeolite protons and the metal species.³⁵

After adsorption of pyridine at 150 °C (Fig. 4) the bands associated to pyridinium ions (PyH⁺, pyridine chemisorbed on Brønsted acid sites) at 1545 cm⁻¹ (ν_{19b}) and 1637 cm⁻¹ (ν_{8a}) decrease in the samples containing Mg and Zn oxides. Coordinated pyridine species (PyL,

pyridine interacting with Lewis acid sites) give rise to bands at $1464\text{--}1445\text{ cm}^{-1}$ (ν_{19b}) and $1600\text{--}1628\text{ cm}^{-1}$ (ν_{8a}). It must be noted that the higher are these wavenumbers, the stronger is the Lewis acidity.³⁶ The parent zeolites present bands at around 1456 cm^{-1} and 1623 cm^{-1} associated to pyridine strongly adsorbed on coordinatively unsaturated Al^{3+} ions. The latter vibration is mainly ascribed to pyridine interacting with Al^{3+} in tetrahedral environment.³⁷ On the other hand, the vibration band at 1444 cm^{-1} is due to the interaction between pyridine and silanols.

As it can be observed in Fig. 4, the spectra of the samples containing Mg and Zn species change noticeably compared to the parent supports, with a shifting of the peak at 1456 cm^{-1} toward lower frequencies (1448 cm^{-1} and 1454 cm^{-1} , respectively) due to their different polarizing power. The presence of these Lewis acid sites, with medium-strong strength is clearly related to the metal incorporation, being also evidenced by the appearance of new bands at 1610 cm^{-1} and 1613 cm^{-1} .³⁸ Interestingly, it seems that the incorporation of Mg and Zn species not only affects to the Brønsted acid sites but also to tri-coordinated aluminum in tetrahedral environment since the band at 1623 cm^{-1} decreases as well. This fact seems to be more pronounced in the case of Mg based materials.

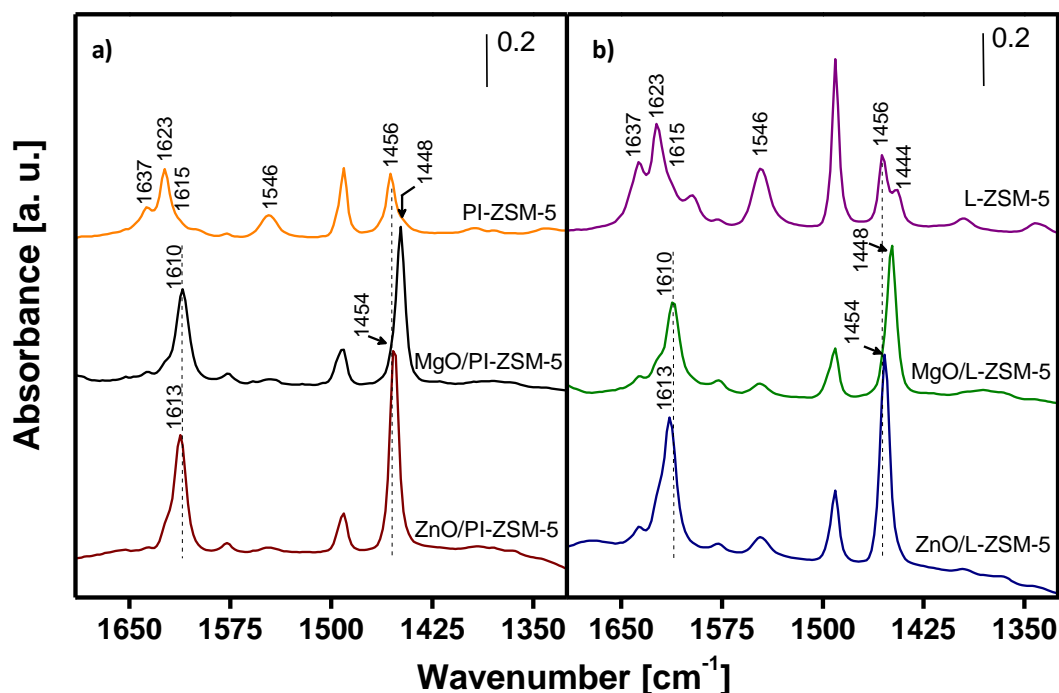


Fig. 4. FTIR spectra in the region of pyridine vibrations for (a) pillared ZSM-5 and (b) lamellar ZSM-5 based materials.

Fig. 5 depicts the concentration of Brønsted and Lewis acids sites at different temperatures for all studied samples, referred to the weight of the zeolitic support. In general, it is observed that the amount of acid centers decreases with the temperature proving the existence of sites with different acid strength. Comparing both supports (PI-ZSM-5 and L-ZSM-5), the introduction of amorphous silica pillars decreases the concentration of Brønsted acid sites (Fig. 5a) in comparison with the lamellar samples (Fig. 5c), although quite smaller differences are found for Lewis acid sites. This is in agreement with the results provided by the ICP-OES measurements showing that the pillared zeolitic support presents a higher Si/Al ratio and suggests that the silica pillars contribute also to the Lewis acidity.

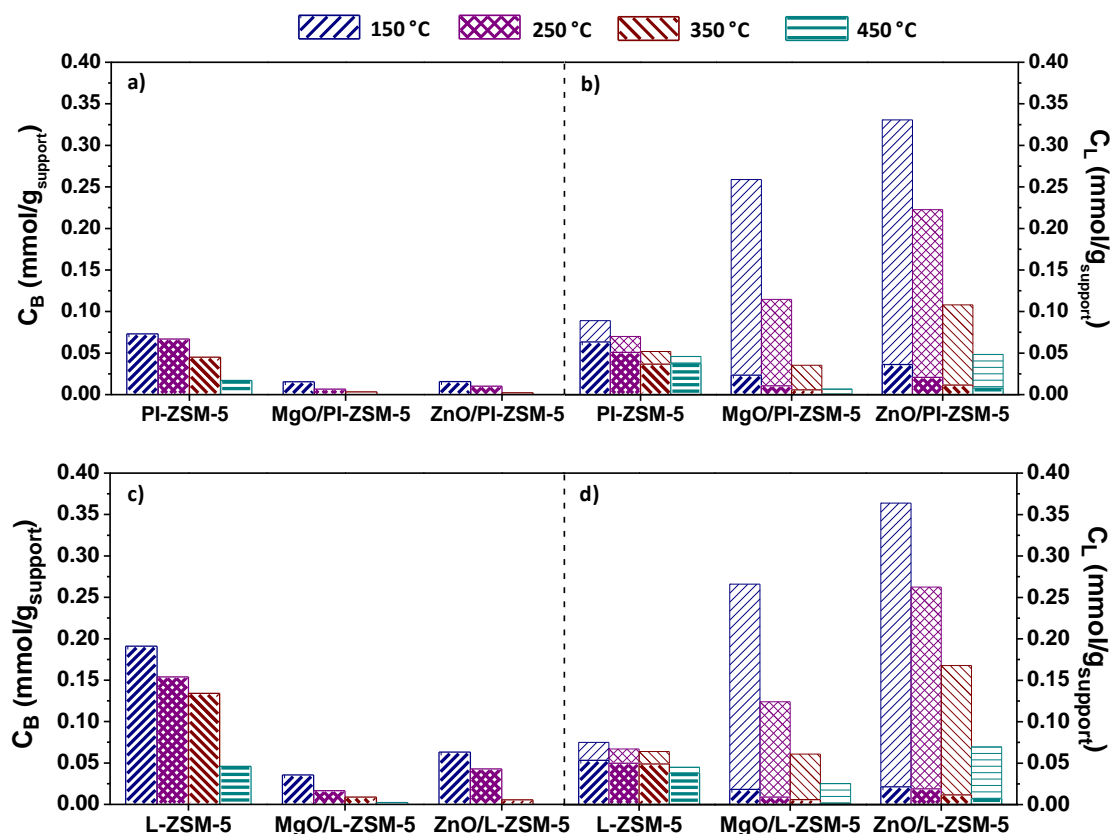


Fig. 5. Concentration of Brønsted, C_B (a, c) and Lewis, C_L (b, d) acid sites in the pillared (PI-) and lamellar (L-) ZSM-5 samples after desorption of pyridine at different temperatures followed by FT-IR. Thick patterns correspond to 1623 cm^{-1} band and thin patterns are ascribed to bands at $1616\text{-}1605\text{ cm}^{-1}$ range.

The incorporation of metal oxides sharply decreases the concentration of Brønsted acid sites for both lamellar and pillared zeolitic materials. Thus, in the case of PI-ZSM-5, the concentration of those sites, detected after pyridine desorption at 150 °C , is just about 21% of that present in the parent support for both Mg and Zn-containing materials. Likewise, for the L-ZSM-5 sample, after the addition of Mg and Zn, only 18% and 33%, of the Brønsted acid sites contained in the raw support are now detected, respectively. It is quite evident that the reductions of the Brønsted acid sites concentration are quite superior than those above commented for the different surface areas of the supports (around 50% in most cases). Therefore, the acidity variations cannot be just assigned to the covering or blockage of the zeolite surface by the incorporated Mg and Zn phases, suggesting that a preferential interaction is established between the added metals and the zeolite Brønsted acid sites, probably by ion exchange with the protons of the latter. In this way, it must be taken into account that the Mg/Al and Zn/Al atomic ratios employed during the metal incorporation by impregnation ranges from 2 up to 10 depending on the metal and the support, being in all cases high enough for not discarding the contribution of ion-exchange phenomena.

Regarding the Lewis acid sites, the incorporation of Mg and Zn leads to an important increase in the overall concentration of this type of acid sites in comparison with the corresponding parent zeolitic materials (Fig. 5b and d). This fact, together with the shift observed in the position of the IR band originated by the adsorption of pyridine on Lewis acid sites, suggests that the incorporation of Mg and Zn oxides causes the generation of additional Lewis acid sites, probably related to the metal oxide particles. In order to distinguish between Lewis

acid sites of the zeolitic support and those originated from the metal oxides, a deconvolution of the IR spectra in the region at 1650-1580 cm^{-1} has been performed. Thereby, the following bands have been considered for the supports: 1637 cm^{-1} (associated to pyridine bonded to Brønsted acid sites), 1623 cm^{-1} and $\sim 1615 \text{ cm}^{-1}$ (both ascribed to pyridine adsorbed on coordinatively unsaturated Al^{3+} ions but probably of different strength and/or environments³⁷-Lewis acidity). Taking into account the areas for the latter two bands, and assuming that the proportion between them is the same in the region of 1456 cm^{-1} (used for quantification), it is possible to differentiate their contributions to the total amount of acid sites. In the case of the samples containing metal oxides, in addition to the bands at 1637 cm^{-1} and 1623 cm^{-1} (coming from the support), new bands at 1610 cm^{-1} and 1613 cm^{-1} were identified in presence of Mg and Zn species, respectively. Thus, the contribution of the signals at 1623 cm^{-1} and in the range 1616–1605 cm^{-1} has been calculated considering the different band areas of the parent zeolites and the metal oxide-containing materials as well as their total concentration of Lewis acid sites. The results so obtained are shown in Fig. 5b and d, distinguishing two zones in the bars. The one marked with thick patterns in this figure indicates the contribution of the band at 1623 cm^{-1} to the total Lewis acidity and the zone having a thin pattern is associated to the bands in the region 1616–1605 cm^{-1} . While for the parent zeolitic supports, the 1623 cm^{-1} signal is predominant, a very important contribution of the latter bands is observed when incorporating Mg and Zn species. This is consistent with the presence of Lewis acid sites directly related to the metal oxide phases. The concentration of Lewis acid sites present in the parent zeolitic supports is also affected by the incorporation of Mg and Zn, although in a lower extension than that earlier commented for the Brønsted acid sites. This fact denotes that this type of acidity is less prone to interact with the Mg and Zn species than in the case of the Brønsted acid sites.

In the case of the Mg-containing zeolite samples, when increasing the pyridine desorption temperature up to 450 °C, they present a lower overall concentration of Lewis acid sites than the parent PI-ZSM-5 and L-ZSM-5 materials. This result evidences that the new Lewis acid sites are weaker compared to those of the zeolitic supports, as it was expected taking into account the observed absorption band shift toward lower wavenumbers (1448 cm^{-1}) after the Mg incorporation. For the ZnO/PI-ZSM-5 and ZnO/L-ZSM-5 samples, although the Lewis acid sites concentration is also strongly reduced when increasing the pyridine desorption temperature, they are still present at 450 °C in similar or even slightly higher concentration of Lewis acid sites than in the corresponding supports. This result agrees well with the Lewis sites band shift observed for the Zn-containing materials (1454 cm^{-1}), which is quite less pronounced than in the case of the samples incorporating Mg oxide.

It can be concluded from these measurements, that the incorporation of Mg and Zn phases causes strong changes in the acidic features of the layered and pillared ZSM-5 zeolites, suppressing in a great extension the Brønsted acidity and generating new types of Lewis acid sites. These changes are expected to have a significant role in the catalytic behaviour of these materials for the lignocellulose catalytic fast pyrolysis.

3.2. Catalytic activity

Biomass pyrolysis produces three main product fractions: solid char, gases and a complex liquid mixture called bio-oil. When the vapors coming from biomass pyrolysis are put into contact with a catalyst, an important variation in the relative proportion of these fractions takes place, as well as the formation of another one, corresponding to the coke deposited on the

catalyst. The results obtained in the present work for non-catalytic and catalytic fast-pyrolysis of eucalyptus woodchips are illustrated in Fig. 6 in the form of mass yield of the different fractions. In addition, Table 2 provides additional information about the composition and properties of the gas and bio-oil products.

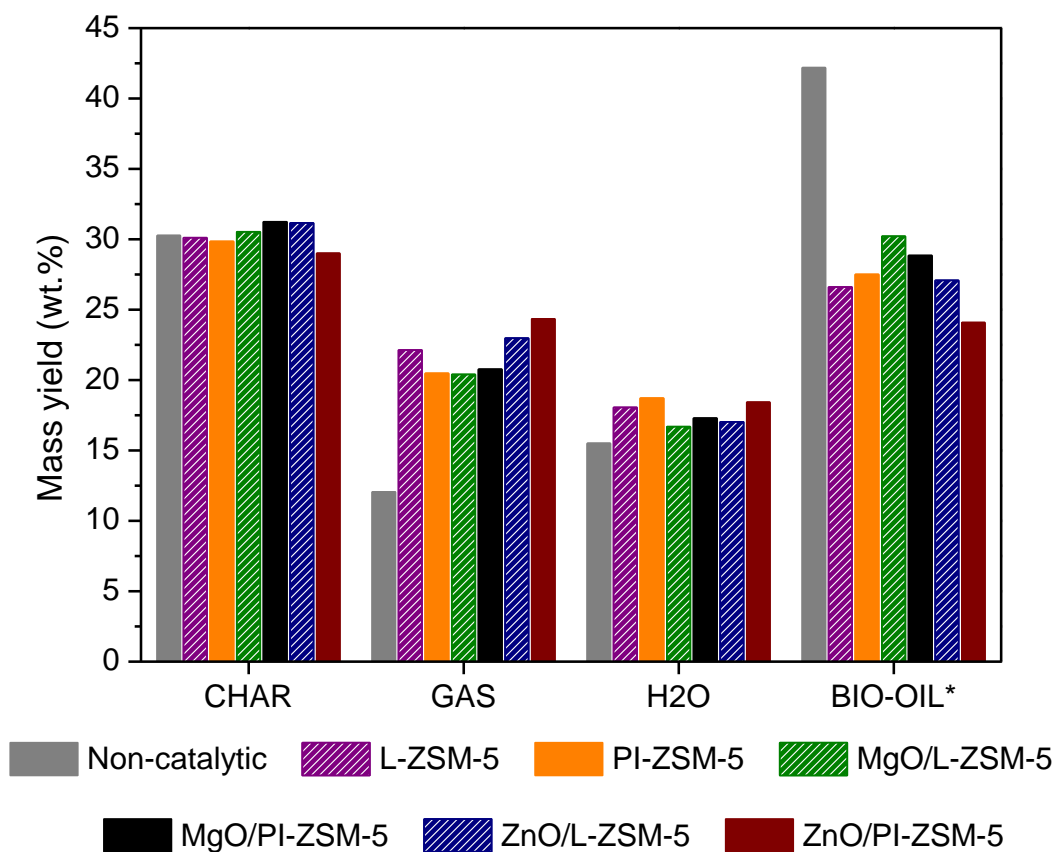


Fig. 6. Products yield distribution obtained in the fast-pyrolysis tests (catalytic and non-catalytic) of eucalyptus woodchips.

Table 2. Composition of the gas and properties of the bio-oil fraction (water free basis) obtained in the catalytic and non-catalytic and catalytic fast-pyrolysis of eucalyptus woodchips.

Catalyst	Gas (wt%)					Bio-oil ^a		
	H ₂	(C ₁ -C ₃) _p	(C ₂ -C ₃) _o	CO	CO ₂	Yield (wt%)	O conc. (wt%)	HHV (MJ/kg _{bio-oil})
Non-catalytic	0.007	0.52	0.10	3.40	8.0	42.2	39.0	23.4
PI-ZSM-5	0.009	0.8	0.9	7.8	11.0	27.5	30.9	28.3
MgO/PI-ZSM-5	0.008	0.8	0.8	7.2	11.9	28.9	32.1	27.8
ZnO/PI-ZSM-5	0.078	1.1	1.1	8.0	14.1	24.1	26.6	30.8
L-ZSM-5	0.007	0.7	1.1	8.3	12.0	26.6	29.6	29.3
MgO/L-ZSM-5	0.006	0.8	1.0	6.8	11.7	30.2	33.5	26.9
ZnO/L-ZSM-5	0.060	0.8	1.3	7.0	13.8	27.1	30.3	28.9

^a Bio-oil properties are expressed in relation to the organic compounds present in the liquid phase, i.e. in a water free basis.

Char is an important by-product of the pyrolysis process that may contain a significant proportion of the chemical energy in the feed material.³⁹ The minimum char yield, in dry basis, should be at least equal to the sum of the fixed carbon and ash contents of the raw biomass (25.3 wt%). Since the reaction system comprises two separated reaction zones (non-catalytic and catalytic), and the catalyst bed is downstream placed regarding the first pyrolysis zone, the type of catalyst does not affect nor modify the char formation. Accordingly, the char yield obtained in the different experiments is very similar, with random variations regarding an average value around 30 wt%. This figure confirms the relevance in quantitative terms of the char. Moreover, taking into account its elemental composition (relatively low oxygen content) and heating value, it can be easily concluded that the char accounts for more than 40% of the chemical energy contained in the initial biomass. Therefore, in order to have a feasible process, the char so produced should find specific applications instead of being considered just a residue of the pyrolysis process. Thus, it could be burnt for providing most of the energy consumed in the overall process, avoiding the use of external energy sources and making the process energy self-sufficient.^{36,37} Likewise, char gasification could be another interesting alternative for producing synthesis gas and/or hydrogen.

In addition to char, coke is formed in significant amounts in all cases over the different catalysts here investigated. In the case of the pure zeolitic catalysts (L-ZSM-5 and PI-ZSM-5), coke yield is about 3 wt% of the total raw biomass, which represents 15 wt% referred to the catalyst weight. This is a high amount for a catalyst based on ZSM-5 zeolite, suggesting that it is formed, at least in a great extension, outside the zeolite micropores. The incorporation of MgO, and particularly of ZnO, to the supports causes some reduction in the amount of coke, which can be considered a consequence of the lower concentration of zeolite Brønsted and Lewis acid sites and the generation of a new Lewis acidity with a lower acid strength, in the metal oxide-containing catalysts.

Non-catalytic pyrolysis of eucalyptus woodchips produces about 12 wt% of gases, formed mainly by CO and CO₂, as well as by minor amounts of C₁–C₃ hydrocarbons. Catalytic fast-pyrolysis markedly increased the total gas yield up to values in the range 20–24 wt%, which is related to the enhanced deoxygenation produced in the catalytic tests through decarboxylation and decarbonylation. The second one seems clearly favored when using both the zeolitic supports, as well as for the catalysts incorporating MgO, since the CO production is enhanced by a factor of around 2 (Table 2). In contrast, the addition of ZnO to the zeolitic supports causes also an important increase in the CO₂ yield, suggesting that this system promotes the decarboxylation pathway. On the other hand, all the catalysts display significant cracking activity of the pyrolysis vapors, increasing the production of gaseous hydrocarbons. This enhancement is particularly important in the case of gaseous olefins, although no clear trend is observed among the different catalysts. It is also noticeable that the hydrogen concentration in the gas stream undergoes a ten-fold increase when using ZnO-containing catalysts.

Water is another major product of biomass pyrolysis. In addition to the humidity that may be present in the raw biomass, water comes from a variety of dehydration reactions undergone by the starting biomass components or by primary and secondary pyrolysis products. Water is recovered as a component of the bio-oil fraction. Depending on the water amount, type and polarity of the organic components in bio-oil and even on the storage conditions, a phase separation may occur, so in this case the bio-oil consists really of two phases: aqueous and organic ones. In the experiments here reported, water has been detected in both of them, showing

that a liquid-liquid equilibrium is really established between both liquid phases rather than occurring a total segregation of the different components. Karl-Fisher analyses of these two phases indicate that their water content is very different with values of 69–75 wt% and 10–15 wt%, for the so called “aqueous” and “organic” phases, respectively. This is a fact to be carefully considered when comparing and discussing bio-oil yields, since the presence of different water contents may lead to not completely consistent conclusions. For this reason, in the present work water and bio-oil yields are given independently, so just the organic components are considered when using bio-oil yield data. The overall water produced in the non-catalytic test was 15.5 wt%, being increased when using catalysts up to 16.7–18.7 wt%, which shows that the different catalysts also promote in some extension dehydration reactions.

In order to get further insights about the different deoxygenation pathways, the selectivity toward dehydration, decarbonylation and decarboxylation has been represented in Fig. 7. The predominant pathway in the case of the non-catalytic pyrolysis dehydration with selectivity values around 64%, followed by decarboxylation and finally decarbonylation.⁴⁰ For the catalytic fast-pyrolysis test, the contribution of dehydration declines, reaching values of c.a. 53–55%, whereas decarbonylation and, in a lesser extension, decarboxylation are more favored undergoing important selectivity enhancements regarding the non-catalytic pyrolysis. Compared to the zeolitic supports, the incorporation of MgO and, in special, of ZnO increases the decarboxylation selectivity. Therefore, it can be postulated that decarboxylation reactions are catalysed in a great part by Lewis acid sites. Taking into account, the gaseous fraction composition (Table 2), the behavior of the ZnO-containing catalysts can be explained by the occurrence of the water gas shift reaction, that leads to the formation of CO₂ and H₂ by reaction between CO and water. ZnO-based systems are well known to catalyze this reaction.^{41,42}

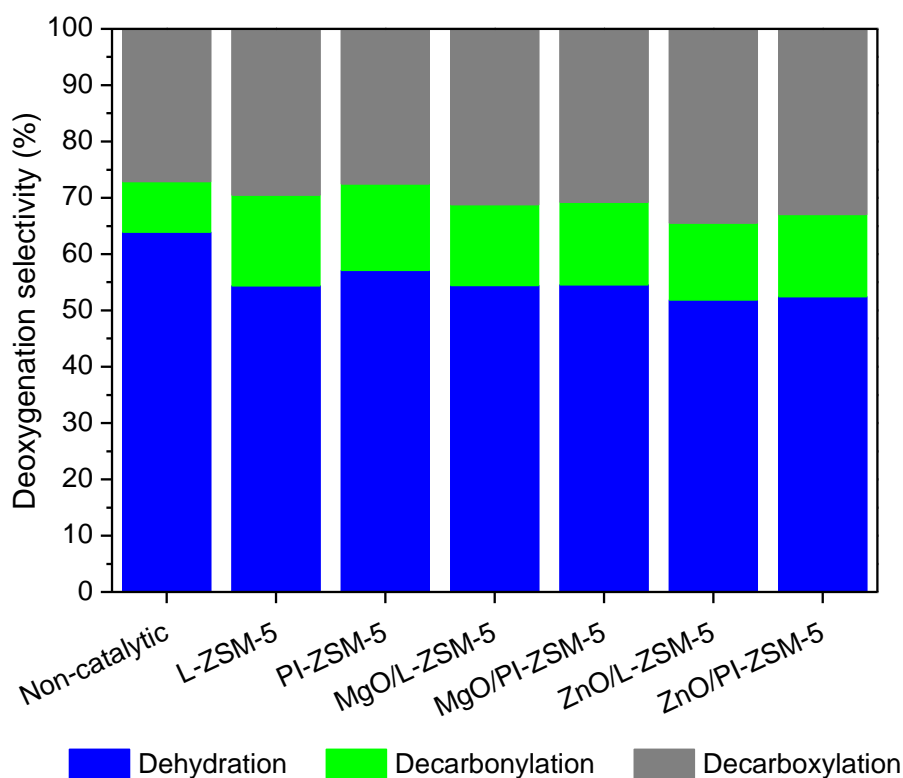


Fig. 7. Deoxygenation selectivity obtained in the fast-pyrolysis tests (catalytic and non-catalytic) of eucalyptus woodchips.

On the other hand, the data in Table 2 indicates that the incorporation of zeolitic catalysts to the process causes a significant reduction of the bio-oil yield (in a water free basis) from about 42 wt% to 24–30 wt%. This reduction was in a great part due to the oxygen removal as the bio-oil undergoes extensive deoxygenation over the catalysts, which in turn implies an improvement of its quality as fuel. This fact is also reflected in the high heating value of the bio-oil, which increases from 23.4 up to 27–31 MJ kg⁻¹ for non-catalytic and catalytic fast-pyrolysis experiments, respectively. Fig. 8 compares the bio-oil yield (excluding the water content) obtained with the different catalysts investigated in this work, confirming the decrease produced in regard to the non-catalytic bio-oil. In addition to deoxygenation reactions, coke deposition and cracking to gaseous hydrocarbons also contribute to the bio-oil yield reduction. While the non-catalytic bio-oil is recovered as a complex mixture without phase segregation, two phases were observed and could be separated in all the catalytic fast-pyrolysis experiments. This is a consequence of both the higher water content of the latter and the larger deoxygenation degree of the organics in the liquid phase since both factors facilitate the separation of the aqueous and organic phases. No significant variations are observed in the yield of the organics present in the aqueous phase, which suggests that this parameter is determined and limited by the water solubility of the organic compounds. However, important differences can be seen in the yield of organic compounds in the organic phase. In this case, the highest yields are obtained with the MgO-containing catalysts, which is consistent with the lower deoxygenation degree obtained with them. As it was shown above, the incorporation of Mg species onto the zeolitic catalysts causes drastic changes in their acidic features, strongly decreasing the concentration of both zeolitic Brønsted and Lewis acid sites. At the same time, the new generated acid sites, associated to MgO, exhibit a weak strength. All together confirm that the Mg-containing catalysts show the weakest acidity and, therefore, the lowest bio-oil deoxygenation activity.

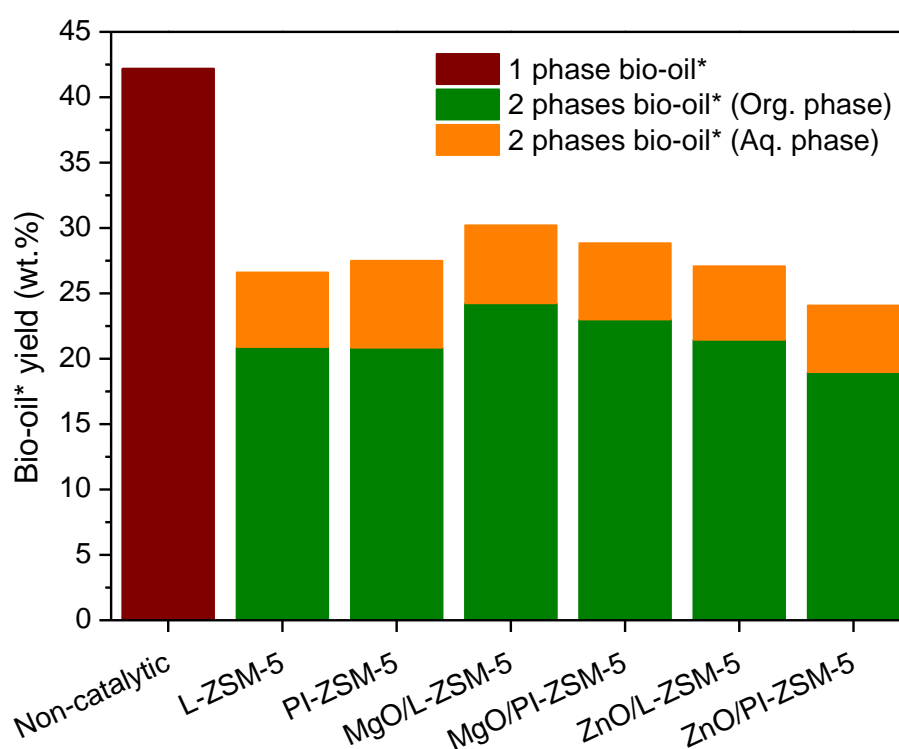


Fig. 8. Organic products yield obtained in the different fast-pyrolysis tests (catalytic and non-catalytic) of eucalyptus woodchips.

Fig. 9 provides semi-quantitative information about the bio-oil composition based on the results obtained by GC-MS analyses for the non-catalytic and catalytic fast-pyrolysis tests. Aqueous and organic phases of the catalytic bio-oils were separately analysed to determine the distribution of the different compound families in both phases, classified according to eight groups: carboxylic acids (AC), aldehydes (ALD), alcohols (ALC), ketones and ethers (KET & ETH), furans (FUR), aromatic hydrocarbons (AR), sugars (SUG) and oxygenated aromatics (O-AR), in addition to the group representing non-identified or unknown compounds (UNK). It must be noted that a critical bottle neck in studying catalytic fast-pyrolysis process is the fact that many bio-oil products cannot be identified with accuracy due to significant fragmentations in EI-MS and/or their absence in the database.^{43,44}

As seen in Fig. 9, non-catalytic fast-pyrolysis bio-oil mostly consists of oxygenated aromatics, 44%, (trimethoxy-toluene 6.7%, syringol 6.4%, trimethoxy-benzene 6.3%, creosol 3.2% and guaiacol 3.1%); followed by carboxylic acids, 15%, (acetic acid 14.4%); sugars, 11.6%, (levoglucosan 11%); ketones and ethers, 11.5% (acetol 5%) and furans, 8.2% (furfural 6.1%). Acetic acid is the most abundant single compound, which confers bio-oil corrosiveness and makes difficult its use as a fuel in engines.⁴⁵

In the case of bio-oils obtained by catalytic fast-pyrolysis, the aqueous phase consists mainly of acids (acetic acid), ketones (acetol) and ethers (1,1,1-trimethoxyethane), whilst the organic phase contains most of the high molecular weight lignin-derived oxygenated aromatics 65–75%, (1,2,4-trimethoxybenzene, syringol and 3,4,5-trimethoxytoluene) and all the aromatic hydrocarbons. At a first glance (Fig. 9), the product distribution in the bio-oils is very different for non-catalytic and catalytic fast-pyrolysis experiments. Thus, the concentration of acetic acid, furans and sugars are significantly lower when the bio-oil vapors enter into contact with the catalysts.

Acetic acid conversion could follow direct deoxygenation pathways (decarbonylation and decarboxylation), as well as ketonisation reactions, which would be consistent with the increase of the ketone concentrations observed with most of the catalysts. Ketonisation of carboxylic acids has been reported to be promoted by both basic^{46,47} and acid⁴⁸ catalysts. This reaction is of high interest in the system here studied as it allows the carboxylic acids concentration to be reduced, removing oxygen in the form of CO₂ and leading to the formation of C-C bonds.

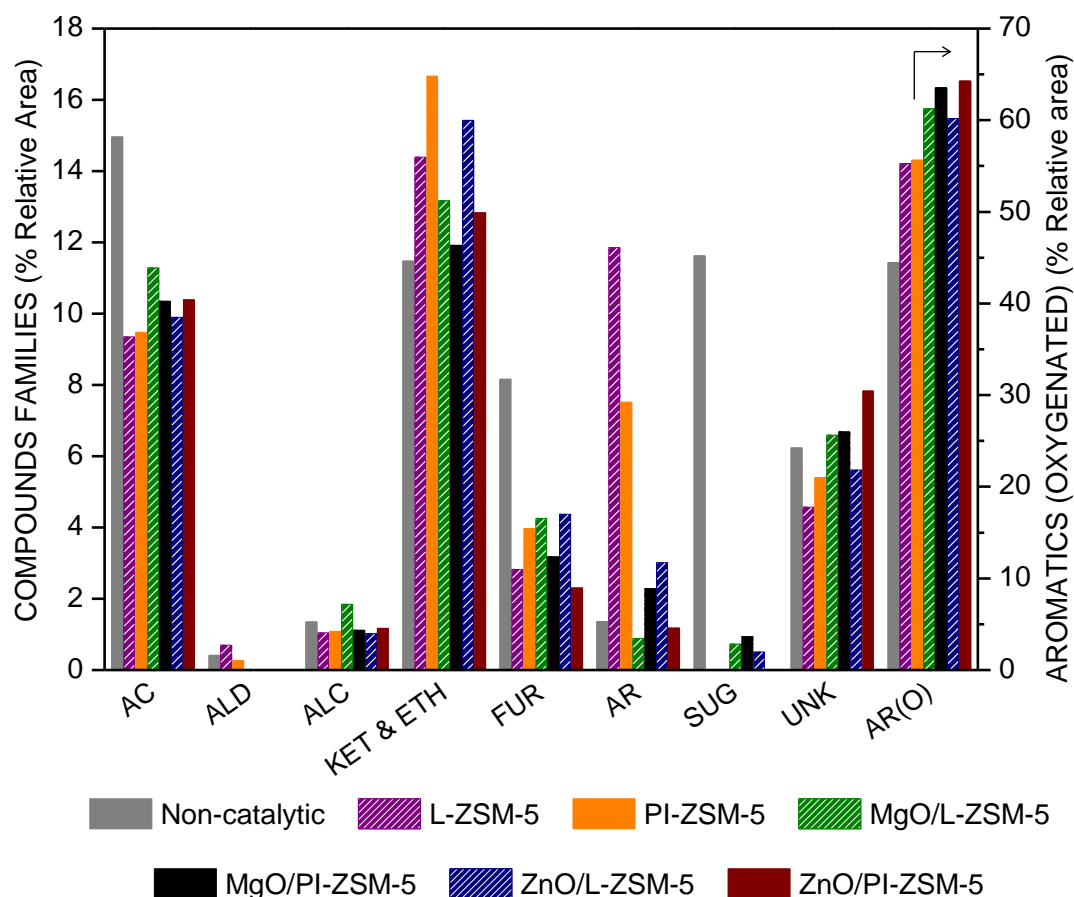


Fig. 9. Composition of the bio-oil in term of organic compounds families (% of relative area from GC-MS analyses) obtained in the different fast-pyrolysis tests (catalytic and non-catalytic) of eucalyptus woodchips.

Levoglucosan is the most important compound derived directly from cellulose decomposition, which is detected in the biomass fast-pyrolysis oil. Interestingly, this compound completely reacted in the case of L-ZSM-5, PI-ZSM-5 and ZnO/L-ZSM-5 catalysts, being not observed in any of the two bio-oil phases. In the rest of the catalysts, levoglucosan was also decomposed at a large extent, and only a small amount was detected in the aqueous phase. According to Mihalcik et al.,¹³ levoglucosan is deoxygenated in two steps, in the first one dehydration to form furans occurs, and then conversion of the latter into aromatic hydrocarbons via consecutive dehydration and decarboxylation reactions. Cheng and Huber⁴⁹ and Dorado et al.⁵⁰ have shown the importance of Diels-Alder condensation and dehydration reactions of furan rings with alkenes (ethylene or propylene) to produce aromatics (benzene, toluene, xylene, etc.) and water over ZSM-5 zeolite.⁴⁹

According to the results obtained in the present work, furfural accounts for 6.1% of the non-catalytic bio-oil, being catalytically converted into furans and CO. Parent zeolites were the most effective catalysts producing aromatic hydrocarbons from the oxygen-rich vapors, increasing the aromatics proportion in the total bio-oil from 1.4 to 11.9 and 7.5% in case of L-ZSM-5 and PI-ZSM-5, respectively. Among aromatic hydrocarbons, the most abundant compounds were styrene, xylene, methyl-styrene, trimethyl-benzene; but also some polyaromatic hydrocarbons (PAHs) like methyl-naphthalene and dimethyl-naphthalene. PAHs are considered hazardous for the environment, and therefore disliked compounds among bio-oil components.^{11,51,52} The

incorporation of MgO and ZnO to both zeolitic supports decreases the overall production of aromatic hydrocarbons in favor of oxygenated aromatics, decreasing as well the formation of undesired PAHs.⁵³⁻⁵⁵ Moreover, the latter are considered to be coke precursors, causing the catalyst deactivation.^{53,56,57} As above denoted, the incorporation of ZnO and MgO into the zeolitic supports modifies strongly their acid features, increasing the Lewis acidsites to the detriment of Bronsted acid sites, which also contributes to a lower coke formation.

4. Conclusions

The in-situ upgrading of eucalyptus woodchips fast-pyrolysis vapors has been investigated over lamellar and pillared ZSM-5 catalysts, modified by impregnation with MgO and ZnO. XRD and TEM measurements indicate that the metal oxides are present in the form of very-small entities with a high dispersion over the supports.

The incorporation of MgO and ZnO causes in all cases a strong decrease in the Ar adsorption in the whole range of relative pressures, confirming that it affects strongly to the support porosity. As a result, the values of the textural properties (surface area and pore values) are significantly lower for the samples incorporating the metal oxides compared to the parent supports. The large decrease in both the zeolite micropore volume and surface after the addition of the metal oxides may be assigned to different phenomena: location within the zeolite micropores, deposition on the mesopores blocking the entrance to the zeolite micropores and introduction by ion exchange of the protons in Si-OH-Al species by Mg²⁺ and Zn²⁺. Likewise, the incorporation of Mg and Zn phases causes strong changes in the acidic features of the layered and pillared ZSM-5 zeolites, suppressing in a great extension the Brønsted and Lewis acidity of the parent zeolites and generating new types of Lewis acid sites, with weaker strength and associated to the metal oxides.

The char yield obtained in the different experiments of eucalyptus woodchips fast pyrolysis is very similar, with random variations around an average value of 30 wt%, accounting for more than 40% of the chemical energy contained in the initial biomass. Therefore, in order to have a feasible process, the char so produced should find specific applications instead of being considered just a residue of the pyrolysis process.

Water is recovered as a component of the bio-oil fraction. Depending on the water amount, type and polarity of the organic components in the bio-oil and even on the storage conditions, a phase separation may occur, so in this case the bio-oil consists really of two phases: aqueous and organic ones. In the experiments here reported, water has been detected in both of them, with values of 69–75 wt% and 10–15 wt% for the so called “aqueous” and “organic” phases, respectively.

Regarding the organic compounds contained in the bio-oil, the incorporation of zeolitic catalysts to the process causes a significant reduction of the bio-oil yield (in a water free basis) from 42 to 24–30 wt%. This reduction is in a great part due to the oxygen removal as the bio-oil undergoes extensive deoxygenation over the catalyst, which in turn implies an improvement of its quality as fuel. This fact is also reflected in the high heating value of the bio-oil, which increases from 23.4 up to 27–31 MJ kg⁻¹ for non-catalytic and catalytic fast-pyrolysis experiments, respectively.

Likewise, drastic variations are also observed when using the different catalysts in the product distribution per type of organic compounds present in the bio-oil. The concentration of

carboxylic acids (formed mainly by acetic acid) decreases, leading to an enhancement in the ketone production. Moreover, sugar derivatives are almost completely transformed in the catalytic fast-pyrolysis tests, whereas furanic compounds also undergo extensive conversion. Both factors lead to the production of large amounts of both oxygenated aromatic compounds and aromatic hydrocarbons. MgO and ZnO incorporation into both lamellar and pillared supports moderates the formation of aromatic hydrocarbons in favor of oxygenated aromatics due to the reduction caused by these metals in the concentration of strong zeolitic acid sites. This fact is of relevance as it affects positively the coke formation on the catalyst and prevents the formation of undesired polyaromatic hydrocarbons.

Acknowledgements

The authors gratefully acknowledge the financial support from the European Union Seventh Framework Programme (FP7/2007-2013) under grant agreement n°604307. J. Č. also acknowledges the Czech Science Foundation for the support through grant P106/12/0189.

References

1. D. Carpenter, T. L. Westover, S. Czernik, W. Jablonski, *Green Chem.*, 2014, **16**, 384–406.
2. D. Kubička, I. Kubičková, J. Čejka, *Catal. Rev.*, 2013, **55**, 1–78.
3. A. Bridgwater, G. Peacocke, *Renew. Sustain. Energy Rev.*, 2000, **4**, 1–73.
4. D. Meier, O. Faix, *Bioresour. Technol.*, 1999, **68**, 71–77.
5. C. Liu, H. Wang, A. M. Karim, J. Sun, Y. Wang, *Chem. Soc. Rev.*, 2014, **43**, 7594–7623.
6. Q. Zhang, J. Chang, T. Wang, Y. Xu, *Energy Convers. Manag.*, 2007, **48**, 87–92.
7. R. H. Venderbosch, *ChemSusChem*, 2015, **8**, 1306–1316.
8. P. A. H. Paul, T. Williams, *Biomass Bioenergy*, 1994, **7**, 223–236.
9. T. R. Carlson, G. A. Tompsett, W. C. Conner, G. W. Huber, *Top. Catal.*, 2009, **52**, 241–252.
10. P. T. Williams, N. Nugranad, *Energy*, 2000, **25**, 493–513.
11. J. Adam, E. Antonakou, A. A. Lappas, *Microporous Mesoporous Mater.*, 2006, **96**, 93–101.
12. T. P. Carlson, T. V. Vispute, G. W. Huber, *ChemSusChem*, 2008, **1**, 397–400.
13. D. J. Mihalcik, C. A. Mullen, A. A. Boateng, *J. Anal. Appl. Pyrolysis*, 2011, **92**, 224–232.
14. J. D. Adjaye, N. N. Bakhshi, *Fuel Process. Technol.*, 1995, **45**, 161–183.
15. M. A. Jackson, D. L. Compton, A. A. Boateng, *J. Anal. Appl. Pyrolysis*, 2009, **85**, 226–230.
16. W. Roth, P. Nachtigall, R. Morris, J. Čejka, *Chem. Rev.*, 2014, **114**, 4807–4837.
17. W. J. Roth, B. Gil, B. Marszalek, *Catal. Today*, 2014, **227**, 9–14.
18. W. J. Roth, J. Čejka, *Catal. Sci. Technol.*, 2011, **1**, 43–53.

19. R. E. Morris, J. Čejka, *Nat. Chem.*, 2015, **7**, 381–388.
20. P. Eliášová, M. Opanasenko, P. S. Wheatley, M. Shamzhy, M. Mazur, P. Nachtigall, W. J. Roth, R. E. Morris, J. Čejka, *Chem. Soc. Rev.*, 2015, **44**, 7177–7206.
21. H. W. Lee, S. H. Park, J. K. Jeon, R. Ryoo, W. Kim, D. J. Suh, Y. K. Park, *Catal. Today*, 2014, **232**, 119–126.
22. E. Pütün, *Energy*, 2010, **35**, 2761–2766.
23. S. D. Jackson, J. S. J. Hargreaves, *Metal Oxide Catalysis*, Wiley-VCH Verlag GmbH & Co. KGaA, 2009.
24. L. Zhou, H. Yang, H. Wu, M. Wang, D. Cheng, *Fuel Process. Technol.*, 2013, **106**, 385–391.
25. S. D. Stefanidis, K. G. Kalogiannis, E. F. Iliopoulou, A. A. Lappas, P. A. Pilavachi, *Bioresour. Technol.*, 2011, **102**, 8261–8267.
26. S. A. Channiwala, P. P. Parikh, *Fuel*, 2002, **81**, 1051–1063.
27. M. Choi, K. Na, J. Kim, Y. Sakamoto, O. Terasaki, R. Ryoo, *Nature*, 2009, **461**, 246–249.
28. K. Na, C. Jo, J. Kim, W. S. Ahn, R. Ryoo, *ACS Catal.*, 2011, **1**, 901–907.
29. Y. He, G. Nivarthi, F. Eder, K. Seshan, J. Lercher, *Microporous Mesoporous Mater.*, 1998, **25**, 207–224.
30. C. A. Emeis, *J. Catal.*, 1993, **141**, 347–354.
31. B. Gil, S. I. Zones, S. J. Hwang, M. Bejblová, J. Čejka, *J. Phys. Chem. C*, 2008, **112**, 2997–3007.
32. K. Na, M. Choi, W. Park, Y. Sakamoto, O. Terasaki, R. Ryoo, *J. Am. Chem. Soc.*, 2010, **132**, 4169–4177.
33. C. O. Arean, M. R. Delgado, P. Nachtigall, H. V. Thang, M. Rubeš, R. Bulánek, P. Chlubná-Eliášová, *Phys. Chem. Chem. Phys.*, 2014, **16**, 10129–10141.
34. M. R. Delgado, R. Bulánek, P. Chlubná, C. O. Arean, *Catal. Today*, 2014, **227**, 45–49.
35. D. Mao, W. Yang, J. Xia, B. Zhang, Q. Song, Q. Chen, *J. Catal.*, 2005, **230**, 140–149.
36. A. Travert, A. Vimont, A. Sahibed-Dine, M. Daturi, J. C. Lavalley, *Appl. Catal. A Gen.*, 2006, **307**, 98–107.
37. C. Poupin, R. Maache, L. Pirault-Roy, R. Brahmi, C. T. Williams, *Appl. Catal. A Gen.*, 2014, **475**, 363–370.
38. L. Lericci, M. Renzini, U. Sedran, L. Pierella, *Energy & Fuels*, 2013, **27**, 2202–2208.
39. A. Bridgwater, *Biomass Bioenergy*, 2012, **38**, 68–94.
40. H. Zhang, R. Xiao, H. Huang, G. Xiao, *Bioresour. Technol.*, 2009, **100**, 1428–1434.
41. A. Haryanto, S. Fernando, N. Murali, S. Adhikari, *Energy & Fuels*, 2005, **19**, 2098–2106.
42. M. Nokkosmäki, E. Kuoppala, *J. Anal. Appl. Pyrolysis*, 2000, **55**, 119–131.

43. D. P. Cole, Y.J. Lee, *J. Anal. Appl. Pyrolysis*, 2015, **112**, 129–134.
44. M. Staš, D. Kubička, J. Chudoba, M. Pospíšil, *Energy & Fuels*, 2014, **28**, 385–402.
45. G. W. Huber, S. Iborra, A. Corma, *Chem. Rev.*, 2006, **106**, 4044–4098.
46. L. Deng, Y. Fu, Q. Guo, *Energy & Fuels*, 2008, **41**, 564–568.
47. C. A. Gaertner, J. C. Serrano-Ruiz, D. J. Braden, J. A. Dumesic, *J. Catal.*, 2009, **266**, 71–78.
48. A. Aho, N. Kumar, K. Eränen, T. Salmi, M. Hupa, D. Y. Murzin, *Fuel*, 2008, **87**, 2493–2501.
49. Y. T. Cheng, G. W. Huber, *Green Chem.*, 2012, **14**, 3114–3125.
50. C. Dorado, C. A. Mullen, A. A. Boateng, *Appl. Catal. B Environ.*, 2015, **162**, 338–345.
51. A. A. Lappas, K. G. Kalogiannis, E. F. Iliopoulou, K. S. Triantafyllidis, S. D. Stefanidis, *Wiley Interdiscip. Rev. Energy Environ.*, 2012, **1**, 285–297.
52. P. T. Williams, P. A. Horne, *Fuel*, 1995, **74**, 1839–1851.
53. G. Caeiro, P. Magnoux, P. Ayrault, J. Lopes, F. Ribeiro, *Chem. Eng. J.*, 2006, **120**, 43–54.
54. H. Zhang, S. Shao, R. Xiao, D. Shen, J. Zeng, *Energy & Fuels*, 2013, **28**, 52–57.
55. H. Zhang, T. R. Carlson, R. Xiao, G. W. Huber, *Green Chem.*, 2012, **14**, 98–110.
56. H. Cerqueira, P. Ayrault, J. Datka, M. Guisnet, *Microporous Mesoporous Mater.*, 2000, **38**, 197–205.
57. I. Graça, J. D. Comparot, S. Laforge, P. Magnoux, J. M. Lopes, M. F. Ribeiro, F. Ramôa Ribeiro, *Energy & Fuels*, 2009, **23**, 4224–4230.

Supporting Information

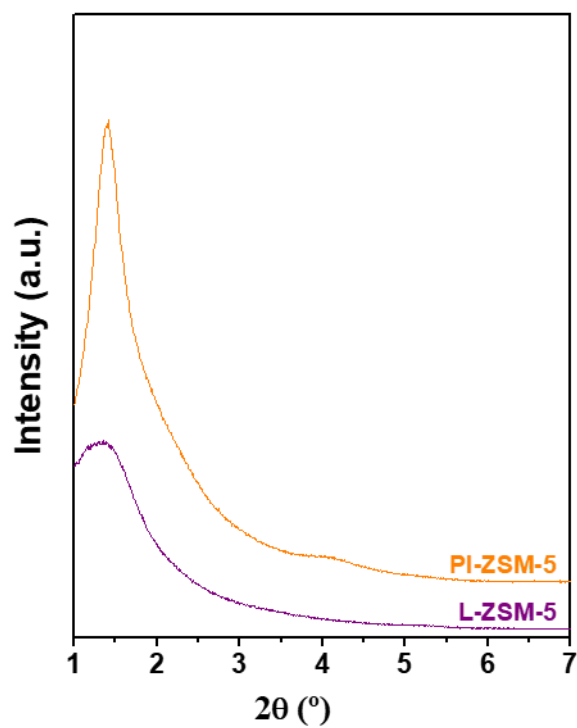


Fig. S1. Low-angle XRD patterns of calcined PI-ZSM-5 and L-ZSM-5.

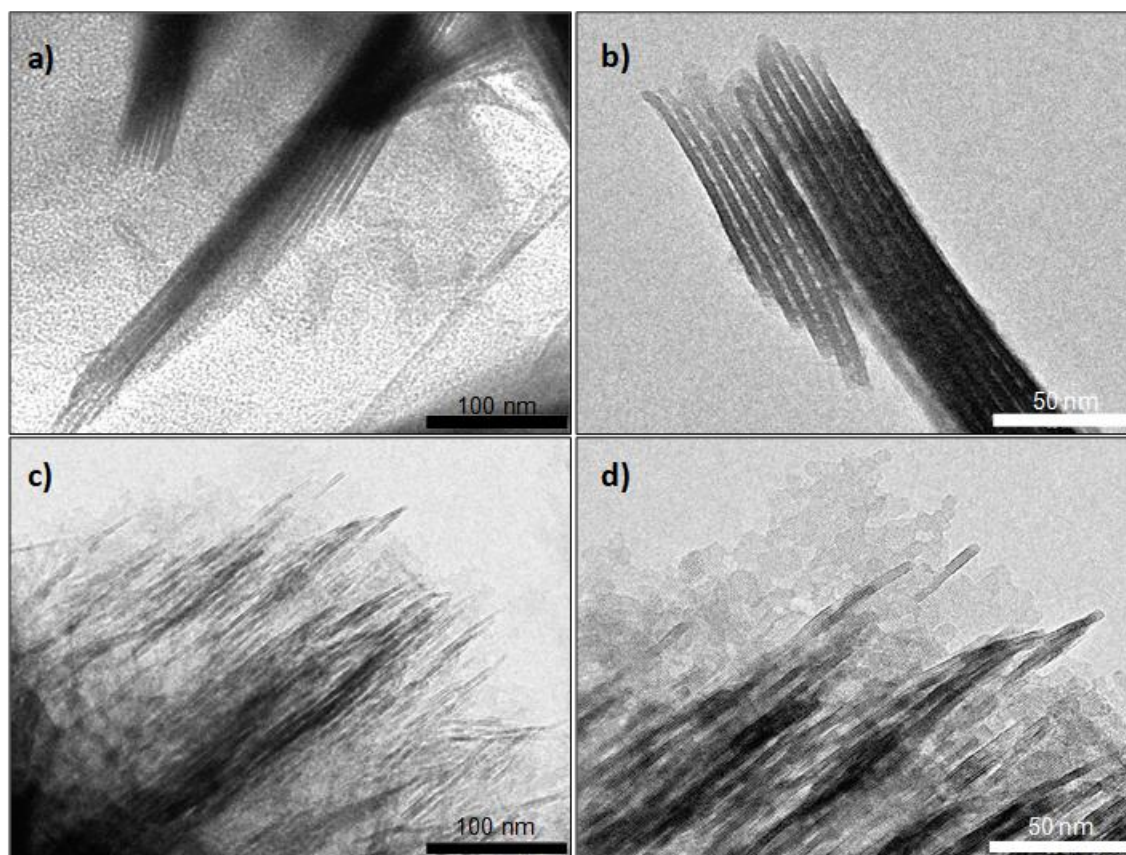


Fig. S2. TEM images of the parent materials after calcination: (a, b) PI-ZSM-5 and (c, d) L-ZSM-5.

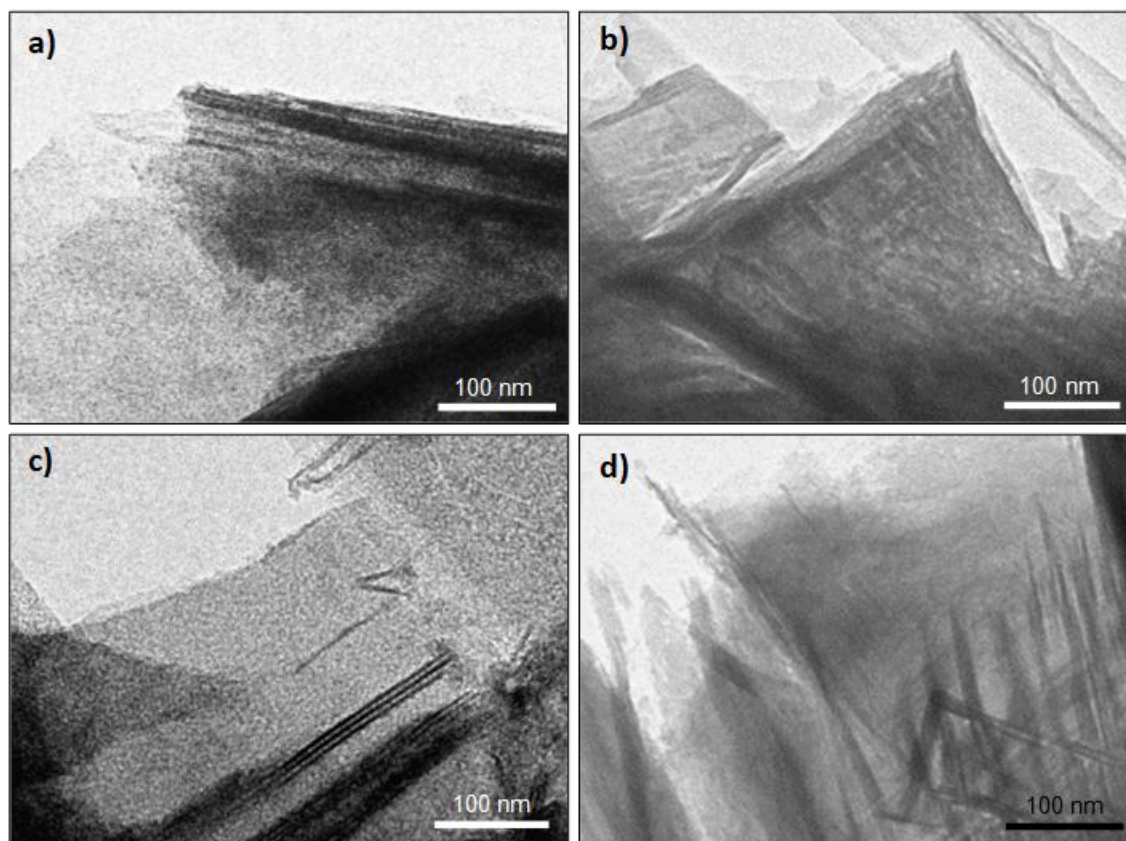


Fig. S3. TEM images of (a) MgO/PI-ZSM-5, (b) MgO/L-ZSM-5, (c) ZnO/PI-ZSM-5 and (d) ZnO/L-ZSM-5.

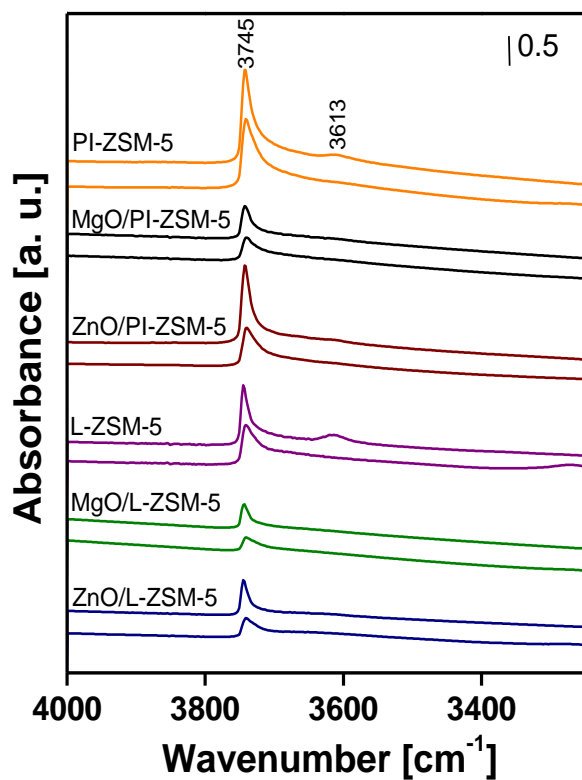


Fig. S4. Hydroxyl vibration region of the materials under study before (top spectra) and after (down spectra) adsorption of pyridine.

Article 6

Assessing biomass catalytic pyrolysis in terms of deoxygenation pathways and energy yields for the efficient production of advanced biofuels

Catalysis Science and Technology, 2016, 6(8), 2829-2843

**Catalysis
Science &
Technology**



PAPER

[View Article Online](#)
[View Journal](#) | [View Issue](#)



Cite this: *Catal. Sci. Technol.*, 2016,
6, 2829

Assessing biomass catalytic pyrolysis in terms of deoxygenation pathways and energy yields for the efficient production of advanced biofuels

H. Hernando,^a S. Jiménez-Sánchez,^a J. Feroso,^a P. Pizarro,^{ab}
J. M. Coronado^a and D. P. Serrano^{*ab}

Impact JCR factor, (JCR 2017): 5.365

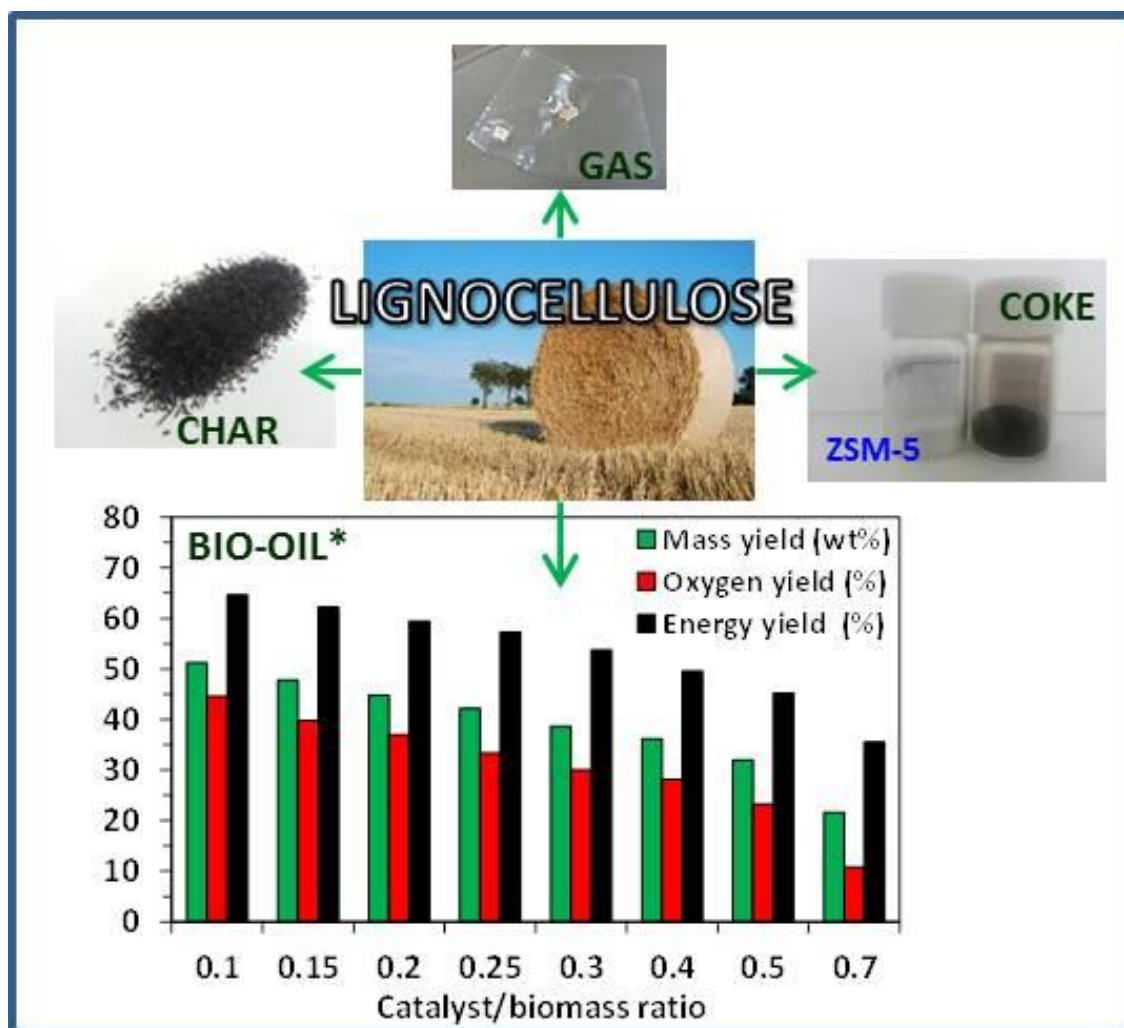
Category: Physical Chemistry. 32 of 147 (Q1)

ABSTRACT

The present work focuses on the pathways through which catalytic pyrolysis of biomass into bio-oil proceeds and the effect of the operation conditions on parameters like bio-oil oxygen composition and mass yield, but also additional indicators, such as the distribution of both the oxygen and the chemical energy contained in the initial biomass among the different products. Acid washed wheat straw was used as biomass feedstock. The pyrolysis tests were performed in a lab-scale downdraft fixed-bed reactor working at atmospheric pressure, employing a nanocrystalline H-ZSM-5 zeolite as catalyst. A systematic study was carried out consisting on decoupling both the thermal and catalytic reactions in order to evaluate the influence of three key variables: temperature of the thermal zone; temperature of the subsequent catalytic step and catalyst/biomass ratio. Increasing the pyrolysis temperature in the thermal zone resulted in more bio-oil* (bio-oil in water-free basis) production to the detriment of char and water fractions. In contrast, a significant reduction in bio-oil* fraction, due to decarbonylation and decarboxylation, occurred when increasing the catalytic bed temperature from 400 up to 500 °C. A similar effect was observed by varying the catalyst/biomass ratio since it increased the production of CO, CO₂, light olefins and coke at expenses of a decline of the bio-oil* yield. Nevertheless, this bio-oil contains oxygen amounts as low as 10 wt%, while retaining about 38% of the energy yield. Char, coke and gaseous hydrocarbons contain a great part of the biomass chemical energy, hence their formation should be suppressed or minimized to further improve the bio-oil* energy yield. At high catalyst/biomass ratios the bio-oil becomes rich in aromatic compounds, both oxygenated and hydrocarbons, while the content of sugars, furans, carboxylic acids, and other oxygenated products is strongly reduced.

Keywords: Lignocellulose. Catalytic pyrolysis. Bio-oil. ZSM-5. Deoxygenation

GRAPHICAL ABSTRACT



1. Introduction

Fossil fuels are still predominant in the transport sector contributing to a high share of the global GHG emissions in spite of the efforts carried out during the last decades for introducing other low carbon options, such as biofuels, hydrogen and electrical vehicles.¹ In particular, biofuels are expected to play a major role in the short to medium term by reducing the dependence from imported fossil fuels and contributing to mitigate the CO₂ emissions. Thus, the European Union has established the goal of increasing the consumption of biofuels to reach a 10% renewable share by 2020 in the transport sector.² However, the so called first generation biofuels have shown to suffer of important limitations, mainly due to the high water and energy consumption during their production and the possible competition for raw materials with the food markets.^{3,4}

Accordingly, a great interest has emerged in developing biofuels produced from non-food biomass, mainly by the transformation of lignocellulosic biomass, such as forestry and agricultural residues.^{4,5} Lignocellulose is the most abundant source of continental biomass and it is usually a low-cost raw material that can be employed for the production of advanced biofuels with reduced environmental impact.⁶

Among the various routes investigated for the conversion of lignocellulose into fuels, pyrolysis has shown to be a promising and relatively simple alternative in which biomass is treated under inert atmosphere to yield gases, liquids (bio-oil) and a solid residue (char).⁷⁻⁹ The bio-oil fraction possesses a high potential as liquid fuel and/or source of chemicals. However, it contains 15-25 wt% water, about 40 wt% of oxygen and is formed by a very complex mixture of oxygenated organic compounds, including carboxylic acids, ketones, aldehydes, furans, phenolics, etc.¹⁰ Consequently, compared with petroleum-derived fuels, pyrolysis bio-oil is a poor quality fuel, possessing low heating value (15-20 MJ kg⁻¹), strong corrosiveness due to its acidic pH, high viscosity, immiscibility with conventional fuels and low chemical stability with polymerisation of components observed on storage.¹¹ These facts hinder the use of bio-oil in many applications and reduce its economic value. These important limitations can be overcome if the bio-oil is subjected to upgrading treatments to improve its properties, which requires a great change in the bio-oil elemental composition by decreasing the O/C ratio and increasing the H/C ratio.

Catalytic pyrolysis has arising in recent years as one of the most efficient alternative for bio-oil upgrading into advanced biofuels, with several processes based on this technology close to reach commercialization.^{6,12} It can be conducted by adding directly the solid catalyst to the pyrolysis reactor (in-situ catalytic pyrolysis) or by using a catalytic reactor close coupled to the pyrolysis system (ex-situ catalytic pyrolysis).¹⁰ A variety of catalysts have been described in the literature for biomass catalytic pyrolysis, including zeolites,¹³⁻¹⁶ metal oxides^{15,17} and metal salts.^{18,19} The catalyst promotes a number of reactions: cracking, oligomerization, cyclization, aromatization and deoxygenation, which are coupled with those already occurring just by thermal degradation of the different lignocellulose components. In particular, deoxygenation may proceed by three main pathways: decarboxylation, decarbonylation and dehydration, leading to the formation of CO₂, CO and H₂O, respectively. A high degree of deoxygenation has been reported using strong acid zeolitic catalysts, which produce large amounts of aromatic hydrocarbons. However, the strong acidity of the catalyst causes also a sharp decrease of the bio-

oil yield as it promotes excessive cracking, whereas the catalyst suffers from extensive coking, which results in its fast deactivation.^{20–24}

The current interest and relevance of catalytic pyrolysis is demonstrated by the huge number of works and reviews published in the past years on this topic.^{18,25–27} This literature has extensively investigated the effect of a large number of parameters and variables: lignocellulose type,²⁴ biomass pretreatment such as torrefaction²⁸ and de-ashing,^{29,30} co-processing of biomass and other raw materials such as plastics,³¹ reaction conditions,^{32,33} reactor type and configuration,⁸ catalyst properties^{21,34,35} and catalyst load,^{34,35} among others. However, most works are mainly focused on the bio-oil properties, such as oxygen content, composition, HHV, pH, viscosity, etc., being aimed at maximizing the bio-oil mass yield, whereas little attention is given to the other fractions formed in the process (char, gases and coke). Moreover, in spite of the products being targeted as fuels almost no information is given on the overall energy yield of the process, i.e. the proportion of the chemical energy contained in the raw biomass that it is retained in the produced bio-oil.

In this context, the present work addresses the development of an exhaustive procedure for assessing the results of biomass catalytic properties according to both mass and energy yields. Thereby, all the fractions formed in the biomass pyrolysis process are characterized in detail: char (carbonaceous residue formed in the pyrolysis zone), coke (carbonaceous deposits on the catalyst), gases and liquid phases (organic and aqueous ones). The methodology here applied allows tracking the oxygen distribution among those fractions (not only in bio-oil) giving essential information to understand the different deoxygenation pathways. Likewise, knowing how the energy yield is shared among the different fractions is a key factor for optimizing the overall process, showing that a large part of the initial biomass chemical energy is lost with the secondary streams, like char, coke and gases.

The catalyst employed in this work is a commercial H-ZSM-5 zeolite with nanocrystalline features. This zeolitic structure has been widely investigated in the literature for biomass catalytic pyrolysis^{32,34,36–38} since it provides a high yield of aromatic hydrocarbons. Moreover, as the material here used is formed by nanocrystals, it presents a relatively high amount of external surface area, which can be very convenient for the conversion of the bulky molecules formed from the decomposition of lignocellulose. In this way, the experiments here performed have covered a large range of catalyst/biomass ratios to find out the main reaction pathways from the early stages of the catalytic upgrading process.

2. Experimental

2.1. Biomass feedstock

The lignocellulose biomass selected to carry out this study was wheat straw (WS). It was ground with a cutter mill and sieved to the desired particle size of 0.5-1 mm. WS was partially de-ashed by means of a mild acid-washing pretreatment trying to avoid the interference of the mineral matter components with the zeolite employed in the catalytic tests. The procedure used for the mentioned washing is described as follows: a representative biomass sample of 50 g was dispersed in 1000 cm³ of an aqueous HNO₃ solution (1 wt%) and subjected to a continuous magnetic stirring at a constant temperature of 50 °C for 2 h. After this pretreatment, the solution was vacuum filtered and washed with mili-Q water until reaching neutral pH. Then, the sample was dried at 105 °C for 2 days. This acid-washed sample is denoted as WS-ac.

Biomass ash was collected by burning 20 g of wheat straw, both raw and acid-washed, in a muffle at 815 °C in air flow for 2 h. The chemical composition of WS and WS-ac ash was measured by inductively coupled plasma-optical emission spectroscopy (ICP-OES) analyses with a Perkin Elmer Optima 3300 DV instrument. A representative amount of each ash sample was digested in a mixture of HF and HNO₃ in an Anton Paar (MW3000) microwave oven. TGA analyses (NETZSCH STA 449) were employed to determine the volatile matter of the biomass sample and the coke deposited on the catalyst after the reaction tests.

The proximate analyses, according to European standards, included for WS and WS-ac samples the determination of the moisture (UNE-EN 14774-1:2010), ash (UNE-EN 14775:2010), volatile matter (UNE-EN 15148:2010) and fixed carbon (determined by difference) contents. In addition, the ultimate analysis was carried out in a micro-elemental analyser (Thermo Scientific) in order to determine the content of C, H, N, S and O (by difference). The composition of raw and de-ashed biomass samples in biopolymers (cellulose, hemicellulose and lignin) was determined by methods described elsewhere.³⁹

2.2. Catalyst sample

For catalytic fast-pyrolysis tests, H-ZSM-5 zeolite supplied by CLARIANT was employed. The amount of aluminium of this sample was determined by ICP-OES, showing a Si/Al molar ratio of 42. Argon physisorption isotherms at -186 °C were measured on a AUTOSORB iQ system (Quantachrome). The surface area was determined using the Brunauer–Emmet–Teller (BET) equation and the pore size distributions were calculated by applying the NLDFT model to the adsorption branch of the isotherm. The specific surface area and micropore volume showed values of 347 m² g⁻¹ and 0.134 cm³ g⁻¹, respectively. The acidity of the zeolite was measured by temperature programmed desorption (TPD) of NH₃ using an AUTOCHEM 2910 system (Micromeritics). The standard procedure for the TPD measurements involved the activation of the sample by flowing He at 600 °C (1 h), cooling to 100 °C, adsorbing NH₃ from a He–NH₃ (15%) mixture, removing the weakly adsorbed NH₃ by flowing He at 100 °C for 30 min, and finally carrying out the TPD experiment by raising the temperature of the catalyst sample with a ramp of 10 °C min⁻¹. H-ZSM-5 zeolite presented an acidity of 0.414 mmol NH₃ g⁻¹, which is in agreement with its Al content (Si/Al = 42). The TPD curve exhibited two desorption peaks, one at about 165 °C associated with weak acidic sites, and a broader, less intense feature at 335 °C, which is attributed to strong acid sites.

Previous to the pyrolysis tests, the zeolite sample was pelletized, crushed and sieved to the desired particle size of 180-250 µm.

2.3. Catalytic activity tests

The schematic diagram of the lab-scale experimental setup used for the fast-pyrolysis experiments of WS-ac sample is shown in Fig. 1. This setup consists of a downdraft fixed-bed stainless steel reactor (16 mm i.d. and 400 mm length) with two separated zones, pyrolysis and catalytic, heated by two independent electrical furnaces. The reaction temperatures are measured by two type K thermocouples, placed on the pyrolysis zone (char bed) and on the catalytic zone (catalyst bed), respectively. For the catalytic experiments, the reactor is loaded with 0.4-2.8 g of catalyst, to operate with a catalyst to biomass ratio of 0.1 to 0.7. The WS-ac sample (4 g) is placed in the biomass tank and kept at room temperature. Two internal stainless steel tubes are placed inside the reactor to separate the catalytic bed from the pyrolysis zone. A quartz wool

sheet and a metallic plate are placed over each tube and over the catalyst particles to avoid possible mixing between the char particles and the catalyst bed. The pyrolysis tests have been carried out at atmospheric pressure and temperatures of 475-600 °C and 400-500 °C for the pyrolysis and catalytic zones, respectively.

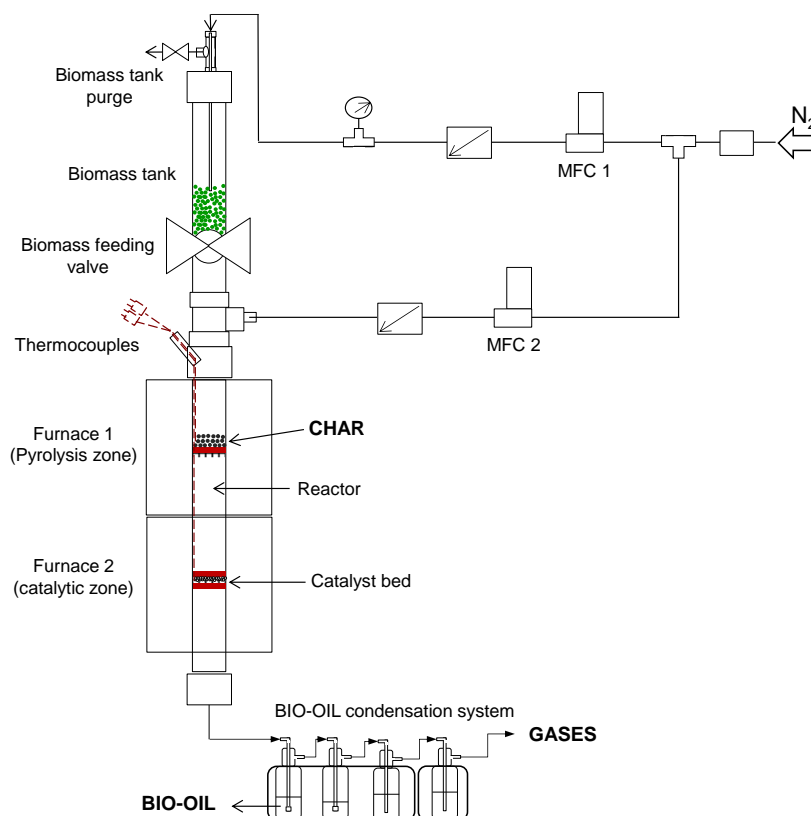


Fig. 1. Schematic flow diagram of the experimental setup used for the WS-ac fast-pyrolysis experiments.

Prior to each pyrolysis experiment and during the heating up of the reactor, the biomass tank and all the reaction system are purged with a N₂ flow delivered by mass flow controllers, until the O₂ concentration levels of the exiting gas drop to < 0.1 vol.%, ensuring that pyrolysis takes place in an inert atmosphere. Once the reactor temperature reaches the desired set point, the feeding valve is open and the biomass falls into the reactor, being subjected to pyrolysis to form a solid carbonaceous residue (char) and vapours. The volatiles so generated in the pyrolysis zone are swept by a N₂ flow of 100 cm³ min⁻¹ and passed through the catalyst bed to leave rapidly the reaction zones, being condensed by means of a condensation system composed by four 125 cm³ flasks connected in series (with a total cooling surface area of around 180 cm²) and refrigerated by an ice-water bath (0-4 °C). Permanent gases and light hydrocarbons (C₁-C₄) are finally collected in a sampling bag for their further analysis in a dual channel Agilent® CP-4900 Micro Gas Chromatograph (Micro-GC), which is equipped with molecular sieve (Molsieve 5 Å) and HayeSep A columns and a thermal conductivity detector (TCD), using Helium as carrier gas. The TCD is periodically calibrated with a standard gas mixture containing N₂ (internal standard), O₂, H₂, CO, CO₂, CH₄, C₂H₄, C₂H₆, C₃H₆ and C₃H₈. Thus, the gas mass yield and its elemental composition (C, H and O) can be calculated.

After the experiments, the char and the used catalyst were collected for their further investigation. Char was characterized in the same way as the biomass, proximate and ultimate analyses being performed. In the case of the coke fraction, its amount was determined as the weight loss experienced by the used catalyst in the TGA test with a heating program of 20 °C min⁻¹ up to 550 °C in air atmosphere. Moreover, elemental analysis of coke was carried out in the same way as that of biomass and char samples.

The bio-oil was characterized by several techniques. In most of the catalytic fast-pyrolysis tests, bio-oil was formed by two phases, being separated by centrifugation. The water content of bio-oil was determined using a Karl-Fischer titration instrument (ASTM E203-08), whilst its elemental composition of C, H, N, S and O (the latter by difference) was calculated with a Thermo-Scientific micro analyser. The bio-oil fraction was considered in a water-free basis, being named as bio-oil*. The components present in bio-oil were analysed by a Gas Chromatograph Mass Spectrometer, GC-MS, Bruker® SCION 436-GC, (Electron Energy 70 eV, Emission 300 V; He flow rate: 1 cm³ min⁻¹; Column WCOT fused silica 30 m x 0.25 mm ID x 0.25 μm). NIST EI-MS spectral library (v2.0) was used for the compounds identification (with a minimum match score of 700). Bio-oil compounds were further grouped in families according to their main functional groups.

Finally, from the weight of the bio-oil and char fractions, and those calculated for coke and gas fractions, the total mass balance was closed to the amount of biomass fed with an experimental error lower than 5 wt% in all tests. Then, the mass yield of any product fraction was calculated according to Eq. (1):

$$\text{Mass yield } i \text{ (wt\%)} = 100 \cdot [\text{mass } i \text{ (g)}/\text{biomass (g)}] \quad (1)$$

where i = gas, char, bio-oil* (bio-oil in water-free basis), water and coke. In addition, Eq. (2) was used to estimate the mass yield of the different components of the gas fraction:

$$\text{Mass yield } j \text{ (wt\%)} = 100 \cdot [\text{mass } j \text{ (g)}/\text{biomass (g)}] \quad (2)$$

where j = H₂, (C₁-C₃)_{paraffins}, (C₂-C₃)_{olefins}, CO and CO₂.

The elemental (C, H and O) mass balances were also assessed from the yield of the different products and their ultimate analyses. Thus, the oxygen distribution, O_{*i*}, between the different i fractions was calculated according to Eq. (3):

$$O_i \text{ (wt\%)} = 100 \cdot [O_i \text{ (g)}/O_{\text{biomass}} \text{ (g)}] \quad (3)$$

where O_{biomass} is the oxygen content in the biomass feed.

The high heating value (HHV) of the biomass and of the different fractions was calculated according to Eq. (4), which is a correlation reported to be valid for solid, liquid and gaseous fuels:⁴⁰

$$\text{HHV}_i \text{ (MJ/kg}^{-1}\text{)} = 0.3491 \cdot \text{C} + 1.1783 \cdot \text{H} + 0.1005 \cdot \text{S} - 0.1034 \cdot \text{O} - 0.0151 \cdot \text{N} - 0.0211 \cdot \text{A} \quad (4)$$

where C, H, O, N, S and A represents carbon, hydrogen, oxygen, nitrogen, sulphur and ash contents of i , expressed in wt% on dry basis. Then, the energy yield of any i fraction was calculated according to Eq. (5):

$$\text{Energy yield } i \text{ (\%)} = 100 \cdot [\text{HHV}_i \cdot \text{mass yield } i / \text{HHV}_{\text{biomass}}] \quad (5)$$

3. Results and discussion

One of the main objectives of this study was to understand better the main pathways through which catalytic pyrolysis of biomass proceeds and the effect of the operation conditions on the yield and quality of bio-oil. Usually, pyrolysis studies have been performed using oxygen content and mass yield of bio-oil as main assessment parameters of the process.^{8,41–43} Here, additional indicators, such as both oxygen and energy distribution among the fractions, are introduced in order to get more realistic outputs about the efficiency of the process/catalyst system. With this purpose, a systematic study was carried out consisting on decoupling both the thermal and catalytic reactions in order to evaluate the influence of three key variables: temperature of the thermal pyrolysis zone; temperature of the subsequent catalytic step and catalyst to biomass ratio.

De-ashed wheat straw (WS-ac) was used as biomass feedstock for the pyrolysis tests. Table 1 summarizes wheat straw proximate and ultimate analyses, as well as the biopolymers composition, before and after de-ashing pretreatment. The biomass de-ashing procedure visibly modified the proximate analysis, increasing the volatiles in 10% and becoming poorer in fixed carbon. Moreover, the composition in biopolymers changes somewhat with an increase of the holocellulose material to the detriment of the lignin content.⁴⁴ The overall effectiveness of this pretreatment was moderate with a total value of 26% de-ashing. However, this percentage reached 98–99% for many of the elements susceptible to interfere in the pyrolysis process, such as alkaline and alkaline earth metals (AAEM):^{18,45} K, Ca, Mg and Na as it is summarized in Table 1. Removal of such inorganic impurities is an effective way to maximize the bio-oil yield since they are known to catalyse carbonization reactions.⁴⁴ Moreover, K promotes gases production by catalysing decarbonylation and decarboxylation reactions of the pyrolysis primary vapors.⁶ On the other hand, other elements, which are expected not to be catalytically active, like Si, were scarcely eliminated.

Table 1. Proximate, ultimate and biopolymers analyses of the raw (WS) and acid-washed (WS-ac) wheat straw biomass samples

Sample	Proximate Analysis, db (wt%)			Ultimate Analysis, daf (wt%)				HHV (MJ/kg _{gas})	Biopolymers distribution (wt%)					
	Ash	Volatile Matter	Fixed Carbon	C	H	N	O		Cellulose	Hemicel.	Lignin			
WS	4.7	75.3	20.0	47.8	5.9	0.5	45.9	17.9	37.8	27.5	34.7			
WS-ac	3.5	83.1	13.4	49.1	6.1	0.5	44.4	18.9	42.3	29.9	27.8			
Sample	Ash elements (wt% · 10 ⁻²)													
	Al	Ba	Ca	Fe	K	Mg	Mn	Na	P	Si	Sn	Sr	Ti	Zn
WS	1.0	0.3	17.3	0.6	28.0	5.0	0.3	4.4	4.7	89.1	0.6	0.3	0.1	0.1
WS-ac	0.6	0.1	0.2	0.3	0.6	0.1	0.0	0.1	0.6	87.2	0.3	0.0	0.0	0.0

db: dry basis

daf: dry ash free

3.1. Influence of the thermal zone temperature

It is well known that biomass pyrolysis is strongly influenced by temperature, in terms of both quantitative and qualitative products distribution. Thus, there is usually a temperature range in which the bio-oil yield can be maximized. The optimal temperature, in terms of bio-oil yield, is generally within the range of 400–550 °C, but it depends on the biomass used as feedstock.⁸ Accordingly, a first set of pyrolysis tests was carried out in the absence of catalyst using the

same reaction conditions but varying the temperature between 475 and 600 °C. Fig. 2 illustrates the product yield (A) and the gas composition (B) attained. Note that the bio-oil yield is given in a water-free basis (denoted as bio-oil*). As expected, higher temperatures lead to larger amount of gases (from 7.1 to 13.5 wt%) and lower yield of char (from 24.4 to 18.4 wt%) in agreement with previous works reported in the literature.^{42,46} Water yield decreases with the temperature, denoting a lower extension of dehydration reactions, whereas the bio-oil* yield reaches a maximum at 550 °C.

Char formation is usually attributed to the thermal carbonization of lignin, which represents 25.9 wt% of the de-ashed wheat straw employed in this study. However, taking into account that oxygen is extensively removed from the lignin fraction during its carbonization and that the ash content of biomass is 3.5 wt%, the mass balance suggests that part of this char was also derived from the holocellulose fraction, primarily hemicellulose.^{6,47} Operating at lower temperatures results in higher yields of char due to a lower extent of thermal decomposition reactions together with a major contribution of condensation reactions.^{33,44} As the temperature increases, less char is produced as a result of the competition between charring and devolatilisation reactions, the latter becoming more favoured.^{46,48}

Fig. 2(B) plots the mass yields of non-condensable gases evolved during pyrolysis, in which CO₂ and CO were the major products during the whole temperature range. Although in a lower extension, significant amounts of gaseous hydrocarbons were also detected in the gas stream, their yield being increased with the temperature. The main components are gaseous olefins, in particular ethylene and propylene. Finally, hydrogen was also present in the gases but in rather small amounts, rising from 0.32 to 2.69 mol% of the gases with increasing the pyrolysis temperature. Steam gasification of the remaining char fraction starts to be noteworthy at high temperatures as denoted by the enhanced production of both CO and H₂ to the detriment of the water formation.

The bio-oil* yield (water-free basis) is positively affected by the increase of the pyrolysis temperature up to 550 °C since the release of larger amounts of pyrolysis vapours is favoured. However, at 600 °C the secondary cracking of pyrolysis vapours start taking precedence over the pyrolysis vapours release, causing a slight decrease in the bio-oil* yield.

From the previous findings, it can be concluded that decarboxylation and decarbonylation are promoted at higher temperatures with a progressively lower contribution of dehydration reactions. Likewise, there is a clear increase on the yield of light hydrocarbons, as a consequence of the aforementioned secondary cracking promotion. This is an undesirable result since it contributes to diminish not only the mass but also the energy yield of the bio-oil. Nevertheless, its effect is counterbalanced by the reduction in the char generation so that the global result is a higher yield of bio-oil*.

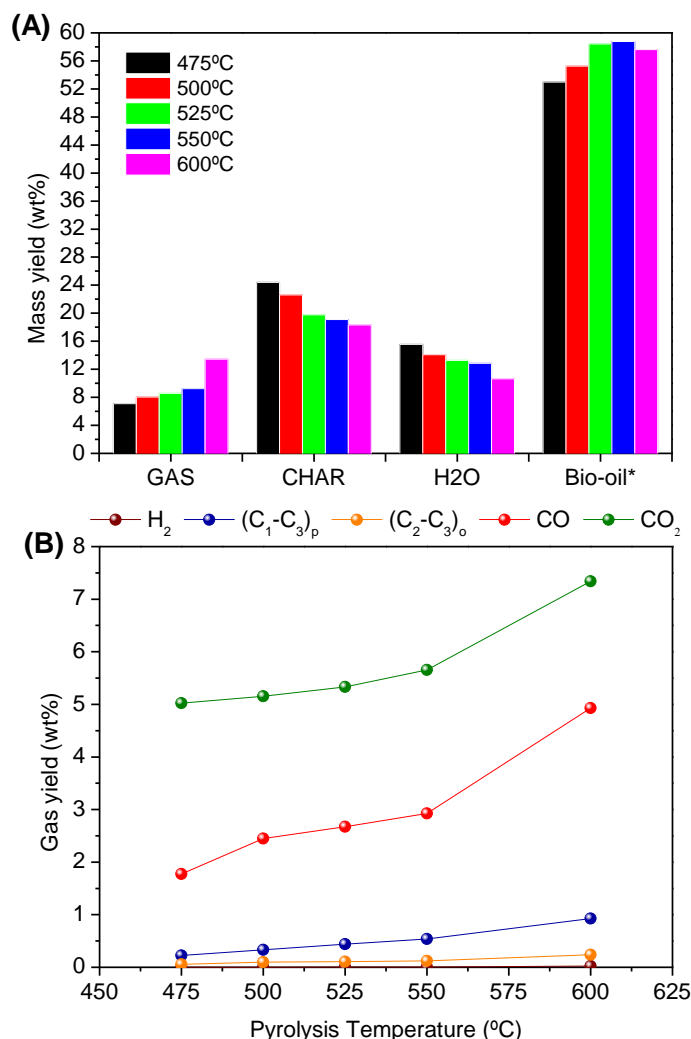


Fig. 2. Products yield (A), and gas composition (B) in the non-catalytic fast-pyrolysis of WS-ac as function of the pyrolysis temperature. (C₁-C₃)_p: paraffins; (C₂-C₃)_o: olefins.

Table 2 reports the elemental analysis (dry basis) and high heating value (HHV) of the char and bio-oil* fractions obtained. In the case of the bio-oil*, no significant differences existed in HHV values as a function of the pyrolysis temperature, which was an expected finding since its composition was just slightly modified. Comparing the raw de-ashed biomass with the bio-oil* there was a decrease in the oxygen concentration from 44.37 to around 40 wt%, which resulted in an increase of the carbon content from 49.08 to around 53 wt%; while that of hydrogen was almost not affected. Accordingly, the HHV also increased from 18.91 in the biomass to 21.8 MJ kg⁻¹ for the bio-oil*. These data show that biomass pyrolysis in the absence of a catalyst is little effective in removing oxygen from the bio-oil* fraction. Regarding the analysis of the char, its oxygen content shows in general a decreasing trend with temperature, due to a higher extent of carbonization reactions.

Most works in the literature assess the biomass catalytic pyrolysis according to the mass yield and oxygen content of the bio-oil*. However, to get a more realistic assessment on the efficiency of the process, other parameters must be evaluated, mainly how the oxygen and chemical energy, initially contained in the biomass, are distributed among the different fractions and products.

Table 2. Elemental analyses and heating value of char and bio-oil* fractions obtained in the non-catalytic fast-pyrolysis of WS-ac as function of the pyrolysis temperature zone.

Temp. (°C)	Char						Bio-oil					
	Ash (wt%)	Elemental analysis (db, wt%)				HHV (MJ/kg _{char})	H ₂ O (wt%)	Bio-oil*				HHV (MJ/kg)
		C	H	N	O			C	H	N	O	
475	15.0	70.5	3.4	0.9	10.2	27.2	22.7	53.8	6.1	0.1	40.0	21.8
500	16.2	72.1	3.0	0.7	8.0	27.5	20.3	52.5	6.3	0.1	41.0	21.6
525	18.5	72.4	3.0	0.8	5.3	27.8	18.5	52.6	6.3	0.1	40.9	21.6
550	19.0	73.0	3.0	0.6	4.4	28.1	18.0	52.7	6.3	0.1	40.8	21.7
600	20.0	70.4	2.5	0.6	6.5	26.4	15.6	52.7	7.0	0.1	40.3	22.4

Fig. 3(A) represents the oxygen distribution as a function of the pyrolysis temperature, whereas Fig. 3(B) illustrates the energy yield corresponding to the different fractions. The bio-oil contains a great part of the oxygen, confirming that a pure thermal treatment does not really promote bio-oil deoxygenation, followed by the water and gaseous fractions, whereas char shows the lowest oxygen accumulation. Working at higher reaction temperatures leads to a lower amount of water and to a decrease of the amount of oxygen contained in the char fraction, increasing the amount of oxygen present in the gases and leading to a maximum of oxygen in bio-oil* at 550 °C.

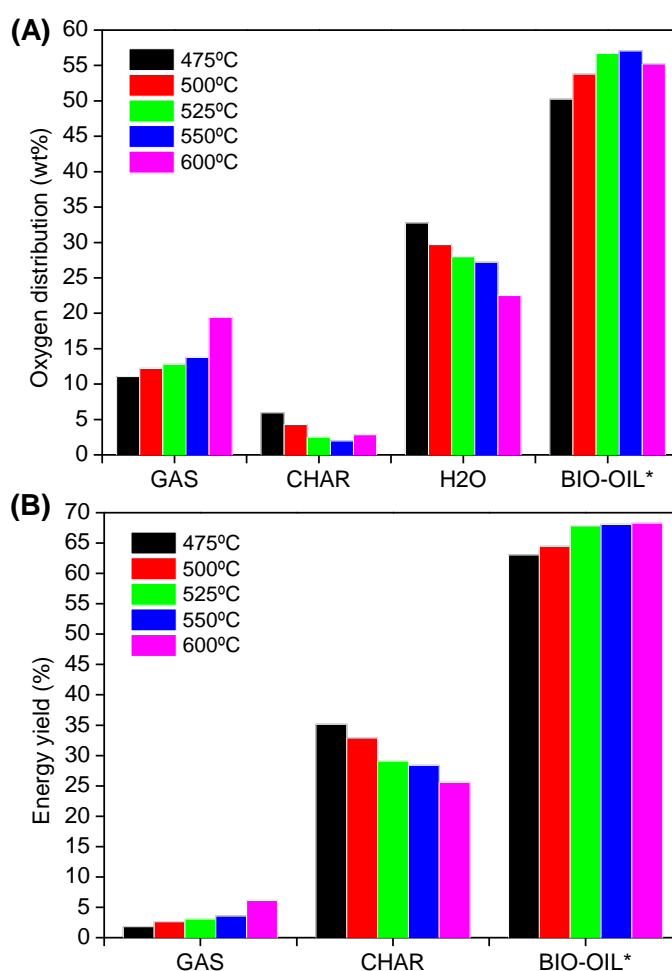


Fig. 3. Oxygen distribution (A), and energy yield (B) in the non-catalytic fast-pyrolysis of WS-ac as function of the pyrolysis temperature.

A different trend is observed when comparing the products in terms of energy yield (Fig. 3(B)). The highest value corresponds with bio-oil*, followed by char and finally the gases. It is remarkable that char may contain up to 34% of the chemical energy that was originally present in the raw biomass, which is a direct consequence of its low oxygen content. Accordingly, reduction of the char formation is an important factor to maximize the bio-oil* energy yield, which can be achieved by working at relatively high temperatures in the pyrolysis zone, although it implies also an enhancement of the gas production. However, if both effects are considered together, the reduction of the char formation with the temperature is predominant, resulting in higher energy yields of the bio-oil* fraction (about 67% in the 500-600 °C range).

3.2. Influence of the catalytic zone temperature

The effect of the catalytic reaction temperature was studied by placing the catalyst bed (H-ZSM-5 zeolite) in-line with the thermal pyrolysis zone, heated with an independent furnace and thermocouple to accurately control the temperature in the catalytic zone (see Fig. 1). Thus, the pyrolysis section was fixed at 550 °C whereas the temperature was varied within the range of 400-500 °C in the catalyst bed. The catalyst to biomass ratio employed was kept constant (0.2) in this series of experiments. Fig. 4 represents the results so obtained in terms of mass yields (A) and gas composition (B), respectively.

As char was entirely produced through thermal pyrolysis and retained in the first zone, its quantity was almost identical in all cases. A distinctive jump in the yields of the other fractions was observed when comparing the purely thermal experiment with the catalytic one, both being performed using the same combination of temperatures in the two reaction zones (550 °C/400 °C). The coupling of the H-ZSM-5 zeolite bed causes a sharp reduction in the bio-oil* yield, while those of gases and water are increased. Moreover, a new fraction appears in the catalytic pyrolysis experiments corresponding to the coke deposited over the zeolite.

Increasing the temperature of the catalytic zone in the range 400-500 °C further reduces the bio-oil* yield, enhancing the production of gases, whereas coke and water formation are quite less affected. As shown in Fig.4(B), the main components in the gases are CO and CO₂, with minor amounts of gaseous paraffins, olefins and hydrogen. In particular CO becomes the major product in the gases when working at a temperature of 450 °C and above, showing that decarbonylation reactions are favoured by increasing the temperature of the catalytic zone.

Among the three possible routes of deoxygenation (dehydration, decarboxylation and decarbonylation) the last one must be minimized from the process efficiency point of view. In this way, Fig. 5 shows how the overall selectivity corresponding to those pathways, estimated from the production (thermal plus catalytic) of H₂O, CO and CO₂, respectively, is affected by the variation of the catalyst bed temperature. It is clearly seen that the increase of temperature favours decarboxylation, and especially decarbonylation, versus dehydration.

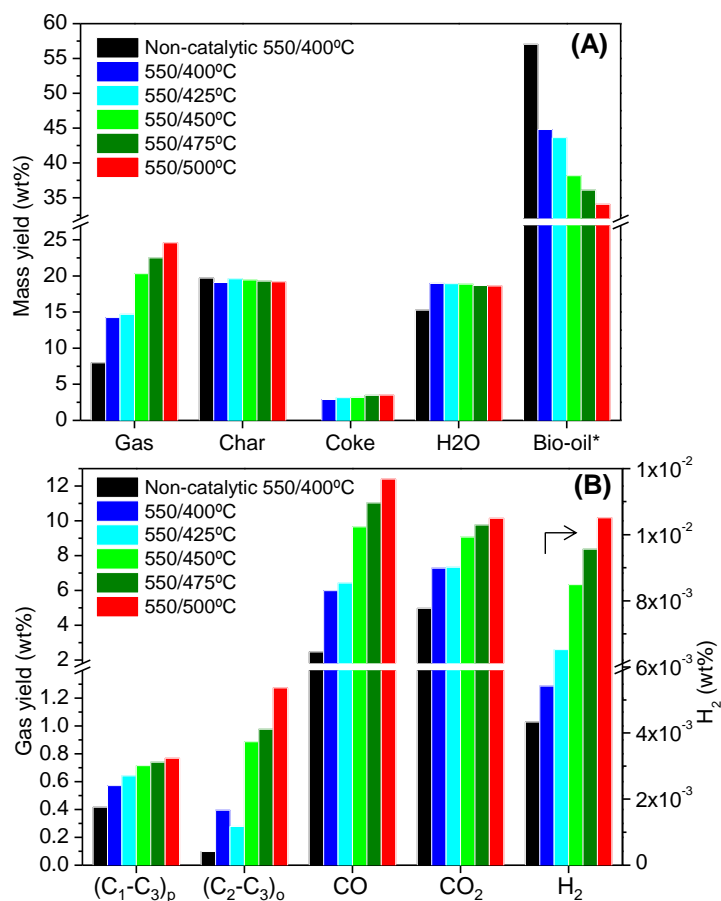


Fig. 4. Products yield (A), and gas composition (B) in the catalytic fast-pyrolysis of WS-ac as function of the catalyst zone temperature. Pyrolysis temperature zone: 550°C. (C₁-C₃)_p: paraffins; (C₂-C₃)_o: olefins.

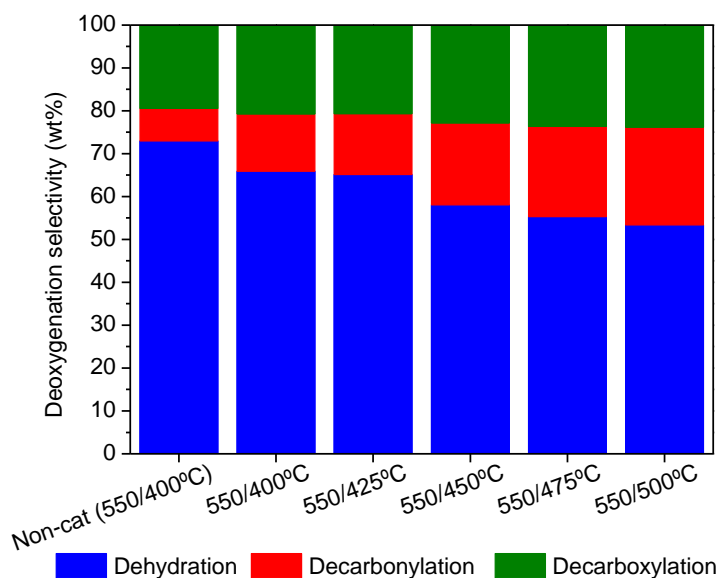


Fig. 5. H-ZSM-5 deoxygenation selectivity in the catalytic fast-pyrolysis tests of WS-ac as function of the catalyst zone temperature.

The distribution of the oxygen initially contained in the biomass among the different fractions is shown in Fig. 6(A). While in the non-catalytic reactions most oxygen was present in the bio-oil*, this trend drastically changed when passing the vapours through the H-ZSM-5 zeolite bed. Thus, in agreement with the promotion of decarbonylation and decarboxylation reactions at higher temperatures, there is a drastic increase in the oxygen contained in the gas phase, which is reflected in the reduction of the oxygen present in the coke and bio-oil* fractions.

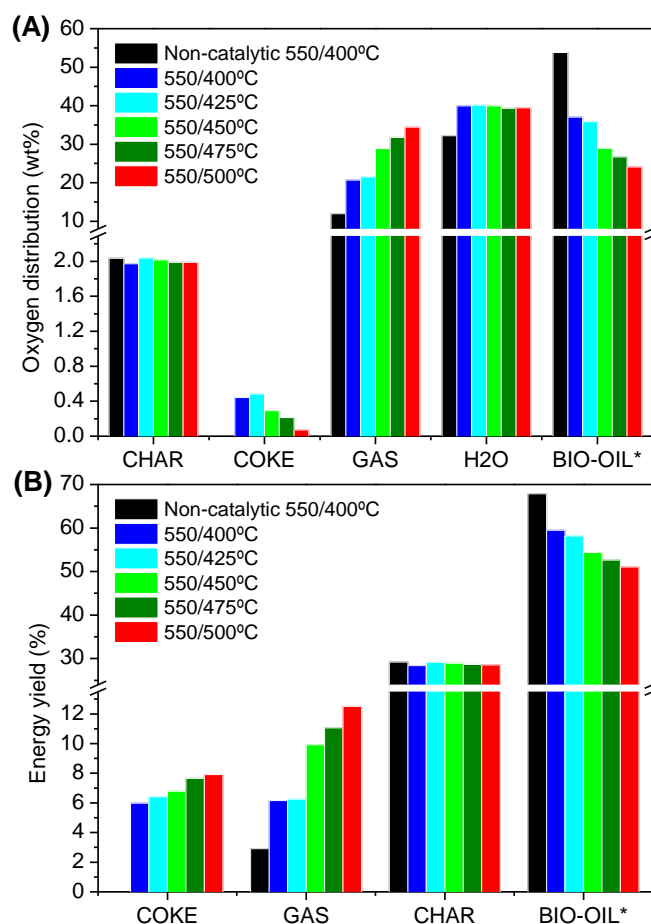


Fig. 6. Oxygen distribution (A), and energy yield (B) in the catalytic fast-pyrolysis of WS-ac as function of the catalytic zone temperature. Pyrolysis temperature zone: 550°C.

These results have a direct effect on the heating value of each fraction, as it can be seen in Table 3 for coke and bio-oil*, as well as on the energy yields, which are represented in Fig. 6(B). Coke deposits, which represent from 13.8 to 20.1 wt% of the spent catalyst weight loss, accounted for just 2.9-3.5 wt% yields (with respect to the biomass fed). However, its contribution is more important in terms of energy yield, as the coke deposits contain between 6 and 8% of the biomass chemical energy. This fact is explained by the coke chemical composition, as it presents a rather low oxygen concentration. Coke formation during biomass catalytic pyrolysis over H-ZSM-5 zeolite reported in the literature varies significantly, 2-12 wt%, depending on a variety of factors such as reactor configuration, operation conditions (temperature, heating rate, etc.) and biomass pretreatment among others.^{21,23,32,33,38,49} In general, the literature values are in good agreement with those here obtained.

Table 3. Parameters of coke and bio-oil* fractions obtained in the catalytic fast-pyrolysis of WS-ac as function of the catalyst temperature zone (pyrolysis temperature zone: 550 °C)

Temp. (°C)	Coke						Bio-oil					
	Coke (wt%)	Elemental analysis (db, wt%)				HHV (MJ/kg _{coke})	H ₂ O (wt%)	Bio-oil*				HHV (MJ/kg)
		C	H	N	O			C	H	N	O	
400	13.8	86.4	7.1	0.1	6.4	37.8	29.7	58.7	6.3	0.1	34.9	24.3
425	14.8	86.8	6.7	0.1	6.4	37.5	30.3	59.0	6.4	0.1	34.5	24.6
450	16.4	88.7	7.3	0.1	3.9	39.2	33.1	61.1	7.0	0.1	31.8	26.3
475	19.1	89.0	8.3	0.1	2.6	40.6	34.1	61.4	7.2	0.2	31.2	26.7
500	20.1	89.8	9.3	0.0	0.9	42.2	35.4	62.2	7.9	0.2	29.7	28.0

Regarding the gaseous fraction, the enhancement in the formation of CO, H₂ and hydrocarbons at higher temperatures causes a rapid increase of its energy yield. Therefore, it is evidenced again the necessity of working at relatively low temperatures in the catalytic zone to reduce the chemical energy lost with the coke and gas fractions, improving consequently the overall energy efficiency of the process.

3.3. Effect of catalyst to biomass ratio

The effect of the catalyst to biomass ratio was investigated by varying the amount of H-ZSM-5 from 0.4 to 2.8 g, and keeping constant the biomass load (4 g). In all these tests, the pyrolysis zone of the reactor was kept at 550 °C, while the temperature of the catalytic bed was fixed at 400°C in order to maximize the mass and energy yield of the bio-oil* fraction.

Fig. 7(A) shows the variation of the proportion of the different fractions obtained by catalytic pyrolysis as a function of the zeolite/biomass ratio. An almost linear decrease of the bio-oil* yield is observed, which goes in parallel to the increase in the formation of gaseous products and coke. As expected, char production remain fairly constant in this series of experiments since there is no direct contact between the char and the catalyst. Likewise, the water yield is little affected by the catalyst/biomass ratio, the largest difference being observed just when comparing the thermal experiment with the catalytic ones. This result indicates that there is just a small amount of OH groups in the bio-oil* that can be removed by the H-ZSM-5 catalyst through dehydration reactions. However, the lower amount of bio-oil* so produced, together with the higher hydrophobicity of their organic components, resulted in phase separation (water rich and organic rich phases, respectively) in the bio-oils obtained with catalyst/biomass ratio > 0.4. The water content in both, aqueous and organic, phases ranged from 60.6 and 15.5 wt% to 88.0 and 7.5 wt%, respectively, when the catalyst to biomass ratio was increased from 0.4 to 0.7.

The data collected in Table 4 show that the percentage of coke, referred to the catalyst weight, decreases from 15.2 to 10.6% by varying the catalyst/biomass ratio from 0.1 to 0.7, although the coke yield regarding the raw biomass weight is significantly increased as shown in Fig. 7(A). In addition, the elemental composition of the coke and its calorific value also changes when varying the amount of catalyst. Thus, the O/H and C/H ratios of this solid fraction decrease appreciably when using higher proportion of H-ZSM-5, leading to carbonaceous deposits richer in hydrogen and, therefore, with superior HHV.

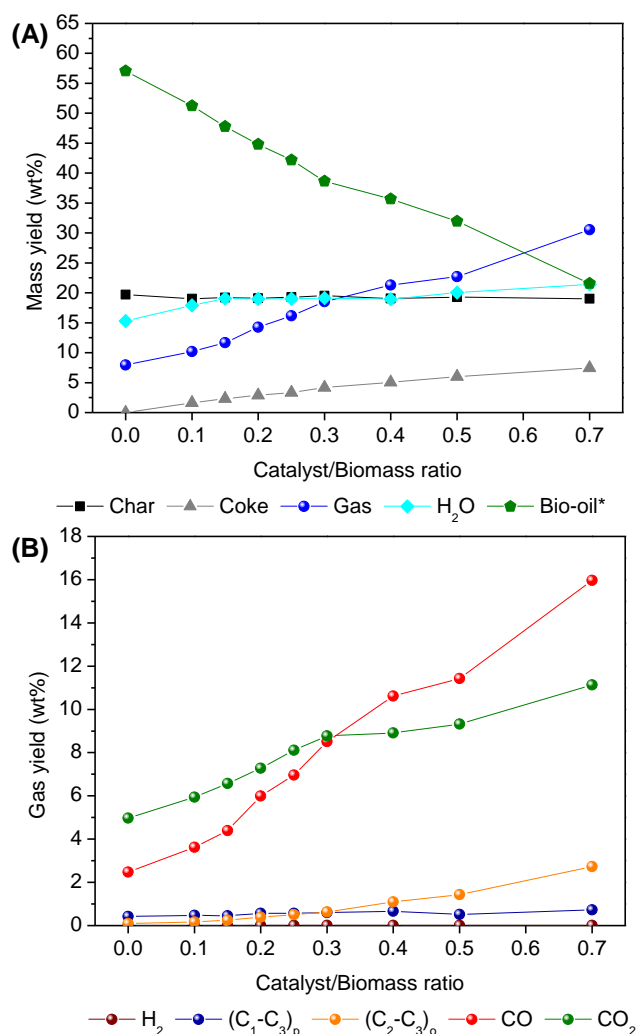


Fig. 7. Products yield (A), and gas composition (B) in the catalytic fast-pyrolysis of WS-ac as function of the catalyst to biomass ratio (0.0-0.7). Pyrolysis/Catalyst temperature zones: 550°C/400°C. (C₁-C₃)_p: paraffins; (C₂-C₃)_o: olefins.

Table 4. Elemental analysis and heating value of coke and bio-oil* fractions obtained in the catalytic fast-pyrolysis of WS-ac at 550 °C/400 °C as function of the catalyst to biomass ratio.

C/B ratio	Coke						Bio-oil					
	Coke in catalyst (wt%)	Elemental analysis (db, wt%)				HHV (MJ/kg _{coke})	H ₂ O (wt%)	Bio-oil*				HHV (MJ/kg _{bio-oil*})
		C	H	N	O			Elemental analysis (db, wt%)				
C	H	N	O	C	H	N	O					
0.10	15.2	82.3	7.5	0.8	9.4	36.6	25.9	57.3	6.0	0.1	36.6	23.2
0.15	14.7	81.0	8.8	0.9	9.3	37.6	28.5	58.9	6.0	0.1	35.0	24.0
0.20	13.8	80.2	9.6	1.1	9.1	38.4	29.7	58.7	6.3	0.1	34.9	24.3
0.25	13.7	79.6	10.7	1.0	8.7	39.4	31.1	60.4	6.4	0.1	33.1	25.2
0.30	13.4	79.7	11.0	1.0	8.3	39.9	33.1	60.6	6.7	0.1	32.6	25.6
0.40	12.7	78.9	12.3	1.1	7.7	41.2	34.7	61.5	6.4	0.1	32.0	25.7
0.50	12.0	79.2	13.3	0.6	6.9	42.6	38.5	63.7	6.1	0.2	30.0	26.3
0.70	10.6	80.0	14.1	0.8	5.1	44.0	49.8	72.6	6.1	0.2	21.1	30.4

Fig. 7(B) displays the evolution of the gas composition as a function of the catalyst/biomass ratio. As in the assays discussed in the previous sections, the most abundant components of the gas fraction are CO and CO₂. It is worth noting that, while when using low amounts of catalyst decarboxylation is more important, for zeolite to biomass ratio higher than 0.3 decarbonylation becomes the dominant route. Significant changes are also observed in other components of the

gas fraction, such as C₂-C₃ olefins, whose concentration remarkably increases. As a consequence, the relative proportion of alkanes (methane to propane) and hydrogen is overpassed by light alkenes.

As it has been above mentioned, reducing the oxygen content in the liquid fraction unavoidably results in lower mass yield of bio-oil* but improved HHV values. In order to study thoroughly these variations, the bio-oil* oxygen concentration is plotted as a function of the bio-oil* mass yield in Fig. 8(A). In this graph, the curves that correspond to the three theoretical deoxygenation pathways (dehydration, decarboxylation and decarbonylation) have been also represented from the non-catalytic bio-oil* point.

It is remarkable that the experimental curve follows a complex trend as it starts close to the decarboxylation pathway but, as the catalyst mass ratio is increased, is shifted towards the left reaching the decarbonylation curve. Moreover, for high catalyst/biomass ratios the experimental bio-oil* yield values are quite lower than those predicted even by the decarbonylation pathway. This apparently anomalous behaviour can be explained by the formation of coke and gaseous hydrocarbons, as coking and cracking reactions occur by conversion of bio-oil components. Therefore, it can be concluded that the sharp influence of the catalytic treatment over the bio-oil* yield is not only due to the different deoxygenation pathways but also to the formation of coke deposits on the catalyst and the occurrence of cracking reactions yielding light olefins.

This finding has a very important effect in terms of energy yields, as depicted in Fig. 8(B). The bio-oil* energy yield is strongly reduced when increasing the catalyst/biomass ratio. Thus, for the highest catalyst/biomass ratio the bio-oil* energy yield is less than half of that corresponding to the non-catalytic bio-oil*. This energy is lost in the gases by formation mainly of CO, light hydrocarbons and hydrogen (see the inset in Fig. 8(B)) and in the coke fraction. Thus, the energy yield of the latter reaches values as high as 17% for the largest catalyst/biomass ratio, as a consequence of both the increased formation of coke and the enhanced H content of these carbonaceous deposits (Table 4). This finding denotes the high relevance of avoiding the formation of both coke and gaseous hydrocarbons in biomass catalytic pyrolysis to achieve the production of bio-oil* with high energy yields.

Fig. 8(C) compares the selectivity towards the deoxygenation pathways, estimated from the oxygen amount in the form of H₂O, CO and CO₂, between the thermal and the catalytic steps and how the latter is affected by the variation of the catalyst/biomass ratio. In the absence of catalyst and at low catalyst/biomass ratios the predominant deoxygenation pathway is dehydration. However, as the catalyst/biomass ratio is varied in the range 0.1 – 0.3, the decarbonylation selectivity is sharply increased, confirming that the H-ZSM-5 catalyst promotes in a large extension the oxygen removal through CO formation. Finally, for catalyst/biomass ratios in the range 0.4 – 0.7 the pattern of deoxygenation selectivity does not change significantly.

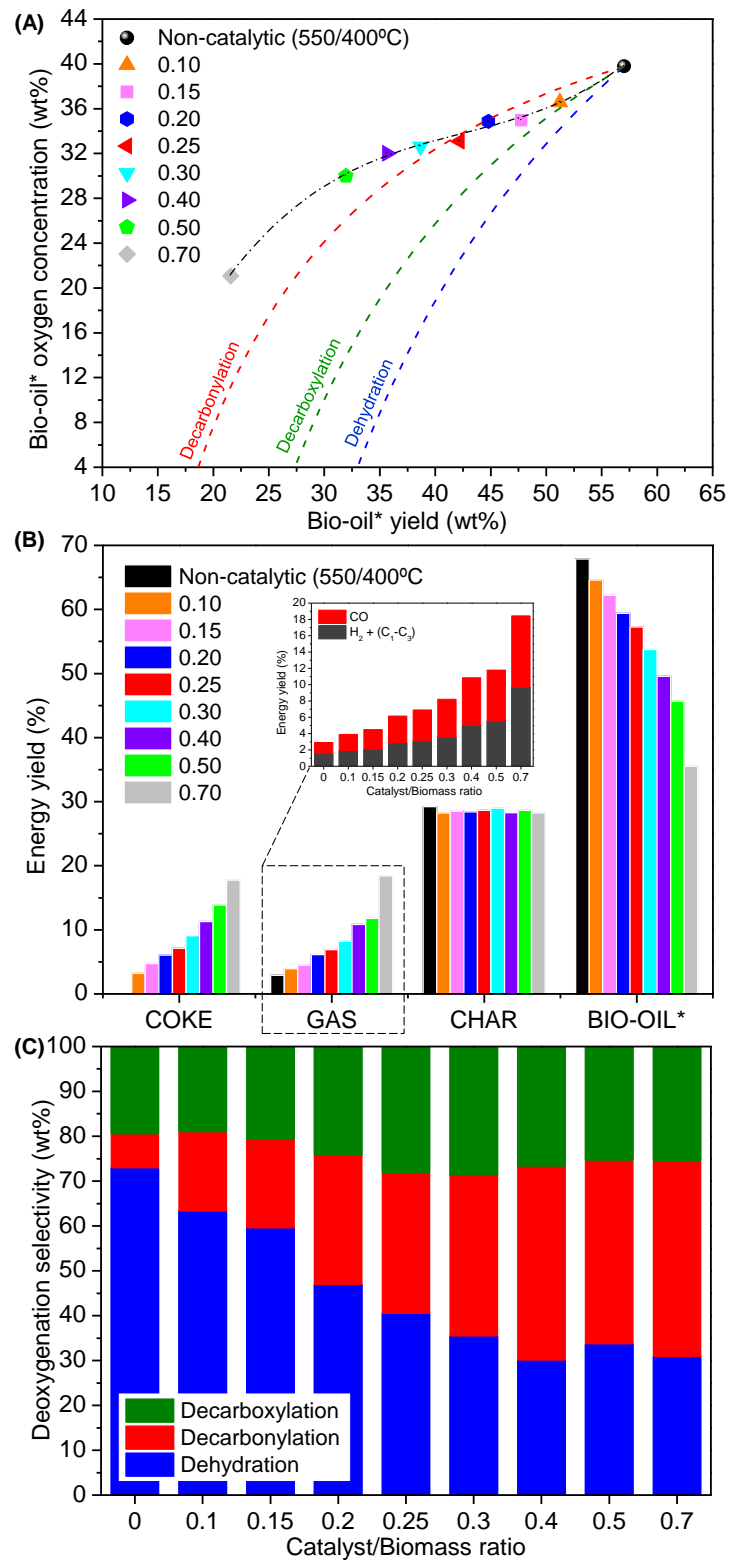


Fig. 8. Catalytic fast-pyrolysis of WS-ac at different catalyst to biomass ratios (pyrolysis/catalyst temperature zones: 550°C/400°C): (A) bio-oil* oxygen concentration versus bio-oil* yield; (B) energy yield distribution of pyrolysis products; and (C) thermal and catalytic deoxygenation selectivity.

3.4. Effect of operation conditions on the bio-oils composition

Despite the limitations of GC-MS for ascertain the complex chemical composition of bio-oils, this technique can provide some useful insights into the effect of the operation variables on the mechanism of catalytic pyrolysis by monitoring variations in the concentration of the main chemicals families present in this liquid fraction. These families have been classified in this work according to nine groups: carboxylic acids (AC), aldehydes (ALD), alcohols (ALC), ketones and ethers (KET & ETH), furans (FUR), amines and amides (AMN & AMD), oxygenated aromatics (O-AR), aromatic hydrocarbons (AR), sugars (SUG) and a last group representing non-identified or unknown compounds (UNK). However, it should be kept in mind that high molecular weight oligomers produced by partial depolymerisation of the biomass cannot be detected by this technique.

Fig. 9 shows the semi-quantitative results (expressed as % of relative area) of the bio-oil's composition in terms of the main chemical groups obtained by fast-pyrolysis of WS-ac. The reaction mechanism for the biomass components decomposition during fast-pyrolysis has been previously studied in the literature.^{13,24,26,55,56} Fig. 10 shows a simplified scheme of the main transformation routes occurring during the lignocellulose fast-pyrolysis that can helps to understand the catalytic and non-catalytic decomposition mechanisms. This scheme has been derived from previous literature works, as well as from the results here commented.

Fig. 9(A) shows the composition of the non-catalytic bio-oil* obtained at different pyrolysis temperatures. The most abundant components are sugars, mainly levoglucosan, which is derived from cellulose pyrolysis. Likewise, degradation of hemicellulose leads to furans and lignin decomposition generates both oxygenated aromatics and small oxygenates. Acetic acid among the carboxylic acids, furfural among the furans, creosol and other substituted methoxy-phenols among the group of oxygenated aromatics, and 2,2-dimethoxypropane as representative ketone, are present in relative high concentration in the thermal bio-oil.

Variation of the pyrolysis temperature in the non-catalytic tests alters only moderately the distribution of the different chemicals groups in the bio-oil. Nevertheless, within each chemical family, some changes in the relative proportion of the different components are observed, such as for example for glycolaldehyde, whose concentration grows with temperature. Similarly, levoglucosan proportion slightly increases from 32 to 41 area % with the reaction temperature. This last observation is consistent with previous reports that confirm that levoglucosan is thermally stable under pyrolysis conditions in absence of catalyst.^{6,51,52}

The use of H-ZSM-5 has a profound influence on the chemicals composition of the bio-oils. Fig. 9(B) displays the distribution of the main chemical groups of the catalytic bio-oil obtained varying the catalyst bed temperature. Differences between the catalytic liquid fraction and the thermal bio-oil become evident, mainly regarding the lower sugar content and the larger proportion of aromatics in the former. In this way, it is well-known that H-ZSM-5 zeolite is an effective catalyst the production of aromatic hydrocarbons production from pyrolysis vapours.^{6,53} In addition, the contribution of ketones, ethers, and furans tend to be larger for the bio-oils obtained using H-ZSM-5.

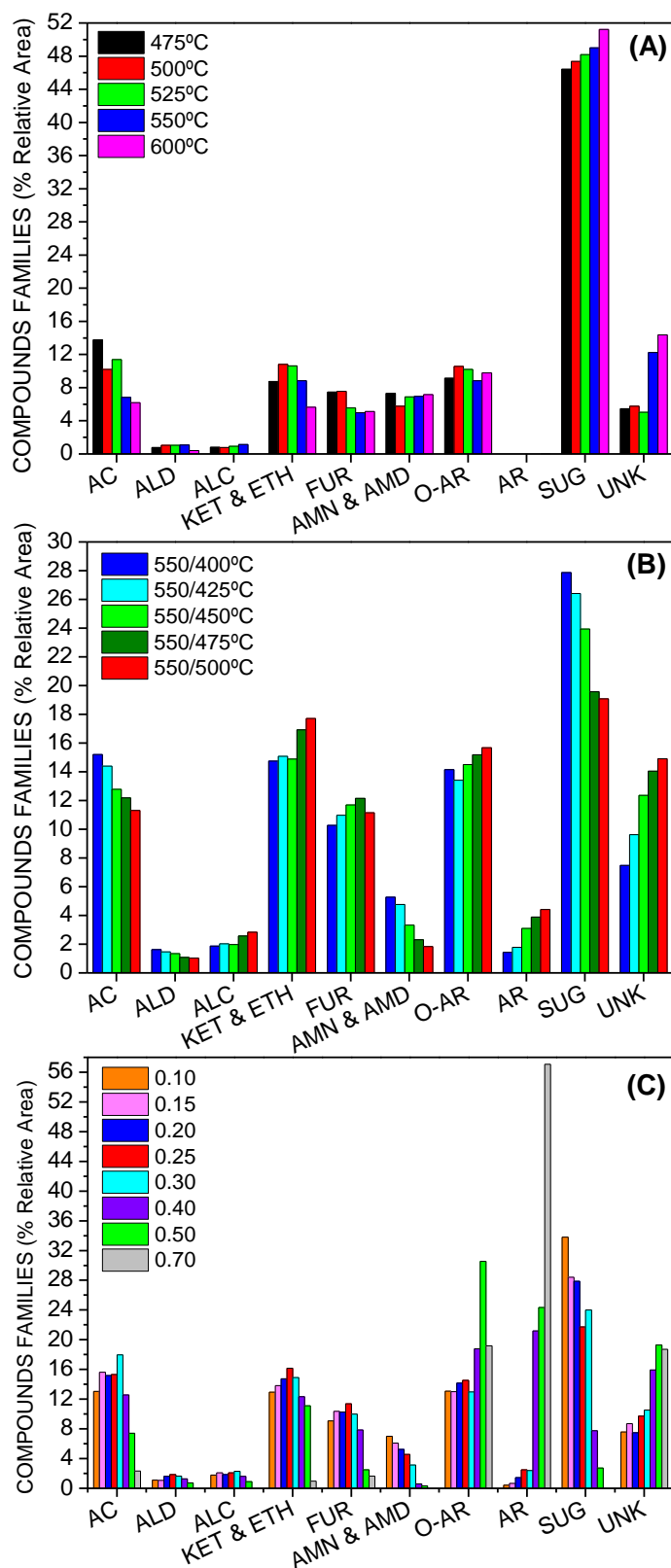


Fig. 9. Main compound families in the bio-oil obtained by fast-pyrolysis of WS-ac. (A) non-catalytic tests at different pyrolysis zone temperature, (B) catalytic tests at different catalytic zone temperature, and (C) catalytic tests at 550°C/400°C and different catalyst to biomass ratio (0.1-0.7).

On the other hand, these results show that the variation of the catalytic bed temperature in the 400–500 °C range has a significant effect. Increasing the operation temperature leads to a progressive reduction in the concentration of acetic acid, which according to Gayubo et al.⁵⁴ first undergoes ketonization to form acetone, and then it follows the same reaction pathways of acetone to form olefins and eventually aromatics.⁶ In parallel, catalytic treatments at higher temperatures lead to a gradual increment of the contribution of ketones and ethers. Due to the great number of chemicals ascribed to this category (more than 40 different molecules belonging to this group have been identified), it is challenging to ascertain the exact transformation routes taking place, but some tendencies can be observed. Thus, formation of cyclic pentanones significantly rises with temperature, which may be produced from sugars, possibly via pyran intermediates.⁵¹ At the same time generation of various benzofurans is also observed to increase with temperature, which may constitute intermediates or by-products of the aromatic formation. It is also worth mentioned that the increase of the catalyst bed temperature favours the formation of phenols and methoxyphenols, most likely due to the higher efficiency of the depolymerisation of lignin fragments.

An important fact is that levoglucosan is catalytically converted over H-ZSM-5. During catalytic pyrolysis, levoglucosan may undergo a variety of reactions, such as dehydration to form furans.^{13,24,47} These furans can be then converted by a series of acid-catalyzed reactions inside the pores of the zeolite to form aromatics and olefins,^{13,47,51} but also could polymerize to form coke on the catalyst.⁴⁷ In this way, several studies have proposed that H-ZSM-5 zeolite promotes the formation of aromatics through the Diels-Alder condensation and dehydration of furans molecules with light alkenes such ethylene or propylene.^{31,55,56} Detection of growing concentrations of these small olefins in the gas phase with increasing the catalytic bed temperature supports this route for the formation of aromatics. On the other hand, the higher percentage of coke deposited on the catalysts at high temperatures can be also related to the larger concentration of polyaromatic hydrocarbons (PAH) being detected.

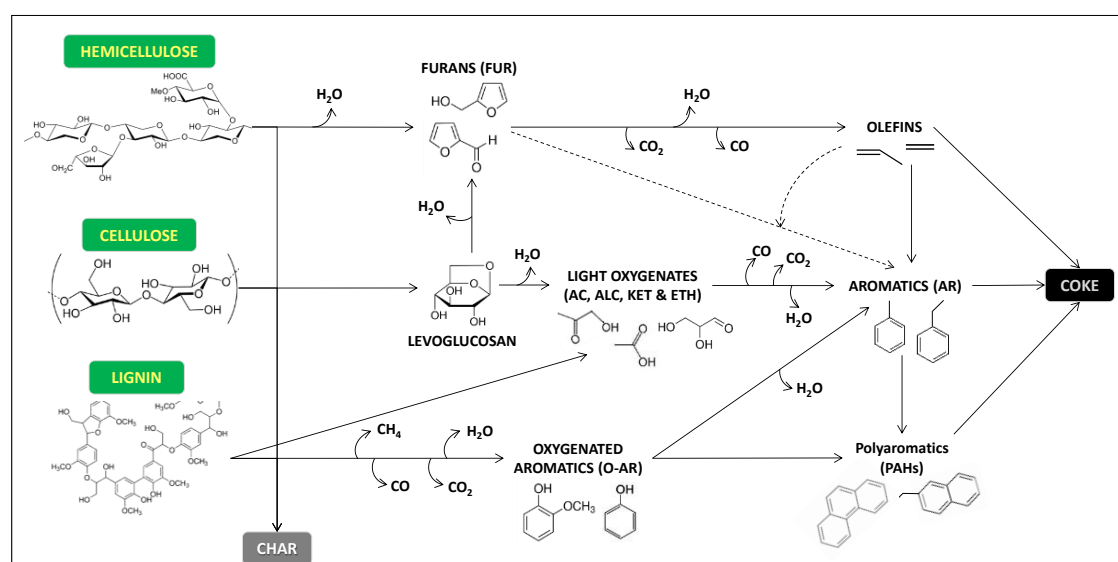


Fig. 10. Scheme proposed showing the main pathways for the catalytic fast-pyrolysis of lignocellulose.

Variations in the product distribution in the bio-oil obtained with different catalyst to biomass ratio are displayed in Fig. 9(C). In the case of the bio-oils produced with

catalyst/biomass ratios over 0.3, the high water concentration induces the separation of the liquid product in two phases, as it has been earlier commented. However, for the sake of a fair comparison within the whole series of tests, the mixture of both the aqueous and the organic components were analysed.

As it can be appreciated in Fig 9(C), changing the H-ZSM-5 proportion has a significant effect in all the chemical families, in particular for the tests carried out with elevated catalysts loadings. Thus, the share of anhydrosugars drops from 34% area to negligible values by increasing the catalyst/biomass ratio from 0.1 to 0.7, while the opposite is observed for aromatic hydrocarbons. These dramatic variations confirm that the removal of sugars is correlated to the formation of aromatics, with furans and light olefins as intermediates. In this way, a maximum is observed in the proportion of furans for a catalyst/biomass ratio of 0.25 denoting their role of reaction intermediates. It is remarkable that most small oxygenated compounds (carboxylic acids, ketones, ethers alcohols and aldehydes) are almost completely converted for high catalyst/biomass ratio. Based on the evolution of the gas composition, deoxygenation of these families occurs mainly by decarbonylation leading to the formation of light olefins (mainly ethylene and propylene). The latter are very reactive compounds that may undergo a variety of transformations. This is the case of the generation of aromatic hydrocarbons, by cyclization-dehydrogenation reactions or through Diels-Alder condensation with furans.^{31,55} Likewise, light olefins may act as precursors to form paraffinic coke, which agrees well with the progressive increase observed in the H/C ratio of the coke deposits from 1.09 to 2.13 as the catalyst/biomass ratio is varied in the range 0.1-0.7. Finally, it must be pointed out that oxygenated aromatics tend to increase with the catalyst/biomass ratio, being not completely converted even for the highest value of this ratio. This result shows that this family of compounds are difficult to be deoxygenated over the H-ZSM-5 catalyst at least under the conditions employed in these experiments.

4. Conclusions

A systematic study on biomass catalytic pyrolysis has been performed decoupling the thermal and catalytic reaction zones in order to evaluate the influence of three key process variables: temperature of thermal pyrolysis zone; temperature of subsequent catalytic reactions and catalyst to biomass ratio.

Acid pretreatment caused the partial biomass de-ashing with a moderate overall effectiveness (26%). However, this percentage reached 98-99% for many of the elements susceptible to interfere in the pyrolysis process, such as alkaline and alkaline earth metals (K, Ca, Mg and Na). Removal of such inorganic impurities is an effective way to maximize the bio-oil yield since they are known to catalyse biomass carbonization and/or gas production by decarbonylation and decarboxylation reactions.

The increase in the thermal zone temperature within the range 475-600 °C leads to lower yield of char and larger amount of gases due to a higher extent of both primary thermal decomposition reactions and secondary cracking of the pyrolysis vapours. When comparing the different fractions in terms of energy yield, the highest value corresponds with bio-oil*, followed by char and finally the gases. Nevertheless, char may contain up to 34% of the chemical energy in the raw biomass, which is a direct consequence of its low oxygen content. Accordingly, reduction of the char formation is important to maximize the bio-oil energy yield, which can be

achieved by working at high temperatures in the pyrolysis zone, although it also implies an enhancement of the gas production. In the purely thermal process, deoxygenation takes place mainly by dehydration with a lower contribution of decarboxylation and decarbonylation. This oxygen removal affects mainly to the char fraction, being little effective for reducing the bio-oil* oxygen content.

Regarding the effect of the catalyst bed temperature, its variation in the 400-500 °C range further reduces the bio-oil* yield, enhancing the production of gases, whereas water formation is quite less affected. The main components in the gases are CO and CO₂, with minor amounts of gaseous hydrocarbons and hydrogen. CO becomes the major product when working at a temperature of 450 °C and above, showing that decarbonylation reactions are favoured by increasing the temperature of the catalytic zone.

A large range of catalyst/biomass ratios (0.1-0.7) was covered to find out the main reaction pathways from the early stages of the catalytic bio-oil upgrading process. It was observed that increasing the catalyst/biomass ratio caused an almost linear decrease of the bio-oil* yield, which occurred in parallel to the increase in the formation of gaseous products: CO, CO₂, ethylene and propylene. For catalyst/biomass ratios larger than 0.3, decarbonylation became the dominant deoxygenation route. Likewise, in contrast with the enhancement observed in the C₂-C₃ olefins yield, the production of gaseous paraffins was quite less affected by the increase of the catalyst/biomass ratio.

At high H-ZSM-5 zeolite loadings the bio-oil* deoxygenation degree increases dramatically, which leads to an oxygen concentration in this fraction as low as 10 wt%, although at the expenses of reducing sharply its mass and energy yield. The distribution of the chemical energy initially contained in the raw biomass among the different fractions shows the relevance of reducing as much as possible the formation of coke and gaseous hydrocarbons during the catalytic step to improve the mass and energy yield of bio-oil*.

GC-MS analyses of the bio-oil* fraction have provided useful information to discern the effect of the operation variables on the main biomass catalytic pyrolysis pathways. As expected, the use of H-ZSM-5 had a strong impact on the chemicals detected in the bio-oil*. In particular, the increase in the catalyst/biomass ratio changed sharply the distribution of all the chemical families, with remarkable increments in the proportion of aromatics compounds (both oxygenated and hydrocarbons), whereas sugars, furans, carboxylic acids and most oxygenated products were almost completely converted.

Acknowledgements

Authors gratefully acknowledge the financial support from the European Union Seventh Framework Programme (FP7/ 2007-2013) under grant agreement n°604307 (CASCATBEL project). CIEMAT (Spain), and in particular Dr. Ignacio Ballesteros, are acknowledged for assessing the biopolymers composition of the biomass.

References

- 1 G. W. Huber, S. Iborra and A. Corma, *Chem. Rev.*, 2006, **106**, 4044–4098.
- 2 Y. Su, P. Zhang and Y. Su, *Renew. Sustain. Energy Rev.*, 2015, **50**, 991–1003.
- 3 T. Koizumi, *Renew. Sustain. Energy Rev.*, 2015, **52**, 829–841.

- 4 S. N. Naik, V. V. Goud, P. K. Rout and A. K. Dalai, *Renew. Sustain. Energy Rev.*, 2010, **14**, 578–597.
- 5 S. K. Karmee, *Renew. Sustain. Energy Rev.*, 2016, **53**, 945–953.
- 6 C. Liu, H. Wang, A. M. Karim, J. Sun and Y. Wang, *Chem. Soc. Rev.*, 2014, **43**, 7594–7623.
- 7 D. A. Bulushev and J. R. H. Ross, *Catal. Today*, 2011, **171**, 1–13.
- 8 A. Bridgwater, *Biomass Bioenergy*, 2012, **38**, 68–94.
- 9 A. Bridgwater and G. Peacocke, *Renew. Sustain. Energy Rev.*, 2000, **4**, 1–73.
- 10 D. A. Ruddy, J. A. Schaidle, J. R. Ferrell III, J. Wang, L. Moens and J. E. Hensley, *Green Chem.*, 2014, **16**, 454–490.
- 11 J. P. Diebold, *A Review of the Chemical and Physical Mechanisms of the Storage Stability of Fast Pyrolysis Bio-Oils*, Golden, Colorado, 2000.
- 12 D. Meier, B. van de Beld, A. V. Bridgwater, D. C. Elliott, A. Oasmaa and F. Preto, *Renew. Sustain. Energy Rev.*, 2013, **20**, 619–641.
- 13 T. Carlson, J. Jae, Y. Lin, G. Tompsett and G. Huber, *J. Catal.*, 2010, **270**, 110–124.
- 14 E. Taarning, C. M. Osmundsen, X. Yang, B. Voss, S. I. Andersen and C. H. Christensen, *Energy Environ. Sci.*, 2011, **4**, 793–804.
- 15 D. Fabbri, C. Torri and V. Baravelli, *J. Anal. Appl. Pyrolysis*, 2007, **80**, 24–29.
- 16 B. Zhang, Z. Zhong, P. Chen and R. Ruan, *Bioresour. Technol.*, 2015, **197**, 79–84.
- 17 X. Zhang, L. Sun, L. Chen, X. Xie, B. Zhao, H. Si and G. Meng, *J. Anal. Appl. Pyrolysis*, 2014, **108**, 35–40.
- 18 K. Wang, J. Zhang, B. H. Shanks and R. C. Brown, *Appl. Energy*, 2015, **148**, 115–120.
- 19 G. Yildiz, F. Ronsse, R. Venderbosch, R. Van Duren, S. R. a. Kersten and W. Prins, *Appl. Catal. B Environ.*, 2015, **168-169**, 203–211.
- 20 C. Mukarakate, M. J. Watson, J. ten Dam, X. Baucherel, S. Budhi, M. M. Yung, H. Ben, K. Iisa, R. M. Baldwin and M. R. Nimlos, *Green Chem.*, 2014, **16**, 4891–4905.
- 21 J. Feroso, H. Hernado, P. Jana, I. Moreno, J. Prech, C. Ochoa-Hernández, P. Pizarro, J. M. Coronado, J. Cejka and D. P. Serrano, *Catal. Today*, 2016, **277**, 171–181.
- 22 H. Cerqueira, P. Ayrault, J. Datka and M. Guisnet, *Micropor. Mesopor. Mater.*, 2000, **38**, 197–205.
- 23 A. Aho, N. Kumar, K. Eränen, T. Salmi, M. Hupa and D. Y. Murzin, *Fuel*, 2008, **87**, 2493–2501.
- 24 D. J. Mihalcik, C. A. Mullen and A. A. Boateng, *J. Anal. Appl. Pyrolysis*, 2011, **92**, 224–232.
- 25 A. Sharma, V. Pareek and D. Zhang, *Renew. Sustain. Energy Rev.*, 2015, **50**, 1081–1096.
- 26 M. Asadieraghi and W. M. A. Wan Daud, *Energy Convers. Manag.*, 2015, **101**, 151–163.

- 27 R. H. Venderbosch, *ChemSusChem*, 2015, **8**, 1306–1316.
- 28 D. Carpenter, T. L. Westover, S. Czernik and W. Jablonski, *Green Chem.*, 2014, **16**, 384–406.
- 29 K. Raveendran, A. Ganesh and K. Khilar, *Fuel*, 1995, **74**, 1812–1822.
- 30 P. Das, A. Ganesh and P. Wangikar, *Biomass and Bioenergy*, 2004, **27**, 445–457.
- 31 C. Dorado, C. A. Mullen and A. A. Boateng, *Appl. Catal. B Environ.*, 2015, **162**, 338–345.
- 32 H. Zhang, R. Xiao, H. Huang and G. Xiao, *Bioresour. Technol.*, 2009, **100**, 1428–1434.
- 33 P. T. Williams and N. Nugranad, *Energy*, 2000, **25**, 493–513.
- 34 Y. Fan, Y. Cai, X. Li, N. Yu and H. Yin, *J. Anal. Appl. Pyrolysis*, 2014, **108**, 185–195.
- 35 S. R. Naqvi, Y. Uemura, S. Yusup, Y. Sugiur, N. Nishiyama and M. Naqvi, *Energy Procedia*, 2015, **75**, 793–800.
- 36 P. T. Williams and P. A. Horne, *Fuel*, 1995, **74**, 1839–1851.
- 37 J. Jae, R. Coolman, T. J. Mountziaris and G. W. Huber, *Chem. Eng. Sci.*, 2014, **108**, 33–46.
- 38 O. D. Mante and F. A. Agblevor, *Biomass Convers. Biorefinery*, 2011, **1**, 203–215.
- 39 J. B. Sluiter, R. O. Ruiz, C. J. Scarlata, A. D. Sluiter and D. W. Templeton, *J. Agric. Food Chem.*, 2010, **58**, 9043–9053.
- 40 S. A. Channiwala and P. P. Parikh, *Fuel*, 2002, **81**, 1051–1063.
- 41 A. Demirbas, *Fuel Process. Technol.*, 2007, **88**, 591–597.
- 42 M. Garcia-Perez, X. S. Wang, J. Shen, M. J. Rhodes, F. Tian, W.-J. Lee, H. Wu and C.-Z. Li, *Ind. Eng. Chem. Res.*, 2008, **47**, 1846–1854.
- 43 S. Papari and K. Hawboldt, *Renew. Sustain. Energy Rev.*, 2015, **52**, 1580–1595.
- 44 I.-Y. Eom, J.-Y. Kim, S.-M. Lee, T.-S. Cho, H. Yeo and J.-W. Choi, *Bioresour. Technol.*, 2013, **128**, 664–672.
- 45 T. Wigley, A. C. K. Yip and S. Pang, *J. Anal. Appl. Pyrolysis*, 2015, **113**, 296–306.
- 46 C. Di Blasi, G. Signorelli, C. Di Russo and G. Rea, *Ind. Eng. Chem. Res.*, 1999, **38**, 2216–2224.
- 47 K. Wang, K. H. Kim and R. C. Brown, *Green Chem.*, 2014, **16**, 727–735.
- 48 J. L. Figueiredo, C. Valenzuela, A. Bernalte and J. M. Encinar, *Fuel*, 1989, **68**, 1012–1016.
- 49 S. Stephanidis, C. Nitsos, K. Kalogiannis, E. F. Iliopoulou, A. A. Lappas and K. S. Triantafyllidis, *Catal. Today*, 2011, **167**, 37–45.
- 50 M. S. Mettler, D. G. Vlachos and P. J. Dauenhauer, *Energy Environ. Sci.*, 2012, **5**, 7797–7809.
- 51 H. Kawamoto, W. Hatanaka, and S. Saka, *J. Anal. Appl. Pyrolysis*, 2003, **70**, 303–313.

- 52 J. D. Adjaye and N. N. Bakhshi, *Fuel Process. Technol.*, 1995, **45**, 185–202.
- 53 A. G. Gayubo, A. T. Aguayo, A. Atutxa, R. Aguado, M. Olazar, and J. Bilbao, *Ind. Eng. Chem. Res.*, 2004, **43**, 2619–2626.
- 54 Y.-T. Cheng and G. W. Huber, *Green Chem.*, 2012, **14**, 3114–3125.
- 55 A. Corma, G. Huber, L. Sauvanaud, and P. Oconnor, *J. Catal.*, 2007, **247**, 307–327.

Article 7

Engineering the acidity and accessibility of the zeolite ZSM-5 for efficient bio-oil upgrading in catalytic pyrolysis of lignocellulose

Green Chemistry, 2018, 20(15), 3499-3511

Green Chemistry



PAPER [View Article Online](#)
[View Journal](#) | [View Issue](#)

 Check for updates

Engineering the acidity and accessibility of the zeolite ZSM-5 for efficient bio-oil upgrading in catalytic pyrolysis of lignocellulose†

Cite this: *Green Chem.*, 2018, 20, 3499

Héctor Hernando, ^a Ana M. Hernández-Giménez,^b Cristina Ochoa-Hernández, ^{†c} Pieter C. A. Bruijninx, ^b Klaartje Houben, ^d Marc Baldus, ^d Patricia Pizarro,^{a,e} Juan M. Coronado, ^a Javier Feroso,^a Jiří Čejka, ^c Bert M. Weckhuysen ^b and David P. Serrano ^{*a,e}

Impact JCR factor, (JCR 2017): 8.586

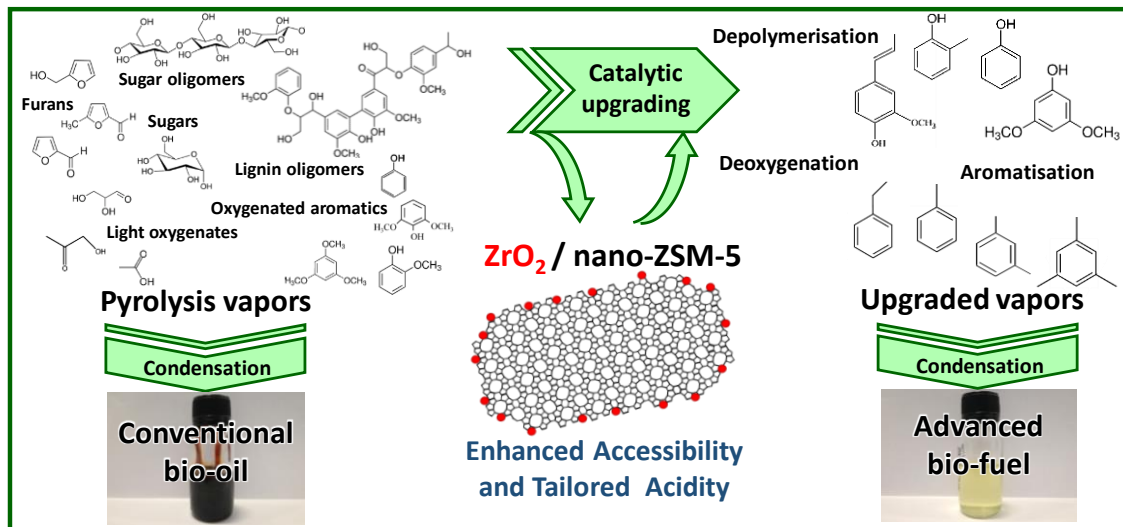
Category: Multidisciplinary Chemistry. 21 of 171 (Q1)

ABSTRACT

The properties of the zeolite ZSM-5 have been optimised for the production and deoxygenation of the bio-oil* (bio-oil on water-free basis) fraction by lignocellulose catalytic pyrolysis. Two ZSM-5 supports possessing high mesopore/external surface area, and therefore enhanced accessibility, have been employed to promote the conversion of the bulky compounds formed in the primary cracking of lignocellulose. These supports are a nanocrystalline material (n-ZSM-5) and a hierarchical sample (h-ZSM-5) of different Si/Al ratios and acid site concentrations. Acidic features of both zeolites have been modified and adjusted by incorporation of ZrO₂, which has a significant effect on the concentration and distribution of both Brønsted and Lewis acid sites. These materials have been tested in the catalytic pyrolysis of acid-washed wheat straw (WS-ac) using a two-step (thermal/catalytic) reaction system at different catalyst/biomass ratios. The results obtained have been assessed in terms of oxygen content, energy yield and composition of the produced bio-oil*, taking also into account the selectivity towards the different deoxygenation pathways. The ZrO₂/n-ZSM-5 sample showed remarkable performance in the biomass catalytic pyrolysis, as a result of the appropriate combination of accessibility and acidic properties. In particular, modification of the zeolitic support acidity by incorporation of highly dispersed ZrO₂ effectively decreased the extent of secondary reactions, such as severe cracking and coke formation, as well as promoted the conversion of the oligomers formed initially by lignocellulose pyrolysis, thus sharply decreasing the proportion of the components not detected by GC-MS in the upgraded bio-oil*.

Keywords: Biomass catalytic pyrolysis. Bio-oil upgrading. ZSM-5 zeolite. ZrO₂

GRAPHICAL ABSTRACT



1. Introduction

Biomass catalytic fast pyrolysis (CFP) is considered one of the most feasible routes for the production of liquid biofuels from lignocellulose, as it is a relatively simple process that takes place at atmospheric pressure, moderate temperatures and with short residence times.^{1,2} In addition to the liquid fraction (bio-oil), gases and a carbonaceous solid (char) are also produced. Bio-oil is viewed as an interesting product that could be applied for both biofuels and bio-based chemicals production.^{3,4} However, it contains a large variety of oxygenated compounds and significant amounts of water, which provides it with a number of undesired properties, such as low calorific value, immiscibility with fossil-derived fuels and acid pH (corrosiveness).¹ Moreover, bio-oil is not a stable product since even at room temperature it undergoes a number of reactions and transformations upon storage, which usually provokes phase separation and formation of solids.^{3,5} Accordingly, the bio-oil produced by thermal degradation of lignocellulose should be regarded as a low-quality fuel with limited economic value.⁶

In recent years, two main chemical routes have been proposed for improving the bio-oil properties: catalytic pyrolysis using acid solids, and hydrodeoxygenation over metal-containing catalysts.^{7,8} Catalytic pyrolysis presents the advantages of operation at the atmospheric pressure and not consuming external hydrogen, although it is limited by extensive formation of carbonaceous deposits leading to catalyst deactivation and reduction in the bio-oil yield.⁹⁻¹³ On the other hand, other catalytic transformations have been recently explored for bio-oil upgrading based on the use of catalysts with ketonization and aldol condensation activities, which allow the oxygen content of the bio-oil to be reduced with simultaneous C-C bond formation, hence increasing the molecular weight of the species present in the bio-oil.¹⁴⁻¹⁷

Bio-oil upgrading by catalytic pyrolysis can be performed in-situ or ex-situ regarding the pyrolysis reactor.^{2,18,19} The second configuration is more convenient since in this case the direct contact of the catalyst with the raw biomass is avoided, limiting at least partially the catalyst deactivation. In addition, both thermal and catalytic steps can be operated under different reaction conditions affording a more efficient biomass conversion and bio-oil upgrading.^{2,9} Indeed, it has been earlier shown that the optimum temperatures for biomass pyrolysis and bio-oil catalytic conversion differ significantly, demonstrating the convenience of ex-situ reaction systems for lignocellulose catalytic pyrolysis.⁹

Among solid catalysts employed in biomass catalytic pyrolysis, zeolites exhibited a remarkable performance in terms of bio-oil quality and deoxygenation degree.^{20,21} In particular, ZSM-5 zeolite has led to promising results, selectively promoting the formation of aromatic hydrocarbons, hence opening the possibility of using the obtained upgraded bio-oil in the formulation of advanced biofuels.²²⁻²⁵ This effect has been mainly related to the medium size of the micropores and strong acidity of ZSM-5 zeolite.²⁶ However, the use of this zeolite in biomass catalytic pyrolysis leads to low bio-oil yields as it also suffers from hindered accessibility to the active sites, coke deposition over the catalyst and occurrence of severe cracking reactions that promote the formation of gaseous hydrocarbons.¹⁸

A strong research effort has been devoted to improve the ZSM-5 behaviour in biomass catalytic pyrolysis. Thereby, the ZSM-5 properties have been modified by

reduction of the crystal size,^{11,23,27} introduction of a secondary porosity in the mesopore range^{11,23,28,29} or use of 2D ZSM-5 materials in order to increase the accessibility of the compounds present in the bio-oil vapours to the active sites.³⁰ Likewise, the addition of metals to ZSM-5 zeolite has been extensively investigated to increase the aromatisation activity and/or to decrease the coke formation during biomass pyrolysis. Thus, numerous works have been published using ZSM-5 zeolites, modified by incorporating a variety of elements, such as Pt, Pd, Ni, Ga, Mg, Zn, Co and Fe, in the catalytic pyrolysis of different lignocellulosic feedstock.^{10,22,31-39}

On the other hand, ZrO₂-based catalysts have been reported in the past years as materials with suitable catalytic properties for different biomass transformations, including not just biomass catalytic pyrolysis, but also other reactions of interest for the conversion of biomass-derived intermediates, such as ketonization,¹⁴ aldol condensation⁴⁰⁻⁴² and esterification.^{42,43} In contrast, almost no examples can be found in the literature exploring the modification of ZSM-5 with ZrO₂ for biomass catalytic pyrolysis. A rare example is provided by Li et al., who have recently investigated the biomass catalytic pyrolysis over Fe-, Zr- and Co-modified ZSM-5 zeolites,^{32,39} showing some positive effects of the incorporation of these elements in terms of product distribution, but providing no information on the deoxygenation degree of the bio-oil neither on its energy yield and on other relevant properties related to the level of upgrading achieved. Moreover, the zeolitic support used by these authors is a standard ZSM-5 of micrometer crystal size and, therefore, with very limited mesopore/external surface and accessibility, which may explain the relatively small effect seen upon zeolite modification.

In this context, the present work aims at adjusting the ZSM-5 properties to overcome its limitations in biomass catalytic pyrolysis for the production of upgraded bio-oil. Thereby, two main properties of the ZSM-5 zeolite are considered in the catalyst engineering strategy: high accessibility and tailored acidity. Thus, enhanced accessibility to the active sites was ensured by using two different non-standard ZSM-5 zeolites: a hierarchical ZSM-5 sample prepared by desilication (h-ZSM-5) and a nanocrystalline ZSM-5 material (n-ZSM-5). Both zeolites have high mesopore/external surface areas and reduced diffusional pathway lengths, properties expected to promote the conversion of the bulky molecules present in the bio-oil vapours. In addition to the variation of the Si/Al ratio, the incorporation of highly dispersed ZrO₂ over these ZSM-5 samples is here reported as a very efficient strategy for modulating and complementing the zeolite acidic features and improving their performance in biomass catalytic pyrolysis, as demonstrated by a variety of characterization techniques. The results obtained in the catalytic tests have been assessed using a quite complete set of parameters, including composition and mass yield of the different fractions obtained in the pyrolysis process (bio-oil, gases, water, char and coke formed over the catalyst), deoxygenation pathways selectivity and energy yield of the produced bio-oil.

2. Experimental

Detailed information about the catalysts preparation and characterization techniques, as well as on the procedure and set up employed for the biomass catalytic pyrolysis tests, is provided as Supporting Information.

3. Results and discussion

3.1. Catalysts properties

Basic characterization of the catalysts. The parent ZSM-5 samples used in this work possess very different Al content with values of the Si/Al molar ratios of 42 and 12 for the n-ZSM-5 and h-ZSM-5 samples, respectively (Table 1). The high Al content of the h-ZSM-5 zeolite is caused by the NaOH desilication treatment employed to generate the secondary porosity present in this material, which provokes extensive silica extraction from the zeolite framework.

High-angle X-ray diffraction patterns of the ZSM-5 samples (Fig. S1) exhibited typical diffraction lines of highly crystalline zeolites with MFI topology. The incorporation of ZrO₂ to the supports had no evident effect on their crystallinity. The fact that the impregnated samples did not exhibit diffraction peaks of pure zirconium oxide phases is indicative of the existence of either ZrO₂ particles with very small size and homogeneous dispersion over the ZSM-5 supports or the absence of crystalline ZrO₂ particles. In line with the XRD data, Raman spectroscopy also did not show any evidence for the presence of a perfectly crystalline ZrO₂ component (Fig. S2). Thus, the main broad band seen in the Raman spectra for both Zr-containing samples at 381 cm⁻¹ coincides with a vibration of monoclinic ZrO₂, but other bands expected for this phase, e.g. at 475, 615 and 637 cm⁻¹ are hardly or not detected.^{44,45} Orthorhombic and tetragonal ZrO₂ phases can also be discarded, as they would show significantly different Raman features than those detected for the ZrO₂/h-ZSM-5 and ZrO₂/n-ZSM-5 samples.^{46,47} These results show that the ZrO₂ present over the zeolitic support is poorly crystalline, most likely amorphous.

The textural properties of the catalysts were determined from the Ar adsorption isotherms at -186 °C applying the NL-DFT model, which allowed the contribution of the zeolite micropores and that of the mesopore/external surface to be distinguished (Table 1). Both parent samples present similar BET areas and a significant amount of mesopore/external surfaces, as expected taking into account their nanocrystalline and hierarchical features. This effect is more pronounced in the case of the h-ZSM-5 sample ($S_{\text{MES+EXT}} = 206 \text{ m}^2 \text{ g}^{-1}$), confirming that the desilication treatment was very effective in generating mesopores. After Zr incorporation, some attenuation of the textural properties was observed for both ZSM-5 samples. This variation was more accentuated for h-ZSM-5, whose micropore surface area and micropore volume were especially affected (32% of reduction), indicating that part of the Zr species are located within the zeolite micropores. In contrast, for the n-ZSM-5 catalyst Zr incorporation had a stronger effect on the mesopore+external surface (reduction of 25%) while no reduction is observed in the micropore one; hence, it can be concluded that in this sample the ZrO₂ is mainly located over the outer part of the zeolite nanocrystals rather than within the micropores.

Table 1. Physicochemical properties of the catalysts

Sample	Si/Al ^a	ZrO ₂ (wt%)	S _{BET} ^b (m ² /g)	S _{MES+EXT} ^c (m ² /g)	S _{MIC} ^d (m ² /g)	V _T ^e (cm ³ /g)	V _{MIC} ^f (cm ³ /g)	C _B (mmol/g)	C _L (mmol/g)
h-ZSM-5	12	---	447	206	241	0.584	0.144	0.192	0.179
ZrO ₂ /h-ZSM-5	12	7.8	362	197	165	0.550	0.100	0.091	0.083
n-ZSM-5	42	---	445	133	312	0.512	0.186	0.134	0.061
ZrO ₂ /n-ZSM-5	42	9.2	413	100	313	0.420	0.190	0.128	0.100

TEM and SEM examination of the h-ZSM-5 zeolite (Fig. 1a and S3a, respectively) showed coffin-shaped crystallites with sizes in the micrometer range (about 1 - 2.5 μm). Moreover, the presence of a high proportion of voids within the crystals is clearly observed, confirming the effectiveness of the desilication treatment for generating mesopores (see high resolution images in Fig. 1a). After zirconia impregnation, no apparent differences can be observed in the hierarchical zeolite catalysts (Fig. 1b), except for a rougher appearance for the Zr-promoted sample (Fig. S3b). Yet, SEM-EDX dot-mapping on $\text{ZrO}_2/\text{h-ZSM-5}$ sample showed Zr (Fig. S3b3) to be homogeneously dispersed over the crystallites, most likely being located within the zeolite micropores, with a Si/Zr molar ratio of ca. 12 (Fig. S4). On the other hand, TEM and SEM images of the n-ZSM-5 zeolite sample showed aggregates between 20-50 μm in size, consisting of crystallites of about 25-50 nm and thus confirming its nanocrystallinity (Fig. 1c and S3c, respectively). The Zr-promoted nanozeolite crystals appeared to be uniformly coated by ZrO_2 nanoparticles of rugged morphology located more on the external surface of the zeolite crystals (Fig. 1d). The SEM-EDX image of the $\text{ZrO}_2/\text{n-ZSM-5}$ (Fig. S3d) indicated that the Zr (d3) is evenly distributed over the sample, as evidenced by EDX dot-mapping, with a Si/Zr molar ratio of ca. 14 (Fig. S4), which is very close to the overall one (Si/Zr = 15).

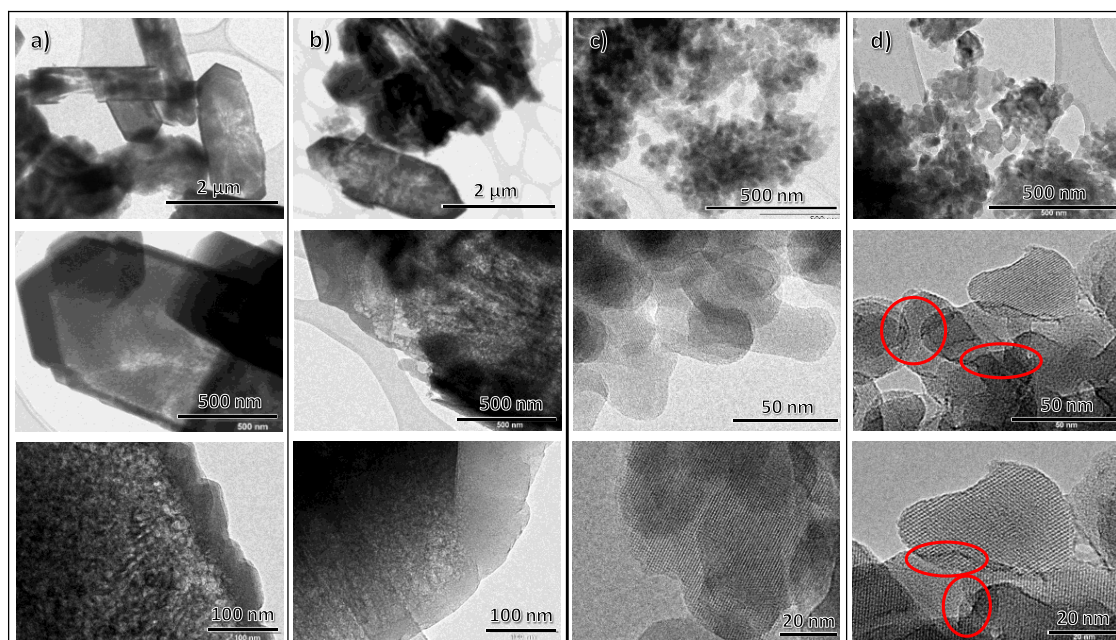


Fig. 1. TEM images of h-ZSM-5 (a), $\text{ZrO}_2/\text{h-ZSM-5}$ (b), n-ZSM-5 (c) and $\text{ZrO}_2/\text{n-ZSM-5}$ (d). The marked areas in d correspond to regions rich in ZrO_2 nanoparticles.

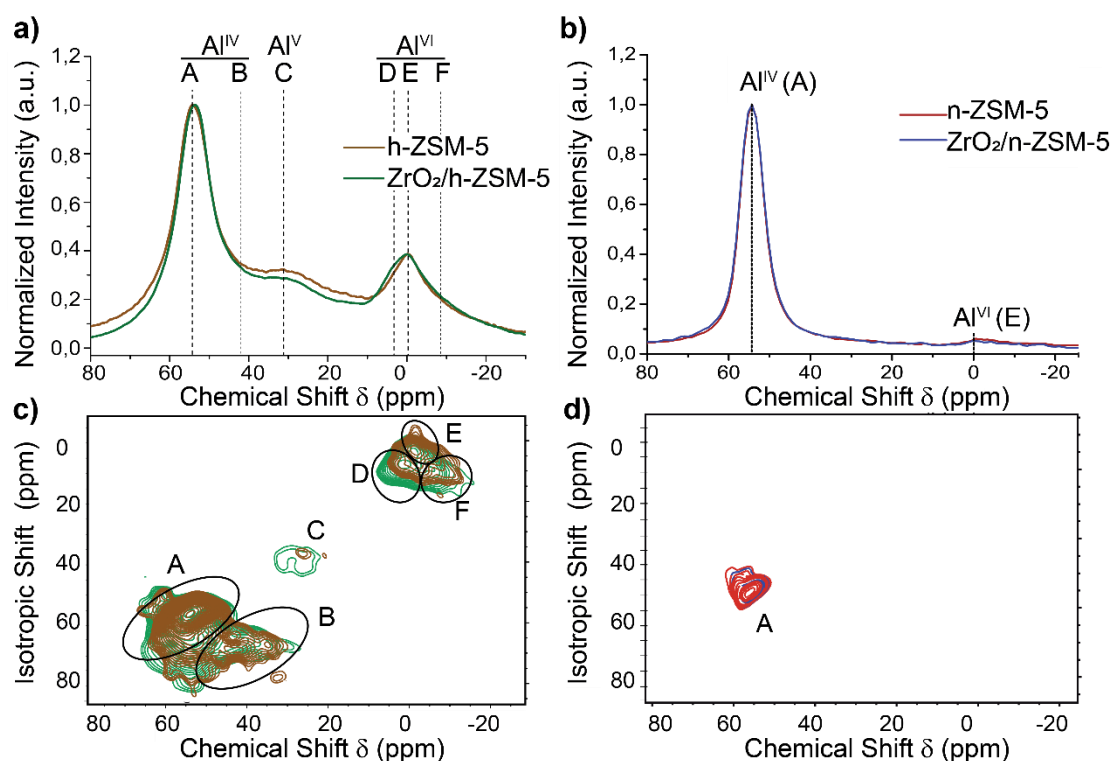


Fig. 2. Normalized ^{27}Al MAS ssNMR (a,b) and overlaid ^{27}Al MQ ssMAS NMR (c,d) spectra of h-ZSM-5 (orange) and ZrO₂/h-ZSM-5 (green) (a,c), and n-ZSM-5 (red) and ZrO₂/n-ZSM-5 (blue) (b,d). A to F correspond to the different contributing Al species which compose the NMR spectrum (see Fig. S5).

Al environment and acidity. Aluminium speciation in the different catalyst samples was examined by solid-state ^{27}Al ssMAS (Fig. 2a,b) and ^{27}Al MQ ssMAS NMR (Fig. 2c,d) analyses. For the h-ZSM-5 sample, in addition to framework tetrahedral (Al^{IV}, 53 ppm, A) and extra-framework octahedral (Al^{VI}, 0 ppm, E) Al,^{48–50} some penta-coordinated extra-framework Al (Al^V; C) is also present, as detected at ca. 30 ppm.⁵¹ Other minor resonances at ca. 40 ppm (B) and -10 ppm (F) correspond to distorted tetrahedral and octahedral Al, respectively, as deduced from the 2D MQ ssMAS NMR spectra (Fig. 2c). This variety of Al environments in the h-ZSM-5 sample is a direct consequence of the desilication treatment applied for the generation of mesoporosity, lowering the Si/Al ratio and generating extraframework Al. ZrO₂ addition (green series in Fig. 2) led to slight distortions of the different signals, in particular of the one associated with species C, whereas a shoulder (species D) is observed in the region of octahedral Al environments. These changes denote the existence of interactions between the Zr and some of the Al species of the zeolite. On the other hand, Zr⁴⁺ incorporation into the framework is excluded, as this would have resulted in more significant distortions and the formation of defects in the structure. The 1D Al spectra of h-ZSM-5 (Fig. S5a) and ZrO₂/h-ZSM-5 samples (Fig. S5b) were fitted, with the number and peak maxima of the Gaussians having been obtained from the MQ MAS spectra (see Table S1). The ratio between framework and extra-framework Al species is also presented in Table S1, suggesting a small drop in framework Al sites after Zr incorporation.^{48,50} In strong contrast with the h-ZSM-5 catalyst, the n-ZSM-5 sample, which was not subjected to any desilication process, almost exclusively showed tetrahedral Al species located at 54 ppm (A, blue series Fig. 2e, f) and very little octahedral Al at 0 ppm (Al^{VI}, E). The same is seen after ZrO₂ addition (red series in Fig. 2e), with the spectrum of ZrO₂/n-ZSM-5 being

practically identical to the one obtained for the pure zeolite. In this case, no interactions between any Zr species and Al seem to be detected, which is consistent with the ZrO₂ location on the external surface of this sample, as suggested by TEM and by Ar physisorption.

The concentration, type and strength of the acid sites have been determined by pyridine adsorption at 150 °C followed by FTIR (Py-FTIR). Table 1 summarizes the results obtained for the different samples in terms of Brønsted and Lewis acid sites concentration (BAS and LAS, respectively). The h-ZSM-5 sample possesses a higher acid sites concentration in line with its lower Si/Al ratio. The incorporation of ZrO₂ to h-ZSM-5 support caused a significant decrease in the concentration of both BAS and LAS, which may be due to a direct interaction between the Zr species and the acid sites and/or to a partial blockage of the zeolite micropores as above denoted from the variation of the textural properties. In the case of the n-ZSM-5 support, the addition of ZrO₂ provoked just a slight decrease in the BAS concentration. However, an increase is observed in the content of LAS. Thus, the ZrO₂/n-ZSM-5 material showed higher LAS concentration than the parent support, denoting that additional LAS were generated upon ZrO₂ incorporation. In order to analyse this last effect in more detail, Fig. 3 compares the FTIR spectra of the n-ZSM-5 and ZrO₂/n-ZSM-5 samples before and after pyridine adsorption followed by evacuation at different temperatures. In the hydroxyl stretching vibration region (Fig. 3a and c), it is observed that before adsorption both samples display two bands at 3745 cm⁻¹ and 3610 cm⁻¹ assigned to terminal silanol groups and acidic bridging OH groups (Si-OH-Al), respectively. The intensity of these bands was slightly lower in the case of ZrO₂/n-ZSM-5. After pyridine adsorption, these bands disappeared, with new ones emerging ascribed to different ring vibration modes of the pyridine interacting with the acid sites (Fig. 3b and d): ν_{8a} (1650-1600 cm⁻¹) and ν_{19b} (1580-1430 cm⁻¹). The new bands at 1636 cm⁻¹ and 1546 cm⁻¹ correspond to pyridine chemisorbed on the BAS of n-ZSM-5 (pyridinium ions, PyH⁺), whereas those at 1624 cm⁻¹ and 1456 cm⁻¹ are attributed to pyridine adsorbed on Al³⁺ ions in tetrahedral environment (Lewis acidity, PyL). Moreover, two additional bands at 1609 cm⁻¹ and 1448 cm⁻¹ could be distinguished for the ZrO₂/n-ZSM-5 sample, which can be assigned to the presence of pyridine interacting with LAS associated to Zr species.⁵² The relative strength of the acid sites can be deduced from the evolution of the pyridine desorption with the temperature. Thus, both samples exhibited a similar behaviour in terms of BAS in the range of evacuation temperatures from 150 °C up to 350 °C. However, the intensity of the bands at 1609 cm⁻¹ and 1448 cm⁻¹, related to ZrO₂, decreased faster upon increasing the temperature than those associated with the zeolitic LAS (Fig. 3d), indicating that the former are of lower strength.

Selective staining of the materials with 4-fluorostyrene (Scheme S1a) was used to probe the (local) Brønsted acidity properties of the zeolites, before and after ZrO₂ addition. On Brønsted sites of sufficient acidity, 4-fluorostyrene reacts to give (cyclic) dimers (see Scheme S1b, compounds 3-5), or higher oligomers, such as trimer (6) species. The formation of cyclic species (7) over the linear oligomers (5, 6) is favoured over stronger Brønsted acid sites (BAS). The in-situ UV-Vis absorption bands recorded for the different samples are displayed in Fig. 4, with the time evolution of selected wavelengths in the in-situ CFM emission spectra shown in Fig. S6.^{53,54} Here, it should be noted that the absorption and emission bands evolve in the same manner.

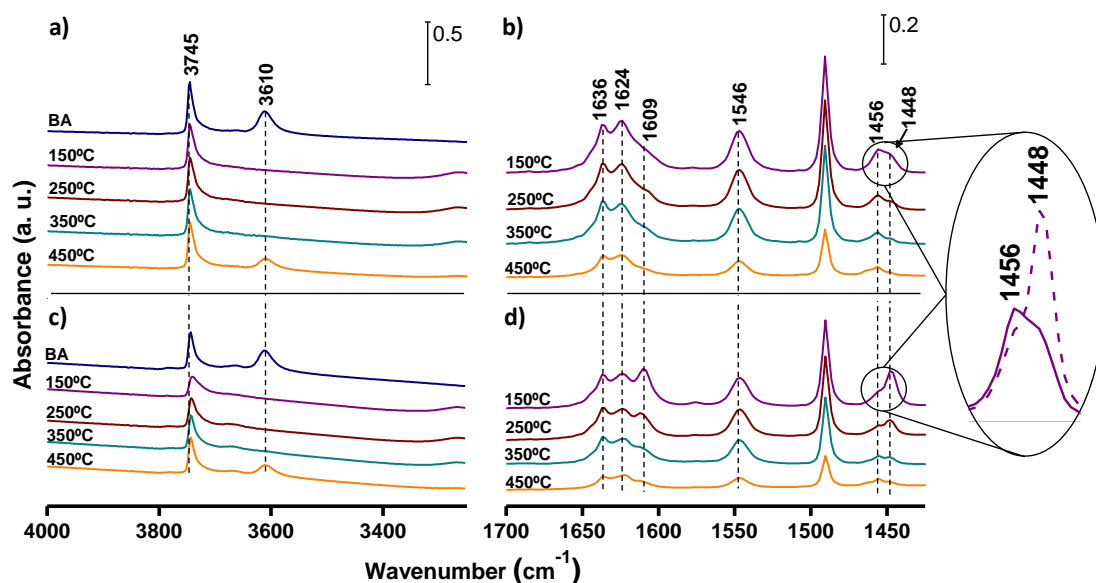


Fig. 3. FTIR spectra of the OH stretching vibration (a and c) and the pyridine vibration regions (b and d) for n-ZSM-5 (a and b) and ZrO₂/n-ZSM-5 (c and d).

The band profiles and peak positions of the maxima seen are similar for all catalyst samples with the main difference being the evolution of the bands with time-on-stream. The high ratio of cyclic to linear species - represented in the right axis of Fig. S6 as the intensity ratio of the 515 nm/555 nm bands⁵⁵ - is in line with the strong, initial Brønsted acidity of both the h-ZSM-5 and n-ZSM-5 zeolites, as shown by Py-FTIR. The staining results confirm that the Brønsted acidity initially present in the pure zeolites is partially preserved after ZrO₂ impregnation. The fact that less of higher oligomers, denoted as 6a and 6b species, are seen for the ZrO₂ impregnated zeolites (Fig. 4 and Fig. S6a-b, c-d) would be in line with less accessible acid sites compared to the parent sample, in particular for the hierarchical zeolite.

While the final UV-Vis spectra of h-ZSM-5 and n-ZSM-5 are very similar (despite their different Si/Al ratios), the time profiles of 5 and 7 (Fig. S6) are rather different. Indeed, the reaction seemed to occur faster on the nano-sized zeolite, likely because of better diffusivity, with the concentration profiles plateauing much faster. This result confirms the existence of a partial micropore blockage in the h-ZSM-5 sample, provoked by the high concentration of extra-framework Al species, which is further enhanced by Zr incorporation, as concluded above from the Ar adsorption-desorption isotherms. Likewise, the optical images of the samples after staining and reaction are included in insets in Fig. 4, showing pink colouration of all samples, except for the ZrO₂/h-ZSM-5 material, which looks purple. The pink colour, over purple, indicates the presence of more cyclic species (7), visually confirming the observation made by Py-FTIR that ZrO₂/h-ZSM-5 has less strong BAS accessible to the pyridine molecules.

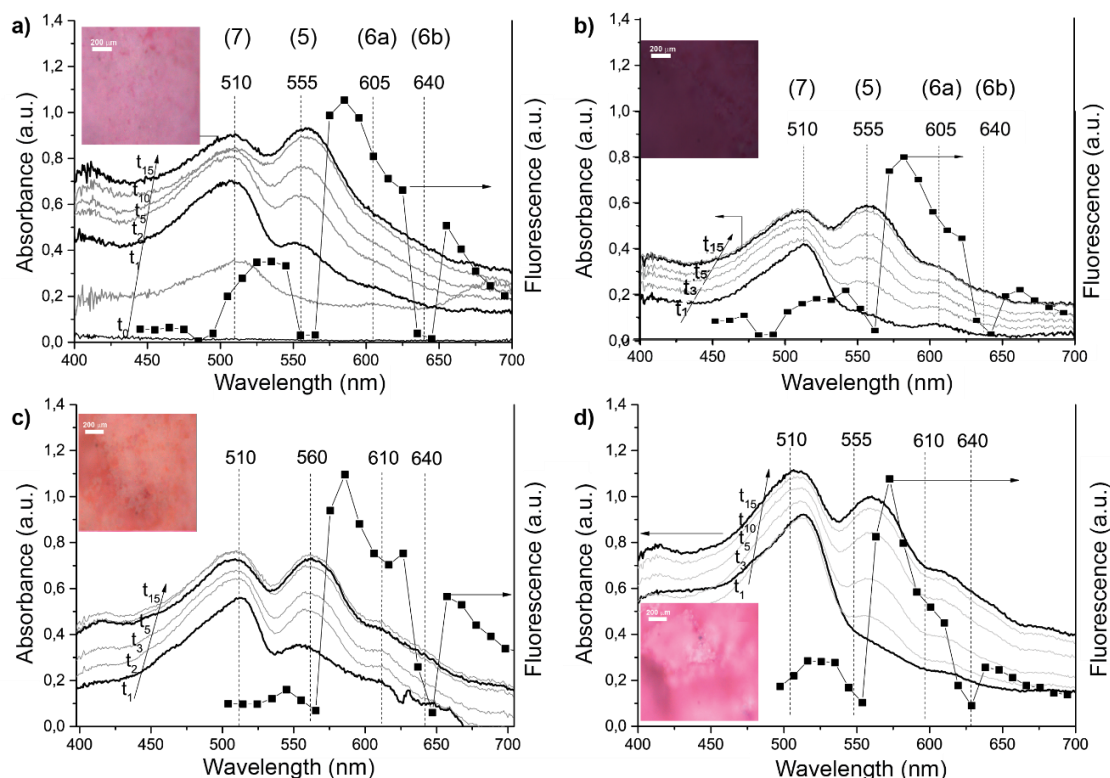


Fig. 4. Evolution of UV-Vis absorption spectra (continuous line) and ex-situ (30 min after reaction) fluorescence spectra (scattered line) of the 4-fluorostyrene oligomerization reaction products recorded at 100 °C for: (a) h-ZSM-5; b) ZrO₂/h-ZSM-5; c) n-ZSM-5; d) ZrO₂/n-ZSM-5. Excitation lasers are fixed at $\lambda = 488, 561, 642$ nm. Insets are optical images of the corresponding samples after 15 min of 4-fluorostyrene oligomerization.

3.2. Biomass catalytic pyrolysis tests

Wheat-straw was employed as biomass feedstock representative of agriculture residues. Prior to the pyrolysis tests, it was subjected to acid washing (WS-ac) to minimize any possible interference associated with indigenously catalytic components naturally present in the raw biomass, such as alkali and alkali earth metals (AAEM).⁵⁶ The catalytic pyrolysis experiments were performed in a two-zone reactor in which the thermal and catalytic conversions take place at different temperatures (550 and 400 °C, respectively), allowing optimization of the bio-oil production in each step. The different catalysts were tested using two catalyst/biomass ratios (0.4 and 0.7 g g⁻¹) in order to obtain results at two levels of bio-oil upgrading. With this configuration, the residual solid fraction (char) formed in the thermal conversion zone was very similar in all cases, with a mass yield of around 19 wt%. This product originated entirely from the initial biomass devolatilization and was retained in the upper reactor zone, avoiding direct contact with the catalyst bed.

Products distribution and bio-oil oxygen content. Fig. 5a depicts the product distribution in terms of mass yield for the catalytic pyrolysis of WS-ac employing the two ZSM-5 supports (n-ZSM-5 and h-ZSM-5) with a catalyst to biomass ratio of 0.7. The products include the organic part of the bio-oil (denoted as bio-oil*), the non-condensable gases, water and the coke deposited over the catalyst. Fig. 5b shows the oxygen content of the bio-oil* obtained in the different pyrolysis experiments, whereas Fig. 5c illustrates the mass yield corresponding to the different

components present in the gas fraction: CO, CO₂, CH₄, gaseous olefins (GO) and gaseous paraffins (GP). As reference, the results corresponding to a pure thermal test are also included in this figure.

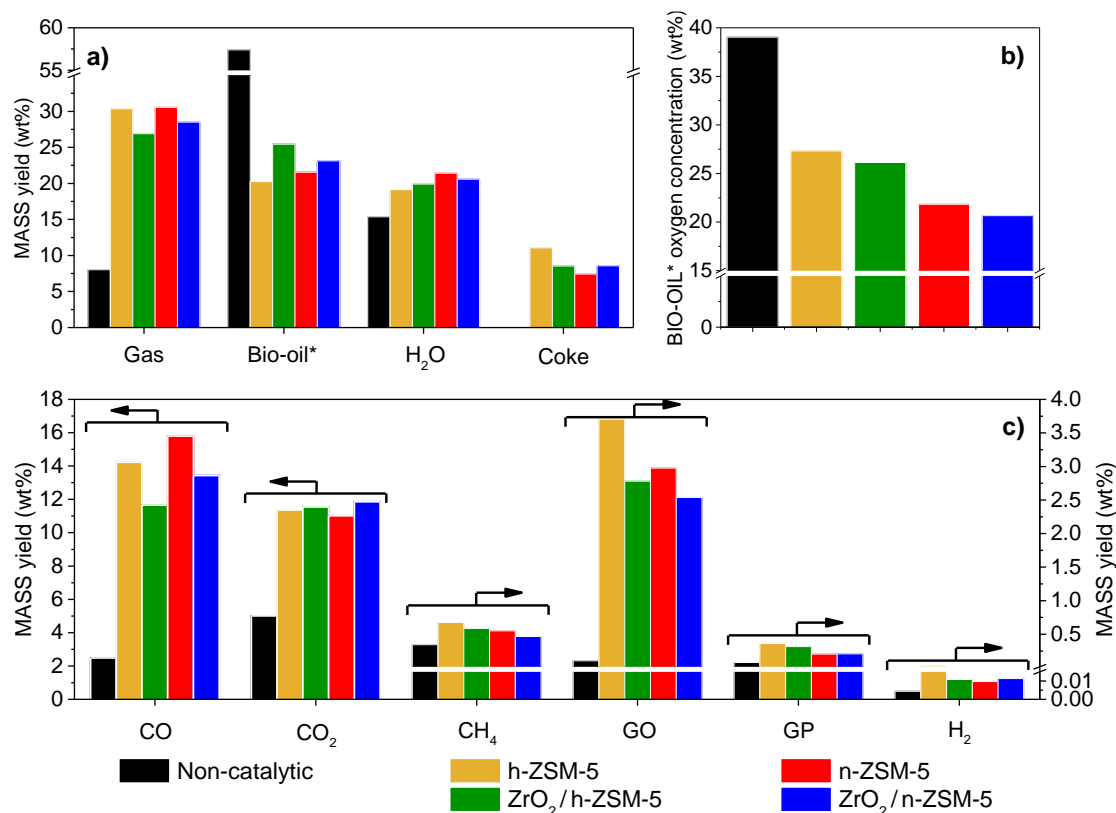


Fig. 5. Products yield distribution (wt%) (a), Bio-oil oxygen concentration (wt%, dry basis) (b) and gaseous components yield (wt%) (c), in the fast-pyrolysis of WS-ac (Catalyst/Biomass = 0.7 g/g, T = 550/400 °C). GO: gaseous olefins (C₂–C₄); GP: gaseous paraffins (C₂–C₄).

As expected, the incorporation of the zeolite catalyst bed for upgrading the bio-oil vapours causes strong changes in both the product distribution and the bio-oil* oxygen content compared to the pure thermal test, showing a high catalytic activity of the two ZSM-5 catalysts here employed. Thus, a notable reduction in the bio-oil* oxygen content is observed from the thermal bio-oil* to the catalytic ones. Note that the thermal bio-oil* presents an oxygen content (39 wt%) quite close to that of the raw biomass (42.8 wt%), indicating that a pure thermal degradation is poorly effective for deoxygenating the liquid organic fraction. In contrast, the use of ZSM-5 catalysts led to the production of bio-oils* with less oxygen, in the range of 20.7–27.3 wt% according to the data shown in Fig. 5b. However, the bio-oil* upgrading by catalytic deoxygenation was accompanied by a strong decrease in the bio-oil* yield at the expense of the enhanced formation of gases and water, as well as of the appearance of a new solid fraction (coke) deposited over catalysts. Within the non-condensable gases, the zeolite catalysts increased strongly the formation of CO, CO₂ and gaseous olefins (mainly propylene), with a more moderate effect on the yields of methane and other gaseous paraffins. The enhanced formation of water, CO and CO₂ occurred in agreement with the bio-oil* deoxygenation by dehydration, decarbonylation and decarboxylation routes, respectively. Likewise, the strong increase in the production of light hydrocarbons, in particular of gaseous olefins, over the zeolite catalysts reflects that these materials also promote severe cracking reactions, which are detrimental for

the bio-oil* yield. Methane has earlier been proposed to originate mainly from the lignin biopolymer¹² by demethylation of the abundant methoxyl groups in the lignin structure. On the other hand, gaseous olefins may be formed through decarbonylation of light oxygenated intermediates or by cracking of alkyl aromatics.⁵⁷

Interesting differences can be denoted in Fig. 5 between the product distribution obtained over both zeolitic supports (n-ZSM-5 and h-ZSM-5), mainly regarding the bio-oil* yield and its oxygen content. Thus, the n-ZSM-5 sample produces more bio-oil* than the h-ZSM-5 material, and with a significantly lower oxygen content, showing its superior properties for bio-oil* upgrading.

The variation in the bio-oil* production can be mainly related to the higher acid site concentration in h-ZSM-5 sample, which promotes the generation of more gases and the formation of more of coke deposits. Increased coking causes a faster zeolite deactivation, explaining the lower bio-oil* deoxygenation degree achieved with the hierarchical ZSM-5 sample.

The results obtained in biomass catalytic pyrolysis when incorporating ZrO₂ over the two ZSM-5 samples have been also included in Fig. 5. For both supports the addition of Zr positively affected bio-oil* yield while reducing the gas production, with minor variations in water formation. Interestingly, this enhanced production of bio-oil* is accompanied by a small but noticeable reduction in its oxygen content. Within the gas fraction, Zr-incorporation decreased mainly the production of CO and CH₄, with little changes in the case of CO₂, gaseous olefins and paraffins. Moreover, for the h-ZSM-5 sample, Zr modification also reduced coke deposition over the catalyst attenuating its deactivation. These results can be directly related to the fine tuning of the zeolite acidity by Zr incorporation, since it reduces the concentration of strong acid sites, limiting undesired severe cracking and coking reactions.

3.3. Deoxygenation selectivity

The oxygen contained in the raw biomass and, subsequently, in the bio-oil* can be removed by a variety of reactions that can be grouped into three main routes, depending on the final product that contains the oxygen atoms: dehydration, decarbonylation and decarboxylation. Least preferred is decarbonylation as it brings a significant loss of both mass and energy yield of the bio-oil*. In term of mass, the oxygen removal through decarbonylation involves the formation of one molecule of CO containing 57.1 wt% of oxygen, i.e. it takes place with a 42.9 wt% carbon loss. In contrast, for decarboxylation and dehydration the respective oxygen contents in CO₂ and H₂O are 72.7 and 88.9 wt% O, which implies considerably lower mass losses of C and H, respectively. Regarding the chemical energy yield, decarbonylation is also a less favourable route compared to decarboxylation and dehydration, since CO still contains a significant heating value (12.6 MJ Nm⁻³). Thus, the term overall deoxygenation selectivity is defined as the mass of oxygen removed from the original biomass by means of CO, CO₂ and H₂O. By subtracting the thermal overall deoxygenation contribution to those of the catalytic experiments, catalytic deoxygenation selectivity was calculated in a similar way.

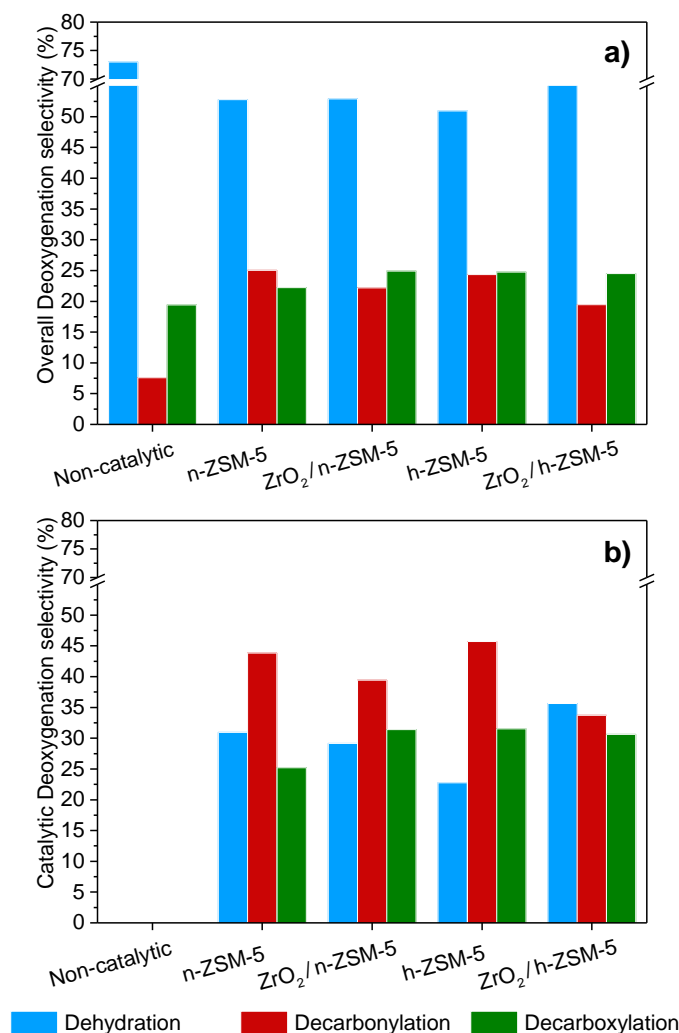


Fig. 6. Overall deoxygenation (a) and catalytic deoxygenation (b) selectivity in the fast-pyrolysis of WS-ac. (Catalyst/Biomass = 0.7 g/g, T = 550/400 °C).

Taking into account the yield of H₂O, CO and CO₂ obtained in the different biomass pyrolysis tests, as well as their oxygen content, the overall deoxygenation selectivity is shown in Fig. 6a. For non-catalytic biomass pyrolysis, the major pathway was dehydration (with a selectivity of 72%), followed by decarboxylation and with a minor contribution of decarbonylation. Nevertheless, it must be taken into account that in the thermal experiment deoxygenation has little effect on the bio-oil* fraction since its oxygen content is just slightly lower than that of the raw biomass. This means that in the non-catalytic pyrolysis the observed deoxygenation pathways are really surpassed for the formation of char, which shows reduced oxygen content compared to the raw biomass, as concluded previously.⁹ For the catalytic experiments, dehydration is still the main overall deoxygenation route, although a larger contribution of decarboxylation and in particular of decarbonylation is observed. By subtracting the thermal contribution to the overall production of H₂O, CO and CO₂, it was possible to assess the catalytic deoxygenation selectivity, as shown in Fig. 6b. For both ZSM-5 supports, decarbonylation is the predominant route of catalytic deoxygenation, followed by dehydration (over n-ZSM-5) or decarboxylation (over h-ZSM-5). Decarbonylation selectivity was higher for the hierarchical ZSM-5 sample, reaching a value of 45.7%. These facts highlight one of the limitations of ZSM-5 zeolite for efficiently upgrading bio-oil as it promotes the least favourable deoxygenation

route, i.e. decarboxylation. However, the addition of Zr to the zeolitic supports, and associated moderation of strong BAS in ZSM-5 zeolites, reduced decarbonylation selectivity, which is a positive effect in terms of both mass and energy yields of the remaining bio-oil* fraction. This result was more pronounced in the case of the h-ZSM-5 sample.

3.4. Energy yield distribution

Since typically the main goal of biomass catalytic pyrolysis is the production of biofuels, one important parameter is how the chemical energy initially present in the biomass is distributed among the different fractions obtained. In this way, Fig. 7 shows the chemical energy distribution per fraction corresponding to the experiments performed with a catalyst/biomass ratio of 0.7, including also the results corresponding to the thermal test.

In the thermal, non-catalytic experiment, almost 70% of the biomass chemical energy is present in the bio-oil* fraction and just a small proportion in the gases. The remainder of the chemical energy is contained in the char produced in the pyrolysis process due to its relatively low oxygen content.

For the catalytic pyrolysis tests, sharp changes are observed in the energy yield distribution. Thus, the h-ZSM-5 and n-ZSM-5 parent zeolites exhibit a relatively low bio-oil* energy yield, with values almost half of that corresponding to the thermal bio-oil, as a great part of the chemical energy is contained in the coke, CO and gaseous olefins formed. This finding denotes the relevance of, not only having a favourable deoxygenation pathway, but also of avoiding the formation of coke and gaseous hydrocarbons during biomass catalytic pyrolysis in order to minimize the bio-oil* energy yield losses during the upgrading process.

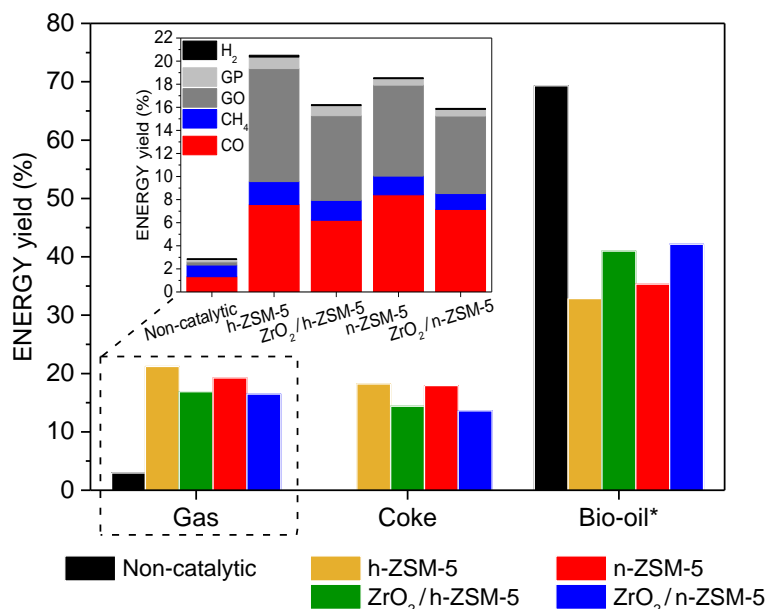


Fig. 7. Energy yield distribution (%) in the fast-pyrolysis of WS-ac. (Catalyst/Biomass = 0.7 g/g, T = 550/400 °C). GO: gaseous olefins (C₂–C₄); GP: gaseous paraffins (C₂–C₄).

Zr incorporation onto both ZSM-5 zeolitic supports had a positive effect on the bio-oil* energy yield, with their modified acidity being responsible for the improved biomass catalytic pyrolysis with lower production of coke, light hydrocarbons and CO.

3.5. Bio-oil upgrading efficiency

The above results show that bio-oil* deoxygenation over zeolite catalysts is accompanied by a sharp decrease in both mass and energy yield of this fraction. To make a proper comparison between the different catalysts, both parameters must be assessed together. Fig. 8 illustrates the evolution of the bio-oil* oxygen content versus the mass and energy yields, respectively, of the bio-oil* fraction. For each catalyst, the results obtained operating at two different catalyst/biomass ratios (0.4 and 0.7 g g⁻¹, respectively) have been represented in this figure to illustrate the corresponding bio-oil* upgrading pathways. As expected, regardless of the zeolite used, a higher catalyst to biomass ratio led to a reduction of the bio-oil* oxygen concentration, although also causing a decrease in the bio-oil* yield. The trend of the curves varies significantly depending on the catalyst employed, which in turn is a result of the efficiency of each material for promoting deoxygenation without paying too much of a penalty in terms of mass and energy yields of the bio-oil* fraction.

The data in Fig. 8 confirm that the n-ZSM-5 support is superior in all cases than the h-ZSM-5 one for catalytic biomass pyrolysis, affording the production of bio-oils* with higher deoxygenation degrees and with higher/superior yields. The microcrystalline h-ZSM-5 zeolite, prepared by desilication hence showing a low Si/Al ratio, was not very efficient at bio-oil upgrading: it led to a strong reduction in the bio-oil* yield with just moderate deoxygenation, due to the occurrence of undesired reactions, as seen in previous sections. On the other hand, this figure illustrates clearly how for the two ZSM-5 supports the incorporation of Zr had a very positive effect, as it improves both the bio-oil* yield and its deoxygenation degree.

The ZrO₂/n-ZSM-5 sample was the most efficient, allowing the production of a highly deoxygenated bio-oil* while reducing the mass and energy losses due to secondary transformations. Thus, for a catalyst/biomass ratio of 0.7 g g⁻¹, this catalytic system was able to decrease the bio-oil* oxygen concentration to reach a value as low as 20 wt% containing still 40% of the biomass chemical energy. Compared to the thermal bio-oil*, these figures show that the oxygen content is halved, retaining about 60% of its chemical energy.

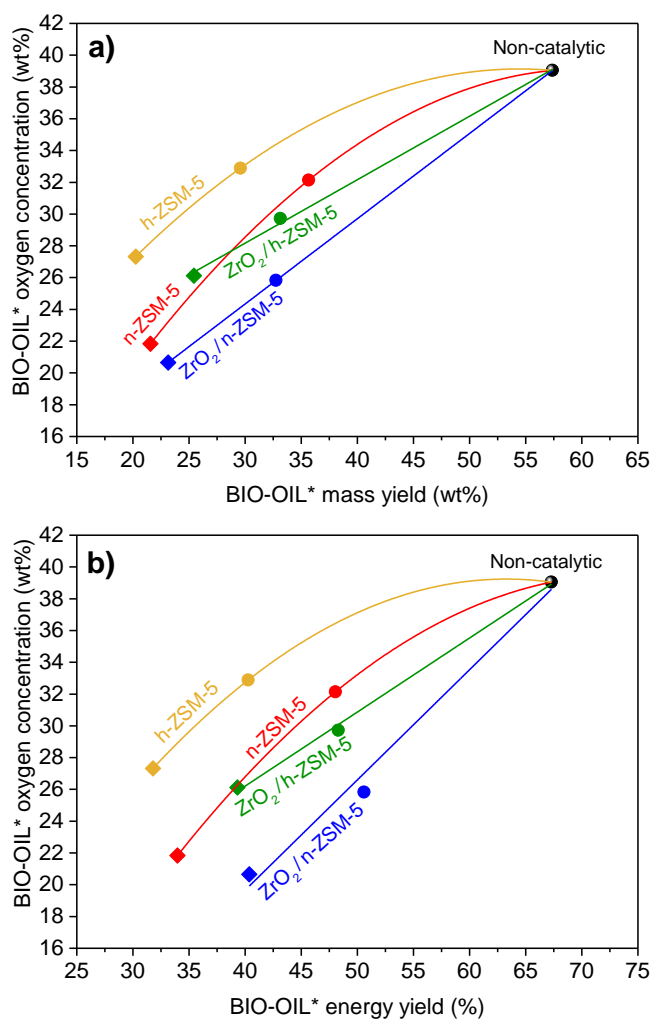


Fig. 8. Bio-oil* oxygen concentration versus bio-oil* mass (a) and energy (b) yields obtained in the fast-pyrolysis of WS-ac varying the catalyst to biomass ratio ($T = 550/400$ °C).

3.6. Bio-oil GC-MS composition

Due to numerous compounds present in the bio-oil, GC-MS is often applied as a semi-quantitative tool for product distribution analysis, based on relative area%, in spite of the large variation between their response factors. Moreover, it is known that the compounds identified by GC-MS represent just a fraction of the total components contained in the bio-oil* sample. In particular, oligomers derived from the partial fragmentation of the three biopolymers in lignocellulose cannot be detected by GC-MS. To avoid these problems, in this work the most abundant components in the different organic products families have been quantified after calibration, allowing the results to be provided as mass yield relative to the initial raw biomass weight. Likewise, from the elemental composition of the quantified matter, its contribution in terms of chemical energy yield was determined. The results obtained from the GC-MS analyses of the bio-oil* produced over the catalysts based on the nanocrystalline ZSM-5 material are shown in Fig. 9 and compared with the thermal bio-oil*.

Bio-oil obtained in the absence of any catalysts consists mainly of not quantified matter, which accounts for about 70% of the total in this sample (Fig. 9a). This result denotes the high content of oligomers in the non-catalytic bio-oil*, showing the limitations of a pure thermal treatment in achieving a total fragmentation of the lignocellulose biopolymers.

In the case of the catalytic pyrolysis tests, Fig. 9a shows that while the overall bio-oil* yield dropped upon addition of the n-ZSM-5 catalyst to the reaction system, the amount of non-quantified matter was significantly reduced, this effect being enhanced at higher catalyst/biomass ratios. This fact highlights the ability of ZSM-5 zeolite to convert the biomass oligomers, although this transformation is not really very efficient from the point of view of upgraded bio-oil* production, as the yield corresponding to the quantified matter does not improve compared to the thermal experiment. Accordingly, it can be concluded that the n-ZSM-5 sample promotes the conversion of the oligomers mainly through non-desired secondary reactions, leading to the formation of gaseous hydrocarbons, CO and carbonaceous residues.

However, this picture is quite different when analysing the results obtained over the ZrO₂/n-ZSM-5 sample. With this catalyst, the reduction in the oligomers is accompanied by an enhancement of the mass yield into the quantified components. This variation is more pronounced when the comparison is made in terms of chemical energy yield due to the high deoxygenation degree of the bio-oil* produced. Therefore, the presence of Zr species over the catalyst and, in particular of new Lewis acid sites, provides it with a remarkable catalytic activity for converting the biomass oligomers into smaller components in the bio-oil* fraction, overcoming the limitations of the parent ZSM-5 support. Thus, for a catalyst/biomass ratio of 0.7 g g⁻¹, the ZrO₂/n-ZSM-5 catalyst leads to the production of a bio-oil* with little oligomers, achieving simultaneously a reduction to half of the oxygen content shown by the thermal bio-oil.

The yields of the main components present in the quantified fraction of the bio-oil are shown in Fig. 9b. Products have been classified according to the following families: carboxylic acids (AC), light oxygenates (LO: aldehydes, ketones, ethers and alcohols), furans (FUR), oxygenated aromatics (O-AR), aromatic hydrocarbons (AR) and anhydrosugars (SUG). For the thermal bio-oil, the major components by far are the anhydrosugars (mainly levoglucosan), with also significant yields of other compounds families such LO and O-AR. In contrast, any hydrocarbons present in this bio-oil fall below the detection limit. In a previous work,⁹ a simplified reaction mechanism scheme was proposed to account for the main transformation routes occurring during the biomass catalytic fast-pyrolysis. According to this scheme, levoglucosan, furans and oxygenated aromatics are considered to be the main products coming from the depolymerisation of cellulose, hemicellulose and lignin, respectively. Their subsequent conversion leads to the formation of other families of oxygenated species, such as carboxylic acids, ketones and ethers.

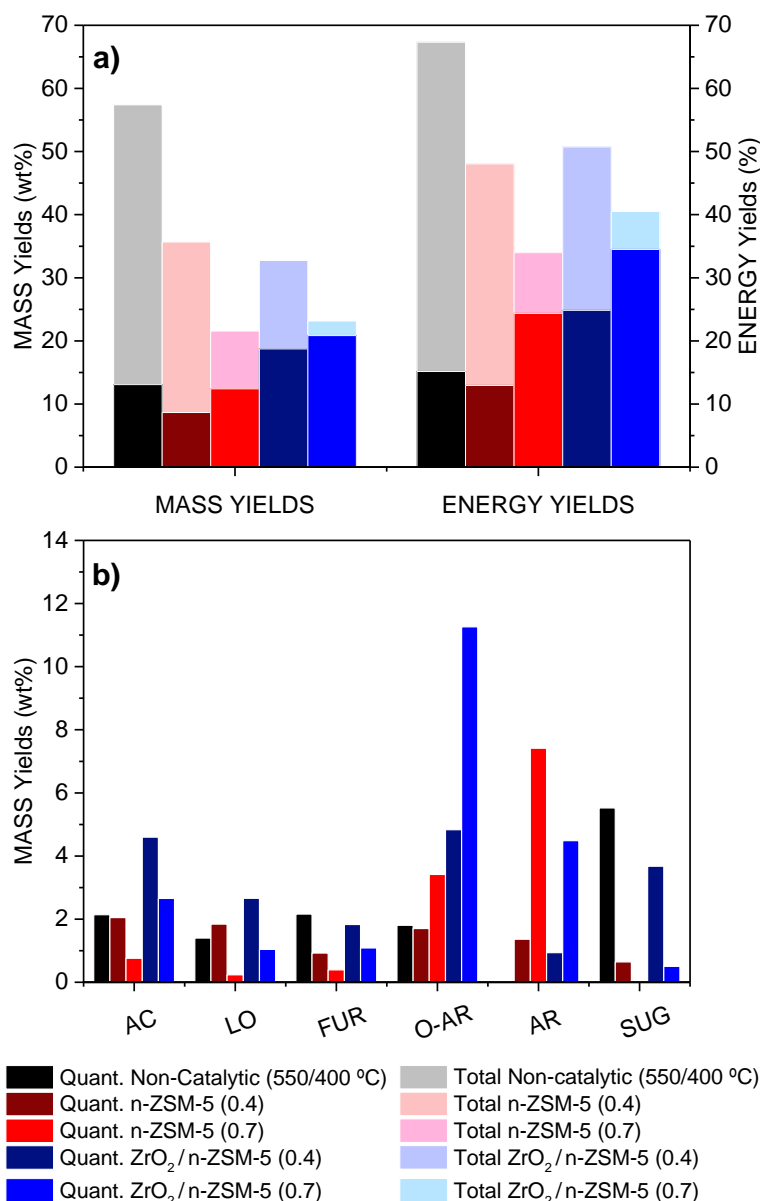


Fig. 9. Total/Quantified bio-oil* components (a), and bio-oil* components mass yields in terms of main organic compounds families (b) obtained in the fast-pyrolysis of WS-ac (Catalyst to biomass weight ratio indicated in brackets, T = 550/400 °C).

As expected, bio-oil product distribution was strongly affected by the incorporation of the n-ZSM-5 catalyst to the reaction system, this effect being more pronounced for the experiment performed at the highest catalyst/biomass ratio. Thus, for the catalytic bio-oil* SUG is no longer the major fraction as levoglucosan is almost completely converted, probably by dehydration into furans.^{58,59} In the same way, the yield corresponding to most of the other oxygenated compounds families (AC, LO and FUR) decreased in the case of the catalytic pyrolysis tests upon increasing the catalyst/biomass ratio. However, this is not the case for O-AR since its yield increases when working at the highest catalyst/biomass ratio. On the other hand, while the thermal bio-oil* does not contain any appreciable amount of hydrocarbons, the n-ZSM-5 catalyst led to the appearance of aromatic hydrocarbons. According to the literature,^{9,60,61} one of the predominant pathways for the formation of these aromatic hydrocarbons consists of first the dehydration of levoglucosan into furans, followed by Diels-Alder condensation of the latter with light alkenes,

mainly propylene, which are present in significant amounts in the non-condensable gas fraction. Nevertheless, the contribution of a carbon-pool type mechanism cannot be discarded in the formation of aromatic hydrocarbons.

Interestingly, the modification of the n-ZSM-5 zeolite with ZrO_2 had a profound effect on the product distribution shown in Fig. 9b. For both catalyst/biomass ratios, an increase in the yield of all families of oxygenated compounds is observed compared to the pure ZSM-5 support, in agreement with the ability of the ZrO_2 -modified catalysts to promote the conversion of the oligomers present in the bio-oil. These enhanced yields are particularly remarkable in the case of oxygenated aromatics and, to a lesser extent, for carboxylic acids (consisting mainly of acetic acid), which can be interpreted as a direct result of the conversion of oligomers into smaller compounds, catalysed by the new types of Lewis acid sites generated upon ZrO_2 incorporation. Accordingly, a remarkable overall upgrading of the bio-oil* fraction is achieved when using the Zr-modified n-ZSM-5 sample.

4. Conclusions

Nanosized and hierarchical ZSM-5 zeolites, showing enhanced accessibility, have been investigated in biomass catalytic pyrolysis to promote the conversion and upgrading of the bulky molecules coming from the thermal fragmentation of the lignocellulose biopolymers into partially deoxygenated bio-oil*. Acid washed wheat straw (WS-ac) has been used as a feedstock representative of agriculture wastes. The tests have been performed in an ex-situ catalytic pyrolysis system, which allows the thermal and catalytic steps to operate under different, previously optimised reaction temperatures.

In spite of the favourable accessibility of these ZSM-5 samples, they still suffer from a number of limitations in biomass catalytic pyrolysis that negatively affect the bio-oil* yield. The excessive presence of strong acid sites in ZSM-5 zeolite favours the occurrence of undesired reactions, such as severe cracking leading to gaseous hydrocarbons and the formation of carbonaceous residues over the catalyst, causing its deactivation. Moreover, among the different deoxygenation pathways, the ZSM-5 zeolite extensively promotes decarbonylation, which is undesired as it results in a significant loss of both mass and energy yields of the bio-oil*. Regarding the composition of the liquid organic fraction, the ZSM-5 catalysts are able to transform a great part of the oligomers present in the bio-oil* compared to the non-catalytic test, significantly increasing the components detected by GC-MS. However, even by working at high catalyst/biomass ratio, the parent ZSM-5 samples cannot completely convert those oligomers, which negatively affects the bio-oil* properties.

Incorporation of Zr to the ZSM-5 supports, in the form of highly dispersed species, modifies the ZSM-5 physicochemical properties and strongly improves its catalytic performance for biomass catalytic pyrolysis. The addition of Zr allows the zeolite acidity to be adjusted, decreasing the concentration of the strong acid sites linked to the zeolitic support and generating a new type of Lewis acid sites associated with the highly dispersed ZrO_2 phase. This effect is more pronounced for the nanocrystalline ZSM-5 catalyst since in this material Zr is mainly in the form of very small ZrO_2 nanoparticles distributed over the external surface of the zeolite crystals. The modification of ZSM-5 with Zr leads to enhanced bio-oil* yields combined with a high deoxygenation degree, as a result of: a decrease in severe cracking reactions, less coke formation and reduction in the extent of deoxygenation by decarbonylation. Moreover, the Zr-

modified catalysts show considerably better activity for the conversion of the oligomers present in the bio-oil*, suggesting the participation of the new population of Lewis acid sites in these reactions. The best results are obtained with the ZrO₂/n-ZSM-5 catalyst, which show the highest bio-oil* yields in terms of both mass and chemical energy, producing a partially deoxygenated liquid organic fraction with low content of oligomeric species.

Acknowledgements

The authors gratefully acknowledge the financial support from: the European Union Seventh Framework Programme (FP7/2007–2013) under grant agreement n° 604307 (CASCATBEL project), and from the Spanish Ministry of Economy and Competitiveness through CATPLASBIO project (Ref: CTQ2014 - 602209 - R). J. Čejka thanks the Czech Science Foundation for the financial support (P106/12/G015). Likewise, the authors thank SILKEM company for the preparation and supply of the hierarchical ZSM-5 sample. The NMR studies were supported by NWO (Middelgrootprogram, grant number 700.58.102 to MB).

References

1. J. Feroso, P. Pizarro, J. M. Coronado and D. P. Serrano, *Adv. Rev.*, 2017, **6**, 1–18.
2. J. Feroso, P. Pizarro, J. M. Coronado and D. P. Serrano, in *Encyclopedia of Sustainability Science and Technology*, ed. R. A. Meyers, Springer, New York, 2017, pp. 1–33.
3. D. Carpenter, T. L. Westover, S. Czernik and W. Jablonski, *Green Chem.*, 2014, **16**, 384–406.
4. A. V Bridgwater, *Biomass and Bioenergy*, 2011, **38**, 68–94.
5. D. Mohan, C. U. Pittman and P. H. Steele, *Energy & Fuels*, 2006, **20**, 848–889.
6. R. H. Venderbosch, *ChemSusChem*, 2015, **8**, 1306–1316.
7. A. V. Bridgwater, *Catal. Today*, 1996, **29**, 285–295.
8. Z. Cao, J. Engelhardt, M. Dierks, M. T. Clough, G. H. Wang, E. Heracleous, A. Lappas, R. Rinaldi and F. Schüth, *Angew. Chemie - Int. Ed.*, 2017, **56**, 2334–2339.
9. H. Hernando, S. Jiménez-Sánchez, J. Feroso, P. Pizarro, J. M. Coronado and D. P. Serrano, *Catal. Sci. Technol.*, 2016, **6**, 2829–2843.
10. Y. Zheng, F. Wang, X. Yang, Y. Huang, C. Liu, Z. Zheng and J. Gu, *J. Anal. Appl. Pyrolysis*, 2017, **126**, 169–179.
11. L. Jia, M. Raad, S. Hamieh, J. Toufaily, T. Hamieh, M. Bettahar, G. Mauviel, M. Tarrighi, L. Pinard and A. Dufour, *Green Chem.*, 2017, **19**, 5442–5459.
12. K. Wang, K. H. Kim and R. C. Brown, *Green Chem.*, 2014, **16**, 727–735.
13. Á. Ibarra, A. Veloso, J. Bilbao, J. M. Arandes and P. Castaño, *Appl. Catal. B Environ.*, 2016, **182**, 336–346.
14. G. Pacchioni, *ACS Catal.*, 2014, **4**, 2874–2888.
15. K. Wu, M. Yang, W. Pu, Y. Wu, Y. Shi and H. sheng Hu, *ACS Sustain. Chem. Eng.*,

- 2017, **5**, 3509–3516.
16. J. Wang, B. Zhang, Z. Zhong, K. Ding, A. Deng, M. Min, P. Chen and R. Ruan, *Energy Convers. Manag.*, 2017, **139**, 222–231.
 17. S. Tosoni, H. T. Chen, R. Puigdollers and G. Pacchioni, *Philos. Trans. R. Soc. A - Math. Phys. Eng. Sci.*, 2018, **376**, 1–19.
 18. C. Liu, H. Wang, A. M. Karim, J. Sun and Y. Wang, *Chem. Soc. Rev.*, 2014, **43**, 7594–7623.
 19. S. Wan and Y. Wang, *Front. Chem. Sci. Eng.*, 2014, **8**, 280–294.
 20. A. Galadima and O. Muraza, *Energy Convers. Manag.*, 2015, **105**, 338–354.
 21. D. Fabbri, C. Torri and V. Baravelli, *J. Anal. Appl. Pyrolysis*, 2007, **80**, 24–29.
 22. Y. T. Cheng, J. Jae, J. Shi, W. Fan and G. W. Huber, *Angew. Chem. Int. Ed.*, 2012, **51**, 1387–1390.
 23. T. C. Hoff, M. J. Holmes, J. Proano-Aviles, L. Emdadi, D. Liu, R. C. Brown and J. P. Tessonnier, *ACS Sustain. Chem. Eng.*, 2017, **5**, 8766–8776.
 24. C. Hu, R. Xiao and H. Zhang, *Bioresour. Technol.*, 2017, **243**, 1133–1140.
 25. A. A. Lappas, K. G. Kalogiannis, E. F. Iliopoulou, K. S. Triantafyllidis and S. D. Stefanidis, *Wiley Interdiscip. Rev. Energy Environ.*, 2012, **1**, 285–297.
 26. D. Kubička, I. Kubičková and J. Čejka, *Catal. Rev. Sci. Eng.*, 2013, **55**, 1–78.
 27. A. Zheng, Z. Zhao, S. Chang, Z. Huang, H. Wu, X. Wang, F. He and H. Li, *J. Mol. Catal. A Chem.*, 2014, **383–384**, 23–30.
 28. J. Li, X. Li, G. Zhou, W. Wang, C. Wang, S. Komarneni and Y. Wang, *Appl. Catal. A Gen.*, 2014, **470**, 115–122.
 29. K. Qiao, X. Shi, F. Zhou, H. Chen, J. Fu, H. Ma and H. Huang, *Appl. Catal. A Gen.*, 2017, **547**, 274–282.
 30. J. Feroso, H. Hernando, P. Jana, I. Moreno, J. Přeč, C. Ochoa-Hernández, P. Pizarro, J. M. Coronado, J. Čejka and D. P. Serrano, *Catal. Today*, 2016, **277**, 171–181.
 31. B. Valle, A. G. Gayubo, A. T. Aguayo, M. Olazar and J. Bilbao, *Energy & Fuels*, 2010, **24**, 2060–2070.
 32. P. Li, X. Chen, X. Wang, J. Shao, G. Lin, H. Yang, Q. Yang and H. Chen, *Energy & Fuels*, 2017, **31**, 3979–3986.
 33. M. M. Yung, A. R. Stanton, K. Iisa, R. J. French, K. A. Orton and K. A. Magrini, *Energy & Fuels*, 2016, **30**, 9471–9479.
 34. L. Sun, X. Zhang, L. Chen, B. Zhao, S. Yang and X. Xie, *J. Anal. Appl. Pyrolysis*, 2016, **121**, 342–346.
 35. M. M. Yung, A. K. Starace, C. Mukarakate, A. M. Crow, M. A. Leshnov and K. A. Magrini, *Energy & Fuels*, 2016, **30**, 5259–5268.
 36. P. He, W. Shan, Y. Xiao and H. Song, *Top. Catal.*, 2016, **59**, 86–93.

37. H. Zhang, J. Zheng and R. Xiao, *BioResources*, 2013, **8**, 5612–5621.
38. W. W. Purwato, D. Supramono, R. Muthia and M. F. Firdaus, *Int. J. Technol.*, 2015, **7**, 1069–1075.
39. P. Li, D. Li, H. Yang, X. Wang and H. Chen, *Energy & Fuels*, 2016, **30**, 3004–3013.
40. W. Shen, G. A. Tompsett, K. D. Hammond, R. Xing, F. Dogan, C. P. Grey, W. C. Conner, S. M. Auerbach and G. W. Huber, *Appl. Catal. A Gen.*, 2011, **392**, 57–68.
41. D. Liang, G. Li, Y. Liu, J. Wu and X. Zhang, *Catal. Commun.*, 2016, **81**, 33–36.
42. S. Wang and E. Iglesia, *J. Phys. Chem. C*, 2016, **120**, 21589–21616.
43. M. Signoretto, F. Menegazzo, L. Contessotto, F. Pinna, M. Manzoli and F. Boccuzzi, *Appl. Catal. B Environ.*, 2013, **129**, 287–293.
44. N. Korsunskaya, V. Papusha, O. Kolomys, V. Strelchuk, A. Kuchuk, V. Kladko, Y. Bacherikov, T. Konstantinova and L. Khomenkova, *Phys. Status Solidi Curr. Top. Solid State Phys.*, 2014, **11**, 1417–1422.
45. R. Fricke, H. Kosslick, V. A. Tuan, I. Grohman, W. Pilz, W. Storek and G. Walther, in *Studies in Surface Science and Catalysis*, 1994, vol. 83, pp. 57–66.
46. E. Djurado, F. Boulc, L. Dessemond, N. Rosman and M. Mermoux, *J. Electrochem. Soc.*, 2004, **151**, 774–780.
47. H. Wang, G. Li, Y. Xue and L. Li, *J. Solid State Chem.*, 2007, **180**, 2790–2797.
48. M. Hunger, in *Zeolite Characterization and Catalysis. A Tutorial*, eds. A. W. Chester and E. G. Derouane, Springer, 2009, pp. 65–105.
49. L. Rodríguez-González, F. Hermes, M. Bertmer, E. Rodríguez-Castellón, A. Jiménez-López and U. Simon, *Appl. Catal. A Gen.*, 2007, **328**, 174–182.
50. A. Samoson, E. Lippmaa, G. Engelhardt, U. Lohse and H. G. Jerschke, *Chem. Phys. Lett.*, 1987, **134**, 589–592.
51. Z. Yan, D. Ma, J. Zhuang, X. Liu, X. Han, X. Bao, F. Chang, L. Xu and Z. Liu, *J. Mol. Catal. A Chem.*, 2003, **194**, 153–167.
52. C. Poupin, R. Maache, L. Pirault-Roy, R. Brahmi and C. T. Williams, *Appl. Catal. A Gen.*, 2014, **475**, 363–370.
53. I. L. C. Buurmans, E. A. Pidko, J. M. de Groot, E. Stavitski, R. A. van Santen and B. M. Weckhuysen, *Phys. Chem. Chem. Phys.*, 2010, **12**, 7032–7040.
54. Z. Ristanović, A. V. Kubarev, J. Hofkens, M. B. J. Roeffaers and B. M. Weckhuysen, *J. Am. Chem. Soc.*, 2016, **138**, 13586–13596.
55. L. R. Aramburo, S. Wirick, P. S. Miedema, I. L. C. Buurmans, F. M. F. de Groot and B. M. Weckhuysen, *Phys. Chem. Chem. Phys.*, 2012, **14**, 6967–6973.
56. J. Feroso, H. Hernando, S. Jiménez-sánchez, A. A. Lappas, E. Heracleous, P. Pizarro, J. M. Coronado and D. P. Serrano, *Fuel Process. Technol.*, 2017, **167**, 563–574.
57. A. Corma, G. Huber, L. Sauvanaud and P. Oconnor, *J. Catal.*, 2007, **247**, 307–327.

58. T. Carlson, J. Jae, Y. Lin, G. Tompsett and G. Huber, *J. Catal.*, 2010, **270**, 110–124.
59. X. Zhang, K. Wilson and A. F. Lee, *Chem. Rev.*, 2016, **116**, 12328–12368.
60. Y.T. Cheng and G. W. Huber, *Green Chem.*, 2012, **14**, 3114–3125.
61. A. Fukutome, H. Kawamoto and S. Saka, *ChemSusChem*, 2015, **8**, 2240–2249.

Supporting information

2. Experimental

2.1. Catalyst preparation

2.1.1. Zeolite samples

Two ZSM-5 zeolites were selected as catalytic supports: a nanocrystalline ZSM-5 provided by CLARIANT (HCZP 90) denoted as n-ZSM-5; and a microcrystalline material (1-4 μm) synthesized by SILKEM, which was subjected to desilication by treatment with a 1.4 M NaOH solution at 65 °C for 30 min (solution/zeolite mass ratio = 5) to generate mesopores, being denoted as h-ZSM-5. After desilication, the sample was ion-exchanged with an ammonium sulphate solution and calcined in air at 550 °C to obtain the acid form.

2.1.2. Zeolite ZrO_2 incorporation

ZrO_2 was introduced in both h-ZSM-5 and n-ZSM-5 in a proportion of 10 wt% by wet impregnation in two steps and using ethanol as solvent, followed by calcination in static air. Initially, 50% of the total metal precursor required (zirconium (IV) acetylacetonate, Aldrich, 97%) was dissolved in ethanol (10 ml $\text{g}_{\text{support}}^{-1}$) and contacted with the support. The mixture was kept stirring for 6 h at 40 °C and the solvent was then removed using a rotary evaporator. After that, the sample was dried at 100 °C in an oven overnight. Using this same procedure, the second half of the zirconium precursor solution was added to the support. Finally, the sample was calcined at 450 °C for 6 h to obtain the final $\text{ZrO}_2/\text{h-ZSM-5}$ and $\text{ZrO}_2/\text{n-ZSM-5}$ samples.

2.2. Catalyst characterisation

2.2.1. X-ray diffraction

X-ray diffraction (XRD) patterns of the parent ZSM-5 zeolites and ZrO_2 supported catalysts were recorded with a Philips PW 3040/00 X'Pert MPD/MRD diffractometer using Cu $\text{K}\alpha$ radiation ($\lambda = 1.542 \text{ \AA}$), operated at 45 kV and 40 mA.

2.2.2. Electronic microscopy - energy dispersive X-ray analysis

The samples were analysed by Transmission Electronic Microscopy (TEM) using a Philips TECNAI 20 instrument operating at 200 kV. Likewise, Scanning Electron Microscopy (SEM) images and energy dispersive X-ray spectroscopy (EDX) were recorded using a FEI XL30SFEG microscope. The samples were sprinkled on an aluminium stub with a carbon sticker. Pt sputter coating was avoided to prevent overlap of the Pt and Zr signals in the EDX measurements. Quantification of Zr average has been based counting on Si, Al, O and Zr elements. SEM images were recorded in secondary electron (SE) mode.

2.2.3. Ar adsorption-desorption isotherms

The textural properties of the assayed catalysts were determined by argon adsorption-desorption isotherms at -186 °C in an AUTOSORB iQ Analyzer System from Quantachrome Instruments. The samples were previously degassed at 300 °C under vacuum for 3 h. The total surface area was determined applying the Brunauer-Emmett-Teller (BET) equation. The pore

size distribution and the contribution of micro- and mesopores to the textural properties were calculated using the adsorption branch of the isotherms by means of the NL-DFT (Non Local Density Functional Theory) model assuming cylindrical pore geometry.

2.2.4. Inductively coupled plasma-optical emission spectroscopy

The aluminium and zirconia contents of the zeolite samples were measured by inductively coupled plasma-optical emission spectroscopy (ICP-OES) using a Perkin Elmer Optima 7300AD instrument. Thereby, the samples were digested in a mixture of HF and HNO₃ in a microwave oven (Anton Paar MW3000).

2.2.5. Acidity measurements

The Brønsted and Lewis acid sites (BAS and LAS, respectively) were quantified by pyridine adsorption, followed by FTIR spectroscopy. Self-supporting wafers (ca. 10 mg/cm²) were prepared and activated at 450 °C for 4 h under vacuum. Subsequently, 3 Torr of pyridine were introduced into the system and the adsorption took place at 150 °C for 20 min. The strength of BAS and LAS was determined at different evacuation temperatures (150, 250, 350 and 450 °C). Thereby, after 20 min of desorption at high vacuum, spectra were recorded at room temperature with a 4 cm⁻¹ resolution in the 4000-400 cm⁻¹ range by means of a Nicolet FTIR spectrometer equipped with a MCT detector. The concentration of BAS (C_B) and LAS (C_L) was calculated using specific FTIR bands and the corresponding molar extinction coefficients, as explained elsewhere.^{1,2}

2.2.6. Raman spectroscopy

Raman spectroscopy was performed with a Renishaw InVia microscope, using 785 nm laser excitation, through a 20x long working distance objective. Spectra were acquired using a 100% laser excitation power, for 5 accumulations at a 20 s exposure. In the case of the monoclinic ZrO₂ powder used as reference (Aldrich, nanopowder, <100 nm), the parameters were the same as for the catalyst powders except for 50% laser excitation power.

2.2.7. Magic angle spinning solid-state nuclear magnetic resonance

²⁷Al magic angle spinning solid-state nuclear magnetic resonance (MAS ssNMR) experiments were performed at 11.7 T (n-ZSM-5) and 9.4 T (h-ZSM-5) (500 and 400 MHz ¹H Larmor frequency) on a Bruker Avance III spectrometer equipped with a 3.2 mm MAS probe. Spectra were recorded at ambient temperature using 18 kHz MAS, for the h-ZSM-5 catalyst, and 15 kHz MAS for the n-ZSM-5 zeolite. RF fields of 50 kHz and 40 kHz were respectively used for the ²⁷Al $\pi/12$ pulse followed by 26 ms acquisition. 10240 scans were accumulated using an inter-scan delay of 1 s. The ²⁷Al chemical shift was externally referenced to an aqueous aluminium nitrate solution. The 1D spectra were processed using a line-broadening of 100 Hz.

A zero-quantum (ZQ) filtered multiple-quantum magic angle spinning (MQ-MAS) pulse-sequence was used to correlate the ²⁷Al isotropic chemical shift (F1) with the quadrupolar line-shape (F2).³ The excitation and conversion pulses were applied with an RF field of 62 kHz. For the selective pulse following the Z-filter delay an RF field of 6.5 kHz was used. The incrementation time for the indirect dimension was set to one rotation period and 36 increments were recorded. The direct acquisition time was set to 2.5 ms and 696 scans were accumulated

using an inter-scan delay of 2 s. MQ-MAS data were Fourier transformed and sheared, using the software of Bruker Topspin3.5, and 250 Hz line-broadening was applied in both dimensions.

The 1D NMR spectra were deconvoluted using a Gaussian multipeak fitting function in the Origin 9.1 software. The areas under the curves were fitted based on the Levenberg-Marquardt least-squares algorithm to generate fits from starting peak positions observed in the corresponding MQ MAS NMR spectra. The areas under the peaks were used to estimate the ratio between framework and extra-framework Al species.

2.2.8. UV-Vis micro-spectroscopy

UV-Vis micro-spectroscopy was performed in an in-situ cell (FTIR600, Linkam Scientific Instruments) equipped with a temperature controller (Linkam TMS 93). The microscopy set-up used is based on an Olympus BX41 upright microscope with a 50 x 0.5 NA-high (NA: numerical aperture) working distance microscope objective. A 75 W tungsten lamp was used for illumination. The microscope was equipped with a 50/50 double-viewpoint tube, which accommodated a CCD video camera (ColorView IIIu, Soft Imaging System GmbH) and an optical fibre mount. A 200 mm-core fibre connected the microscope to a CCD UV/Vis spectrometer (AvaSpec-2048TEC, Avantes).

Selective catalyst staining by 4-fluorostyrene oligomerization was followed in-situ by UV-Vis micro-spectroscopy. After preheating the catalysts at 100 °C for 10 min, 15 µl of 4-fluorostyrene was added per 10 mg of sample. The first in-situ spectra of the stained powder catalyst were recorded 5 min after addition for 15 min.

2.2.9. Confocal fluorescence microscopy

Confocal fluorescence microscopy (CFM) images of the stained materials were acquired using a Nikon Eclipse 90i confocal microscope with a 100 x 0.73 NA dry objective. Excitation light was provided by focusing three specific laser lines, 488, 561 and 642 nm, simultaneously on the desired sample, located in an open cell (Linkam Instruments, FTIR 600). The microscope was equipped with a Nikon A1 scan head, accommodating the optics, which couple fibre optics for excitation and emission light microscope. A spectral analyser in the Nikon A1 system was equipped with 32 photomultiplier tubes (PMTs) set to collect emission light in the region of ca. 450–700 nm, with a resolution of 6 nm. Following the same procedure as for in-situ UV-Vis micro-spectroscopy, 4-fluorostyrene oligomerization staining was also followed in-situ by CFM. In addition, ex-situ fluorescence spectra were recorded on the samples 30 min after the reaction.

2.3. Biomass feedstock

The lignocellulosic biomass employed in this study was acid-washed wheat straw (WS-ac), obtained from agricultural residues of Segovia province (Spain). The raw biomass was ground into a particle size of 0.5-1 mm and then subjected to a de-ashing treatment by acid washing. Thereby, a representative amount of biomass was dispersed into a 1 wt% HNO₃ solution (20 ml_{dis} g⁻¹_{biomass}) at 50 °C for 2 h. The sample was then filtered, washed with Milli-Q water till neutral pH and finally dried at 105 °C for 2 days. This pre-treatment was applied to minimize the interferences of the intrinsic catalytic effects of the mineral matter present in the raw biomass.

2.4. Biomass pyrolysis tests

The details of the lab-scale experimental setup here used for the catalytic fast-pyrolysis tests have been provided elsewhere.⁴ The reaction system consists of a downdraft fixed bed reactor with two differentiated zones physically separated, one for the primary thermal pyrolysis and other for the vapour catalytic upgrading, heated and controlled by two independent electric furnaces and K thermocouples, respectively. All the experiments were carried out using 4 g of WS-ac sample. For the catalytic experiments, 1.6 and 2.8 g (0.4 and 0.7 g g⁻¹ catalyst/biomass ratio, respectively) were loaded. Catalysts were pelletized into particles with a size between 0.180 – 0.250 mm to avoid an excessive pressure drop and to ease their recovery after reaction. The pyrolysis tests were carried out at atmospheric pressure and temperatures of 550 and 400 °C for the pyrolysis and catalytic zones, respectively, using 100 cm³ min⁻¹ of N₂ as carrier gas.

Once the levels of O₂ were dropped down to < 0.1 vol% in the reaction system and the selected temperatures were reached, the biomass feeding valve was opened and the biomass was introduced into the reactor. Consequently, the pyrolysis reaction occurred and char (carbonaceous solid by-product) and pyrolysis vapours were formed. The solid fraction was accumulated in the thermal zone, while vapours and permanent gases were swept by the N₂ flow and passed through the catalyst bed. The vapours leaving the reactor were condensed by a series of 125 cm³ flasks refrigerated by an ice-water bath kept at 0 °C. The non-condensable gases were passed to a sampling bag placed at the end of the line.

The different fractions formed in the pyrolysis process (bio-oil, char, coke and non-condensable gases) were collected, quantified and subjected to detailed compositional analysis, as next described. The bio-oil fraction expressed on a water-free basis is denoted as bio-oil*.

2.5. Characterization of the products obtained in the biomass pyrolysis tests

Proximate analyses of the biomass were performed following European standards, including moisture (UNE-EN 14774-1:2010), ash (UNE-EN 14775:2010), and volatile matter (UNE-EN 15148:2010) contents. The moisture content was determined by weight difference of a representative amount of biomass sample after being dried in an oven at 105 °C for 3 h. The ash content present was calculated by combusting a representative amount of biomass (20 g, previously dried) at 815 °C with 100 cm³ min⁻¹ air flow for 2 h. The chemical composition of the ash was measured by ICP-OES. Volatile matter of biomass and char was determined by thermogravimetric analysis (TGA) using a NETZSCH STA 449 thermobalance from the weight loss of a certain amount of sample heated up to 900 °C for 7 min under an inert flow of Ar. The amount of fixed carbon was determined by difference.

The ultimate analyses of biomass and pyrolysis products (bio-oil, char and coke) were performed in a Thermo Scientific FLASH 2000 CHNS/O micro-elemental analyser. C, H, N and S elements were directly measured, whilst O was determined by difference. The coke deposited over the catalysts was quantified by TGA. Thereby, a certain amount of the used catalyst was heated up to 550 °C at 20 °C min⁻¹ under air flow and coke was calculated by weight difference. The water content of the bio-oil fraction was measured by means of a Mettler-Toledo V20S compact volumetric Karl-Fischer titrator (ASTM E203-08).

The individual components of the bio-oil fraction were analysed by a Gas Chromatograph coupled to Mass Spectrometer (GC/MS), GC-MS, Bruker® SCION 436-GC, (Electron Energy: 70 eV; Emission: 300 V; He flow rate: 1 cm³ min⁻¹; Column: WCOT fused silica 30 m x 0.25

mm ID x 0.25 μm). For tentative identification of pyrolysis products, all mass spectra were compared to the NIST EI-MS spectral library (v2.0) with a minimum match score of 700. Due to the high complexity of the bio-oil components, the compounds identified by comparing the mass spectra with the NIST database have been classified according to their main functional groups as follows: carboxylic acids (AC), light oxygenates (LO: aldehydes, alcohols, ketones and ethers), furans (FUR), amines and amides (AMN & AMD), oxygenated aromatics (O-AR), aromatic hydrocarbons (AR) and anhydrosugars (SUG). From the response factors corresponding to a number of compounds representative of those families, it was possible to estimate their concentration in the bio-oil* samples.

The gas fraction was analysed using a dual channel Agilent® CP-4900 Micro Gas Chromatograph (μ -GC), equipped with molecular sieve (Molsieve 5 Å) and HayeSep A columns and a thermal conductivity detector (TCD), using He as carrier gas. The equipment was periodically calibrated with standard gas mixtures of different gas concentrations containing N₂ (internal standard), O₂, H₂, CO, CO₂, CH₄, C₂H₄, C₂H₆, C₃H₆, C₃H₈, C₄H₈ and C₄H₁₀. Thus, the gas mass yield of the gas fraction and its elemental composition (C, H and O) could be calculated.

The high heating value (HHV) of the gases was determined from those of the individual compounds. The HHV of the biomass, bio-oil, char and coke were calculated from the elemental composition using an empirical correlation.⁵

By adding the measured weights of the different products, the total mass balance was closed to the amount of biomass fed with an experimental error lower than 5 wt% in all tests. Details on the procedure used for the mass balance calculations in the catalytic and non-catalytic biomass pyrolysis tests can be found elsewhere.⁴ Energy yield associated with a specific pyrolysis product was calculated as the proportion of chemical energy (HHV) retained in this product respecting to that of raw biomass. Likewise, the overall selectivity towards the different deoxygenation products (H₂O, CO and CO₂) was determined from the relative molar production of these compounds in each test taking into account its oxygen content. The catalytic deoxygenation selectivity was calculated in a similar way but subtracting the contribution of a thermal pyrolysis test to the overall H₂O, CO and CO₂ production.

Figure captions

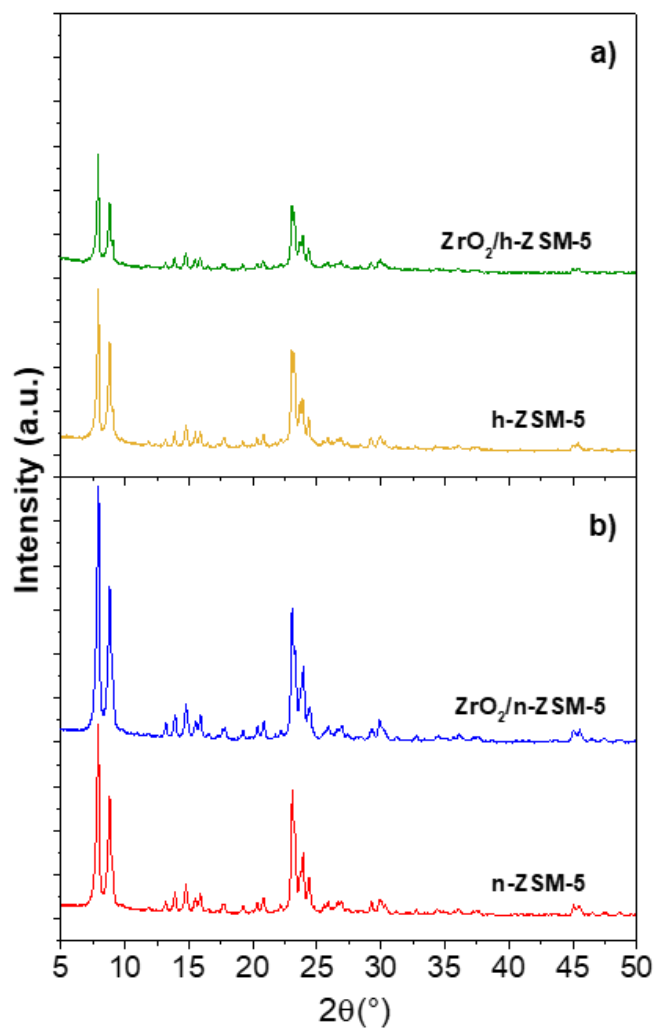


Fig. S1. XRD patterns of calcined (a) desilicated and (b) nanocrystalline ZSM-5 based materials.

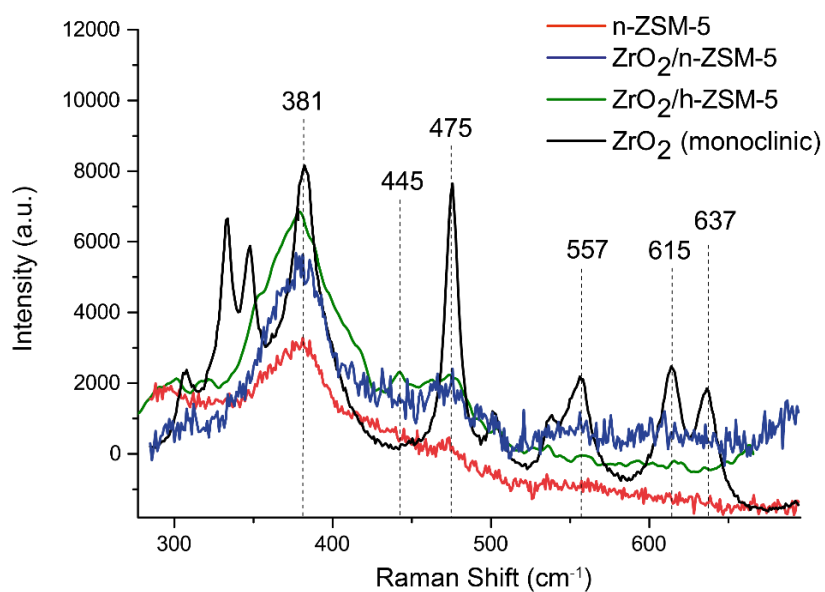


Fig. S2. Raman spectra of n-ZSM-5 (red), $\text{ZrO}_2/\text{n-ZSM-5}$ (blue), $\text{ZrO}_2/\text{h-ZSM-5}$ (green) and monoclinic ZrO_2 (black), used as reference. Excitation source $\lambda = 785$ nm.

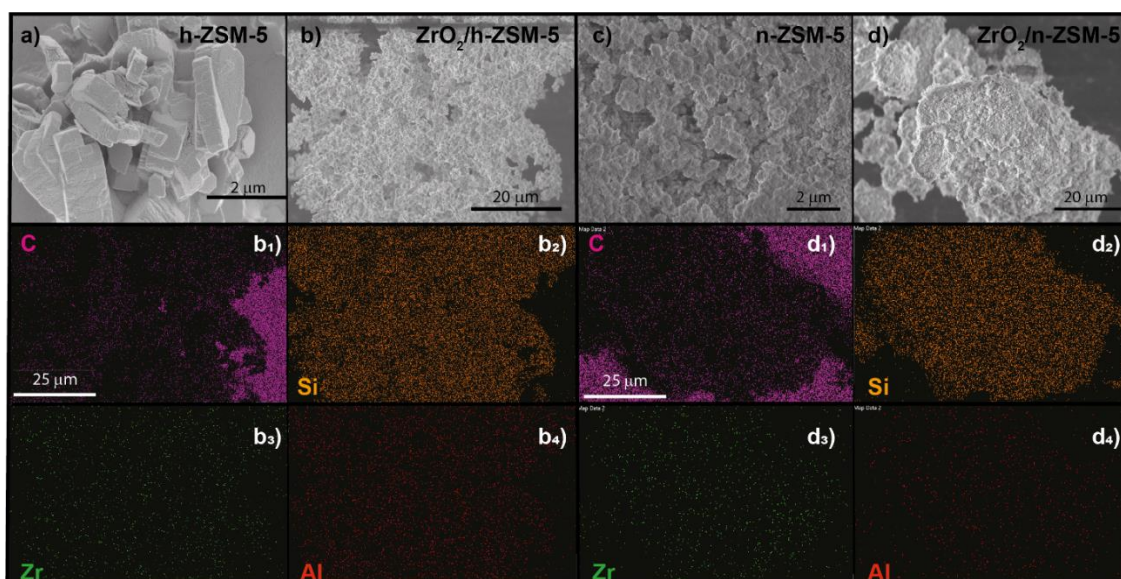


Fig. S3. SEM images of: h-ZSM-5 (a) and n-ZSM-5 (c); and SEM-EDX images and corresponding elements maps for: ZrO₂/h-ZSM-5 (b) and ZrO₂/n-ZSM-5 (d) catalysts. Note that dot-mapping of C (b₁, d₁), present in the carbon sticker which holds the powder sample, is used as reference for defining the negative of the aggregate's contour.

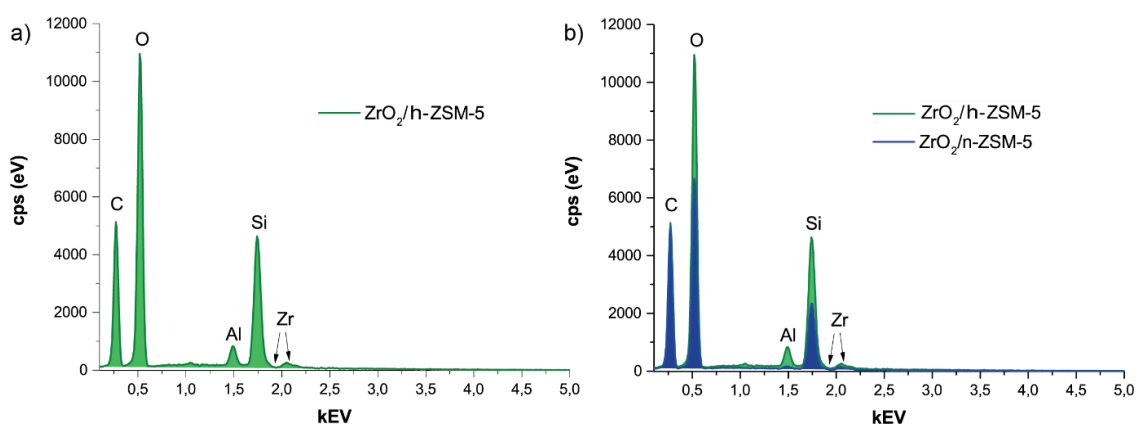


Fig. S4. Map sum spectrum derived from the EDX dot mapping of: a) ZrO₂/h-ZSM-5, b) ZrO₂/n-ZSM-5 compared to ZrO₂/h-ZSM-5.

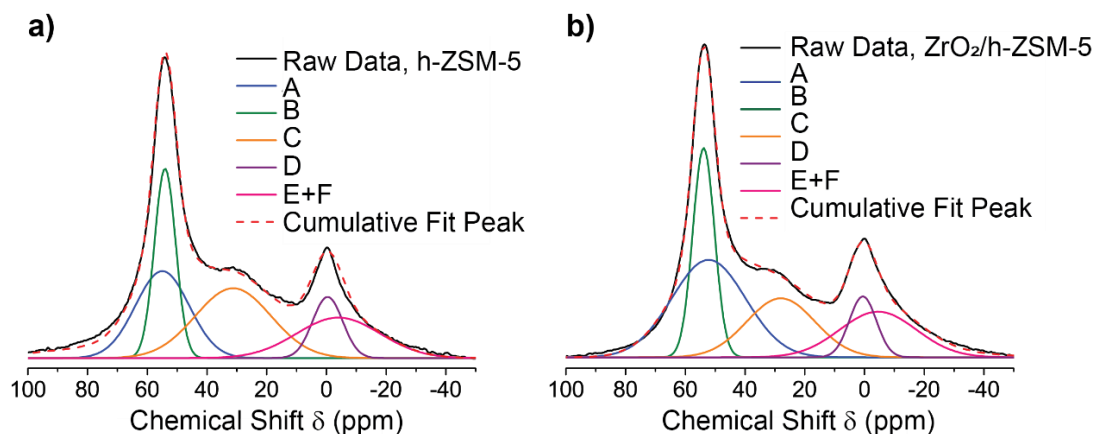


Fig. S5. Deconvolution and fit of the ^{27}Al MAS ssNMR spectra of h-ZSM-5 (a) and $\text{ZrO}_2/\text{h-ZSM-5}$ (b).

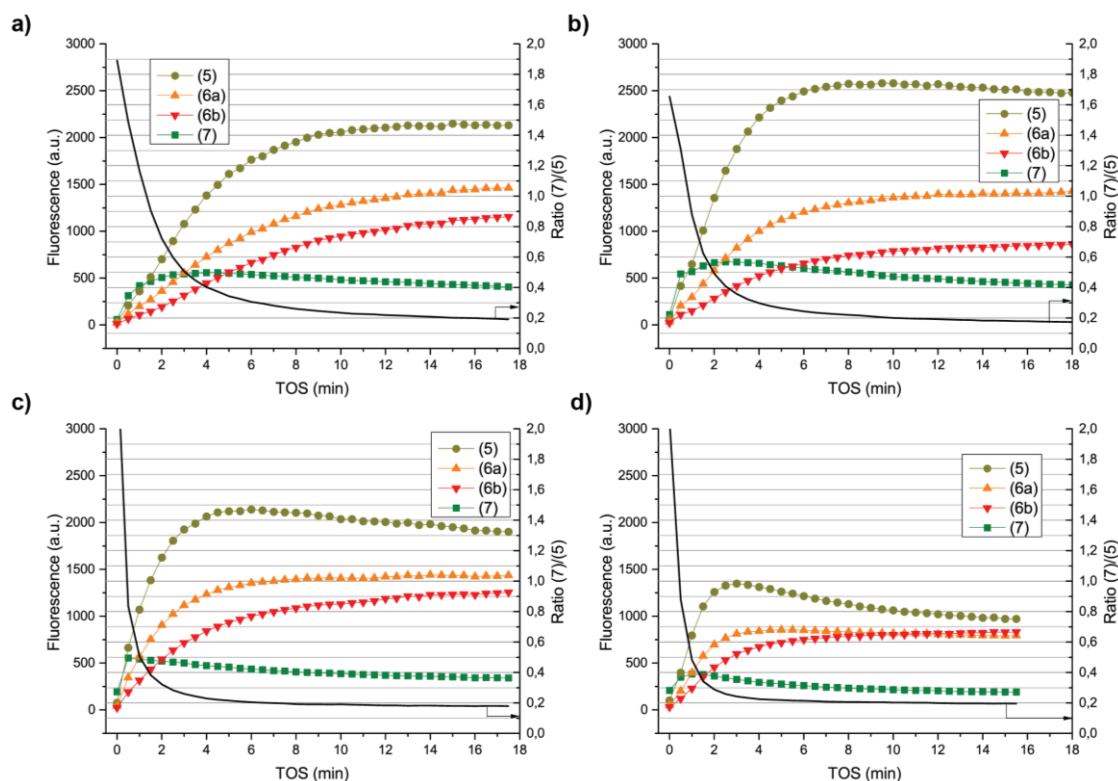
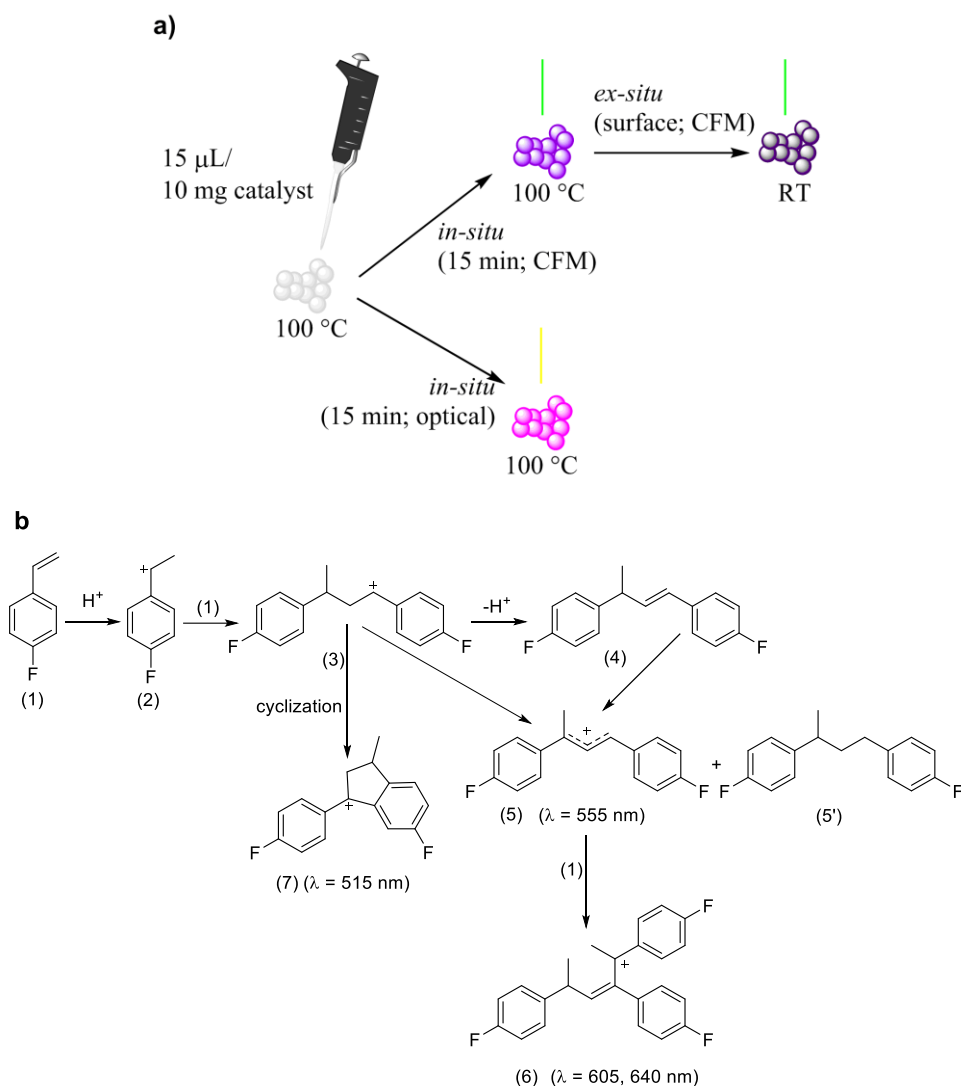


Fig. S6. Left axis: Time evolution of the intensities of the fluorescent emission bands during the 15 min of 4-fluorostyrene oligomerisation at $100\text{ }^\circ\text{C}$ on: (a) h-ZSM-5, (b) $\text{ZrO}_2/\text{h-ZSM-5}$, (c) n-ZSM-5; (d) $\text{ZrO}_2/\text{n-ZSM-5}$. According to Scheme S1, the corresponding series are assigned to: the cyclic oligomer product (7), linear oligomer (5), dimer (6a) and trimer (6b). Excitation lasers: 404, 488, 561, 642 nm. Right axis: Ratio of intensities of the emission bands assigned to cyclic (7) and linear (5) carbocations at selected times during the 4-fluorostyrene oligomerisation reaction.

Table S1. Resolution of the fitted peaks for the ^{27}Al MAS ssNMR spectra of h-ZSM-5 and $\text{ZrO}_2/\text{h-ZSM-5}$ catalysts and ratio of Al species after fitting for both solid catalysts.

		h-ZSM-5		ZrO ₂ /h-ZSM-5	
		Value	Standard Error	Value	Standard Error
Peak A	center (ppm)	54.96	0.44	53.84	0.99
Peak A	area	2.79E+06	3.24E+04	7.93E+06	1.02E+06
Peak A	width	17.96	0.75	26.50	0.62
Peak B	center (ppm)	54.05	0.02	52.20	0.66
Peak B	area	2.42E+06	5.72E+04	5.32E+06	47432
Peak B	width	7.14	0.07	8.33	0.03
Peak C	center (ppm)	31.24	0.48	30.56	0.75
Peak C	area	3.16E+06	6.52E+05	6.09E+06	2.33E+06
Peak C	width	25.27	2.37	29.64	5.48
Peak D	center (ppm)	-0.40	0.08	1.03	0.08
Peak D	area	1.10E+06	7.58E+04	1.58E+06	174783
Peak D	width	10.04	0.28	9.66	0.30
Peak E+F	center (ppm)	-3.99	2.13	-3.72	1.49
Peak E+F	area	2.03E+06	5.35E+04	1.67E+06	815078
Peak E+F	width	28.00	2.18	18.19	2.30
		R² 0.93168	Reduced chi-sqr 9.53E8	R² 0.99822	Reduced chi-sqr 2.84E7
Sample		Al ^{IV} / Al ^{VI}	Al ^{IV} / Al ^V	Al ^{IV} / Al ^V	Al ^{IV} / (Al ^{VI} + Al ^V)
h-ZSM-5		3.0	3.8	3.8	1.7
ZrO ₂ /h-ZSM-5		2.2	2.9	2.9	1.3



Scheme S1. a) Schematic representation of staining of the catalyst under study and in-situ examination by optical microscopy (white light source) and by confocal fluorescence microscopy (CFM) (green to red light source). b) Reaction pathways in the Brønsted acid-catalysed oligomerization of 4-fluorostyrene on H-ZSM-5 zeolites.^{6–8} 4-fluorostyrene is protonated in the presence of Brønsted acid sites (BAS) giving benzylic carbocation (2). Dimerization with a second 4-fluorostyrene monomer (1) yields the linear dimeric 1,3-bis(4-fluorophenyl)-1-butylium cation (3), which can be transformed either into a conjugated linear dimeric 1,3-bis(4-fluorophenyl)-2-buten-1-yl cation (5) by deprotonation, or into 3-methyl-1,4-fluorophenylindanyl by cyclization (7). Conjugate linear dimeric carbocation (5) can further oligomerize trimeric and longer oligomer species (6). The wavelengths in brackets indicate the literature 6 assignment to the carbocationic species shown.

References

1. C. A. Emeis, *J. Catal.*, 1993, **141**, 347–354.
2. A. Peral, J. M. Escola, D. P. Serrano, J. Prech, C. Ochoa-Hernandez and J. Cejka, *Catal. Sci. Technol.*, 2016, **6**, 2754–2765.
3. J. P. Amoureux, C. Fernandez and S. Steuernagel, *J. Magn. Reson.*, 1996, **123**, 116–118.
4. H. Hernando, S. Jiménez-Sánchez, J. Feroso, P. Pizarro, J. M. Coronado and D. P. Serrano, *Catal. Sci. Technol.*, 2016, **6**, 2829–2843.
5. S. A. Channiwala and P. P. Parikh, *Fuel*, 2002, **81**, 1051–1063.
6. I. L. C. Buurmans, E. A. Pidko, J. M. de Groot, E. Stavitski, R. A. van Santen and B. M. Weckhuysen, *Phys. Chem. Chem. Phys.*, 2010, **12**, 7032–7040.
7. Z. Ristanović, A. V. Kubarev, J. Hofkens, M. B. J. Roefsaers and B. M. Weckhuysen, *J. Am. Chem. Soc.*, 2016, **138**, 13586–13596.
8. L. R. Aramburo, S. Wirick, P. S. Miedema, I. L. C. Buurmans, F. M. F. de Groot and B. M. Weckhuysen, *Phys. Chem. Chem. Phys.*, 2012, **14**, 6967–6973.

Article 8

The crucial role of clay binders on the performance of ZSM-5 based materials for biomass catalytic pyrolysis

Catalysis Science and Technology, 2019, 9, 789-802

**Catalysis
Science &
Technology**



PAPER

[View Article Online](#)
[View Journal](#)



Cite this: DOI: 10.1039/c8cy02116c

The crucial role of clay binders in the performance of ZSM-5 based materials for biomass catalytic pyrolysis†

Héctor Hernando, ^{ab} Cristina Ochoa-Hernández, ^{†c} Mariya Shamzhy, ^c Inés Moreno,^{ab} Javier Feroso, ^a Patricia Pizarro,^{ab} Juan M. Coronado, ^{§a} Jiří Čejka ^c and David P. Serrano ^{*ab}

Impact JCR factor, (JCR 2017): 5.365

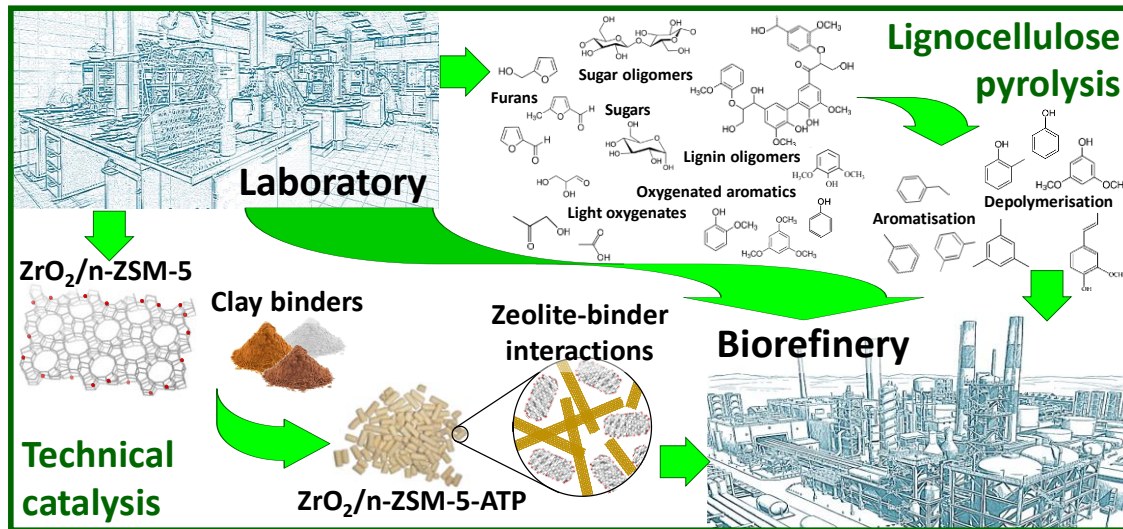
Category: Physical Chemistry. 32 of 147 (Q1)

ABSTRACT

The effect of the agglomeration of the $\text{ZrO}_2/\text{n-ZSM-5}$ catalyst with two different clays (bentonite and attapulgite) on lignocellulose catalytic pyrolysis has been investigated. The reaction tests have been carried out with an “ex-situ” configuration of the reaction system, which allowed the thermal and catalytic zones to operate at different temperatures (550 and 400 °C, respectively). The behavior of the agglomerated catalysts has been compared with those of the binder-free material and the pure clays. The catalyst samples have been characterized by X-ray diffraction, microscopy, chemical analysis and Ar adsorption measurements, as well as by FTIR of both adsorbed pyridine and CO_2 to probe their acid-base properties. The occurrence of synergetic effects between the different catalyst components in the agglomerated materials has been denoted in lignocellulose catalytic pyrolysis. Agglomeration caused opposite effects on the catalyst performance depending on the clay. With bentonite as binder, the technical catalyst showed a reduced bio-oil deoxygenation activity due to a loss of most of its strong acidity by ion-exchange of Na^+ cations from the clay. However, the agglomerated catalyst incorporating attapulgite exhibited an enhanced activity leading to the production of a bio-oil with significantly lower oxygen content. For this system a migration of Mg^{2+} occurs from the attapulgite towards both the zeolitic and ZrO_2 components of the parent catalyst. Although this fact partially decreases the concentration of the zeolite Brønsted acid sites, it also has a promotion effect on both Lewis acidity and basicity due to the interaction between the migrating Mg^{2+} species and the ZrO_2 phase. As a result, the technical catalyst agglomerated with attapulgite exhibits a well-balanced distribution of acid and basic sites, which is responsible for the remarkable enhancement observed in the bio-oil deoxygenation activity in comparison with the binder-free material.

Keywords: Catalytic pyrolysis. Biomass. ZSM-5. ZrO_2 . Clays. Attapulgite. Bentonite.

GRAPHICAL ABSTRACT



1. Introduction

Thermochemical processes for the transformation of biomass, from torrefaction to gasification, have recently received a great deal of attention in connection with the interest in developing more sustainable biorefineries schemes, since these conversion routes provide flexibility in products generation, as well as maturity and technical reliance. Among them, biomass pyrolysis represents a direct route to the production of a high throughput of liquid products. However, it is well-known that the physicochemical characteristics of pyrolysis bio-oils are far from ideal due to their high oxygen content. This liquid bioproduct is formed by a complex blend of a number of functionalized molecules, such as phenol derivatives, furans, anhydro-sugars, ketones, aldehydes and carboxylic acids, in addition to large oligomers that are difficult to characterize.¹⁻⁴ This composition results in a number of undesirable properties: acidic pH and corrosiveness, high instability and viscosity, along with moderate heating values.⁵ Accordingly, several catalytic processes have been proposed for either in-situ or subsequent upgrading of the bio-oils. In this way, catalytic pyrolysis can be viewed as a primary bio-oil deoxygenation step to be subsequently coupled with other upgrading treatments. Thus, although hydrodeoxygenation (HDO) can achieve a high degree of transformation of bio-oils into hydrocarbons, the requirement of an external hydrogen source and extreme operation conditions, calls for a previous refinement of bio-oils, which could be accomplished by catalytic pyrolysis.

A variety of catalysts have been tested for biomass catalytic pyrolysis including basic metal oxides such as MgO,⁶⁻⁹ red mud,¹⁰⁻¹³ clays^{7,10,14} and ordered mesoporous materials.^{15,16} However, most of the studies have been focused on the use of zeolites,¹⁷⁻¹⁹ ZSM-5 being one of the most used because it presents adequate acidic properties and pore structure, which reduces formation of coke deposits and favours the production of aromatics.²⁰⁻²⁴ In the search for an ideal conjunction of activity and selectivity, the incorporation of additional active phases to conventional zeolitic materials has opened new conversion pathways, becoming a hot topic in the field.^{20,25-28} In a recent work, the incorporation of ZrO₂ over both nanocrystalline and partially desilicated hierarchical ZSM-5, was highly beneficial for the process by inducing a sharper deoxygenation of the bio-oil*, enhancing the liquid energy yield and also promoting depolymerisation of larger oligomers.²⁹

An additional difficulty for optimising the process under real conditions arises from the fact that zeolite catalysts in technical form also contain usually a significant proportion of binder additives, which provide them with convenient mechanical properties. These solid modifiers, which in most cases are alumina or natural clays, in principle are expected to act as diluents of the active phase, although very often they have inhibitory effects. Thus, agglomeration of zeolite catalyst using clay binders has been reported to reduce the activity in toluene disproportionation and n-octane hydroisomerisation.^{30,31} These findings have been assigned to different phenomena induced by the binders, such as pore blockage and/or neutralisation of the acid sites in the zeolite catalyst. In a recent work, the occurrence of interactions between zeolites and clays during the agglomeration process has been studied for thiophene conversion into light absorbing oligomers as an acid-catalysed staining reaction test, showing that the binder heavily impacts the reactivity and product selectivity and concluding that the type of binder plays a vital role.³² Interestingly, in rare examples some promoter effects have been identified when using clays for zeolite agglomeration. Thus, attapulgite increased the longevity of hierarchical ZSM-5 zeolite in methanol-to-hydrocarbons, also influencing positively the olefin selectivity. This has been

explained in terms of the reversible neutralisation of the zeolite acid sites by mobile Mg species from the clay.³³

On the other hand, when considering the use of clay binders for catalytic biomass pyrolysis, it should be taken into account that the clay itself may possess some catalytic properties. In this way, different types of clays, being low-cost materials, have been tested as catalysts for biomass pyrolysis although their capacity for improving bio-oil characteristics was low.^{10,34} Nevertheless, a recent work has shown that acid-modified bentonite possesses a significant activity for the pyrolysis of lignin.¹⁴

The present work focuses on the catalytic effect of two natural clays (bentonite and attapulgite) as binders of the $\text{ZrO}_2/\text{ZSM-5}$ system for lignocellulose catalytic pyrolysis. The results obtained indicate that these binders induce sharp changes in the catalytic behaviour of the zeolite, but with opposite trends when comparing both clays. Thus, while bentonite attenuates the activity of the parent catalyst, a strong enhancement of the bio-oil deoxygenation is provoked by agglomeration with attapulgite. These results have been correlated with the textural and acidic properties of the technical catalysts, as well as through the study of the acidity/basicity of the materials by FTIR monitoring the adsorption and interaction of probe molecules (pyridine and carbon dioxide) with the catalyst.

2. Experimental

2.1. Catalyst preparation

The parent ZSM-5 sample was provided by CLARIANT (HCZP 90). Being nanocrystalline, this sample was denoted here as n-ZSM-5. 10 wt% of ZrO_2 was incorporated into the n-ZSM-5 sample by wet impregnation in two steps to favor a better dispersion of the active phase. Initially 50% of the total metal precursor required (zirconium (IV) acetylacetonate 97%, Aldrich) was dissolved in ethanol, the support being added to the solution ($10 \text{ ml g}_{\text{support}}^{-1}$). The mixture was kept under stirring for 6 h at 40 °C and the solvent was then removed in a rotary evaporator. After that, the sample was dried at 110 °C in an oven overnight. In the same way, the second half of the zirconium precursor was incorporated, repeating the procedure earlier described. Finally, the sample was calcined at 550 °C for 5 h to obtain the $\text{ZrO}_2/\text{n-ZSM-5}$ material.

The agglomerated catalysts were prepared using two different clay binders: bentonite (CLARIANT) and attapulgite (CMS), denoted here as BNT and ATP, respectively. The extruding process was based in an earlier work.³⁵ The first step to obtain the extruded paste consisted in a physical dry mixing of the catalyst and the inorganic binder (70/30 w/w), in addition to methylcellulose (Aldrich, 20 wt% referred to the total paste mass). Once the mixture was completely homogeneous, distilled water (1.6 ml of distilled water per 1 g of paste) was added to the powder mixture while keeping the stirring. The paste was kept airtight for 1 h and then extruded in a Caleva Mini Extruder at 50 rpm ending in a circular nozzle of 1 mm of diameter. The so-obtained cylindrical bodies were cut into 3 mm length and kept under controlled temperature and humidity conditions (40 °C and 10% of humidity) in a CTS GmbH C +10/200 climate chamber for 48 h. Finally, the catalyst pellets were calcined under continuous flow of air ($100 \text{ cm}^3 \text{ min}^{-1}$) to remove the remaining water and the organics and to enhance their mechanical strength. The calcination program involved heating the catalyst up to 440 °C at 0.5 °C min^{-1} , keeping constant the latter temperature for 1 h and then increasing the temperature at a rate of 1 °C min^{-1} up to 550 °C, which is maintained for 4 h.

2.2. Catalyst characterization

2.2.1. X-ray diffraction

X-ray diffraction (XRD) patterns of the catalysts were recorded with a Philips PW 3040/00 X'Pert MPD/MRD diffractometer using Cu K α radiation ($\lambda = 1.5406 \text{ \AA}$), operated at 45 kV and 40 mA.

2.1.1 Ar adsorption-desorption isotherms

The textural properties of the zeolite-based catalysts were determined by argon adsorption-desorption isotherms at $-186 \text{ }^\circ\text{C}$ in an AUTOSORB iQ Analyzer System (Quantachrome Instruments). The samples were previously degassed at $300 \text{ }^\circ\text{C}$ under vacuum for 3 h. The total BET area was determined applying the Brunauer-Emmett-Teller (BET) equation in the range of $P/P_0 = 0.05-0.20$. The pore size distributions and the contributions of micro- and mesopores to the values of surface area and pore volume were calculated using the adsorption branch of the isotherm by means of the NL-DFT (Non Local Density Functional Theory) model assuming cylindrical pore geometry.

2.1.2 Inductively coupled plasma-optical emission spectroscopy

The aluminium and zirconium contents of the catalysts were measured by inductively coupled plasma-optical emission spectroscopy (ICP-OES) using a Perkin Elmer Optima 7300AD instrument. The samples were digested in a solution of HF/HNO $_3$ in a microwave oven (Anton Paar MW3000).

2.1.3 FTIR monitoring of the adsorption of probe molecules

The catalyst and binder samples were pressed into self-supporting wafers with a density of $8.0-12 \text{ mg cm}^{-2}$ and activated *in-situ* at $T = 450 \text{ }^\circ\text{C}$ for 4 h under high vacuum. The adsorption of pyridine was performed at 3 Torr and $150 \text{ }^\circ\text{C}$ for 20 min. Desorption of pyridine was carried out at $150 \text{ }^\circ\text{C}$, $250 \text{ }^\circ\text{C}$, $350 \text{ }^\circ\text{C}$ and $450 \text{ }^\circ\text{C}$ for 20 min at each temperature. Before adsorption, pyridine was degassed by freeze-pump-thaw cycles. The concentrations of Lewis and Brønsted acid sites were evaluated from the integral intensities of bands at $1444-1455 \text{ cm}^{-1}$ (cL) and 1545 cm^{-1} (cB) using extinction coefficients, $\epsilon(\text{L}) = 2.22 \text{ cm } \mu\text{mol}^{-1}$ and $\epsilon(\text{B}) = 1.67 \text{ cm } \mu\text{mol}^{-1}$, respectively.³⁶

On the other hand, the adsorption of CO $_2$ was carried out at $25 \text{ }^\circ\text{C}$. CO $_2$ was repeatedly adsorbed in the sample in small aliquots ($7-10 \text{ } \mu\text{mol g}^{-1}$ catalyst) until integral intensities of absorption bands observed in $2400-2200 / 1700-1400 \text{ cm}^{-1}$ region reach maximal values. CO $_2$ was added from a gas admission compartment with a volume of $11.40 \pm 0.03 \text{ cm}^3$. The pressure in this compartment was determined with the aid of PfeifferTM Vacuum CMR 363 capacitance-type pressure meter with a measurement range $p = 1 \cdot 10^{-3} - 11 \text{ hPa}$ and accuracy $\pm 0.20\%$. The amount of added CO $_2$ was estimated from ideal gas law. A spectrum was recorded 30 min after each CO $_2$ addition. Spectra recorded after longer time intervals show no significant difference.

All spectra were recorded using Nicolet 6700 spectrometer equipped with MCT/B detector with a resolution of 4 cm^{-1} by collecting 128 scans for a single spectrum at room temperature. All the spectra were normalized to a wafer density of 10 mg cm^{-2} .

2.1.4 Compression mechanical tests of the technical catalysts

To certify that both binders provide physical strength to the shaped cylinders, compression mechanical tests were performed over the lateral surfaces of the cylinders in a Chatillon Model MT Tension/Compression Mechanical Test instrument.

2.2 Biomass feedstock

The lignocellulosic biomass employed in this study was wheat straw (*WS-ac*), grounded into a particle size of 0.5-1 mm, de-ashed and dried. Its selection as raw biomass was based on previous studies.³⁷⁻³⁹ The de-ashing pretreatment step (washing with a 1 wt% nitric acid solution at 50 °C for 2 h) was applied to minimize interferences from catalytic effects of the mineral matter contained in the raw biomass.^{38,39}

2.3 Biomass pyrolysis tests

The lab-scale experimental setup used for the catalytic pyrolysis tests consists in a downdraft fixed bed reactor with two zones physically separated, the first one for the primary thermal pyrolysis and the second for the vapour catalytic upgrading, as shown in detail in previous works.^{37,38} All the experiments were carried out using 4 g of biomass fed through a manual valve. The ZrO₂/n-ZSM-5 catalyst in powder form was pelletized into a 180-250 μm particle size to avoid an excessive pressure drop. The pyrolysis tests were carried out at temperatures of 550 °C and 400 °C for the thermal and catalytic zones, respectively, atmospheric pressure and 100 cm³ s⁻¹ of N₂ as carrier gas. For the tests performed with the technical catalysts the overall catalyst/biomass (C/B) ratio was 0.2857 w/w, whereas in the experiments carried out using the binder-free catalyst and the pure clays the C/B ratio was adjusted to operate with loadings of those components similar to those employed with the agglomerated catalysts (0.2 w/w for ZrO₂/n-ZSM-5 and 0.0857 w/w for bentonite and attapulgite).

Once the reaction system was completely inert (O₂ < 0.1 vol%) and the set temperatures were reached, the biomass-feeding valve was opened and the pyrolysis reaction started. The carbonaceous solid fraction (char) was accumulated in the thermal zone, while vapours and incondensable gases passed through the catalyst bed. The vapours were condensed by a series of 125 cm³ flasks refrigerated at 0 °C. The gases were collected in a sampling bag at the end of the line. The bio-oil, char and the used catalyst were recovered and weighted. The bio-oil fraction in water-free basis has been named as bio-oil*.

2.4 Products characterisation and data treatment

2.4.1 Proximate and ultimate analyses

The proximate analyses were performed according to the European standards, including moisture (UNE-EN 14774-1:2010), ash (UNE-EN 14775:2010) and volatile matter (UNE-EN 15148:2010) contents, the amount of fixed carbon being determined by difference. The chemical composition of the ash was measured by ICP-OES. The ultimate analyses of biomass and pyrolysis products (bio-oil, char and coke) were performed in a Thermo Scientific FLASH 2000 CHNS/O micro-elemental analyser. C, H, N and S elements were directly measured, whilst O was determined by difference. The coke deposited over the catalysts after the biomass catalytic pyrolysis tests was quantified by TGA, heating up the spent catalyst to 550 °C at 20 °C min⁻¹ under 80 cm³ min⁻¹ air flow.

2.4.2 Karl-Fischer titration

The water content of the bio-oil fraction was measured by means of a Mettler-Toledo V20S compact volumetric Karl-Fischer titrator (ASTM E203-08).

2.4.3 Gas chromatography

The gas fraction was analysed by a dual channel Agilent® CP-4900 Micro Gas Chromatograph (μ -GC), equipped with two different columns (Molsieve 5 Å and HayeSep A) and a thermal conductivity detector (TCD), using He as carrier gas. The equipment was periodically calibrated with standard gas mixtures of different gas concentrations containing N₂ (internal standard), O₂, H₂, CO, CO₂, CH₄, C₂H₄, C₂H₆, C₃H₆, C₃H₈, C₄H₈ and C₄H₁₀.

2.4.4 Gas chromatography coupled to mass spectrometry

The individual components of the bio-oil* fraction were analysed by a Gas Chromatograph coupled to a Mass Spectrometer (GC-MS), Bruker® SCION 436-GC (electron energy: 70 eV; emission: 300 V; He flow rate: 1 cm³ min⁻¹; column: WCOT fused silica 30 m x 0.25 mm ID x 0.25 μ m). The NIST EI-MS spectral library (v2.0) was used to identify the products. Due to a wide range of molecules present in the bio-oil*, they were classified according to their main functional groups as follows: carboxylic acids (AC), light oxygenates (LO: aldehydes, alcohols, ketones and ethers), furans (FUR), amines and amides (AMN & AMD), oxygenated aromatics (O-AR), aromatic hydrocarbons (AR) and anhydrosugars (SUG). An external calibration of the GC-MS was carried out using the most representative compounds of each group. More details about the calibration for GC-MS quantification is included in the ESI.

2.5 Mass and energy yield calculations

The high heating value (HHV) of the gas fraction was calculated from the individual compounds in the same way as in previous studies.^{27,37-40} The HHV of the biomass, bio-oil, char and coke was calculated by the correlation proposed by Channiwala and Parikh.⁴¹ This equation is valid for a wide range of composition of solid, liquid and gaseous fuels.

The total mass balance was closed with an experimental error lower than 5 wt% of the biomass for all the experiments. The equations and details of the mass balances applied to evaluate the pyrolysis tests can be found elsewhere.³⁷ The total chemical energy balance was carried out by addition of the energy yields corresponding to the different fractions, determined by combining their mass yield and HHV.

3. Results and discussion

3.1 Properties of the catalysts

Structural and surface characterisation of the technical catalysts, prepared by agglomeration of the ZrO₂/n-ZSM-5 material with bentonite and attapulgite, is first discussed to determine the influence of the extrusion process on their physicochemical properties. As reference, both the parent binder-free catalyst and the two pure clays have been included in the study.

XRD patterns of the agglomerated catalysts are shown in Fig. 1, including also those of the clays used as binders. Most of the XRD diffraction lines observed for the technical catalysts correspond with the reflections typical of the MFI zeolite structure, although being observed with a lower intensity than in the parent material. This fact can be assigned to dilution and

shielding effects caused by the distribution of the clay particles between and around the zeolite nanocrystals. The absence of XRD amorphous background indicates that the zeolite component keeps its crystallinity during the agglomeration process. The presence of clays is not obviously revealed by XRD due to a relatively low intensity of their characteristic peaks. The sharp peak at 26.6° present in both BNT and ATP corresponds to quartz, which is frequently found as an impurity in clays,⁴² being also observed as a small signal in the technical catalysts. ZrO_2 phase, supported on the n-ZSM-5 zeolite, does not provide any additional feature to the XRD patterns, as it has been previously indicated,²⁹ since it is highly dispersed over the external surface of the zeolite nanocrystals.

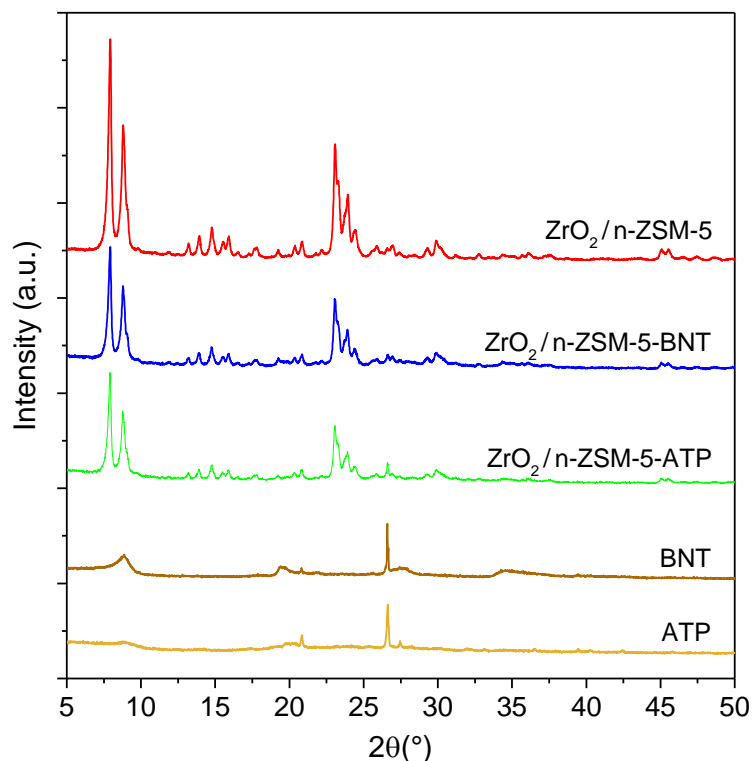


Fig.1. XRD patterns of both pure clays and ZSM-5 based catalysts.

The main physicochemical characteristics of the extruded catalysts and pure clays are summarized in Table 1. Elemental analysis shows that ZrO_2 content is close to the theoretical one added by impregnation (10 wt%), being little affected by the agglomeration with clays. On the other hand, both extruded catalysts exhibit a mechanical strength somewhat lower than those of the pure clays but still significant, with values obtained in the rupture test of 16 and 12 N when using bentonite and attapulgite as binders, respectively.

The textural properties of the samples determined from Ar adsorption isotherms, are collected in Table 1. The pure clays exhibit low BET areas (57 and $107 \text{ m}^2 \text{ g}^{-1}$ for bentonite and attapulgite, respectively) compared to the parent $\text{ZrO}_2/\text{n-ZSM-5}$ catalyst ($375 \text{ m}^2 \text{ g}^{-1}$). No microporosity is detected in the pure clays, hence their surface area arises from the external surface of the clays particles having lamellar and needle morphology in the case of bentonite and attapulgite, respectively. The incorporation of the binders to the parent $\text{ZrO}_2/\text{n-ZSM-5}$ sample causes a decrease in both the surface area and the pore volume. This reduction is very close to that expected considering the dilution effect caused by the agglomeration with 30 wt% of binder.

Thus, BET areas of the catalysts extruded with BNT and ATP (269 and 296 m² g⁻¹, respectively) match quite well with those obtained by combining linearly the values corresponding to the individual catalyst components (280 and 295 m² g⁻¹). These results evidence that the agglomeration with clays causes almost no blockage of the zeolite pores so both technical catalysts are expected to keep a high accessibility to the active sites.

Table 1. Physicochemical properties of both pure clays and ZSM-5 based catalysts.

Catalyst	ZrO ₂ loading ^a (wt%)	Rupture test (N)	S _{BET} ^b (m ² /g)	S _{MES+EXT} ^c (m ² /g)	S _{MIC} ^d (m ² /g)	V _T ^e (cm ³ /g)	V _{MIC} ^f (cm ³ /g)	Acidity ^g (mmol/g)	
								C _B	C _L
BNT	-	20 ± 1	57	57	-	0.099	-	-	0.008
ATP	-	24 ± 3	107	107	-	0.455	-	0.004	0.039
ZrO ₂ /n-ZSM-5	9.2	-	375	91	284 ^d	0.378	0.169	0.116	0.091
ZrO ₂ /n-ZSM-5-BNT	9.8	16 ± 1	269	77	192 ^d	0.326	0.114	0.018	0.121
ZrO ₂ /n-ZSM-5-ATP	10.5	12 ± 1	296	65	231 ^d	0.382	0.138	0.059	0.088

^a Measured by ICP-OES. ^b BET surface area. ^c Mesopore + external surface area. ^d Micropore surface area. ^e Total pore volume at P/P₀ ≈ 0.98. ^f Micropore volume. ^g From FTIR/pyridine, values calculated from desorption at 150 °C

3.2 Pyrolysis of wheat straw using technical catalysts

Fig. 2A compares the mass yields of the different fractions obtained in the wheat straw catalytic pyrolysis tests over the parent ZrO₂/n-ZSM-5 sample and the technical catalysts produced by agglomeration with bentonite and attapulgite. The oxygen content of the bio-oil* fraction is shown in Fig. 2B, whereas the composition of the gases is illustrated in Fig. 2C. The results corresponding to a thermal test, as well as those obtained using the pure clays are also included in this graph. The products obtained in the pyrolysis experiments have been grouped according to the following fractions: char (carbonaceous residue produced in the thermal zone of the reactor), coke (carbonaceous residue deposited over the catalyst), gases, water and bio-oil* (organic components of the liquid phases). In all experiments the char yield was almost constant (about 19 wt%), which was an expected result since it is generated in the thermal zone of the reactor prior to the contact of the generated vapours with the catalytic bed. In each test, the catalyst/biomass ratio was adjusted to work with the same loading of zeolitic and clay components as those present in the technical catalysts (ZrO₂/n-ZSM-5-BNT and ZrO₂/n-ZSM-5-ATP).

The pure clays exhibit a low activity for wheat straw catalytic pyrolysis, at least with the catalyst loadings employed in these tests, showing results very similar to those of the thermal experiment. Nevertheless, a slight decrease in the yield and oxygen content of the bio-oil* occurs with the pure clays, in addition to the formation of small amounts of coke (0.5-1.0 wt% referred to the raw biomass) and some enhancement in the yield of specific gaseous components (CO, CO₂ and CH₄). Overall, these variations are not very significant, showing that the parent clays almost do not contribute to the biomass catalytic pyrolysis process. Accordingly, it could be expected that, if no interaction exists between the catalyst components, the incorporation of these clays to the parent ZrO₂/n-ZSM-5 material should not have a remarkable effect. However, as shown in Fig. 2, this is not the case, since the use of both bentonite and attapulgite as binder causes significant variations in the yield of the different fractions and components, as well as on the bio-oil* oxygen content. Moreover, bentonite and attapulgite show mainly opposite trends, when added as binders to the parent zeolitic catalyst. As a first conclusion, these results evidence

that a strong interaction exist between the ZSM-5 based catalyst and both clays, which remarkably affect the biomass catalytic pyrolysis.

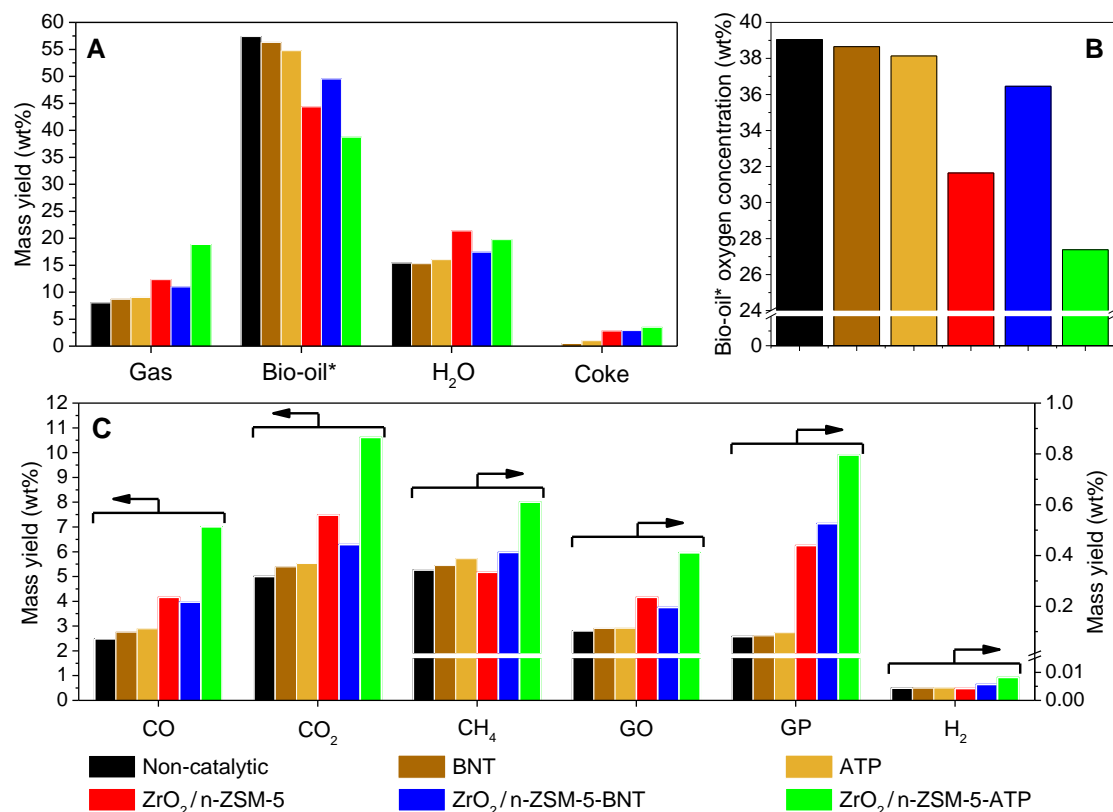


Fig. 2. Product yield (wt%) (A), bio-oil* oxygen concentration (B), and yield of gaseous components (wt%) (C), obtained in the WS-ac pyrolysis over both pure clays and ZSM-5 based catalysts.

The use of bentonite as binder is quite detrimental for the catalytic activity, leading to a product distribution between those of the parent zeolitic catalyst and the thermal test. Thus, compared with binder-free ZrO₂/n-ZSM-5, the technical catalyst agglomerated with bentonite exhibits a lower production of gases, water, and a higher yield of bio-oil*, as well as a quite larger oxygen content of the last one. Therefore, the catalyst agglomerated with bentonite possesses a small deoxygenation activity.

A very different behaviour is observed for the technical catalyst agglomerated with attapulgite. In this case, the presence of the clay binder does not affect negatively to the wheat straw catalytic pyrolysis but, on the contrary, it reinforces significantly the activity of the parent ZrO₂/n-ZSM-5 material. This is reflected in the lower oxygen content and yield of bio-oil* and the enhanced formation of gases in comparison with the binder-free material. Thus, the degree of bio-oil* deoxygenation achieved by agglomeration with attapulgite is around 1.6 higher than over the parent ZrO₂/n-ZSM-5 catalyst. Likewise, from the product distribution in the gaseous fraction, it can be concluded that the catalyst agglomerated with attapulgite exhibits enhanced production of all components and, in particular, of CO and CO₂, generated by decarbonylation and decarboxylation reactions, respectively. Since the pure attapulgite presents a low activity for wheat straw catalytic pyrolysis, these findings evidence a remarkable synergetic effect coming from the interaction between the zeolitic and attapulgite components of the technical ZrO₂/n-ZSM-5-ATP catalyst.

Regarding the production of gaseous hydrocarbons (see Table S1), the most relevant components in terms of yield are methane, propylene, ethylene and ethane. Catalytic cracking of alkyl chains in bulky molecules, particularly those derived from lignin, as well as deoxygenation of light organic compounds, are the most likely origins of these light hydrocarbons. When using the pure clays, the yields of these components are very similar to those obtained in the thermal test. For the technical catalysts, agglomeration with bentonite causes just slight variations (mainly an increase in the methane production), whereas the use of attapulgite as binder leads to an enhancement in the yield of all gaseous hydrocarbons.

In addition to the char formed in the thermal zone of the reactor, a second carbonaceous phase (coke) is generated over the catalysts. The amount and elemental composition of the coke deposits are summarized in Table S2. When using the pure clays, the coke content is higher for attapulgite than for bentonite and the same occurs when comparing the technical catalysts. Regarding the parent $\text{ZrO}_2/\text{n-ZSM-5}$ catalyst, the agglomeration with bentonite leads to a lower coke formation, which is in agreement with the reduced activity of bentonite for biomass catalytic pyrolysis. On the other hand, when using attapulgite as binder, the coke deposited per amount of catalyst is not increased in comparison with the parent zeolitic catalyst in spite of the observed activity enhancement. Likewise, important differences are observed on the coke composition. For the parent $\text{ZrO}_2/\text{n-ZSM-5}$ material the coke deposited is very rich in C (81.2 wt%), whereas the oxygen content is relatively small (11.1 wt%). In contrast, the coke formed over the technical catalysts contain quite less carbon and rather more oxygen, showing that the incorporation of the clays increases the affinity of the catalysts by oxygenated compounds. As a consequence, the chemical energy yield lost in the coke deposits decreases when agglomerating the parent $\text{ZrO}_2/\text{n-ZSM-5}$ catalyst.

An important parameter in biomass catalytic pyrolysis is the deoxygenation pattern as it determines largely the degree of bio-oil* upgrading achieved. According to a simplified scheme, deoxygenation may take place by three main routes: decarboxylation, decarbonylation and dehydration, whose extension can be easily quantified from the production of CO_2 , CO and H_2O , respectively.

The overall deoxygenation selectivities obtained in the thermal and catalytic experiments of the present work are illustrated in Fig. 3. As it has been earlier reported^{26,37,38,40} for non-catalytic biomass pyrolysis, dehydration is the main pathway for removing oxygen, accounting for a 73% selectivity, followed by decarboxylation and finally by decarbonylation. Nevertheless, it must be taken into account that the purely thermal process is little efficient from the point of view of oxygen removal in the bio-oil* fraction, as the latter presents a high oxygen content, which in fact is very close to that of the raw biomass. Therefore, the overall deoxygenation selectivities are more linked to the formation of char, which shows reduced oxygen,³⁷ than to the bio-oil upgrading process. For this reason, just relatively small differences are observed in the catalytic tests in terms of overall deoxygenation selectivity, as shown in Fig. 3A. Just in the case of the catalyst agglomerated with attapulgite a clear deviation is observed from the thermal deoxygenation pattern.

In order to isolate the effect of the thermal and catalytic contribution on the deoxygenation pathways, Fig. 3B represents the deoxygenation selectivity corresponding just to the catalytic step, which has been calculated from the incremental production of CO_2 , CO and H_2O that takes place in the catalytic tests in comparison with the thermal experiment. In this graph the

selectivities corresponding to the tests using the pure clays as catalysts have not been included due to the almost negligible catalytic activity of the latter. For the parent $\text{ZrO}_2/\text{n-ZSM-5}$ catalyst dehydration is still the main deoxygenation catalytic route, although with a lower contribution compared to the thermal step. Agglomeration of this material with bentonite causes a further reduction in the dehydration selectivity, increasing the contribution of decarboxylation and especially of decarbonylation. Interestingly, for the technical catalyst agglomerated with attapulgite, decarboxylation becomes the major deoxygenation route (with 39% selectivity), followed by dehydration and decarbonylation, denoting the crucial effect of this clay binder on changing the bio-oil* deoxygenation pathways and explaining the enhanced deoxygenation activity observed with this material. On the other hand, this result is also quite relevant from the point of view of the efficiency of the bio-oil* upgrading process since decarboxylation is a quite favourable deoxygenation route, which minimize the loss of chemical energy and contribute to increase the H/C ratio, approaching the bio-oil composition to that of the current fossil-derived transportation fuels.

Bio-oil* upgrading through deoxygenation involves also a progressive decrease of the bio-oil* yield, hence both parameters should be assessed together. In this way, Fig. 4 plots the oxygen concentration of the bio-oil* fraction as a function of the bio-oil* energy yield, the latter representing the proportion of the chemical energy contained in the raw biomass which is retained in the liquid organic product for each of the evaluated catalysts. As a reference, the result obtained with the purely thermal pyrolysis is also shown in the graph. The trend followed in the upgrading process of the thermal bio-oil* according to this figure depends on the relative contribution of the three deoxygenation routes, but also on the extension of other transformations, such as the formation of coke and light hydrocarbons, which subtracts energy to the liquid fraction without provoking its deoxygenation.³⁷

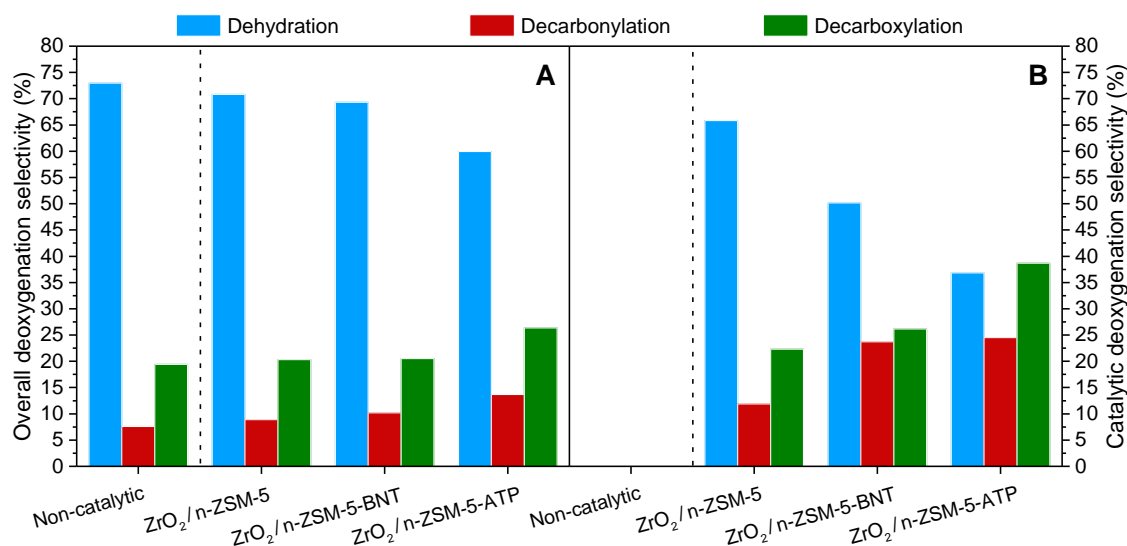


Fig. 3. Relative contribution of the deoxygenation routes obtained in the WS-ac pyrolysis: overall deoxygenation selectivity in both thermal and catalytic tests (A) and catalytic deoxygenation selectivity for the ZSM-5 based catalysts (B).

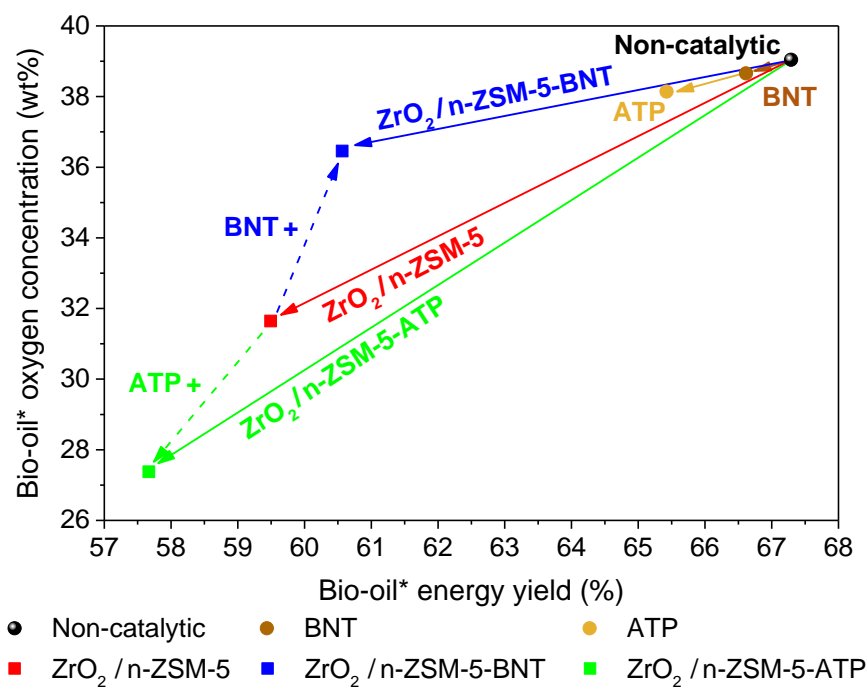


Fig. 4. Bio-oil* oxygen concentration versus bio-oil* energy yield obtained in the WS-ac pyrolysis over both pure clays and ZSM-5 based catalysts.

The points corresponding to bio-oils* obtained over the pure clays are very close to that of the thermal test, as expected from their almost negligible catalytic activity for bio-oil* upgrading. When incorporated as binders into the technical catalysts, the two clays exhibit completely opposite tendencies in this graph. The effect of bentonite is confirmed to be clearly detrimental, leading to an important decrease in the deoxygenation activity with just a moderate increase of the energy yield regarding the parent ZrO₂/n-ZSM-5 catalyst. On the contrary, attapulgite incorporation has a remarkable beneficial influence leading to a bio-oil* with reduced oxygen content (about 27 wt%) and high energy yield (57.6%). Moreover, the slope of the line connecting with the point of the thermal bio-oil* is higher for the technical catalyst agglomerated with attapulgite than that of the parent ZrO₂/n-ZSM-5 material, inducing the former a more efficient bio-oil* deoxygenation pathway. These positive results appear to be related to the promotion of the decarboxylation route when using attapulgite as binder, which is the most favourable for achieving a good balance between low oxygen content and high energy yield in the bio-oil* fraction.

The composition of the bio-oil* fraction has been assessed by GC-MS, the different products identified being grouped into the following families: carboxylic acids (AC), light oxygenates (LO; including mainly aldehydes, ketones and ethers), furans (FUR), sugars (SUG; mostly levoglucosan), oxygenated aromatic compounds (O-AR) and aromatic hydrocarbons (AR). By calibration of the main components in each family it has been possible to determine the corresponding mass yield. Moreover, the difference between the overall bio-oil* yield and the addition of the yields obtained by GC-MS has been assigned to the species present in the bio-oil* that cannot be detected by this technique, which includes mainly oligomers coming from the decomposition of the three lignocellulose biopolymers.

As shown in Fig. 5A, non-detected GC-MS components account for about 70% of all the species present in the bio-oil* obtained in the thermal test, which confirms the reduced effectiveness of the biomass pyrolysis process in the absence of catalysts. For the experiment

performed with the $\text{ZrO}_2/\text{n-ZSM-5}$ catalyst the yield in components detected by GC-MS is almost two-fold of that in the thermal test, showing that this material is able to transform a great part of the oligomeric species. Agglomeration of this catalyst with clays causes mainly changes in the yield of the non GC-MS detected matter, opposite effects being again denoted for bentonite and attapulgite. Thus, the bio-oil* produced over the catalyst agglomerated with bentonite possesses a quite higher proportion of oligomeric species than when using attapulgite as binder. In this last case, the introduction of the clay causes a small but noticeable increase in both mass and energy yield of components detected by GC-MS, confirming the positive effects derived from the agglomeration of the ZSM-5 based catalyst with attapulgite.

According to Fig. 5B, the main component families present in the bio-oil* obtained over the parent $\text{ZrO}_2/\text{n-ZSM-5}$ catalyst are SUG, followed by O-AR and AC, and lower yields of LO and FUR. The high concentration of SUG in this catalytic bio-oil* is a consequence of the mild reaction conditions here employed ($C/B = 0.2$, $T = 400\text{ }^\circ\text{C}$) to compare the different catalysts. As shown in a previous work,³⁷ increasing the C/B ratio over the binder-free catalyst leads to a drastic reduction in the SUG concentration and a sharp increase in the AR yield. The technical catalyst agglomerated with bentonite produces a bio-oil* with even higher SUG yield but decreasing the formation of O-AR, whereas aromatic hydrocarbons are almost not detected. On the contrary, when using attapulgite for the agglomeration, the SUG yield is reduced, increasing those of AC, FUR, O-AR and AR in respect to the parent binder-free catalyst. These results are in line with an enhanced activity of the technical catalyst prepared using the attapulgite clay.

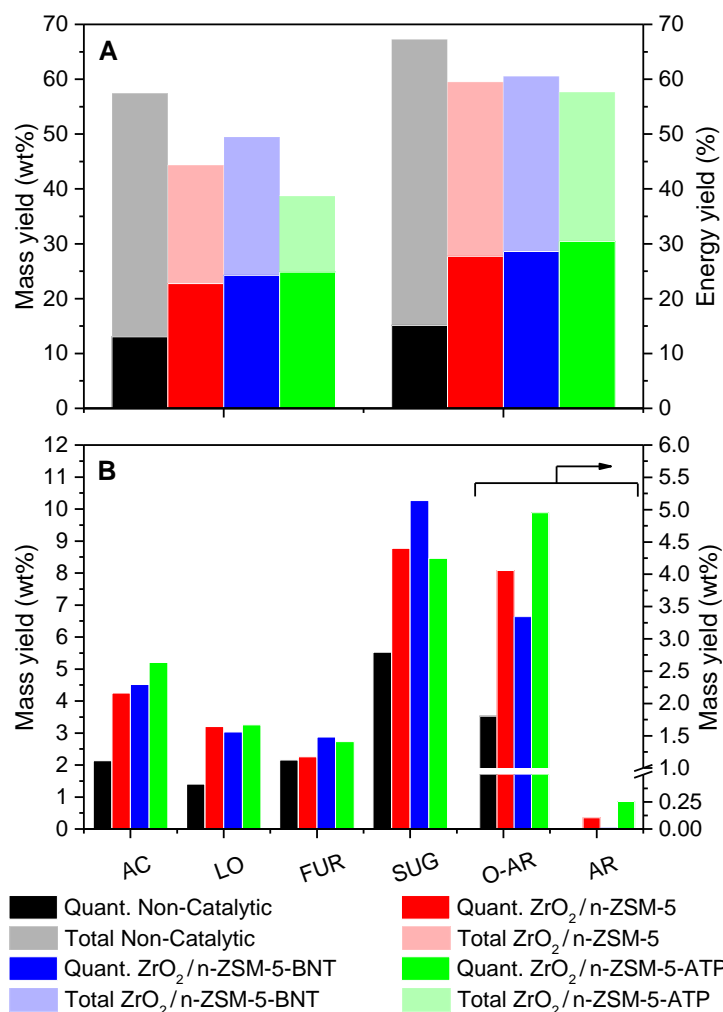


Fig. 5. GC-MS analysis of the bio-oil* obtained in the WS-ac pyrolysis over the ZSM-5 based catalysts: mass yield of total/quantified components (A), mass yield of the quantified components according to families of compounds (B).

3.3 FTIR study of the acid-basic properties of the catalysts

In order to gain further understanding on the changes induced by the clay binders on the acid-base properties of the catalyst, the ZrO₂/n-ZSM-5 system (including both parent and agglomerated samples) has been explored systematically by means of FTIR following pyridine and CO₂ adsorption.

3.3.1 FTIR/pyridine tests

Type, strength and concentration of acid sites in the catalysts were determined by pyridine adsorption/desorption monitored by FTIR. The overall concentration of the different types of acid centres was determined from the areas of the bands at 1546 cm⁻¹ (Brønsted acid sites, BAS) and in the range 1444-1455 cm⁻¹ (Lewis acid sites, LAS), being gathered in Table 1. More detailed information on the strength of these centres can be found in Fig. 6, showing the concentration of acid sites capable to retain adsorbed pyridine at certain temperature. Likewise, the main FTIR signals originated by the adsorption of pyridine on both Brønsted and Lewis sites are illustrated in Fig. 7.

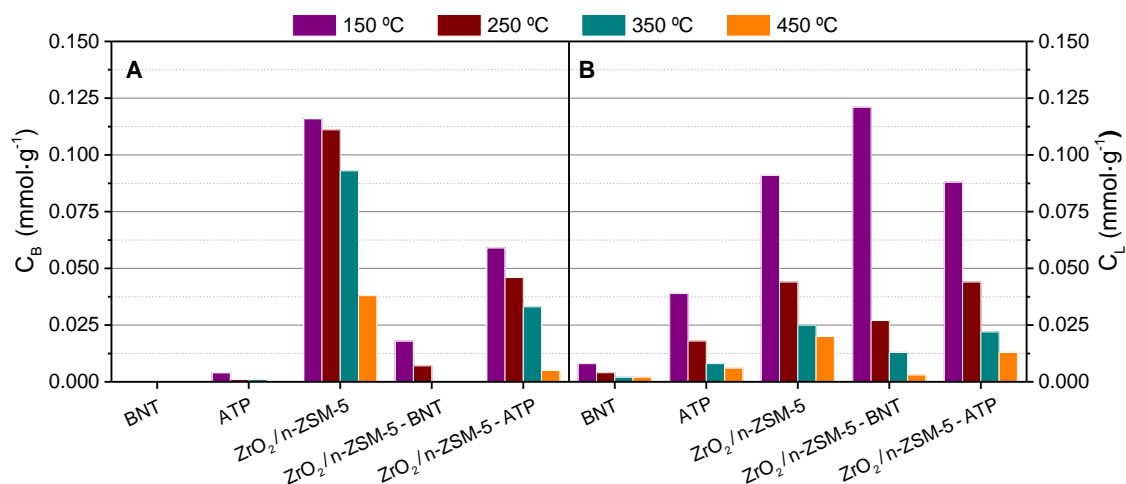


Fig. 6. Brønsted (C_B), and Lewis (C_L) acid sites strength distribution determined for different catalysts using thermodesorption of pyridine monitored with FTIR adsorption.

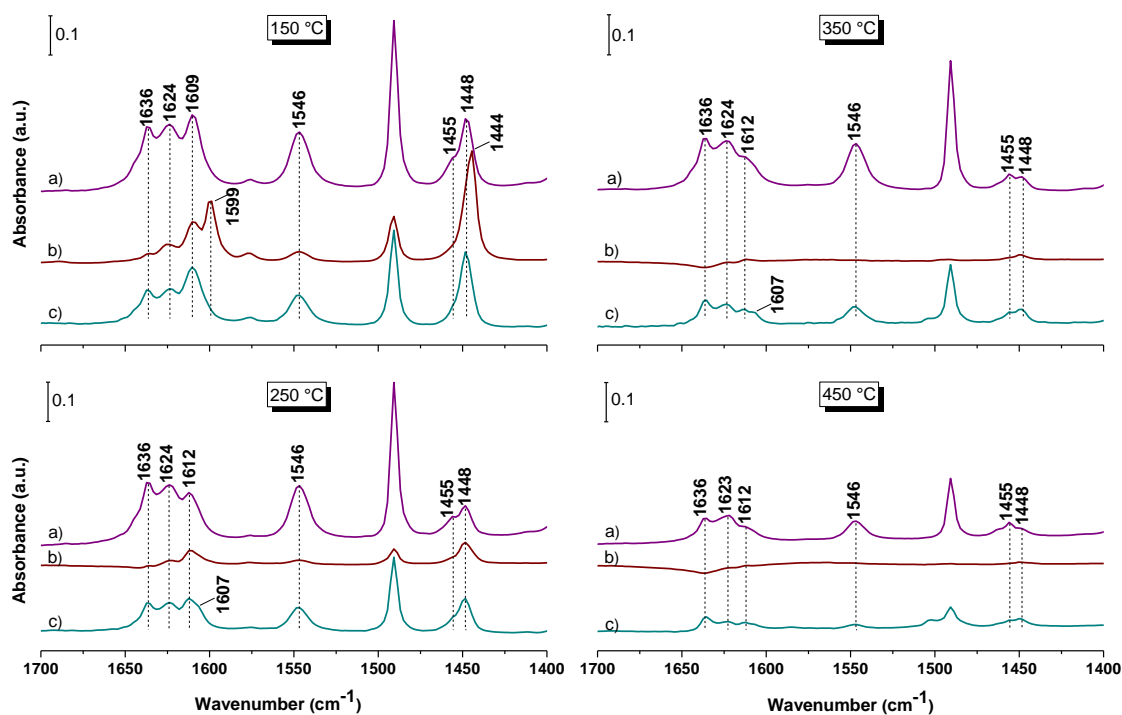


Fig. 7. FTIR spectra of a) ZrO₂/n-ZSM-5, b) ZrO₂/n-ZSM-5-BNT and c) ZrO₂/n-ZSM-5-ATP after adsorption of pyridine, using different evacuation temperatures.

In the case of the pure binders, the FTIR/pyridine measurements show that bentonite has almost no acidity, whereas some Lewis acid sites are present in attapulgite. On the other hand, both Brønsted and Lewis sites are detected in the ZrO₂/n-ZSM-5 catalyst, showing a LAS/BAS ratio = 0.8, which is higher than that typically found in this zeolite.⁴³ As reported in a previous work,²⁹ this effect is due to the presence of ZrO₂ that causes the generation of new LAS (bands at 1448 and 1609 cm⁻¹ in Fig. 7).

From the FTIR/pyridine data it becomes evident that incorporation of bentonite is rather detrimental for Brønsted acidity (bands at 1546 and 1636 cm⁻¹). Thus, taking into account the dilution effect of the binder, it can be estimated that the zeolite component in the technical

catalyst agglomerated with bentonite has suffered about 78% BAS reduction in comparison with the parent $\text{ZrO}_2/\text{n-ZSM-5}$ sample. The reason for this strong decrease in the BAS concentration is the occurrence of ion-exchange between Na^+ cations, which are abundant in the interlayer space of bentonite, and the protons of the zeolite Brønsted sites, as it has been previously described in the literature.^{30,44} On the contrary, the effect of attapulgite on the BAS concentration is quite less pronounced, showing that in this case migration of the Mg^{2+} cations, contained in this clay, affects just partially to the BAS of the zeolite. Thus, the zeolite component in the $\text{ZrO}_2/\text{n-ZSM-5-ATP}$ catalyst still retains about 73% of the BAS concentration in respect to the binder-free catalyst.

On the other hand, the overall Lewis acidity is not negatively affected by the incorporation of the binders but, on the contrary, an increment of the concentration of this type of acid sites is observed when comparing the technical catalysts and the parent one. Thus, the overall Lewis acidity of the $\text{ZrO}_2/\text{n-ZSM-5-BNT}$ material ($0.121 \text{ mmol g}^{-1}$) is quite superior to the theoretical one ($0.066 \text{ mmol g}^{-1}$), calculated from the contribution of the individual components. Although less pronounced, this effect is also denoted for the LAS concentration in the $\text{ZrO}_2/\text{n-ZSM-5-ATP}$ catalyst ($0.088 \text{ mmol g}^{-1}$), being somewhat higher than the theoretical value ($0.075 \text{ mmol g}^{-1}$). These results denote that a synergetic effect arises in respect to Lewis acidity from the interaction of both the zeolite-based catalyst and the clays. However, a closer inspection of the LAS bands (see Fig. 7) indicates that in reality the agglomeration with bentonite has a negative impact on the Lewis acidity related with Al species (reduction in the intensity of the bands at 1455 and 1624 cm^{-1}), whereas the LAS band appearing at 1448 cm^{-1} , assigned in a previous work to the ZrO_2 phase, becomes quite more intense. Moreover, a new band at 1599 cm^{-1} appears in the spectra of the $\text{ZrO}_2/\text{n-ZSM-5-BNT}$ sample that could be related with ion-exchanged Na^+ cations. In the case of the catalyst agglomerated with attapulgite, the Al-associated LAS bands at 1455 and 1624 cm^{-1} are less affected by the clay, whereas an increase is also observed in the intensity of the 1448 cm^{-1} band. These findings can be related with different phenomena occurring during agglomeration that affect to the Lewis acidity: I) neutralization of LAS linked to Al species, II) generation of new LAS, associated to cations ion-exchanged into the zeolite, III) modification of the Zr-associated Lewis acidity by interaction with the cations migrating from the clay component. In this way, it must be taken into account that the ZrO_2 is present on the external surface of the zeolite nanocrystals with a loading of 10 wt%, thus being quite accessible to the clay-migrating cations.

Interestingly, the two binders provoke different effects on the position and intensity of the ZrO_2 -linked LAS band at 1448 cm^{-1} . Thus, for the technical catalyst agglomerated with bentonite the band is shifted to 1444 cm^{-1} in the spectra recorded at $150 \text{ }^\circ\text{C}$, showing a high intensity, in fact quite superior to that in the parent $\text{ZrO}_2/\text{n-ZSM-5}$ catalyst. A similar effect has been earlier observed in the literature after ion-exchange of zeolite Beta with K^+ .⁴⁵ Accordingly, for the technical catalyst agglomerated with bentonite, the 1444 cm^{-1} band can be assigned to Lewis acid features of the ion-exchanged Na^+ cations present in the zeolitic component of the catalysts, which is also reflected in the appearance of the 1599 cm^{-1} band. Moreover, both bands disappear quite fast when increasing temperature, being almost not observed above $250 \text{ }^\circ\text{C}$. This finding evidences that the Na^+ -linked Lewis acidity is very weak and the strong ZrO_2 -associated Lewis acid sites, present in the parent binder-free material, are almost not detected in the technical catalyst agglomerated with bentonite.

For the catalyst prepared using attapulgite as binder the band at 1448 cm^{-1} , arising from the ZrO_2 Lewis acidity, is not shifted after agglomeration, although it shows also an increase in its relative intensity compared to the parent binder-free catalyst (note that in the technical catalyst the zeolite component accounts for 70% of the whole sample, which must be taken into account when comparing the intensities of the bands in Fig. 7). Other remarkable fact is that for the catalyst agglomerated with attapulgite this band is still visible at the highest pyridine evacuation temperature ($450\text{ }^\circ\text{C}$), hence it is originated by strong Lewis acid sites, as it occurred in the binder-free catalyst. These results suggest that, in contrast with the effect of Na^+ , the migration of Mg^{2+} from attapulgite, not only does not affect negatively to the ZrO_2 -linked Lewis acidity, but it induces a promotion effect of the latter.

3.3.2 FTIR/ CO_2 tests

The use of CO_2 as a probe molecule allows to address both Lewis acid and basic sites of the catalysts by analysing absorption bands characteristic of CO_2 linearly adsorbed on extra-framework cations ($2400\text{-}2200\text{ cm}^{-1}$)⁴⁶ or those attributed to CO_2 chemisorbed on basic sites (carbonate species, $1400\text{-}1700\text{ cm}^{-1}$).^{47,48}

Assessing the spectra of adsorbed CO_2 in the region characteristic of molecular coordination of probe molecule with metal cations (Lewis acid sites) provides further evidence of the interactions occurring between zeolite-based catalyst and inorganic binders (Fig. 8A). All materials under investigation showed a blue shift $\Delta\nu_3$ with respect to gaseous CO_2 ($\nu_3 = 2349\text{ cm}^{-1}$). Such upward shift agrees with the molecular coordination of CO_2 with metal cations through one of the oxygen atoms. A correlation between the value of $\Delta\nu_3$ and the polarisation strength of the extra-framework cation was shown in ⁴⁹. Thus, a weak band at 2355 cm^{-1} is observed for pure bentonite containing interlayer Na^+ cations, while attapulgite possessing Mg^{2+} counterions shows two weak and overlapping bands at 2368 and 2350 cm^{-1} . The latter can be related to CO_2 linearly adsorbed on slightly different sites of attapulgite. In contrast, n-ZSM-5 only shows a band of moderate intensity at 2347 cm^{-1} (spectrum not shown), which is close to the frequency of gas phase CO_2 , suggesting that a weak interaction occurs between the solid surface and the CO_2 adsorbed on the pure ZSM-5 sample. Incorporation of ZrO_2 results in the formation of an additional band at 2362 cm^{-1} , which is more clearly visible at lower CO_2 pressures. This result gives another evidence for generation of new types of LAS after modification of the n-ZSM-5 zeolite by deposition of the ZrO_2 phase. The intensity of the band at 2362 cm^{-1} further raises after attapulgite incorporation, showing again the occurrence of interactions between this clay and the ZrO_2 present in the catalyst. When using bentonite as binder the increasing number of weak LAS is evidenced by the shift of the 2362 cm^{-1} band characteristic of $\text{ZrO}_2/\text{n-ZSM-5}$ to 2355 cm^{-1} and by a strong enhancement in its intensity.

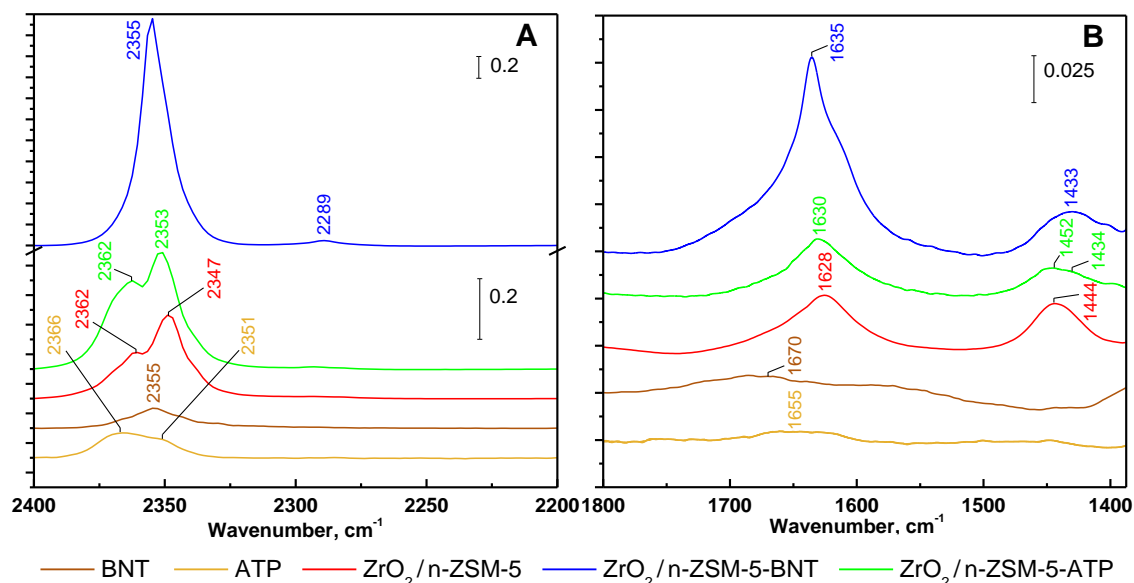


Fig. 8. FTIR spectra of adsorbed CO_2 ($\sim 30 \mu\text{mol g}^{-1}$ catalyst) over both pure clays and ZSM-5 based materials in the ranges of $2200\text{-}2400 \text{ cm}^{-1}$ (A) and $1300\text{-}1800 \text{ cm}^{-1}$ (B).

Likewise, the adsorption of CO_2 was monitored by means of FTIR in the area of the C-O stretching mode of carbonate ion ($1400\text{-}1700 \text{ cm}^{-1}$) in order to determine the basic properties of these materials. The obtained spectra can be observed in Fig. 8B. Both pure clays show just low intensity and broad bands in the range $1630\text{-}1670 \text{ cm}^{-1}$, which suggests they contain a small concentration of basic sites that could be assigned to the formation of bidentate or even bridged carbonates.^{47,50} The raw n-ZSM-5 zeolite does not exhibit any significant band in this region (spectrum not shown), which is in agreement with the known lack of basicity of zeolites in protonic form^{47,51}. In contrast, the $\text{ZrO}_2/\text{n-ZSM-5}$ sample presents two well-defined bands at 1444 and 1628 cm^{-1} , denoting that the incorporation of ZrO_2 provokes the generation of basic sites, which is consistent with its amphoteric properties. Based on previous studies on ZrO_2 ^{52,53} both bands could be assigned to hydrogen carbonates species formed by the interaction of CO_2 with hydroxyl groups. Nevertheless, the assignment of the band at 1444 cm^{-1} is not evident since bands in this region have been also earlier related with monodentate and bridged carbonates.⁵⁴ Agglomeration of the $\text{ZrO}_2/\text{n-ZSM-5}$ sample with bentonite leads to sharp changes in the FTIR/ CO_2 spectrum, an intense band appearing at 1635 cm^{-1} , which can be explained by the formation of new basic sites originated by the Na^+ ion-exchange from the clay into the zeolite. On the other hand, the ZrO_2 band at 1444 cm^{-1} is slightly shifted to 1433 cm^{-1} , suggesting that some interaction also occurs between the Na^+ cations and the ZrO_2 phase. Likewise, the use of attapulgite as binder induces some changes in the FTIR/ CO_2 spectrum of the parent $\text{ZrO}_2/\text{n-ZSM-5}$ material, in particular by the appearance of several overlapping bands in the region $1420\text{-}1450 \text{ cm}^{-1}$. This result indicates the occurrence of a higher diversity of basic sites after agglomeration with ATP, which can be also related with the migration of Mg^{2+} species from the clay and their subsequent interaction with the ZrO_2 phase deposited over the zeolite nanocrystals.

3.4 Relationship between the changes in the acid-basic properties and the biomass catalytic activity

Characterisation of the technical catalysts has shown that the agglomeration with both clays provokes little blockage of the zeolite micropores, but it affects drastically to their acid-basic properties due to the occurrence of strong interactions between cations in the binders and the components in the parent $\text{ZrO}_2/\text{n-ZSM-5}$ material.

In the case of the bentonite, Na^+ cations from the clay are ion-exchanged into the zeolite during agglomeration removing most of its Brønsted acid sites, although providing it with basic properties. The Na^+ migration also affects negatively to the Lewis acidities associated to both Al octahedral species and the ZrO_2 phase deposited over the external surface of the zeolite nanocrystals. Therefore, the lack of strong acidity in the $\text{ZrO}_2/\text{n-ZSM-5-BNT}$ catalyst is the reason of its reduced activity for biomass catalytic pyrolysis, in particular for promoting bio-oil* deoxygenation reactions and the formation of aromatic hydrocarbons by Diels-Alder condensation between furans and light olefins. This results in the production of a bio-oil* with higher oxygen content than that obtained over the binder-free catalyst.

When using attapulgite as binder, migration of cations from the clay (Mg^{2+}) also occurs during the agglomeration process but, unlike the case of bentonite, this provokes just a small decrease of the zeolite Brønsted and Lewis acid sites. Moreover, interaction between Mg^{2+} species, migrating from the clay, with the ZrO_2 phase, deposited over the outer part of the ZSM-5 nanocrystals, seems to reinforce the Lewis acidity of the catalyst, while generating a higher variety of basic sites. In this sense, Zr-Mg mixed oxides have been widely reported in the literature as materials with amphoteric properties, being successfully employed as catalysts in a number of reactions, such as aldol condensation, transesterification, etherification, alcohol dehydration and dehydrogenation, etc.⁵⁵⁻⁵⁸ Accordingly, it can be envisaged that the enhanced activity of $\text{ZrO}_2/\text{n-ZSM-5-ATP}$ for biomass catalytic pyrolysis is originated by the generation of additional acid-base pairs, due to Mg^{2+} - ZrO_2 interaction, which promotes the bio-oil* deoxygenation through decarboxylation and decarbonylation pathways.

4. Conclusions

Agglomeration of the $\text{ZrO}_2/\text{n-ZSM-5}$ catalyst with two different clays (bentonite and attapulgite) induced drastic changes in lignocellulosic biomass pyrolysis. Synergetic effects have been denoted when comparing the catalytic properties of the technical catalysts with those of both the parent ZSM-5 based material and the pure clays, showing that important interactions take place between the components in the agglomerated materials. However, depending on the clay, agglomeration causes opposite effects on the catalyst behaviour in lignocellulose pyrolysis.

When using bentonite as binder, the technical catalyst showed a reduced bio-oil deoxygenation activity, which was assigned to the loss of most of the ZSM-5 acidity by ion-exchange with Na^+ cations from the clay. However, the agglomerated catalyst incorporating attapulgite exhibited an enhanced activity leading to the production of a bio-oil with significantly lower oxygen content. This fact was accompanied by a change in the relative contribution of the deoxygenation routes, an increase of the decarboxylation and decarbonylation selectivities being observed for the material prepared using attapulgite as binder.

Detailed FTIR characterisation of the samples indicated that for the technical catalyst agglomerated with attapulgite a migration of Mg^{2+} occurs from the clay towards both the zeolitic

and ZrO₂ components of the catalyst. This caused a partial decrease of the concentration in the zeolite Brønsted acid sites. However, this effect was compensated by the enhancement produced in the concentration of strong Lewis acid sites and the generation of a higher variety of basic sites by interaction of Mg and Zr species.

The improved bio-oil deoxygenation activity of ZrO₂/n-ZSM-5-ATP can be assigned to the occurrence of an adequate equilibrium between different types of acidic and basic sites in this material, leading to a remarkable performance in a reaction system with high chemical complexity, as it is the case of biomass catalytic pyrolysis.

Acknowledgements

The authors gratefully acknowledge the financial support from the European Union Seventh Framework Programme (FP7/2007–2013) under grant agreement n° 604307 (CASCATBEL project). J. Čejka thanks the Czech Science Foundation for the financial support (P106/12/G015). CLARIANT is highly appreciated for supplying the HCZP 90 zeolite sample (*n*-ZSM-5).

References

1. D. A. Ruddy, J. A. Schaidle, J. R. Ferrell III, J. Wang, L. Moens and J. E. Hensley, *Green Chem.*, 2014, **16**, 454–490.
2. J. Feroso, P. Pizarro, J. M. Coronado and D. P. Serrano, *Adv. Rev.*, 2017, **6**, 1–18.
3. X. Bai, K. H. Kim, R. C. Brown, E. Dalluge, C. Hutchinson, Y. J. Lee and D. Dalluge, *Fuel*, 2014, **128**, 170–179.
4. X. Gong, Y. Yu, X. Gao, Y. Qiao, M. Xu and H. Wu, *Energy and Fuels*, 2014, **28**, 5204–5211.
5. C. Liu, H. Wang, A. M. Karim, J. Sun and Y. Wang, *Chem. Soc. Rev.*, 2014, **43**, 7594–7623.
6. E. Pütün, *Energy*, 2010, **35**, 2761–2766.
7. S. D. Stefanidis, S. A. Karakoulia, K. G. Kalogiannis, E. F. Iliopoulou, A. Delimitis, H. Yiannoulakis, T. Zampetakis, A. A. Lappas and K. S. Triantafyllidis, *Appl. Catal. B Environ.*, 2016, **196**, 155–173.
8. R. Mahadevan, R. Shakya, S. Neupane and S. Adhikari, *Energy and Fuels*, 2015, **29**, 841–848.
9. M. Auta, L. M. Ern and B. H. Hameed, *J. Anal. Appl. Pyrolysis*, 2014, **107**, 67–72.
10. A. Veses, M. Aznar, J. M. López, M. S. Callén, R. Murillo and T. García, *Fuel*, 2015, **141**, 17–22.
11. A. Güngör, S. Önenç, S. Uçar and J. Yanik, *J. Anal. Appl. Pyrolysis*, 2012, **97**, 39–48.
12. B. K. Yathavan and F. A. Agblevor, *Energy and Fuels*, 2013, **27**, 6858–6865.
13. S. Wang, M. Xu, F. Wang and Z. Li, *Int. J. Agric. Biol. Eng.*, 2016, **9**, 177–183.
14. A. M. Elfadly, I. F. Zeid, F. Z. Yehia, M. M. Abouelela and A. M. Rabie, *Fuel Process. Technol.*, 2017, **163**, 1–7.

15. Q. Lu, Z. Tang, Y. Zhang and X. Zhu, *Ind. Eng. Chem. Res.*, 2010, **49**, 2573–2580.
16. E. H. Lee, M. J. Jeon, J. K. Jeon, D. J. Suh, S. H. Park, B. Seo, S. H. Joo and Y. K. Park, *J. Nanosci. Nanotechnol.*, 2014, **14**, 2343–2351.
17. A. Galadima and O. Muraza, *Energy Convers. Manag.*, 2015, **105**, 338–354.
18. D. Fabbri, C. Torri and V. Baravelli, *J. Anal. Appl. Pyrolysis*, 2007, **80**, 24–29.
19. D. P. Gamliel, H. J. Cho, W. Fan and J. A. Valla, *Appl. Catal. A Gen.*, 2016, **522**, 109–119.
20. Y. T. Cheng, J. Jae, J. Shi, W. Fan and G. W. Huber, *Angew. Chem. Int. Ed.*, 2012, **51**, 1387–1390.
21. T. C. Hoff, M. J. Holmes, J. Proano-Aviles, L. Emdadi, D. Liu, R. C. Brown and J. P. Tessonier, *ACS Sustain. Chem. Eng.*, 2017, **5**, 8766–8776.
22. C. Hu, R. Xiao and H. Zhang, *Bioresour. Technol.*, 2017, **243**, 1133–1140.
23. T. R. Carlson, G. A. Tompsett, W. C. Conner and G. W. Huber, *Top. Catal.*, 2009, **52**, 241–252.
24. T. C. Hoff, D. W. Gardner, R. Thilakaratne, K. Wang, T. W. Hansen, R. C. Brown and J. P. Tessonier, *ChemSusChem*, 2016, **9**, 1473–1482.
25. S. Kelkar, C. M. Saffron, Z. Li, S.-S. Kim, T. J. Pinnavaia, D. J. Miller and R. Krieger, *Green Chem.*, 2014, **16**, 803–812.
26. J. Feroso, H. Hernando, P. Jana, I. Moreno, J. Přeč, C. Ochoa-Hernández, P. Pizarro, J. M. Coronado, J. Čejka and D. P. Serrano, *Catal. Today*, 2016, **277**, 171–181.
27. H. Hernando, I. Moreno, J. Feroso, C. Ochoa-Hernández, P. Pizarro, J. M. Coronado and D. P. Serrano, *Bioresour. Technol.*, 2017, **7**, 289–304.
28. E. F. Iliopoulou, S. Stefanidis, K. Kalogiannis, A. C. Psarras, A. Delimitis, K. S. Triantafyllidis and A. A. Lappas, *Green Chem.*, 2014, **16**, 662–674.
29. H. Hernando, A. M. Hernández-Giménez, C. Ochoa-Hernández, P. C. A. Bruijninx, K. Houben, M. Baldus, P. Pizarro, J. M. Coronado, J. Feroso, J. Čejka, B. M. Weckhuysen and D. P. Serrano, *Green Chem.*, 2018, **20**, 3499–3511.
30. M. A. Uguina, J. L. Sotelo and D. P. Serrano, *Appl. Catal.*, 1991, **76**, 183–198.
31. A. de Lucas, J. L. Valverde, P. Sánchez, F. Dorado and M. J. Ramos, *Ind. Eng. Chem. Res.*, 2004, **43**, 8217–8225.
32. G. T. Whiting, A. D. Chowdhury, R. Oord, P. Paalonen and B. M. Weckhuysen, *Faraday Discuss.*, 2016, **188**, 369–386.
33. N. Michels, S. Mitchell and J. Pérez-Ramírez, *ACS Catal.*, 2014, **4**, 2409–2417.
34. K. Ding, Z. Zhong, B. Zhang, J. Wang, A. Min and R. Ruan, *J. Anal. Appl. Pyrolysis*, 2016, **122**, 55–63.
35. D. P. Serrano, R. Sanz, P. Pizarro, I. Moreno, P. De Frutos and S. Blázquez, *Catal. Today*, 2009, **143**(1-2), 151–157.

36. C. A. Emeis, *J. Catal.*, 1993, **141**, 347–354.
37. H. Hernando, S. Jiménez-Sánchez, J. Feroso, P. Pizarro, J. M. Coronado and D. P. Serrano, *Catal. Sci. Technol.*, 2016, **6**, 2829–2843.
38. J. Feroso, H. Hernando, S. Jiménez-Sánchez, A. A. Lappas, E. Heracleous, P. Pizarro, J. M. Coronado and D. P. Serrano, *Fuel Process. Technol.*, 2017, **167**, 563–574.
39. H. Hernando, J. Feroso, I. Moreno, J. M. Coronado, D. P. Serrano and P. Pizarro, *Biomass Convers. Biorefinery*, 2017, **7**, 277–287.
40. H. Hernando, J. Feroso, C. Ochoa-Hernández, M. Opanasenko, P. Pizarro, J. M. Coronado, J. Čejka and D. P. Serrano, *Catal. Today*, 2018, **304**, 30–38.
41. S. A. Channiwala and P. P. Parikh, *Fuel*, 2002, **81**, 1051–1063.
42. J. Liu and G. Zhang, *Phys. Chem. Chem. Phys.*, 2014, **16**, 8178–8192.
43. D. P. Serrano, R. A. García, G. Vicente, M. Linares, D. Procházková and J. Čejka, *J. Catal.*, 2011, **279**, 366–380.
44. D. Haffad, A. Chambellan and J. C. Lavalley, *Catal. Letters*, 1998, **54**, 227–233.
45. O. Kikhtyanin, R. Bulánek, K. Frolich, J. Čejka and D. Kubička, *J. Mol. Catal. A Chem.*, 2016, **424**, 358–368.
46. R. Bulánek, K. Frolich, E. Frýdova and P. Čičmanec, *Top. Catal.*, 2010, **53**, 1349–1360.
47. S. Bordiga, C. Lamberti, F. Bonino, A. Travert and F. Thibault-Starzyk, *Chem. Soc. Rev.*, 2015, **44**, 7262–7341.
48. Y. Ganjkhanelou, R. Bulánek, O. Kikhtyanin and K. Frolich, *J. Therm. Anal. Calorim.*, 2018, **133**, 355–364.
49. T. Montanari and G. Busca, *Vib. Spectrosc.*, 2008, **46**, 45–51.
50. J. C. Lavalley, *Catal. Today*, 1996, **27**, 377–401.
51. G. Busca, *Microporous Mesoporous Mater.*, 2017, **254**, 3–16.
52. M. Bensitel, V. Moraver, J. Lamotte, O. Saur and J. C. Lavalley, *Spectrochim. Acta - Part A Mol. Spectrosc.*, 1987, **43**, 1487–1491.
53. E.-M. Köck, M. Kogler, T. Bielz, B. Klötzer and S. Penner, *J. Phys. Chem. C*, 2013, **117**, 17666–17673.
54. B. Bachiller-Baeza, I. Rodríguez-Ramos and A. Guerrero-Ruiz, *Langmuir*, 1998, **14**, 3556–3564.
55. L. Faba, E. Díaz and S. Ordóñez, *ChemSusChem*, 2013, **6**, 463–473.
56. I. Sádaba, M. Ojeda, R. Mariscal, R. Richards and M. López Granados, *ChemPhysChem*, 2012, **13**, 3282–3292.
57. A. Rabee, J. Manayil, M. Isaacs, C. Parlett, L. Durndell, M. Zaki, A. Lee and K. Wilson, *Catalysts*, 2018, **8**, 228.
58. X. Ding, Y. Li, F. Fang, D. Sun and Q. Zhang, *J. Mater. Chem. A*, 2017, **5**, 5067–5076.

Supporting information

2. Experimental

2.2 Products characterisation and data treatment

2.2.6 Gas chromatography coupled to mass spectrometry

An external calibration of the GC-MS was carried out using the most representative compounds of each group, which included a total of 13 compounds (acetic acid, diethoxypropane, furfural, phenol, guaiacol, cresol, creosol, syringol, toluene, xylene, trimethylbenzene, naphthalene and levoglucosan), being calibrated using 10 different concentrations. With these standards, a relative area of at least 67% was accurately quantified for the experiments included in this article. The response factors of the remaining compounds were estimated as the average response factor of the corresponding group.

3. Results and discussion

3.2 Pyrolysis of wheat straw using technical catalysts

Table S1. Mass yield of gaseous hydrocarbons obtained in the WS-ac pyrolysis over both pure clays and ZSM-5 based catalysts.

Sample	Light paraffins (wt%·10 ⁻²)				Light olefins (wt%·10 ⁻²)		
	CH ₄	C ₂ H ₆	C ₃ H ₈	C ₄ H ₁₀	C ₂ H ₄	C ₃ H ₆	C ₄ H ₈
Non-catalytic	34.3	5.6	2.0	0.4	5.5	4.5	0.4
BNT	36.1	6.4	2.1	0.5	6.3	5.0	0.5
ATP	38.7	7.4	2.2	0.6	6.4	4.9	0.5
ZrO ₂ /n-ZSM-5	33.4	6.7	2.6	1.2	8.5	12.8	2.3
ZrO ₂ /n-ZSM-5-BNT	41.2	7.7	2.5	1.1	8.3	9.1	2.1
ZrO ₂ /n-ZSM-5-ATP	61.0	11.8	4.0	2.8	14.7	22.3	4.1

Table S2. Amount (referred to the raw catalyst weight) and elemental composition of the coke deposited over both pure clays and ZSM-5 based catalysts during WS-ac pyrolysis.

Catalyst	%Coke	Ultimate analysis (wt%)			
		C	H	N	O
BNT	5.2	36.0	9.7	0.2	54.2
ATP	10.7	58.9	5.9	1.3	33.9
ZrO ₂ /n-ZSM-5	12.8	81.2	6.2	1.5	11.1
ZrO ₂ /n-ZSM-5-BNT	9.3	60.2	11.7	1.1	27.0
ZrO ₂ /n-ZSM-5-ATP	12.2	57.6	4.8	1.6	36.1

Article 9

Scaling-up of Bio-oil Upgrading during Biomass Pyrolysis over ZrO₂/ZSM-5-Attapulgite

ChemSusChem, 2019, 12, 2428-2438



DOI: 10.1002/cssc.201900534

CHEMSUSCHEM
Full Papers

Scaling-Up of Bio-Oil Upgrading during Biomass Pyrolysis over ZrO₂/ZSM-5-Attapulgite

Héctor Hernando,^[a, b] Ana M. Hernández-Giménez,^[c] Santiago Gutiérrez-Rubio,^[a]
Tomaz Fakin,^[d] Andrej Horvat,^[d] Rosa M. Danisi,^[e] Patricia Pizarro,^[a, b] Javier Feroso,^[a]
Eleni Heracleous,^[f] Pieter C. A. Bruijninx,^[c] Angelos A. Lappas,^[f] Bert M. Weckhuysen,^[c] and
David P. Serrano^{*[a, b]}

Impact JCR factor, (JCR 2017): 7.411

Category: Multidisciplinary Chemistry. 24 of 171 (Q1)

ABSTRACT

Ex-situ catalytic biomass pyrolysis is investigated at both laboratory and bench scales using a zeolite ZSM-5 based catalyst for selectively upgrading the bio-oil vapors. The catalyst consists of nanocrystalline ZSM-5, modified by incorporation of ZrO₂ and agglomerated with attapulgite (ZrO₂/n-ZSM-5-ATP). Characterization of this material by means of different techniques, including CO₂ and NH₃ TPD, NMR, UV-Vis micro-spectroscopy and fluorescence microscopy, shows that it possesses the right combination of accessibility and acid-base properties for promoting the conversion of the bulky molecules formed by lignocellulose pyrolysis and their subsequent deoxygenation to upgraded liquid organic fractions (bio-oil). The results obtained at laboratory scale by varying the catalyst-to-biomass ratio (C/B) indicate that the ZrO₂/n-ZSM-5-ATP catalyst is more efficient for bio-oil deoxygenation than the parent zeolite n-ZSM-5, producing upgraded bio-oils with better combination of mass and energy yields with respect to the oxygen content. The excellent performance of the ZrO₂/n-ZSM-5-ATP system is confirmed by working with a continuous bench scale plant. The scale-up of the process, even with different raw biomasses as feedstock, reaction conditions and operation modes, is in line with the lab scale results, leading to deoxygenation degrees of about 60% with energy yields around 70% in respect to those of the thermal bio-oil.

Keywords: Catalytic pyrolysis • Biomass • ZSM-5 • Technical catalyst • Scaling

1. Introduction

Biomass pyrolysis has attracted much interest for the production of liquid biofuels, mainly when using lignocellulosic residues as raw material.¹ It is a relatively simple process that takes place in a non-oxidative medium at atmospheric pressure. The optimum conditions for maximizing the yield of the liquid fraction (bio-oil) comprise intermediate temperatures, typically in the range of 500-600 °C, and high heating rates (fast pyrolysis).^{2,3} The bio-oil so obtained contains high amounts of oxygen and water, having low heating value, acidic pH and low stability.⁴

Bio-oil upgrading has been investigated by a variety of physical and chemical methods. Chemical transformations applied to the bio-oil include catalytic pyrolysis, hydrodeoxygenation, ketonization, aldol condensation, esterification and alkylation.^{2,5-9} In most cases, these transformations are aimed to reduce (at least partially) the oxygen content of the bio-oil, thus approaching its chemical composition to that typical of fossil-derived fuels. Catalytic pyrolysis presents the advantage of operating at atmospheric pressure, and can thus be easily combined with the biomass thermal step.¹⁰ This can be accomplished by adding the catalyst directly to the pyrolysis reactor (in situ system) or by connecting the catalyst bed in series with the pyrolysis zone (ex situ system).^{3,4,11} In the latter scheme, it is possible to operate the thermal and catalytic steps at different temperature, while avoiding the direct contact between the biomass and the catalyst. The solid fraction (char) produced by thermal biomass pyrolysis is accumulated in the thermal zone in the ex-situ configuration, being not in contact with the catalyst, which helps in attenuating catalyst deactivation.^{3,10}

A large number of solid catalysts have been tested in biomass catalytic pyrolysis, including zeolites,^{12,13} amorphous silica-alumina,^{14,15} ordered mesoporous materials^{16,17} and metal oxides.¹⁸⁻²¹ Most of the work has been focused on the use of zeolites due to their excellent performance in catalytic cracking reactions. In particular, zeolite ZSM-5 has shown remarkable properties for biomass catalytic pyrolysis leading to the formation of upgraded bio-oils with a high concentration of aromatic hydrocarbons.²²⁻²⁵ However, zeolitic catalysts suffer from fast deactivation by the deposition of carbonaceous residues, whereas the yield finally obtained for the upgraded bio-oil is often very low due to the extensive formation of gases and coke.⁴ Accordingly, a great research effort has been devoted in past years to tune the properties of zeolite-based catalysts to improve their accessibility, suppress secondary reactions and decrease the coke deposition. Thus, zeolite ZSM-5 has been modified by reducing its crystal size, introducing secondary porosity and incorporating a variety of metals and metal oxide phases.^{10,26-34} Most studies in literature have been performed at laboratory scale using catalysts in powder form. Investigation of the scale-up of the process with the use of technical catalysts has been scarcely covered.

In a recent work, we have demonstrated the remarkable and positive effect of modifying zeolite ZSM-5 in nanocrystalline form by impregnation of ZrO₂ over the external surface of the zeolite nanocrystals, since this moderates and complements the zeolite acidity.³⁵ We showed in a further work that the use of clay binders for the agglomeration of pyrolysis catalysts has also a noticeable influence on their behaviour in biomass catalytic pyrolysis. In particular, the use of attapulgite as binder enabled the production of upgraded bio-oil with enhanced yield and low oxygen content.³⁶ Within this context, the current work reports on the excellent performance of the ZrO₂/n-ZSM-5-ATP catalyst material for the production of bio-oil with improved properties

by lignocellulose pyrolysis using reaction systems operating at different scales and operation modes, i.e. batch and continuous. Moreover, the effect of the catalyst-to-biomass ratio is assessed, providing valuable information on the main reaction pathways occurring during bio-oil upgrading over this catalyst.

2. Experimental

Detailed information about the preparation of the catalysts and characterization techniques used, as well as on the procedure and set up employed for the biomass catalytic pyrolysis tests, is provided as ESI.

3. Results and discussion

3.1 Catalyst properties

The main physicochemical properties of the technical $\text{ZrO}_2/\text{n-ZSM-5-ATP}$ catalyst, the pure zeolite and the impregnated $\text{ZrO}_2/\text{n-ZSM-5}$, are summarized in Table 1. The influence of using attapulgite as binder was analyzed in depth in previous work.³⁶ Synergetic effects between the zeolite and the clay were found to occur in the technical $\text{ZrO}_2/\text{n-ZSM-5-ATP}$ catalyst, affecting both the acidic and basic features of the material. The quantity of ZrO_2 incorporated into the zeolitic support, determined by ICP-OES, matches well with the theoretical value (10 wt%). A reduction in the textural properties is observed after agglomeration of the parent $\text{ZrO}_2/\text{n-ZSM-5}$ material with attapulgite, which is a direct consequence of the lower surface area of the pure clay ($107 \text{ m}^2 \text{ g}^{-1}$). In this way, the decrease of the micropore surface area is well correlated with the dilution effect caused by incorporation of 30 wt% of attapulgite, taking into account that the latter has no microporosity. This result denotes that both the integrity and accessibility of the ZSM-5 micropores are maintained after the agglomeration process.

The acid and basic properties of the catalysts have been evaluated by NH_3 and CO_2 TPD, respectively (see Table 1). Incorporation of ZrO_2 to zeolite n-ZSM-5 increases the overall acidity due to the generation of a new type of acid sites, having also an enhancement effect on the concentration of basic sites. These findings can be directly assigned to the amphoteric properties of ZrO_2 . On the other hand, it can be concluded that the agglomeration with attapulgite barely alters the overall catalyst acidity, while it increases the concentration of basic sites, which has been earlier related to the interaction of Mg^{2+} species, migrating from the attapulgite, with both the zeolitic and ZrO_2 components.³⁶ Accordingly, the technical $\text{ZrO}_2/\text{n-ZSM-5-ATP}$ catalyst exhibits singular acid-base properties, showing a combination of Brønsted and Lewis acidity, as well as of basic sites.

Table 1. Physicochemical properties of the zeolite ZSM-5 based samples.

Catalyst	Si/Al ^a	ZrO ₂ ^a (wt%)	S _{BET} ^b (m ² /g)	S _{MES+EXT} ^c (m ² /g)	S _{MIC} ^d (m ² /g)	V _T ^e (cm ³ /g)	V _{MIC} ^f (cm ³ /g)	Acidity ^g (mmol/g)	Basicity ^h (μmol/g)
n-ZSM-5	42	-	445	133	312	0.512	0.186	0.28	3.26
ZrO ₂ /n-ZSM-5	42	9.2	395	105	290	0.620	0.173	0.39	11.01
ZrO ₂ /n-ZSM-5-ATP	42	10.5	325	102	223	0.445	0.133	0.38	18.39

^a Si/Al ratio of the zeolite component, measured by ICP-OES. ^b BET surface area. ^c Mesopore + external surface area. ^d Micropore surface area. ^e Total pore volume at $P/P_0 \approx 0.98$. ^f Micropore volume. ^g Measured by TPD-NH₃. ^h Measured by TPD-CO₂.

Figure 1 illustrates SEM and TEM images of the different materials employed for the preparation of the technical catalyst. The binder-free n-ZSM-5 and ZrO₂/n-ZSM-5 samples are formed by nanocrystallites of ca. 40-60 nm, aggregated into 20-50 μm particles,³⁵ whereas attapulgite shows its characteristic needle-like morphology,^{37,38} as well as some impurities associated with quartz (highlighted in image). SEM-EDX analysis of the ZrO₂/n-ZSM-5-ATP catalyst (e-i) indicates that Zr is evenly distributed over the sample, as evidenced by EDX dot-mapping, with a Si/Zr molar ratio of ca. 43 (Figure S1). The Zr content of the ternary sample is slightly lower than that of the ZrO₂/n-ZSM-5 catalyst (ca. 14, blue series Figure S1) due to both the dilution of the material with attapulgite and to the newly incorporated Si naturally present in the clay. Likewise, Mg could also be found very homogeneously distributed alongside the catalyst surface (Si/Mg~21), indicative of an even zeolite/clay distribution.

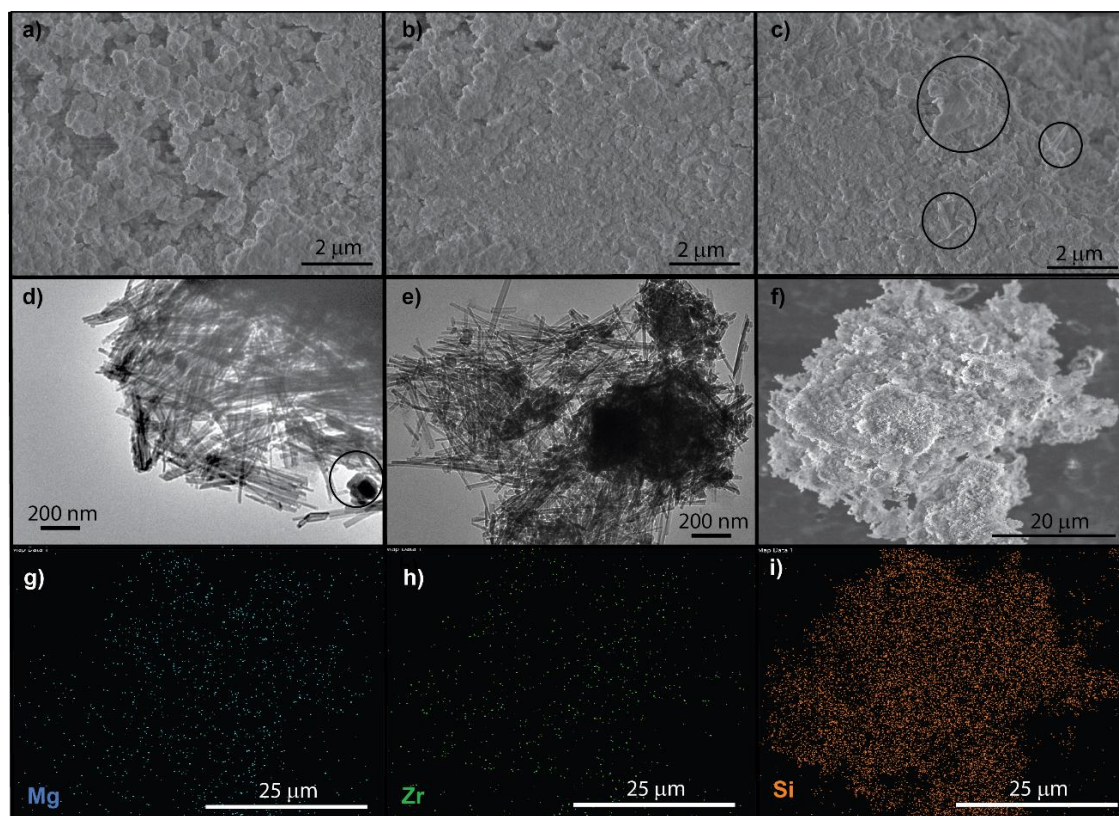


Fig. 1. SEM (a-c) and TEM (d,e) images of n-ZSM-5 (a), ZrO₂/n-ZSM-5 (b), ATP (d) and ZrO₂/n-ZSM-5-ATP (c,e) catalysts. (f-i) SEM and derived elemental EDX dot maps for ZrO₂/n-ZSM-5-ATP catalyst.

Figure S2 shows the XRD pattern of the ZrO₂/n-ZSM-5-ATP catalyst, compared to the parent materials, the pure zeolite n-ZSM-5 and impregnated ZrO₂/n-ZSM-5. The ternary catalyst, as the parent materials, shows the orthorhombic phase of the MFI framework (Pnma, PDF 00-044-0003).^{39,40} While ZrO₂ is X-ray invisible due to the lack of crystallinity of the ZrO₂ nanoparticles and/or their small size,³⁵ the attapulgite phase is evidenced in the XRD of the ZrO₂/n-ZSM-5-ATP catalyst by the presence of a small amount of quartz phase, a common impurity of this clay also detected by TEM (Figure 1d), at 31.1 2θ° (Figure S2c).

Aluminum speciation was examined by solid-state ²⁷Al MAS (Figure 2a) and ²⁷Al MQ MAS NMR (b) analyses. Zeolite n-ZSM-5 (black series) contains almost exclusively tetrahedrally coordinated Al species, located at 54 ppm, and very little presence of octahedrally coordinated

Al (signal at 0 ppm).⁴¹⁻⁴³ The same is seen after ZrO₂ addition (green series), with the NMR spectrum of ZrO₂/n-ZSM-5 being practically identical to that of the pure zeolite. The lower intensity of the resonance at 54 ppm is due to the incorporation of 9.2 wt% ZrO₂. Attapulgite (orange series), which contains about 5 wt% of Al, presents different Al species: tetrahedral at ~62 ppm⁴⁴ and 58 ppm, penta-coordinated at 25 ppm, and octahedral at 3 ppm.⁴⁵ The mixing of ZrO₂/n-ZSM-5 with attapulgite and the further extrusion leads to changes in the Al environment.⁴⁶ The framework Al^{IV} species, yet at 54 ppm, suffer some distortion evidenced by the broadening and increase in anisotropy of the resonance for the ternary ZrO₂/n-ZSM-5- ATP catalyst. At the same time, an enhancement in the extra-framework Al occurs, as evidenced by the hump at 35-25 ppm assigned to penta-coordinated Al^V species, and the increase in octahedral Al^{VI} species that appear at higher chemical shift, at ca. 2 ppm (a).

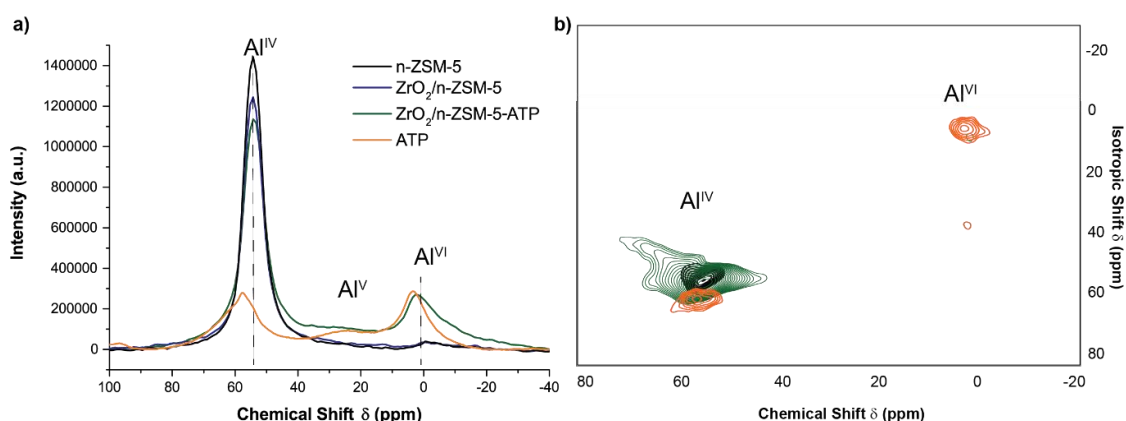


Fig. 2. a) ²⁷Al MAS ssNMR spectra of n-ZSM-5 (**black**), ZrO₂/n-ZSM-5 (**blue**), ZrO₂/n-ZSM-5-ATP (**green**) and ATP (**orange**). b) Overlapping of ²⁷Al MQ MAS ssNMR spectra. $\pi/12$ ²⁷Al pulse excitation source (0.87 μ s), MAS 18 kHz, T_{set} 298 K.

The 4-fluorostyrene oligomerization reaction was carried out to study the effect of attapulgite on Brønsted acidity and catalyst accessibility.⁴⁷⁻⁵⁰ In the reaction catalyzed by ZrO₂/n-ZSM-5-ATP (Figure 3a,b), styrene oligomers can be seen forming but at lower extent than on the n-ZSM-5 (c) and ZrO₂/n-ZSM-5 (d) catalysts. The intensity evolution of the cyclic oligomers (7), favored in zones with high density of Brønsted acid sites, is particularly low for the ZrO₂/n-ZSM-5-ATP catalyst. On the contrary, the formation of linear dimer (5) is more pronounced, especially in the first 5 min of reaction; afterwards, the relative amount of trimer oligomers (6a and 6b) increases.

The evolution of band intensities for the three catalysts and the related profiles obtained (a) indicate a progressive loss in Brønsted acidity suffered by the zeolite n-ZSM-5 upon ZrO₂ addition and especially after attapulgite inclusion. This can be visually confirmed by the images, shown in Figure S4. The optical images vary in color from light to dark pink and finally to violet for n-ZSM-5 (a), ZrO₂/n-ZSM-5 (b) and ZrO₂/n-ZSM-5-ATP (c) catalysts, respectively. This indicates the higher presence of cyclic oligomers (7) absorption bands, evolving at 515 nm for the n-ZSM-5 catalyst, and the higher presence of linear oligomers (5) absorption bands, evolving at 555 nm for ZrO₂/n-ZSM-5-ATP. Complementary confocal fluorescence microscopy pictures demonstrate that the fluorescence ranges from green- to more orange-like (Fig. S4 e-g). Note that pure attapulgite, which cannot catalyze this styrene oligomerization reaction given its lack in Brønsted acidity, does not change in color (d) and, hence does not undergo any fluorescence by the presence of the styrene monomer, as indicated by the black confocal fluorescence image

(h). The partial loss of Brønsted acidity after agglomeration with attapulgite has been earlier reported, although this effect is compensated by an increase in the amount of Lewis acid sites.³⁶

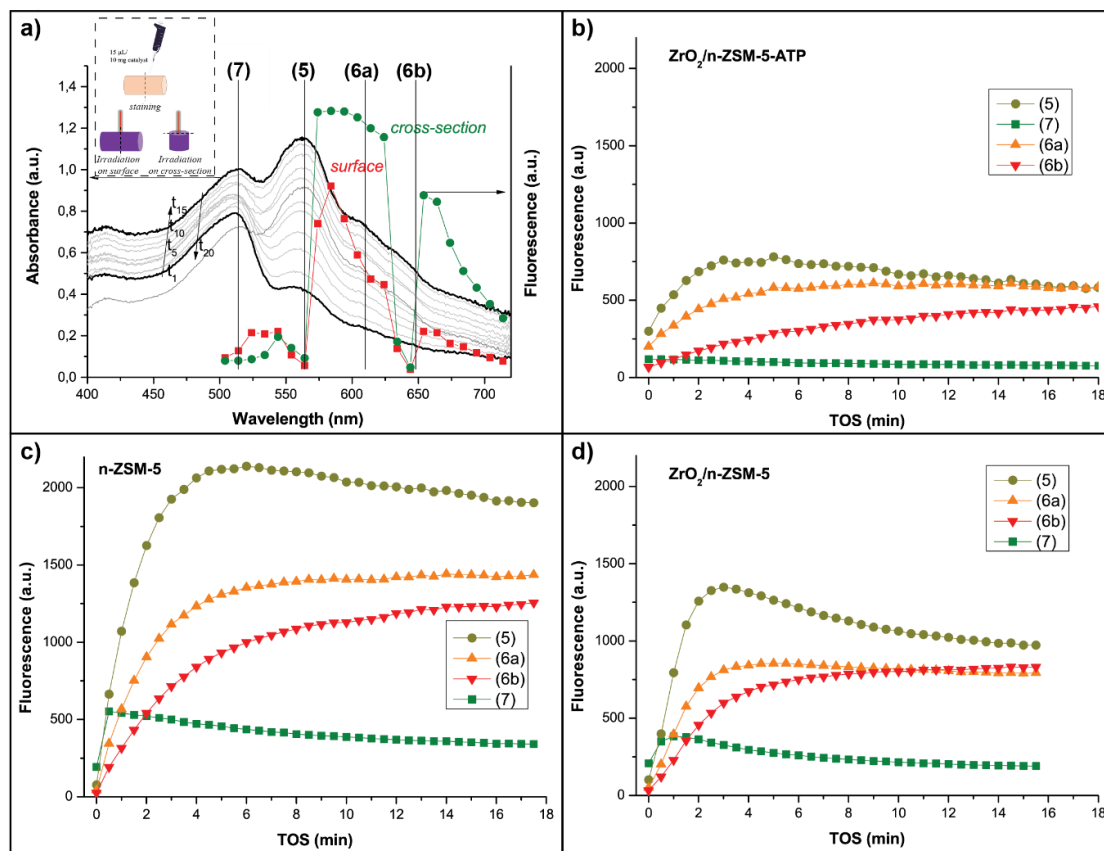


Fig. 3. (a) In-situ absorption UV-Vis (continuous line) and ex-situ fluorescence spectra (scattered line; red for recorded on surface, green for cross-section) of the 4-fluorostyrene oligomerization reaction products recorded at 100 °C on the ZrO₂/n-ZSM-5-ATP catalyst. Inset: scheme of the impregnation and recording process. (b-d) Evolution of emission bands during reaction for ZrO₂/n-ZSM-5-ATP, (b), n-ZSM-5 (c), and ZrO₂/n-ZSM-5 (d) catalysts, for the sake of comparison. Excitation lasers are fixed at $\lambda = 488, 561$ and 642 nm.

The ZrO₂/n-ZSM-5-ATP extrudate shows good accessibility, as demonstrated by confocal fluorescence microscopy. The ex-situ emission spectrum taken on the cross-section of the catalyst after reaction (green scattered series, Figure 3a, right axis) shows more intense fluorescence than the one taken on the surface where the catalyst staining was performed (red series). This observation confirms the good diffusivity/accessibility of the nanocrystalline ZrO₂/n-ZSM-5-ATP extrudate for styrene derivatives.

3.2 Biomass catalytic pyrolysis

3.2.1 Laboratory scale tests

The activity of the ZrO₂/n-ZSM-5-ATP catalyst was tested in wheat straw catalytic pyrolysis using an ex-situ lab-scale reactor with different reaction temperatures in the thermal (550 °C) and catalytic (400 °C) zones, operating in batch mode by discharging at once 4 g of biomass into the reactor. In order to avoid interferences from the inorganic components present in the raw biomass, that could act as indigenous catalysts favoring the formation of char in detriment of the

bio-oil yield, the wheat straw was subjected to an acid-washing pre-treatment affording the removal of 98 wt% of the alkaline and alkaline earth metals (AAEM), being named as WS-ac. A detailed description of the properties of this biomass can be found elsewhere.^{10,26}

The performance of the $\text{ZrO}_2/\text{n-ZSM-5-ATP}$ material in the catalytic pyrolysis of de-ashed wheat straw was tested using six catalyst/biomass ratios ($C/B = 0.1, 0.2, 0.3, 0.4, 0.5$ and 0.7 g g^{-1}) in order to get insights about the progression of the pyrolysis vapors upgrading as a function of the catalyst loading. In the reactor configuration herein employed, the residual solid fraction (char), which originates entirely from the initial biomass decomposition, is retained in the upper reactor zone, avoiding the direct contact with the catalyst bed. The char yield was around 19 wt% for all the experiments, value that was independent of the C/B ratio.

Figure 4a illustrates the product distribution, in terms of mass yield, corresponding to the different fractions (char excluded) as a function of the C/B ratio. The products herein displayed include the non-condensable gases, the liquid phases and the coke deposited over the catalyst. The liquid fraction is separated in water and bio-oil on dry basis. The results obtained in a pure thermal test, carried out with no catalyst, are also included in this graph as a reference. Likewise, the oxygen content of the bio-oil fraction is shown in Figure 4b.

In line with previous studies,^{10,35} the presence of the catalyst causes strong changes in the yield of the different fractions compared to the pure thermal test. A strong decrease of the bio-oil yield and an enhancement in the production of non-condensable gases and water is observed, in addition to the formation of coke over the catalyst. These variations are accompanied by a significant reduction in the oxygen content of bio-oil, from about 39 wt% (thermal test) down to 17 wt% (catalytic test with $C/B = 0.7 \text{ g g}^{-1}$), showing the effectiveness of the catalyst in promoting deoxygenation reactions. Using progressively higher C/B ratios leads to increased bio-oil deoxygenation but also to higher production of gases and coke, at the expense of the bio-oil yield. The water yield does not change too much on the whole range of C/B values, denoting that the catalyst here employed does not favor specifically dehydration reactions.

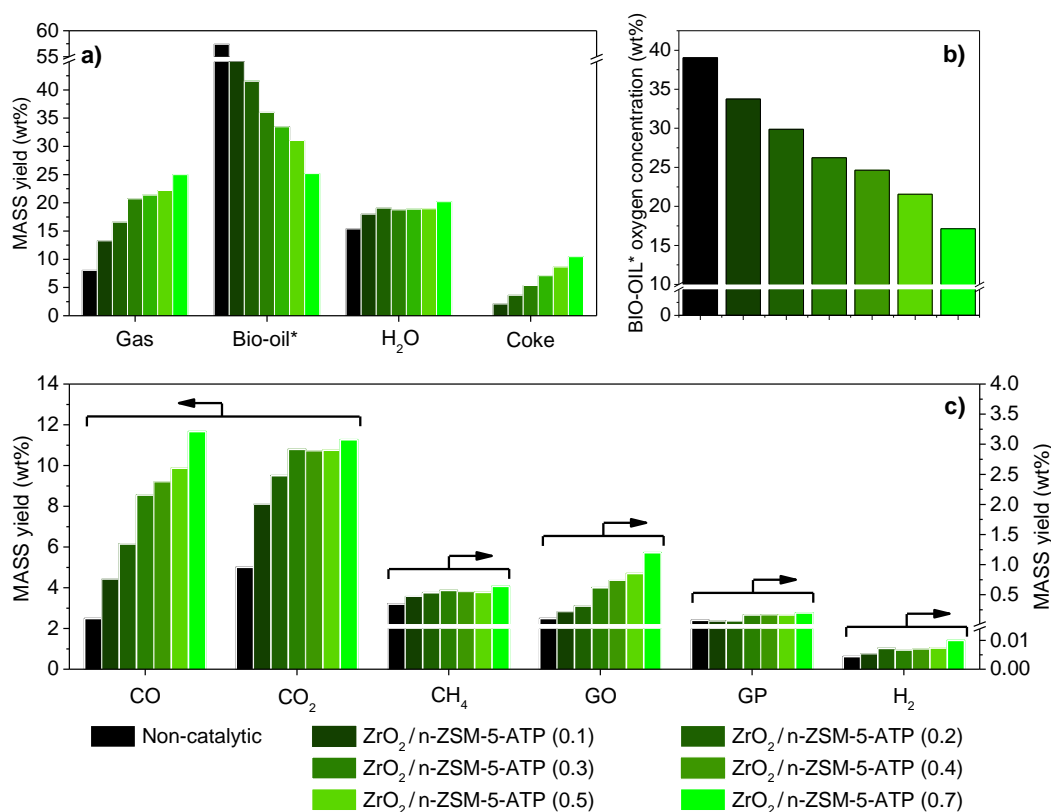


Fig. 4. Products yield distribution (wt%) (a), bio-oil oxygen concentration (wt%) (b), and gaseous components yield (wt%) (c), obtained in the WS-ac pyrolysis over the $\text{ZrO}_2/\text{n-ZSM-5-ATP}$ catalyst using different C/B ratios. GO: gaseous olefins ($\text{C}_2\text{-C}_4$); GP: gaseous paraffins ($\text{C}_2\text{-C}_4$).

The main components present in the gaseous fraction include CO, CO_2 , CH_4 , gaseous olefins (GO) and gaseous paraffins (GP), their yield shown in Fig. 4c as a function of the C/B ratio. For all the gases, the yield increases with the C/B ratio, but with two different patterns. In the case of CO and gaseous olefins, the yield variation is more or less proportional to the C/B ratio. However, for CO_2 , methane, gaseous paraffins and hydrogen, the yield increase is pronounced for C/B up to 0.2, suggesting that the species and functional groups that generate these products are mainly consumed in the initial steps of the biomass catalytic pyrolysis process. As shown in Table 3, methane is the predominant component within gaseous paraffins, whereas propylene is the major one within gaseous olefins in the whole range of C/B ratios investigated.

As shown in Figure 4a, the yield of the coke deposited over the catalyst increases almost linearly with the C/B ratio. Note that these values refer to the initial biomass weight, reaching about 10 wt% at the highest C/B ratio. Therefore, if char and coke are grouped together, it means that for this C/B ratio about 29 wt% of the biomass is transformed into carbonaceous residues, denoting the relevance of minimizing the production of these fractions, as well as finding applications for them. In this context, both char and coke could be combusted to provide a great part of the energy consumed in the overall catalytic pyrolysis process. Thus, Table 4 discloses the composition of char and coke, their High Heating Values and the amount of coke referred to catalyst weight. Regarding the char, the data indicate that this fraction accumulates most of the ash still contained in the raw biomass, but it has little oxygen and therefore possesses a relatively high HHV. In the case of the coke deposits, it is interesting to note that the amount of coke

expressed per gram of catalyst decreases with the C/B ratio but in a short range, from 13.1 wt% (C/B = 0.1) to 10.5 wt% (C/B = 0.7), which suggests that its formation is limited by the porosity of the catalyst. One other interesting fact is that the coke composition is very different to that of the char, showing less C and H, similar N and quite higher amounts of oxygen, which in turn leads to lower HHV. These results point out that the zeolite-based catalyst tends to accumulate highly oxygenated compounds. The oxygen content of the coke deposits exhibits a maximum at C/B ratio 0.5, whereas the N proportion decreases continuously, which evidences some changes in the nature of the species retained over the catalyst.

Table 3. Mass yield into gaseous hydrocarbons obtained in the WS-ac pyrolysis over the ZrO₂/n-ZSM-5-ATP catalyst using different C/B ratios.

Catalyst	Light paraffins (wt% · 10 ⁻²)				Light olefins (wt% · 10 ⁻²)		
	CH ₄	C ₂ H ₆	C ₃ H ₈	C ₄ H ₁₀	C ₂ H ₄	C ₃ H ₆	C ₄ H ₈
Non-catalytic	34.3	5.6	2.0	0.4	5.5	4.5	0.4
ZrO ₂ /n-ZSM-5-ATP (0.1)	47.2	3.2	3.0	0.7	11.1	10.6	0.8
ZrO ₂ /n-ZSM-5-ATP (0.2)	53.3	3.1	3.4	3.9	12.6	18.5	1.6
ZrO ₂ /n-ZSM-5-ATP (0.3)	57.2	12.0	4.3	4.9	22.7	38.9	6.6
ZrO ₂ /n-ZSM-5-ATP (0.4)	55.2	11.9	4.3	5.4	26.7	47.0	7.8
ZrO ₂ /n-ZSM-5-ATP (0.5)	54.0	12.0	4.4	5.9	30.6	54.8	8.1
ZrO ₂ /n-ZSM-5-ATP (0.7)	63.8	14.1	5.6	7.8	45.9	74.1	11.1

Table 4. Char and coke composition, and corresponding HHV values, obtained in the WS-ac pyrolysis over the ZrO₂/n-ZSM-5-ATP catalyst using different C/B ratios.

	Ultimate Analysis (wt%)			Proximate Analysis (wt%)				HHV (MJ/kg)
	Vol.	Ash	F. C.	C	H	N	O	
Char	12.8	19.0	68.2	72.1	2.7	0.8	5.3	27.4
Catalyst	Coke over catalyst (wt%)			Proximate Analysis (wt%)				HHV (MJ/kg)
ZrO ₂ /n-ZSM-5-ATP (0.1)	13.1			58.7	5.7	1.0	34.6	23.6
ZrO ₂ /n-ZSM-5-ATP (0.2)	12.6			56.2	5.0	1.3	37.5	21.6
ZrO ₂ /n-ZSM-5-ATP (0.3)	12.5			49.9	5.4	0.6	44.7	19.2
ZrO ₂ /n-ZSM-5-ATP (0.4)	12.4			52.3	4.3	0.6	43.4	18.8
ZrO ₂ /n-ZSM-5-ATP (0.5)	12.1			47.1	4.9	0.5	48.1	17.2
ZrO ₂ /n-ZSM-5-ATP (0.7)	10.5			55.9	5.7	0.2	38.4	22.2

Bio-oil deoxygenation takes place through a complex scheme of reactions that lead to the generation of water, CO and CO₂ as final products according to three main deoxygenation routes: dehydration, decarbonylation and decarboxylation, respectively. With the aim of preserving as much as possible the chemical energy of the bio-oil and increasing its H/C ratio, decarboxylation should be the preferred one. Figure 5a shows the changes in the overall deoxygenation selectivity towards the three routes with increasing C/B ratio, defined as the mass of oxygen in the form of CO, CO₂ or H₂O, respectively, referred to the total amount of oxygen present in these three compounds. The most pronounced one is dehydration, followed by decarboxylation and finally decarbonylation. However, it must be taken into account that a great part of the formation of water, CO₂ and CO occurs during the thermal step, which causes little deoxygenation of the bio-

oil phase, its effect being in reality reflected on the composition of the char fraction that possesses a low oxygen content as above indicated. Accordingly, the deoxygenation selectivity of the catalytic step has been defined similarly to the overall selectivity but taking into account the incremental productions of CO, CO₂ or H₂O that take place when the vapors generated in the thermal zone are passed through the catalyst bed. Thereby, the results obtained in the pure thermal test have been taken as reference. The deoxygenation selectivity of the catalytic step is more representative of the bio-oil deoxygenation pathways than the overall one. As shown in Figure 5, and in contrast with non-catalytic pyrolysis, in which dehydration is by far the predominant deoxygenation route, the use of the ZrO₂/n-ZSM-5-ATP catalyst leads to a quite balanced scheme. Thus, for C/B = 0.1 g g⁻¹ dehydration and decarboxylation contribute almost to a similar extent, followed by decarbonylation. However, at higher C/B ratios the decarbonylation selectivity increases progressively, becoming the major one for C/B = 0.7. These results denote that the bio-oil deoxygenation promoted by the catalyst is a balanced combination of the three routes, whose relative contribution varies with the C/B ratio.

The variation of the elemental composition of the bio-oil in the tests performed using different catalyst loadings is shown in Figures 6a and b in the form of van Krevelen graphs, representing the overall and effective H/C ratios versus the O/C one, respectively. The latter has been defined in earlier works^{51,52} as $H_{\text{eff}}/C = (H-2O-3N-2S)/C$ to account only for the hydrogen that could be finally available if all the oxygen present in the bio-oil is removed in the form of water. The results obtained with the parent zeolite n-ZSM-5 are also included as reference. According to Figure 6a, for the ZrO₂/n-ZSM-5-ATP catalyst, passing from the raw biomass first to the thermal bio-oil, and then to that produced in the catalytic pyrolysis tests, involves a significant reduction in the O/C ratio, whereas the overall H/C ratio just slightly increases. However, the emerging picture is more positive when assessing the results obtained in the form of H_{eff}/C (Figure 6b), as they show clearly an increasing trend that approaches progressively the composition region typical of fossil-derived fuels. Interestingly, the pathways followed in the van Krevelen graphs when using the parent n-ZSM-5 catalyst are quite less favorable compared to the catalyst here investigated, with a reduction in the values of the overall H/C ratio and a lower increase in the H_{eff}/C . These results denote the positive effects caused by the modification of zeolite ZSM-5 by incorporation of ZrO₂ and agglomeration with attapulgite in terms of bio-oil composition upgrading aimed at the production of advanced biofuels. More detailed information about the elemental compositions of the bio-oils* can be found in Table S1.

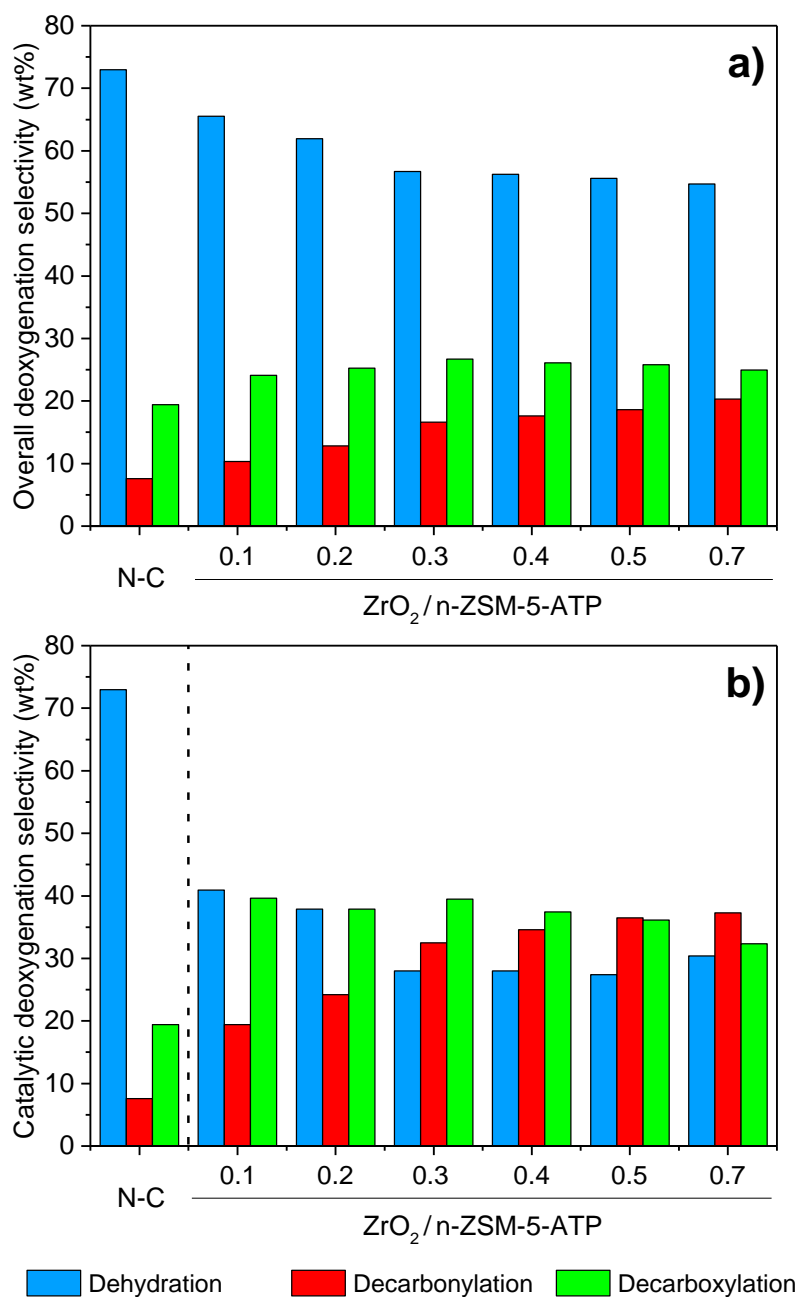


Fig. 5. Overall deoxygenation selectivity (a) and catalytic deoxygenation (b), obtained in the WS-ac pyrolysis over the ZrO₂/n-ZSM-5-ATP catalyst using different C/B ratios. *N-C*: non-catalytic.

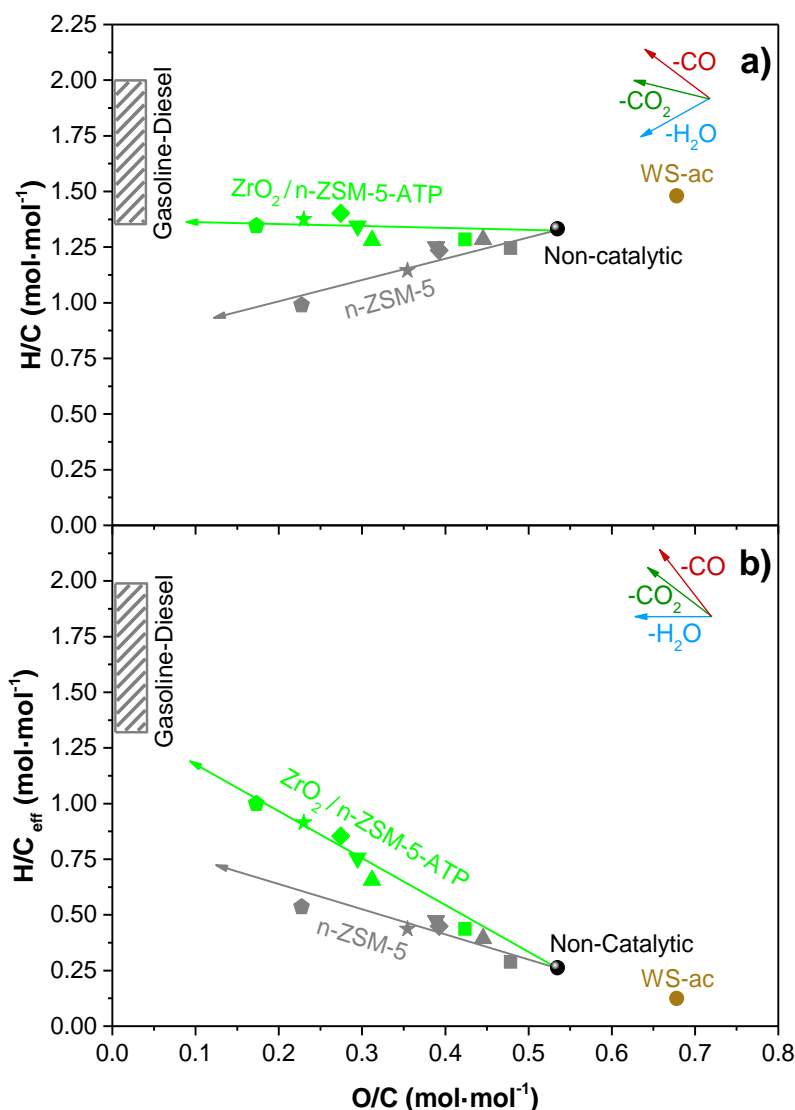


Fig. 6. Van Krevelen graphs obtained in the WS-ac pyrolysis over the $\text{ZrO}_2/\text{n-ZSM-5-ATP}$ catalyst in comparison with the parent zeolite n-ZSM-5, varying the C/B ratio.

Other essential parameter to be taken into consideration in biomass catalytic pyrolysis is the energy yield, which reveals how the chemical energy initially contained in the raw biomass is shared among the different pyrolysis products. Figure 7 illustrates the energy yield corresponding to the different fractions obtained in the catalytic pyrolysis process and its variation with the increase of the C/B ratio. The bio-oil energy yield decreases continuously with the C/B ratio, whereas the opposite occurs with the chemical energy contained in the gases and coke. Within the gaseous fractions more than half of the chemical energy corresponds to CO, followed by light olefins, methane and light paraffins, whereas the contribution of hydrogen is almost negligible due to its low concentration.

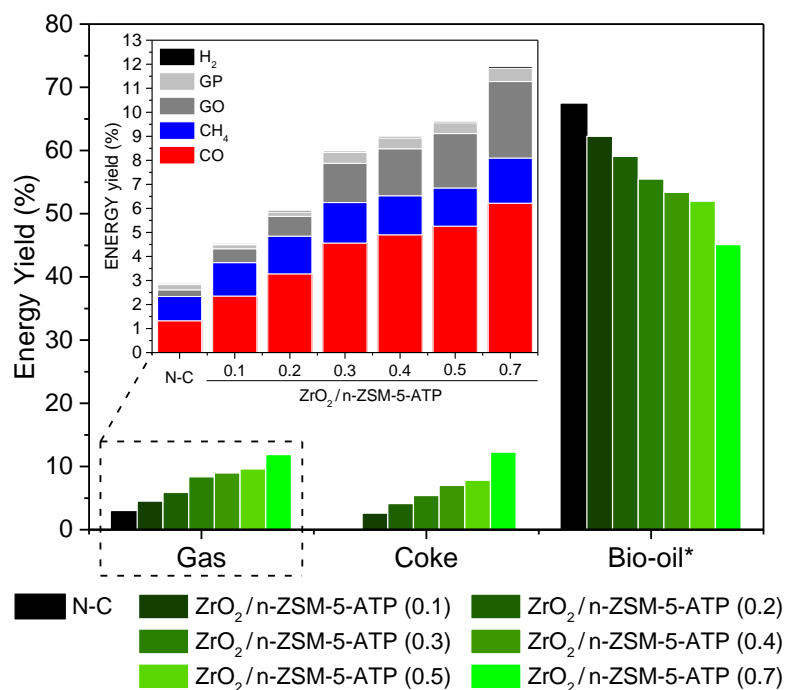


Fig. 7. Energy yield distribution (%) obtained in the WS-ac pyrolysis over the $\text{ZrO}_2/\text{n-ZSM-5-ATP}$ catalyst as a function of the C/B ratio (0.1-0.7 g g^{-1}). N-C: non-catalytic.

The above results evidence that the variation of the C/B ratio is effective for provoking the bio-oil upgrading through deoxygenation reactions, but this parameter induces also significant losses in terms of both mass and energy yields, mainly due to the occurrence of a variety of non-desired secondary transformations. The relationship between oxygen content and yield of the bio-oil fraction when varying the C/B ratio is illustrated in Figure 8, comparing again the results obtained with the catalyst here investigated and those corresponding to the parent zeolite n-ZSM-5. This figure highlights the great relevance of fine-tuning the zeolite properties to improve its performance in biomass catalytic pyrolysis. For the parent n-ZSM-5, bio-oil deoxygenation implies a sharp reduction in both mass and energy yield. In contrast, these negative effects are quite less pronounced for the $\text{ZrO}_2/\text{n-ZSM-5-ATP}$ catalyst. Thus, for a bio-oil oxygen content of about 22 wt%, the bio-oil energy yield corresponding to the parent zeolite is just 34%, whereas it increases up to 52% over the modified ZSM-5 catalyst. Moreover, with the latter catalyst is possible to reach deoxygenation levels of the bio-oil quite superior to those of the parent n-ZSM-5, reducing the bio-oil oxygen content to values as low as 17 wt% and still retaining 45% of the chemical energy initially present in the raw biomass. These results denote that modification of the zeolite ZSM-5 with ZrO_2 and attapulgite leads to a significantly more efficient pathway during the bio-oil upgrading process.

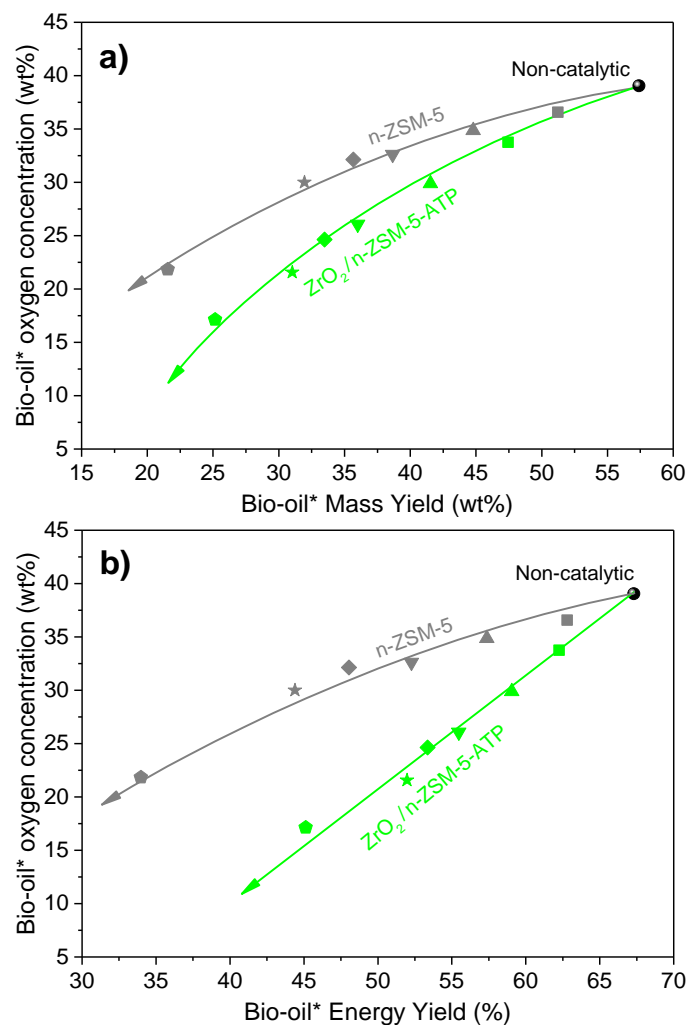


Fig. 8. Bio-oil* oxygen concentration versus mass (a) and energy (b) yields obtained in the WS-ac pyrolysis over the ZrO₂/n-ZSM-5-ATP catalyst in comparison with those corresponding to the parent zeolite n-ZSM-5, varying the C/B ratio.

3.2.2 Bench scale tests

In order to validate the promising performance of the ZrO₂/n-ZSM-5-ATP catalyst at larger scale, ex-situ biomass catalytic pyrolysis tests were performed in a bench scale unit, working with continuous biomass feeding at different catalyst to biomass ratios (C/B = 0.20, 0.25, 0.43 and 0.50 g g⁻¹). In these tests, the catalyst loading was varied in the range of 20 - 50 g, i.e. an order of magnitude higher than the catalyst amount used for the lab scale tests reported above.

Figure 9 compares the mass yield of the main products obtained using the ZrO₂/n-ZSM-5-ATP catalyst in the lab and bench plant experiments for two C/B ratios. A deeper conversion of the bio-oil fraction occurs for the tests performed in the bench plant, as denoted by the lower bio-oil yield, as well as by its reduced oxygen content. For both scales, increasing the C/B ratio provokes a progressive reduction of the bio-oil yield, which is accompanied by a decrease of its oxygen content. For the bench reaction system, a higher production of the different gaseous components is observed: methane, olefins, paraffins and especially CO and CO₂. However, the water yield is very similar in both series of experiments, remaining almost constant in respect to the variation of the C/B ratio, which confirms that the employed catalyst promotes to a higher extend decarboxylation and decarbonylation reactions rather than dehydration ones.

The differences between the results obtained in the two experimental sets up can be assigned mainly to the longer residence time of the bio-oil vapors, in addition to the higher temperature of the catalytic bed, when using the bench scale, which provokes a more pronounced conversion and deoxygenation of the bio-oil in comparison with the lab scale system. In this way, it must be noted that the biomass pyrolysis proceeds in the laboratory scale in two separated zones (thermal and catalytic) located within the same reactor, whereas in the case of the bench plant the thermal pyrolysis and the catalytic upgrading steps take place in two different reactors connected in series. This fact leads to significant differences in the residence times of the bio-oil vapors in the respective thermal zones (about 1 s in the lab setup versus 7 s in the bench scale plant), while the residence time in both catalytic beds are very similar (in the range 0.5-1 s).

Regarding the coke deposited over the catalyst, its yield is more pronounced at higher C/B ratios, with higher quantity forming in the case of the lab scale tests. This negative effect is counterbalanced by the decreasing amount of oxygen in the liquid organics with increasing catalyst loading in the upgrading reactor. Thus, for the bench plant experiments, at the highest C/B ratio investigated ($C/B = 0.5 \text{ g g}^{-1}$), a very good quality bio-oil with only 10 wt% oxygen content is produced at a mass yield of ~16 wt%, which corresponds to about 1/3 of the initial chemical energy in the biomass feedstock.

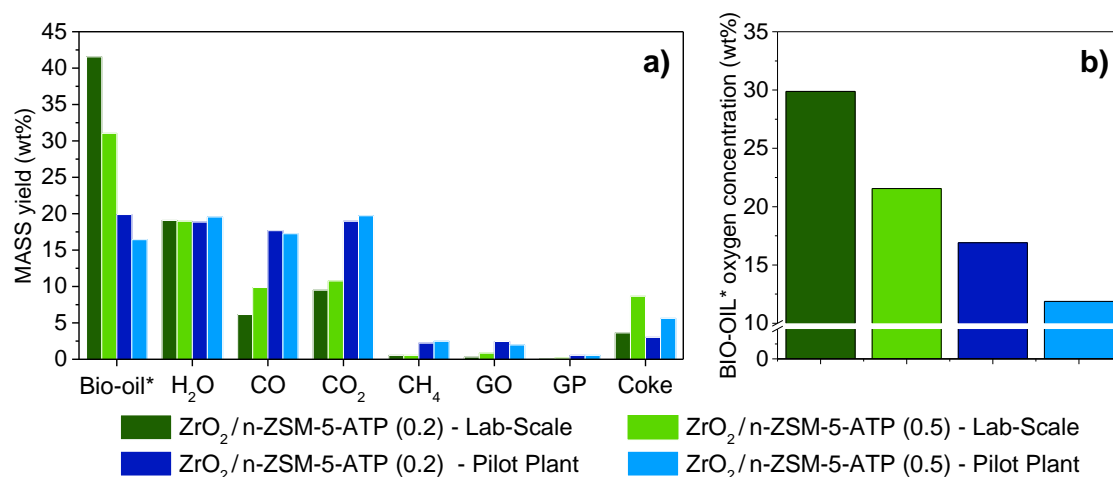


Fig. 9. Products yield distribution (wt%) (a) and bio-oil oxygen concentration (wt%) (b), obtained in the biomass pyrolysis at both laboratory and bench plant scales over the ZrO₂/n-ZSM-5-ATP catalyst using different C/B ratios (0.2 and 0.5). GO: gaseous olefins (C₂-C₄); GP: gaseous paraffins (C₂-C₄).

For comparing the relationship between the yield and oxygen content of the bio-oil obtained at lab and bench scales, it is important to take into account that the starting point, i.e. the yield and composition of the thermal bio-oil, is different in both series of tests. Accordingly, the deoxygenating degree of the bio-oil attained in the catalytic upgrading step has been referred to the oxygen content of the thermal bio-oil. In the same way, the energy yield of the bio-oil has been computed taking as reference those corresponding to the bio-oils produced in absence of catalyst for both series of experiments. Accordingly, Figure 10 compares the relationship between the bio-oil deoxygenation degree and its energy yield, referred to those of the thermal bio-oils, providing thus information on the catalytic effects of the ZrO₂/n-ZSM-5-ATP system for upgrading the organics produced in the thermal zones of the corresponding reaction systems. It can be observed that both series of points exhibit a similar trend in spite of the differences in

the conditions and sets up between them. This is a remarkable result as it demonstrates that the $ZrO_2/n-ZSM-5-ATP$ system exhibits similar catalytic properties when using different raw biomasses, reaction conditions and operation modes, providing deoxygenation degrees up to 60% with energy yields around 70% in respect to those of the thermal bio-oils. Moreover, it can be concluded that this excellent performance is maintained when scaling up the process from batch lab system to a continuous bench plant.

The actual liquid biofuel obtained from the bench plant tests was collected and analyzed to determine its suitability for use in fuel applications. It should be noted that the total liquid product produced from thermal biomass pyrolysis followed by upgrading of the vapors in the consecutive catalytic reactor segregated into two phases: an aqueous light phase, containing mainly water and a low amount of polar organic compounds, and an organic-rich heavy phase, with low moisture and high organics content. This organic phase was separated from the aqueous phase for the tests at C/B ratio 0.25 and 0.50 and was characterized to determine its water content, elemental composition, TAN number and heating value. These results, together with the percentage of the organic phase in the total liquid, are summarized in Table 5. This organic phase has favorable properties for fuel use as it has little water and the oxygen content is very low compared to typical pyrolysis bio-oil without the use of hydrogen in the process and merely due to the effective deoxygenation induced by the $ZrO_2/n-ZSM-5-ATP$ catalyst. This is also reflected in the high heating value, which is close to that of fossil-based fuels.

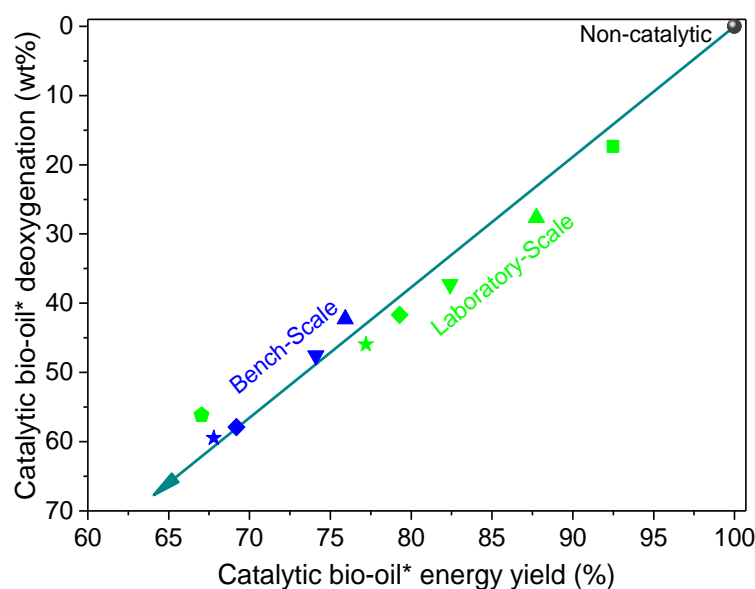


Fig. 10. Bio-oil* deoxygenation degree versus bio-oil energy yield of the catalytic step (referred to those of the thermal bio-oil), obtained in the biomass pyrolysis at laboratory and bench scales over the $ZrO_2/n-ZSM-5-ATP$ catalyst using different C/B ratios.

Table 5. Characterization of the bio-oil organic phase obtained in the oak pyrolysis at bench scale over the $ZrO_2/n-ZSM-5-ATP$ catalyst.

C/B	Percentage of total liquid product (%)	H_2O (wt%)	Elemental composition (wt% db)			TAN (mg_{KOH}/g)	HHV (MJ/kg_{db})	Energy Yield (%)
			C	H	O			
0.25	45.8	3.6	80.6	7.3	12.0	8.5	35.8	33.0
0.50	42.8	2.7	83.5	7.6	8.8	2.6	37.6	30.2

Another important property for fuel applications is the TAN number, which corresponds to the acidity, and thus corrosiveness, of the fuel. In the case of both organic liquids, the TAN number is very low due to the effective removal of oxygen from the acidic molecules in the bio-oil vapors.

The organic phase of the bio-oil sample obtained from the bench scale pyrolysis tests at catalyst/biomass ratio of 0.25 was also analyzed by GC-MS to determine the composition of the produced liquid. The bio-oil compounds were identified and grouped in families according to their functional groups. Figure 11 shows the semi-quantitative GC-MS results (expressed as % of relative area) in terms of the main chemicals groups. The organic bio-oil consists mainly of aromatics, phenols, aliphatic compounds and polyaromatic hydrocarbons, consistent with the high deoxygenation activity of the $ZrO_2/n-ZSM-5-ATP$ catalyst, which resulted in the production of bio-oil with low oxygen content and high heating value. Moreover, the amount of oxygenates, such as aldehydes, ketones and acids, is very low, also indicative of the efficiency of this catalyst and in line with the reduced TAN number of the biofuel.

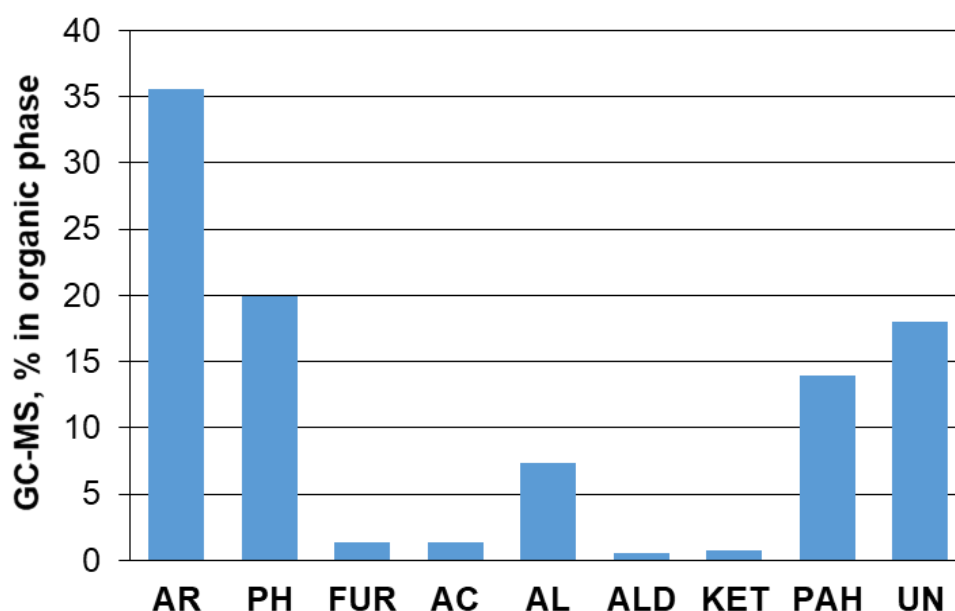


Fig. 11. Semi-quantitative analysis of the organic phase of bio-oil obtained in the fast-pyrolysis of lignocellulosic biomass at bench scale over the $ZrO_2/n-ZSM-5-ATP$ catalyst at C/B ratio 0.25 with GC-MS. AR: aromatics; PH: phenols; FUR: furanics; AC: acids; AL: aliphatic compounds; ALD: aldehydes; KET: ketones; PAH: polyaromatic hydrocarbons; UN: unidentified compounds.

4. Conclusions

The $ZrO_2/n-ZSM-5-ATP$ material is an efficient catalyst for the upgrading of the bio-oil vapors produced by biomass pyrolysis using an ex-situ configuration. In addition to high accessibility for bulky molecules, provided by the nanocrystalline nature of the ZSM-5 sample, this material exhibits a right balance of acid and basic sites, which is essential for catalyzing the variety of reactions taking place during biomass pyrolysis and bio-oil upgrading. As a consequence, the $ZrO_2/n-ZSM-5-ATP$ catalyst leads in the laboratory scale tests to a quite more selective deoxygenation pathway when varying the catalyst-to-biomass ratio, as denoted by the

improved relationship between the bio-oil yield and its oxygen content in comparison with that of the parent n-ZSM-5 sample. Likewise, the pathways followed in the van Krevelen graphs when using the parent n-ZSM-5 catalyst are quite less favorable compared to the catalyst material here investigated, with a reduction in the values of the overall H/C ratio and a lower increase in the H_{eff}/C one, which confirms the remarkable positive effects derived of the zeolite modification by ZrO_2 impregnation and agglomeration with attapulgite. In the bench scale tests, performed using the $ZrO_2/n\text{-ZSM-5-ATP}$ catalyst, a lower bio-oil yield is obtained although showing also less oxygen content in comparison with the laboratory scale results. These differences can be assigned mainly to the longer residence time of the bio-oil at bench scale, which provokes a more pronounced conversion and deoxygenation of the bio-oil.

Interestingly, the $ZrO_2/n\text{-ZSM-5-ATP}$ system exhibits similar catalytic properties for upgrading the thermal bio-oil vapors even when using different raw biomasses, reaction conditions, scales and operation modes, providing deoxygenation degrees up to 60% with energy yields around 70% in respect to those of the thermal bio-oils. Moreover, this finding confirms the feasibility of scaling-up the biomass catalytic pyrolysis process from laboratory to bench scale.

Acknowledgements

The authors gratefully acknowledge the financial support from: the European Union Seventh Framework Program (FP7/2007–2013) under grant agreement n° 604307 (CASCATBEL project), and from the Spanish Ministry of Economy and Competitiveness through CATPLASBIO project (Ref: CTQ2014 - 602209). R. J. Wijten (Utrecht University, UU) is acknowledged for performing the SEM-EDX measurements. Dr. K. Houben (UU) and Prof. M. Baldus (UU) are thanked for carrying out the ^{27}Al (MQ) MAS NMR measurements.

References

1. A.V. Bridgwater, *Biomass and Bioenergy* 2012, **38**, 68–94.
2. J. Feroso, P. Pizarro, J.M. Coronado, D.P. Serrano, *Adv. Rev.* 2017, **6**, 1–18.
3. J. Feroso, P. Pizarro, J.M. Coronado, D.P. Serrano, *Transportation Biofuels via the Pyrolysis Pathway: Status and Prospects*, in: R.A. Meyers (Ed.), *Encycl. Sustain. Sci. Technol.*, Springer, New York, 2017: pp. 1–33.
4. C. Liu, H. Wang, A.M. Karim, J. Sun, Y. Wang, *Chem. Soc. Rev.* 2014, **43**, 7594–7623.
5. A.V. Bridgwater, *Catal. Today* 1996, **29**, 285–295.
6. Z. Cao, J. Engelhardt, M. Dierks, M.T. Clough, G.H. Wang, E. Heracleous, A.A. Lappas, R. Rinaldi, F. Schuth, *Angew. Chem. Int. Ed.* 2017, **56**, 2334–2339.
7. R.W. Snell, E. Combs, B.H. Shanks, *Top. Catal.* 2010, **53**, 1248–1253.
8. M. Milina, S. Mitchell, J. Pérez-Ramírez, *Catal. Today.* 2014, **235**, 176–183.
9. T.N. Pham, D. Shi, D.E. Resasco, *Appl. Catal. B Environ.* 2014, **145**, 10–23.
10. H. Hernando, S. Jiménez-Sánchez, J. Feroso, P. Pizarro, J.M. Coronado, D.P. Serrano, *Catal. Sci. Technol.* 2016, **6**, 2829–2843.

11. S. Wan, Y. Wang, *Front. Chem. Sci. Eng.* 2014, **8**, 280–294.
12. A. Galadima, O. Muraza, *Energy Convers. Manag.* 2015, **105**, 338–354.13.
13. T. Carlson, J. Jae, Y. Lin, G. Tompsett, G. Huber, *J. Catal.* 2010, **270**, 110–124.
14. M. Zabeti, T.S. Nguyen, L. Lefferts, H.J. Heeres, K. Seshan, *Bioresour. Technol.* 2012, **118**, 374–381.
15. M. Zabeti, J. Baltrusaitis, K. Seshan, *Catal. Today* 2016, **269**, 156–165.
16. Q. Lu, Z. Tang, Y. Zhang, X. Zhu, *Ind. Eng. Chem. Res.* 2010, **49**, 2573–2580.
17. E.H. Lee, M.J. Jeon, J.K. Jeon, D.J. Suh, S.H. Park, B. Seo, S.H. Joo, Y.K. Park, *J. Nanosci. Nanotechnol.* 2014, **14**, 2343–2351.
18. D. Fabbri, C. Torri, V. Baravelli, *J. Anal. Appl. Pyrolysis* 2007, **80**, 24–29.
19. X. Zhang, L. Sun, L. Chen, X. Xie, B. Zhao, H. Si, G. Meng, *J. Anal. Appl. Pyrolysis* 2014, **108**, 35–40.
20. S.D. Stefanidis, S.A. Karakoulia, K.G. Kalogiannis, E.F. Iliopoulou, A. Delimitis, H. Yiannoulakis, T. Zampetakis, A.A. Lappas, K.S. Triantafyllidis, *Appl. Catal. B Environ.* 2016, **196**, 155–173.
21. M.I. Nokkosmäki, E.T. Kuoppala, E.A. Leppämäki, A.O.I. Krause, *J. Anal. Appl. Pyrolysis* 2000, **55**, 119–131.
22. Y.T. Cheng, J. Jae, J. Shi, W. Fan, G.W. Huber, *Angew. Chem. Int. Ed.* 2012, **51**, 1387–1390.
23. T.C. Hoff, M.J. Holmes, J. Proano-Aviles, L. Emdadi, D. Liu, R.C. Brown, J.P. Tessonnier, *ACS Sustain. Chem. Eng.* 2017, **5**, 8766–8776.
24. A.A. Lappas, K.G. Kalogiannis, E.F. Iliopoulou, K.S. Triantafyllidis, S.D. Stefanidis, *Wiley Interdiscip. Rev. Energy Environ.* 2012, **1**, 285–297.
25. C. Hu, R. Xiao, H. Zhang, *Bioresour. Technol.* 2017, **243**, 1133–1140.
26. J. Feroso, H. Hernando, S. Jiménez-Sánchez, A.A. Lappas, E. Heracleous, P. Pizarro, J.M. Coronado, D.P. Serrano, *Fuel Process. Technol.* 2017, **167**, 563–574.
27. H. Hernando, J. Feroso, I. Moreno, J.M. Coronado, D.P. Serrano, P. Pizarro, *Biomass Convers. Biorefinery* 2017, **7**, 277–287.
28. H. Hernando, I. Moreno, J. Feroso, C. Ochoa-Hernández, P. Pizarro, J.M. Coronado, D.P. Serrano, *Biomass Convers. Biorefinery* 2017, **7**, 289–304.
29. J. Feroso, H. Hernando, P. Jana, I. Moreno, J. Přeč, C. Ochoa-Hernández, P. Pizarro, J.M. Coronado, J. Čejka, D.P. Serrano, *Catal. Today* 2016, **277**, 171–181.
30. Y.T. Cheng, G.W. Huber, *Green Chem.* 2012, **14**, 3114–3125.
31. E.F. Iliopoulou, S. Stefanidis, K. Kalogiannis, A.C. Psarras, A. Delimitis, K.S. Triantafyllidis, A.A. Lappas, *Green Chem.* 2014, **16**, 662–674.
32. A. Zheng, Z. Zhao, S. Chang, Z. Huang, H. Wu, X. Wang, F. He, H. Li, *J. Mol. Catal. A Chem.* 2014, **383–384**, 23–30.

33. R. French, S. Czernik, *Fuel Process. Technol.* 2010, **91**, 25–32.
34. M.M. Yung, A.R. Stanton, K. Iisa, R.J. French, K.A. Orton, K.A. Magrini, *Energy & Fuels* 2016, **30**, 9471–9479.
35. H. Hernando, A.M. Hernández-Giménez, C. Ochoa-Hernández, P.C.A. Bruijninx, K. Houben, M. Baldus, P. Pizarro, J.M. Coronado, J. Feroso, J. Čejka, B.M. Weckhuysen, D.P. Serrano, *Green Chem.* 2018, **20**, 3499–3511.
36. H. Hernando, C. Ochoa-Hernández, M. Shamzy, I. Moreno, J. Feroso, P. Pizarro, J.M. Coronado, J. Čejka, *Catal. Sci. Technol.* 2019, **9**, 789–802.
37. J. Zhang, X. Liu, *Phys. Chem. Chem. Phys.* 2014, **16**, 8655–8560.
38. W.F. Bradley, *Minerologist* 1940, **25**, 405–410.
39. E.L. Wu, S.L. Lawton, D.H. Olson, A.C. Rohrman Jr., G.T. Kokotailo, *J. Phys. Chem.* 1979, **83**, 2777–2781.
40. A.G. Alvarez, H. Viturro, R.D. Bonetto, *Mater. Chem. Phys.* 1992, **32**, 135–140.
41. M. Hunger, *Solid-State NMR Spectroscopy*, in: A.W. Chester, E.G. Derouane (Eds.), *Zeolite Charact. Catal. A Tutor.*, Springer, Berlin, 2009: pp. 65–105.
42. L. Rodríguez-González, F. Hermes, M. Bertmer, E. Rodríguez-Castellón, A. Jiménez-López, U. Simon, *Appl. Catal. A Gen.* 2007, **328**, 174–182.
43. A. Samoson, E. Lippmaa, G. Engelhardt, U. Lohse, H.G. Jerschkewitz, *Chem. Phys. Lett.* 1987, **134**, 589–592.
44. S.Y. Choi, Y.S. Park, S.B. Hong, K.B. Yoon, *J. Am. Chem. Soc.* 1996, **118**, 9377–9386.
45. Z. Yan, D. Ma, J. Zhuang, X. Liu, X. Han, X. Bao, F. Chang, L. Xu, Z. Liu, *J. Mol. Catal. A Chem.* 2003, **194**, 153–167.
46. J.S.J. Hargreaves, A.L. Munnoch, *Catal. Sci. Technol.* 2013, **3**, 1165–1171.
47. I.L.C. Buurmans, E.A. Pidko, J.M. de Groot, E. Stavitski, R.A. van Santen, B.M. Weckhuysen, *Phys. Chem. Chem. Phys.* 2010, **12**, 7032–7040.
48. I.L.C. Buurmans, J. Ruiz-Martinez, W.V. Knowles, D. van der Beek, J.A. Bergwerff, E.T.C. Vogt, B.M. Weckhuysen, *Nature Chemistry* 2011, **3**, 862–868.
49. I.L.C. Buurmans, J. Ruiz-Martinez, S.L. van Leeuwen, D. van der Beek, J.A. Bergwerff, W.V. Knowles, E.T.C. Vogt, B.M. Weckhuysen, *Chem. Eur. J.* 2012, **18**, 1094–1101.
50. Z. Ristanović, A.V. Kubarev, J. Hofkens, M.B.J. Roeffaers, B.M. Weckhuysen, *J. Am. Chem. Soc.* 2016, **138**, 13586–13596.
51. N.Y. Chen, T.F. Degnan Jr., L.R. Koenig, *Chem. Tech.* 1986, **16**, 506–511.
52. W.O. Haag, P.G. Rodewald, P.B. Weisz, US Patent 4,300,009, 1981.

Supporting information

2. Experimental

2.1 Biomass feedstock

The lignocellulosic biomass selected for performing the laboratory scale batch tests was wheat straw (WS), obtained from agricultural residues of Segovia province (Spain). The raw sample was subjected to a series of pre-treatments that comprise: mill into a particle size of 0.5-1 mm, de-ashing and drying to obtain the final sample denoted as WS-ac. The de-ashing pre-treatment step was employed to remove the mineral matter of raw biomass, especially alkaline and alkaline-earth metals, which are known to have important intrinsic catalytic effects, favouring the char formation. The acid washing consisted in dispersing the raw biomass sample in an aqueous HNO₃ solution (1 wt%) with a ratio of 20 ml g_{biomass}⁻¹, stirred at a constant temperature of 50 °C for 2 h. After this pre-treatment, the solution was vacuum filtered and the biomass was washed with mili-Q water until reaching a pH of 6-7. Then, the sample was dried at 105 °C for 2 days.^{1,2}

For the bench scale tests, with continuous supply of biomass, a typical lignocellulosic material (oak) with low ash content was employed as it could be easily fed to the reaction system. The biomass was sieved and the fraction with particle size 0.5-1 mm was used for the tests. The feedstock was provided by ENCE in Spain having the following composition: Moisture 8.6 wt%; ash 0.6 wt%; C 49.6 wt% d.b.; H 5.9 wt% d.b.; O 43.9 wt% d.b. (by difference).

2.2 Catalyst preparation

The catalyst was synthesized from a nanocrystalline ZSM-5 zeolite provided by CLARIANT (HCZP 90) denoted as n-ZSM-5, which was selected as according to an earlier work on lignocellulose catalytic pyrolysis.³ The incorporation of ZrO₂ to the n-ZSM-5 support by wet impregnation, as well as the agglomeration of the resulting material with attapulgite, were carried out following the procedures described elsewhere.^{4,6}

The catalyst preparation recipe was adapted for the scaling at bench scale. Regarding the wet impregnation of Zr over the n-ZSM-5 support, ethanol was substituted for deionized water as solvent of the precursor. The suspension was stirred at 300 rpm for 6 h at 40 °C. After that, the water was slowly evaporated at 50 °C, then dried at 100 °C and finally calcined at 550 °C. Respecting the granulation, the impregnated zeolite (3 kg) was mixed with the respecting amount of attapulgite (Attagel, BASF, 1.29 kg) in an Eirich intensive mixer (Pilot R01). Once a complete physical admixture of both components was achieved, ~2.5 kg of deionized water was added to prepare the final extruding paste. Cylinders of 3 mm diameter and 5-6 mm length were produced in an industrial extruder. Moisture was removed in a fluid-bed dryer with an air inlet temperature of 70 °C afterwards, so that they became a physically stable. Final calcination of ZrO₂/n-ZSM-5-ATP granules was performed at 550 °C for 2h.

2.3 Catalyst characterization

2.3.1 Electronic microscopy – energy dispersive X-ray analysis

The catalyst and support samples were analyzed by Transmission Electron Microscopy (TEM) using a Philips TECNAI 20 instrument operating at 200 kV. Likewise, Scanning Electron Microscopy (SEM) images and energy dispersive X-ray spectroscopy (EDX) were recorded using a FEI XL30SFEG microscope. The samples were sprinkled on an aluminium stub with a carbon sticker. Pt sputter coating was avoided to prevent overlap of the Pt and Zr signals in the EDX measurements. Quantification of Zr average has been based counting on Si, Al, O, Mg and Zr elements. SEM images were recorded in secondary electron (SE) mode.

2.3.2 X-ray diffraction

XRD patterns were obtained using a Bruker AXS D2 phaser diffractometer, in Bragg-Brentano mode, equipped with a Lynxeye detector. The radiation source used was cobalt $K\alpha_{12}$ ($\lambda_{12} = 1.79026 \text{ \AA}$), operating at 30 kV and 10 mA. Samples were measured at room temperature in the $5\text{-}70^\circ 2\theta$ with a scan step of $0.01^\circ 2\theta$ and 0.25 s scan^{-1} . The lattice parameters were determined using Le Bail⁷ full-profile fit provided by the software Topas^{5,8}. Peak shapes were fitted using fundamental parameters, while the background was fitted with a 5-term Chebyshev polynomial.

2.3.3 Magic angle spinning solid state nuclear magnetic resonance

²⁷Al magic angle spinning solid state nuclear magnetic resonance (MAS ssNMR) experiments were performed at 11.7 T on a Bruker Avance III spectrometer equipped with a 3.2 mm MAS probe. Spectra were recorded at ambient temperature using 15 kHz MAS. RF fields of 50 kHz and 40 kHz were respectively used for the ²⁷Al $\pi/12$ pulse followed by 26 ms acquisition. 10240 scans were accumulated using an inter-scan delay of 1 s. The ²⁷Al chemical shift was externally referenced to an aqueous aluminium nitrate solution. The 1D spectra were processed using a line-broadening of 100 Hz.

A zero-quantum (ZQ) filtered multiple-quantum magic angle spinning (MQ-MAS) pulse-sequence was used to correlate the ²⁷Al isotropic chemical shift (F1) with the quadrupolar line-shape (F2). The excitation and conversion pulses were applied with an RF field of 62 kHz. For the selective pulse following the Z-filter delay an RF field of 6.5 kHz was used. The incrementation time for the indirect dimension was set to one rotation period and 36 increments were recorded. The direct acquisition time was set to 2.5 ms and 696 scans were accumulated using an inter-scan delay of 2 s. MQ-MAS data were Fourier transformed and sheared using the software of Bruker Topspin3.5 and 250 Hz line-broadening was applied in both dimensions.

The 1D ssNMR spectra were deconvoluted using a Gaussian multipeak fitting function in the Origin 9.1 software. The areas under the curves were fitted based on the Levenberg-Marquardt least-squares algorithm to generate fits from starting peak positions observed in the corresponding MQ MAS ssNMR spectra. The areas under the peaks were used to estimate the ratio between framework and extra-framework Al species.

2.3.4 UV-Vis micro-spectroscopy

UV-Vis micro-spectroscopy was performed in an in-situ cell (FTIR600, Linkam Scientific Instruments) equipped with a temperature controller (Linkam TMS 93). The microscopy set-up used is based on an Olympus BX41 upright microscope with a 50 x 0.5 NA-high (NA: numerical aperture) working distance microscope objective. A 75 W tungsten lamp was used for illumination. The microscope was equipped with a 50/50 double-viewport tube, which accommodated a CCD video camera (ColorView IIIu, Soft Imaging System GmbH) and an optical fibre mount. A 200 mm-core fibre connected the microscope to a CCD UV/Vis spectrometer (AvaSpec-2048TEC, Avantes).

Catalyst staining by 4-fluorostyrene oligomerization was followed in-situ by UV-Vis micro-spectroscopy. After preheating the catalyst at 100 °C for 10 min, 15 µl of 4-fluorostyrene was added per extrudate (~10 mg of sample) on the external surface, centred on a side. After letting the probe compound penetrate the extrudate catalyst for 5 min, spectra of the stained material were recorded for 15 min.

2.3.5 Confocal fluorescence microscopy

Confocal fluorescence microscopy (CFM) images of the stained materials were acquired using a Nikon Eclipse 90i confocal microscope with a 100 x 0.73 NA dry objective. Excitation light was provided by focusing three (or four) specific laser lines, (404), 488, 561 and 642 nm, simultaneously on the desired sample, located in an open cell (Linkam Instruments, FTIR 600). The microscope was equipped with a Nikon A1 scan head, accommodating the optics, which couple fibre optics for excitation and emission light microscope. A spectral analyzer in the Nikon A1 system was equipped with 32 photomultiplier tubes (PMTs) set to collect emission light in the region of ca. 450–700 nm, with a resolution of 6 nm. Following the same procedure as for in-situ UV-Vis micro-spectroscopy, 4-fluorostyrene oligomerization staining was also followed in-situ by CFM. In addition, ex-situ fluorescence spectra were recorded at room temperature on the cross-section and on the side of the reacted extrudate, approx. 30 min after finalizing the reaction.

2.3.6 Ar adsorption-desorption isotherms

The textural properties of the catalyst were assessed by argon adsorption–desorption tests at –186 °C in an AUTOSORB iQ Analyzer System from Quantachrome Instruments. The sample was previously degassed at 300 °C under vacuum for 3 h. The total surface area was determined applying the Brunauer–Emmett–Teller (BET) equation. The pore size distributions and the contributions of micro- and mesopores to the surface and volume, were calculated using the adsorption branch of the isotherm by means of the NL-DFT (Non-Local Density Functional Theory) model assuming cylindrical pore geometry.

2.3.7 Temperature Programmed Desorption of probe molecules

Ammonia (NH₃) and carbon dioxide (CO₂) were selected as probe molecules to measure the overall acidity and basicity, respectively, of the catalysts by means of temperature programmed desorption using an AUTOCHEM 2910 instrument (Micromeritics), equipped with a TCD. In the NH₃-TPD tests, the catalyst sample (0.1 g) was degassed under He flow at 600 °C for 6 h followed by saturation at 120 °C using a He–NH₃ mixture. The sample was then purged for 30

min under He flow in order to remove the weakly physisorbed ammonia. NH_3 -TPD profiles were subsequently recorded increasing the temperature from 120 to 600 °C using a ramp rate of 10 °C min^{-1} . A final isotherm at 600 °C of 25 min was added in order to ensure a complete NH_3 desorption.

In the CO_2 -TPD measurements, the catalyst sample was preconditioned by heating up to 600 °C during 6 h by flowing 100 ml min^{-1} of He. After cooling to 100 °C, the sample was exposed to 50 ml min^{-1} of 5% CO_2/He gas for 30 min and then the system was then purged in flowing He for 1 h to remove physisorbed CO_2 . Finally, the catalysts were heated from 100 to 550 °C in He flow. A final isotherm of 20 min at 600 °C was added at the end of the program to record the complete desorption of CO_2 at that temperature.

2.4 Biomass pyrolysis tests

2.4.1 Laboratory scale experimental setup

The lab-scale experimental setup employed for the biomass catalytic pyrolysis tests consists of a downdraft fixed-bed reactor with two temperature zones physically separated, one for the primary thermal pyrolysis and other for the vapour catalytic upgrading. The schematic diagram and the detailed description of the unit can be found in previous studies.³ The pyrolysis tests were carried out at temperatures of 550 and 400 °C for the pyrolysis and catalytic zones, respectively, atmospheric pressure and use of 100 $\text{cm}^3 \text{ s}^{-1}$ of N_2 as carrier gas. All the experiments were conducted with 4 g of de-ashed wheat straw (WS-ac sample) as feedstock, whilst the catalyst load was progressively incremented from 0.4 to 2.8 g of zeolite material, to yield catalyst to biomass ratios (C/B) from 0.1 to 0.7 g g^{-1} , respectively.

Once the operating conditions of temperature and reaction atmosphere ($\text{O}_2 < 0.1 \text{ vol}\%$) were reached, the biomass-feeding valve was opened to initiate the pyrolysis reaction. The carbonaceous solid residue (char) was accumulated in the thermal zone, while vapours and non-condensable gases passed through to the catalyst bed. The upgraded vapours were then condensed by a series of three 125 cm^3 flasks refrigerated at 0-4 °C, and the non-condensable gases passing through the reaction system were finally collected in a sampling bag for further analysis. Bio-oil, char and the used catalyst were recovered and weighted for their further characterization, as described next. The bio-oil fraction on water free basis is denoted as bio-oil*.

2.4.2 Bench plant experimental setup

The bench scale pyrolysis tests were carried out in a fully automated continuous biomass pyrolysis plant unit consisting of two reactors, a fluidized bed and a catalytic bed reactor, connected in series. The first reactor was used to perform the thermal pyrolysis step of the process, while in the second reactor the catalytic upgrading of the bio-oil vapours took place. Biomass was introduced in the fluidized bed reactor through a screw feeder. At the same time, N_2 (5 l min^{-1}) was inserted at the bottom of the reactor to achieve fluidization. The reactor was loaded with inert material and was heated by an external furnace at 550 °C, with the temperature being controlled by suitable thermocouples. All the gas and pyrolysis vapours from the fluidized bed reactor (about 7-8 l min^{-1}) were introduced into the second reactor, which contained the catalyst and was heated by a different furnace at 450 °C. The exit stream was directed to the

product separation and collection section of the unit. In all tests, the liquid and gaseous products were separated, collected and measured.

In order to investigate the catalytic performance at different catalyst to biomass ratios (C/B), the total amount of biomass fed to the reactor was kept constant at 100 g, while the catalyst loading in the reactor was varied between 20 to 50 g to obtain C/B ratios ranging from 0.20 to 0.50 g g⁻¹.

2.5 Product characterization

2.5.1 Laboratory scale biomass pyrolysis

The proximate analyses were performed according to the European standards, including moisture (UNE-EN 14774-1:2010), ash (UNE-EN 14775:2010) and volatile matter (UNE-EN 15148:2010) contents, the amount of fixed carbon being determined by difference. The chemical composition of the ash was measured by ICP-OES.

The ultimate analyses of biomass and pyrolysis products (bio-oil, char and coke) were performed in a Thermo Scientific FLASH 2000 CHNS/O micro-elemental analyzer. C, H, N and S elements were directly measured, whilst O was determined by difference.

The coke deposited over the catalyst after the experiments was quantified by weight difference in a TGA. The program used consisted of heating up to 550 °C at 20 °C min⁻¹ under 80 cm³ min⁻¹ air flow.

The water content of the bio-oil fraction was measured by means of a Mettler-Toledo V20S compact volumetric Karl-Fischer titrator (ASTM E203-08).

The gas fraction was analyzed by a dual channel Agilent® CP-4900 Micro Gas Chromatograph (μ -GC), equipped with two different columns (Molsieve 5 Å and HayeSep A) and a thermal conductivity detector (TCD), using He as carrier gas. The equipment was periodically calibrated with standard gas mixtures of different gas concentrations containing N₂ (internal standard), O₂, H₂, CO, CO₂, CH₄, C₂H₄, C₂H₆, C₃H₆, C₃H₈, C₄H₈ and C₄H₁₀.

The HHV of the biomass, bio-oil, char and coke was calculated by the correlation proposed by Channiwala and Parikh. The HHV of the gas fraction was calculated from its individual molecules.¹⁰

The total mass balance was closed with an experimental error lower than 5 wt% of the biomass for all the experiments. The equations and details of the mass balances applied to evaluate the pyrolysis tests can be found elsewhere.³ The energy yield corresponding to the different fractions was determined from the chemical energy contained in each product with respect to the initial biomass.

2.5.2 Bench scale biomass pyrolysis

The liquid product was collected in two separate vessels and was analyzed after mixing into a single sample. The water content of the bio-oil was determined by Karl-Fischer titration (ASTM D6304). Carbon and hydrogen were determined concurrently in a LECO-800 CHN analyzer, measured as CO₂ and H₂O by selective infrared cells (detectors). The oxygen content was calculated by difference. The organic phase of the bio-oil was analyzed by GC-MS using an Agilent 7890A/5975C gas chromatograph-mass spectrometer system (Electron energy 70 eV;

Emission 300 V; Helium flow rate: $0.7 \text{ cm}^3 \text{ min}^{-1}$; Column: HP-5MS (30 m x 0.25 mm ID x 0.25 μm). Internal libraries were used for the identification of the compounds found in the bio-oil and their categorization into main functional groups. The analysis performed was semi-quantitative and the results refer to the relative area of the peaks of the different compounds in the chromatograph. Gases were analyzed in a GC (determination of CO_2 , CO , H_2 , CH_4 , C_2 , C_2^- , C_3 , C_3^- and other light hydrocarbons up to C_6), while solid products (char & coke) were measured together during the regeneration stage, by replacing the nitrogen in the bed with air and increasing the bed temperature of both reactors to $650 \text{ }^\circ\text{C}$.

3. Results and discussion

Table S1. Properties of the bio-oil* obtained in the WS-ac pyrolysis over the $\text{ZrO}_2/\text{n-ZSM-5}$ -ATP catalyst, varying the C/B ratio.

	Bio-oil* Elemental Analysis (wt%)				O/C (mol/mol)	H/C (mol/mol)	H_{eff}/C (mol/mol)	HHV (MJ/kg)
	C	H	N	O				
Non-catalytic	54.8	6.1	0.1	39.0	0.53	1.33	0.26	22.20
n-ZSM-5 (0.1)	57.3	6.0	0.1	36.6	0.48	1.26	0.30	23.20
n-ZSM-5 (0.2)	58.7	6.3	0.1	34.9	0.45	1.29	0.40	24.30
n-ZSM-5 (0.3)	60.6	6.7	0.1	32.6	0.40	1.33	0.52	25.60
n-ZSM-5 (0.4)	61.5	6.4	0.1	32.0	0.39	1.25	0.47	25.70
n-ZSM-5 (0.5)	63.7	6.1	0.2	30.0	0.35	1.15	0.44	26.30
n-ZSM-5 (0.7)	72.6	6.1	0.2	21.1	0.22	1.01	0.57	30.40
$\text{ZrO}_2/\text{n-ZSM-5-ATP}$ (0.1)	59.7	6.4	0.1	33.8	0.42	1.28	0.44	24.90
$\text{ZrO}_2/\text{n-ZSM-5-ATP}$ (0.2)	63.2	6.8	0.1	29.9	0.35	1.29	0.58	27.00
$\text{ZrO}_2/\text{n-ZSM-5-ATP}$ (0.3)	66.3	7.4	0.2	26.1	0.29	1.34	0.75	29.20
$\text{ZrO}_2/\text{n-ZSM-5-ATP}$ (0.4)	67.3	7.9	0.2	24.6	0.27	1.40	0.85	30.20
$\text{ZrO}_2/\text{n-ZSM-5-ATP}$ (0.5)	70.2	8.0	0.2	21.6	0.23	1.37	0.91	31.80
$\text{ZrO}_2/\text{n-ZSM-5-ATP}$ (0.7)	74.3	8.3	0.2	17.1	0.17	1.35	1.00	34.00

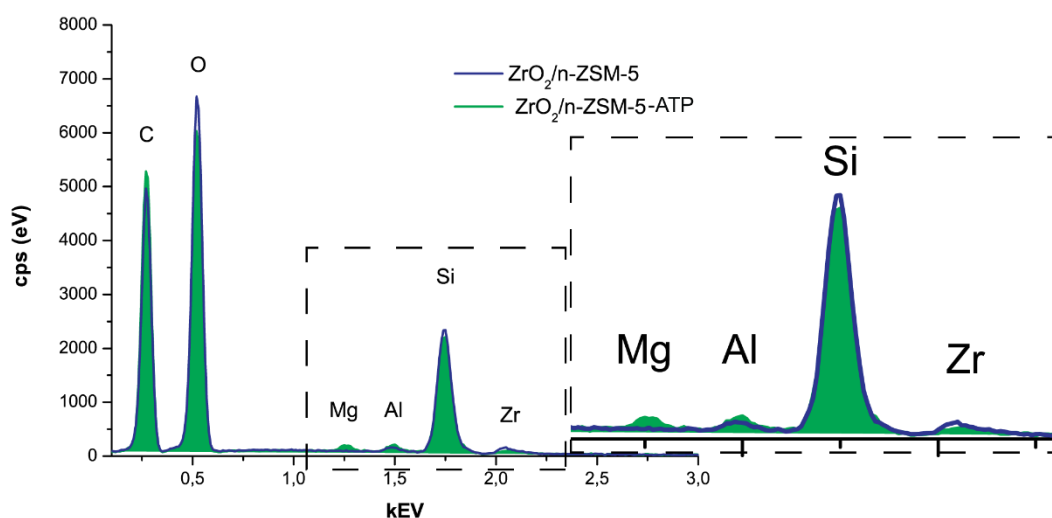


Figure S1. Map Sum Spectrum derived from the EDX dot mapping of $\text{ZrO}_2/\text{n-ZSM-5-ATP}$ (green) and, as reference, $\text{ZrO}_2/\text{n-ZSM-5}$ (blue) catalysts.

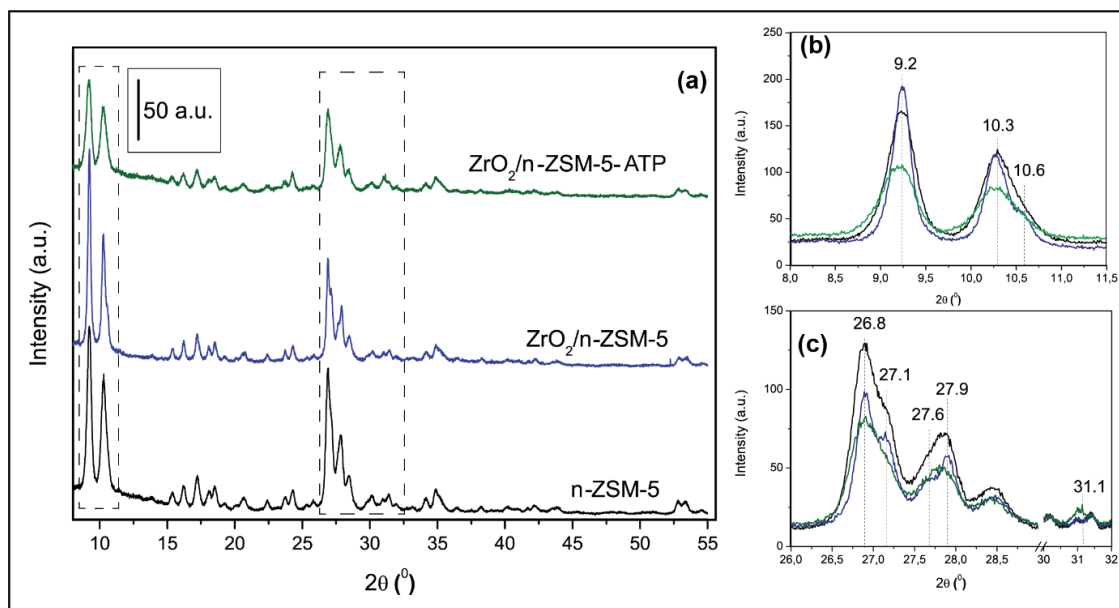


Figure S2. XRD patterns of n-ZSM-5 (black), ZrO₂/n-ZSM-5 (blue) and ZrO₂/n-ZSM-5-ATP (green) catalysts. (a) $2\theta = 8\text{-}55^\circ$; (b) $2\theta = 8\text{-}11.5^\circ$; (c) $2\theta = 26\text{-}32^\circ$.

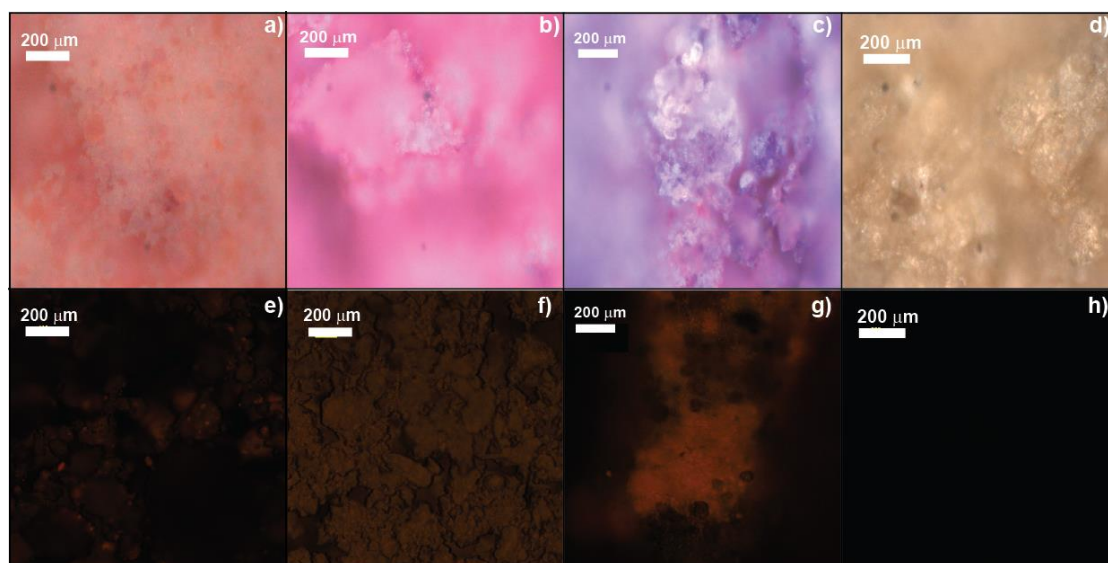


Figure S3. Optical (a-d) and CFM images (e-h) after 15 min of 4-fluorostyrene oligomerization at 100 °C for: (a,e) n-ZSM-5; (b,f) ZrO₂/n-ZSM-5; (c,g) ZrO₂/n-ZSM-5-ATP; (d,h) ATP. Excitation lasers fixed at $\lambda = 404, 488, 561, 642$ nm. Note that attapulgite, whose colour absorbed and emitted are the same, shows no fluorescence.

References

1. H. Hernando, J. Feroso, I. Moreno, J.M. Coronado, D.P. Serrano, P. Pizarro, *Biomass Convers. Biorefinery* 2017, **7**, 277–287.
2. J. Feroso, H. Hernando, S. Jiménez-Sánchez, A.A. Lappas, E. Heracleous, P. Pizarro, J.M. Coronado, D.P. Serrano, *Fuel Process. Technol.* 2017, **167**, 563–574.
3. H. Hernando, S. Jiménez-Sánchez, J. Feroso, P. Pizarro, J.M. Coronado, D.P. Serrano, *Catal. Sci. Technol.*, 2016, **6**, 2829–2843.
4. H. Hernando, A.M. Hernández-Giménez, C. Ochoa-Hernández, P.C.A. Bruijninx, K. Houben, M. Baldus, P. Pizarro, J.M. Coronado, J. Feroso, J. Čejka, B.M. Weckhuysen, D.P. Serrano, *Green Chem.* 2018, **20**, 3499–3511.
5. D.P. Serrano, R. Sanz, P. Pizarro, I. Moreno, P. De Frutos, S. Bla, *Catal. Today* 2009, **143**, 151–157.
6. H. Hernando, C. Ochoa-Hernández, M. Shamzy, I. Moreno, J. Feroso, P. Pizarro, J.M. Coronado, J. Čejka, D.P. Serrano, *Catal. Sci. Technol.* 2019, **9**, 789-802.
7. A. Le Bail, H. Duroy, J.L. Fourquet, *Mater. Res. Bull.* 1988, **23**, 447–452.
8. Bruker AXS, TOPAS, V5.0, (2011).
9. S.A. Channiwala, P.P. Parikh, *Fuel* 2002, **81**, 1051–1063.
10. D.W. Green, R.H. Perry, *Perry's Chemical Engineers' Handbook, 8th Edition*, McGraw-Hill Osborne Media.

